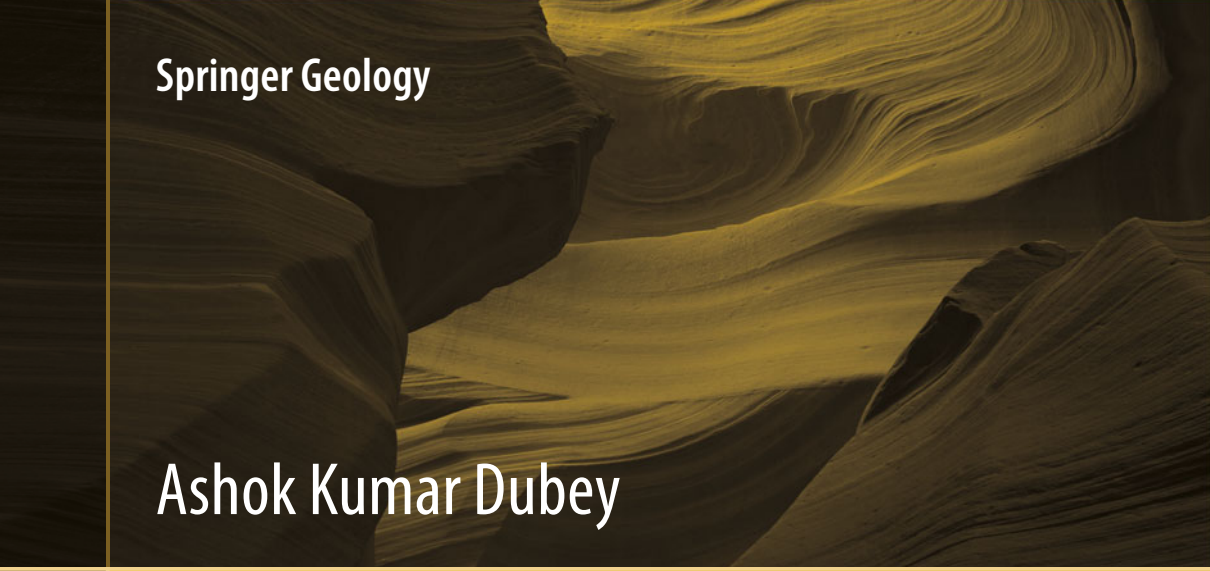

Springer Geology

Ashok Kumar Dubey

Understanding an Orogenic Belt

Structural Evolution of the Himalaya

Springer

Springer Geology

For further volumes:
http://www.springer.com/series/10172

Ashok Kumar Dubey

Understanding an Orogenic Belt

Structural Evolution of the Himalaya

Springer

Ashok Kumar Dubey
Wadia Institute of Himalaya
Dehradun
India

ISBN 978-3-319-05587-9 ISBN 978-3-319-05588-6 (eBook)
DOI 10.1007/978-3-319-05588-6
Springer Cham Heidelberg New York Dordrecht London

Library of Congress Control Number: 2014941098

Printed on acid-free paper

Springer is part of Springer Science+Business Media (www.springer.com)

To my teachers:

John G. Ramsay
Peter R. Cobbold
John W. Cosgrove
Mike P. Coward

Preface

Structural geology is the study of deformation features in rocks from microscopic to map scale. The required data are collected in field and supplemented by laboratory studies, aerial photographs, satellite imageries, and subsurface data (mostly obtained by geophysical methods). A geologist must explore an area with an open mind and interpretations and hypothesis must be based on actual field observations. Any evidence, however small, contradictory to a popular belief or hypothesis must not be ignored and should be taken into account in the final interpretation. Geophysical investigations are useful but some of the techniques are based upon certain assumptions that allow alternate explanations for the same data, in many cases. One such example can be cited from the Himalaya where deep seismic sounding (DSS) studies were performed under an International Geodynamic Project and investigations were carried out along the Tien Shan-Pamirs-Karakoram-Himalaya geotraverse. A number of lithospheric sections were drawn and these sections show very well-marked steep or vertical faults that reach to a depth of ~90 km and displace the Moho (Kaila et al. 1978). However, later subsurface sections that emerged after popularization of the thin-skinned thrust tectonics model illustrate a marked basal decollement with a number of splay thrusts (Allegre et al. 1984). The maximum possible error in case of dip measurements can be 90° and that can be seen in the available sub-surface sections!

Recently, a problem has cropped up because of the modern evaluation system of measuring the quality of research. A certain scale is definitely needed to measure the importance of scientific contributions but with increasing importance of certain Indexes and factors, a negative trend is emerging. Field observation or laboratory data, which is contradictory to a widely accepted hypothesis is sometimes ignored by researchers to be in the frontline of research. It must be kept in mind that because of the heterogeneous nature of the earth's crust, different stress conditions, and different temperature–pressure conditions during deformation, structural evolution of each area is unique and each hypothesis must be modified with additional parameters to highlight this uniqueness. It is really painful if field data is fit into a particular theory of tectonics without considering the possible alternatives. One of the objectives of the present book is to bring out the limitations of some of the modern concepts, related interpretations and propose an alternate model for evolution of the Himalaya.

In the modern times of super specialization, a field geologist may not be very well conversant with certain aspects of recent developments in a particular topic. This has been observed especially in case of the Himalaya where fieldworks have been done mainly for understanding the regional stratigraphy and structure. The problem is aggravated by absence of continuous rock exposures (especially in the NE Himalaya) and lack of sub-surface data for most of the regions. Hence the cross-sections are approximate and can be extrapolated to fit into a previously conceived model. Since there are several aspects in earth sciences that cannot be proved for want of suitable data, it is always better to work with multiple models so that with gradual increase in database, the final model can withstand the test and verification from different approaches.

Structural evolution of the Himalaya is largely attributed to collision followed by subduction of the Indian plate below the Tibetan plate. The model explains large-scale tectonics of the region but while doing so some of the important structural features, e.g. the early rift phase in the Himalayan region, occurrence of younger rocks on the thrust hanging wall, superposed deformation, etc., are ignored by many. The history of Himalayan evolution does not initiate from the Tertiary but from the Proterozoic when the normal listric faults initiated during the rift phase. Relicts of some of these faults can be observed in older rocks.

The object of the book is to provide structural evolution of the Himalaya with relevant basic information so that earth scientists of other specializations will find it easy to comprehend. Hence the book is divided into two parts. Part I describes the basic principles of structural geology and Part II describes the structural evolution of the Himalaya. The book is not intended to be a substitute for an undergraduate coursework because many of the structural geology topics (e.g. joints, unconformities, plotting of field data, etc.) have not been incorporated. However, the book can be used as a supplementary teaching aid.

Dehradun Ashok Kumar Dubey

References

Allegre CJ et al (1984) Structure and evolution of the Himalaya–Tibet orogenic belt. Nature 307:17–22

Kaila KL, Krishna VG, Roy Chowdhury K, Narain H (1978) Structure of the Kashmir–Himalaya from deep seismic soundings. J Geol Soc India 19:1–20

Acknowledgments

I am indebted to my teachers Professors J. G. Ramsay, P. R. Cobbold, J. W. Cosgrove, and M. P. Coward for igniting my interest in structural geology. Their influence can be seen throughout the book. Many of the ideas discussed in the book have emerged as a result of joint field studies and innumerable discussions with M. I. Bhat. Constructive discussions with V. C. Thakur and N. S. Virdi were very helpful. I am also thankful to my colleagues especially, R. Jayangondaperumal, S. S. Bhakuni, S. J. Sangode, N. S. Gururajan, S. K. Ghosh, Rohtash Kumar, Koushik Sen, P. Banerjee, Upasana Devrani, Kavita Tripathi, and A. D. Selokar for continuous support in field and in laboratory Special thanks to Mr. Rambir Kaushik who helped at different stages of book writing and its organisation. Mr. Tajinder Ahuja and Mrs. Rama Pant helped in all computer related matters. Mr. Saeed Ahmad and Mr. S. S. Bhandari helped in collection of relevant scientific publications.

I am indebted to J. G. Ramsay, K. S. Valdiya, V. C. Thakur, D. H. Tarling, B. E. Hobbs, J. Suppe, V. Raiverman, and S. K. Paul for permission to reproduce their diagrams. I am also thankful to American Geophysical Union, Blackwell Publishing Asia, Cambridge University Press, Elsevier, Geological Society of America, Geological Society of London, John Wiley & Sons, NRC Research Press, Royal Society of London, Royal Society of Edinburgh, Seismological Society of America, and Taylor & Francis Group for reproduction of some of their figures.

Finally but not least I thank my wife Usha, and son Chinmay for their constant help and support.

Dehradun Ashok Kumar Dubey

Contents

Part I
Basic Concepts

Chapter 1
Stress and Strain

Abstract The chapter provides basic information about stress and different types of strain. Significance of orientation of layering with respect to stress orientation is described. Homogeneous and inhomogeneous strains are illustrated. Flinn diagram is described to represent shapes of three-dimensional strain ellipsoids on a two dimensional diagram. Different methods for determination of finite strain are based on certain assumptions that should be kept in mind while interpreting the results. The relevant precautions are briefly described such as: (i) Strain data obtained from one rock type is generally not representative of the regional or bulk strain ellipsoid. Strain values can also vary along a fold profile depending on the mechanism of folding. (ii) When a method is based on measurement of grain shapes, competence contrast between the grain and matrix should be minimum otherwise only the matrix will undergo deformation (if least competent) and the grain will not reveal the true strain ellipsoid. Similarly a deformed fossil will indicate strain suffered by the fossil, not by the entire rock. (iii) Reduction spots can be used as strain markers provided the reduction pre-dates the strain. (iv) Methods based on measurement of buckle shortening ignore initial layer parallel strain (homogeneous shortening) that has occurred prior to development of the fold. (v) Magnetic strain, obtained by anisotropy of magnetic susceptibility method, provides bulk strain, i.e. of the entire rock sample including the matrix. Hence petrofabric and magnetic strains can differ noticeably.

The earth has been continuously acted upon by a large number of chemical and physical processes during the course of its evolution. The intensity of these processes varied in time and space and led to changes in shape and position of constituent materials. Most of these changes take place deep inside the earth and various geological processes bring the resulting structures, preserved in deformed rocks, to the surface. The final product is thus available for studies but the initial shape, composition, temperature–pressure conditions and stages of its evolution etc. are not known. Hence a geologist has a formidable task to initiate studies on a finished product and then go back to predict its initial properties, conditions of deformation, displacement path, and amount of translation, if any. The study is performed

A. K. Dubey, *Understanding an Orogenic Belt*, Springer Geology,
DOI: 10.1007/978-3-319-05588-6_1,

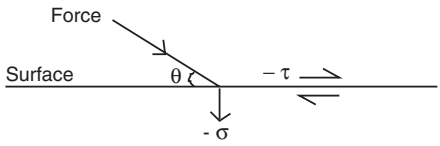

Fig. 1.1 The resolution of force acting on a surface of area 'a' into normal (σ) and shearing stress (τ) components

on various scales from microscopic to map-scale. Most of the basic parameters to describe these processes have been adopted from physics and chemistry, and modified to suit the requirements of earth scientists.

Some of the important fundamental concepts of displacement and changes in length and angles are described here. An exhaustive account of the subject is given by Ramsay (1967), Hobbs et al. (1976), and Ramsay and Huber (1983). Many of the definitions used in the present book are adopted from their work.

1.1 Stress

Forces, which can be a source of deformation, are classified into two types: (i) body forces, and (ii) surface forces. The body forces act on the whole material and are proportional to mass of the substance (e.g. gravity, centrifugal force, magnetic force). These are measured by force per unit volume. The surface forces act on surface of a body, measured by force per unit area and are known as stress. The stress gives a measure of intensity of reaction of the material which lies on one or the other side of the surface (Ramsay, 1967).

The stress is of two types: normal stress (or direct stress, σ), and shearing stress (τ) (Fig. 1.1). When a force acts parallel to a plane, the stress is called as shear stress and when it acts normal to a plane, the stress is called as normal stress. The normal stress can be either compressive or tensile. The compressive stress is directed toward the surface on which it acts, and tensile stress is directed away from the surface on which it acts. Compressive, tensile and shear stresses, respectively resist the tendency of the parts to approach, separate, or mutually slide under the action of applied forces (Roark and Young, 1982).

The general convention in structural geology is to use positive sign for tensile stress and negative sign for compressive stress. If a force vector F acts on surface area 'a' and makes an angle 'θ' with the surface then,

$$\sigma = \mathrm{F} \sin \theta / \mathrm{a}, \text{ and}$$

$$\tau = \mathrm{F} \cos \theta / \mathrm{a}$$

Three mutually perpendicular planes passes through any point in a stressed body, the stress on each of these is purely normal, tensional, or compressional. These planes are the principal planes for that point and the stresses on these planes are the principal stresses. One of the planes represents the maximum stress at the point, and one of them represents the minimum stress at the point. In a special

condition when one of the principal stresses is zero, the condition is one of plane stress and when two of them are zero, the condition is one of uniaxial stress. The distribution of stress is represented by stress trajectories, which are orthogonal lines (planes in three dimensions) representing directions of principal stresses. All points in a stressed body where the corresponding principal stresses have the same direction are called as isoclinic lines. Isotropic points have equal values (strength) of the principal stresses. The principal stresses are represented by a stress ellipsoid, which represents the state of stress at a given point in a body and defined as an ellipsoid whose half axes are equal to the principal stresses.

When all the three principal stresses are equal and no shearing stress exist in the material, the state of stress is called as hydrostatic stress. The effect of hydrostatic stress is to produce change in volume but not in shape. The change in shape is caused by stress difference, which is the algebraic difference between the maximum and minimum principal stresses.

The following two terms are normally associated with geological processes.

Paleostresses are early stresses active during formation of a geological structure. No precise time frame can be deduced for paleostresses using structural data alone.

Neotectonic stresses are prevalent in the earth's crust from Pliocene (late part of Tertiary) to the Present. A special subdivision called as active stress is formed under this category to define the present stresses, which are responsible for very recent deformations and are of particular interest in earthquake studies especially seismic predictions.

1.2 Strain

Bulk transport of a body from one place to another is known as translation and any change in geometrical shape or internal configuration of a body, produced by stress, is called as deformation or strain. Normally, translation is accompanied by internal deformation (e.g. klippe structure) but internal deformation may not necessarily be accompanied by translation. For example, Fig. 1.2a shows stretching of a wire (tensional stress) with initial length l_0 to an increased final length l_1 (Fig. 1.2b). The increase in length is expressed by longitudinal strain, i.e. extension 'e', which is defined as change in unit length. This is obtained as follows.

$$e = l_1 - l_0/l_0 = \delta l / l_0$$

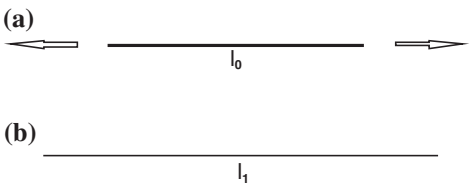

Fig. 1.2 A thin wire with initial length l_0 (**a**), stretched to an extended length l_1 (**b**) under tensional stress

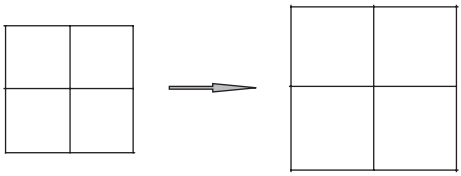

Fig. 1.3 Change in volume of a body without any change in shape resulting in dilation

In the above case, the extension is positive but when compressive stress results in reduction in length, the extension is negative. Sometimes the longitudinal strain is described in terms of quadratic elongation (λ), which is defined as square of the length of a line of originally unit dimensions.

$$\lambda = (l_1/l_0)^2 = (1 + e)^2$$

When deformation results in change in volume without any change in shape, the resulting strain is called as dilational strain (Fig. 1.3). The dilation can be positive (increase in volume) or negative (decrease in volume). The deformation is related to hydrostatic stress and signifies equal extension or shortening in all the three principal directions. When deformation is considered in three-dimensions, the increase in volume is expansion, and decrease in volume is contraction.

This is in contrast to distortional strain, which is accompanied by a change in shape with or without volume change as described below.

1.2.1 Simple Shear

When all the material lines are deflected parallel to one of the reference planes (x-axis in Fig. 1.4), the volume remains constant but the initial angle between intersecting lines is changed. When the initial angle between the intersecting lines is 90°, any deflection from the right angle (i.e. Ψ) is angular shear. This type of deformation is called as simple shear that can be simulated by sliding a pack of cards one against the other. The deformation is expressed as

$$x_1 = x + \tan\Psi y; \quad y_1 = y$$

The shear strain (γ) is defined as

$$\gamma = \tan\Psi$$

The deflection of the perpendicular to the reference direction can be either clockwise or anticlockwise. If the initial perpendicular is rotated clockwise relative to the specific direction, the angular shear strain is negative; if rotated anticlockwise then positive. For example, Fig. 1.4b shows negative shear strain.

In simple shear deformation, orientation of layering with reference to the shear direction is of special significance. For example, ABCD (Fig. 1.5a) is deformed by simple shear to A′B′C′D′ (Fig. 1.5b). All layers parallel to AB does not undergo

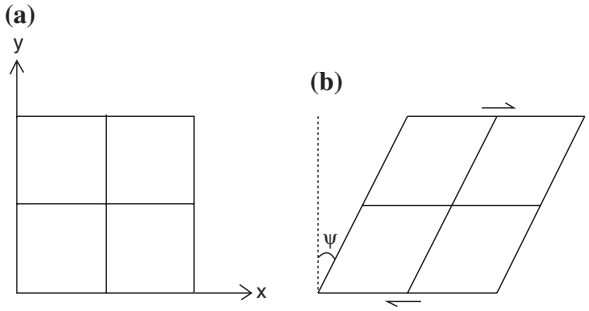

Fig. 1.4 **a** An undeformed body. **b** Simple shear deformation with no change in volume. The initial right angle is deflected by an amount Ψ

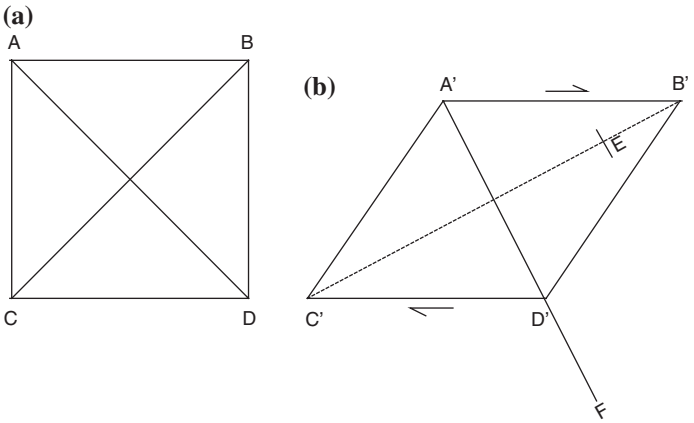

Fig. 1.5 Initial (**a**) and final (**b**) orientations and lengths of layering in simple shear

any change in their length (A′B′) hence their will neither be compressional nor extensional structures in this orientation. Layers parallel to AD take up a new position A′D′ (initial length A′F) with reduction in their length thereby resulting in compressional structures. In contrast, layers parallel to BC are stretched during deformation and takes up a position B′C′ (initial length CE) resulting in extensional structures. Hence simple shear can result in different structures depending upon orientation of layering with reference to the direction of shear.

1.2.2 Homogeneous and Inhomogeneous Strain

A deformed or distorted body shows changes in length of lines and/or initial angles (Fig. 1.6). When the deformation is such that straight lines remain straight, parallel lines remain parallel and all the lines in one direction reveal constant

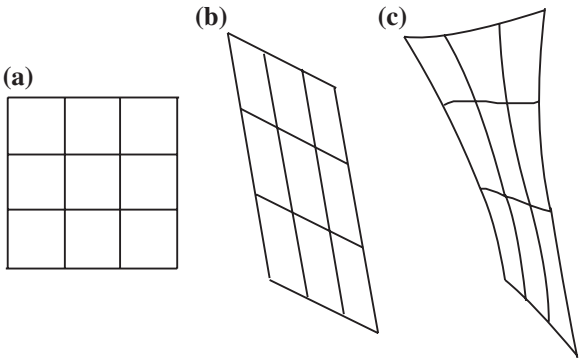

Fig. 1.6 Different strain patterns. **a** Undeformed body. **b** Homogeneous strain. **c** Inhomogeneous strain

values of e, λ, γ, and Ψ, the strain is homogeneous (Fig. 1.6b). In case of inhomogeneous deformation (Fig. 1.6c) the straight lines become curved, parallel lines lose their parallelism, and values of e, λ, γ, and Ψ vary in any given direction in the deformed body.

1.2.3 Extensional and Compressional Structures

In two dimensional deformation studies, it is observed that extension in one direction is accompanied by compression in the perpendicular direction to keep the volume fix, as shown in Fig. 1.7 (details in Ramsay, 1967). The circular object is stretched in one direction (Fig. 1.7a) and the extension is accommodated by shortening in the perpendicular direction (Fig. 1.7b). The extension results in formation of boudins (separation of competent layer into a number of long cylindrical pieces lying side by side when competence contrast between the layer and the matrix is high) (Fig. 1.8) or thinning of the layer (when the competence contrast is low or nil) whereas the shortening results in formation of folds (when competence contrast between the layer and the matrix is high) (Fig. 1.9) or thickening of the layer (when the competence contrast is low or nil). Hence it is to be remembered that extensional and shortening structures may develop simultaneously depending upon orientation of the layering with reference to the stress field. However for the sake of convenience, these structures are normally described separately in text books.

Figure 1.7a represents a unit circle where the diameter is equal in all directions. After the deformation, the circle changes to an ellipse with a short axis (parallel to the axis of maximum compression) and a long axis (parallel to the axis of maximum extension). The axial ratio of the minimum to maximum axes in the diagram (Fig. 1.7b) is 1:3. This quantity provides a measure of intensity of deformation. The large axial ratios indicate large deformations. In some exceptional cases it is known that the initial object was circular (e.g. oolites; spherical in three dimensions) and the axial ratios can be measured directly under a microscope using thin-sections. However, initial geometrical shapes of deformed objects are not always

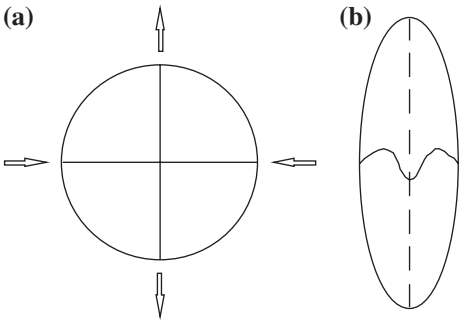

Fig. 1.7 Simultaneous development of extensional and compressional structures to preserve the total volume. **a**. A unit circle showing two perpendicular layers. The extension and compression directions are shown by arrows. **b**. Development of boudins (broken lines) along the direction of extension and folds along the direction of compression

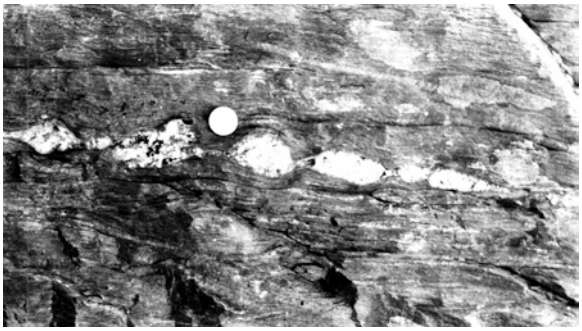

Fig. 1.8 Competent quartz boudins enclosed in less competent host of phyllitic rock (Bhanjraru, Himachal Lower Himalaya)

known hence other methods have to be applied for determining the axial ratios. An exhaustive account of various methods of determining the axial ratios and finite strain are given by Ramsay and Huber (1983).

When the deformation is reversible, i.e. the deformed body comes back to its initial shape after removal of the stress field, the deformation is elastic and when the geometrical shape change is irreversible (permanent), the strain is plastic as observed in geological horizons. An elastic stress or elastic strain is a stress or strain, respectively within the elastic limit.

When a body is deformed at comparatively upper levels of the earth's crust where the rocks are brittle, the dominant result is formation of joints and faults whereas at deeper levels, the rocks behave as ductile material and the dominant structures to be formed are folds and ductile shears. At the intermediate level, the rock behaves as brittle–ductile and this zone is characterized by simultaneous development of folds, faults and shear veins. The rheological properties of rocks at various depths cannot be predicted precisely because of interplay of a number

Fig. 1.9 Development of folds in competent limestone and incompetent slate as a result of layer parallel compression (Tattapani, Himachal Lower Himalaya)

of erratic or unknown physical and chemical factors. For example, the rate of increase of temperature with depth will vary inside a plate and at a plate margin. Composition of rocks is also heterogeneous and the rheological properties will vary depending on pore-fluid pressure, hydrostatic pressure, rate of deformation, etc. Hence a tectonic model proposed for structural evolution of an area may not necessarily be applicable in toto to a different area. The problem will multiply manifold when different orogenic belts formed at different times over different time scales are considered. It is therefore essential that a structural geologist is well versed with basic concepts of the subject and knows the limitations of different analytical techniques. Most importantly, there is no substitute for detailed field investigations and analysis of field data on different scales. The modern day computers and other sophisticated equipments are extremely helpful but inherent assumptions in the used softwares should be taken care of before arriving at a conclusion.

1.2.4 Strain Ellipsoid

The strain ellipsoid represents the state of strain at any given point in a body. It is derived by homogeneous strain of an original sphere with unit radius. It has three orthogonal axes, which are called the principal axes of strain with directions X, Y and Z (Fig. 1.10), with semi-axis lengths $1 + e_1$, $1 + e_2$ and $1 + e_3$. The

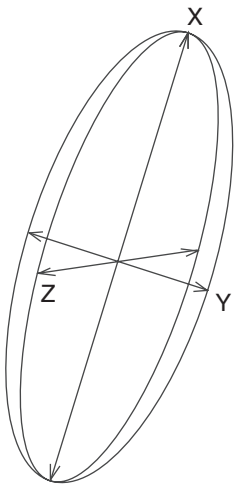

Fig. 1.10 The strain ellipsoid

parameters $e_1 \geq e_2 \geq e_3$ are the three principal longitudinal strains. The planes containing two of the principal axes are known as the principal planes. The strain ratios on these principal planes are the principal plane strain ratios R_{xy}, R_{yz}, R_{zx}.

1.2.5 Strains Associated with Homogeneous Deformation

Different types of strains are associated with constant volume homogeneous deformation, when considered in three dimensions (Fig. 1.11; Hobbs et al., 1976). These are described below.

1. Axially symmetric extension (Fig. 1.11a)

This type of strain involves extension in one principal direction and corresponding equal shortening along the remaining two principal directions, at right angles. The resulting strain ellipsoid is a prolate spheroid.

2. Axially symmetric shortening (Fig. 1.11b)

This involves shortening in one principal direction and corresponding equal extension along the other two principal directions, at right angles. The resulting strain ellipsoid is an oblate spheroid.

3. Plane strain (Fig. 1.11c)

In plane strain, shortening and extension occur parallel to the two principal directions and the third principal direction maintains its original length (now the intermediate axis). Since all the three principal axes have different lengths, the strain ellipsoid is triaxial.

4. General strain (Fig. 1.11d)

This involves extension or shortening along all the three principal directions and the strain ellipsoid is triaxial.

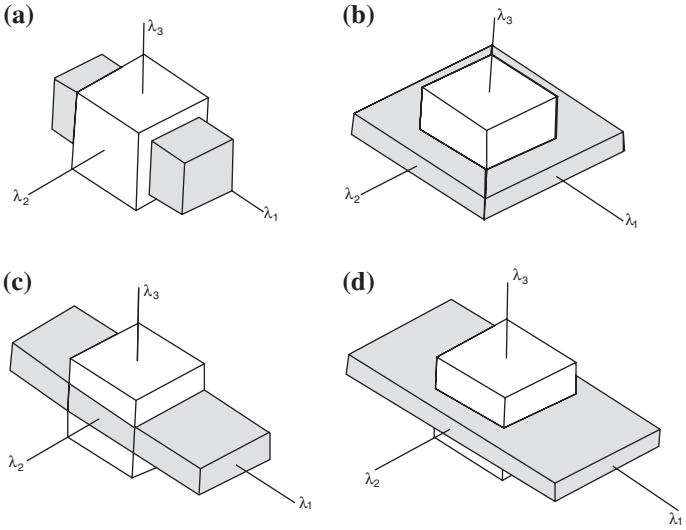

Fig. 1.11 Different types of homogeneous deformation patterns [From Hobbs et al. (1976), © B. E. Hobbs. Published with permission of B. E. Hobbs.]

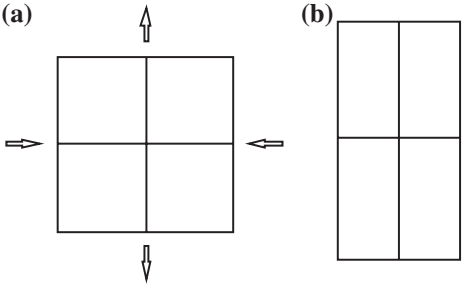

Fig. 1.12 Pure shear deformation. **a** An undeformed square where the intersecting lines make an angle of 90°. **b** Pure shear, plane strain deformation with no change in volume and initial angle between the intersecting lines

1.2.6 Pure Shear

Pure shear signifies homogeneous deformation and incorporates either plane strain or general strain. A simple example is shown in Fig. 1.12 in which a square is deformed into a rectangle. There is no change in volume and the intersecting lines maintain the original angular relationship. Compression along one axis (horizontal, $1 + e_1$) is compensated by extension along the perpendicular axis (vertical, $1 + e_2$) (Fig. 1.12b) with the following relationship.

$$1 + e_1 = 1/1 + e_2$$

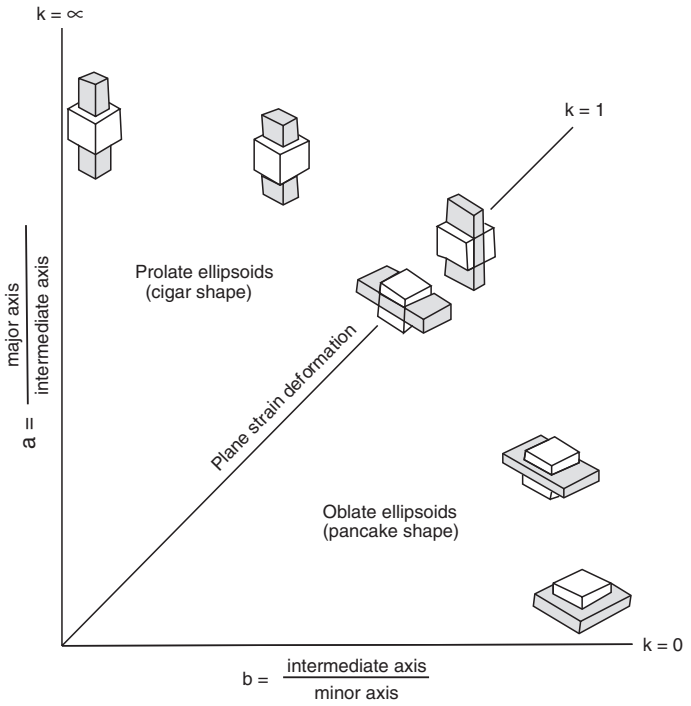

Fig. 1.13 Flinn diagram to represent the shapes of three dimensional strains [From Hobbs et al. (1976), © B. E. Hobbs. Published with permission of B. E. Hobbs.]

This is also referred to as an irrotational deformation (or irrotational strain).

1.3 Flinn Diagram

The Flinn diagram (Fig. 1.13) is a method of graphical representation of homogeneous stain. The method was originally employed by Zingg for recording the shapes of pebbles and later developed by Flinn (1962) for use in structural geology. The method is based on ratios of principal extensions and not on absolute values of the principal extensions, which are not always possible to obtain from naturally deformed rocks. The origin of the graph represents a cube (or sphere) where all the three principal axes are equal. The ratio $(1 + e_1)/(1 + e_2)$ (major axis/intermediate axis) = a is plotted as ordinate, and $(1 + e_2)/(1 + e_1)$ (intermediate axis/minor axis) = b as abscissa. Flinn has also suggested a parameter k, which is the slope of a line joining the plot of the ellipsoids to the origin (point 1, 1) and is defined by

$$k = \frac{a - 1}{b - 1}$$

The parameter has been used to divide the constant volume ellipsoids into five types.

$k = 0$	uniaxial oblate type (pancake shape)
$1 > k > 0$	flattening type
$k = 1$	plane-strain type
$\infty > k > 1$	constriction type
$k = \infty$	uniaxial prolate type (cigar shape)

Despite several advantages, the diagram is of limited use in areas of weak deformation because of clustering of points close to origin of the graph.

1.4 Determination of Finite Strain: Precautions

Strain in deformed rocks can be estimated by using a method depending upon an available geological marker (details in Ramsay and Huber, 1983). The different techniques are extremely useful in understanding and quantification of deformation but the following points should be kept in mind while interpreting the results.

1. Finite homogeneous strain does not generally exist in layered rocks (Treagus, 1981). Strain data obtained from one rock type is generally not representative of regional or bulk strain ellipsoid. The competent (high viscosity) layers reveal relatively low strain as compared to incompetent (low viscosity) layers. Cleavage in competent layers forms sub-perpendicular to bedding becoming closer in attitude to bedding with increase in deformation. In incompetent layers cleavage forms oblique to bedding and remains oblique throughout the deformation. Cleavage, generally assumed to represent the principal plane of flattening in a rock can vary in attitude at intersection with another layering in a multilayer sequence thereby forming cleavage refraction. Strain values can also vary along a fold profile depending on the mechanism of folding.
2. If the method is based on measurement of grain shapes, the competence contrast between the grain and the matrix should be minimum otherwise only the matrix will undergo deformation (if least competent) and the grain will not reveal the true strain ellipsoid. Similarly a deformed fossil will indicate strain suffered by the fossil not by the entire rock.
3. Reduction spots can be used as strain markers but the reduction must pre-date strain because later formed joints or bedding planes can also provide paths for reduction (Borradaile and Henry, 1997).
4. Methods based on measurement of buckle shortening ignore initial layer parallel strain (homogeneous shortening) that has occurred prior to the development of folds. Similarly methods based on geometry of flattened parallel folds (Srivastava and Shah, 2006) yields only a part of total deformation related to late stage flattening of fold limbs.
5. The magnetic strain, obtained by anisotropy of magnetic susceptibility method, provides the bulk strain, i.e. of the entire rock sample including the matrix.

In areas of weak deformation, the method yields good results but in areas of superimposed deformation, the magnetic strain tends to reset to the latest (superposed) deformation.

References

Borradaile GJ, Henry B (1997) Tectonic applications of magnetic susceptibility and its anisotropy. Earth Sci Rev 42:49–93

Flinn D (1962) On folding during three-dimensional progressive deformation. Quaternary J Geol Soc Lond 118:385–433

Hobbs BE, Means WD, Williams PF (1976) An outline of structural geology. John Wiley & Sons Inc, New York 571 pp

Ramsay JG (1967) Folding and fracturing of rocks. McGraw Hill, New York 568 pp

Ramsay JG, Huber MI (1983) The techniques of modern structural geology, vol 1., Strain analysis Academic Press, Waltham 307 pp

Roark J, Young WC (1982) Formulas for stress and strain. McGraw Hill, New York 624 pp

Srivastava DC, Shah J (2006) A rapid method for strain estimation from flattened parallel folds. J Struct Geol 28:1–8

Treagus SH (1981) A theory of stress and strain variations in viscous layers, and its geological implications. Tectonophysics 72:75–103

Chapter 2
Anisotropy of Magnetic Susceptibility

Abstract Anisotropy of magnetic susceptibility is an important technique which depicts preferred orientation of magnetic minerals in a rock or unconsolidated sediments. Hence the property is used for study of primary structures and rock fabric. The technique is non-destructive and can be used in nearly all types of rocks because it does not need a rock to contain specific strain markers like deformed fossils, reduction spots, ooids, etc. The method has an advantage as it can determine weak deformation even where lineation and foliation have not developed. In rocks with well developed tectonic fabrics, the principal magnetic susceptibility directions are closely related to orientation of structural features (e.g. fold, fault, foliation, lineation). Different types of AMS fabrics are described. Differences between magnetic and petrofabric strains are highlighted. Importance of sampling in a region of superimposed deformation is described. It is emphasized that objectives of the study should be formulated prior to selection of sample sites. Hrouda diagram is described for understanding the roles of simple and pure shear deformations in a region of simultaneous development of folding and thrusting. The technique has been successfully employed to ascertain the displacement patterns along some of the prominent Lower Himalayan thrusts.

When a magnetic field is applied on a rock sample, the intensity of magnetization is not always uniform in all directions but varies with orientation of the constituent minerals. Hence the property can be used for study of rock fabric. The dependency of induced magnetization on orientation of the applied magnetic field in a rock is called as anisotropy of magnetic susceptibility (AMS) and it depicts the preferred orientation of magnetic minerals in a rock or unconsolidated sediments (Hrouda 1982, Tarling and Hrouda 1993). The first systematic study in this field was performed by Voight and Kinoshita (1907). It was later used as a petrofabric marker by Ising (1942) and Graham (1954). The technique is non-destructive and does not need a rock to contain specific strain markers like deformed fossils, reduction spots, ooids etc. Hence it can be used in nearly all types of rocks. The method has an advantage as it can determine weak deformation even where lineation and foliation have not developed (Tarling and Hrouda 1993; Borradaile and Henry 1997; Evans et al. 2003).

A. K. Dubey, *Understanding an Orogenic Belt*, Springer Geology,
DOI: 10.1007/978-3-319-05588-6_2,

In rocks with well developed tectonic fabrics, the principal magnetic susceptibility directions are closely related to orientation of structural features (e.g. folds, faults, foliation, lineation) (Hrouda and Janak 1976; Borradaile 1988; Averbuch et al. 1992; Robion et al. 2007; Borradaile and Jackson 2010). Some of the important aspects of the technique are described here (details in Tarling and Hrouda 1993).

2.1 Different Forms of Magnetization

The technique can be applied to rocks even where the magnetic minerals are absent because the magnetic properties arise from motion of electrically charged particles. When electron shells are complete (even atomic numbers) in a substance, application of a magnetic field results in electron spin and generate magnetization. The strength of magnetization is measured in different orientations and the difference is then interpreted in terms of net shape of the grains or degree of their crystalline alignment (petrofabric). Depending on the nature of this magnetization and the magnetization when the field is removed, different forms of magnetization can be identified.

A material is called as diamagnetic when the generated magnetization is in opposite direction to that of the applied field and it is lost immediately after removal of the external magnetizing field (Fig. 2.1a). Since the field is produced in opposite direction to that of the applied field, the diamagnetic substances have negative susceptibilities (~10^{-5} SI) for common rock forming minerals (e.g. quartz, calcite, dolomite). All other substances, with incomplete electron shells, are described as paramagnetic (Fig. 2.1b). These substances are characterized by a magnetic moment that follows the direction of the applied field. The paramagnetism also disappears immediately after removal of the applied field. Paramagnetic minerals have positive susceptibilities that range between 10^{-2} and 10^{-4} SI for common rock forming minerals (e.g. hornblende, chlorite, biotite, muscovite, tourmaline).

A few substances with strong positive susceptibilities can also carry a strong ramanent magnetization (magnetization that remains after the external magnetizing field has been removed). These substances are called as ferromagnetic or loosely as magnetic (Fig. 2.1c). Ferromagnetism is characteristic of substances in which magnetic vectors and the applied field are in the same direction and retain their magnetic alignment after removal of the field (e.g. magnetite, haematite). These materials acquire and retain a very strong magnetism that is superposed on paramagnetic character. Thus if the ferromagnetic properties are destroyed (e.g. by heating), the previously ferromagnetic materials behave as paramagnetic. When the two lattices are strongly magnetized in equal amount, the mineral grains will have no net magnetization resulting in antiferromagnetic substances (e.g. haematite) (Fig. 2.1d) and are characterized by a sub-division in their lattices (designated as A and B sub-lattices). The atomic moments of A and B are aligned antiparallel to each other. Hence when the magnetic moments are equal, they cancel each other and the resultant magnetic moment is nil. When, the lattice is more strongly

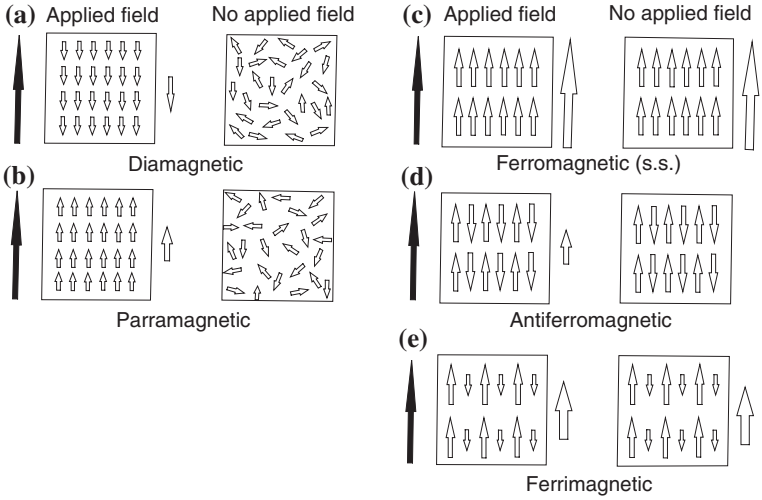

Fig. 2.1 Different forms of magnetization. The *left hand* diagrams in the pairs of illustrations 'a' to 'e' show the magnetization (*hollow arrow outside the square*) that a substance acquires in an applied magnetic field (*solid arrow*). The *right hand* diagrams depict the magnetization present after the field has been removed. **a** Diamagnetic materials become weakly magnetized in opposite direction to that of the applied field, but electron spins randomly on removal of the field. **b** Paramagnetic materials (e.g. olivine, pyroxene) become weakly magnetized in the same direction as that of the applied field, but randomize on its removal. (**c**), (**d**) and (**e**) Ferromagnetic materials retain their magnetic alignment after removal of the field. **c** Ferromagnetic materials acquire and retain a very strong magnetization. **d** The magnetic alignments of antiferromagnetic materials are exactly anti-parallel and most paramagnetic effects are completely dominated by these very strong internal fields. These materials have no external magnetic field after removal of the applied field. **e** The alignments within ferromagnetic materials are antiparallel but not of equal magnitude, so they retain a weaker external magnetization than a ferromagnetic material when the applied field is removed [From Tarling and Hrouda (1993), © D. H. Tarling. Published with permission of D. H. Tarling]

magnetized resulting in weak net magnetic field (e.g. magnetite) the substances are called as ferrimagnetic (Fig. 2.1e). These substances have unequal atomic moments in their sub-lattices and a net spontaneous magnetization, which gives rise to a weak ferromagnetism (Dunlop and Ozdemir 1997). The antiferromagnetic and ferrimagnetic are together referred as ferromagnetic.

2.2 Anisotropy of Magnetic Susceptibility

A natural rock contains a variety of minerals with ferromagnetic, paramagnetic, or diamagnetic properties. Depending on the magnetic properties, each grain contributes to the total (bulk) susceptibility and its anisotropy. When ferromagnetic minerals exceed 0.1 volume percentage of the whole rock, they control the magnetic

properties. In absence of these minerals, the susceptibility of paramagnetic minerals tends to dominate the diamagnetic minerals provided they constitute more than 1 % of the rock.

The susceptibility also depends on temperature and strength of the applied field. Since these are not constant features, the measurements are normally done at room temperature [~20 °C at magnetic fields of <1 mT (milli Tesla)].

The magnitude of anisotropy of magnetic susceptibility, determined from measurements of susceptibility in a weak field, depends on two factors; (i) anisotropy of particles themselves, and (ii) degree of their alignment. The individual particles may represent crystalline or shape anisotropy. The crystalline anisotropy depends upon action of lattice forces and resulting magnetization along specific directions, e.g. a crystalline axis or plane, termed as easy axis or easy plane. In shape anisotropy, the induced magnetization is normally oriented along the long axis of the grains. The ratio of crystalline and shape anisotropies varies in different minerals. For example, in magnetite, the crystalline anisotropy is weak and the shape anisotropy is dominant. In a special condition when crystalline 'easy' axes and long (shape) axes of the grains have the same orientation, the magnetic anisotropy of the rock is maximum.

When strength of induced magnetization per unit volume is directly proportional to strength of the applied magnetic field, it can be represented as:

$$M \alpha H$$
$$M = KH$$
$$K = M/H$$

where,

M Strength of the induced magnetization per unit volume
K Constant of proportionality defined as magnetic susceptibility of the material, and
H Strength of the applied magnetic field

Any difference in magnetic strength of the constituent minerals can be deduced in terms of net shape of the grains and degree of their crystalline alignment. This can be interpreted in the same way as other petrofabric techniques normally employed in structural geology (Tarling and Hrouda 1993; Borradaile and Henry 1997; Evans et al. 2003).

2.3 Equipment

Directional susceptibility of rocks is generally measured by low field bulk susceptibility (details in Tarling and Hrouda 1993). Anisotropy of a sample is determined by measurement of magnitude of susceptibility along at least six directions so that the susceptibility ellipsoid can be drawn. A common type

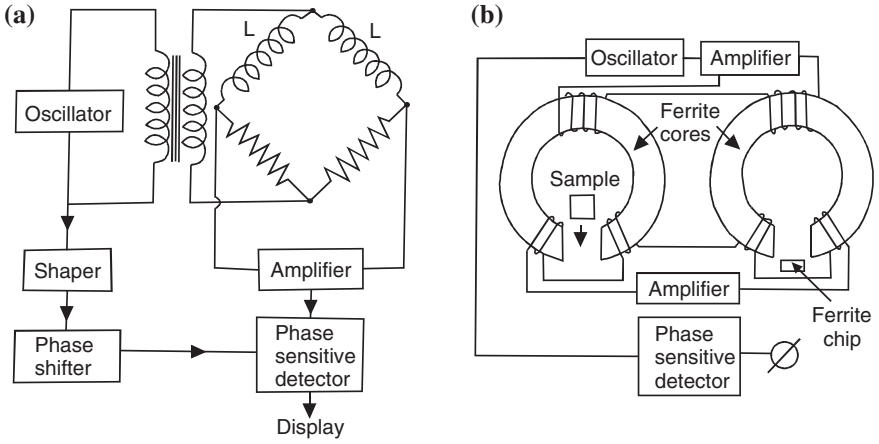

Fig. 2.2 Directional susceptibility meters. Two bridge systems for determination of magnetic susceptibility along the direction of a coil. **a** An equal-impedance bridge. The specimen can be inserted into one of the coils (*L*). **b** The balanced-transformer system where the specimen is placed inside a ferrite ring. The extent of unbalancing the circuit is proportional to susceptibility of the specimen in the direction of circumference of the ring [From Tarling and Hrouda (1993), © D. H. Tarling. Published with permission of D. H. Tarling]

of instrument is a modified a.c. bridge, one arm of which is an inductive coil (Fig. 2.2a). When a rock sample is placed in the coil, the change in inductance of the coil is proportional to the sample susceptibility. Initial calibration is normally done by using a specimen holder containing a known volume of a salt of known susceptibility (e.g. copper sulphate). Subsequent calibrations are performed with a strip of recording tape (meghamite) whose susceptibility has been measured by using the salt sample.

In the balanced-transformer equipment (Fig. 2.2b), a sample is surrounded by one of the sensing coils. Insertion of the sample alters the mutual inductance between the two coils producing a net output voltage in an associated circuit.

The specimen's susceptibility is measured in 15 orientations using a rotatable case. From these values six independent components of susceptibility tensor and statistical errors are calculated using the SUSAM software.

2.4 Collection of Samples

AMS studies require carefully chosen oriented rock samples. These should be fresh i.e. free from weathering and solution activities. In presence of prominent cleavage or thin bedding, the sample is likely to split during drilling. On the other hand, if the rock is hard and massive, it is difficult to extract an oriented sample. Hence a field geologist, who intends to do AMS (and petrofabric strain) studies,

should always carry a light and a heavy hammer, set of chisels, nylon and wire brushes (to wipe a sample for necessary markings prior to its extraction), and a small sprit level for marking the horizontal plane.

Prior to extraction of a sample, the rock surface is marked for strike and dip directions, amounts, and an upright arrow. Structural data (e.g. bedding, flow indicators, lineation, foliation, minor faults) are measured and recorded in a field note book along with the location. The structural data should be recorded as close to the sample as possible, especially in areas of superimposed deformation. Each sample is given a distinct name and number. Since a good number of drill cores (5–10) are required for analysis, it is advisable to collect large samples ($\geq 15 \times 10 \times 5$ cm). The samples are brought to laboratory and fixed firmly in its natural orientation either by using cement or by clamping by a set of vices. The samples are then drilled, cores are taken out and cut to the required size. In an ideal situation, each specimen for anisotropic studies should be a sphere but it is not convenient to cut an oriented sphere from a rock specimen. Hence two most common standard shapes are cylinders with a diameter of 2.5 cm and height of 2.1 cm, and cubes of 2.0 cm side (Tarling and Hrouda 1993). Cubes are normally cut in semiconsolidated sediments. Portable drilling machine are available for obtaining drill cores in field but the machine requires a continuous supply of water or lubricant. This is not very convenient because it is difficult to carry large quantities of water/lubricant while tracking or climbing a mountain. Proper care should be taken for safe transit of the samples although it is possible to reassemble broken samples by using non-magnetic fast setting epoxy glues. The nonmagnetic property of the glue must be tested before its application because many of the glues are quite strongly magnetic when set.

Soft samples are collected by pushing a plastic cylinder (normally a diameter of 55 mm) or box (sides 2.0–2.1 cm) into sediments. Copper or brass tubes can be used for comparatively harder sediments. The orientations are marked on the body of the container and the required length is later cut in laboratory. Unconsolidated lake sediments or marine sequences are sampled with coring devices that penetrate the surface by gravity loading or with the help of hydraulic pressure. The gravity corers consist of nonmagnetic materials like aluminium. The sediment core is then preserved inside a properly sealed plastic tube for transportation. The sealing is an important part of sampling as drying of the sample can alter the properties. The bulk susceptibility of sediments can be measured by using long core devices but in order to determine the anisotropy of susceptibility, the samples need to be tailored to the required size of the equipment container. Special care should be taken to check the geometry of the tube or box as asymmetric shapes can induce significant error in measurements. The samples should ideally be stored at 2–3 °C to avoid any physical (shape) or chemical changes and the analysis should be performed as early as possible. Samples with high water content can deform during sampling (while pushing the sample tube or box). However this deformation is confined near the walls of the container and bulk of the sample contains the original fabric. This can also be avoided by using cylinders of large diameter so that the peripheries

can be cut and removed prior to the measurements. Some of the soft samples can acquire a fabric, which is oriented along the pushing direction of the cylinder. In order to preserve orientation marks on friable rocks, the marks are made on a flat plastic or wood disc glued to the sample (normally top of the sample).

2.4.1 Importance of Sampling in an Area

The deformation pattern is unlikely to be distributed uniformly in a region and part of the region (sample site) may show only a part of the structure. This is further exemplified by using a deformed modeling clay layer surface (Fig. 2.3a). The multilayer model was deformed in two horizontal directions during successive stages of deformation. The first compression resulted in displacement along the thrust and early folds. The second compression was orthogonal to the early axis of maximum compressive stress, and it formed superposed folds, extensional faults and a strike-slip fault. Selection of sample sites is very important in such a region. A sample collected at site 1 (in vicinity of a thrust; Fig. 2.3b) will reveal the thrust related strain pattern. Sample site 2 is located on an early antiformal hinge related to the early deformation. A sample collected at site 3 is likely to show a reversal of the axes of maximum and minimum compression as compared to site 2 because of the superposed deformation. Site 4 is located near an extensional fault hence this will exhibit maximum compression axis in the vertical direction and the minimum compression in the horizontal direction. On the contrary, site 5 (strike-slip fault) will show the maximum and minimum compression axes in two horizontal directions. Site 6 is located at a distance from all the dominant structures hence this site will reveal the minimum strain values. These variations will be reflected in orientations of developing foliation, lineation, etc. and the magnetic susceptibility. Hence minor structures in close vicinity of the sample site should be carefully recorded and a correlation between orientation of susceptibility axes and strain should not be assumed but established.

Location of sample sites is also important in regions, which have undergone a single phase of deformation because geological structures initiate from a point and then propagate with progressive deformation (details in Chap. 3). Strain values can vary along a thrust, across a thrust, in different fold geometries, and even in two limbs of a fold. The values will be different in thin and thick layers of a single fold, in overturned fold limbs, in an earlier formed fold of a single fold complex, and at the culmination point of a fold surface. Hence the purpose of strain determination should be clear in mind before initiating the study. For example, whether the study is for understanding fold interference patterns, propagation of a fault, strain variation along or across a shear zone or across fold limbs. It is suggested that an area where strain studies are to be performed should be carefully mapped for geological structures and their geometries. This should be followed by selection of sample sites keeping in view the objectives of the study.

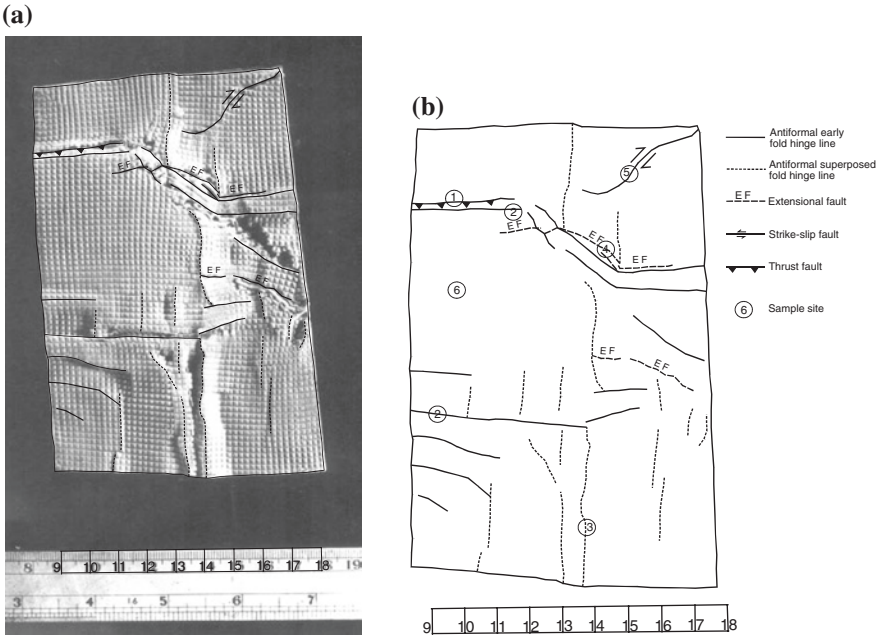

Fig. 2.3 **a** A deformed layer surface after 11 % total model shortening in the first phase and 17 % shortening in the second phase of superposed deformation when the axis of maximum compression was orthogonal to the first axis of maximum compression. A square grid pattern was embossed on the layer surface prior to the deformation. The deformed grids reveal that the surface strain pattern is not uniform throughout the layer. **b** Structural features and sample sites observed on the layer

2.5 Magnetic Anisotropy

When strength of magnetization depends on sample orientation within a magnetic field and the susceptibility varies in different directions, the rock is called as magnetically anisotropic. In anisotropic rocks, the magnetic susceptibility can be represented as a second order symmetric tensor that can be represented geometrically as an ellipsoid with three principle susceptibility axes. The maximum susceptibility is designated as K1, the intermediate as K2, and the minimum as K3 (Kmax > Kint > Kmin). The intensity of these parameters can also vary with relative proportions of ferromagnetic and paramagnetic minerals in the specimen.

Different minerals are characterized by different anisotropies. For example, the crystalline anisotropy is weak in magnetite and the shape anisotropy is dominant whereas in hematite the crystalline anisotropy is dominant. Because of their strong magnetic properties, the ferro- and ferromagnetic minerals are important for magnetic susceptibility studies but in weakly metamorphosed rocks and sediments, the paramagnetic minerals control the AMS (Rochette 1987; Pares 2004).

2.5.1 Mean Susceptibility (Km)

AMS measures the bulk-preferred orientation of ferromagnetic, paramagnetic, and diamagnetic minerals and/or crystal lattices (Hrouda 1982). When the induced magnetization has equal strength in all directions, the rock sample is magnetically isotropic. The mean (average) susceptibility (Kmean) of a specimen is mean value of the directional susceptibilities and is given by:

$$\text{Kmean} = \frac{\text{K1} + \text{K2} + \text{K3}}{3}$$

Another important parameter, normalized anisotropy degree (H) is obtained as follows.

$$\text{H} = \text{K1} - \text{K3}/\text{Kmean}$$

2.5.2 Magnitude of Anisotropy

The anisotropy degree (P or P2) is ratio of the maximum and minimum susceptibilities, i.e.

$$\text{P} = \text{P2} = \text{K1}/\text{K3}$$

The eccentricity of an ellipsoid can also be expressed in terms of axial ratios as follows.

P1 = K1/K2 (the ratio is also known as lineation, L)
P3 = K2/K3 (the ratio is also known as foliation, F)

It is generally accepted that in regions of strong deformation, magnetic lineation is parallel to extension direction (Kmax) and orientation of Kmin axis is parallel to shortening direction (Borradaile and Henry 1997; Housen et al. 1996; Sagnotti et al. 1994; Pares et al. 1999).

Orientation of the susceptibility ellipsoid can be determined precisely in three dimensions and orientation of the susceptibility axes can be used to infer the primary lineations (e.g. flow direction in sediments, emplacement directions in intrusive and extrusive rocks). AMS is particularly useful in characterizing soft sediment deformation (Schwehr and Tauxe 2003) as it can unravel the susceptibility ellipsoid orientation in weakly deformed sediments and rocks, where tectonic fabric has not developed (Borradaile and Henry 1997; Pares 2004). Hence the study has been used extensively for Quaternary deformation and seismotectonic studies (Sagnotti and Speranza 1993; Housen et al. 1996; Sagnotti et al. 1998; Pares et al. 1999; Lee and Angelier 2000, Borradaile and Hamilton 2004, Levi et al. 2005). These studies demonstrate that AMS is an effective tool to distinguish components of sedimentary fabric (resulting from compaction) and earthquake induced structures. Levi et al. (2006) have analyzed sedimentary and seismic origin of clastic dikes in the

Dead Sea Basin and observed that AMS can be very well used for paleoseismic records. AMS has also helped in unraveling coseismic faulting in a trenched fault zone in late Holocene sediments (Jayangondaperumal et al. 2010).

2.6 Different Types of AMS Fabrics

AMS studies in different tectonic settings and particularly in fold-and-thrust belts have described three major categories of AMS fabric types based on relationship between bedding plane and magnetic foliation plane (Sagnotti et al. 1998; Pares et al. 1999; Saint-Bezar et al. 2002; Pares 2004; Robion et al. 2007). Type 1 pattern is essentially sedimentary where the bedding and magnetic foliation are parallel with weak development of magnetic lineation. Type 2 pattern is characterized by magnetic lineation normal to shortening direction and parallel to fold hinge line while the magnetic foliation is parallel to bedding. This is also referred to as mixture of sedimentary and tectonic fabrics (Borradaile and Tarling 1981; Kissel et al. 1986). In type 3 pattern, magnetic lineation is developed perpendicular to shortening direction and bedding plane makes an angle with magnetic foliation plane (Borradaile and Henry 1997).

Later, Robion et al. (2007) have suggested six types of fabric patterns (type 1 to type VI). The sedimentary and tectonic fabrics were differentiated by the angle between mean K3 axes and pole to bedding. Type I and II are sedimentary fabric where K3 is parallel to bedding pole or the angle between K3 and the bedding pole varies from 0° to 15°. Type III corresponds to an intermediate fabric in which K3 is parallel or oblique to bedding (15°–75°). However scattering of K3 around bedding plane may indicate overprinting of tectonic fabrics. When K3 lies within bedding plane, and angle between K3 and bedding pole is greater than 75°, the fabric is described as type IV or cleavage fabric (Pares 2004). Types V and VI are characterized by scattering of K1 around K3 or well grouping of the two, normal to bedding plane. It is to be noted that in all AMS studies, especially in fold-and-thrust belts, sedimentary fabric pattern progressively change to tectonic fabric (Kissel et al. 1986; Housen and van der Pluijm 1991; Aubourg et al. 1995; Pares et al. 1999).

2.7 Plotting of Magnitude and Shape of Susceptibility Ellipsoid

Chapter 1 describes the three-dimensional plot of strain ellipsoid on a two dimensional Flinn diagram. Conceptually, plotting of the susceptibility ellipsoid shapes and their magnitudes is not much different from the Flinn plot. The axial ratios of a magnetic ellipsoid are plotted in the susceptibility plot with foliation (F = K2/K3) along the horizontal axis and lineation (L = K1/K2) along the

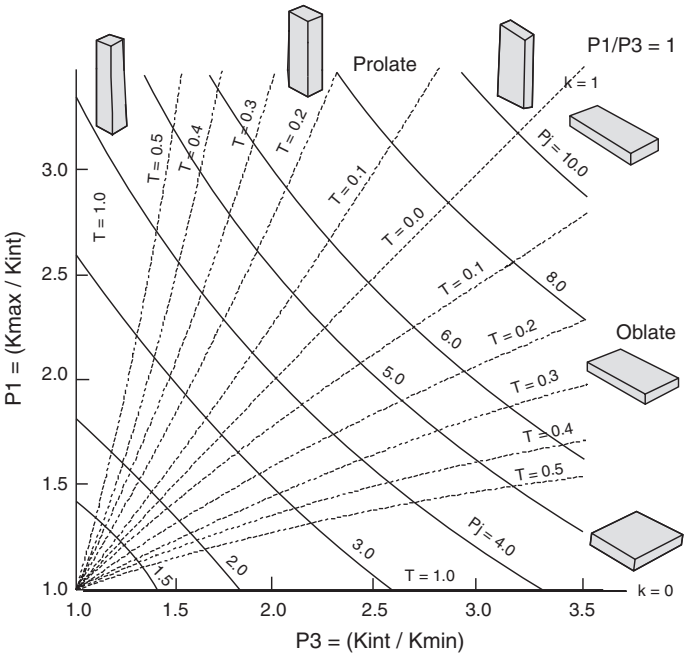

Fig. 2.4 Shapes of AMS ellipsoids in terms of anisotropy degree (Pj) [From Tarling and Hrouda (1993), © D. H. Tarling. Published with permission of D. H. Tarling]

vertical axis (Fig. 2.4). The 45° slope represents the plane strain (triaxial) ellipsoids and divides the area of oblate (disc shape) strain in the lower part and prolate (cigar shape) strain in the upper part. All the ellipsoids with increasing axial ratios plot at increasing distance from the origin.

The technique can provide some help in differentiating the fabrics developed during lithogenesis or during a subsequent tectonic event. For example, depositional or compactional loading normally results in oblate ellipsoid whereas a sheath fold (Chap. 3) reflects a prolate ellipsoid. The diagram also helps in correlation of magnetic and tectonic strains.

In case of unconsolidated sediments the following shape parameter (q) is used.

$$q = \frac{K1 - K2}{K1 + K2/2} - K3$$

The fabric is oblate when $q < 0.69$ and prolate when $q > 0.69$

The shape parameter (T) combines the lineation and foliation parameters to provide a single measure of both properties as follows.

$$T = (\ln L - \ln F/(\ln L + \ln F)$$

The shape parameter (T) has an advantage because it includes all the three principal susceptibilities in its calculation and is symmetrical in its distribution of

values over the full range of ellipsoid shapes. Oblate (disc) shape corresponds to $0 < T \leq 1$, whereas negative values, $-1 \leq T < 0$ correspond to prolate (cigar or rod) shapes (Fig. 2.4). For neutral (plane-strain) ellipsoids, $T = 0$.

The corrected anisotropy degree (Pj) (Jelinek 1981) is intrinsic anisotropy, which either reflects the degree of alignment of minerals as a function of strain intensity or magnetic mineralogy that is linear to bulk susceptibility (Km) (Borradaile 1988; Pares and van der Pluijm 2002).

The parameter can be obtained as follows.

$$\text{Ln (Pj)} = \sqrt{2((\ln K_{MAX}/k))^2 + (\ln(K_{INT}/k))^2 + (\ln(K_{MIN}/k))^2)^{1/2}}$$

The parameter Pj is based on logarithmic values of susceptibility, which are more appropriate in view of lognormal distribution of this property. Most importantly, it incorporates both the intermediate and mean susceptibilities rather than just the maximum and minimum values hence this is a more informative parameter as compared to P_2 alone.

2.7.1 Jelinek Plot (Shape Plot)

This is another two-dimensional plot for depicting the magnitude and shape of susceptibility ellipsoids where the parameters Pj and T are used (Fig. 2.5; Jelinek 1981). Pj is plotted along the horizontal axis ($1 < Pj$) and the shape parameter (T) is plotted along the vertical axis ($-1 < T < 1$). All the prolate shapes have negative values, the triaxial (plane strain ellipsoid) shapes have zero value, and the oblate shapes have positive values tending towards 1.0. Hence both magnitudes and shapes are revealed as the values are plotted linearly with distance. Thus ellipsoid pattern in an area can be observed at a glance.

In some of the minerals (e.g. tourmaline), the longer crystallographic axis (c-axis) corresponds to K3. The property is known as inverse anisotropy and such minerals cannot be used for plotting the AMS ellipsoid.

Shape of the AMS and strain ellipsoids are described in the same way as follows.

Oblate $x = y > z$
Neutral $x/y = y/z$
Prolate $x > y = z$

The above concept appears to be similar to finite strain ellipsoid but the two ellipsoids differ in the following aspects (Borradaile and Jackson 2010).

The strain ellipsoid is dimensionless (i.e. of unit volume) but represents the shapes of strained objects and quantifies these in form of an ellipsoid which can be compared in different outcrops. Strain estimation using a deformed object of known shape provides accurate measurement of strain but this strain value is representative of the object, and not of the entire rock. The matrix and the object may have undergone different amounts of shortenings depending on their rheological

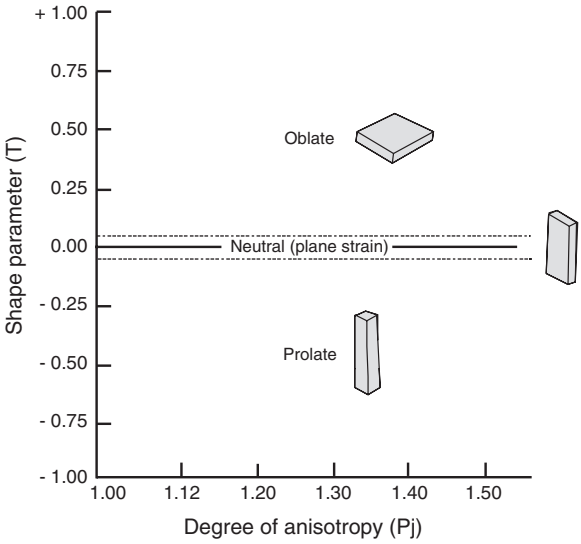

Fig. 2.5 Jelinek plot showing the relationship between degree of anisotropy, Pj, and shape parameter, T [From Tarling and Hrouda (1993), © D. H. Tarling. Published with permission of D. H. Tarling]

properties. Similarly, finite strain determined from fold shapes (unfolding of ptygmatic folds or flattened parallel folds) provide the maximum strain when measurements are made on the maximum amplitude fold with lowest interlimb angle in a competent layer. Adjacent folds with comparatively larger interlimb angles reveal lower strain values. It is also to be noted that layers of the same competence may reveal different finite strain values as a result of variation in fold geometries across a multilayer fold profile and variation in the ratio of layer parallel to buckle strain. Additional complications arise because of three-dimensional variations in fold shapes and superimposed folding (Chap. 3). On the contrary, magnitudes of AMS ellipsoids are the result of different mineral assemblages in the rock samples. Hence the AMS ellipsoid represents the anisotropy of a physical property and the mean susceptibility reveals relative AMS for different specimens obtained from different outcrops. The AMS ellipsoid is a fabric ellipsoid, which may not directly relate to strain. It should be regarded as a petrofabric tool which represents orientation distribution of all minerals and all sub-fabrics in a specimen. Magnitudes of the ellipsoid axes are properties of the state of matter and it can vary in shape and magnitude because different specimens can differ in mean susceptibility (k). However the AMS ellipsoid has an advantage over the finite (petrofabric) strain ellipsoid because it can isolate the sedimentary (depositional), tectonic, and overprint tectonic fabrics. The AMS ellipsoid combines the influence of all minerals forming the sample although the most abundant, high-k, and strongly anisotropic minerals control the rock AMS. For example, high susceptibility of the common oxides (e.g. magnetite) and sulphides of iron (e.g. pyrite) are of special significance. Some of the rocks (e.g. quartzite, limestone, tonalite, rhyolite) may reveal very low susceptibilities ($k \sim 0$ or $k < 0$ along some axes) thereby making it impossible to draw a magnitude ellipsoid. Since a rock is an aggregate

of different minerals with variable properties, for a successful AMS analysis, a sample should be sufficiently homogeneous and the grain size should not be very large. Hence the AMS ellipsoid depends on the mineral abundances and different mineral AMS (Borradaile and Jackson 2010). Further, the AMS ellipsoids can vary in shape and magnitude because of different mean susceptibility (k) in different specimens.

The AMS principal directions can be used to obtain stress and finite-strain directions from weakly deformed rocks at low temperatures. However, shape of the strain ellipsoid (magnitude of strain) is difficult to obtain because strong preferred orientations produced by stress-controlled crystallization have a maximum AMS that cannot increase with strain (Borradaile and Henry 1997). Additional problems arise at low and strong deformations. For a valid correlation between AMS magnitudes and strain it is essential that the maximum shortening is >30 % so that primary AMS fabrics (e.g. compaction during sedimentation) are obliterated. In regions of intense deformation, where the shortening is ~70 %, the mineral alignments are saturated and Pj acquires a plateau. Moreover, there are certain strain markers that are larger than the standard AMS core (e.g. lava pillows, pebbles, xenoliths, etc.). These markers reveal the grain strain and alignment but the inter-granular motion cannot be detected by AMS. These features demand that in order to have a better comparison, the same sample should be used for AMS and strain measurements because the proportions of constituent magnetic minerals may differ in different samples. The finite strain indicators reveal a sum of several increments of strain that may have acted in different directions. Thus it is possible to identify the principal strain directions but it is difficult to predict any systematic angular relationship to principal stress directions during progressive deformation (Borradaile and Henry 1997).

Anisotropy of susceptibility is controlled by crystallographic orientations of the mineral grains but is not affected by grain shape. It is also to be noted that AMS axes and crystal axes rarely show a one-to-one correspondence (Borradaile 1988). The magnitude of strain is normally less in AMS as compared to the strain.

2.7.2 Plotting of the Principal Axes

Directions of the principal axes of susceptibility ellipsoids can be plotted on equal area or equal angle stereographic projections. However, keeping the uniformity of structural plots of field data (bedding, field lineations, field foliations etc.), structural geologists prefer the lower hemisphere, equal area plots. This helps in plotting of field and magnetic data on one diagram for a quick comparison between the two. The axes of maximum, intermediate and minimum susceptibility are plotted as squares, triangles and circles, respectively (Fig. 2.6). As a normal practice all points plotted in the lower hemisphere are solid symbols but hollow, if plotted on the upper hemisphere. The minerals crystallizing in orthorhombic and tetragonal systems are easy to interpret because principal susceptibilities and crystal axes are generally

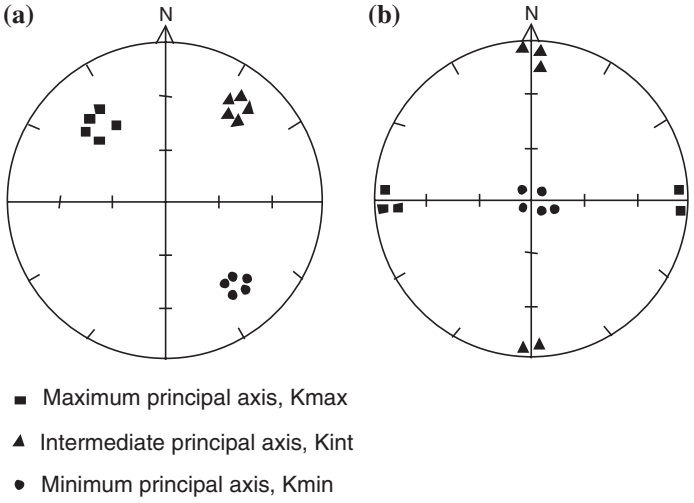

Fig. 2.6 Plotting of the three principal susceptibility axes on lower hemisphere of the equal area net. **a** All the three axes are inclined. **b** The minimum principal axis is vertical whereas the other two are horizontal

parallel. However most of the rock forming silicates are monoclinic in which only one axis corresponds to one of the principal susceptibilities. The triclinic minerals are more complicated because no susceptibility axis is parallel to a crystal axis. The precise orientations of susceptibility axes with respect to crystal axes are yet to be understood completely (Borradaile and Jackson 2010).

2.8 Hrouda Diagram

The Hrouda diagram is based on the property that platy minerals rotate and align during deformation. Initially the minerals may have random orientation (Fig. 2.7a) but with increase in simple shear, the minerals rotate and align parallel to the shear direction thereby producing a preferred orientation (Fig. 2.7b).

Thrusting in orogenic belts involves a combination of pure- and simple-shear mechanisms. The simple-shear is regarded as lying on the thrust surface and parallel to the direction of displacement under the plane-strain condition. The constituent minerals rotate and tend to align parallel to the thrust surface. The degree of alignment of minerals is proportional to magnitude of the simple shear. After the alignment, the minerals have a nearly uniform angular relationship with the thrust surface, which is normally the bedding (flat thrust). Hence a relationship can be established between orientation of constituent platy minerals (magnetic foliation), bedding and other parameters related to deformation. One such relationship was proposed by Hrouda (1991) in which angle (f) between bedding and magnetic

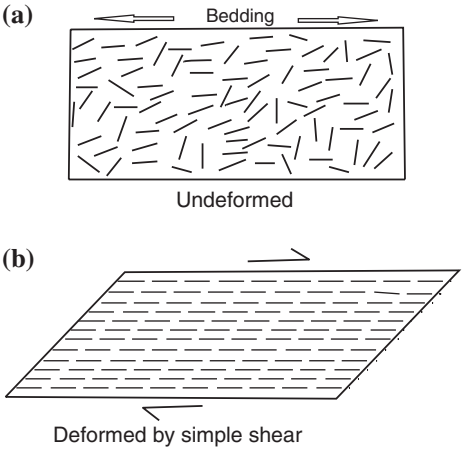

Fig. 2.7 Reorientation of platy minerals during simple shear. **a** Random orientation of platy minerals prior to deformation. **b** Alignment of the minerals parallel to the shear direction

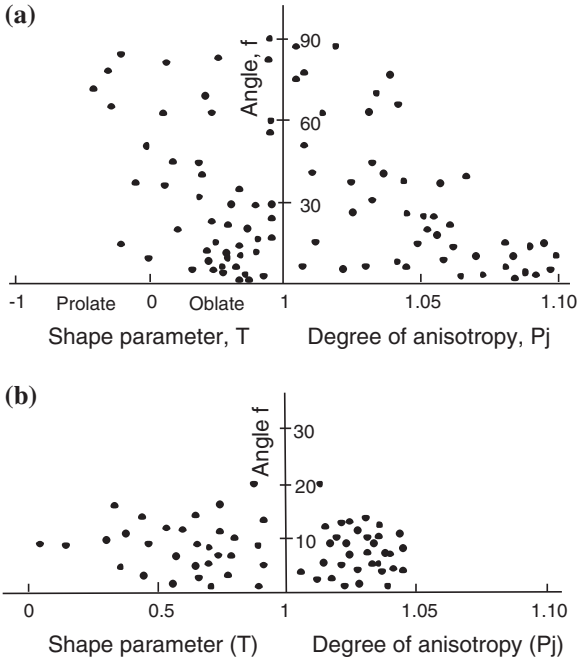

Fig. 2.8 Hrouda diagram illustrating relationships of angle between bedding and magnetic foliation, degree of anisotropy and shape parameter. **a** Weak deformation. **b** Strong deformation

foliation was plotted along the vertical axis whereas the degree of anisotropy (Pj), and shape parameter (T, oblate to plane strain to prolate) were plotted along the horizontal axis (Fig. 2.8). At the outset of deformation, the platy minerals display a random orientation and their angle with the bedding may vary from 0° to 90° (Fig. 2.8a). At large deformations, bedding and magnetic foliation tend to acquire parallelism (i.e. decreasing angle f) (Fig. 2.8b). Hence distribution pattern of different

sites can indicate the extent of deformation. The shape parameter and degree of anisotropy, though not conclusive, can suggest the intensity of deformation. A large variation of 'f' in a strongly deformed rock sequence normally indicates pure shear deformation with a large number of smaller folds.

The diagram is effective in evaluating the extent of simple shear in an area, which has undergone thrusting. However complications may arise in areas of superimposed deformation. Superposed folds (later formed folds) have their own geometries and these can affect the early relationship between bedding and foliation. In such areas it is advisable to ignore locations of superposed folds while collecting samples for construction of the diagram. The samples must be at a safe distance from superposed folds where the effect of superposed strain is minimal.

References

Aubourg C, Rochette P, Bergmuller F (1995) Composite magnetic fabric in weakly deformed black shales. Tectonophysics 87:267–278

Averbuch O, Lamotte DF, Kissel C (1992) Magnetic fabric as a structural indicator of the deformation path within a fold-thrust structure: a test case from the Corbieres (NE Pyrenees, France). J Struct Geol 14:461–474

Borradaile GJ, Hamilton T (2004) Magnetic fabrics may proxy as neotectonic stress trajectories, Polis rift, Cyprus. Tectonics 23(TC1001):1–11. doi:10.1029/2002TC001434

Borradaile GJ, Henry B (1997) Tectonic applications of magnetic susceptibility and its anisotropy. Earth Sci Rev 42:49–93

Borradaile GJ, Jackson M (2010) Structural geology, petrofabrics and magnetic fabrics (AMS, AARM, AIRM). J Struct Geol 32:1519–1551

Borradaile GJ, Tarling DH (1981) The influence of deformation mechanisms on magnetic fabric in weakly deformed rocks. Tectonophysics 77:151–168

Borradaile GJ (1988) Magnetic susceptibility, petrofabrics and strain. Tectonophysics 156:1–20

Dunlop D, Ozdemir O (1997) Rock magnetism, fundamentals and frontiers. Cambridge Studies in Magnetism, Cambridge University Press, Cambridge, p 272

Evans MA, Lewchuk MT, Elmore RD (2003) Strain partitioning of deformation mechanism in limestones: Examining the relationship of strain and anisotropy of magnetic susceptibility (AMS). J Struct Geol 25:1525–1549

Graham JW (1954) Magnetic susceptibility anisotropy, an unexploited petrofabric element. Geol Soc Am Bull 65:1257–1258

Housen BA, van der Pluijm BA (1991) Slaty cleavage development and magnetic anisotropy fabrics (AMS and ARMA). J Geophys Res 96:9937–9946

Housen BA, Tobin HJ, Labaume P, Leitch EC, Maltman AJ, Ocean Drilling Program Leg 156 Shipboard Science Party (1996) Strain decoupling across the decollement of the Barbados accretionary prism. Geology 24:127–130. doi:10.1130/0091-7613

Hrouda F (1982) Magnetic anisotropy of rocks and its application in geology and geophysics. Geophys Surv 5:37–82

Hrouda F (1991) Models of magnetic anisotropy variations in sedimentary thrust sheets. Tectonophysics 185:203–210

Hrouda F, Janak F (1976) The changes in shape of the magnetic susceptibility ellipsoid during progressive metamorphism and deformation. Tectonophysics 34:135–148

Ising G (1942) On the magnetic properties of varved clay. Arkiv for Matematik, Astronomi och Fysik 29A:1–37

Jayangondaperumal R, Dubey AK, Kumar BS, Wesnousky SK, Sangode SJ (2010) Magnetic fabrics indicating Late Quaternary seismicity in the Himalayan foothills. Int J Earth Sci 99:S265–S278. doi:10.1007/s00531-009-0494-5

Jelinek V (1981) Characterization of the magnetic fabrics of rocks. Tectonophysics 79:T63–T67

Kissel C, Barrier E, Laj C, Lee TQ (1986) Magnetic fabric in 'undeformed' marine clays from compressional zones. Tectonics 5:769–781

Lee TQ, Angelier J (2000) Tectonic significance of magnetic susceptibility fabrics in Plio-Quaternary mudstones of south-western foothills, Taiwan. Earth Planet Space 52:527–538

Levi S, Nabelek J, Yeats RS (2005) Paleomagnetism based limits on earthquake magnitudes in northwestern metropolitan Los Angeles, California, USA. Geology 33:401–404. doi:10.1130/G21190.1

Levi T, Weinberger R, Aifa T, Eyal Y, Marco S (2006) Earthquake-induced clastic dikes detected by anisotropy of magnetic susceptibility. Geology 34:69–72. doi:10.1130/G22001.1

Pares JM, van der Pluijm BA (2002) Evaluating magnetic lineations (AMS) in deformed rocks. Tectonophysics 350:283–298

Pares JM (2004) How deformed are weakly deformed mudrocks? Insights from magnetic anisotropy. In: Martin-Hernandez F, Aubourg C, Jackson M (eds) Magnetic fabrics: methods and applications, vol 238. Special Publication Geological Society of London, pp 191–203

Pares JM, van der Pluijm BA, Dinares-Turell J (1999) Evolution of magnetic fabrics during incipient deformation of mudrocks (Pyrenees, northern Spain). Tectonophysics 307:1–14

Robion P, Grelaud S, Frizon de Lamotte D (2007) Pre-folding magnetic fabrics in fold-and-thrust belts: why the apparent internal deformation of the sedimentary rocks from the Minervois Basin (NE Pyrenees, France) is so high compared to the Potwar Basin (SW Himalaya, Pakistan)? Sed Geol 196:181–200

Rochette P (1987) Magnetic susceptibility of the rock matrix related to magnetic fabric studies. J Struct Geol 9:1015–1020

Sagnotti L, Faccenna C, Funiciello R, Mattei M (1994) Magnetic fabric and structural setting of Plio-Pleistocene clayey units in an extensional regime: the Tyrrhenian margin of central Italy. J Struct Geol 16:1243–1257

Sagnotti L, Speranza F (1993) Magnetic fabric analysis of the Plio-Pleistocene clayey units of the Sant'Arcangelo Basin, southern Italy. Phys Earth Planet Inter 77:165–176

Sagnotti L, Speranza F, Winkler A, Mattei M, Funiciello R (1998) Magnetic fabric of clay sediments from the external northern Apennines (Italy). Phys Earth Planet Inter 105:73–93

Saint-Bezar B, Hebert RL, Aubourg C, Robion P, Swennen R, de Lamotte DF (2002) Magnetic fabric and petrographic investigation of hematite-bearing sandstones within ramp-related folds: examples from the South Atlas Front (Morocco). J Struct Geol 24:1507–1520

Schwehr K, Tauxe L (2003) Characterization of soft sediment deformation: detection of cryptoslumps using magnetic methods. Geology 31:203–206

Tarling DH, Hrouda F (1993) The magnetic anisotropy of rocks. Chapman & Hall, London 217 pp

Voight W, Kinoshita S (1907) Bestimmung absoluter Werte von Magnetiserungszahlen, inbesondere fur Kristalle. Annale der Physic 24:492–514

Chapter 3
Folds and Folding

Abstract Some of the basic information related to development of folds are provided, e.g. why, where, and how do they develop. Fold propagation and fold geometries resulting from interference of simultaneously developing folds are described in two and three dimensions along with causes of noncylindricity. Variations of fold geometry along the hinge line, and with depth along the axial surface are shown by natural examples. Attention is drawn to importance of culmination point along a fold hinge line. Sheath and eyed folds are described as separate entities formed by different mechanisms. Late stages in the development history of folds are explained by using deformed physical models. Significance of buckle shortening and layer parallel strain across fold profiles is highlighted. Development of boudins, normal, and thrust faults on fold limbs are discussed. The sequence of deformation suggests that the second order folds should not be described as parasitic folds because the term does not have a correct genetic implication. The chapter highlights the importance of folding in mountain building and how a clear understanding of early and superposed folding can help in resolving the complete deformation history of a region.

The compressional regime exists at converging plate margins where collision between two plates can produce gigantic mountains like the Himalaya. The effect of compression can be seen not only on large-scales but also on small scales including microscopic. The structures may have formed on different scales but they are closely related to one another provided they have formed under the same stress condition. Compressive stresses, which lead to reduction in length of layering, produce fold structures. The resulting folds present a variety of geometrical shapes. Early geologists might have found it relatively easy to explain the origin of faults in terms of mechanical breaks but without an accurate knowledge of temperature-pressure conditions inside the earth and rheology of rocks, it must have been difficult for them to imagine how hard rocks could be forced to make folded forms. With the advancement of knowledge, now we know that folds result from inhomogeneous deformation under ductile or brittle-ductile conditions and form over a period of several thousands of years. The state of strain within a folded layer cannot be determined

A. K. Dubey, *Understanding an Orogenic Belt*, Springer Geology,
DOI: 10.1007/978-3-319-05588-6_3,

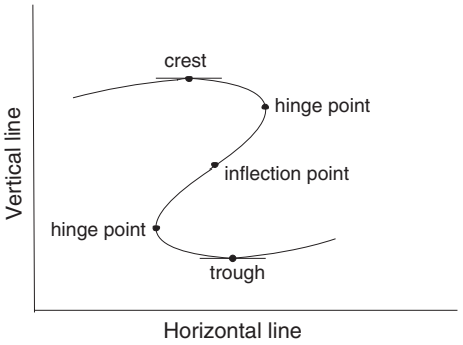

Fig. 3.1 The position of crest, trough, hinge, and inflection points on a cross section (profile) of a folded surface (after Ramsay 1967)

by the shape alone because similar shapes can arrive by different strain patterns. The magnitude of strain around a fold profile can be determined by using some objects of known initial shape but the strain rates cannot be determined. Similarly the orientation of principal stresses can be obtained from folds only when the strain is small and the mechanism of folding is known (Hudleston and Lan 1993).

The geometrical shapes of folds have been studied and an exhaustive account is provided in the available text books (e.g. Hobbs et al. 1976; Davis 1984; Ragan 1985; Ramsay and Huber 1987; Price and Cosgrove 1990). Hence only a few important aspects will be described here.

3.1 Fold Geometry

An individual fold is a departure from planarity and a group of folds normally occurs as wavy structures in practically all types of rocks. A careful study of folds requires observation and measurements in three dimensions. However it is not always possible to observe folds in three dimensions because of limited exposures or overburden of rocks. Hence most of the studies are performed in two dimensional cross-sections in cliffs, river sections, roads, rail cuttings etc. Fold shapes and their orientations can be described with the help of a few basic parameters. Some of these parameters are related to a horizontal datum whereas the others are invariant features of folds, i.e. independent of their orientation with a fixed reference frame.

A point occurring at the highest elevation with respect to horizontal and vertical datum planes is called as crest and a point at the lowest elevation is called as trough (Fig. 3.1). Curvature of fold varies along the profile and the point of maximum curvature is defined as hinge point. The limits of an individual fold is defined by inflection points where the rate of change of slope is zero (an antiform changes to a synform and vice versa).

Most of the folds have a single hinge and are described as single hinge folds (Fig. 3.2a). The line joining the successive hinge points on a fold surface is called as hinge line. Part of a fold in vicinity of hinge is generally known as

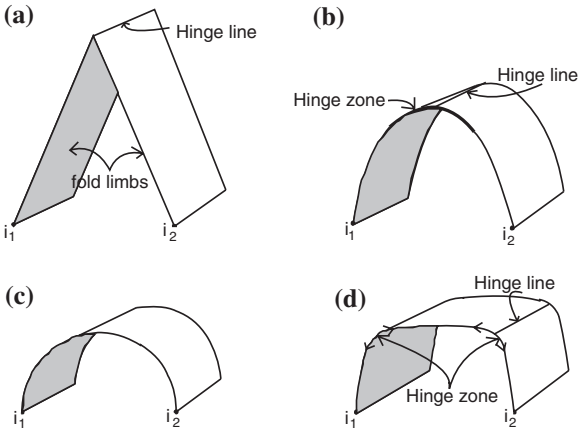

Fig. 3.2 Types of single folded surfaces based on curvature. 'i_1 i_2', inflection points (after Ramsay 1967)

hinge zone but Ramsay (1967) has provided a better definition by comparing the fold curvature to that of a circular arc drawn with i_1 i_2 (two successive inflection points) as diameter. Part of a fold surface where the curvature of fold surface exceeds that of a circular arc is hinge zone and where the curvature is less than that of the circular arc are fold limbs (Fig. 3.2b). In a special case when the fold curvature is constant (as in part of a circular arc, Fig. 3.2c), the hinge point is considered as midpoint of the circular arc. If fold curvature varies between two limbs so that it reaches two or more maxima, the fold has two or more hinge lines. These folds are called as multiple hinge folds. A fold with two hinge points is called a box fold (Fig. 3.2d).

When traced in the third dimension, crest, trough, and inflection define the crest line, trough line, and inflection line respectively (Fig. 3.3). The orientation of these lines may vary with geometry of the fold surface. A hinge line can plunge in one or two directions along the fold surface away from the crest. Such folds are called as plunging folds. A section drawn normal to the hinge line is profile section. On joining the successive positions of fold hinge lines in a profile section, a plane is derived known as axial plane, or axial surface when curved (Fig. 3.4) (Hobbs et al. 1976).

Planar fold limbs and sharp angular hinges define kinks on a small scale (microscopic to hand specimen (Fig. 3.5) and chevron folds on a larger scale. When two limbs of a kink are not equal (asymmetric kinks), a long narrow zone is formed by the successive short limbs. A zone so formed is defined as a kink band.

Conjugate and box folds have a somewhat similar geometry as both the folds are two hinge folds and the adjacent axial surfaces dip towards each other. However folds with straight limbs and sharp hinges can be described as conjugate folds (Fig. 3.6a) and folds with broad hinge zones can be classified as box folds (Fig. 3.6b). Conjugate folds normally occur in thin-bedded rocks on microscopic to outcrop-scale. The small-scale conjugate folds are described as conjugate kink folds.

In case of plunging folds, when the anticlinal fold surface is cut by erosion and the synclinal fold surface is not exposed, the line of intersection of the ground surface and the axial surface is termed trace of the axial surface or simply axial trace (Fig. 3.7).

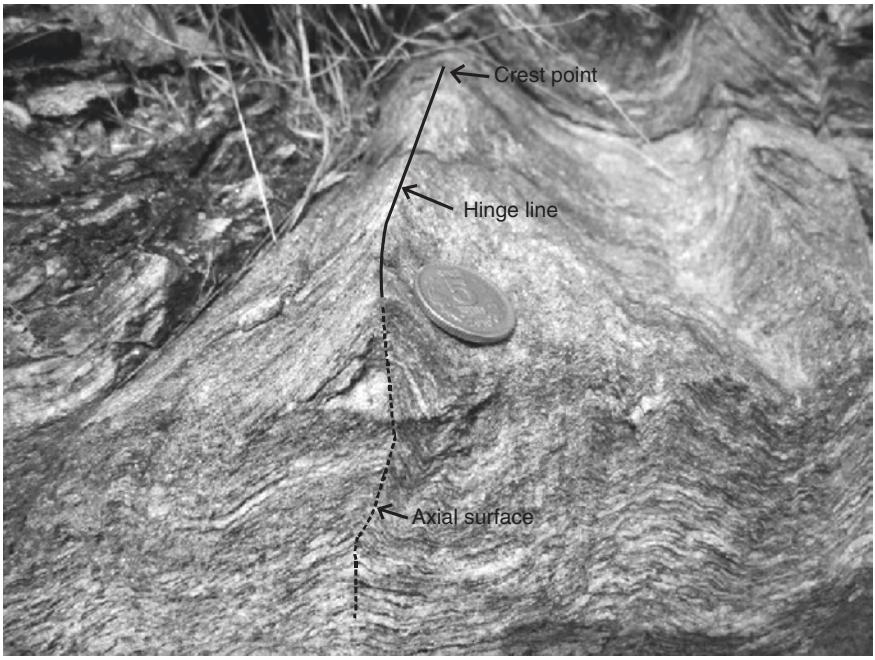

Fig. 3.3 Crest point, hinge line and axial surface of a fold (Wangtu Gneiss, Himachal High Himalaya) [from Sen et al. (2012). © Elsevier. Published with permission of Elsevier]

When considered in three dimensions, folds can be broadly classified into two categories, cylindrical and noncylindrical. A cylindrical fold (Fig. 3.8a) is a part of cylinder and its cross-sectional shape remains the same along the fold hinge line. Since the fold curvature is unchanged, the fold axis can move parallel to itself along the fold surface or the fold axis can generate the fold surface by moving parallel to itself. The noncylindrical folds are characterized by deviation from a true cylindrical geometry. For a better comprehension they can be compared to symmetrical half of a cone (Fig. 3.8b, c). These folds do not have a fold axis because of absence of a line that can move parallel to itself along the fold surface. In order to generate the fold surface, one end of the line remains fixed at the termination and the other end moves along the fold surface. Hence these folds have a hinge line but not a fold axis. Perfect cylindrical folds are extremely rare in geological horizons and the term is normally used for an approximate cylindrical geometry. Hence a structural geologist must be careful in use of the term "fold axis". The noncylindrical folds are also characterized by a point of maximum amplification along a fold hinge line called as culmination point. This definition makes culmination as an invariant feature of folds and is particularly useful in describing the noncylindrical fold geometries in sedimentary or weakly metamorphosed rocks. In sharp contrast to the ideal cylindrical folds, these folds are characterized by convergence of beds (Fig. 3.7) away from the fold culmination (normally the crest or

Fig. 3.4 Axial surface (*broken line*) of chevron folds formed in limestone and shales (Tattapani, Himachal Lower Himalaya)

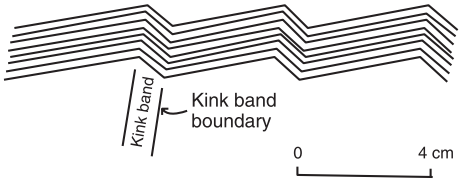

Fig. 3.5 Asymmetric kink bands

trough points). The point of convergence of folded beds is called as termination point.

Fold hinge lines need not be horizontal and the fold surface can tilt along the hinge to make it plunge. The fold plunge can vary depending on orientation of the fold surface. In case of upright folds (axial surface vertical), the plunge amount generally does not exceed 30° (Figs. 3.9a and 3.10). Large plunge amounts are characteristic of sheath or eyed folds (Fig. 3.9b, c). These two folds have similar geometry and signify an eye shape pattern of rocks when the culmination is

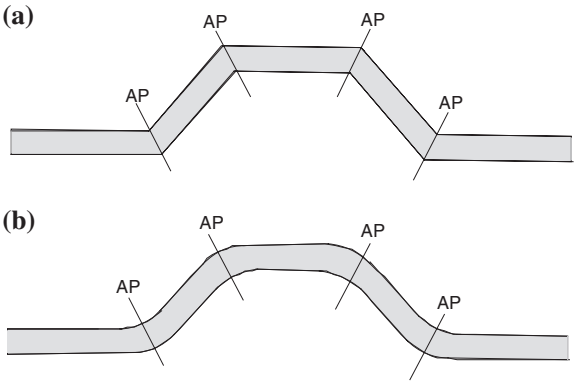

Fig. 3.6 Two hinge folds with different widths of the hinge zones. **a** Conjugate fold. **b** Box fold (*AP* axial plane)

Fig. 3.7 Axial trace of plunging syncline and anticline in graywacke and shale sequence (Bude, England). The synclinal beds are converging towards the front of the photograph and the anticlinal beds are converging towards back of the photograph

eroded (Ramsay 1962; Mukhopadhyay and Sengupta 1979) (Fig. 3.11). However these can be differentiated on the basis of their genesis. The eyed folds form as a result of extreme compression during early and superposed deformations forming a compressed dome and basin type pattern. The sheath folds are formed as a result of large shear strains normally associated with thrusting.

Sometimes more than one order of fold size exists in a single fold surface. These sizes are determined by drawing the median surfaces (i.e. lines joining the

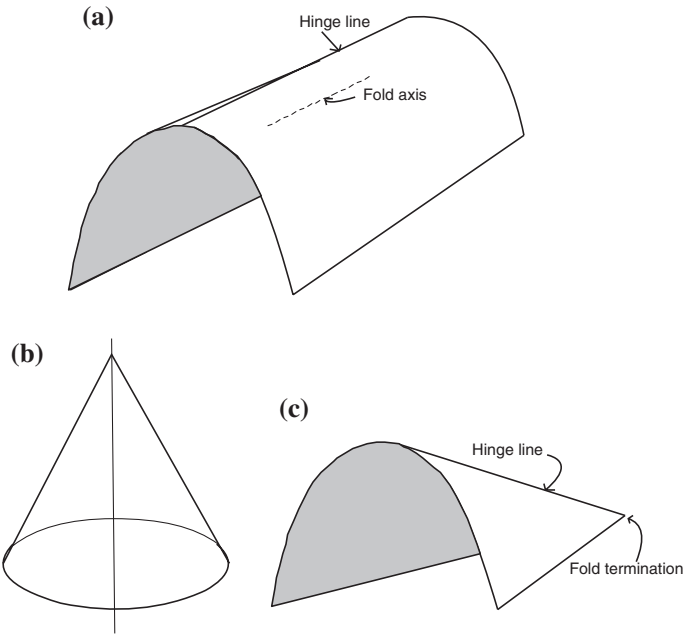

Fig. 3.8 Geometry of fold surfaces. **a** A cylindrical fold surface. **b** A conical surface to be cut in symmetrical halves along a plane shown by the *broken line*. **c** One of the symmetrical halves representing a noncylindrical fold

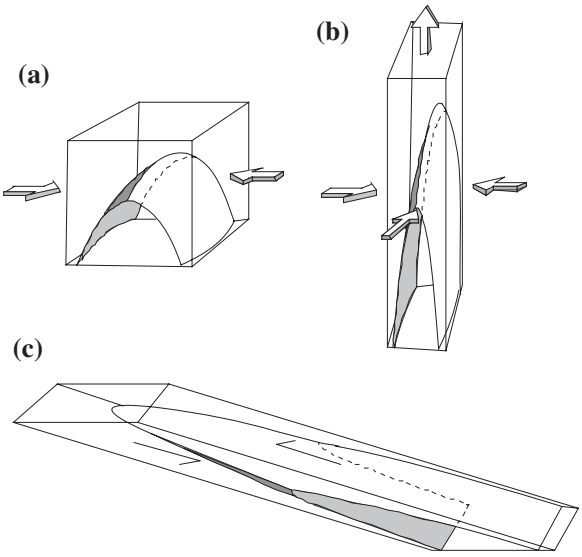

Fig. 3.9 **a** A gently plunging noncylindrical upright fold. The *arrows* indicate the axis of maximum compression. **b** An eyed fold formed as a result of compression in two *horizontal directions* and maximum extension in *vertical direction*. **c** A sheath fold formed as a result of large shear strain. The strain ellipsoid in eyed and sheath folds is essentially of prolate type (after Mukhopadhyay and Sengupta 1979; Ramsay 1980)

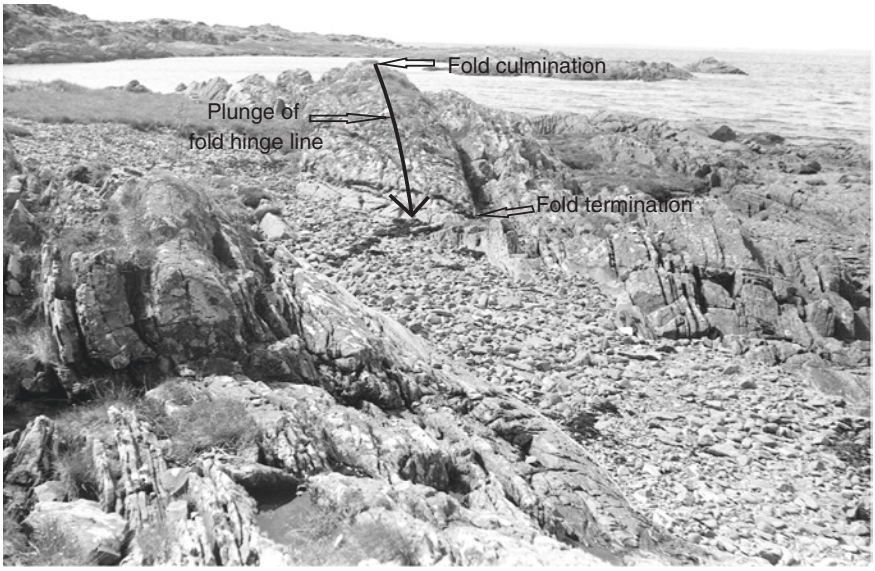

Fig. 3.10 A plunging upright anticline. The plunge direction is shown by an *arrow* (Kirkandrews Bay, Kirkcudbrightshire, Scotland)

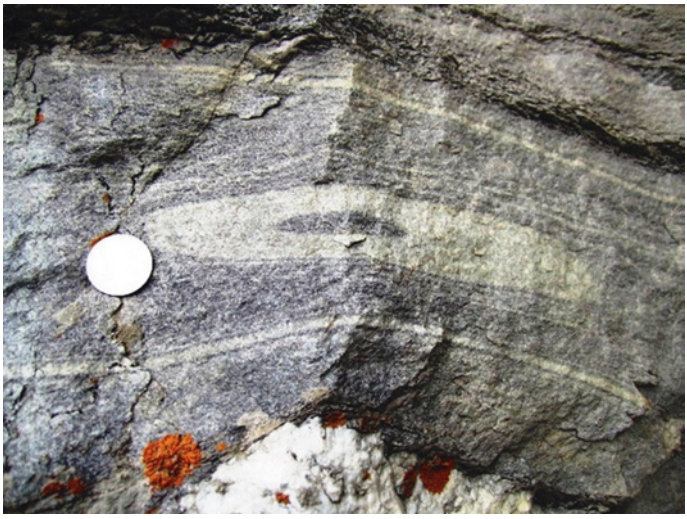

Fig. 3.11 Eroded culmination of a sheath fold in gneissic rock (Sangla valley, Himachal High Himalaya). The fold has formed as a result of large shear strain along the Vaikrita thrust [from Sen et al. (2012). © Elsevier. Published with permission of Elsevier]

successive inflection points) of different fold forms. If these median surfaces are folded, the amplitude and wavelength for that order of fold wave is determined. For example, two fold sizes are present in Fig. 3.12 and the fold is a second order fold. Depending on the number of fold waves present, the fold can be a third order fold.

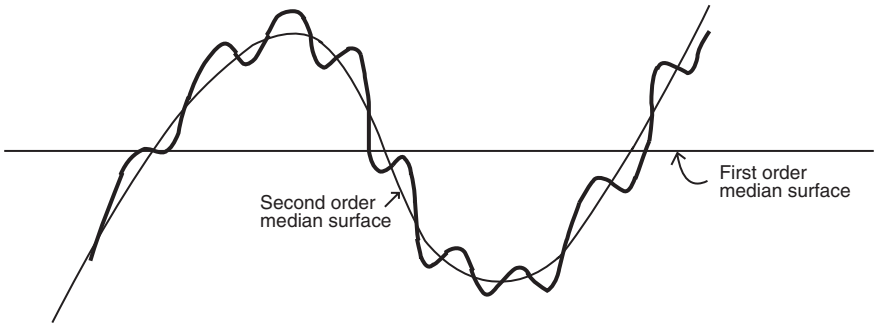

Fig. 3.12 First order (*large wavelength*) and second order (*small wavelength*) folds derived from curvature of the median surfaces (after Ramsay 1967)

3.2 Fold Classification

One of the most widely used classification of folds is based on geographic orientation of axial surface and hinge line (Fig. 3.13; Table 3.1). The classification can explain the attitude of folds in their natural occurrence.

Fleuty (1964) has suggested another fold classification essentially based on fold interlimb angles (Fig. 3.14; Table 3.2).

The classification holds good for single layers although geometrical variations can exist in the outer and inner fold arcs in a single layer. Moreover, different layers in a multilayer fold sequence can provide a variety of fold interlimb angles and width of hinge zones along the axial surface (Fig. 3.15).

The geometry of inner and outer single folded layers can be better expressed by using the dip isogon classification (Ramsay 1967). The dip isogons are lines of the same slope (equal dip) on adjacent fold surfaces in a profile section. These isogons are drawn on a fold profile and the resulting pattern falls in one of the categories shown in Fig. 3.16.

3.2.1 Class 1, Convergent

Curvature of the inner fold arc exceeds that of the outer arc and the dip isogons converge towards the fold axial surface when followed from the outer to the inner arc. The folds can be subdivided into three sub classes depending on the degree of convergence of the dip isogons; strongly convergent (class 1A), moderately convergent (class 1B) and weakly convergent (class 1C). Class 1A is characterized by small orthogonal thickness of the folded layer at the hinge as compared to the fold limbs. Class 1B is also called as parallel folds because the layer maintains a constant orthogonal thickness throughout the fold profile, and the dip isogons are always perpendicular to the fold surface. In class 1C folds, the orthogonal thickness of the folded layer at the hinge is more as compared to the fold limbs.

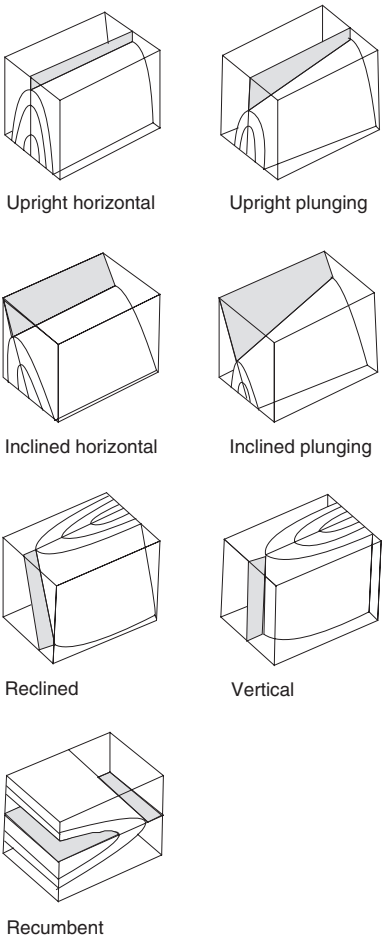

Fig. 3.13 Fold classification based on orientation of fold hinge line and axial surface (after Fleuty 1964; Hobbs et al. 1976). The axial surface is marked in *gray*

Table 3.1 Classification of cylindrical folds based on orientation (after Turner and Weiss 1963)

Orientation of axial surface	Orientation of fold hinge line		
	Horizontal	Plunging	Vertical
Vertical	Upright horizontal	Upright plunging	Vertical
Dipping	Inclined horizontal	Inclined plunging (strike of axial plane oblique to trend of fold hinge line)	
		Reclined (strike of axial plane perpendicular to trend of fold hinge line)	
Horizontal	Recumbent		

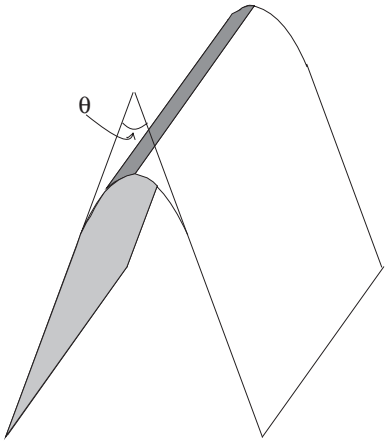

Fig. 3.14 The interlimb angle (θ) of a fold

Table 3.2 Fold classification based on interlimb angles (after Fleuty 1964)

Description of fold	Angle (in degrees) between surface inclinations measured at the two inflection points
Gentle	180 to 120
Open	120 to 70
Close	70 to 30
Tight	30 to 0
Isoclinal	0
Elasticas	Negative value (mushroom shaped)

3.2.2 Class 2, Folds with Parallel Isogons (Similar)

Fold curvatures and the geometrical forms of the outer and inner arcs are identical thereby resulting in parallel dip isogons. Orthogonal layer thickness at the hinge is greater than the thickness at limbs.

3.2.3 Class 3, Divergent

In contrast to class 1, these folds are characterized by a greater curvature of the outer arc as compared to the inner arc. The dip isogons are divergent from the axial surface when traced from the outer to the inner arc. The hinge zone is thicker as compared to the fold limbs.

It is commonly observed that class 1 folds are developed in more competent layers and class 2 and 3 in less competent layers in a multilayer sequence.

Fig. 3.15 Multilayer folds in greywacke and shale sequence of rocks showing different interlimb angles along the axial surface (Bude, North Cornwall, England)

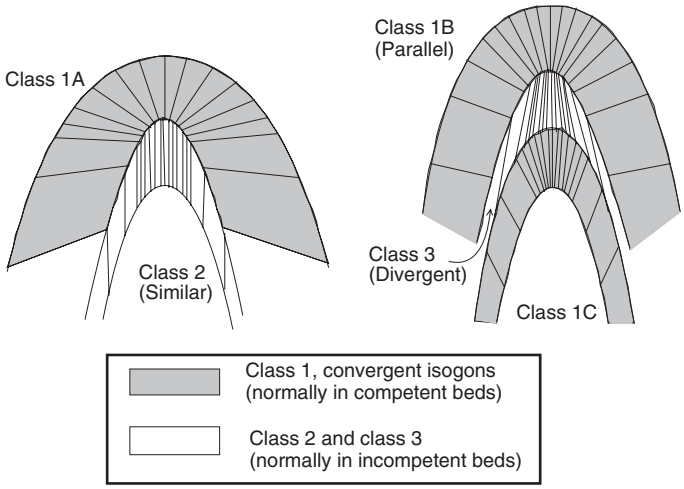

Fig. 3.16 Dip isogon classification of folds (after Ramsay 1967)

3.3 Why Folds Develop

One of the main obstacles, which geologists face in understanding the evolution of fold forms is that it is impossible to observe the formation of folds in their natural environment. Most folds are formed a few kilometers beneath the surface of the

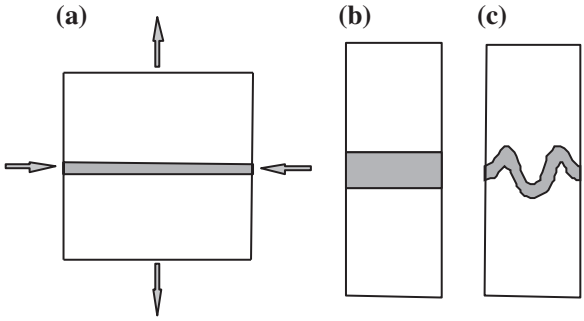

Fig. 3.17 Deformation pattern of a layer embedded in a matrix. **a** An undeformed layer. The *arrows* indicate the stress directions. **b** Homogeneous or layer parallel shortening. **c** Inhomogeneous or buckle shortening

earth, probably over a time scale of 10^5 years and it will always be impossible to observe the natural processes during their course of evolution. Hence geologists have to adopt some indirect approaches to understand the mechanism of fold formation. Such an approach should be practicable and quick to deliver reliable results. One such method was evolved by Hubbert (1937) in his classic work of theory of scale modeling of natural geologic structures. The theory is based on the assumption that two massive bodies can be geometrically and kinematically similar only provided the masses of the one, point by point are proportional to the corresponding masses of the other and that the corresponding forces point by point have the same directions and proportional magnitudes. The modeling approach has formed the basis of most of the studies performed to understand the evolution of folds. The model materials mostly used are modeling clay, Painters putty, silicone putty (Ramberg 1967), Plasticine (McClay 1976), sand (McClay 1989; McClay and Buchanan 1992), wax (Cobbold 1975), Gelatin (Johnson 1977), rubber strip in gelatin (Currie et al. 1962), sand, silicone putty and golden syrup (Davy and Cobbold 1991).

It is a common site in areas of weak and moderate deformations to observe folding in competent layers (e.g. limestone, quartzite) and absence of folding in less competent layers although all the layers have undergone the same deformation. The phenomenon can be explained in terms of homogeneous and inhomogeneous shortenings. When a single layer embedded in host is compressed parallel to the layering, it may reveal either homogeneous shortening (layer parallel shortening or layer thickening) or buckle shortening (heterogeneous shortening leading to folding) (Fig. 3.17). The homogeneous shortening takes place when competence contrast between the layer and the host is nil or minimal, whereas a large competence contrast results in prominent folds.

The ratio of buckle shortening to layer parallel strain can vary in a multilayer sequence and the maximum ratio is observed in layers with better amplification of buckle folds. As a result of variation of layer parallel strain in different layers in a folded sequence, primary lineations present in the layers (e.g. sedimentary structures indicative of current direction, magmatic lineation showing flow direction) can reveal different orientations after deformation. The maximum rotation of lineation will be observed in a layer, which has undergone the maximum amount of layer parallel strain. Figure 3.18 shows an undeformed layer marked with

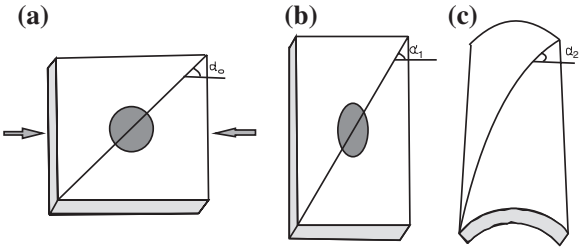

Fig. 3.18 Rotation of a primary lineation during deformation. **a** An undeformed layer with a lineation oriented at an angle α_0 to the axis of maximum compression (shown by *arrows*) **b** Homogeneous layer parallel shortening resulting in rotation of the lineation to a new orientation α_1. The shortening is shown by a strain *ellipse*. **c** Folding of the layer along with the lineation resulting in further change in the angle from α_1 to α_2. A simple unfolding of the layer cannot reveal the initial orientation of the lineation (α_0) [from Ghosh (1974). © Elsevier. Published with permission of Elsevier]

primary lineation oriented at an angle α_0 (Fig. 3.18a). A subsequent layer parallel compression resulting in homogeneous shortening with decrease in the length of the layer and increase in the thickness will change the initial angle α_0 to α_1 (Fig. 3.18b). The layer is subsequently folded (Fig. 3.18c) by a combination of layer parallel strain and buckle shortening when α_1 changes to α_2. Now, a simple unfolding of the layer (e.g. using a stereographic net; Chap. 5 in Ragan 1985) cannot reveal the initial angle (α_0). The initial orientation of the lineation can be determined only if an accurate knowledge of the layer parallel and buckle strains are known. This also leads to a conclusion that a multilayer sequence with different competence contrast of the layers will unravel different initial orientations of an early primary lineation.

3.4 Selection of Wavelength

When compressive stress acts parallel to an initially planar layer, the result may be departure from planarity and decrease in length of the layer measured in the direction of the compressive stress. The phenomenon is called as buckling (Bayly 1971). This simple (mechanical) definition of buckling does not involve any kinematic specifications (e.g. pattern of layer parallel slip or shapes of strain ellipses, mechanism of stress). After initiation of buckling, the layer quickly acquires a wavy form. The earlier work on the initial wavelength of folds was done by Biot (1961), and Currie et al. (1962) who discussed the development of wavelength in elastic layers when compressed along its length. Biot (1961) has considered an elastic plate surrounded by a viscous material and subjected to an axial load F. The plate develops a wavelength W, which is independent of viscosity of the surrounding material, and its value is given by:

$$W = \pi h \sqrt{E \Big/ \left(1 - v^2\right) F}$$

where

h Thickness of the elastic plate,
E Young's modulus of the plate, and
v Poison's ratio for the elastic material

Natural rocks may have some elastic properties but these tend to be overshadowed by viscous properties during folding processes (Biot 1961; Ramberg 1964). Hence the concept was extended to visco-elastic and viscous materials (details in Ramsay 1967; Ramsay and Huber 1987). Some simple assumptions were made in these calculations, e.g. (1) the deformation is plane strain with no volume change (2) the material is isotropic (3) the relationship between stress and strain (or strain rate) is linear, and (4) the effects of inertial or gravitational forces and homogeneous shortening, which accompanied buckling are negligible.

Bearing in mind the limitations, which these assumptions impose on natural geological situations, the results appear to be applicable to natural rocks. Ramsay (1967) has summarized the results of these theoretical studies and discussed their applicability to behaviour of natural rocks deforming as fluids with very high viscosities (10^{17} to 10^{22} poises).

Biot (1964) and Ramberg (1964) have shown that compressive stresses lead to initiation of buckling instabilities with several wavelengths. The rate of development of one is faster than the rest, and this wavelength is termed as the dominant wavelength. Both Biot and Ramberg have derived the following equation for the dominant wavelength, W_d.

$$W_d = 2\pi\, t \sqrt[3]{\mu_1/6\mu_2}$$

Where μ_1 is the viscosity of the layer of thickness t, enclosed in a less viscous medium of viscosity μ_2. The equation shows that the wavelength is proportional to thickness of the layer and viscosity contrast between the layer and the matrix (Fig. 3.19). When μ_1 and μ_2 are equal, the values of W_d/t are less than 5 and no folds can develop in such a situation (Ramsay 1967). This equation is different from the one describing the behaviour of elastic layers because the dominant wavelength in a viscous layer is independent of compressive load and the strain rate. Since the wavelength is independent of the strain rate no such estimates can be made with wavelengths of natural folds.

The concept of dominant wavelength in multilayer situations was also investigated by Biot (1961) and Ramberg (1964). Biot (1961) has shown that if the interlayer boundaries are allowed to slip than the dominant wavelength is larger by a factor $n^{1/3}$

$$W_d = 2\pi\, t \sqrt[3]{n\mu_1}/6\mu_2$$

where n is the number of competent layers.

Sherwin and Chapple (1968) and Hudleston (1973) took account of the initial layer shortening, which may occur before well marked folds begin to form, and Hudleston modified the initial Biot-Ramberg equation to the following form

$$W_d = 2\pi t \sqrt[3]{n\mu_1(s-1)}/6\mu_2\, 2S^2$$

Fig. 3.19 A larger fold wavelength in the competent thick quartzite bed and smaller wavelengths in the incompetent thin mica schist layers (Munsiari Formation, Jakhri, Himachal High Himalaya)

where $S = \lambda_1/\lambda_3$; λ_1 and λ_3 being principal quadratic elongations for the total finite bulk strain.

Initially it was pointed out by Biot (1961) that in order to have clear-cut folding, the viscosity of the layer should be 100 times more than the viscosity of the matrix. Later, Hudleston (1973) developed prominent folds in a single layer where the viscosity contrast was between 10 and 100. However the relationship holds well when cohesion between the layer and the host is strong. In case of multilayers with weak interlayer boundaries, the individual layers slip over one another (flexural-slip mechanism) resulting in development of folds even without any competence contrast between the layers and the matrix.

Ramberg (1964) compared the amounts of fold buckling and initial homogeneous layer shortening in models with layers of different viscosities and found out that layers of differing viscosities had different amounts of initial shortening before folds began strong amplification. Such a phenomenon in natural rock strata might give a wrong impression that the amount of shortening is different in each layer.

An important factor that controls the initiation of folds is presence of irregularities on the layer surface. It was observed in experiments, performed with physical models, that folding initiates either from a compositional irregularity in the layer or irregularity in the stress field. Once folding initiates, it quickly amplifies with increase in shortening (Cobbold 1975; Dubey and Cobbold 1977). An additional factor regarding the initiation and amplification of folds is the imposed boundary condition. The different conditions of bulk deformation can lead to different ratios of bulk shortening to layer parallel strain (Ghosh 1974). It was observed in experiments that with similar composition, thickness, and number of layers, when the

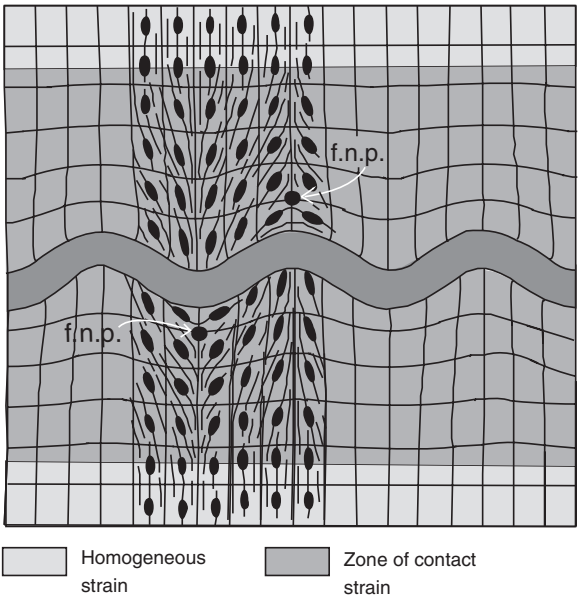

Fig. 3.20 Zone of contact strain and homogeneous strain associated with development of a single buckled layer. F.n.p., finite neutral point where the finite strains are zero (after Ramsay 1967)

direction of maximum extension is parallel to the fold axial surface and normal to hinge, fold initiation takes place at an early stage of deformation (3–10 % overall shortening). However when the direction of maximum extension is parallel to the fold hinge lines, fold initiate between 12–19 % overall shortening. Hence the ratio is less when the direction of maximum extension is parallel to the fold hinge line and more when the direction of maximum extension is perpendicular to the hinge line and parallel to the axial surface.

3.5 Zone of Contact Strain

Amplification of folds in a competent layer affects the enclosing matrix and produces a characteristic strain pattern. The axes of principal extensional strain converge towards synclinal folds and diverge above antiformal folds (Fig. 3.20) (Ramsay 1967).

The variation in orientation of the strain ellipses is reflected in orientation of slaty cleavage or schistosity, which is divergent in the competent host above an antiform. The variation in strain pattern (inhomogeneous shortening) can be observed above (and below) the fold complex only for a certain distance known as the zone of contact strain. The zone is overlain by homogeneous strain pattern. Ramberg (1961) investigated with model experiments, width of the zone of contact strain, which develops in matrix during buckling of a single competent layer. The effect of contact strain was found to be negligible outside a zone about one initial wavelength wide on either side of the folded layer.

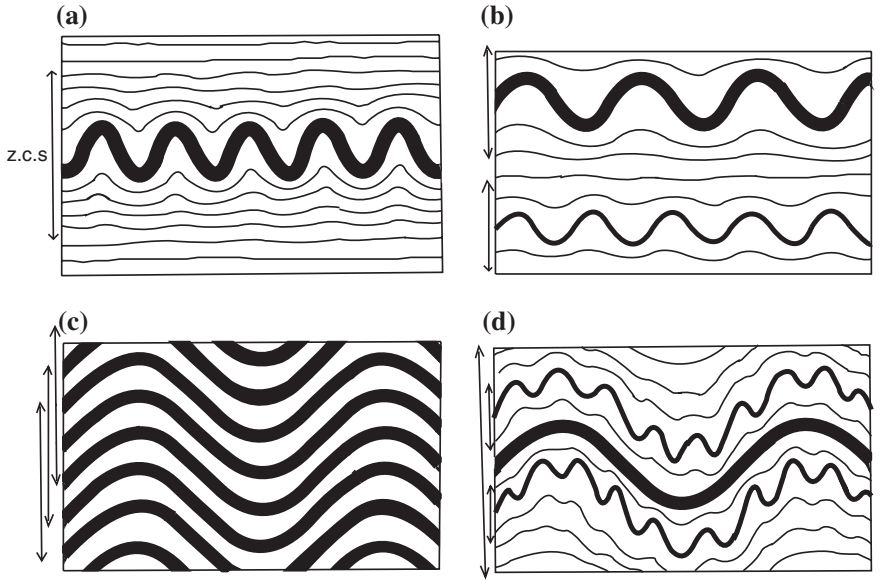

Fig. 3.21 Development of different types of fold patterns based on the interactions of the zones of contact strain (*z.c.s*). *Black* competent layer; *white* incompetent layer [from Ramsay and Huber (1987). © Elsevier. Published with permission of Elsevier]

3.6 Development of Multilayer Folds

Development of multilayer folds is a bit complex process because a variety of fold geometries can result from variation in number and thickness of layers in the multilayer packet, viscosity contrast between individual layers and layers and matrix, and distance between comparatively stiff layers. Another important factor is the zone of contact strain developed around a competent layer. For example, when a competent layer is enclosed in an incompetent host, folds may develop in the competent layer whereas the incompetent host in the zone of contact strain may reveal gradually decreasing deflections with increasing distance from the folds (Fig. 3.21a). When two competent layers (may be of differing thicknesses) are outside the zone of contact strain of each other, the resulting folds will not have a similar periodic structure and wave forms. Since the two waves are not in harmony, the folds are disharmonic (Fig. 3.21b). Competent layers of uniform thickness and viscosity spaced uniformly in a multilayer sequence will form harmonic folding (Fig. 3.21c). When a single thin layer (or layers) is placed in the zone of contact strain of a thick layer, polyharmonic folds (with more than one wavelength) develop (Fig. 3.21d) (Ramberg 1961).

The development of folds in single and multilayers with different rheological properties was very well reviewed by Hudleston and Treagus (2010) (Fig. 3.22).

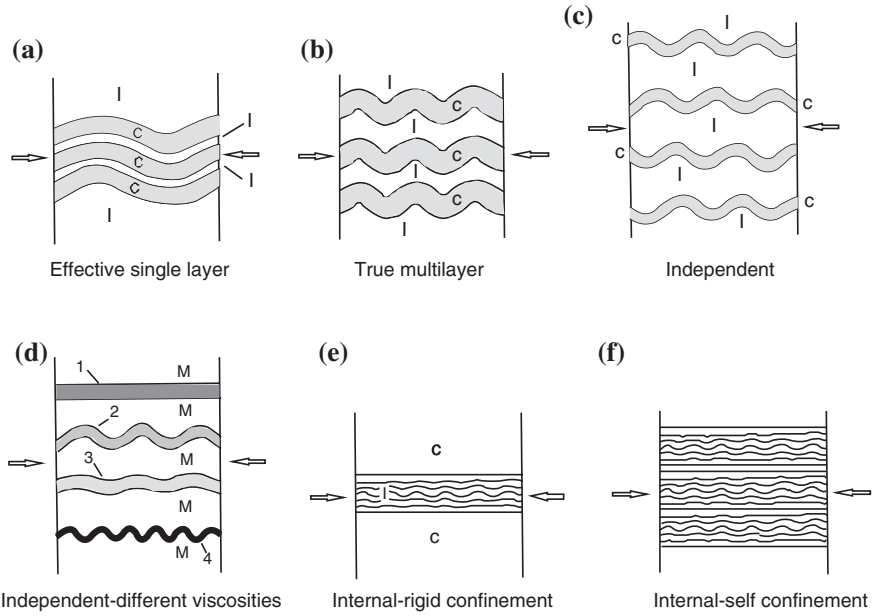

Fig. 3.22 Different fold geometries in deformed multilayer sequences [from Hudleston and Treagus (2010). © Elsevier. Published with permission of Elsevier]

The described geometries were the result of theoretical and experimental works but such folds are quite common in naturally deformed rocks. When stiff layers (high viscosity) of the same viscosity (C in Fig. 3.22a) and thickness are closely spaced in a matrix of lower viscosity, all the layers show harmonic folding or effective single layer. An increase in spacing between these competent layers may result in different fold geometries where the stiff layers show class 1B and the incompetent layers (I in Fig. 3.22b) show class 3 geometries. The structure was termed as true multilayer behavior. Further increase of spacing between the stiff layers where the spacing is greater than the single layer dominant wavelength (i.e. outside the zone of contact strain), the individual competent layers fold as independent units (Fig. 3.22c). The resulting folds have the same dominant wavelength but the overall multilayer fold geometry is that of disharmonic type. Layers with different viscosities fold in different ways. Layers with the minimum viscosity show the maximum layer parallel shortening whereas a layer with the maximum viscosity will show the maximum buckle shortening (Fig. 3.22d). Layer 4 with the minimum thickness shows the smallest wavelength. A multilayer packet with comparatively thin layers with easy lubrication may show initiation of folding in a layer. The folds gradually propagate along the layering (Cobbold 1976). However during the initial stages of development, the folds describe the internal buckle shortening (Fig. 3.22e). Simultaneous initiation of folds in different layers may result in "internal self confinement" (Fig. 3.22f).

3.7 Development of Sinusoidal Buckles in Experiments

Mathematical theories of development of dominant wavelength in layers apply only to first few increments of deformation. Numerical methods have been used to describe the development of folds in large deformations (e.g. up to 77.7 % overall shortening; Dietrich 1970) but the results do not explain; (1) development of boudins in competent layers, extension faults in incompetent layers, limb thinning, hinge thickening, hinge dilation, limb thrusts etc., and (2) development of conjugate set of cross-cutting thrusts at late stages of folding. Hence model deformation studies were employed to understand structural features especially that develop at late stages of fold formation (Dubey 1980). These models were deformed under controlled boundary conditions using specially designed equipments. Plasticine was chosen in many of the experiments as model material because its rheological properties are similar to rock when considered at the scale of the model (McClay 1976). It also provides the following advantages over other model materials such as gelatin, wax or putty.

1. The construction of multilayer models is simple and does not need any elaborate instruments. Interlayer slip during folding can be facilitated by dusting the layer contacts with talc powder. The interior of the model can be observed by cutting the model using a thin wire or nylon thread. Strain studies can be performed by embossing an orthogonal grid pattern on the layer surface or in the cross-section, using a serrated roller.
2. The experiments are performed at room temperature and the deformed models can be kept for a few years without deterioration or shape change.
3. It is possible to take out a deformed model from the press, expose the interior, take a photograph, and then reassemble the model for further shortening.
4. Painter's putty or petroleum jelly can be mixed up in an appropriate amount for change in viscosity.

3.7.1 Construction of Multilayer Plasticine/Modeling Clay Models

Individual layers are made by rolling or extruding Plasticine between two plates to the required uniform thickness. All surfaces can be coated with talc powder to reduce interlayer friction and the layers were then stacked loosely together to form a multilayer unit with planar layering. The initial planarity can be deliberately disturbed by introducing deflections in the layering in the following way. With half the total number of layers stacked together, a shaped object is pressed into the surface of the uppermost layer. The resulting deflection is transmitted to all the underlying layers, but with the deflection amplitude decreasing downwards. The remaining layers are then pressed lightly into position one by one, in such a way as to leave no gaps until the multilayer is complete. Finally, the multilayer unit can be sandwiched between two thick slabs of lower competence.

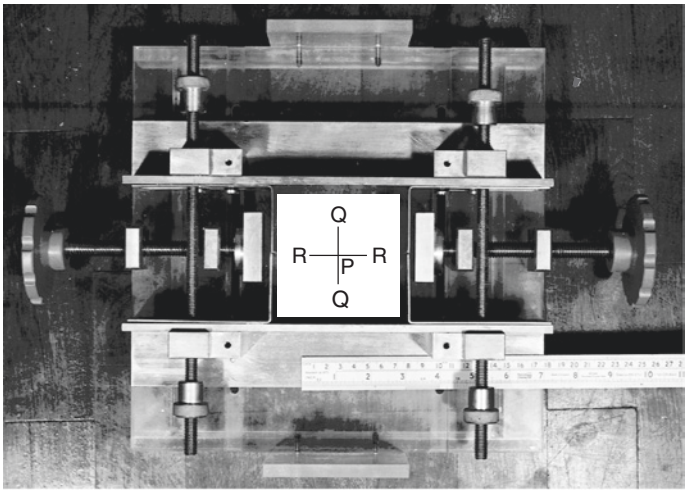

Fig. 3.23 The biaxial press used for model deformation. *R* axis of maximum compression; *P* vertical axis of the press

3.7.2 Biaxial Press

The models are normally deformed in a simple press (e.g. Fig. 3.23; Cobbold et al. 1971). The internal plates of the press act as planar boundaries and these are lubricated by petroleum jelly to minimize frictional effects. The layering before deformation can be either vertical (PR plane) or horizontal (QR plane). Vertical layering facilitates study of evolution of folds in profile sections. Progressive deformation is continuously photographed or a video is prepared through the top Perspex plate for a complete sequence of deformation. The model is shortened along R using hand operated or mechanical screws fitted with step down gears and it is allowed to extend along Q or P under the plane strain boundary condition or in both the directions under the general strain boundary condition. The deformation is affected in stages when the layering is horizontal to allow internal examination of the models. After each deformation stage the model is removed carefully from the press and photographs taken of the fold profiles at the model boundaries and of the layer surfaces after removing the top thick slab. The model can then be replaced in the press for the next stage of deformation. The deformation can thus be studied in stages. The layering can be positioned in an inclined manner for study of compression oblique to the layering.

At the end of an experiment, a series of cross-sections can be observed by cutting the model with a thin wire of high tensile strength. The technique produces very clean and planar cuts in Plasticine and modeling clay models.

An important work on initiation of buckle folds was done by Cobbold (1975) by performing experiments with single layer paraffin wax models (Fig. 3.24). When the layer was compressed along the layering (Fig. 3.24a), folding initiated at a central heterogeneity (marked deliberately) producing an antiform.

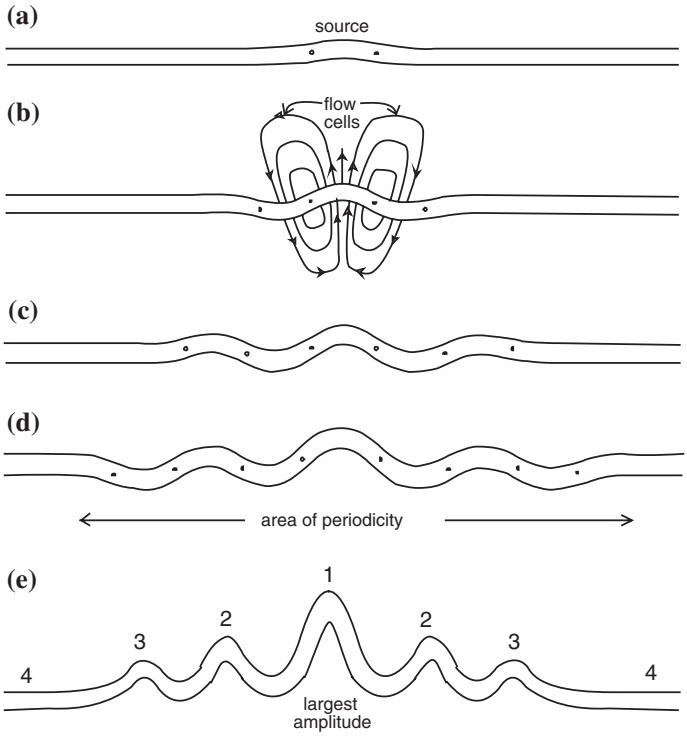

Fig. 3.24 Lateral spreading of folds as transverse fold propagation. The minimum interlimb angle is observed at the largest amplitude fold initiated at the initial irregularity [from Cobbold (1975). © Elsevier. Published with permission of Elsevier]

Amplification of the fold was accompanied by two flanking synforms (Fig. 3.24b). These three folds then continued to amplify causing a cell like flow of adjacent particles in the matrix. With the amplification of the synforms, new antiforms developed on their flanks (Fig. 3.24c) triggering initiation of new flow cells. The process repeats itself in time and space resulting in serial appearance of new folds and their propagation along the layering (Fig. 3.24d). The minimum interlimb angle was observed at the initial irregularity fold. Fold propagation in which lateral spreading of a fold takes place as a periodic structure is called as transverse fold propagation. The concept of fold propagation is important because it explains as to why fold interlimb angles vary in a single fold complex (Fig. 3.24e).

Cobbold (1976) has described fold history in four stages (Fig. 3.25). The first stage, nucleation, consists of initiation of a fold from an irregularity. The fold amplifies with increase in deformation followed by propagation along the layer and across the multilayer sequence. The growth involves amplification or active buckling till the stage of rotation hardening (fold locking) is acquired at small interlimb angles. All the folds do not acquire low interlimb angles and consequent rotation hardening at one instant of deformation. Further deformation leads to

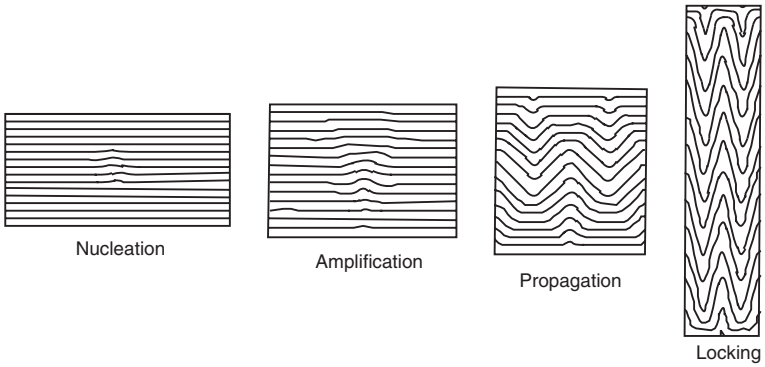

Fig. 3.25 Evolution history of folds [from Cobbold (1976). © Royal Society of London. Published with permission of Royal Society of London]

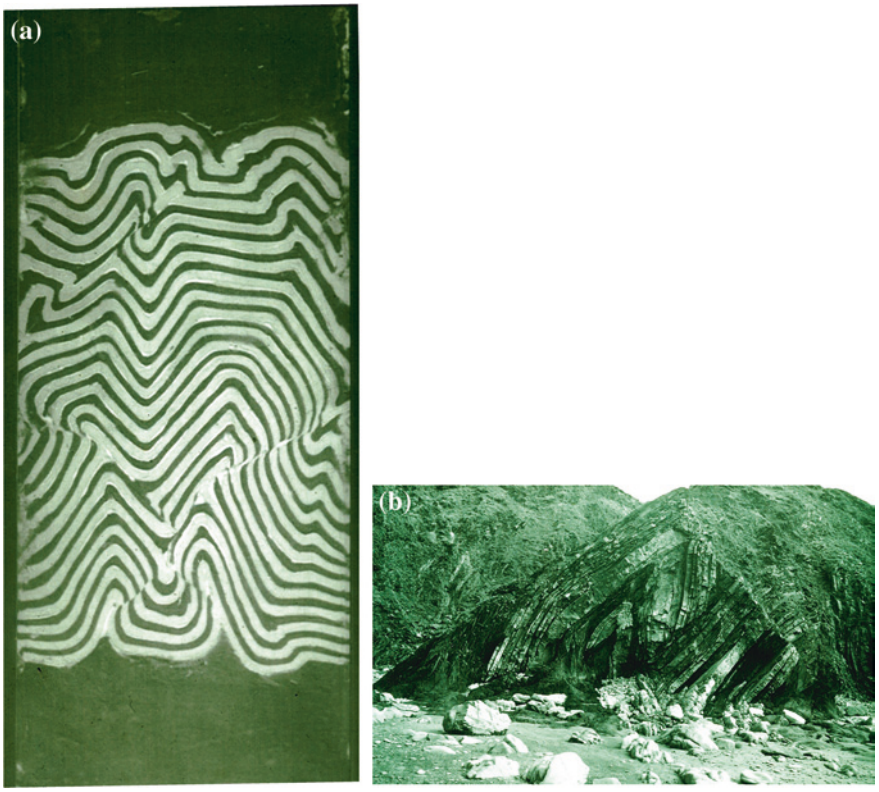

Fig. 3.26 Development of thrust faults at a late stage of folding when the axis of maximum extension remains parallel to the axial surface of the folds, normal to the hinge. **a** A deformed Plasticine model showing conjugate set of thrust faults developed in a multilayer sequence of chevron folds. Hinge dilation, limb thinning and hinge thickening have also developed in the sequence (after Dubey and Behzadi 1981). **b** A chevron fold sequence cut by thrust faults (Bude, England)

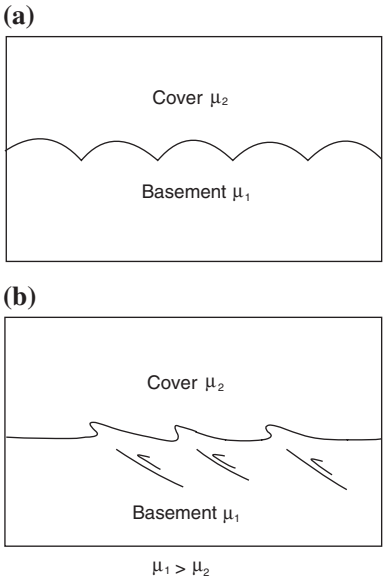

Fig. 3.27 Fold shapes at the contact of contrasting viscosities. The basement has a higher viscosity. **a** Broad antiforms and pinched synforms as a result of buckling. The pinched fold forms point towards the higher viscosity. **b** Pinched asymmetric antiforms (fault propagation folds) as a result of propagation of thrust faults

flattening followed by initiation and development of thrust faults (when the axis of maximum extension is parallel to the axial surface and normal to hinge (Fig. 3.26) or development of conjugate set of strike-slip faults (when the axis of maximum extension is parallel to the fold hinge line). Once thrusting or strike-slip faulting initiates in the multilayer system, growth of the folds ceases and folds with large interlimb angles also acquire stable fold geometry.

Ghosh (1993) has described three stages of buckle folding, i.e. nucleation, amplification, and kinematic growth. Treagus (1997) described the three stages as initial layer parallel shortening, active buckling and late fold flattening. The ratio of the three may differ with number of layers, their rheological properties and conditions of deformation.

It was observed in experiments that when interface separating materials of different viscosities is shortened, the deformation of the contact initially produces a series of wavy forms, the wavelength of which depends on viscosity ratio on the two sides. With progressive deformation this form modifies to broad antiformal folds with low curvatures separated by sharply curved pinched synforms (Fig. 3.27a). These forms occur at the basement—cover interface in orogenic belts on a large scale, and as mullion structure or load cast on a small scale (Ramsay 1967). The pinched synforms points toward the higher viscosity. However when a reversal of the geometry occurs and pinched antiforms points towards the lower viscosity, the structure is likely to be a result of fault propagation folds (Fig. 3.27b).

Most of the experimental work related to development of minor structures ignores the effect of gravity and inertia. Ramberg (1967) has performed experiments with centrifuge models but these experiments mainly deal with development of diapiric structures formed by density contrast between layers or top and bottom strata.

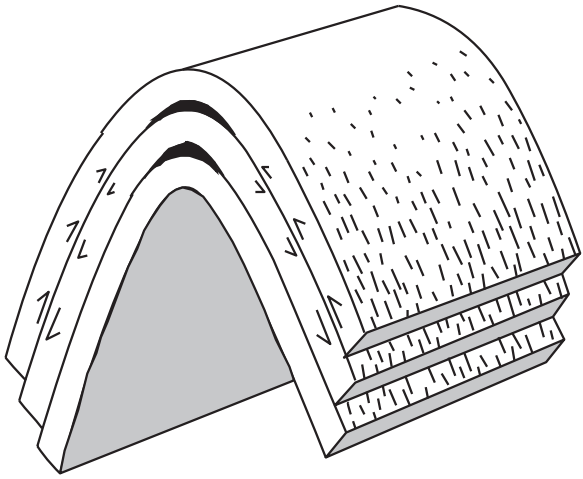

Fig. 3.28 A flexural slip fold. The layer parallel slip gradually decrease towards the hinge and result in formation of slickensides on the bedding surfaces. *Black filling*, hinge dilation (after Ramsay 1967)

3.8 Development of Flexural Slip Folds

These folds develop in multilayers with alternate competent (e.g. sandstone, limestone, quartzite, greywacke) and incompetent layers (e.g. shale, slate, phyllite) in brittle or brittle-ductile environment (Fig. 3.28). The condition exists in sedimentary and metasedimentary rocks. The contact between layers should be relatively weak so as to allow interlayer slip (Ramsay 1967). During the development of fold, the outer layer slips over the inner layer towards the fold hinge. The simple shear strain is inhomogeneously distributed throughout the layer, with gradual decrease in the slip towards the hinge. The development of flexural-slip folds is normally accompanied by formation of an open space or void above the hinge known as hinge dilation (Ramsay 1974). The space may be later filled-up by secondary minerals like quartz or calcite.

In an ideal condition when geometrical shapes of folded layers resemble to that of a parallel fold (class 1B), a relationship can be established between angular shear strain and dip of the layer (Ramsay 1967) (Fig. 3.29). However it was observed in many natural folds that they are characterized by extension parallel to the fold limbs at late stages of fold formation. As a result of this, fold limbs may reveal normal faults (Fig. 3.30), boudins (Fig. 3.31) or limb thinning and hinge thickening. The intensity of boudins and normal faults gradually diminishes towards the hinge. When folds do not maintain a constant orthogonal thickness around the fold profiles, the angular shear strain shows a higher value before the folds lock up (Fig. 3.29).

The development of boudins along a fold limb differs from boudins developed normally as extensional features. Generally, the boudins are formed when a competent layer is enclosed in an incompetent host. The maximum compression is normal to the layering and the maximum extension is parallel to the layering. The

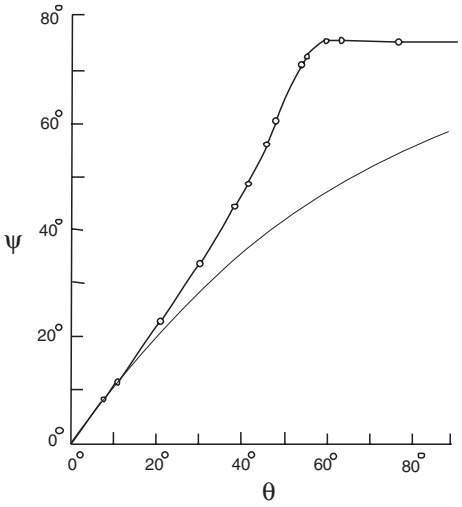

Fig. 3.29 The relationship between angular shear strain (Ψ) and limb dip (θ) in flexural slip folds. *Broken line* fold with parallel geometry (after Ramsay 1967); *continuous line* fold developed in a deformed Plasticine model where the fold limb showed extension with increase in deformation till the fold lock up (after Behzadi and Dubey 1980)

Fig. 3.30 An incompetent shale layer showing extension faults in a chevron fold limb (Bude, England) (after Dubey and Behzadi 1981)

geometrical shape of the boudins depends upon competence contrast between the layer and the host. The most competent layers show rectangular boudins whereas the least competent layers show pinch and swell structure (Fig. 3.32). During the progressive development of boudins, the distance between individual boudins increases gradually and the incompetent material fills-up the gap created by displacement of the boudins.

Fig. 3.31 Boudinage in a siltstone layer enclosed in shale in a chevron fold limb (Bude, England) (after Dubey and Behzadi 1981)

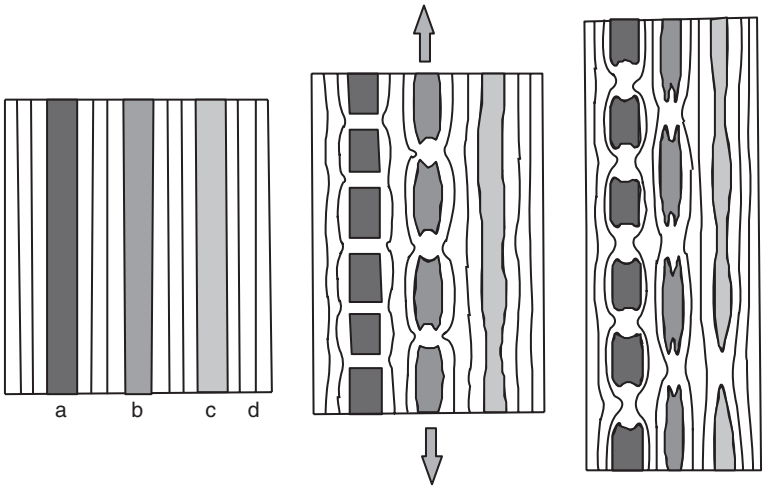

Fig. 3.32 Progressive development of boudinage structure; competence contrast: a > b > c > d. The *arrows* show the direction of maximum extension [from Ramsay and Huber (1983). © Elsevier. Published with permission of Elsevier]

At late stages of fold formation, tensile stresses lead to extension of fold limbs and development of boudins in competent layers (Fig. 3.33a). The amount of extension gradually decreases towards the hinge. The maximum tensile stresses are concentrated midway between two subsequent fold hinges hence the first boudin is likely to be formed in this region. This is followed by initiation of new boudins toward the fold hinges on either side (Fig. 3.33b). The rate of movement of the early boudins is more than the late boudins hence during their sequential

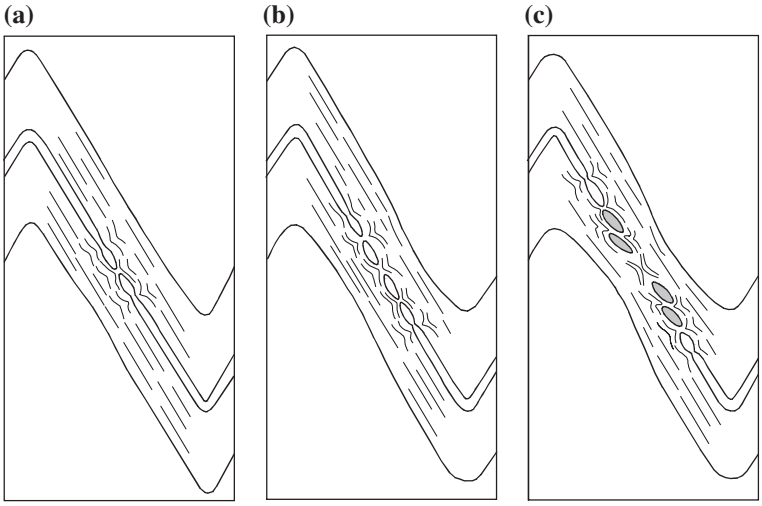

Fig. 3.33 Progressive development of overlapping boudins in a fold limb (after Dubey and Behzadi 1981)

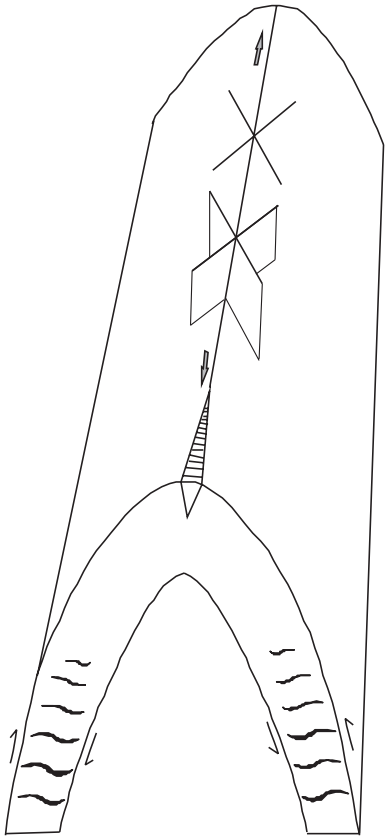

Fig. 3.34 Development of triangular tension gashes at the outer arc of the fold hinge, and sigmoidal gashes at the fold limbs during early stages of fold formation. Fracture planes oblique to the hinge form at late stages of fold formation when the maximum extension is parallel to the fold hinge line

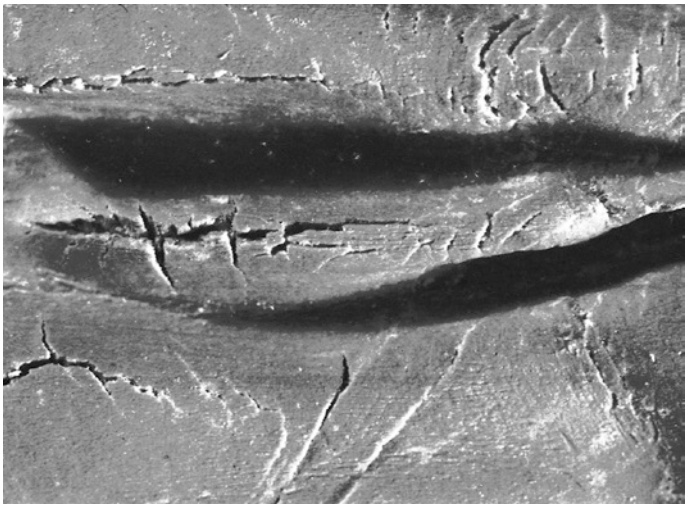

Fig. 3.35 A folded modeling clay layer showing triangular tension gashes and later fractures normal and oblique to the fold hinge line

development, the earlier formed boudins overlap the latter ones and produce overlapping boudins (Fig. 3.33c). An essential condition for formation of the structure is constant fold amplitude at late stages of fold formation as a result of fold locking.

Flexural slip fold limbs are also characterized by en echelon tension fissures filled-up later by secondary quartz or calcite. The intensity of their development gradually decreases toward the hinge. If the flexural slip is accompanied by bending at the hinge, outer arc extension gashes in filled by secondary minerals may form at the hinge. These gashes are triangular in cross-section and taper downwards (Fig. 3.34). The fissures and veins can be traced in the third dimension along the fold surface. The veins cut the folded surfaces of both open and gentle folds but in close and tight folds, the veins are themselves cut and occasionally displaced by later steep veins (Figs. 3.35 and 3.36). These veins are relatively narrow and are perfectly planar when traced across the fold hinge. The orientation of calcite and quartz fibres in the later veins indicates elongation parallel to the fold hinge lines. The feature suggests that there has been a change in the direction of bulk extension during progressive development of folds. In the early history of fold development, the direction of maximum extension was parallel to the fold axial surfaces and normal to the hinge whilst during the later stages, the incremental strains were predominantly extensive along the fold hinge line. Thrust faults are noticeably absent in folds, which show elongation parallel to the fold hinge lines.

Presence of triangular gashes at the hinge, tapering downwards, is also a typical feature of folds form by tangential longitudinal strain whose typical strain pattern is shown in Fig. 3.37. The outer arc of the fold is characterized by extensional

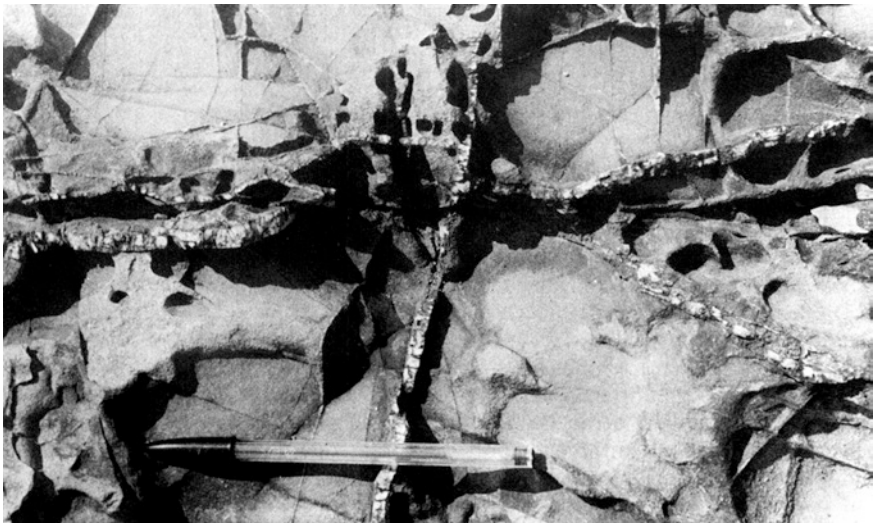

Fig. 3.36 Displacement of an outer arc extension vein by a secondary vein. The pen is parallel to the fold hinge line (Bude, England) [from Dubey (1980). © Elsevier. Published with permission of Elsevier]

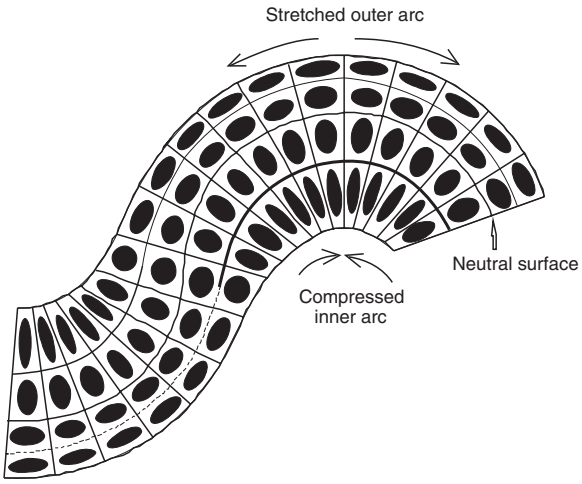

Fig. 3.37 Strain patterns in a fold profile developed by tangential longitudinal strain (after Ramsay 1967). *Thick line* compressed inner arc; *broken line* stretched outer arc; *continuous line* neutral surface

strains whereas the inner arc is characterized by compressional strains. There is a line of neutral surface (no finite longitudinal strain) somewhere in between. The strain pattern at the hinge can also result in development of normal faults in the outer arc and thrust faults in the inner arc.

Fig. 3.38 Asymmetric folds developed as a result of shearing along the Vaikrita thrust (Sangla valley, Himachal High Himalaya). The sense of shear is shown by *half arrows*

3.9 Development of Asymmetric Folds

Folds are not always formed as a result of layer parallel compression under the pure shear condition but also form under predominant simple shear condition resulting in asymmetric or inclined folds (Fig. 3.38). These folds are characterized by dip of the axial surfaces from 10° to 80°. The simple shear can be associated with flexural slip folding where the fold limbs are allowed to slip over one another. Large simple shear is associated with large scale thrusting in orogenic belts.

Fold asymmetry can be used to determine the sense of shear in an area but care has to be taken while interpreting the sense in ductile shear zones with very large shear strain because the asymmetry in such cases can point towards the opposite direction (Fig. 3.39). However, it is not difficult to isolate the reverse sense of shear because all folds do not initiate at the same time and the amount of shear strain is also not equal. Hence sense of shear should be determined from folds exhibiting low shear strain.

In upright folds, the dip direction represents the direction of younging of beds. However in some inclined fold limbs, the younging direction is opposite to the dip direction. Such folds in which one of the limbs is stratigraphically inverted are called as overturned folds (Fig. 3.40).

Overturning of the beds can be identified by the following.

1. By sedimentary structures
   (a) Gradual coarsening of grains upwards in graded bedding.
   (b) Gentle lamellae points upward and steep lamellae downwards in current bedding.

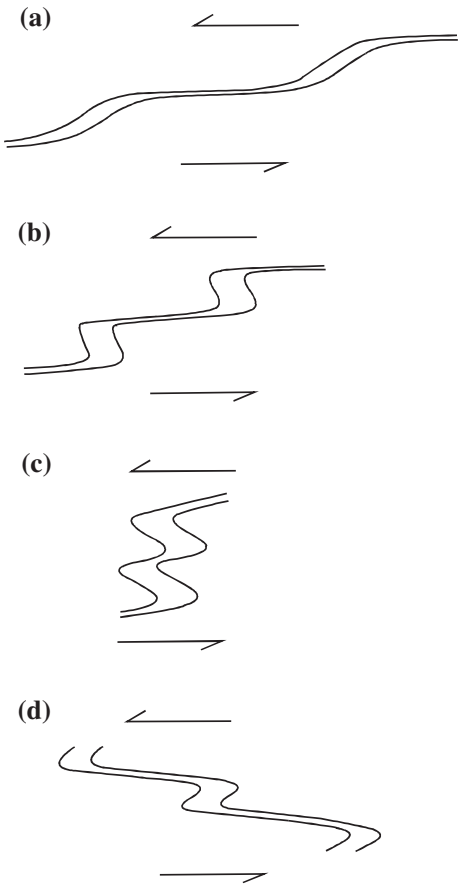

Fig. 3.39 Change in fold asymmetry with progressive shear strain. **a** Initiation of folds in a ductile shear zone. **b** Amplification of the folds with progressive deformation. **c** Rotation of axial surfaces, which tend to become parallel to the shear zone boundaries. **d** Further increase in shear leading to reversal in sense of asymmetry that can lead to wrong prediction of sense of shear [from Hudleston and Lan (1993). © Elsevier. Published with permission of Elsevier]

(c) Open and gentle forms upward in symmetric ripple marks. Asymmetric ripple marks cannot be used for younging direction.

2. By cleavage—bedding relationship in deformed beds
   In upright folds, the axial plane cleavage dips steeper than the bed (Fig. 3.40a). However with rotation of the fold, when one limb becomes overturned (inverted), the bedding is steeper than the cleavage (Fig. 3.40b). The bedding-cleavage relationship related to overturning can also be observed near the hinge of a recumbent fold (axial plane horizontal) (Figs. 3.40c and 3.41). However the relationship is not valid when bedding and cleavage dip in opposite directions.

A large shear can result in formation of extensional structures in overturned fold limbs as shown sequentially in Fig. 3.42.

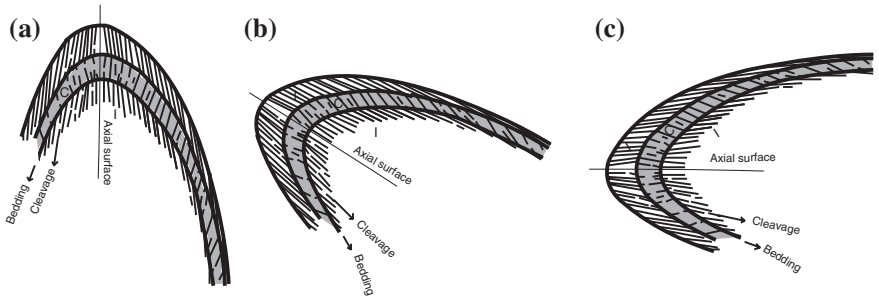

Fig. 3.40 **a** An upright fold showing axial plane cleavage. In incompetent beds (*white*), the layer and the cleavage dip in the same direction but the cleavage dips steeper than the layer. Younging of the beds is in dip direction of the fold limbs, i.e. the anticlinal core consists of the oldest rock. **b** In the inverted limb of an overturned fold, the cleavage and bedding dip in the same direction but bedding dips steeper than the cleavage. In the overturned limb the younging is opposite to the dip direction of the beds (after Ramsay and Huber 1987). **c** The bedding-cleavage relationship of overturned beds can also be observed in vicinity of a recumbent fold hinge. In the competent bed (*gray*), the layer and the cleavage dip in opposite directions hence the relationship is not valid

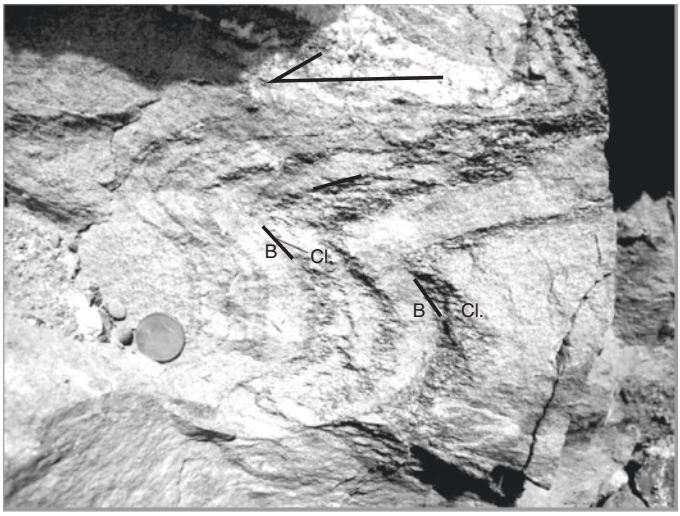

Fig. 3.41 A recumbent fold in quartzite and slate layers, Vaikrita Formation (Karcham, Himachal High Himalaya). The sense of shear is from top to the left. The bedding and cleavage dip in the same direction but dip of the cleavage is less than the dip of the bed. *B* bedding; *Cl* cleavage

3.10 Development of Noncylindrical Folds

Three-dimensional fold surfaces are not always exposed in field but experiments with physical models have greatly helped in understanding their evolution (Ghosh and Ramberg 1968). Folding was observed to initiate from irregularities in

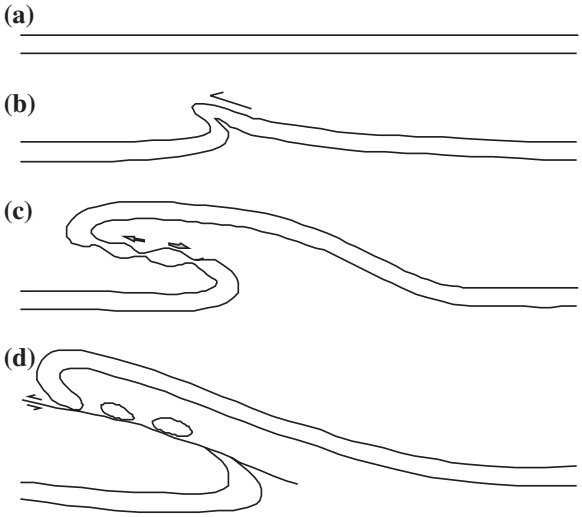

Fig. 3.42 Development of extensional structures in an overturned fold limb under predominant shear regime. **a** An undeformed layer. **b** Initiation of an asymmetric fold. The sense of shear is shown by a *half arrow*. **c** Amplification of the fold along with stretching of the overturned limb and formation of boudins. **d** Separation of the boudins and development of a thrust fault along the overturned limb

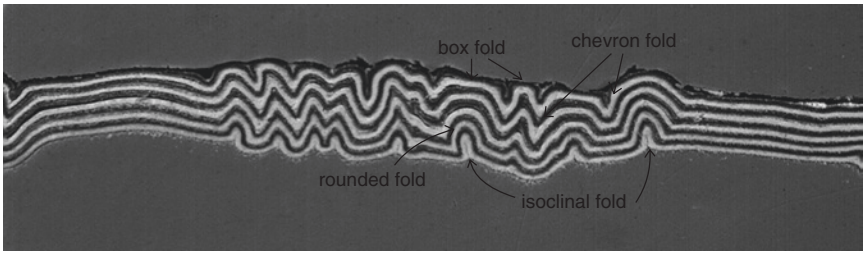

Fig. 3.43 Changing fold shapes with depth along the axial surface

layering or stress field and each fold amplifies by increasing its amplitude with increase in deformation. The geometric shape evolution depends on; (a) shape of initial irregularity at the site of fold initiation, (b) frictional effects on the layer surfaces, and (c) position of the folded layer within the multilayer unit. Fold shape, amplitude and wavelength tend to vary with depth along the axial surface (Figs. 3.43 and 3.44).

Individual folds propagate by forming a series of antiforms and synforms along the direction of compression (transverse fold propagation) and this is simultaneous with propagation by extending the length of hinge line (longitudinal fold propagation). When this propagation is relatively slow, the fold remains noncylindrical. At one stage of deformation, the profile shape of a fold can vary with position

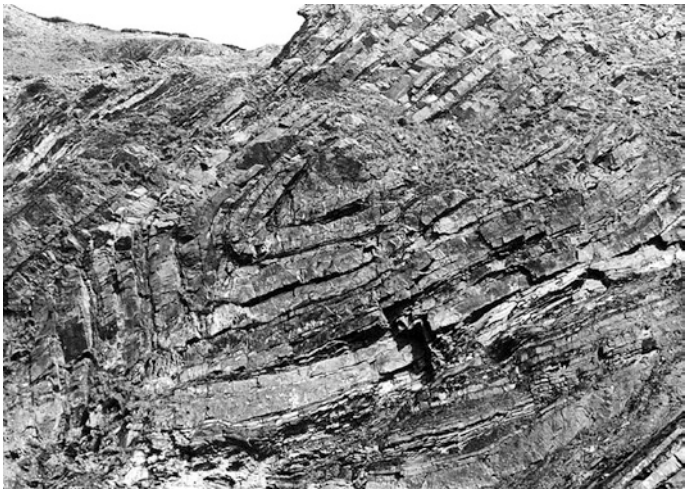

Fig. 3.44 Fold shapes changing from chevron to box folds along the axial surface in greywacke-shale sequence of Bude Formation, Bude, England

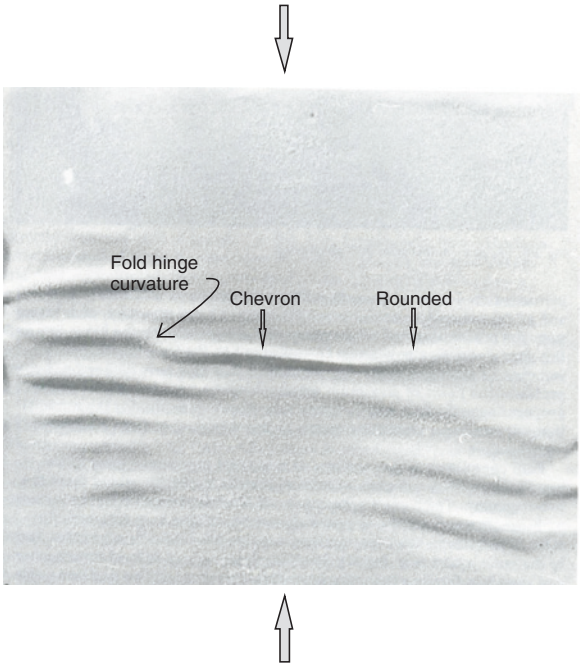

Fig. 3.45 Fold propagation parallel and perpendicular to the direction of compression (shown by *arrows*) on a deformed Plasticine layer. The central fold exhibits a distinct variation in cross-sectional shape along the hinge, and a curvature of the hinge line [from Dubey and Cobbold (1977). © Elsevier. Published with permission of Elsevier]

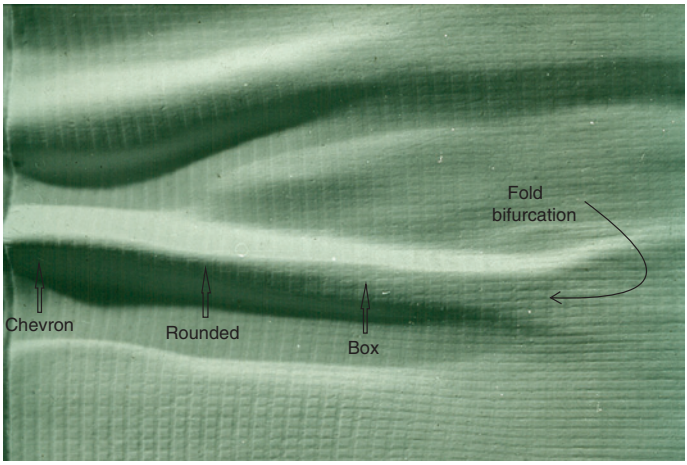

Fig. 3.46 A folded Plasticine layer showing variation in cross-sectional shapes along the fold hinge

Fig. 3.47 The "Whale's Back fold", Bude, North Cornwall, England. *C* culmination point; *E* eastern end of the fold; *CH* curvature of fold hinge [from Dubey and Cobbold (1977). © Elsevier. Published with permission of Elsevier]

along the hinge line. For example, a fold can have a chevron shaped profile at the point of maximum amplitude and a rounded profile at the propagating ends (Fig. 3.45; Dubey and Cobbold 1977). The rounded profile can also change to a box fold profile and a single fold may bifurcate into two folds (Fig. 3.46). Similar fold structures have also been observed in the Carboniferous Formation of Bude, SW England (Figs. 3.47, 3.48 and 3.49), Scottish Highlands (Fig. 3.50), and Irish Variscan fold belt (Bamford and Ford 1990).

Fig. 3.48 Culmination point of the Whale's Back showing a chevron fold style (after Dubey and Cobbold 1977)

Fig. 3.49 Eastern end of the Whale's Back showing a rounded cross-section (after Dubey and Cobbold 1977)

3.10.1 Importance of the Culmination Point

In noncylindrical folds a difference can be made between culmination and crest points. The culmination can be described as the point of maximum amplitude along an antiformal fold hinge line. The definition makes it an invariant feature of folds and its importance lies in the fact that it denotes the place of fold initiation where the maximum heterogeneous strain took place along the hinge line.

Fig. 3.50 An anticlinal rounded fold in the middle distance splitting into two anticlines and an intervening syncline towards the front of the photograph (Kirkandrews Bay, Kirkcudbrightshire, Scotland)

Small-scale structures, which are associated with late stages of formation of folds (e.g. hinge dilation or saddle reef, hinge collapse, limb thrust, limb thinning, hinge thickening, boudinage, extensional faulting associated with layer elongation, cleavage, etc.) initiate at the culmination point and gradually propagate along the hinge, towards the terminations. Hence they may die out away from the culmination. A study of these structures can help in location of mineral deposits when they are related to fold geometry.

3.10.2 Interference Patterns of Simultaneously Developing Fold Complexes

After initiation of a fold from an irregularity, it spreads along the layering by transverse and longitudinal fold propagations. It is most likely that the layering contain more than one irregularity hence folding can initiate from more than one location. In such situations, the individual fold complexes propagate toward one another and then interfere in a manner, depending upon the relative positions, wavelengths, and shapes of approaching complexes. As with other wavelike phenomena, the most critical factor is the phase difference between approaching complexes. As illustrated in a two-dimensional profile section, if the interfering waves are in phase with one another they will link-up without any significant change in fold geometry in the area of interference (Fig. 3.51a). However if they are out of phase, the resulting fold shape in the interference area will have a different (irregular) geometry (Figs. 3.51b and 3.52).

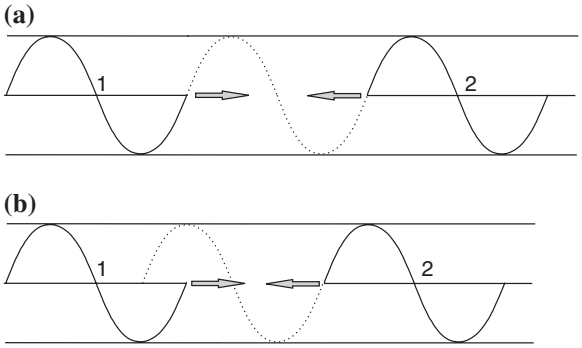

Fig. 3.51 In phase (**a**) and out of phase (**b**) waveforms (1 and 2) propagating towards one another. The direction of propagation is shown by *arrows*

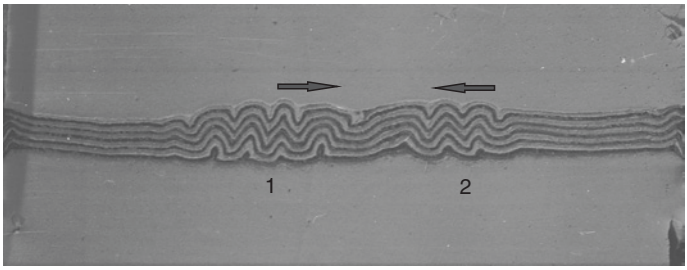

Fig. 3.52 Interference of two out of phase fold waves 1 and 2 in a profile section. The compression was along the layering and the direction of propagation is marked by *arrows* [from Dubey and Cobbold (1977). © Elsevier. Published with permission of Elsevier]

Two fold waves can also interfere with one another during the longitudinal fold propagation. The resulting fold geometry in the area of interference will depend upon the location of propagating anticlines and synclines (Fig. 3.53). When an anticline is positioned in front of an anticline and a syncline in front of a syncline, they link-up directly, anticline with anticline and syncline with syncline (Fig. 3.53a, b). If they are out of phase, i.e. an anticline is positioned in front of a syncline and vice versa, they cannot link directly but may link obliquely. For example, in Fig. 3.53c two complexes have propagated along the direction of their hinges (Y) and have linked together by curving of axial surfaces and hinge lines (the curved hinge lines later tend to become straight with progressive deformation). Where the approaching complexes are totally out of phase, they appear to prevent one another from propagating rather than actively destroy one another. Where they are in phase, the complexes appear to link without any significant increase in amplitude.

If two interfering complexes have differing wavelengths because of different shapes of initial deflections, some folds may link while others are prevented from

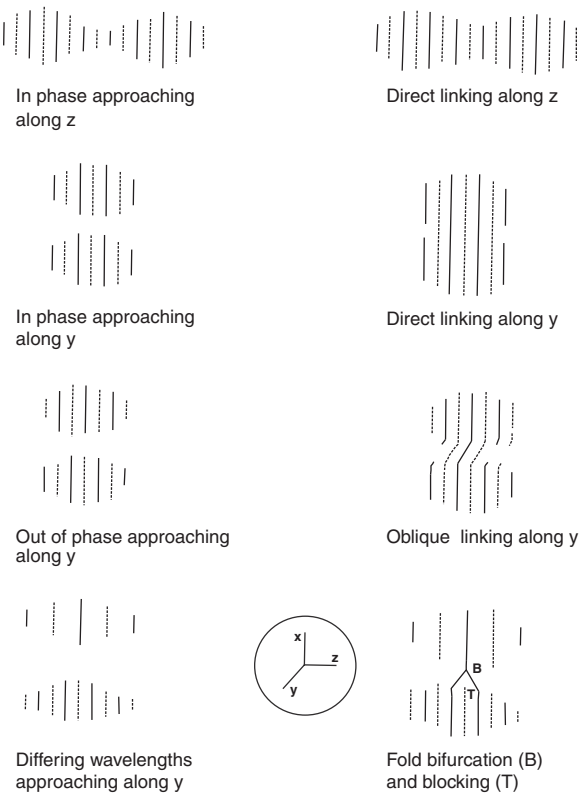

Fig. 3.53 A simplified illustration of interference between two fold complexes of different phase angles and wavelengths. The continuous and broken lines represent anticlinal and synclinal axes. Z is the axis of maximum compression [from Dubey and Cobbold (1977). © Elsevier. Published with permission of Elsevier]

propagating further and acquire steeply plunging terminations (Fig. 3.53d). It is then possible for two anticlines (or synclines of one complex to link with a third anticline (or syncline) of the other complex. The resulting structure has a hinge that bifurcates away from the interfering fold culminations (Ghosh and Ramberg 1968). This type of bifurcation does not imply self-induced subdivision of a propagating fold, but results from mutual fold interference.

The described interference patterns are different from those predicted and observed in other wave processes where the motions are adequately described by linear equations (e.g. small vibrations). In the linear processes, amplitudes of interfering waves are additive, and interference is therefore constructive or destructive, depending upon the phase difference. For the buckling process in natural rocks, the interference apparently involves linking and blocking of anticlines and synclines. Intuitively such a process would consume less energy than the active destruction of one fold by another (Dubey and Cobbold 1977).

The noncylindricity in folds results from; (a) folds initiating at noncylindrical deflections, (b) hinge lengthening not being rapid relative to amplification, and (c) interference between simultaneously propagating folds. The first two factors are responsible for a periclinal fold geometry and the fold interference often

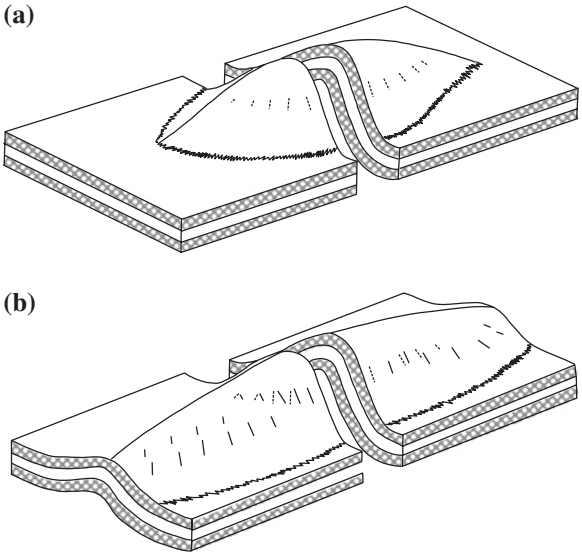

Fig. 3.54 Pattern of interlayer slip during noncylindrical flexural slip folding. **a** Two orientations of fibres (slip directions) during initial stages of fold development resulting from increase of fold amplitude at the culmination. **b** Overlapping fibres in vicinity of the culmination point as a result of increase in fold amplitude with longitudinal fold propagation. *Broken lines* early slip direction; *continuous line* later slip direction

causes an extra curving of hinges. The interference can also cause a significant warping of axial surfaces when two folds amplify simultaneously in different layers in a multilayer sequence.

Orientation of quartz fibres and slicken sides indicating the direction of slip on fold surfaces also helps in understanding the nature of interlayer slip during longitudinal fold propagation (Price and Cosgrove 1990). The direction of slip varies during the fold evolution. For example, Fig. 3.54 shows the pattern of fibre growth on a noncylindrical fold surface at an initial stage of fold formation. At the fold culmination, the fibres are oriented nearly orthogonal to the fold hinge line (Figs. 3.54a and 3.55a). However with increasing distance from the culmination along the hinge, the fibre orientation shows a gradual decrease in angle with the fold hinge line (Figs. 3.54a and 3.55b). The oblique growth is a result of fold amplification (increase in amplitude) at the culmination. The pattern of slip modifies with the longitudinal fold propagation. The fold amplitude increases along the hinge and a greater area is gradually covered by slip normal to the hinge. Hence two orientations of overlapping fibres are visible at some distance from the fold culmination (Figs. 3.54b and 3.55c).

Oblique orientation of slickensides with respect to fold hinge line can also result from buckling of layers, which are asymmetrically oriented with respect to the axes of bulk strain (Ramsay 1967). The two can be differentiated by presence of overlapping fibres at some distance from the culmination.

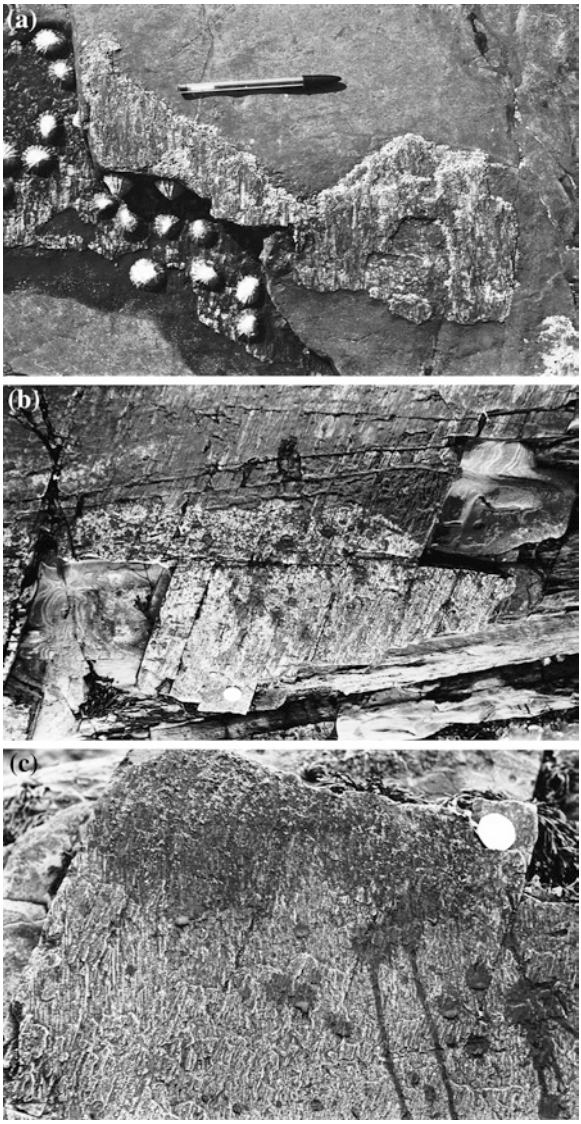

Fig. 3.55 Orientation patterns of fibres along noncylindrical fold surfaces. **a** Quartz fibres normal to hinge line at a fold culmination (Bude, North Cornwall, England). **b** Oblique orientations of quartz fibres near a fold termination (McDuff, Banffshire, Scotland). **c** Overlapping quartz fibres between the fold culmination and the termination (McDuff, Banffshire, Scotland)

3.11 Development of Polyharmonic Folds

Fold waves with two or more orders of wavelengths and amplitudes are known as polyharmonic folds (Ramsay and Huber 1987). These can form in a number of ways as described below.

The effect of contact strain (Fig. 3.20) is evident within a zone about one initial wavelength wide on either side of the folded sheet. Hence polyharmonic folds can

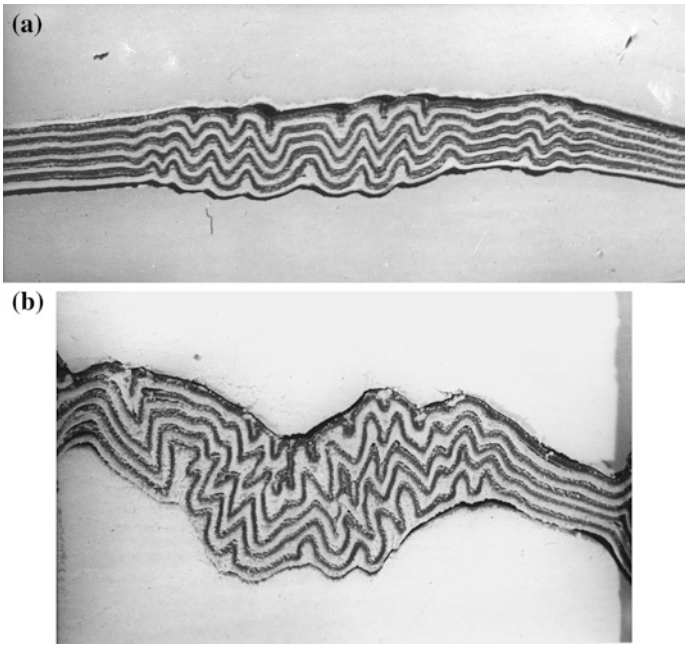

Fig. 3.56 Polyharmonic folds. **a** Cross-sectional fold shapes in a multilayer Plasticine model (49 % shortening). The model was compressed along the layering and the resulting extension took place parallel to the fold hinge lines. **b** The same model after 64 % shortening. After 49 % shortening the direction of maximum compressive stress remained the same, the extension was allowed to take place perpendicular to the fold hinge lines along the *vertical axis* of the press [from Dubey (1980). © Elsevier. Published with permission of Elsevier]

be developed in a layer by placing it in the zone of contact strain of a thick layer (Ramberg 1961).

The dominant wavelength (W_d) is proportional to thickness of the layer (i.e. a thicker layer results in a larger fold wavelength as compared to a thinner layer) and viscosity contrast between the layer and the matrix. Hence the smaller wavelength folds may initiate simultaneously with the large wavelength folds when layers of differing viscosities or differing thicknesses undergo a compressive strain (Ramberg 1963; Ghosh and Ramberg 1968).

At late stages of fold development when the interlimb angles are low (individual folds close or tight), the folds acquire locking or rotation hardening. The reason for fold locking is that the interlayer slip ceases at steep limb dips because of increase in friction on the layer surfaces and resultant requirement of large energy (de Sitter 1958). This stage is normally followed by a change in the direction of maximum extension. The structures that develop after fold locking depend upon the boundary conditions and the ease with which the folds can extend either normal or parallel to the hinge line. Small wavelength folds generally initiate at early stages of compressive strain but when the folds acquire locking,

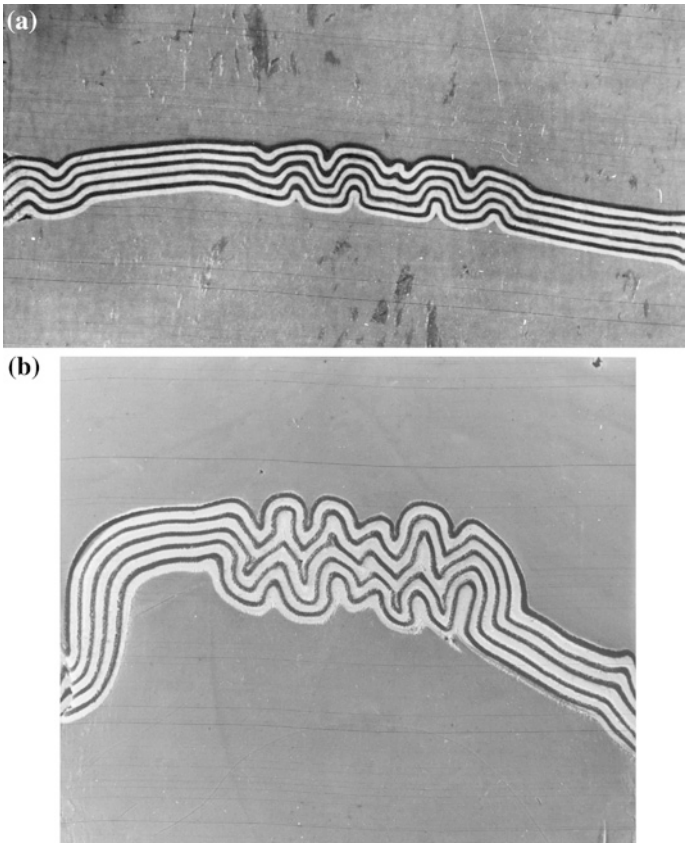

Fig. 3.57 Polyharmonic folds. **a** Cross-sectional fold shapes in a multilayer Plasticine model (19 % shortening). The model was compressed along the layering and the resulting extension took place normal to the fold hinges. **b** The same model after 42 % shortening. After 34 % shortening, the direction of maximum compressive stress remained the same, the extension was allowed to take place along the fold hinge lines. Note that the folds have acquired small interlimb angles but thrust fault has not developed in the layers [from Dubey (1980). © Elsevier. Published with permission of Elsevier]

the multilayer sequence behaves like a single layer and larger wavelength folds develop at late stages of fold development. The multilayer units may be of uniform layer thicknesses and the alternating layers have nearly the same viscosity. A change in the direction of maximum extension at late stages of fold development can also lead to formation of polyharmonic folds in a multilayer sequence. Polyharmonic folds developed under different modes of deformation are shown in Figs. 3.56, 3.57 and 3.60.

While studying fold profile sections, observations should be made for stretch structures and limb thrusts. Absence of these structures in close and tight folds indicates an extension along or oblique to the fold hinge lines (Fig. 3.58). This is

Fig. 3.58 Chevron folds with small interlimb angles in greywacke-shale sequence of Bude Formation, Bude, England. Absence of thrust fault indicates extension parallel to the fold hinge line at late stages of formation of folds

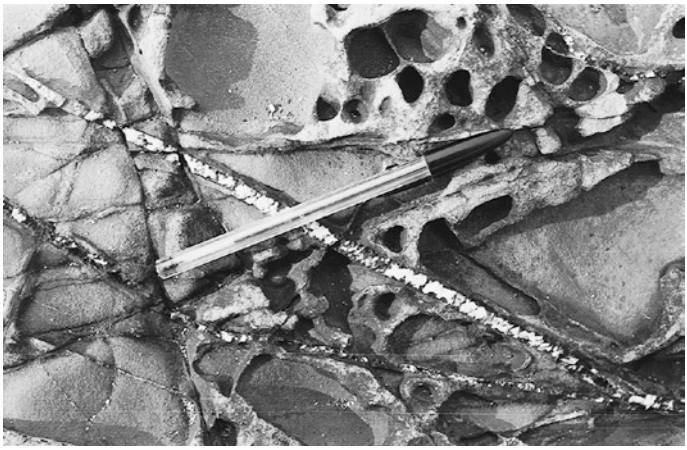

Fig. 3.59 A vein oblique to the fold hinge line. The orientation of vein quartz crystals shows an oblique extension of the fold surface with a component of extension parallel to the hinge line (*top edge of the photograph*) (Bude, North Cornwall, England)

evidenced by presence of tension gashes with orientation of fibres oblique to the fold hinge line indicating an oblique extension of the fold surface while changing from hinge normal to hinge parallel extension (Fig. 3.59).

When small wavelength folds form under the influence of large wavelength folds, they may be described as parasitic folds but when the smaller folds initiate earlier than the large folds and the geometry of the latter is controlled by the geometry and distribution of the former, the smaller folds should not be described as parasitic folds because the term does not have a correct genetic implication.

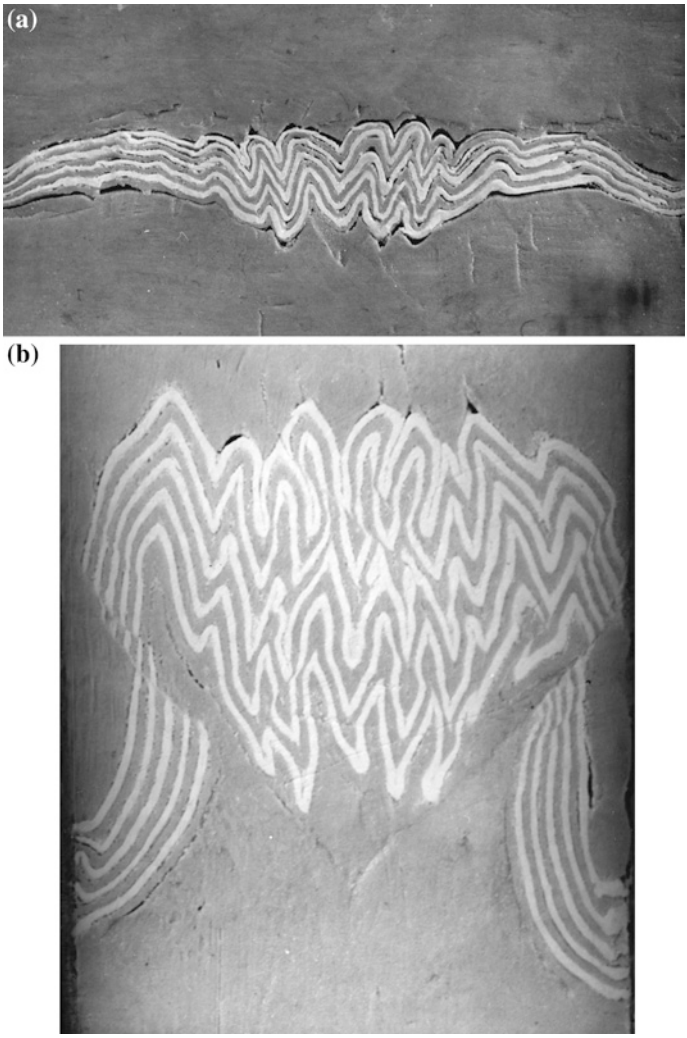

Fig. 3.60 Polyharmonic folds. **a** Cross-sectional fold shapes in a multilayer model (40 % shortening). The model was compressed along the layering and the resulting extension took place normal to the fold hinge lines, parallel to axial surfaces of the developing folds. **b** The same model after 80 % shortening, with no change in the mode of deformation. Thrust faults have developed in the model [from Dubey (1980). © Elsevier. Published with permission of Elsevier]

Where the folds are described as first-order and second-order folds, the different orders refer to size of the fold wavelength and should not be confused with the order of their origin (Fig. 3.60).

Small wavelength folds situated in two limbs of a larger fold, have a characteristic geometry. These folds are asymmetric and the axial surfaces dip away from the axial surface of the larger antiformal fold. Hence the geometry helps in locating the

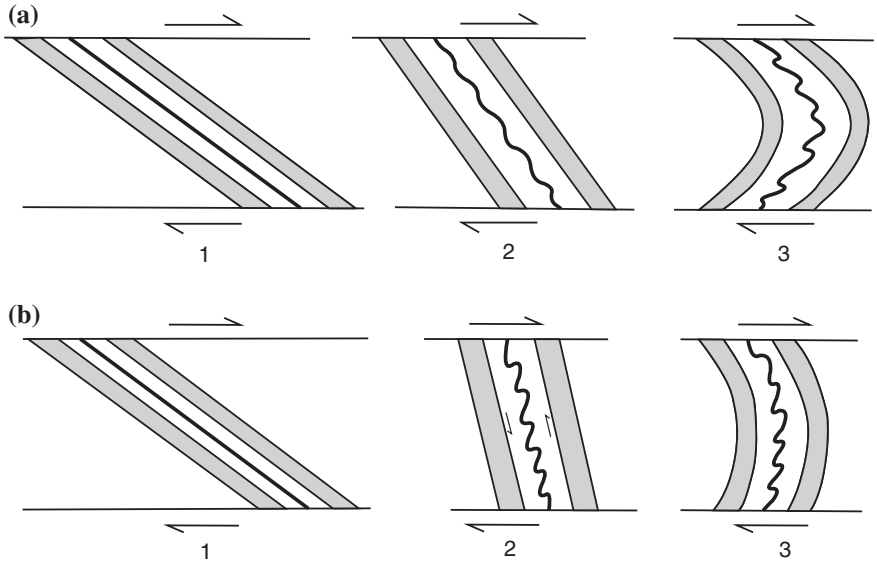

Fig. 3.61 **a** Formation of two orders of folds when the multilayer is tilted to the direction of simple shear. The *central black layer* is competent, *white layers* are incompetent and the *gray layers* have intermediate competent contrast. Buckling of the *gray layer* initiated early before the folds in the black competent layer could be tilted by layer parallel shear strain to form asymmetric folds. **b** Formation of asymmetric small folds with similar vergence in both the limbs of the larger fold. The *gray layer* started buckling at a late stage of deformation when the black competent layer had already acquired asymmetric geometry by layer parallel shear strain [from Ghosh (1966). © Elsevier. Published with permission of Elsevier]

large-scale antiformal and synformal fold hinges (Fig. 3.61a). However this happens when small wavelength folds initiate either at an early stage or simultaneously with the larger fold. In a different situation, when the small-scale asymmetric folds develop throughout the multilayers as a result of strong layer parallel shearing, and buckling of the multilayer (initiation of the large-scale fold) takes place at a late stage of deformation, the asymmetricity of the small folds remains the same in both limbs of the large fold (Fig. 3.61b). However these folds are rarely observed in naturally deformed rocks.

3.12 Structures Developing on Fold Surfaces at Late Stages of Fold Development

It is to be noted that theoretical aspects regarding the development of dominant wavelength in layers applies only to first few increments of deformation. Computation methods have been used to describe the development of folds at large deformations (e.g. up to 77.7 % shortening by Dietrich 1970), but as pointed

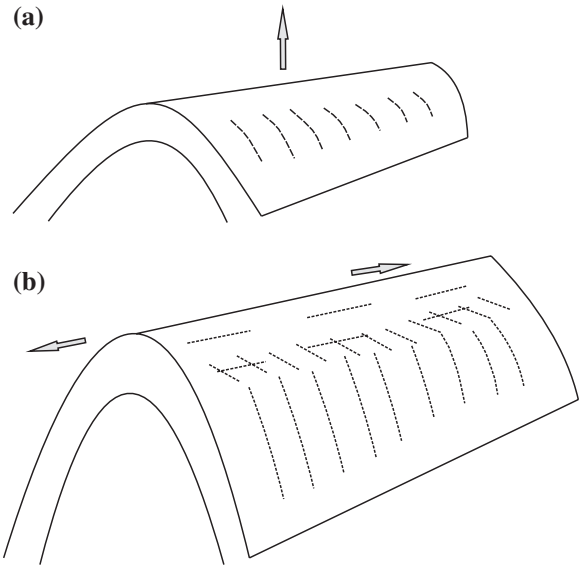

Fig. 3.62 A simplified diagram to illustrate the orientation of lineations during evolution of a fold. **a** Early lineation is formed normal to the fold hinge line when the maximum extension is parallel to the axial surface, normal to the hinge. **b** Later lineation parallel to the hinge line when the maximum extension is parallel to the hinge. The intervening region is marked by oblique orientation of the lineation

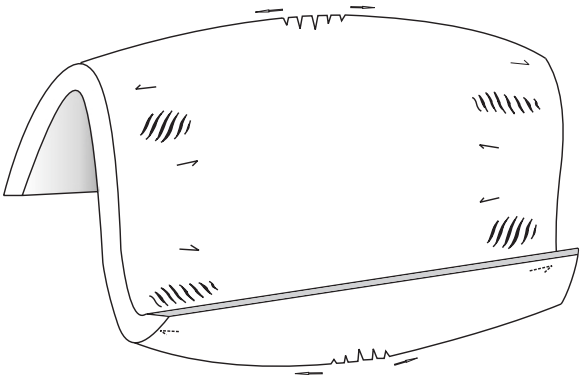

Fig. 3.63 A simplified diagram illustrating the development and orientations of sigmoidal tension gashes on a fold surface

out by Chapple (1968), the method is not appropriate enough to study late stages in the deformational history of folds because of inherent theoretical considerations, especially the assumption of inextensibility of fold limbs does not remain valid and there is no consideration for initiation and development of fractures.

The stretching mineral lineation can also change its trend at late stages of folding. When the maximum extension is parallel to the axial surface and normal

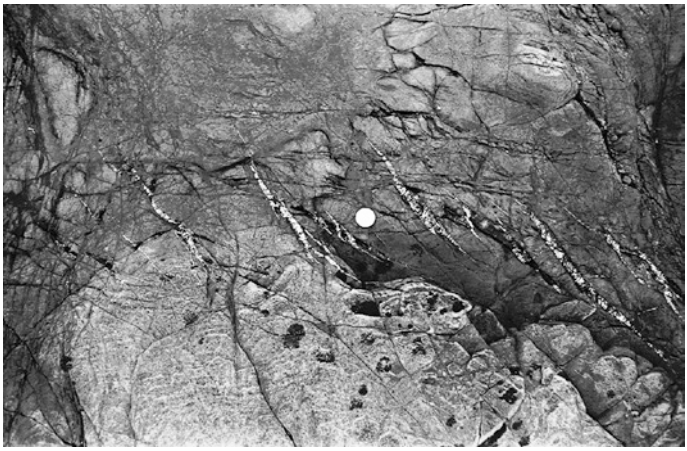

Fig. 3.64 Sigmoidal tension gashes on a fold surface in greywacke-shale sequence of Bude Formation, Bude, England

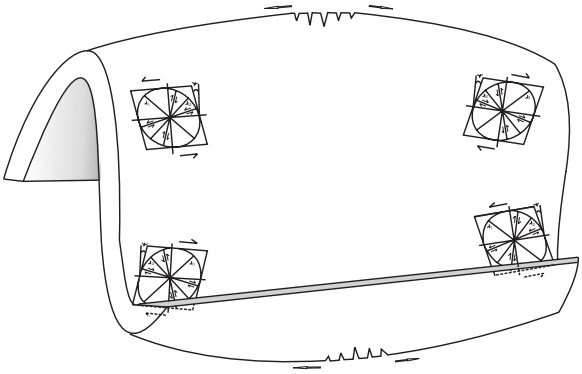

Fig. 3.65 A simplified diagram illustrating the development of reverse faults on a fold surface

to hinge, the lineation is likely to develop normal to the hinge (Fig. 3.62a). After the fold lock-up, maximum extension parallel to the fold hinge line can result in formation of lineation parallel to the fold hinge line (Fig. 3.62b). Between these two extreme cases, orientation of the lineation will be oblique to the hinge line. Hence different orientations of mineral lineations can result on a fold surface at different stages of fold formation.

The magnitude of extension parallel to the hinge line varies along the fold surface and the maximum extension occurs at the culmination point where the interlimb angle is small. The variation of extension results in initiation of simple shear on the fold surface thereby leading to the formation of triangular fractures normal to fold hinge, sigmoidal tension gashes (Figs. 3.63 and 3.64) or reverse faults (Figs. 3.65 and 3.66), in different orientations.

An essential component of transverse fold propagation is that individual folds of a fold complex vary in interlimb angles. The first formed fold on an initially

Fig. 3.66 Reverse faults on a fold limb exposed on an intertidal rock platform in greywacke-shale sequence of Bude Formation, Bude, England

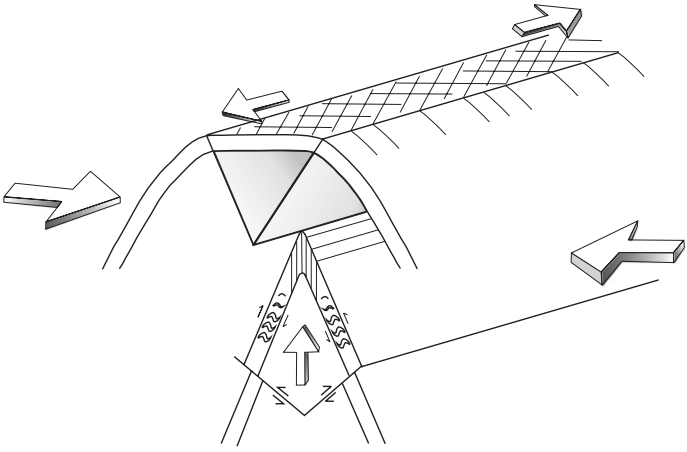

Fig. 3.67 Variation of structural features across a fold profile. The *lower layer* shows development of a conjugate set of thrust faults as a result of extension parallel to the axial surface and normal to hinge line. The *upper layer* shows extension parallel to the hinge line and development of conjugate set of strike-slip faults

planar layering amplifies (i.e. increase in amplitude) with gradual decrease in interlimb angles. This is simultaneous with formation of new folds with gentle geometry. Since the folds lock-up at small interlimb angles, the first formed fold normally locks up prior to the later formed folds. The extension along the fold hinge after the lock-up is not limited to the locked-up fold only but also affects the adjacent folds that may reveal an extension oblique to the fold hinge line.

Apart from variation in fold geometry with depth along the axial surface, deformation pattern may be characteristic of distinct levels in a multilayer profile. Part of a

multilayer sequence which is characterized by fold limb thrust shows extension parallel to the axial surfaces and normal to hinge whereas other folds in the profile may shows extension parallel to the fold hinge (Fig. 3.67) (Dubey 1983). The hinge parallel extension results in formation of strike-slip faults at late stages of deformation.

3.13 Superimposed Folding

When early fold geometry is modified by refolding of the hinge line and/or axial surface by simultaneous or subsequent deformation, the result is a more complex fold geometry. The first formed folds are called early folds, the later formed folds superposed folds, the combined geometry as superimposed folds, and the process as superimposed deformation. When the folding episodes are associated with formation of new minerals or intrusion of dikes (e.g. along the axial surface) their ages, obtained by suitable geochronological methods, can help in deciphering the ages of different episodes.

A careful study of deformed foliations and lineations can help in identifying the different phases of deformation and stress orientation that may have existed during their formation. Hence the geometrical shapes, foliations and lineations are an essential part of the study of superimposed deformation. Normally the two generations of folds are identified by folding of cleavages and their cross-cutting relationships as shown in Fig. 3.68. The diagram shows two foliations S1 and S2 on a fold. Foliation S1 has undergone folding whereas the axial plane foliation (i.e. foliation parallel to the axial plane of the fold) S2 is unfolded. Hence S1 should have formed during an earlier deformation episode because it existed at the initiation of the subsequent deformation. The fold with the later unfolded cleavage is younger in age hence superposed fold.

A slightly different example of superimposed fold is shown in Fig. 3.69. Figure 3.69a shows a fold profile with development of axial plane foliation (AP1). The fold limbs and the axial plane are folded during a subsequent deformation to form a superimposed fold (Fig. 3.69b). The superposed fold has folded the earlier cleavage (AP1) and produced a second axial plane cleavage (AP2). The early fold hinge can be identified on the basis of the fact that the early cleavage AP1 is unfolded around the hinge zone.

The superimposed folds are formed in the following environments (Ramsay 1967).

3.13.1 Crossing Orogenic Belts

When an area undergoes deformation in two successive orogenies with distinct stress patterns, separated by a large time interval, superposed folds may result. The depth of deformation may vary in the two orogenies hence the metamorphic history of the region will need a detailed study of the minerals and their

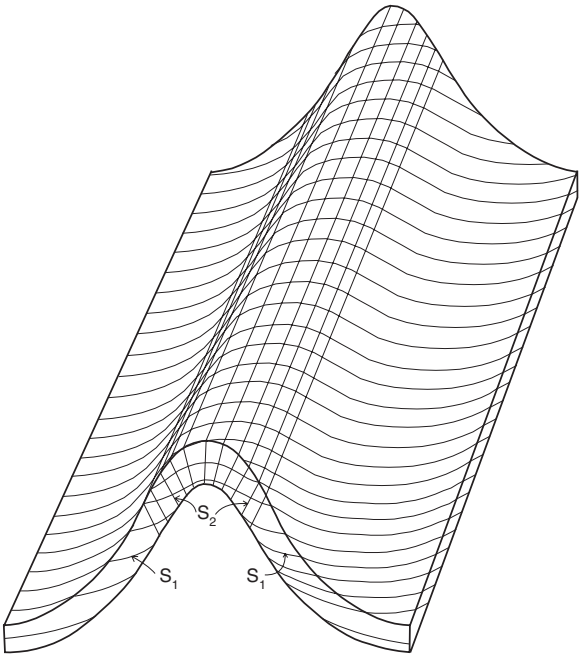

Fig. 3.68 Two foliations on a superposed fold surface. The early foliation (S_1), oblique to the fold hinge line, is folded whereas the later foliation (S_2), parallel to the fold hinge is unfolded

characteristics. Swiss and French Alps are examples of this type where the folded basement was subsequently deformed during the Alpine orogenic movements.

3.13.2 Successive Deformation Phases in One Orogenic Cycle

In the plate tectonics model, the individual plates are moving with a distinct geometric pattern causing deformations. The strain rates, physical state of the rock, and boundary conditions can change during a large single deformation and this can lead to superimposed folding that may also differ geometrically at different topographic levels. Examples of this type have been cited from the Caledonian orogenic belt of the Scottish Highlands (Ramsay 1963).

3.13.3 Successive Folding During a Single Progressive Deformation

Progressive deformation of layered sequences can lead to change in orientation of the layering resulting in oblique straining of the structures and superimposed folding at late stages of deformation, without any change in the regional stress

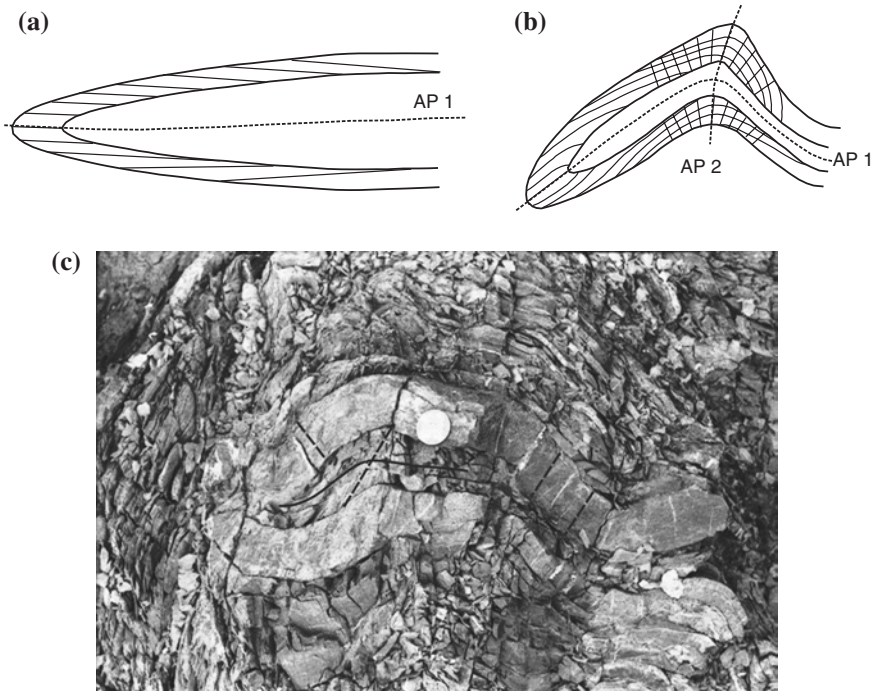

Fig. 3.69 Two foliations in a fold profile. **a** Development of axial plane foliation sub-parallel to the fold axial plane (AP1). **b** Folding of the early axial plane foliation during superposed folding and development of a new foliation parallel to the axial plane of the superposed fold (AP2). AP1 remains unfolded in the hinge region of the early fold. **c** A superposed fold at Rishikesh in the Chandpur Formation of the Garhwal Lower Himalaya. *Continuous line* early (folded) foliation; *broken line* later (unfolded) foliation

pattern (Ramsay and Huber 1983). This type of deformation is observed at late stages of fold formation after the folds lock-up. The stage of lock-up is followed by a change in the direction of maximum extension from normal to hinge line to parallel to the hinge (Fig. 3.70). When the boundary conditions (e.g. presence of oblique ramp or strike-slip fault) do not allow fold hinges to extend, the superimposed folds are formed by curvature of the hinge lines.

3.13.4 Simultaneous Folding in Several Directions During One Deformation

When a layer undergoes a constrictive type of three-dimensional strain, folding may develop simultaneously with the hinge lines oriented in various directions depending on the prevailing stress condition (Ghosh 1968; Ramsay and Huber 1983). A uniform radial compression is a rare possibility in nature but simultaneous compression in more than one direction is possible.

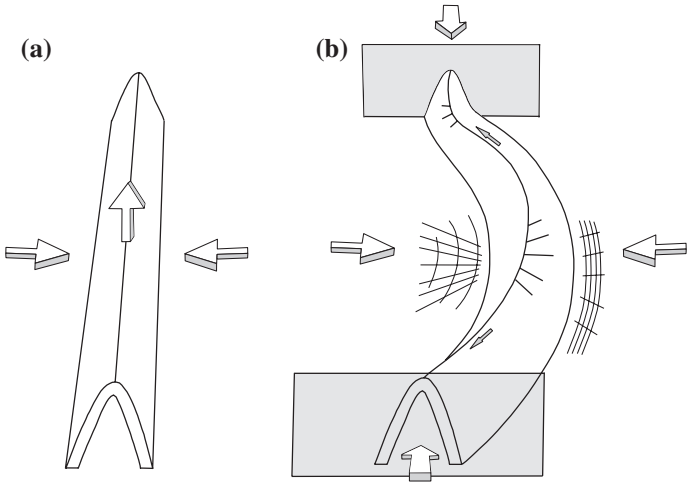

Fig. 3.70 Curvature of a fold hinge line at late stage of fold formation. **a** Development of a cylindrical fold with the axis of maximum extension parallel to the fold axial surface and normal to the hinge line as shown by the *vertical arrow*. **b** Extension of the fold surface parallel to the fold hinge line at late stage of fold formation, obstruction in the extension by boundary condition (e.g. oblique fault ramp, strike-slip fault, etc.; shown by *gray rectangles*) resulting in curvature of the hinge line. In the curved fold surface, the outer arc is characterized by extension and the inner arc is characterized by compression

3.14 Interference Patterns

Ramsay (1962, 1967) has presented an outstanding description where identification of superimposed folds in two-dimensional cross-sections can lead to understanding of their three-dimensional geometries, and kinematic evolution. The description is based upon interference of two sets of fold waves. The following four patterns of interference are most common (Fig. 3.71) (Ramsay and Huber 1987; Thiessen and Means 1980).

3.14.1 Type 0: Redundant Superposition

This type is described as type 0 because the hinge lines and the axial planes of the interfering folds are parallel and the resulting geometries are similar to folds described in single phase deformation. The geometries in the region of interference depend on fold wavelengths of the interfering folds and whether the waves are in phase or out of phase. The development of polyharmonic folds where the large wavelength folds have formed either simultaneously or after locking-up of the early formed small wavelength folds may fall in this category although they are not true superimposed folds.

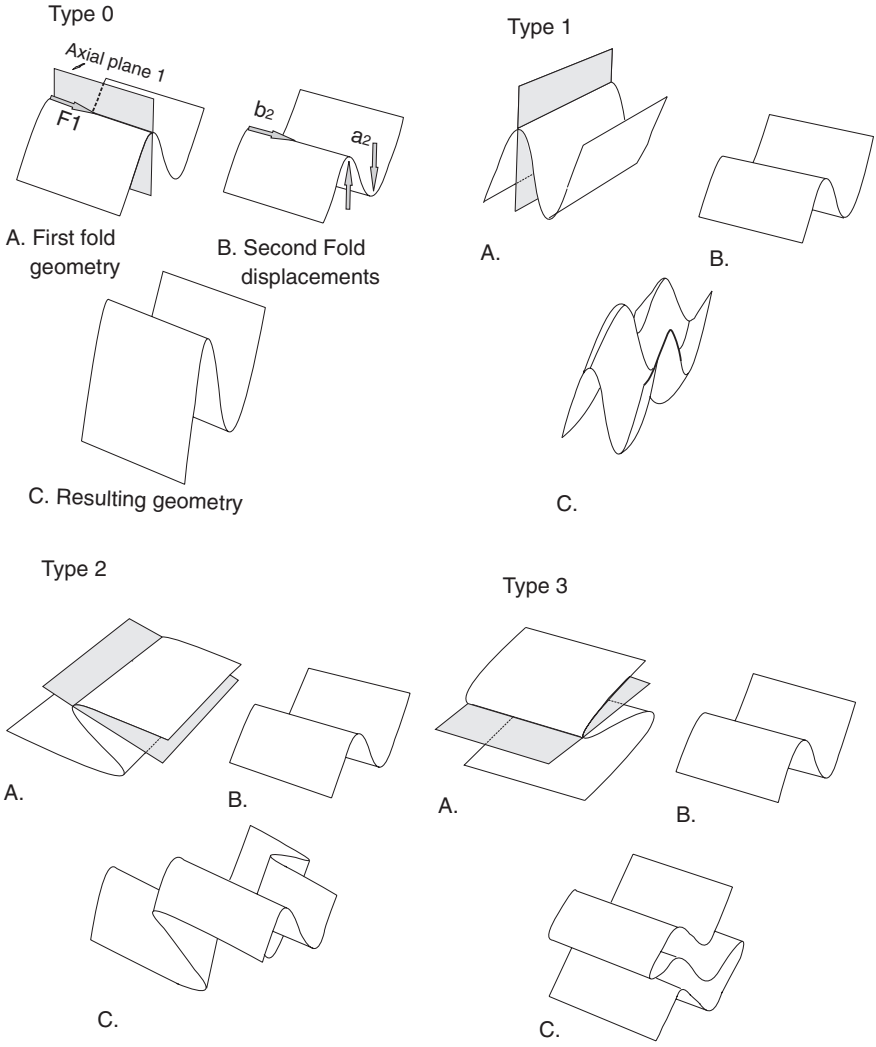

Fig. 3.71 Different types of interference patterns in superimposed folding [from Ramsay and Huber (1987). © Elsevier. Published with permission of Elsevier]

3.14.2 Type 1: Dome-basin Pattern

The dome-basin pattern is formed when the fold hinge lines and axial planes of the two interfering folds make a large angle with one another. The resulting pattern consists of a series of domes and basins resembling cardboard egg cartons. The two deformations that lead to the generation of interfering waves may be either

simultaneous (constrictive type of strain ellipse) or subsequent. The sequence of the deformations can be inferred from the successive cleavages.

3.14.3 Type 2: Dome-crescent-mushroom Pattern

The pattern consists of refolding of overturned folds. After erosion of a part of the fold surface, the characteristic pattern of crescent or mushroom shape appears on the outcrop. The refolding of the first fold produces the dome-basin pattern but differs from type 1 in the fact that the first folds are overturned and this geometry is preserved after the second deformation.

3.14.4 Type 3: Convergent-Divergent Pattern

The type is termed as convergent-divergent pattern because the outcrop traces of the first folds show continuously converging or diverging forms. This is characterized by low angle between the interfering fold hinge lines and high angle between the axial planes. The axial plane of the first fold is refolded but the early fold hinge direction does not show much deflection from the initial orientation.

The interference patterns described above were also tested by deforming models of Plasticine, modeling clay, and putty. The experiments where the two deformations had an orthogonal relationship (Type 1) and the early fold geometry was characterized by cylindrical folds, the superposed deformation resulted in;

(a) gradual opening of interlimb angles along the early fold hinge (Flinn 1962; Ghosh 1974) (an observation, which is difficult to prove in natural folds), or
(b) termination of superposed folds at the early fold surface (superposed folds of the first type, Ghosh and Ramberg 1968), or
(c) curvature in hinge of the early folds (superposed folds of the second type (Ghosh and Ramberg 1968; Watkinson 1981), or
(d) noncylindrical superposed folds at the fold surface of the early fold (Ghosh and Ramberg 1968).

The maximum curvature is normally observed in isoclinal folds and minimum in open and gentle folds during superposed deformation. The early folds also reveal tight or isoclinal geometry (Hobbs et al. 1976) because; (a) the early folds with large interlimb angles may undergo unfolding during superposed deformation, and (b) the early folds with small interlimb angles are generally tightened-up during later folding when axial surface is bent by the later folding (Ghosh 1976).

The longitudinal propagation of superposed folds and their linking with the early folds produce a variety of interference patterns (Fig. 3.72) (Dubey 1984). The main effect is to produce extra curvature in the hinge line and fold blockings. For example Fig. 3.72a shows superposed folds approaching early folds at

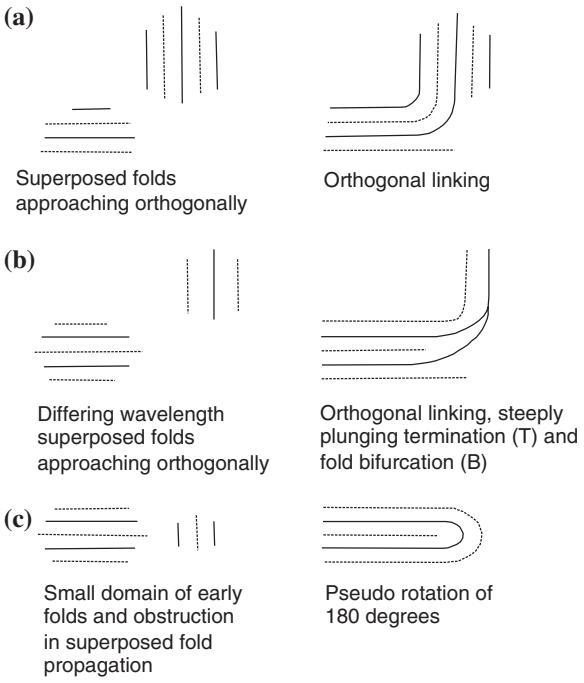

Fig. 3.72 A simplified illustration to show the interference between noncylindrical early and superposed folds. The *continuous* and *broken lines* represent antiformal and synformal hinge lines, respectively. The *vertical lines* represent early folds and the *horizontal lines* represent superposed folds

an angle of 90°. The interference results in orthogonal linking, i.e. an antiform link with an antiform and a synform link with a synform. A difference in the wavelengths between the early and superposed folds results in steeply plunging termination (T) and fold bifurcation (B) (Fig. 3.72b). Two antiformal hinge lines of superposed folds may link with an early noncylindrical antiform to produce folds where the hinge lines show a pseudo rotation of 180° (Fig. 3.72c).

The knowledge of the interference patterns helps in resolving complex geometrical fold shapes in outcrops and maps. For example, superimposed folds are prominently developed in Jutogh schists in the Simla area, Himachal Himalaya (Fig. 3.73). The pattern appears to be complicated at first glance but a careful observation can separate the fold shapes into early and superposed folds making it apparent that the folds have developed by maximum compression in orthogonal directions.

It is to be noted that fold hinge lines and axial surfaces can show prominent curvature during a single phase of deformation hence the superimposed folds must not be identified on the basis of geometrical shapes alone. A particular shape can result from more than one mechanism and a single mechanism can result in more than one geometrical shape. For example, Fig. 3.74 depicts two geometries developed in an asymmetric fault propagation fold. With progressive deformation, the basement thrust undergoes a rotation and acquires a steep dip. The resultant subvertical push from underneath as a result of thrusting can modify the fold geometry to type 3 pattern (Fig. 3.74a). However, if the asymmetric fold develops a

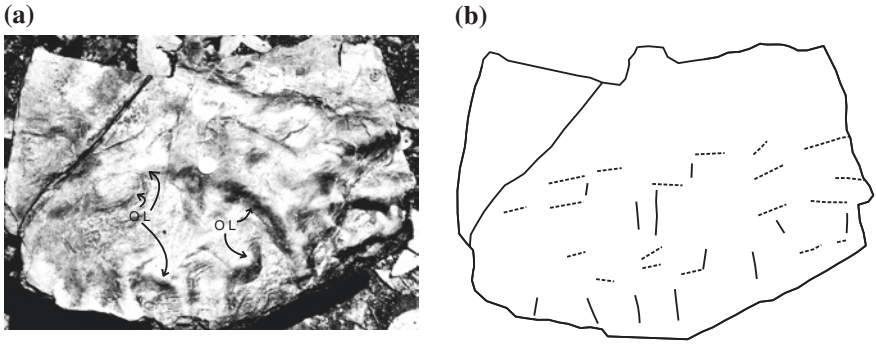

Fig. 3.73 **a** Superposed folds marked by curvature of fold hinge lines in Jutogh schist, Simla, Himachal Himalaya. *OL* orthogonal linking. **b** A possible orientations of the early (*continuous lines*) and superposed (*broken lines*) fold hinge lines prior to the interference

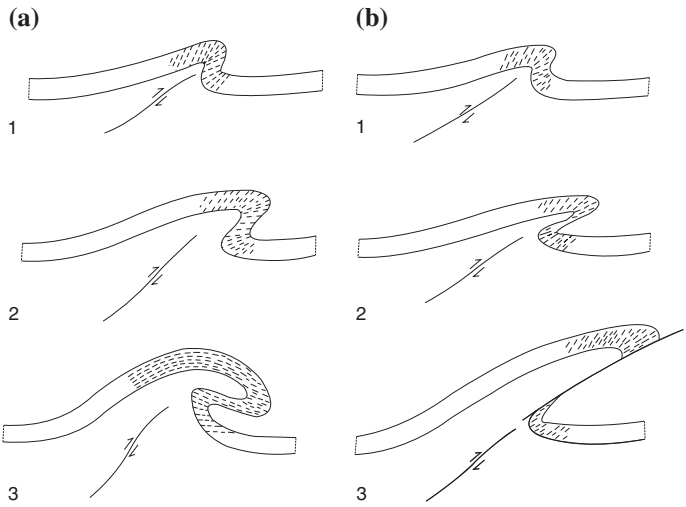

Fig. 3.74 Simplified diagrams to illustrate the geometrical modification of folds above an active thrust. **a** Type 3 interference pattern. **b** Development of limb thrust and normal drag pattern along the thrust (after Dubey and Bhat 1986)

limb thrust with increase in asymmetry, the type 3 pattern is unlikely to develop (Fig. 3.74b).

While analyzing superposed folds, the following points should be taken into account.

1. Oblique linking of fold hinge lines

Orientation of fold hinge lines is sometimes used as a criterion to distinguish between different generations of folds. However this may sometimes lead to erroneous inferences. For example, Fig. 3.75a shows oblique linking of two fold

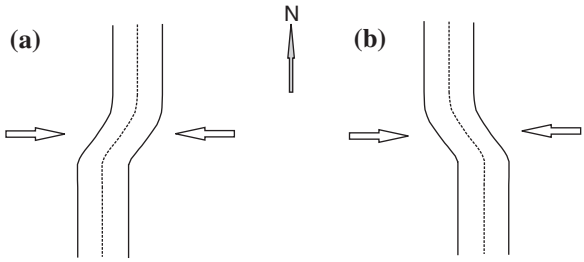

Fig. 3.75 Oblique linking of simultaneously developing folds. **a** *Right* lateral or dextral oblique linking. **b** *Left* lateral or sinistral oblique linking

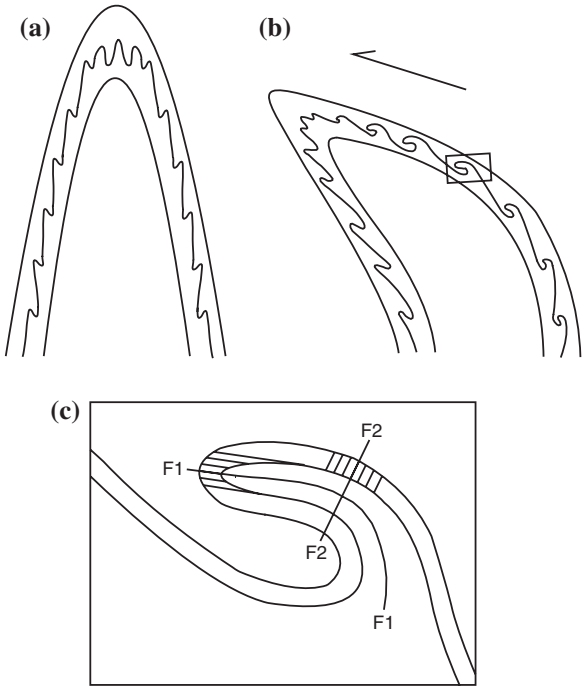

Fig. 3.76 Development of refolded fold geometries as a result of folding of polyharmonic folds. **a** An upright polyharmonic fold. **b** Bending of the axial surface during a subsequent shearing. The sense of shear is shown by a *half arrow*. **c** An *enlarged view* of a refolded fold *inside the rectangle* shown in (**b**). *F1* early axial surface; *F2* later axial plane. The two axial plane cleavages are at a large angle to one another

complexes with orientation of fold hinge lines in N–S, and NE–SW direction (in the region of interference). In a different pattern of oblique linking (Fig. 3.75b), the hinge line orientations are in N–S and NW–SE directions. The three orientations of the hinge lines have developed in a single deformation with predominant E–W maximum compression. Following the terminology of strike-slip faults, fold linking in Fig. 3.75a may be described as right lateral oblique linking and Fig. 3.75b may be described as left lateral oblique linking.

2. Refolding of polyharmonic folds

Refolding of upright polyharmonic folds by later shear strains can modify the fold geometries to refolded shapes. For example, a polyharmonic fold is shown in Fig. 3.76a. Later shearing in the same or at a subsequent phase of deformation can produce a curvature of axial surface of the larger fold and refolding of the

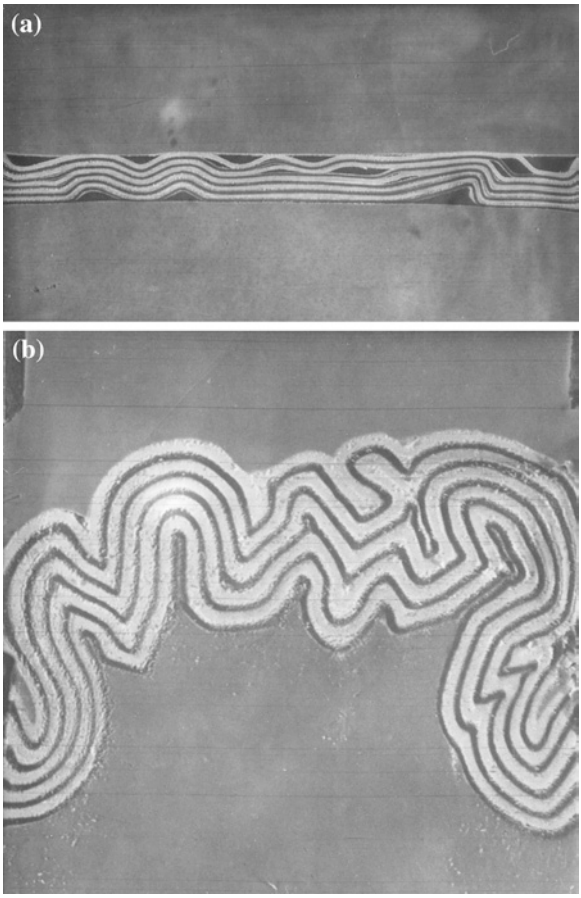

Fig. 3.77 **a** Cross-sectional fold shapes and multiple decollement in a multilayer Plasticine model (10 % shortening). The model was compressed along the layering and the resulting extension took place normal to the fold hinge lines. **b** The same model after 74 % shortening. After 49 % shortening, the direction of maximum compression remained unchanged, the extension was allowed to take place along the fold hinge lines [from Dubey (1980). © Elsevier. Published with permission of Elsevier Scientific Publishing Company]

smaller folds (Fig. 3.76b). These refolded folds resemble type 3 interference pattern (Fig. 3.76c). Two axial plane foliations can also be seen along the early (F1) and the later (F2) folds.

3. Variation of fold interlimb angles

After initiation, the fold laterally propagates by forming a series of antiforms and synforms. During the sequential initiation of folds, the first formed fold is characterized by the lowest interlimb angle with gradual increase in the angle towards the fold propagation directions. Hence folds of one generation can show different interlimb angles, which cannot be used as a criterion for distinguishing different phases of folding.

4. Presence of plane of decollement

Presence of a plane of decollement (plane of relatively easy slip) at the basement-cover interface or planes of decollement within a multilayer sequence can have

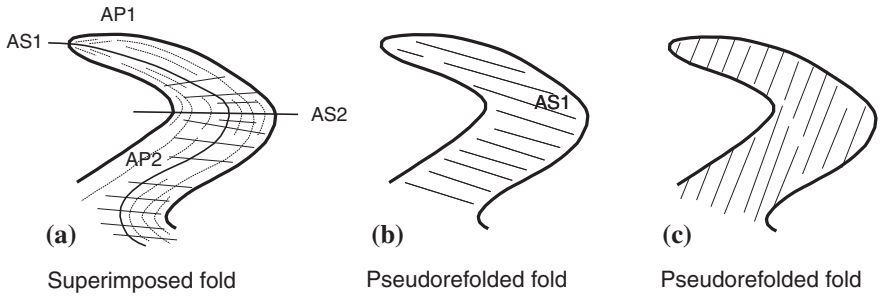

Fig. 3.78 **a** A superimposed fold characterized by two axial plane cleavages. *AS1* early axial surface; *AP1* early axial plane cleavage; *AS2* superposed axial surface; *AP2* later axial plane cleavage. **b**, **c** A pseudo-refolded fold. The geometrical shape resembles a superimposed fold but there is only one cleavage. The cleavage may be unrelated to the axial surface(s) of the fold(s)

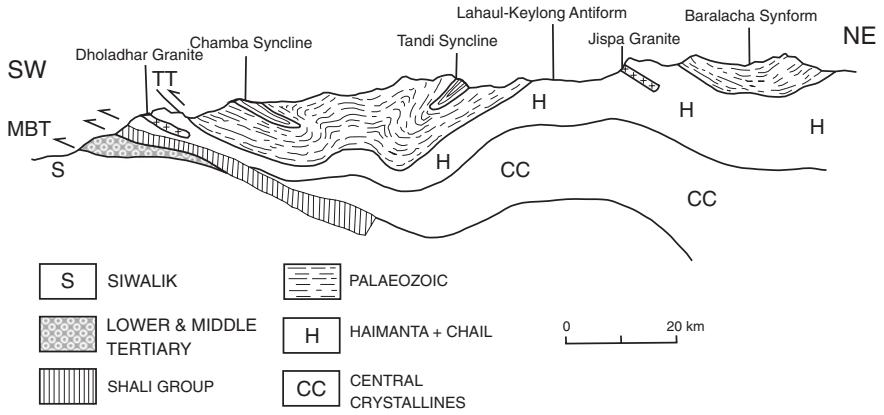

Fig. 3.79 A cross-section through the Himachal Himalaya. Note that the axial surfaces of Chamba and Tandi synclines are dipping towards each other as a result of plane of decollement at the base [from Thakur (1992). © Elsevier. Published with permission of Elsevier]

significant effect on the developing fold geometries. The decollements can result from decrease in boundary load at the onset of deformation (e.g. at upper levels of the earth's crust). Compressive stresses along a multilayer with multiple decollement results in formation of dilation spaces of irregular size, spacing, and distribution (Fig. 3.77a; Dubey 1980). These spaces can result in a large number of fold shapes, e.g. chevron, rounded, box, isoclinal, elastica, and recumbent (Fig. 3.77b). After locking of these folds, the second order folds can also form. It is easier to visualize a plane of decollement at the basement-cover interface but in a multilayer fold profile these planes will not be visible at late stages of fold formation. In such situations, different orientations and curvature of the axial surfaces may resemble the geometrical shapes of superimposed folds. However a careful study of fold geometries along a profile plane or bedding-cleavage relationships

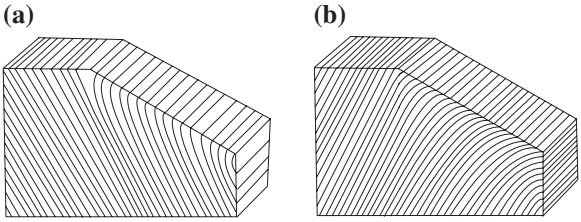

Fig. 3.80 Creep structures on opposite dipping beds at uniform hill slope (after Billings 1954)

in isolated outcrops can differentiate between the superimposed refolded folds (Fig. 3.78a) and pseudo-refolded folds (Fig. 3.78b). The superimposed fold has two axial plane cleavages whereas the pseudo-refolded fold has only one axial plane cleavage. Moreover, the cleavage orientation may not be related to the fold axial surface (Fig. 3.78c).

These fold geometries can occur on large scale as well. One such example is shown from the Tethys Himachal Himalaya (Fig. 3.79) (Thakur 1992). The high grade metamorphic rocks of the Central Crystallines occur at the base and the Palaeozoic metasedimentary rocks occur as cover. The contact is a plane of decollement. The Chamba and Tandi synclines have opposite vergence whereas the intermediate rocks display a box fold geometry.

3.15 Creep

Most of the structural features are governed by processes that take place deep inside the earth's crust. However once these features appear on the surface they are acted upon by superficial processes. One of these processes is time dependent strain known as creep. This is produced in rocks over long time duration under continuous deformation, which is well below the rupture strength of the rock. Normally a rock, which is supposed to behave as a brittle substance may acquire viscous properties if low strain is applied over a long period. Out of these the hillside creep is particularly interesting because it produces deceiving fold structures. Examples of this kind are shown in Fig. 3.80. The figures show dipping beds in opposite directions and resulting curvature of beds as a result of creep. A natural example of the hillside creep are shown in Fig. 3.81 where the creep has produced superimposed fold like structure in turbidite sequence of alternate greywacke and shale layers from the Carboniferous Culm Series of SW England.

3.16 Concluding Remarks

While interpreting a large-scale structure using small-scale structures, the following precautions are necessary.

1. Field studies are normally confined to observations on two-dimensional profile sections of few meters whereas a geological structure may have an extent of

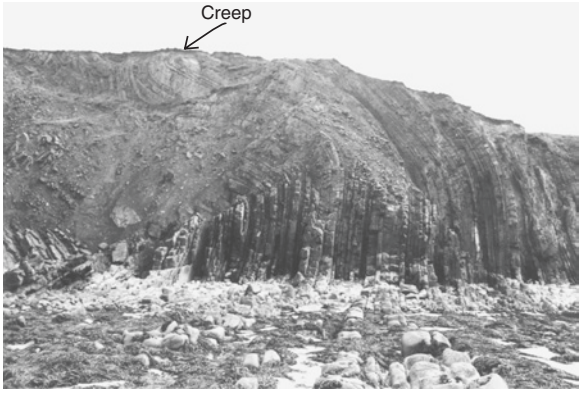

Fig. 3.81 Creep structure in turbidite sequence of rocks, Bude, SW England

several square kilometers in three dimensions. This needs careful interpretation. For example, one has to be sure whether overturning of layers is a result of minor overturned folds or the overturning is a regional feature.

2. Quartzite should be regarded as the least reliable marker bed because of colour, textural and mineralogical similarities between different quartzite beds. Additional evidence must be sought for interpretation of a large-scale structure.
3. Evolution of folds in sedimentary and low grade metamorphic rocks clearly indicate that folds lock at low interlimb angles and isoclinals folds can only develop in presence of a prominent plane of decollement or a number of decollement planes.
4. Fold propagation and interference effects are simple and these can be applied to large-scale structures as well. For example, there are syntaxial bends on the eastern and western borders of the Himalaya. These syntaxial bends can result from either bending of the fold belts (involving a complicated deformation and complex strain patterns) or simply by fold initiation at different points, longitudinal propagation and linking without involving much deformation and complicated strain patterns.

References

Bamford MLF, Ford M (1990) Flexural shear in a periclinal fold from the Irish Variscides. J Struct Geol 12:59–67

Bayly MB (1971) Similar folds, buckling and great circle patterns. J Geol 79(110):118

Behzadi H, Dubey AK (1980) Variation of interlayer slip in space and time during flexural folding. J Struct Geol 2:453–457

Billings MP (1954) Structural geology. Prentice Hall, Englewood Cliffs, 514 pp

Biot MA (1961) Theory of folding of stratified visco-elastic media and its implications in tectonics and orogenesis. Geol Soc Am Bull 72:1595–1620

Biot MA (1964) Theory of internal buckling of a confined multilayered structure. Geol Soc Am Bull 75:563–568

Chapple WM (1968) A mathematical theory of finite amplitude folding. Bull Geol Soc Am 79:47–68

Cobbold PR (1975) Fold propagation in single embedded layers. Tectonophysics 27:333–351
Cobbold PR (1976) Fold shapes as functions of progressive strain. Philos Trans R Soc Lond A 283:129–138
Cobbold PR, Cosgrove JW, Summers JM (1971) Development of internal structures in deformed anisotropic rocks. Tectonophysics 12:23–53
Currie JB, Patnode HW, Trump RP (1962) Development of folds in sedimentary strata. Geol Soc Am Bull 73:655–674
Davis GH (1984) Structural geology of rocks and regions. Wiley, New York 492 pp
Davy Ph, Cobbold PR (1991) Experiments on shortening of a 4-layer model of the continental lithosphere. Tectonophysics 188:1–25
De Sitter LU (1958) Boudins and parasitic folds in relation to cleavage and folding. Geol Mijnbouw 20:277–288
Dietrich JH (1970) Computer experiments on mechanics of finite amplitude folds. Can J Earth Sci 7:467–476
Dubey AK (1980) Late stages in the development of folds as deduced from model experiments. Tectonophysics 65:311–322
Dubey AK (1983) Variation in nature of deformation across a multilayer fold profile and its geological implications. Geosci J 4:105–116
Dubey AK (1984) Superimposed buckle folding in multilayers: interference patterns and simultaneous development with transcurrent faults. Geosci J 5:59–72
Dubey AK, Behzadi H (1981) Development of flexural slip folds, overlapping boudins and extension faults in multilayered materials: field evidence and experimental model. J Geol Soc India 22:274–284
Dubey AK, Bhat MI (1986) The role of reactivation of pre- rift basement listric faults in the structural evolution of the Himalaya: an experimental study. Himalayan thrusts and associated rocks. Curr Trends Geol 9:265–290
Dubey AK, Cobbold PR (1977) Noncylindrical flexural slip folds in nature and experiment. Tectonophysics 38:223–239
Fleuty MJ (1964) The description of folds. Proc Geol Assoc 75:461–492
Flinn D (1962) On folding during three-dimensional progressive deformation. Quat J Geol Soc Lond 118:385–433
Ghosh SK (1966) Experimental tests of buckling folds in relation to strain ellipsoid in simple shear deformations. Tectonophysics 3:169–185
Ghosh SK (1968) Experiments on buckling of multilayers which permit interlayer gliding. Tectonophysics 6:207–249
Ghosh SK (1974) Strain distribution in superposed buckling folds and the problem of reorientation of early lineations. Tectonophysics 21:249–272
Ghosh SK (1976) Interfering buckle folds—a review of experimental results. Bhu Vidya 34:C47–C55
Ghosh SK (1993) Structural geology: fundamentals and modern developments. Pergamon Press, Oxford, 589 pp
Ghosh SK, Ramberg H (1968) Buckling experiments on intersecting fold patterns. Tectonophysics 5:89–105
Hobbs BE, Means WD, Williams PF (1976) An outline of structural geology. Wiley, New York 571 pp
Hubbert MK (1937) Theory of scale models as applied to the study of geologic structures. Bull Geol Soc Am 48:1459–1520
Hudleston PJ (1973) An analysis of single layer folds developed experimentally in viscous media. Tectonophysics 16:189–214
Hudleston PJ, Lan L (1993) Information from fold shapes. J Struct Geol 15:253–264
Hudleston PJ, Treagus SJ (2010) Information from folds: a review. J Struct Geol 32:2042–2071
Johnson AM (1977) Styles of folding: mechanics and mechanism of folding of natural elastic materials. Elsevier, Amsterdam, 426 pp

McClay KR (1976) The rheology of Plasticine. Tectonophysics 33:T7–T15
McClay KR (1989) Analogue models of inversion tectonics. In: Cooper MA, Williams GD (eds) Inversion tectonics. Geological Society of London Special Publication No. 44, pp 41–59
McClay KR, Buchanan PG (1992) Thrust faults in inverted extensional basins. In: McClay KR (ed) Thrust tectonics. Chapman & Hall, London, pp 93–104
Mukhopadhyay D, Sengupta S (1979) "Eyed folds" in Precambrian marbles from southeastern Rajasthan, India. Geol Soc Am Bull 90:397–404
Price NJ, Cosgrove JW (1990) Analysis of geological structures. Cambridge University Press, Cambridge, 502 pp
Ragan DM (1985) Structural geology. An introduction to geometrical techniques, 3rd edn. Wiley, New York, p 393
Ramberg H (1961) Contact strain and folding instability of a multilayered body under compression. Geolgie Rundschau 51:405–439
Ramberg H (1963) Fluid dynamics of viscous buckling applicable to folding of layered rocks. Bull Am Assoc Pet Geol 47:484–505
Ramberg H (1964) Selective buckling of composite layers with contrasted rheological properties. Tectonophysics 1:307–341
Ramberg H (1967) Gravity, deformation and the Earth's crust as studied by centrifuged models. Academic Press, New York 241 pp
Ramsay JG (1962) Interference patterns produced by superposition of folds of "similar" type. J Geol 70:466–481
Ramsay JG (1963) Structure and metamorphism of the Moine and Lewisian rocks of the North West Caledonides. In: The British Caledonides. Oliver & Boyd Ltd, Edinburgh, pp 143–175
Ramsay JG (1967) Folding and fracturing of rocks. McGraw Hill, New York 568 pp
Ramsay JG (1974) Development of chevron folds. Bull Geol Soc Am 85:1741–1754
Ramsay JG (1980) Shear zone geometry: a review. J Struct Geol 2:83-99. doi:10.1016/0191-8141(80)90038-3
Ramsay JG, Huber MI (1983) The techniques of modern structural geology, vol 1. Strain analysis. Academic Press, New York, 307 pp
Ramsay JG, Huber MI (1987) The techniques of modern structural geology, vol II. Folds and fractures. Academic Press, New York, pp 309–700
Sen K, Dubey AK, Tripathi K, Pfänder JA (2012) Composite mesoscopic and magnetic fabrics of the Paleo-Proterozoic Wangtu Gneissic Complex, Himachal Himalaya, India: Implications for ductile deformation and superposed folding of the Himalayan basement rocks. J Geodyn 61:81–93
Sherwin JA, Chapple WM (1968) Wavelengths of single layer folds: a comparison between theory and observation. Am J Sci 266:167–179
Thakur VC (1992) Geology of Western Himalaya. Pergamon, New York, 363 pp
Thiessen RL, Means WD (1980) Classification of fold interference patterns: a reexamination. J Struct Geol 2:311–316
Treagus SH (1997) Modelling deformation partitioning in folds. In: Sengupta S (ed) Evolution of geological structures in micro-to macro-scales. Chapman & Hall, London, pp 341–372
Turner FJ, Weiss LE (1963) Structural analysis of metamorphic tectonites. McGraw Hill, New York 545 pp
Watkinson AJ (1981) Patterns of fold interference: influence of early fold shapes. J Struct Geol 3:19–23

Chapter 4
Thrust Fault

Abstract Thrust fault and its classification is described. Formation of normal and reverse drags is explained in terms of frictional effects along the thrust surface. Flat and ramp, and smooth trajectory thrusts are illustrated along with the associated cleavage patterns. Evolution of planar and listric faults is depicted in an inverted basin. A new model is proposed for development of duplex structures. Decollement upwarps have been identified in the foreland basin of the Himalaya and a model is proposed for their evolution. The model implies that formation of upwarp structures inhibits displacement along basal decollements. Formation of oblique thrust ramps and associated structures are highlighted. A new model, called as basement wedge klippe model, is proposed for formation of klippe structure. Problems related to restoration of deformed sections are described. An unrestorable section does not mean a wrong construction. The thin-skinned model for evolution of fold and thrust belts may not be universally applicable to all the orogenic belts.

Three important mechanisms, which control the deformation patterns in geological horizons are extension, shortening, and shearing. These mechanisms result in distinct structural features. Faulting of rocks is one of them. Faults are fractures along which there is visible displacement. Out of different types of faults, thrust faults play a crucial role in development of mountains because they cause uplift and translation of huge rock masses. These faults are formed in predominant compressional regimes when the maximum compression is in horizontal direction and the maximum extension (minimum compression) is in vertical direction (Fig. 4.1). Strike of the fault remains parallel to the intermediate axis of compression (i.e. normal to the vertical section). The stress condition results in formation of gently inclined thrust fault where the hanging wall moves up relative to the footwall. The upward movement of the hanging wall brings older layers of the hanging wall in contact with younger layers of the footwall. For example, the oldest layer of sequence 'A' (Fig. 4.1a) is in contact with the younger layer B in the footwall (Fig. 4.1b), across the fault. Similarly B is in contact with C, and so on.

A. K. Dubey, *Understanding an Orogenic Belt*, Springer Geology,
DOI: 10.1007/978-3-319-05588-6_4,

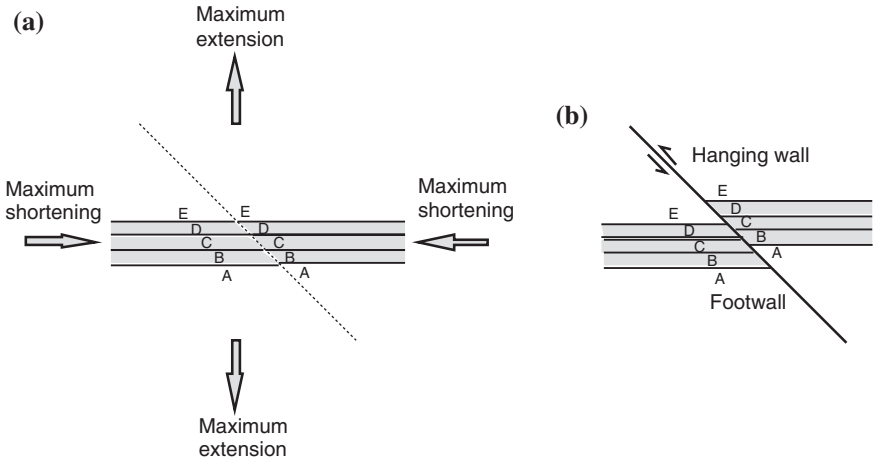

Fig. 4.1 Displacement along a thrust fault. **a** Initial disposition of a multilayer sequence with directions of maximum shortening and extension. **b** Upward displacement of the hanging wall (or downward displacement of the footwall, or both) resulting in formation of a thrust fault

4.1 Reverse and Normal Drags

Displacement along a thrust fault can vary from few mm to more than 100 km. For a larger magnitude of displacement, the fault surface should have a minimum friction, which is provided by proper lubrication. The fault lubrication is facilitated by fluids derived from surrounding rocks in high temperature–pressure conditions. At upper levels of the earth's crust, the lubrication is provided by favourable lithological beds like gypsum, salt, graphite etc. A good lubrication facilitates displacement with low energy and avoids crumpling of the rock mass during the push. The hanging wall and footwall layers are displaced and stretched in the direction of relative displacement along the thrust forming a reverse drag (Fig. 4.2a) (cf. Hamblin 1965). In contrast, friction along a fault is likely to produce normal drag (Fig. 4.2b). Increased frictional effects can result in intense crushing and formation of fault breccia along the fault surface.

Thrusts are best studied in cross-sectional profiles because displacement magnitudes along minor faults can be measured and development of associated structural features can be observed.

4.2 Classification of Thrust Faults

Thrusts can be broadly classified into the following categories based on their cross-sectional geometries.

1. *Planar fault*

The fault surface cutting across a layered sequence is planar (Fig. 4.1). Normally these faults occur on small-scale. At large scales, they tend to acquire curved forms.

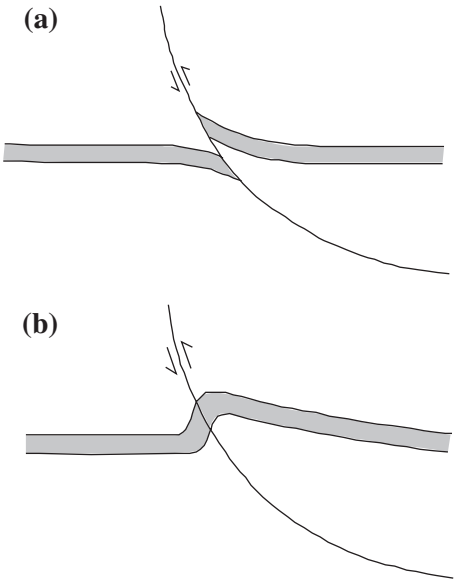

Fig. 4.2 Displacement of a layer across a thrust leading to formation of reverse drag (**a**), and normal drag (**b**). [From Dubey and Bhakuni (1998), © Elsevier. Published with permission of Elsevier]

2. *Flat and ramp faults*

Rich (1934) was one of the early workers who conceptualized the ramp and flat geometry of thrust faults while working in the Appalachian Mountains. The formation of folds was explained as superficial structures formed by passive translation of thrust blocks over ramps on detachment surfaces. The internal strains in these rocks are of minimal values. Later, the concept was applied to the Canadian Rockies, Idaho-Wyoming thrust belt, Pyrenees, and Scottish Highlands. The model, based on volume conservation, eventually led to formation of thin-skinned tectonics. Due to simplicity of the model, clear geometrical assumptions, and its ability to restore deformed cross-sections to determine shortening amounts, the model became popular amongst a large section of structural geologists. This has also been proved useful for hydrocarbon explorations, especially in Canada, America, and the North Sea (Britain). However, a few inherent geometrical assumptions, discussed below, compel the structures to have identical geometries and therefore cross-sections from different orogenies, varying in rheological properties and deformation conditions, have identical cross-sections (Ramsay and Huber 1987; Casey and Dietrich 1997).

Flats are essentially parallel to an incompetent horizon. Deformation is concentrated above a plane of decollement and basement remains undeformed (Fig. 4.3). The existence of a floor or sole thrust depends on the presence of a prominent incompetent bed that acts as a lubricating horizon. The situation is common in orogenic belts where the basement is high grade metamorphic rock. However because of inhomogeneous nature of the rock and boundary conditions, the fracture cannot propagate for a very long distance. Hence the flat geometry represents the early stage of thrust initiation and propagation. The geometry is followed by step-like ramp geometry across a more competent layer and finally merging into another incompetent

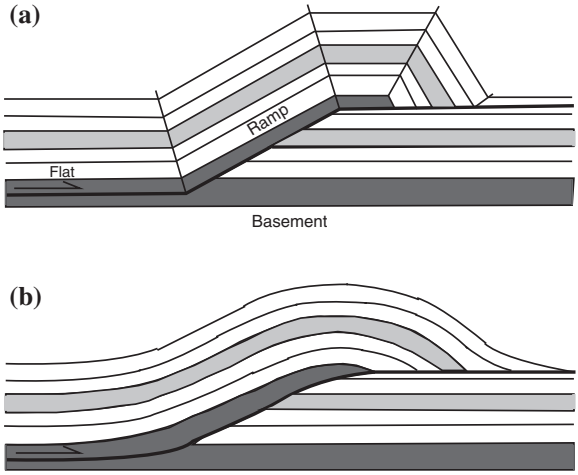

Fig. 4.3 Geometry of hanging wall folds controlled by geometry of the ramp. **a** Flat and ramp fault geometries. The fault propagation has resulted in development of angular folds in the overlying layers. **b** Smooth trajectory thrust resulting in curved folds in the overlying layers. [From H. Fossen (2010), © Cambridge University Press. Published with permission of Cambridge University Press, Cambridge]

bed as flat. Displacement of hanging wall layers over a ramp results in bending of the layers in harmony with the ramp geometry and formation of fault-bend folds. Kink band geometry of the flat and ramp structure is reflected in hanging wall folds (Fig. 4.3a). The fault geometry represents an initial stage of fault propagation and the sharp kinks can acquire a gradual curvature or smooth trajectory thrust with increase in deformation (Fig. 4.3b). The kink band geometry is preferred by many structural geologists because the layer parallel (homogeneous) shortening can be ignored and the folded layers can be easily restored to their supposedly initial orientation. Since the faults terminate at the basement and does not penetrate very deep into the earth's crust, the mechanism is described as thin-skinned tectonics. The tectonic style has been described as characteristic of foreland foothill belts consisting of sedimentary rocks deformed independently of an underlying basement (Dahlstrom 1969; Elliott 1976; Boyer and Elliott 1982; Suppe 1985).

Fabric of a rock can differ in staircase-trajectory and smooth-trajectory thrusts (Cooper and Trayner 1986) (Fig. 4.4). In the ideal staircase trajectory model, the footwall remains undeformed, i.e. there is no fabric or strain development and the beds are planar (unfolded) during the thrust propagation (Fig. 4.4a). The hanging wall anticline reveals strains related to passive fold formation. However strain studies in fold-and thrust-belts contradicts these essential requirements. The footwall is mostly deformed and the hanging wall shows deformation not entirely related to thrusting (Fig. 4.4b). In case of smooth-trajectory thrust, the footwall displays folding of the beds, strains and/or development of fabrics.

3. *Listric faults*

Listric faults have a smooth curvature and they may not necessarily terminate into a lower horizon of incompetent rock. These faults are characterized by gradual

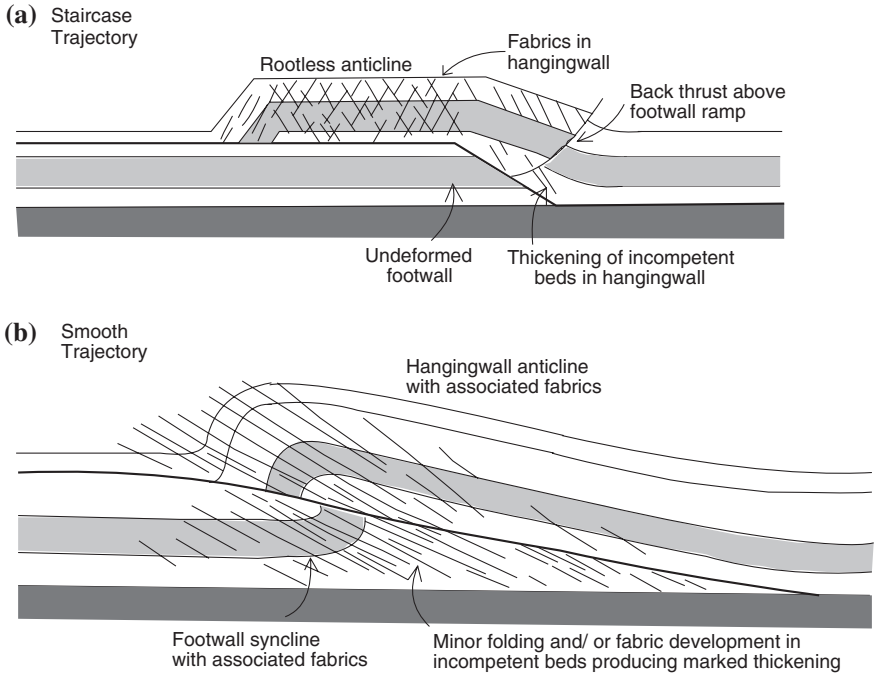

Fig. 4.4 Deformation features associated with angular and smooth trajectory thrusts. **a** Flat and ramp (staircase) trajectory. **b** Smooth-trajectory. [From Cooper and Trayner (1986), © Elsevier. Published with permission of Elsevier]

variation of dip with depth. Positive listric faults show gradual decrease in fault dip with increase in depth whereas negative listric faults show gradual increase in dip with increasing depth (Fig. 4.5). Since the dip is continuously changing with depth, the fault cannot be classified strictly into thrust (fault dip $< 45^{\circ}$), reverse fault (fault dip $> 45^{\circ}$), or overthrust (fault dip $< 10^{\circ}$). The hanging wall and footwall layers are deformed simultaneously. Fault displacement varies along the fault and a higher fault dip results in a larger rotation of hanging wall layers. Hence positive listric faults are expected to show a decrease in layer rotation with increase in depth.

Since the listric faults have a smooth trajectory, displacement along the fault is easier provided frictional effects are minimal along the fault surface.

Results of sand model experiments and related theoretical studies are shown in Fig. 4.6. One sided layer parallel compression resulted in development of asymmetric folds. Geometry of the folds, boundary stresses, and approximate pattern of stress distribution is shown in Fig. 4.6a. Figure 4.6b illustrates an approximate pattern of principal stress trajectories, which are tangential curves to principal stresses at every point. Since the principal stresses are mutually perpendicular, three principal stress trajectories one each for σ_1, σ_2, and σ_3 pass through each point. In a two-dimensional stress system on a plane parallel to σ_1 and σ_3, two families of orthogonal stress trajectories, one everywhere parallel to σ_1 and the

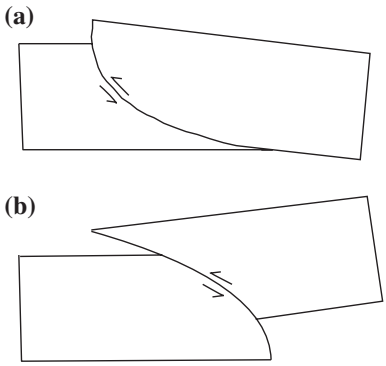

Fig. 4.5 Two types of listric faults **a** Positive listric fault **b** Negative listric fault

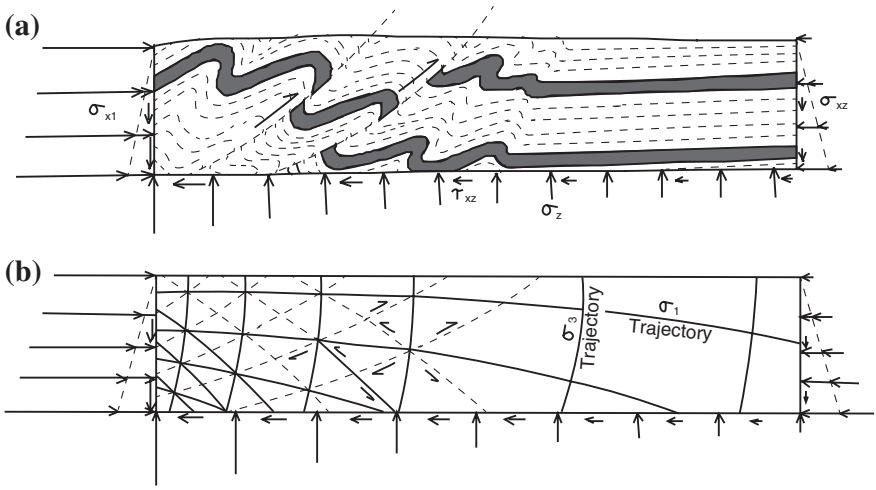

Fig. 4.6 **a** Two-dimensional stresses acting upon boundaries of a block consisting of multilayers. **b**. Principal stress trajectories (*solid lines*) and potential reverse fault surfaces (*broken lines*) compatible with the boundary stresses of the *top figure* (**a**). [From Hubbert (1951), © Geological Society of America. Published with permission of Geological Society of America.]

other to σ_2, exist (Hubbert 1951; Hafner 1951). The family of greatest stress trajectories, σ_1, is convex upward, plunge downward and divergent to the right. The family of least-stress trajectories, σ_3, is orthogonal to this pattern. It is tempting to relate the slip lines to listric geometry of the developing faults but it has been shown by Jackson and McKenzie (1983) that the slip lines within such a system are not discrete surfaces on which slip is concentrated and across which there is a velocity discontinuity. The velocity is continuous throughout the deforming region and cannot concentrate on faults. Hence no effort should be made to relate the slip lines and faults.

4.2.1 Basal Decollement

The term decollement is used as a plane of relatively easy slip during folding whereas basal decollement is used as an interface between the competent basement and comparatively softer overlying sediments that are mechanically detached from the basement. In the thin-skinned model all faults initiate from a basal decollement and occur as splay faults. In contrast, a basal decollement can occur in the listric fault model but all major listric faults may or may not join the basal decollement. These faults become gentler at depth and they may terminate prior to reaching the decollement. Hence it is more likely that they form a zone of basal decollement rather than a plane of basal decollement.

4.3 Flat and Ramp Model

A model for the evolution of thrust with flat and ramp geometry was proposed by Suppe (1983, 1985). The model involves deformation of hanging wall rocks with kink geometry whereas the footwall remained inactive and undeformed (Fig. 4.7). The axial planes of the kinks develop simultaneously with displacement along the thrust and the planes migrate through the layers during folding.

The limbs of the kink gradually increased in length with increase in fault displacement and formation of hanging wall ramp anticline (an antiformal structure developed above a thrust ramp). The development results in variation in the shear state in various sectors of the fold as shown in Fig. 4.8 (Ramsay and Huber 1987). The positive and negative sense of bedding parallel shear is marked by their respective sign.

The shear sense in different sectors of a kink fold can be accommodated but development of kink geometry in hanging wall rocks simultaneously with displacement along thrust imposes a few problems. For example Fig. 4.8a shows two sectors A and B marked in gray. The sector A (marked with circles) represents an undeformed region and sector B (marked with positive sign) represents positive shear in rear limb of the kink. The frontal limb of the kink is characterized by negative shear. Figure 4.8b represents an advanced stage in the development of kink and thrust translation where the sectors A and B occupy new positions. Sector A moves to a new position A′ in the rear limb of the kink thereby changing its position from an undeformed region to a region undergoing positive shear. Sector B moves to a new position B′ adapting to a new geometry as a result of negative shear.

With continued displacement along the thrust, sector A′ moves to position B, then to position B′ and subsequently B′ moves to an unstrained sector on the hinge zone of the kink. The process repeats itself in time and space and the hanging wall rock undergoes a complicated history of straining and unstraining. It is difficult to envisage such a mechanism for natural rock deformation. The process will further complicate if reactivation and reversal of displacement along a fault is considered during inversion tectonics.

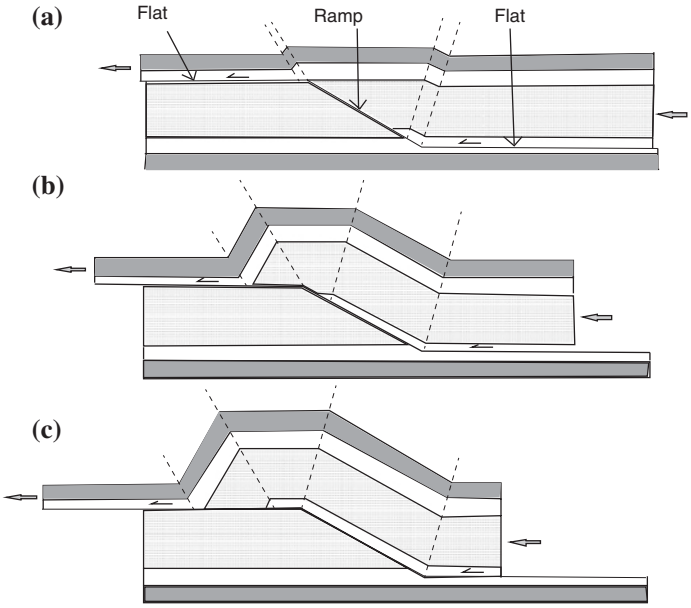

Fig. 4.7 Development of flat and ramp geometry along a thrust. The footwall is undeformed. **a** Initiation of flat in an incompetent layer and ramp in a more competent layer. As a result of thrust displacement, axial planes of a kink fold develop in the hanging wall overlying layers. **b** Propagation of the axial planes and formation of a kink fold in the hanging wall. **c** Propagation along the thrust with kink band geometry. [From Suppe (1985), © J. Suppe. Published with permission of J. Suppe]

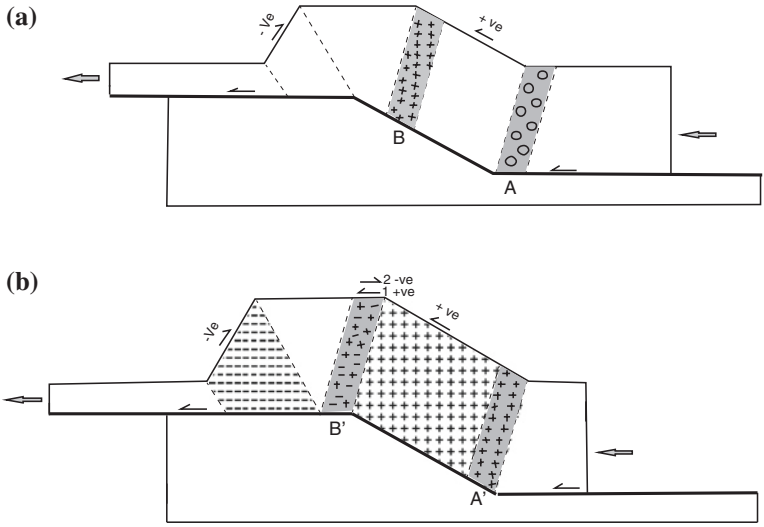

Fig. 4.8 Shear state in various sectors of a kink fold hanging wall structure. [From Ramsay and Huber (1987), © Elsevier. Published with permission of Elsevier]

The staircase or flat and ramp model of thin-skinned thrust tectonics excludes the possibility of deformation in the footwall. However after a detailed field study of the Caledonides of NW Scotland, Ramsay (1997) found out that the basement possessed almost the same ductility as the cover and an unconformity at the basement-cover interface was not a site of localized detachment. The formation of schistosity and ductile mylonites was also found to be the same in the basement and the cover. Layer parallel shortening of cover sediments and the basement (up to ~30 %) during the tectonic development in the Eriboll region is also an important factor.

4.4 Problems with the 'Rocky Mountain' Thrust Model

The Appalachian 'Rocky Mountain' thrust model (Fig. 4.7) may not be applicable to all the orogenic belts because of the following reasons (Ramsay 1992).

1. Folding is closely associated with thrusting. The individual layers are deflected and folded as the thrust sheet translates over irregularities in the thrust surface or develop as a fault tip propagates through unfaulted rock. At the same time, a large number of buckle folds develop as a result of layer parallel shortening, at a distance from the thrust (Allmendinger 1982). In the Himalaya, folds on different scales have developed both during the early and superposed deformations. Asymmetric folds near the thrust and upright folds at a distance from a thrust is a characteristic feature of several parts of the Himalaya. Most of these upright folds have little relationship with thrusting.
2. The rheological properties of individual layers have no significant role in controlling the fold geometry in the model. However in the Helvetic nappes of Switzerland and in the Himalaya, lithologies do have a considerable influence on development of structures in the nappes and the folds are not just a result of passive layer bending above a variably inclined thrust surface.
3. When thrust surfaces having a gentle dip cut upwards across the stratigraphy and travel for a long distance, shearing and layer parallel shortening acts together in the transported hanging wall block (Fig. 4.9). This shortening leads to buckle folds in the more competent layers with initial wavelengths controlled by layer thickness, competence contrast, and number of layers in the sequence (Chap. 3). This deformation is ignored in the Rocky Mountain model.
4. In the classic model of fault bend folding, folds are developed only in the hanging wall rock sequence (Fig. 4.10a). However deformed footwall with no deformation in the hanging wall rocks (Fig. 4.10b), and footwall synforms with hanging wall antiforms have also been observed (Fig. 4.10c). The model cannot explain the formation of footwall synforms that mirrors the hanging wall antiforms.
5. The model also ignores the footwall folds that form as a result of localized shear displacements directly beneath the thrust surface as a result of strong ductile shear strains in proximity of the thrust surface (Fig. 4.11; also see experimental folds Fig. 7.1, 7.2, 7.4). A number of mechanisms have been suggested for development of folds in the footwall.

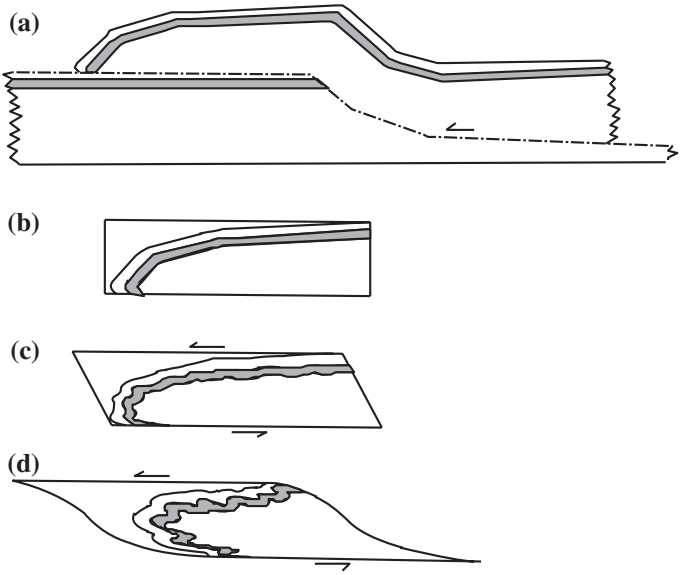

Fig. 4.9 An evolutionary model for geometric features of the frontal part of the Morcles nappe. **a** Displacement of the hanging wall rocks along a ramp and flat geometry. **b** The frontal part of the overthrust. **c** Further shortening of competent layer (*gray band*) and folding with superposed simple shear strain. **d** The effects on the fold shapes where the superposed simple shear is heterogeneous and is particularly strong along the upper and lower nappe contacts. [From Ramsay (1992)]

6. Natural folds with kink band geometry are normally observed on a centimetric or decimetric scale. Large-scale kink band geometry as envisaged in the fault bend fold model is extremely rare. Continuation of the kink band geometry for a larger distance in the hanging wall requires a considerable input of energy into the system. Normally, the deflection of incompetent material around a buckled layer progressively decreases away from the surface of the buckled layer in the zone of contact strain (Chap. 3). Such geometry gives the least work energy configuration of the system.
7. The ramp-flat model fails to explain the kinematics of the Helvetic nappes of Switzerland because the structures needed a more distributed deformation model. Hence the structure was explained by an overthrust shear zone model (Casey and Dietrich 1997). Each shear zone starts broad and narrows down to a high strain zone as it develops, ultimately forming a thrust fault. The model is applicable to other orogenies where the deformation took place at temperatures of sub-greenschist facies and above.
8. Basement rocks are also deformed in several orogenies (including the Himalaya) along with the cover rocks and no prominent plane of decollement exists above the basement.
9. Seismic sections can help in interpreting structural geometry in foreland regions but they have severe limitations in basement rocks. The seismic methods allow us to locate reflectors with low inclinations but steeply inclined reflectors give rise to transparent data windows. Moreover, without borehole data (as in the Himalaya), the reflection data can sometimes be made to fit in several kinematic models.

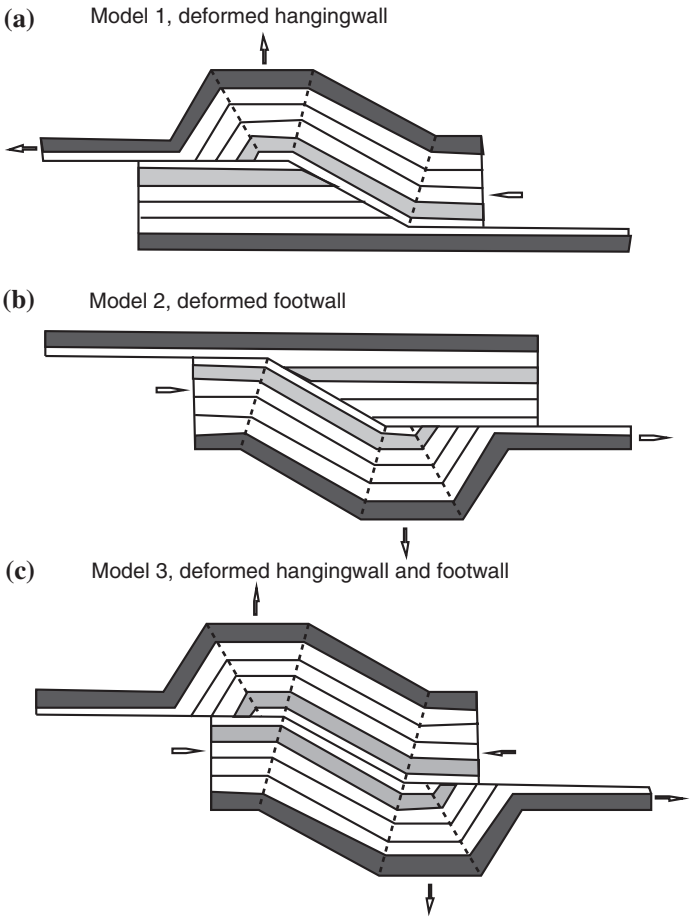

Fig. 4.10 Three models for development of hanging wall and footwall structures. [From Ramsay (1992)]

4.5 The Kimmeridge Bay Model

Considering the above points and based on field observations, Ramsay (1992) has proposed the Kimmeridge Bay model. A comparison of the Fault bend fold model and the Kimmeridge Bay model is shown in Fig. 4.12. Figure 4.12a depicts the overall shear between the hanging wall and footwall, flat and ramp geometry of the thrust, undeformed footwall, and kink band geometry of the hanging wall layers. Figure 4.12b shows a more realistic model incorporating the hanging wall and footwall deformations, additional shear planes associated with folding, zone of contact strain, and variation of strain in incompetent layers at different locations with respect to the fold.

Watkinson (1993) has also described a thrust fault from the Montana fold and thrust belt. Footwall of the thrust has taken most of the main fault deformation and

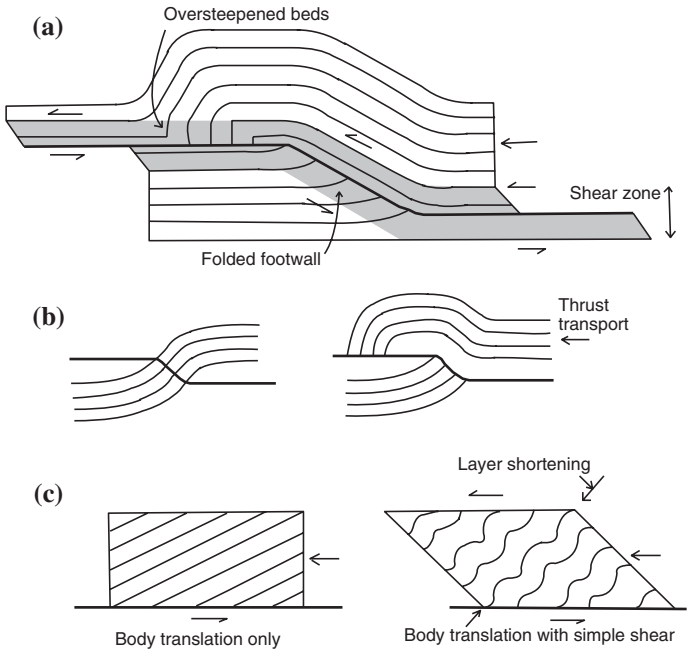

Fig. 4.11 Different mechanisms for development of folds in footwall. **a** Ductile shear in a zone (*gray*) along the thrust. **b** Development of ramp and flat structure in previously folded rocks. **c** Folds developed by thorough going simple shear in a transported thrust sheet. [From Ramsay and Huber (1987), © Elsevier. Published with permission of Elsevier]

depicts well-ordered system of subsidiary minor faults. Considering the demerits of the fault bend fold model, Ramsay (1997) has cautioned of inherent danger of building oversimplified and even incorrect structural analyses by forcing field data to fit a previously chosen model.

4.6 Imbricate Thrusts

One or more thrust faults can initiate simultaneously depending upon the available planes of weakness with suitable orientation. Normally the faults initiate from an incompetent lithology and propagate upwards through the more competent lithology. When the lower incompetent layer is a prominent horizon, a number of thrusts can initiate from this sole (or floor) thrust and propagate with an asymptotic geometry. These faults may continue upwards and merge in another prominent incompetent horizon called as roof thrust. Such a structure is called as duplex and the individual thrust nappes are called horses (Figs. 4.13a and 4.14). In absence of a roof thrust, the pattern of thrust surfaces is called as imbricate (or schuppen) structure. The individual fractures may differ in magnitude of fault

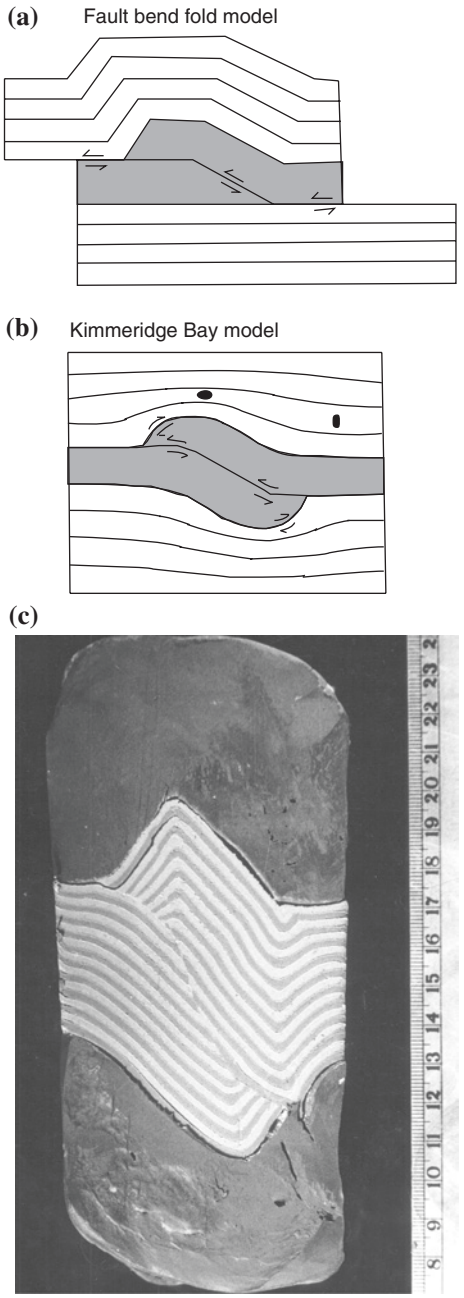

Fig. 4.12 Two models for thrust propagation. **a** The Fault bend fold model. *Half arrows* depicts overall shear between the hanging wall and footwall. **b** The Kimmeridge Bay model. *Half arrows* show additional shear planes on the hanging wall and footwall fold limbs. The strain ellipse shows strain patterns at different points in an incompetent layer. [From Ramsay (1992). **c** A deformed multilayer modeling clay model showing deformation of hanging wall and footwall

displacement and in order of their initiation. Sequential initiation of individual fractures and propagation towards the foreland is described as leading imbricate fan (Fig. 4.13b) or 'piggy back' because a new fracture carries the older fractures

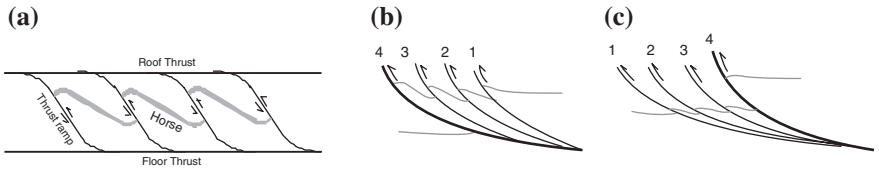

Fig. 4.13 Imbricate fan and horse structures. A marker horizon is shown in *gray*. **a** Duplex structure. **b** Leading imbricate fan. **c** Trailing imbricate fan. The sequence of fault initiation is shown by numbers. *1* is the oldest and *4* is the youngest (after Ramsay and Huber 1987)

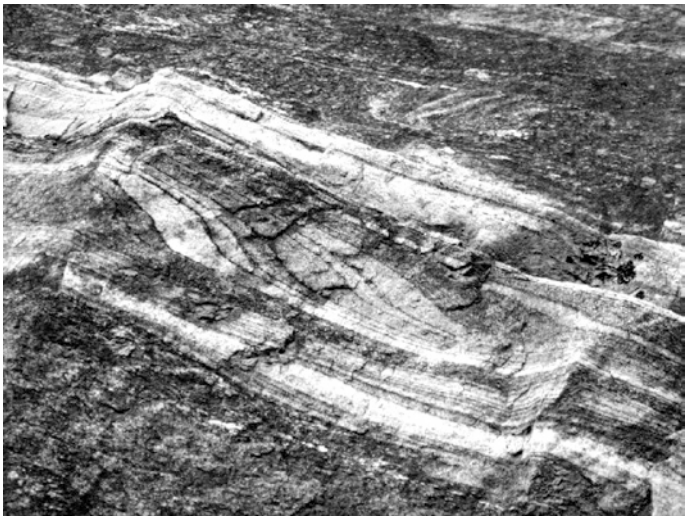

Fig. 4.14 A duplex structure in the Vaikrita Group gneiss (Sangla valley, Himachal High Himalaya)

on its back. In another situation when the sequence of formation of faults is in a reverse order and a new fault initiates towards the hinterland, the structure is known as out of sequence thrusts (Fig. 4.13c).

4.7 Development of Duplex Structure

In view of the problems associated with the Appalachian Rocky Mountain thrust model, a new model is envisaged where the thrust initiates with kink geometry but gradually modifies to a more geologically realistic geometry of smooth planes. Figure 4.15a shows initiation of a fracture in a layered sequence of competent beds and its propagation under a predominant compressional regime. The fault acquires kink band geometry after encountering incompetent horizons at both

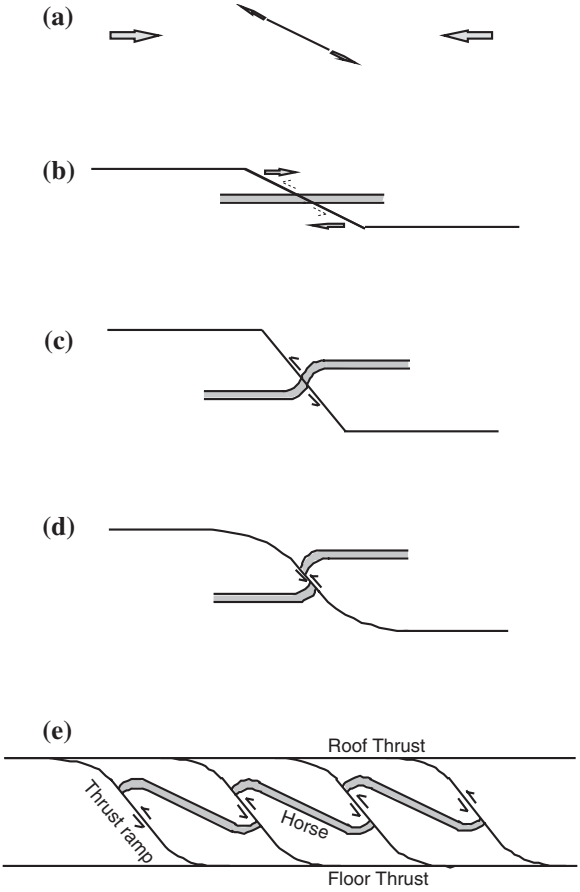

Fig. 4.15 A schematic model to show the development of duplex structure

ends (i.e. flats at incompetent horizon and ramp at a more competent horizon; the horizons not shown in the diagram) (Fig. 4.15b). Increase in fault displacement at the ramp with progressive deformation results in formation of drag folds in the competent bed across the ramp and rotation of the thrust ramp to a steeper geometry (Fig. 4.15c). The fault gradually acquires a smooth geometry so that sharp hinges of the kink gradually smoothens to a sigmoidal geometry to facilitate the increase in thrust displacement (Fig. 4.15d) (cf., Cooper and Trayner 1986). A number of fractures can initiate simultaneously at the onset of deformation (depending upon the available planes of weakness) or a new fracture can form after locking of a thrust at steep dips. The process repeats itself and a large number of thrusts can develop with similar stages of development. If the incompetent horizons at the base and the top are very prominent, a duplex structure is formed (Fig. 4.15e). The basal decollement surface is floor thrust whereas the top flat surface is roof thrust. The individual steep thrusts are ramps and the displaced

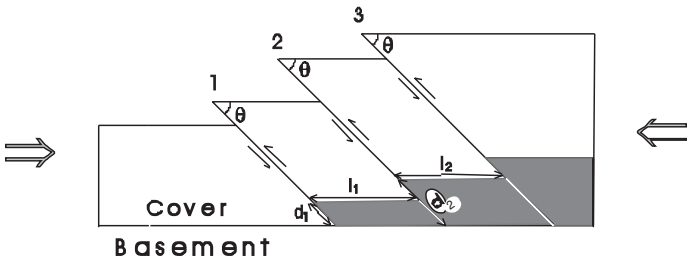

Fig. 4.16 A simplified diagram illustrating thrusting and formation of dilation spaces (marked in *gray*) above the basement. [From Dubey (2004), © John Wiley and Sons. Published with permission of John Wiley and Sons]

geological horizons are horses. In absence of prominent incompetent beds at the base and top, the fractures may initiate at different depths and the ramp structures may acquire different heights thereby resulting in a number of listric faults.

4.8 Development of Decollement Upwarp Structure

A non-planar basal decollement can also form as shown in the following simplified geometrical models.

4.8.1 Model 1

Figure 4.16 illustrates displacement of homogeneous and competent blocks along a number of planar thrusts above the basement-cover interface. The number of faults, their dip, and displacements can vary along a section. If it is assumed that all blocks are detached from the basement, the geometric outcome of the process will be formation of dilation spaces above the basement. The cross-section area of the dilation spaces (Δ) beneath the blocks is;

$$\Delta = \sum d_1 l_1 \sin\theta + \cdots d_1 l_1 \sin\theta$$

where

d distance between the interface and base of the cover block parallel to the thrust,
l length of the block parallel to the initial basement-cover interface, and
θ dip of the faults (assuming that all the faults have the same dip amount).

It is likely that any dilation created by thrusting would be filled in by folding of the interface and uplift of the basement, along with some secondary minerals. An antiformal structure so formed at the junction of basement flat and thrust ramp is termed as decollement upwarp.

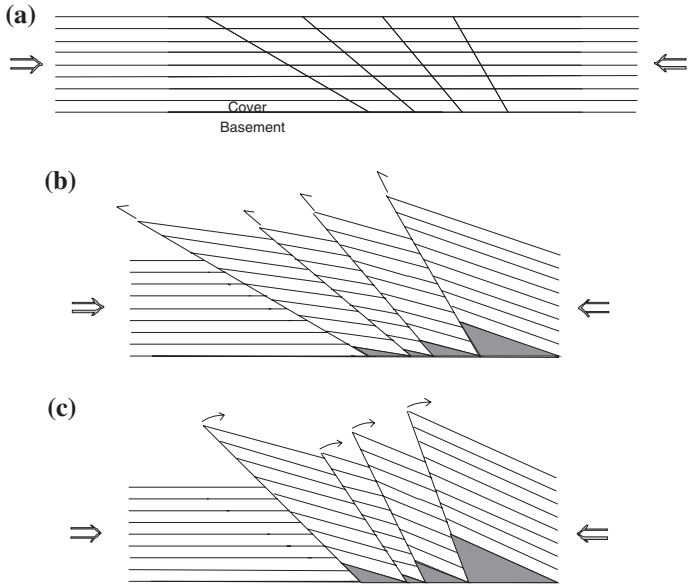

Fig. 4.17 A simplified diagram illustrating layer rotation and formation of dilation spaces (marked in *gray*) above the basement. **a** Initial disposition of layers and thrusts. **b** Rotation of hanging wall layers during thrusting. **c** Simultaneous rotation of layers and thrust planes. The dilation spaces have increased in size because of rotation of thrusts (shown by *arrows*). [From Dubey (2004), © John Wiley and Sons. Published with permission of John Wiley and Sons]

4.8.2 Model 2

In a predominant brittle environment, hanging wall layers can rotate along a thrust with increase in displacement. Figure 4.17 shows four such faults, which are resting over a basement. The faults crosscut horizontal layers and have different initial dips. Assuming frictionless fault surfaces, the layers rotate during thrusting with larger rotation along steeper faults. An approximate disposition of the layers after 25 % shortening is shown in Fig. 4.17b. Prominent dilation spaces can be seen at the basement-cover interface. Figure 4.17c depicts simultaneous rotation of the layers and the thrust planes. As a result of larger rotation along the steeper faults, larger dilation spaces have formed at the same amount of shortening.

The hanging wall layers rotate during thrusting and produce reverse drag (Fig. 4.2a) in vicinity of the thrust surface accompanied by a dilation space at the interface (Fig. 4.18a). The available relief leads to curvature of the footwall layers in the normal drag sense (Fig. 4.2b) and formation of a basement upwarp (Fig. 4.18b). The size of the upwarp depends upon the dip and geometry of the listric thrust fault, initial dip of the hanging wall layers, friction along the thrust, nature of the basement-cover interface, and amount of shortening.

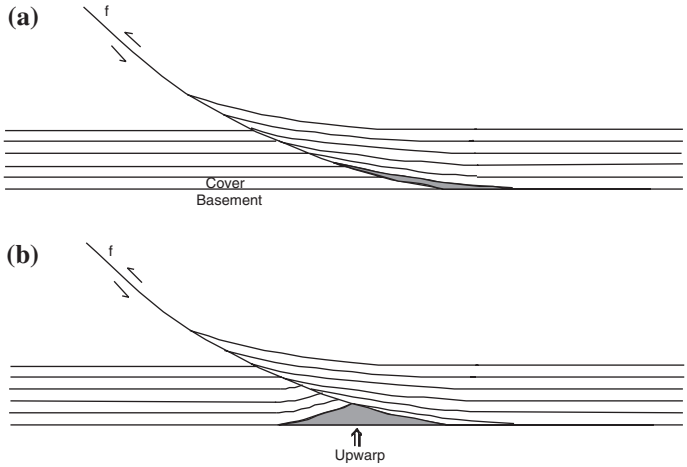

Fig. 4.18 Formation of a decollement upwarp at the basement-cover interface. **a** Displacement along the listric fault (*f*) accompanied by rotation of the hanging wall layers resulting in formation of a dilation space (marked *gray*) above the basement. **b** Curvature of the lower footwall layers to occupy the dilation space and formation of a decollement upwarp (marked in *gray*). [From Dubey (2004), © John Wiley and Sons. Published with permission of John Wiley and Sons]

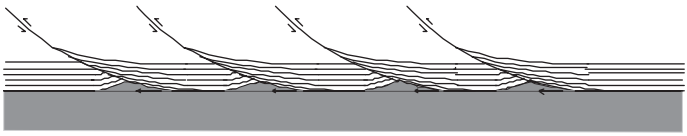

Fig. 4.19 Development of decollement upwarps along a series of listric faults inhibiting motion of the thrust sequence. In order to be a planar structure, the basal decollement should propagate by cutting across the upwarps in the direction indicated by the arrows. [From Dubey (2004), © John Wiley and Sons. Published with permission of John Wiley and Sons]

With progressive deformation a number of decollement upwarps can develop along a series of listric faults (Fig. 4.19). An individual upwarp may not affect the displacement along the adjacent listric fault but the entire thrust sheet will propagate along the basal decollement with bumpy movements. Alternatively, the basal decollement thrust may penetrate and crosscut the basement upwarps. This is a difficult proposition because of absence of a weak plane across the upwarps. Hence the thrust propagation is likely to form a zone of decollement rather than a plane of decollement and the hanging wall thrust sheet may incorporate a part of the basement. The model predicts that presence of a number of decollement upwarps will result in a greater inhibition in the motion of a thrust sequence.

Geological cross-sections across the Foreland Foothill Belt of the Himalaya (Chap. 10) demonstrate a poorly developed surface of decollement at the pre-Tertiary—Tertiary boundary (Fig. 4.20) (Raiverman et al. 1995). The rocks below

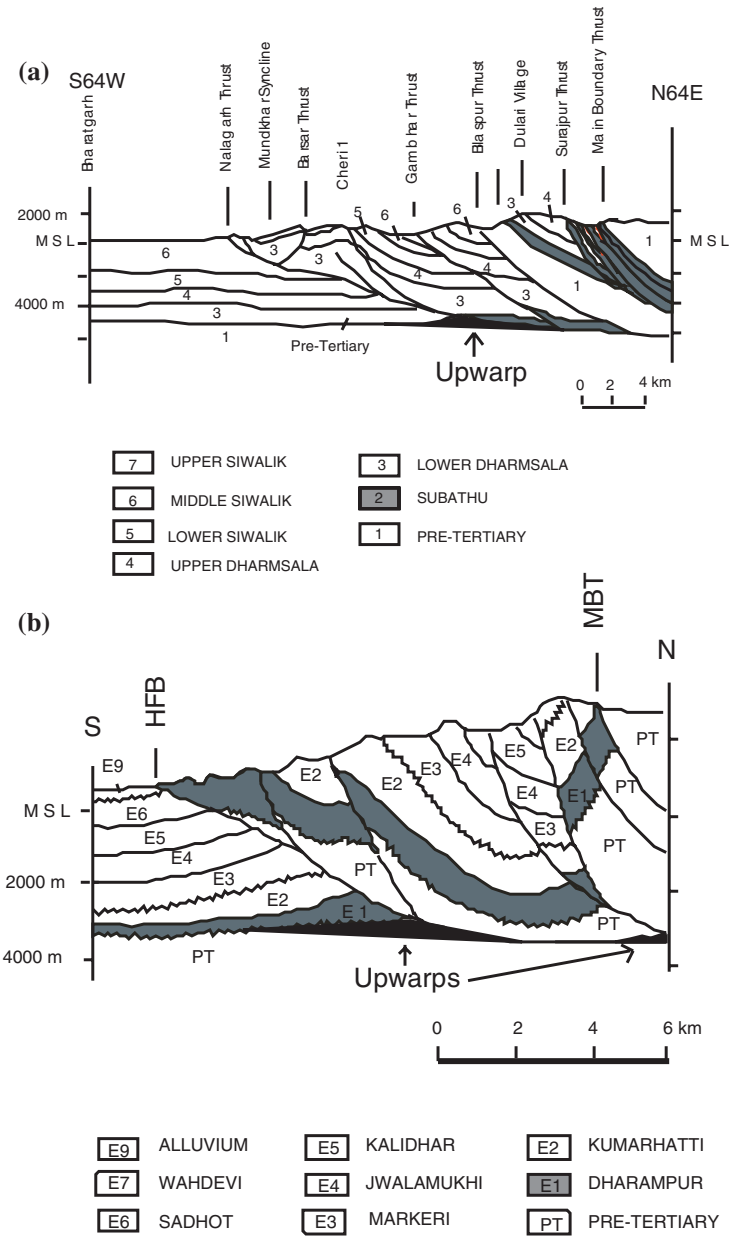

Fig. 4.20 Geologic cross-sections of the Siwalik Foreland Basin showing decollement upwarps (marked in *black*). **a** Section across the Sub-Himalaya, SE of the Simla klippe, Himachal Himalaya. **b** Section across the Sub-Himalaya west of Tanakpur, Kumaun Himalaya (after Raiverman et al. 1995)

the decollement consist of pre-Tertiary sedimentary and metasedimentary rocks (mainly shale, slate, quartzite and limestone with minor phyllite) whereas the cover rocks consist of Tertiary sedimentary rocks (mainly shale, sandstone, and limestone with minor conglomerate). Hence the rocks above and below the surface have comparable rheological properties. The subsurface data does not easily fit in the ideal thin-skinned model because; (i) the decollement at the Tertiary—pre-Tertiary boundary is not very prominent as the pre-Tertiary rocks are also involved in thrusting, and (ii) the decollement surface is slightly undulatory because it is marked by upwarps at the contact of thrust ramps with the pre-Tertiary rocks.

4.9 Thrust Locking

After initiation, thrusts do not propagate for an indefinite period but lock (i.e. fault displacement cease) after a certain stage of development. Following are the main reasons for thrust locking.

1. Fault surface gradually rotates away from the axis of maximum shortening with a result that the fault steepens and displacement cannot take place along a steep fault surface (Dubey and Behzadi 1981).
2. Once a thrust surface is folded, the resulting geometrical shape is not favourable for further thrust displacement.
3. A listric fault has an inbuilt restriction on the amount of total thrust displacement because of non-planar geometry. The lower part of the fault has a gentle dip with a greater horizontal displacement whereas the upper part (near the surface) is steep thereby supporting a greater vertical component of displacement. This variation in the nature of displacement results in smaller displacement as compared to a planar gentle dip fault.
4. The resistance to slip (frictional properties) along a fault is likely to increase with increase in displacement (Coward 1983).

4.10 Frontal and Oblique Fault Ramps

Frontal fault ramp is a fault structure which cuts across a stratigraphic section and is perpendicular to the main transport direction (Fig. 4.21a). The fault displacement (d, Fig. 4.21b) takes place in the dip direction implying that there is no strike-slip component of displacement along the fault.

An oblique ramp is a fault structure which cuts across a stratigraphic section and is oblique to the main transport direction (Fig. 4.21c) (McClay 1992). The frontal and oblique ramps describe the orientation of a fault with respect to stress directions. Since these structures are not constrained by relative sense of displacement they can occur in thrust as well as normal faults. However oblique thrust ramps have a greater occurrence in shallow fold and thrust belts.

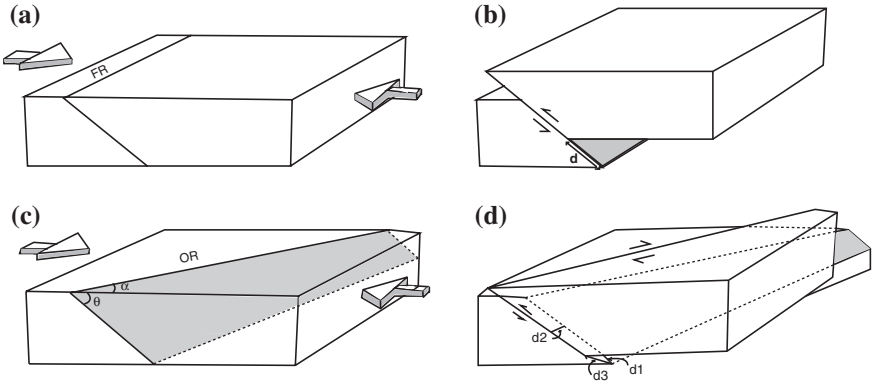

Fig. 4.21 Displacement patterns along frontal and oblique thrust ramps. **a** Initial orientation of the frontal thrust ramp (*FR*). The *arrows* represent the maximum compression direction. **b** Displacement along the frontal thrust ramp under plane strain boundary condition. (*d*) dip slip displacement. **c** Initial orientation of the oblique thrust ramp (*OR*). (θ) thrust dip; (α) angle between oblique ramp and axis of maximum compression. **d** Displacement along oblique ramp under general strain boundary condition. *d1* dip slip; *d2* strike-slip; *d3* oblique slip

In oblique fault ramps, there are components of dip slip (d1), strike-slip (d2, also called as displacement out of the tectonic transport plane) and oblique slip (d3) displacements. The magnitude of these displacements depends upon the angle between strike of the oblique ramp and the maximum compression direction (α, Fig. 4.21c). A large angle results in a greater dip-slip component whereas a small angle results in a greater strike-slip component. Oblique fault ramps are associated with stress concentration and they inhibit motion of thrust sheets (Apotria et al. 1991).

Simultaneous development of frontal and oblique ramps is facilitated by general strain boundary condition that allows components of vertical and horizontal displacements.

4.10.1 Formation of Oblique Fault Ramps

In heterogeneous brittle rocks there are several weak cohesion points. A number of faults can initiate from these points and propagate simultaneously by extending their lengths along the strike direction and width (depth) in the dip direction. Simultaneous propagation of different faults may result in various types of linking. For example, faults 1 and 2 have initiated simultaneously and are propagating by extending their lengths (in strike direction) (Fig. 4.22a). Since they are positioned in front of each other they link as direct linking forming a frontal ramp (Fig. 4.22b). In another situation, the two faults are positioned as shown in Fig. 4.22c, the faults take a curved route and link with each other. The curved linking forms an oblique ramp (OR) (Fig. 4.22d) When a fault in front is positioned

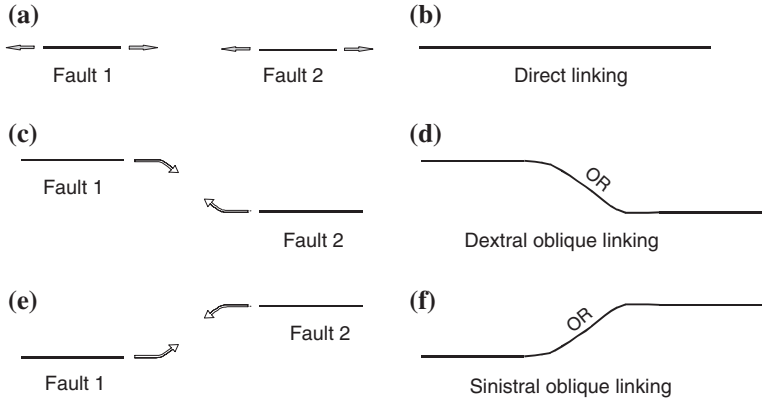

Fig. 4.22 Development of oblique fault ramps by linking. **a** Initiation of faults *1* and *2* from different points located in front of one another. The direction of propagation is shown by *arrows*. **b** Direct linking of the two faults. **c** Initiation of two faults *1* and *2* en echelon to one another. **d** Curvature in the direction of propagation and dextral (*right handed*) oblique linking (*OR*) of the faults. **e**, **f** A different location of the propagating faults would result in sinistral oblique linking (*OR*)

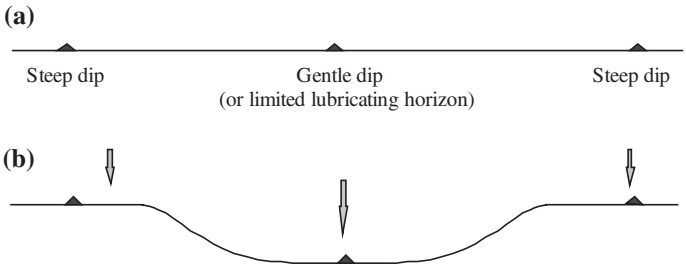

Fig. 4.23 Formation of oblique ramp structures along a thrust. **a** A thrust fault with a gentler dip in the central part and/or the central part has a lubricating stratum of limited extent. **b** A larger displacement in the central segment of the thrust and formation of oblique ramps

towards right the linking is right lateral or dextral oblique linking and when the fault is positioned towards left, the linking is left lateral or sinistral oblique linking (Fig. 4.22e, f).

The length of an oblique ramp can vary from outcrop scale to several kilometers (e.g. ~200 km in the Kangra recess, Himachal Himalaya).

Variation of thrust dip along strike can lead to locking of the thrust at different stages in different segments. The steep dip segments are likely to be locked at an early stage as compared to the gentle dip segment. The differential displacement may form oblique ramps (Fig. 4.23). Similar structure will result when a lubricating geological strata has a limited extent along the thrust.

When two linked faults make an angle of 90°, the structure is called as lateral ramp. A special category of faults, called as transfer faults are characterized by transfer of displacement from one fault to the other (Davis 1984).

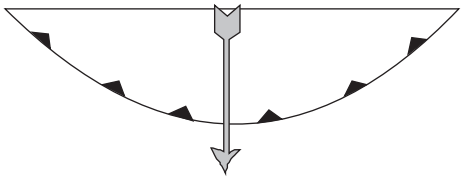

Fig. 4.24 An arcuate thrust with an arrow denoting the direction of tectonic transport (after Elliott 1976)

When the fault has an arcuate strike, the tectonic transport direction can be deduced by bow and arrow rule (Fig. 4.24) (Elliott 1976). A straight line is drawn connecting two ends of the trace of a thrust. The perpendicular bisector of this line gives the displacement direction though the displacement magnitude cannot be determined from the length of this line.

4.11 Models of Thrusting

A number of models have been proposed to understand the geometry, displacement and dynamics of thrusting along with evolution of associated structures. Each model has its own limitations because of some inherent assumptions. A simple model to understand the relationship between thrust displacement and rotation of hanging wall layer is described here (Fig. 4.25) (Dubey and Bhakuni 1998).

Line A′B represents a thrust plane dipping at an angle θ. A horizontal layer BC′ joins the thrust at point B and forms a horizontal hanging wall layer. A compressive stress along the layer results in its rotation and displacement along the thrust. After a few increments of shortening, the layer occupies a new position CA, provided there is no folding, layer length is unchanged (i.e. no layer parallel shortening), and displacement along the fault is relatively easy (i.e. absence of friction on the fault surface). Distance AB represents fault displacement and angle ACB represents rotation of the layer. If the initial layer BC′ is divided into 10 equal parts then rotation of the layer can be measured for every 10 % increase of shortening. For example, the angle ACB represents a rotation after 10 % shortening and the angle A′C″B represents a rotation after 20 % shortening. The angle ACB and other angles with increasing shortening can be calculated by the following geometric relationship.

$$\cos\ \mathrm{ACB} = \frac{\mathrm{BC}^2 + \mathrm{AC}^2 - \mathrm{AB}^2}{2\mathrm{BC} \cdot \mathrm{AC}}$$

This helps in establishing the relationships between layer dips and fault dips with increasing shortening (Fig. 4.26a, b).

The following inferences can be drawn from the diagrams.

Thrust and layer dipping in the same direction

1. Dip of the layer increases steadily with increase in shortening depending on the fault dip and initial layer dip (Fig. 4.26a). The rate of increase of layer dip is lower in gentle thrusts. Hence a greater variation in the layer and thrust dips lead to an initial higher increase in layer dip.

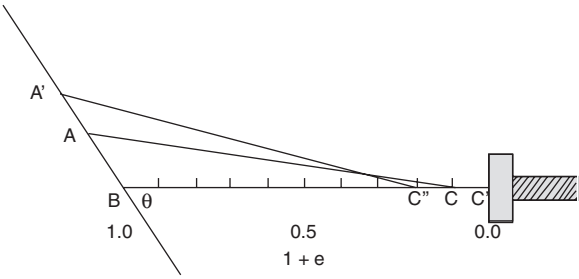

Fig. 4.25 A geometrical representation of rotation of a hanging wall layer BC' along a thrust fault $A'B$ with increase in shortening. [From Dubey and Bhakuni (1998), © Elsevier. Published with permission of Elsevier]

2. Individual lines on the diagram (Fig. 4.26a) represent orientations where length of a layer remains constant. The region above the line represents extension whereas the underlying region represents shortening of the layer.

Thrust and layer dipping in opposite directions

1. The layer rotates clockwise with increase in shortening thereby resulting in decrease of dip. The rate of layer rotation is low and nearly uniform for gently dipping layers whereas steep layers show a greater rotation during the early stages of shortening (Fig. 4.26b).
2. Individual lines on the diagram (Fig. 4.26b) represent rotation of the layer while maintaining a constant length. The region above the line represents shortening whereas the underlying region represents stretching of the layer (cf. Fig. 4.26a).
3. At a fault dip of 30°, the lines intersect prior to 10 % shortening, indicating that these layers undergo early contraction (Fig. 4.27a). Similarly at fault dips of 60° and above, the layers shorten to rotate along the fault plane (Fig. 4.27b). Hence fault dips of more than 60° could not be included in the diagram.
4. Subvertical and vertical layer dips should not be considered in a thrusting model because; (i) the layers are unlikely to be oriented vertically in a rifted terrain, and (ii) any compression normal to vertical layers is likely to extend layers instead of its rotation and displacement along thrust.
5. Rotation of the layers gradually brings them to horizontal position when additional rotation follows the pattern shown in Fig. 4.26a.

The amount of layer rotation along a well lubricated fault is proportional to dip of the thrust hence a steeper dip results in a larger rotation (Fig. 4.26). This implies that a positive listric fault is expected to show a decrease in layer rotation with increase in depth. The variation of layer rotation may result in formation of a number of dilation spaces along the thrust (Fig. 4.28). The area of each dilation depends on amount of dip change, frictional effects along the thrust surface, and dip of the hanging wall layers. Slow deformation with good fault lubrication results in a larger dilation space.

Variation of layer dip across an angular unconformity can also result in formation of dilation spaces (Fig. 4.29). Location of these spaces, which may serve as sites for secondary mineral deposits including oil traps, can be predicted with

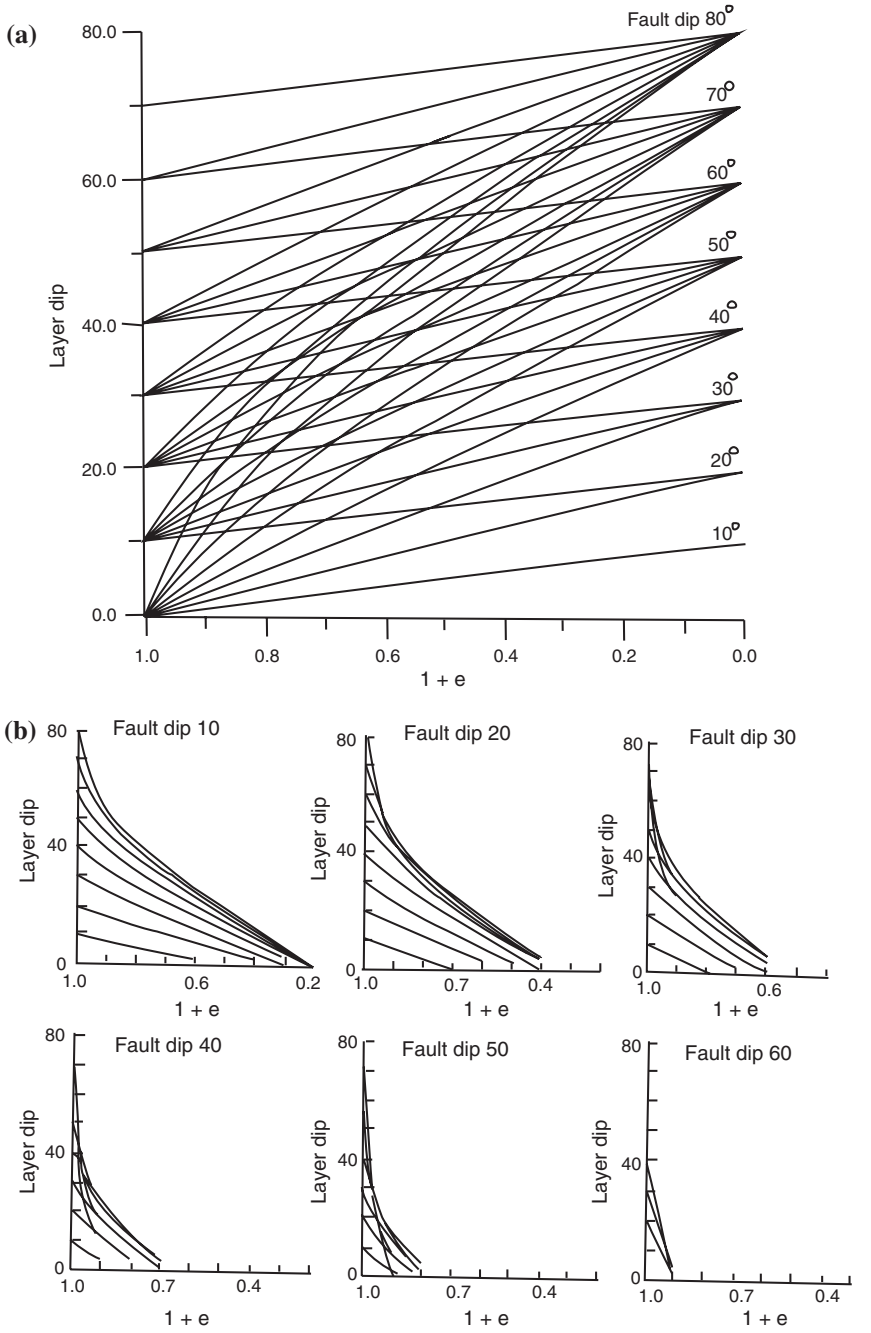

Fig. 4.26 **a** Relationships between shortening (1 + e) and layer dip, for different fault dips when fault and layer dip in the same direction. **b** Relationships between shortening (1 + e) and layer dip, for different fault dips when fault and layer dip in opposite directions. [From Dubey and Bhakuni (1998), © Elsevier. Published with permission of Elsevier]

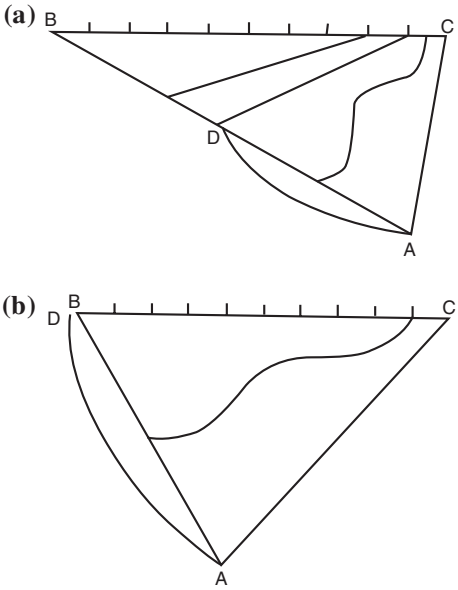

Fig. 4.27 Geometrical representations of changes in length of hanging wall layers (initial position *AC*) during rotation along a thrust (*AB*). **a** Fault dip 30°, layer dip 80°. **b** Fault dip 60°, layer dip 50°. The curve *AD* represents rotation of the line *AC* while maintaining a constant length during deformation. [From Dubey and Bhakuni (1998), © Elsevier. Published with permission of Elsevier]

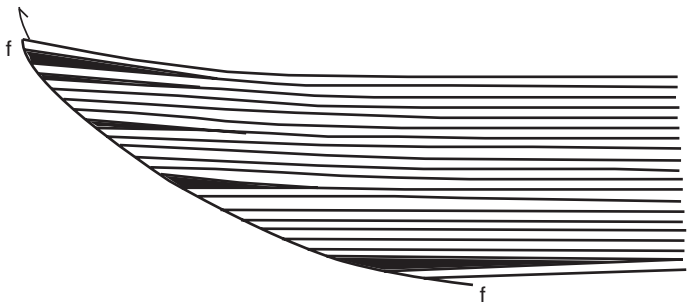

Fig. 4.28 Formation of dilation spaces (marked *black*) as a result of variation of layer rotation along a listric fault (*f–f*). [From Dubey and Bhakuni (1998), © Elsevier. Published with permission of Elsevier]

accurate knowledge of thrust geometry and initial orientation of hanging wall layers. Different layer dips at an angular unconformity will result in folds with different geometries on the two sides.

Variation in fault geometry and associated layer rotations can also result in different fold geometries within a stratigraphic sequence. For example, Fig. 4.30a depicts a pre- to

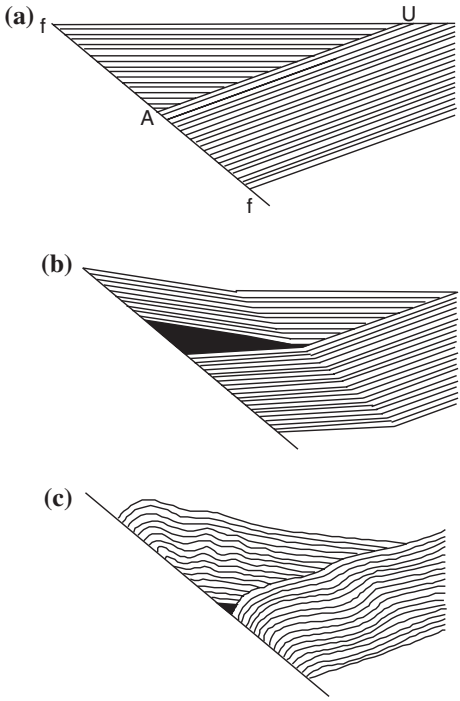

Fig. 4.29 Deformation features across an angular unconformity. **a** Initial configuration of an angular unconformity (*A–U*), and a fault (*f–f*). **b** Variation in rotation of hanging wall layers as a result of variation in initial dip of the layers and formation of a dilation space (marked *black*) in a predominant brittle regime. **c** Development of different fold geometries in the older and younger sequence of rocks with formation of a dilation space in a brittle-ductile regime. [From Dubey and Bhakuni (1998), © Elsevier. Published with permission of Elsevier]

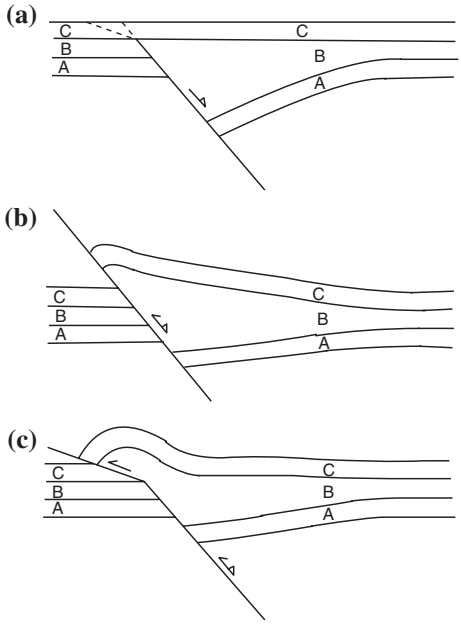

Fig. 4.30 Effect of fault geometry on the development of hanging wall folds. **a** Initial configuration of the stratigraphic sequence. *A* pre-rift; *B* syn-rift; *C* post-rift sequence. **b** Formation of an asymmetric fold at a uniformly dipping thrust. **c** Formation of a ramp anticline over a ramp-flat profile. [From Dubey and Bhakuni (1998), © Elsevier. Published with permission of Elsevier]

post-rift sequence. A subsequent compressional phase results in reactivation of the earlier normal fault as thrust. A layer with a dip opposite to dip direction of the thrust (layer A) undergoes a larger rotation as compared to a horizontal layer (layer C), along a fault of uniform dip (Fig. 4.30b). The larger rotation of layer A in the profile accompanied by resistance to displacement of layer C from above, results in formation of an asymmetric fold in the overlying layer (C) near the thrust (cf. Berger and Johnson 1980; Gillcrist et al. 1987; Letouzey 1990). Decrease in thrust dip with depth is not an essential condition for the described model. If the fault geometry is characterized by a ramp-flat structure (Fig. 4.30c), rotation of a horizontal layer is further reduced on a low dip segment of the fault thereby resulting in a ramp anticline.

4.12 Formation of Thrust Ramps

A number of mechanisms have been suggested for the formation of thrust ramps (Fig. 4.31) (Wiltschko and Eastman 1983). One of these includes pre-existing folds (Fig. 4.31a). A flat thrust may propagate into an antiformal core and terminate in the core. However it is difficult to prove whether the fold is pre-existing or it has formed as a fault propagation fold. The fault may also propagate further and intersect the fold limb. Normally it has been observed that a thrust terminates in the core of an open antiform and intersects a folded sequence in close or tight folds that have already acquired locking and are characterized by limb thinning and hinge thickening (Chap. 3). Stratigraphic inhomogeneities (e.g. pinching of an incompetent unit, Fig. 4.31b) can also form a fault ramp where the fault propagates from an incompetent unit to a competent unit. Geometry and distribution of basement warps can also lead to formation of fault ramps during propagation as shown in Figs. 4.31c, d). Warps in Fig. 4.31d are results of listric, normal faults formed during a pre-orogenic extensional phase.

Another possible mechanism for the formation of thrust ramp is shown in Fig. 4.32. Figure 4.32a depicts displacement along the floor thrust but the amount of slip decreases because of sticking or drag at point ‘S’. A continuous push from the back and sticking at a point in front lead to curvature of the slip plane and a ramp is formed (Fig. 4.32b). The deformation proceeds by amplification of folds in the overlying layers. At Heilam (Scottish Highland), the thrust cuts across the overturned fold limb. It is possible that the ramp propagates upward and on meeting an incompetent bed switch over to a flat once again.

4.13 Development of Klippe

The terms klippe and window are associated with thrusting that involves large translation of hanging wall rocks. Klippe is an exposure of older rocks above a thrust completely surrounded by younger rocks below it (Fig. 4.33). A window

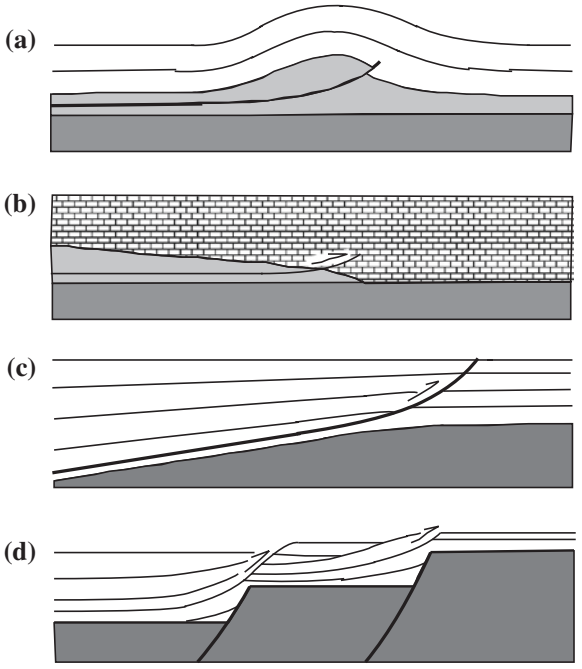

Fig. 4.31 Four regional stress concentration mechanisms for the formation of thrust ramps. [From Wiltschko and Eastman (1983), © Geological Society of America. Published with permission of Geological Society of America]

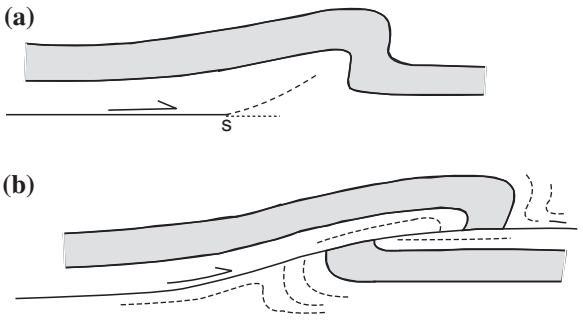

Fig. 4.32 Initiation of a thrust ramp as a result of sticking or drag on the floor thrust; a model for the Heilam sheet. [From Fischer and Coward (1982), © Elsevier. Published with permission of Elsevier]

(or fenster) is an exposure of younger rocks below a thrust fault that is completely surrounded by older rock above the thrust. Windows are exposed after erosion of the overlying thrusted mass. The hinterland region from where the thrust has initiated its journey is known as root zone. The distance between klippe and window provides the minimum displacement along the thrust (Fig. 4.33) subject to the following conditions (Hobbs et al. 1976).

1. The rocks beneath the thrust (window rocks) are younger than the rocks above it (thrust rocks).

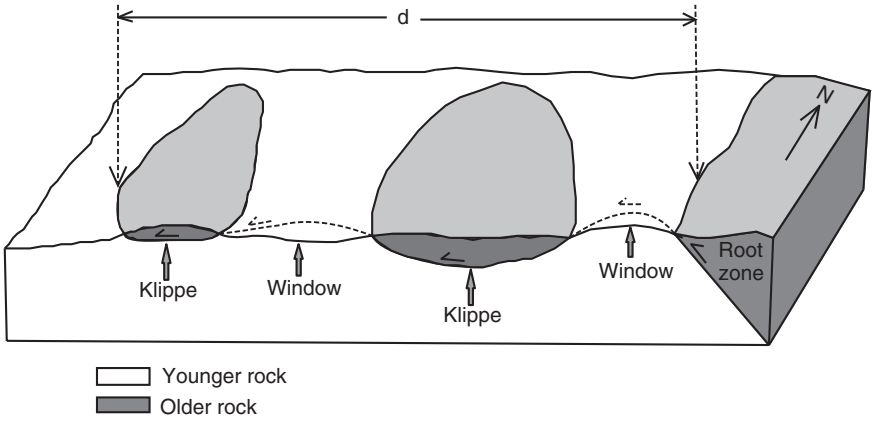

Fig. 4.33 Klippe and window structures. *Half arrows* show the direction of thrust displacement. The diagram also shows klippe-to fenster (window) method for obtaining a minimum estimate of thrust displacement (*d*)

2. No stratigraphic inversion has taken place (e.g. recumbent folding) prior to thrusting.
3. A line drawn from window to klippe is approximately parallel to the direction of displacement (tectonic transport direction).
4. The thrust displacement must have occurred in a direction approximately normal to the outcropping trace of the fault (i.e. E–W displacement in Fig. 4.33).

Large-scale displacement of the order of hundreds of kilometers along thrust faults has remained a problem. Questions have been raised because the enormous hanging wall mass will yield and internally crushed under its own weight instead of undergoing a very large displacement when pushed from one side. The possible solutions to the objection include the following.

1. A lubricant horizon (e.g. graphite, salt, gypsum) at the base of the thrust,
2. Overpressure close to lithostatic pressure in the basal thrust zone which considerably decreases the push required to move the thrust nappe (Hubbert and Rubey 1959),
3. A very large number of shear planes with small increments of slip.
4. During uplift of the thrust mass, gravity takes up a large part of energy involved in thrust displacements. The rate of uplift is more in steep faults hence the required energy is more (Coward 1983). After acquiring a higher elevation, the rocks may slide under the influence of gravity with minimum energy.

The klippe like structures can be generated by a number of thrust mechanisms (Figs. 4.34, 4.35). The first model (Fig. 4.34a) is similar to Fig. 4.33 and is also called as allochthonous. The model is normally preferred for large-scale displacement along a thrust. Steep faults, if present, are ascribed either to simple rotation or to folding. Displacement along vertical faults, (Fig. 4.34b, vertical tectonics model)

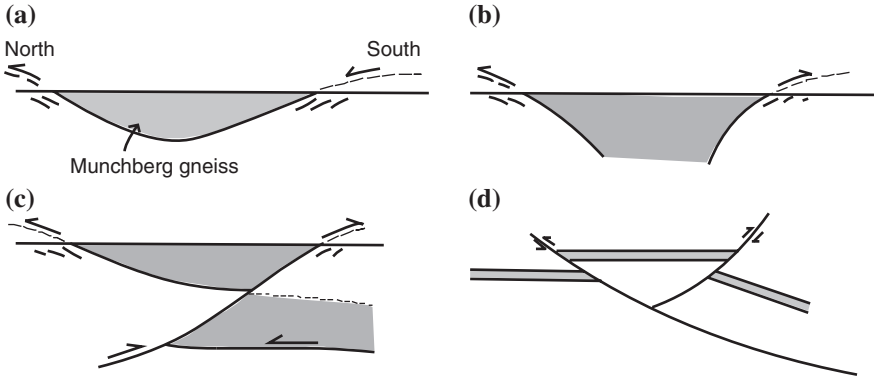

Fig. 4.34 Different models for the formation of klippe structure. [From Coward (1983), © Elsevier. Published with permission of Elsevier]

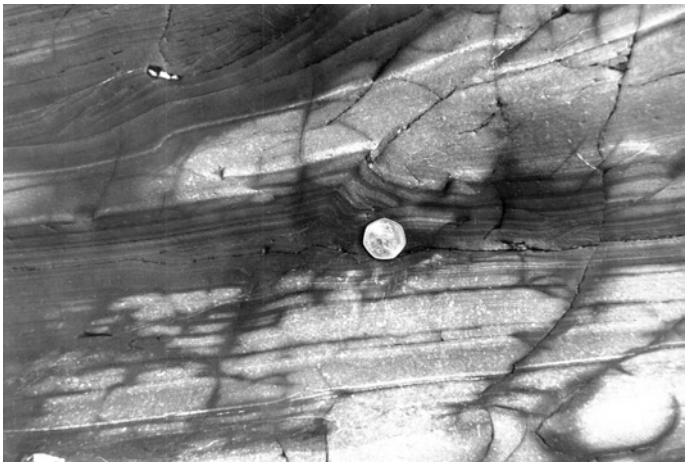

Fig. 4.35 A small-scale pop-up structure developed in greywacke and shale sequence (Bude, North Cornwall)

involves nearly vertical movements without significant horizontal displacements. The model is normally not preferred by structural geologists because fault displacement along a vertical fault is difficult to explain. The displacement is possible in situations where lighter rocks are overlain by denser rocks and the rocks have come-up as a result of lighter density. This model is described as diapiric or autochthonous model. The third model involving a sequence of hinterland dipping thrust followed by a back thrust (foreland dipping) is described as "pop-up" klippen model. The back thrust can either cut the hinterland dipping early thrust (Fig. 4.34c) or it can rest over the hinterland dipping thrust (Fig. 4.34d). It is to be noted that the surface

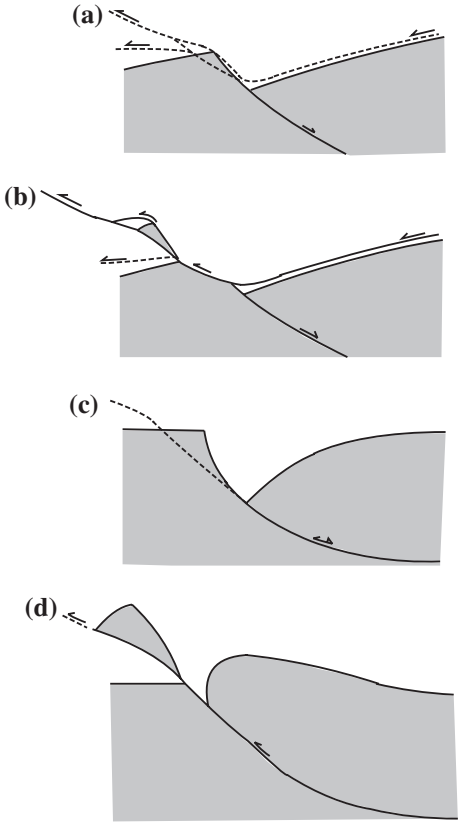

Fig. 4.36 Models to suggest evolution of the Grand Chatlard massif. **a** Large-scale translation at the basement-cover interface over a rifted basement. For easy translation the contractional fault has sliced through the basement. **b** Displacement of the sliced portion of the basement along the thrust and its possible new position over the cover rocks (Beach 1981). **c** Rifted basement blocks with roll-over anticline in the hanging wall. **d** Reactivation of the early normal fault as thrust, slicing of a portion of the angular basement block for easy translation and its deposition on the cover rocks. [From Gillcrist et al. (1987), © Elsevier. Published with permission of Elsevier]

exposures of Fig. 4.34b, c, and d have a similar sense of relative movement along the thrust.

Another model for detached klippe was described by Gillcrist et al. (1987) for the Grand Chatlard massif, French Alps (Fig. 4.36).

Inspired by the above models, a new type of basement wedge klippe is proposed here. The model is essentially based on inversion tectonics (i.e. change in stress orientation from extensional to compressional). The evolutionary stages consist of rotation of hanging wall blocks along a listric fault, curvature of the fault to a sigmoidal geometry, break-up of the top of the basement and subsequent folding as described below.

Figure 4.37a shows initial configuration of a basement with initiation of listric faults during rift phase. Figure 4.37b represents normal fault displacement along the listric faults, anticlockwise rotation of the hanging wall (because of the listric fault geometry), formation of half grabens and deposition of cover rocks (CR) over the basement (B). The displacement along different faults may be either simultaneous or sequential. With increase in extension, the fault surfaces rotate away from the axis of maximum compression (i.e. vertical). However the rate of rotation is not uniform and there is a greater rotation in the central part resulting in sinusoidal geometry of the faults (Figs. 4.37c and 5.3). With the onset of an orogeny, the extensional phase changes to compressional phase with reactivation of earlier normal faults as thrusts (Fig. 4.37d). The magnitude of thrust displacement varies along individual faults because of fault dip variations in the sinusoidal and listric geometries. The maximum displacement takes place in central part of the fault where the dip is minimum and favourable for thrust displacement. The upper and lower segments of the fault where the dip is steep are locked for thrust displacement. The maximum displacement in the central part lead to fault propagation by extending its length shown by broken lines in Fig. 4.37d. The lower, now inactive, segments of the fault remain as relicts of the early normal faults. During upward propagation, the thrust penetrates into upper part of the basement which is then detached and translated as a hanging wall block (Fig. 4.37e). With progressive deformation, the displaced basement wedge may be folded (Fig. 4.37f). Since this is surrounded by younger rocks on all sides, the structure is a klippe but the amount of translation is likely to be much less as compared to an allochthonous model.

Rotation of normal faults during extension leads to gentler dips resulting in locking of the normal faults. However the gentle dips provide a suitable orientation for development of thrust faults during inversion tectonics. Reactivation of early normal faults as thrusts has been observed on various scales in several geological horizons (Jackson 1980; Stoneley 1982; Cohen 1982). One such example of the Birmingham Anticlinorium is depicted here (Fig. 4.38). The stratigraphic data from wells reveal that there is an increase in depth to the basement of at least 4 km over a distance of 20 km from northwest to southeast (Schedl and Wiltschko 1987). The difference was interpreted as an evidence for presence of a basement normal fault which was initiated during Eocambrian rifting (Fig. 4.38a). Variation in stratigraphic thicknesses across the anticlinorium suggests episodic movement along the basement normal fault during the Mid-Cambrian, Mid-Silurian and Early Mississippian extensions. The fault displacement has resulted in formation of a drape fold in the younger sequence (Fig. 4.38b). Reactivation of the fault as thrust initiated during Early post-Pennsylvanian compressional phase and formed a thrust ramp below the drape fold (Fig. 4.38c). The thrust fault did not use the earlier normal fault as a displacement surface but cuts across the earlier structure. The fold was carried by the ramp and is now positioned as crest of the Anticlinorium (Fig. 4.38d).

It is possible that the basement flat at the lower level may propagate as smooth trajectory thrust cross-cutting a part of the basement (Fig. 4.39).

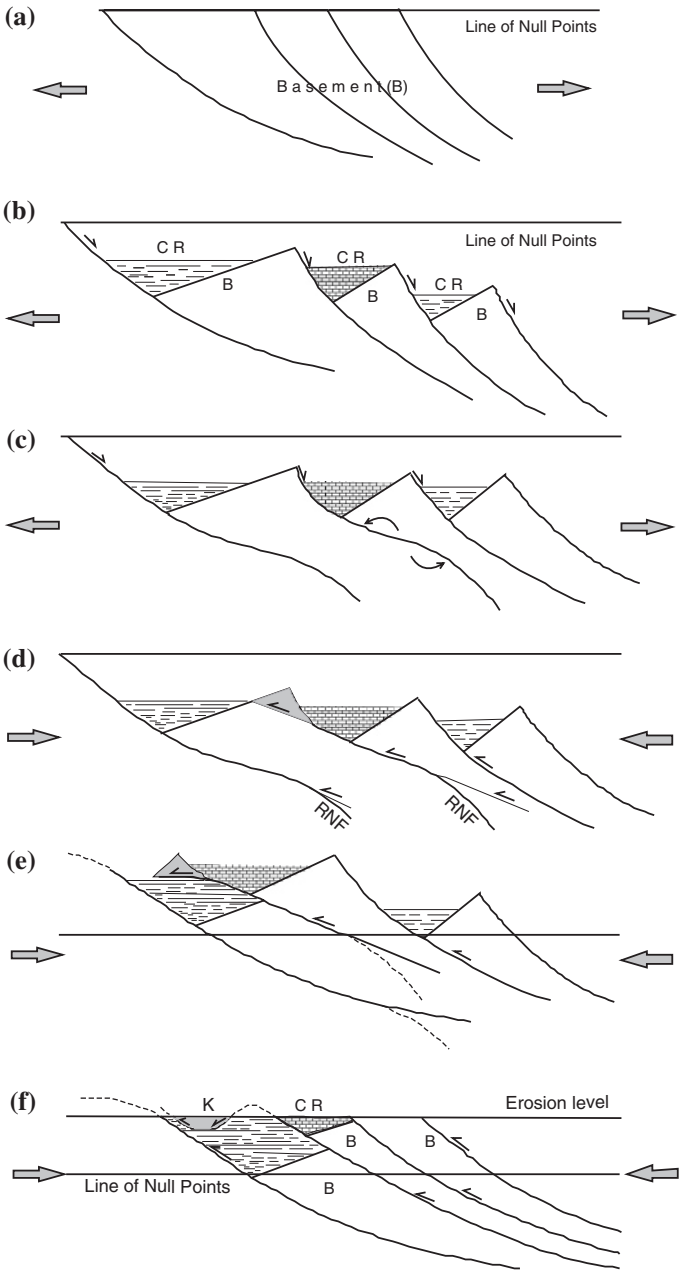
(a)
Line of Null Points
Basement (B)
(b)
Line of Null Points
CR
B
CR
B
CR
B
(c)
(d)
RNF
RNF
(e)
(f)
K
CR
Erosion level
B
B
Line of Null Points
B

◀ **Fig. 4.37** The basement wedge klippe model. **a** Initiation of normal faults during a tensional regime. The maximum extension direction is shown by *arrows*. The line of null points denotes an undisturbed pre-fault plane. **b** Displacement along the normal, listric faults, anticlockwise rotation of the basement blocks (*B*), formation of half grabens and deposition of cover rocks (*CR*). It is possible that different types of rocks are deposited in different half grabens. **c** A larger rotation of the faults, away from the axis of maximum compression (i.e. *vertical*) in the central part, and modification to sigmoidal geometries. The pattern of rotation is shown by *arrows*. **d** Initiation of compressional phase and reactivation of early normal faults as thrusts. A greater displacement along the gentle dip segment of the faults. During upward propagation, the thrust intrudes into the basement wedge. RNF = remnant normal fault. **e** Translation of the basement wedge over the cover rock. **f** Folding of the basement wedge and formation of a klippe

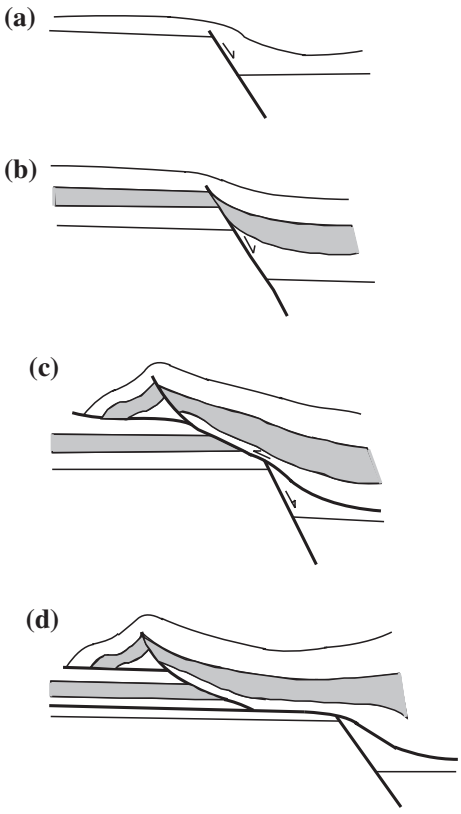

Fig. 4.38 Reactivation of a normal fault as thrust. Schematic evolution of the Birmingham Anticlinorium. **a** Initiation of a basement normal fault in the Eocambrian. **b** A drape fold observed in the basement normal fault after Mid-Cambrian, Mid-Silurian and Early Mississippian movements. **c** Initiation of a thrust ramp in the early post- Pennsylvanian. **d** Cratonward propagation of the thrust fault. [From Schedl and Wiltschko (1987), © Elsevier. Published with permission of Elsevier]

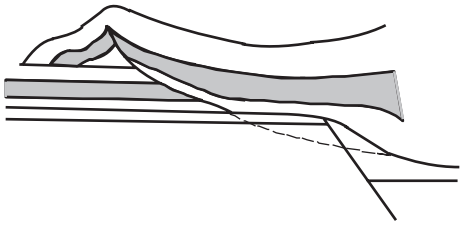

Fig. 4.39 Propagation of basal thrust flat (shown by *broken line*) into the basement to form a smooth trajectory thrust

4.14 Restoration (Balancing) of Deformed Cross-Sections

The balancing of deformed cross-sections was first attempted at Calgary, Canada and the results were quite useful for oil exploration in the region. Dahlstrom (1969) set out the rules for section balancing or restoration of deformed cross-sections. The most important rule is that the section should be geometrically compatible. Compatibility implies that the body translations, rotations and strains developed in a deformed rock mass follow certain geometric rules that are requisites for the rock mass to remain coherent after deformation (Ramsay and Huber 1987). The geometric features of a deformed section must be restorable to a pre-deformational form without loss of material volume and the lengths and thicknesses of individual strata restore to reveal a coherent picture or palinspastic reconstruction. The section construction should start from field observations in cliffs, road cuts, mountain sides, railway cutting etc. (Elliott 1983). This should be substantiated by seismic and/or bore-hole data to construct the subsurface structures. It has been suggested that construction of a section should be simultaneously restored. However many of the geological sections are not restorable hence an unrestorable section does not necessarily mean wrong construction.

The Line length balancing method assumes that finite strains within the developed folds in the section are not of high values and the deformation has taken place mainly by layer parallel shear (e.g. flexural-slip; Chap. 3). In such situations the fold profiles keep the initial bed length and cross-section areas of original layers also remain unchanged. However it is necessary to check the uniform thickness of the folded layers and absence of internal layer strain prior to applying the method as described below (Ramsay and Huber 1987).

1. Fossils, which lie on the bedding surfaces, should be undeformed.
2. The incompetent layers should be free from overshear developed as a result of concentration of shear displacement in the layers.
3. There should not be any penetrative cleavage (parallel to XY) at angles greater than about 40° to the bedding surfaces.
4. The folds should have a parallel form (Class 1B, Chap. 3).
5. Metamorphic grade of the rocks should not exceed low greenschist facies so that there is no ductile flow and associated layer parallel extension or shortening.

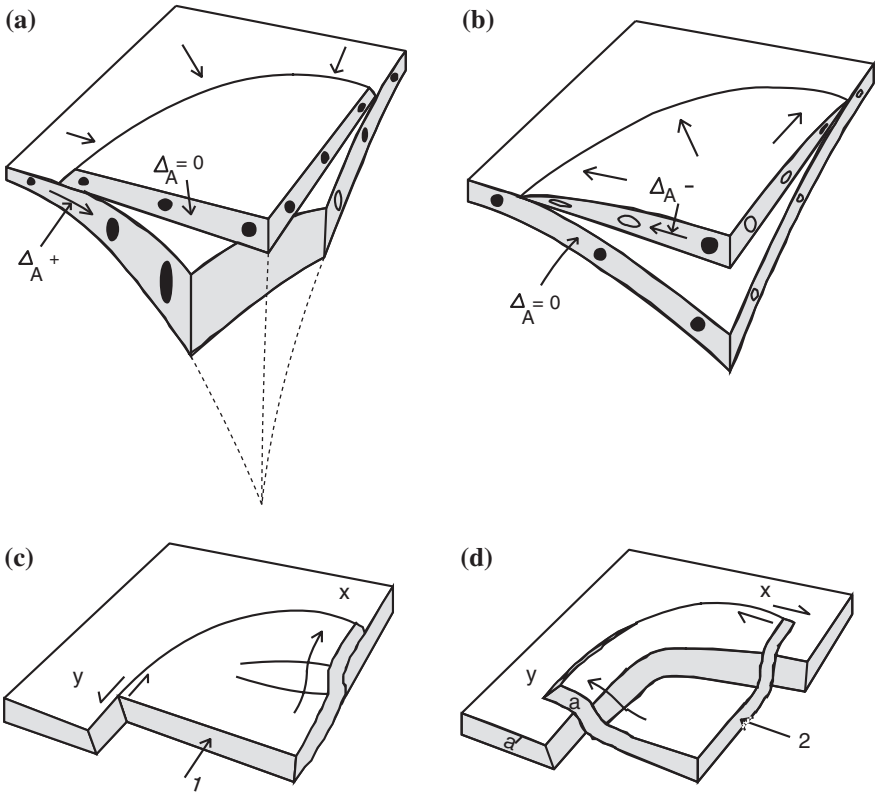

Fig. 4.40 Geometric effects of developing thrusts and folds with arcuate traces. **a** Convergent movement of the footwall leading to increase in thickness of the footwall ($\Delta A+$). **b** Divergent movement of the hanging wall leading to thinning ($\Delta A-$). **c** and **d** Two stage developments of an arc by successive simple shear displacements. [From Ramsay and Huber (1987), © Elsevier. Published with permission of Elsevier]

6. The deformation must be under plane strain so that there is no extension normal to the plane of the section. Hence the method is not applicable to regions where the extension is also parallel to the fold hinge lines. The condition further requires absence of strike slip faults (maximum and minimum compression in horizontal directions; Chap. 6).
7. The technique cannot be applied to arcuate fold zones because these can form in a number of ways with different strain patterns (Fig. 4.40) (Ramsay and Huber 1987). The arcuation can be a result of single deformation (Fig. 4.40a, b, c) or multiple deformation (Fig. 4.40d). In a single deformational event, the geometric features of a profile section depend on whether the convex side of the fold arc has been active (as a result of convergent flow of the footwall region (Fig. 4.40a) or the concave side has been transported over a foreland (resulting in divergent flow of the hanging wall region (Fig. 4.40b). These two situations lead to different

strain patterns as shown in the diagram and result in area and length changes of layers in a profile section. In a third model the overthrust sheet is developed along a curved fracture by two (or more) differently oriented transports. It is possible that an early movement at one point (at x) is simply overthrust whereas at another position (at y) the movement is taken up only by horizontal strike-slip movement. Between these two points the movement proceeds by a combination of overthrust and horizontal strike-slip motions. If the region is undergoing superposed deformation at a later stage (Fig. 4.40d), a second movement vector in a different direction can give rise to horizontal motions only at x, and overthrust motions at y. It is clear from Fig. 4.40d that continuous sections drawn perpendicular to the thrust front (or normal to the local fold axes) cannot be balanced. For example the material in the thrust sheet at position 'a' was originally in the same line of section as position 'a'. Hence this would be geometrically incoherent with the profile section directly under position 'a'. In such situations, the only section lines that can be used for matching and balancing are those which contain the direction of the total displacement vector. In some cases the movement vector can be determined from shear fibre structures on fault surfaces or by the "bow and arrow" rule (Fig. 4.24).

4.15 Estimation to the Depth of Detachment

Depth to the basal detachment is crucial for drawing a balanced section. An error in the depth measurement can significantly misrepresent the geometry of the restored section. In some areas the depth data are available from seismic studies. In other areas it is possible to determine the depth assuming a true thin-skinned model. Figure 4.41 shows one such method (Ramsay and Huber 1987). An undeformed layer of length l is lying over a basal detachment (Fig. 4.41a). Displacement over a flat and ramp geometry following the thin-skinned tectonics reduces the initial length to l′. If there is no loss of rock volume and no change in the cross-sectional area, the volume of material removed by shortening of the sedimentary pile is equal to that of the uplifted portion shown by gray in Fig. 4.41b. Considering the plane strain deformation (no extension or contraction perpendicular to the section, parallel to the fold hinge line), the geometry can be described by the following relationship.

$$A = d(l - l').$$

where d is the depth to the decollement surface below a particular marker level x. The uplifted area A can be measured by a planimeter or by using a transparent square grid and counting the number of full and half squares. The final length (l′) can be directly measured and the initial length (l) is assumed to equal the total length of a marker bed in the deformed section. In order to avoid any change in the length, the most competent bed should be chosen as the marker horizon. Once the values of area (A) and shortening ($l - l'$) are known, the depth of detachment can be easily calculated.

Some parts of the restored section where thickening of the beds is observed can be further corrected by area balancing method (Fig. 4.42). If the area A of a horse

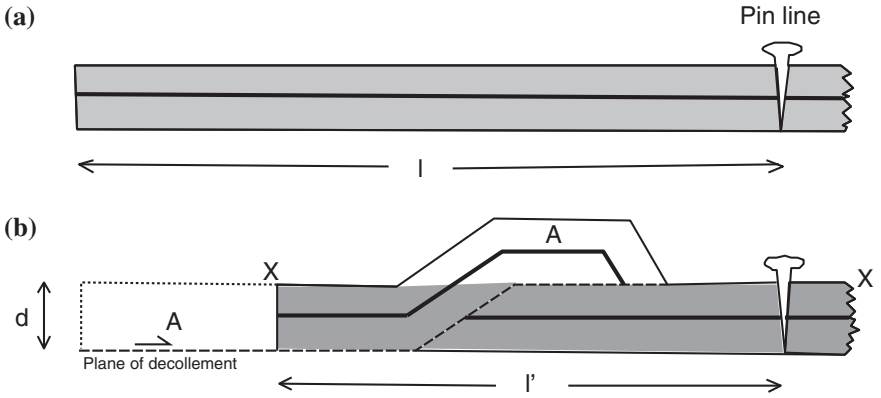

Fig. 4.41 Relationship between uplifted area *A* and initial geometry. *d* is the depth to decollement below level *x* (after Ramsay and Huber 1987)

Fig. 4.42 Changes in bed length and bed thickness as a result of layer thickening keeping the cross-sectional area (*A*) constant (after Ramsay and Huber 1987)

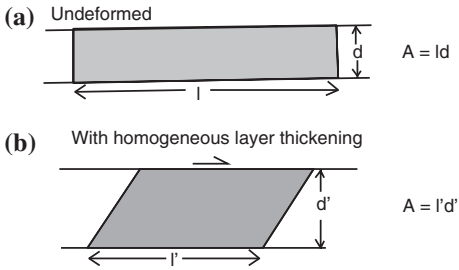

unit is divided by the initial stratigraphic thickness d, the initial layer length can be obtained.

In a duplex structure, individual horse units (Fig. 4.13 or Fig. 4.15) can be area balanced and the thickness corrections can be made.

4.16 Step-by-Step Construction of Balanced Cross-Section

1. Prepare a structural map of the area and compile the subsurface seismic and bore hole data.
2. Draw a section line parallel to the direction of tectonic transport (follow the bow and arrow rule in arcuate fold belts, normal to fold hinge lines in linear fold belts, or stretching mineral lineation). In a mountainous region, it may not be possible to collect the structural data along the projected section line but keep as close to the section line as possible to minimize the error.
3. Project in the subsurface data and up- and down-plunge geologic data.

4. Draw a separate restored stratigraphic layer cake or wedge using the youngest unit as a horizontal datum. Use thickness data from surface and subsurface measurements for each layer in the thrust sheet for subsurface reconstruction.
5. Find the depth to basement (seismic data or Fig. 4.41) and draw in the basement surface on the deformed section.
6. Mark the thicknesses of stratigraphic units above the basement to give a guide for the depths of thrust sheets trailing edges.
7. Draw a foreland pin line (reference line) in the section to correspond to the foreland edge of the restored section. The structural data must start from the pin line.
8. Extend surface geology to depth based on dip isogons, axial plane intersections, depth-to-detachment calculations or stratigraphic separation diagrams. Have the trailing edge of each major sheet return to original above basement.
9. Given hanging wall cutoff geometries on the surface or as reconstructed from unfolding, try to fit the subsurface footwall geometries.
10. Fill deep holes with imbricates, horses, and duplexes as seems appropriate in a thin-skinned model.
11. Measure bed lengths from the foreland pin point back through the section for each horizon (i.e. L_1, L_2, … L_n between thrusts). In absence of enough data, measure only key beds and the positions of local pin lines in each sheet.
12. Measure the same bed lengths from the foreland margin of the restored stratigraphic wedge. This locates all faults in the restored section.
13. Make sure that all local pin lines, or well-constrained surface geometries are preserved in the restored section. The observed surface and interpreted subsurface structures should be coherent.
14. Make sure that respective hanging wall and footwall cutoffs correspond. No gaps or overlaps in the restored section are permitted (as observed in the listric fault models).
15. Measure the area of each thrust sheet in the deformed section and in the restored section for equal values, i.e. area change is not allowed.
16. If thrust sheet areas are not equal find where your stratigraphic thicknesses are wrong or whether this is a result of deviation from the plane strain deformation (this can be checked with the field data).
17. When thrust sheet areas are equal, measure formation or other subunit areas in both the deformed and restored sections. They should also be equal.
18. Compare the deformed and balanced sections. The two should have the same bed lengths and areas. Individual thrusts should dip in one direction, i.e. no reversal of the dip direction. If these conditions are not fulfilled, the deformed section is unrestorable (but not necessarily wrong).
19. The deep structures may need to be area balanced because bed-length details will probably be incomplete.
20. Your level of confidence in the section should be directly proportional to the amount of manipulation done for rotation of beds to fill the gaps, overcome the overlaps, and rotation of faults for a uniform regular dip.
21. Not all geological sections can be balanced. Hence if you fail to balance a section do not get discouraged. Have confidence in your structural data and go ahead for a suitable interpretation.

The method is useful in certain geological areas but as pointed out by Ramsay and Huber (1987) the following limitations are associated with balancing a section.

1. The thin-skinned thrust tectonics model assumed for balancing is applicable to marginal regions of orogenic zones. It considers a relatively thin (1–6 km) sequence of continental shelf sediments originally deposited on a continental type basement of crystalline gneisses and igneous rocks. The basement is very competent relative to the overlying sediments and the cover is mechanically detached from the basement along a decollement fault (basal decollement). The cover rocks are involved in folding and thrusting but the crystalline basement remains undeformed. Hence the method cannot be applied universally in all the orogenies because these conditions are not always prevalent. For example, all the available rocks in the Himalaya are deformed in a similar manner including the crystalline basement.
2. The fault surface can undergo folding or further fracturing at a late stage of deformation.
3. There is no consideration for viscosity contrast between the layers, and superimposed folding.

References

Allmendinger RW (1982) Analysis of micro-structures in the Meade Plate of the Idaho-Wyoming foreland thrust belt, USA. Tectonophysics 85:221–251

Apotria TG, Snedden WT, Spang JH, Wiltschko DV (1991) Kinematic models of deformation at an oblique ramp. In: McClay K (ed) Thrust tectonics. Chapman & Hall, New York, pp 141–154

Beach A (1981) Thrust structures in the eastern Dauphinois Zone (French Alps), north of the Pelvoux massif. J Struct Geol 3:299–308

Berger P, Johnson AM (1980) First-order analysis of deformation of a thrust sheet moving over a ramp. Tectonophysics 70:T9–T24

Boyer SE, Elliott D (1982) Thrust systems. AAPG Bull 66:1196–1230

Casey M, Dietrich D (1997) Overthrust shear in mountain building. In: Sengupta S (ed) Evolution of geological structures in micro- to macro scales. Chapman & Hall, London, pp 119–142

Cohen CR (1982) Model for a passive to active continental margin transition: implication for hydrocarbon exploration. AAPG Bull 66:708–718

Cooper MA, Trayner PM (1986) Thrust surface geometry: implications for thrust belt evolution and section balancing techniques. J Struct Geol 8:305–312

Coward MP (1983) Thrust tectonics, thin skinned or thick skinned and the continuation of thrusts to deep in the crust. J Struct Geol 5:113–123

Dahlstrom CDA (1969) Balanced cross-sections. Can J Earth Sci 6:743–757

Davis GH (1984) Structural geology of rocks and regions. Wiley, New York 492 p

Dubey AK (2004) Formation of decollement upwarps during thrusting. Terra Nova 16:91–94

Dubey AK, Behzadi H (1981) Development of flexural slip folds, overlapping boudins and extension faults in multilayered materials: field evidence and experimental model. J Geol Soc India 22:274–284

Dubey AK, Bhakuni SS (1998) Hangingwall bed rotation and the development of contractional and extensional structures around a thrust fault: geometric and experimental models. J Struct Geol 20:517–527

Elliott D (1976) The energy balance and deformation mechanisms of thrust sheets. Philos Trans R Soc Lond A 283:289–312

Elliott D (1983) The construction of balanced cross-sections. J Struct Geol 5(101):35 doi:10.1016/0191-8141(83)90035-4
Fischer MW, Coward MP (1982) Strains and folds within thrust sheets: an analysis of the Heilam sheet, Northwest Scotland. Tectonophysics 88:291–312
Fossen H (2010) Structural geology. Cambridge University Press, Cambridge 463 p
Gillcrist R, Coward MP, Mugnier J-L (1987) Structural inversion and its controls: examples from the Alpine foreland and the French Alps. Geodinamica Acta (Paris) 1:5–34
Hafner W (1951) Stress distribution and faulting. Bull Geol Soc Am 62:373–398
Hamblin WK (1965) Origin of "reverse drag" on the downthrown side of normal faults. Bull Geol Soc Am 76:1145–1164
Hobbs BE, Means WD, Williams PF (1976) An outline of structural geology. Wiley, New York 571 p
Hubbert MK (1951) Mechanical basis for certain familiar geologic structures. Bull Geol Soc Am 62:355–372
Hubbert MK, Rubey WW (1959) Role of fluid pressure in mechanics of overthrust faulting: I. Mechanics of fluid filled porous solids and its application to overturned faulting. Bull Geol Soc Am 70:115–166
Jackson JA (1980) Reactivation of basement faults and crustal shortening in orogenic belts. Nature 283:343–346
Jackson J, McKenzie D (1983) The geometrical evolution of normal fault systems. J Struct Geol 5:471–482
Letouzey J (1990) Fault reactivation, inversion and fold thrust belt. In: Letouzey J (ed) Petroleum and tectonics in mobile belts. Editions Technip, pp 101–128
McClay KR (ed) (1992) Thrust tectonics. Chapman & Hall, London
Raiverman V, Srivastava AK, Prasad DN (1995) On the foothill thrust of northwestern Himalaya. Himalayan Geol 16:237–256
Ramsay JG (1992) Some geometric problems of ramp-flat thrust models. In: McClay KR (ed) Thrust tectonics. Chapman & Hall, London, pp 191–200
Ramsay JG (1997) The geometry of a deformed unconformity in the Caledonides of NW Scotland. In: Sengupta S (ed) Evolution of geological structures in micro- to macro-scales. Chapman & Hall, London, pp 445–472
Ramsay JG, Huber MI (1987) The techniques of modern structural geology, vol II: folds and fractures. Academic Press, pp 309–700
Rich JL (1934) Mechanics of low angle overthrust faulting as illustrated by Cumberland thrust block, Virginia, Kentucky, and Tennessee. AAPG Bull 18:1584–1596
Schedl A, Wiltschko DV (1987) Possible effects of pre-existing basement topography on thrust fault ramping. J Struct Geol 9:1029–1037
Stoneley R (1982) On the structural development of the Wessex basin. J Geol Soc London 139:543–554
Suppe J (1983) Geometry and kinematics of fault bend folding. Am J Sci 283:684–721
Suppe J (1985) Principles of structural geology. Prentice Hall, New Jersey
Watkinson AJ (1993) A footwall system of faults associated with a foreland thrust in Montana. J Struct Geol 15:335–342
Wiltschko D, Eastman D (1983) Role of basement warps and faults in localizing thrust fault ramps. Mem Geol Soc Am 158:177–190
Woodward NB, Boyer SE, Suppe J (1989) Balanced geological cross-sections: an essential technique in geological research and exploration, vol 6. Short Course in Geology, American Geophysical Union, Washington, D.C., 132 p

Chapter 5
Normal Fault

Initiation, propagation, and modification of normal fault geometry from planar to sigmoidal shape are described. How normal faults of one generation can have a variety of dips, geometry and displacements are discussed. Relay ramps and bookshelf gliding are illustrated. Co-existence of normal and (pseudo) thrust faults are shown. Formation of half grabens, angular unconformities and associated structures are shown diagrammatically. Displacement patterns of planar and listric (both positive and negative) faults are described. Models of lithospheric extension are highlighted. Finally, identification of a rift phase by geochemical methods is discussed. The downward movement of the hanging wall brings younger layers of the hanging wall in contact with older layers of the footwall. For example, the youngest layer E of the hanging wall is in contact with an older layer D of the footwall, across the fault. Similarly D is in contact with C, and so on (Fig. 5.1b). Extension fault is a synonym for normal fault because they are associated with maximum horizontal extension.

It is to be remembered that movement along a fault is always relative because absolute movements cannot be determined in natural strata. This means that; (i) only one block (either hanging wall or footwall) moves and the other remains stationary, (ii) both the blocks move in opposite directions, (iii) both the blocks move in one direction but with different amounts of displacement magnitudes. In order to signify this point, the directions of displacements along a fault are always marked by half arrows.

When normal faults evolve simultaneously with sedimentation during growth of a basin, the hanging wall beds gradually subsides with concomitant sedimentation thereby resulting in greater thickness of the hanging wall beds as compared to the footwall beds (Fig. 5.2). These faults can occur on different scales and are called as growth faults.

5.1 Fault Propagation and Termination

After initiation, a fault propagates by extending its length (Fig. 5.3a). The propagation is simultaneous with rotation of the fault resulting in gradual reduction in fault dip (Fig. 5.3b). The magnitude of rotation is not uniform along the fault and

A. K. Dubey, *Understanding an Orogenic Belt*, Springer Geology,
DOI: 10.1007/978-3-319-05588-6_5,

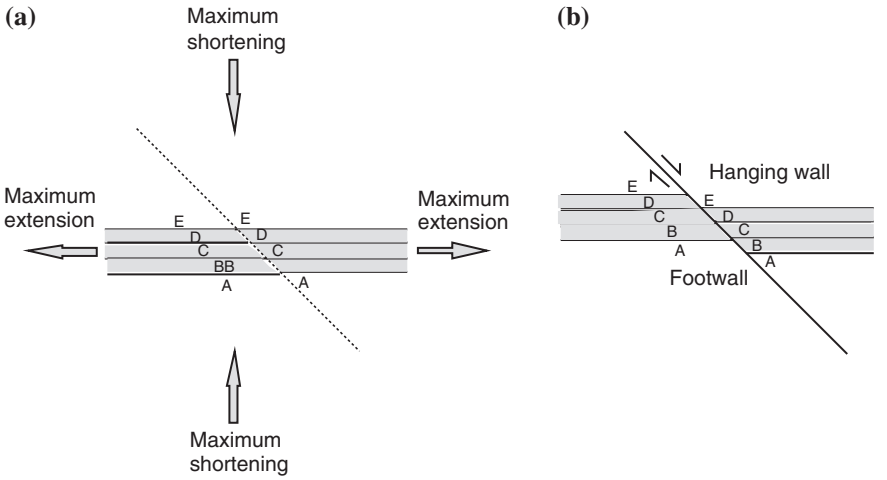

Fig. 5.1 Development of a normal fault. **a** Initial disposition of a multilayer sequence with directions of maximum shortening and extension. **b** Downward displacement of the hanging wall

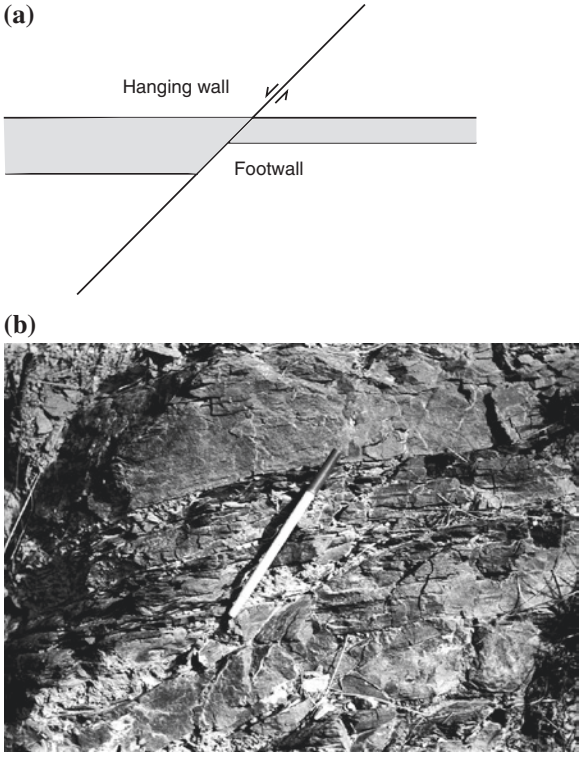

Fig. 5.2 **a** A growth fault showing greater thickness of the hanging wall bed. **b** A growth fault in weakly metamorphosed Simla Group of rocks. The *pen* is *parallel* to the fault plane. Thickness of the slate layer has increased in the hanging wall (down thrown side). The top quartzite layer is unfaulted (Kiarighat, Simla Lower Himalaya)

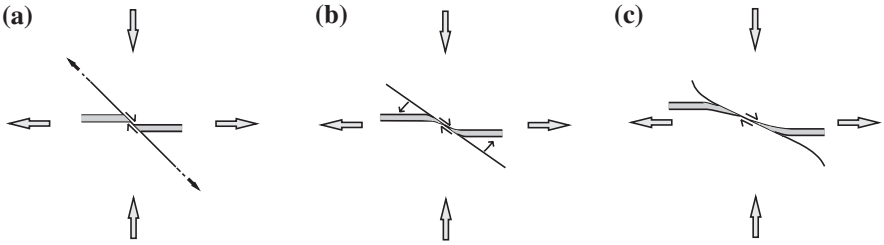

Fig. 5.3 Modification in normal fault geometry with progressive deformation. **a** Initiation of normal fault with steep dip. The stress orientation is shown by *large arrows* and fault propagation (increase in fault length) by *small arrows*. **b** Rotation of the fault away from the axis of maximum compression leading to decrease in dip. **c.** Fault locking by curvature of the fault towards the receding side. The fault acquires a sinusoidal geometry at this stage

the maximum rotation takes place in the central part. Apart from variation in the rotation amount, the displacement magnitude also varies along the fault. The maximum displacement occurs in the central part and gradually decreases to zero at the terminations. The combined effect of rotation and displacement variations is to modify the cross-sectional fault geometry to sinusoidal shape followed by fault locking (Fig. 5.3c). If the same stress conditions prevail, a new normal fault is initiated with planar geometry. Hence it is possible that normal faults of the same generation may reveal a variety of dips and geometries in one region.

The nature and magnitude of fault displacement vary during deformation history. The initial extension is likely to be more diffusive and scattered in natural heterogeneous rocks and this will result in a large number of normal faults with limited amounts of displacements. In succeeding stages, the deformation is more concentrated with increased fault displacements along a few selective faults having suitable dips and good lubrication.

The relationship between shortening and displacement along a fault has a sigmoidal pattern (Fig. 5.4). The initial fault displacement is slow (domain A, Fig. 5.4) followed by an increase (domain B) and finally the displacement decreases once again with increase in fault rotation (domain C). In case of a normal fault, it locks up at gentle dips. Fault locking is followed by initiation of a new fault with similar deformation history. Hence the different faults of one generation will not only have different dips but also different amounts of total displacement at any one instant of deformation.

In addition to gradual decrease in displacement towards terminations, the propagation of faults also results in a converging pattern of displacement directions when viewed in three-dimensions (Fig. 5.5). The displacement is normal to strike of the fault in the central part (point of fault initiation) with gradual decrease in the angle towards the terminations. The varying sense of displacement directions is reflected in orientation of mineral fibres or slicken lines (i.e. lines marked on the fault surface).

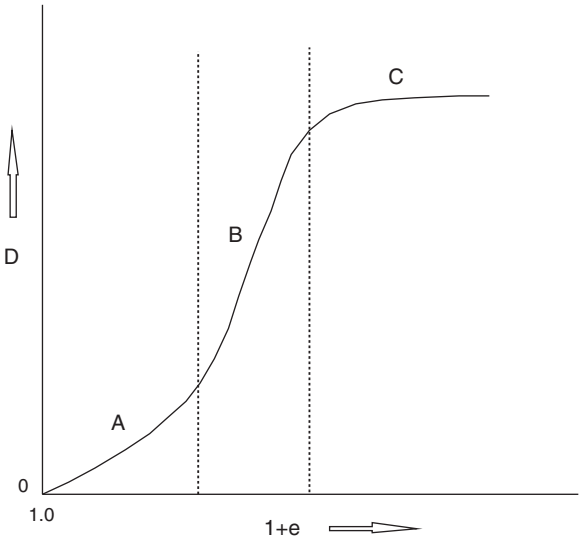

Fig. 5.4 A simplified relationship between shortening (1 + e) and fault displacement (*D*). The *arrows* indicate direction of increase

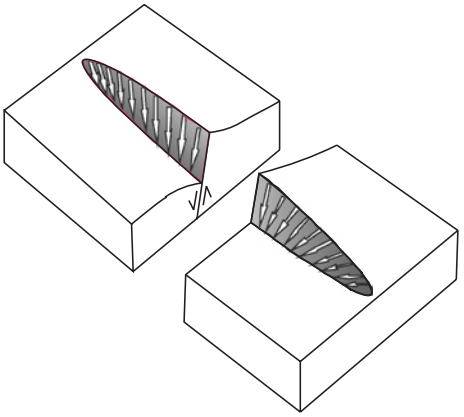

Fig. 5.5 Converging pattern of fault displacement with fault propagation [From Maniatis and Hampel (2008), © Elsevier. Published with permission of Elsevier.]

Two parallel (or nearly parallel) normal faults may be joined by a relay ramp, which is described as an area of reoriented bedding which transfers displacement between the faults (Fig. 5.6) (Larsen 1988). The tilt of the relay ramp gradually increases with increase in fault displacement and the tilted block may be deformed by extensional strains.

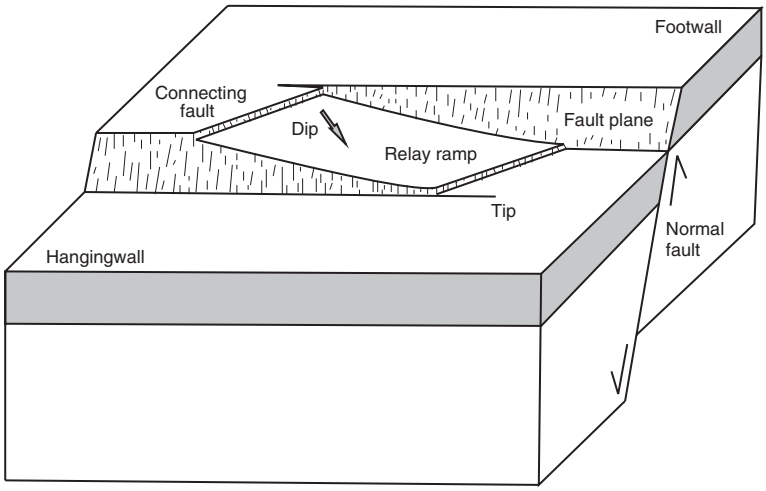

Fig. 5.6 A relay ramp between two normal faults [From Peacock and Sanderson (1995), © Elsevier. Published with permission of Elsevier.]

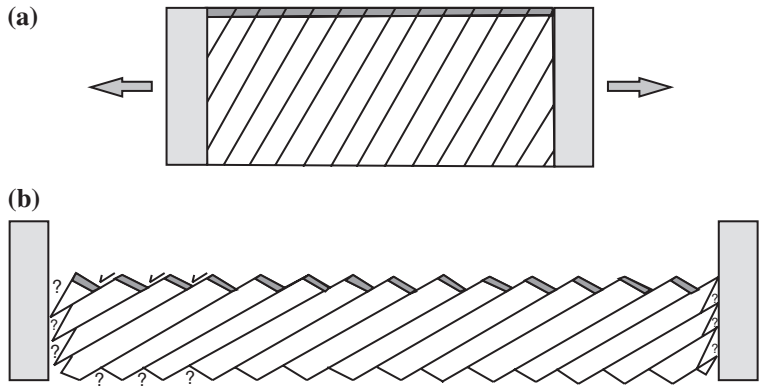

Fig. 5.7 Bookshelf gliding. **a** An initial multilayer sequence. The *arrows* indicate extension direction. **b** A series of parallel normal faults resulting in bookshelf gliding. The *question mark* shows dilation spaces formed as a result of rotation of the faults [From Wernicke and Burchfiel (1982), © Elsevier. Published with permission of Elsevier.]

5.2 Bookshelf Gliding

A variety of normal fault geometries can result during a tensional regime. One of the simplest geometry is domino or bookshelf model (Fig. 5.7).

The extension leads to formation of a series of parallel normal faults. The retaining blocks on either side may remain undeformed and move apart parallel to the axis of maximum extension. The individual faulted blocks do not show internal

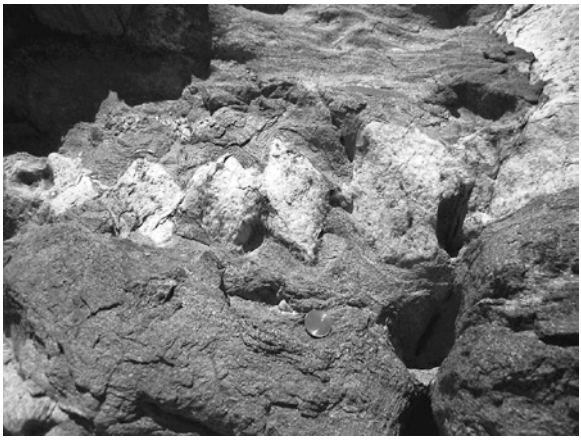

Fig. 5.8 Rotation of a series of fault blocks displacing a quartz vein (Ladakh Himalaya). The dilation spaces are filled-up by ductile flow of the granitic matrix

deformation but rotate as rigid blocks and are displaced by faulting. The amount of rotation of individual blocks may vary. A number of compatibility space problems arise during their development because of formation of triangular dilation spaces around the collapsing blocks. A solution to the problem was suggested by Ramsay and Huber (1987) by filling the upper block spaces by sediments and magma intrusion in the lower block spaces. The open voids cannot remain for a larger time scale because of the necessity of supporting blocks for the top load. Hence the magmatic intrusion should be simultaneous with formation of the faults (Fig. 5.8).

5.3 Fault Dip, Displacement and Extension

The relationship between fault dip, extension, and displacement is shown in Fig. 5.9. The diagram represents a cross-sectional profile in which line AB is parallel to the axis of maximum extension (shown by broad arrows) (also represents the horizontal component of fault displacement) and a normal fault 'f–f' dipping at an angle θ. The normal fault displacement results in movement of the hanging wall block ABC to a new position A′B′C′. 'E' (=A′B′) and 'D' represents the extension and fault displacement respectively. The geometrical relationship between the extension and fault displacement can be expressed as follows.

$$\text{Displacement} = \frac{\text{Extension}}{\cos\theta}$$

Fault displacements for the same amount of extension are shown in Fig. 5.10. Fault dip in Fig. 5.10a is 40° whereas in Fig. 5.10b, the dip is 30°. A comparison of the two figures reveals that for the same amount of extension, a larger displacement results in large fault dip.

The above relationship is shown graphically in Fig. 5.11 for different fault dips. It is apparent from the diagram that a larger displacement results in steeper faults

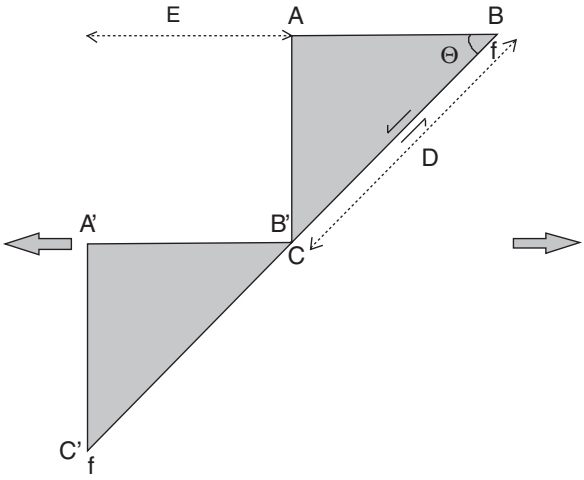

Fig. 5.9 A simplified diagram showing relationship between fault dip (θ), displacement (D) and extension (E) in a normal fault (f–f). The extension direction is shown by *large gray arrows*

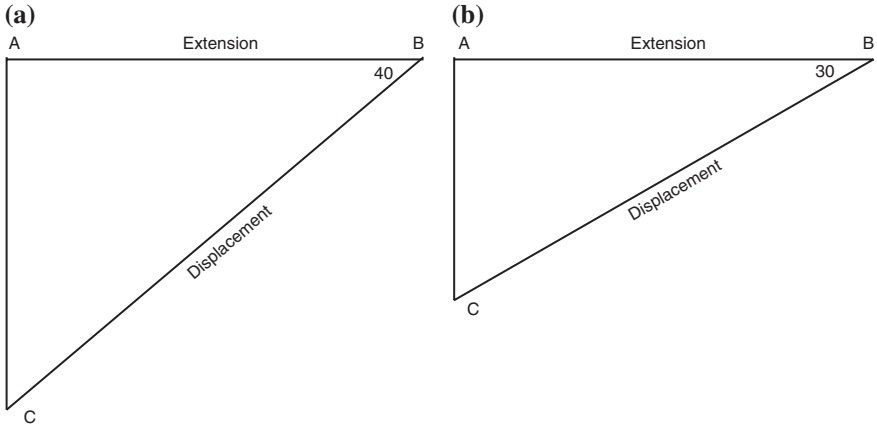

Fig. 5.10 Simple relationships between fault dip (θ), displacement, and extension for normal faults (B–C). **a** Fault dip, 40°. **b** Fault dip, 30°

for the same amount of extension. It has been shown earlier (Fig. 5.3) that dip of the normal fault gradually decreases with increase in deformation. Hence during the early stages of normal faulting, the rate of fault displacement will be more but the rate of extension will be slow followed by decrease in fault displacement and increase in extension. The geological implication of this is important because a greater depth of rift basin is obtained during early stages of deformation. It has been observed that in absence of a weak layer, planar normal faults can reach to a depth of about 10 km with dip amount of approximately 45°. Seismic evidence for

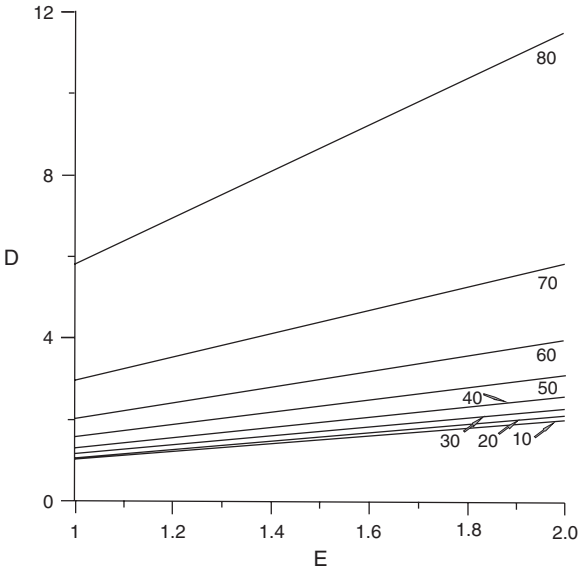

Fig. 5.11 Relationships between extension (E) and fault displacement (D) for different fault dips

such normal faults has been found in Central Greece and western Turkey where the active faults are approximately planar and reach to depths of about 10 km (Jackson and McKenzie 1983).

Generally, normal faults of regional dimensions have a curved geometry to accommodate rotation of the fault surfaces and are characterized by a gradual decrease or increase of dip amount with depth. These faults are called as listric faults (Chap. 4). The earlier studies (Hafner 1951; Price 1977) have shown that normal faults on a crustal scale form with initial listric shape. In most of the geological horizons, the faults show a gradual decrease of dip with depth and are described as positive listric faults in contrast to negative listric faults that show increase of dip with depth. The fault curvature results from variation in stress orientation with depth and rheological changes mainly resulting from geothermal gradients or to fluid overpressure during compaction (Hubbert and Rubey 1959; Jackson and McKenzie 1983).

5.4 Curvature of Faults and Associated Dilation Spaces

The kinematics of planar faults is simple because the displacements take place without rotation of the hanging wall. However listric faults present somewhat complicated patterns of displacements. Further, the curvature of listric faults prevent accurate estimate of extension from surface observations of fault dip and displacement. An example is shown in Fig. 5.12 where initiation of a positive normal, listric fault (Fig. 5.12a) is followed by displacement along the fault. The displacement leads to formation of dilation spaces along the fault. Depending of the

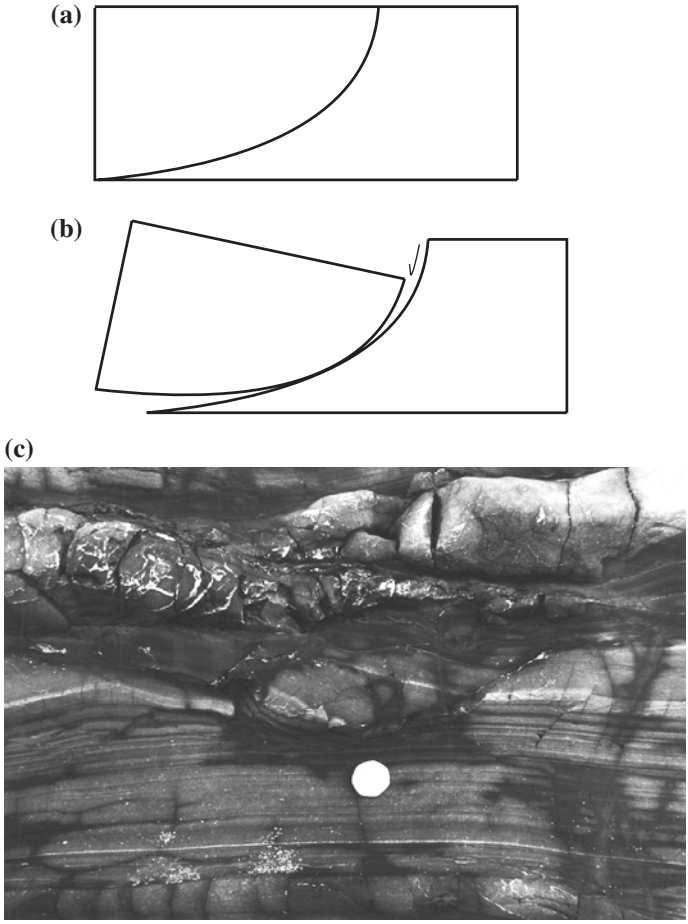

Fig. 5.12 Development of a listric fault. **a** Initiation of a positive listric fault. **b** Dilation spaces as a result of displacement along a curved fault surface. **c** Tilting of a hanging wall block during normal faulting in a greywacke shale sequence. Minor thrust faults are later tectonic structures (Bude, England)

location of displacement along the fault, the dilation spaces can form at two levels as shown in the diagram (Fig. 5.12b) or only at one level.

A number of geometrical solutions have been suggested to overcome the problem of dilation spaces. For example, Fig. 5.13a shows initiation of a listric fault, rotation of the hanging wall beds, and formation of a dilation space. The dilation space can be filled-up by curvature of the hanging wall beds under the influence of gravitational forces (Fig. 5.13b). An alternate solution can be curvature and formation of open fissures in the hanging wall beds (Fig. 5.13c).

Experimental results using sand box (McClay and Ellis 1987) reveal that the extensional faults can form either by domino-type model (Fig. 5.7) or by a group

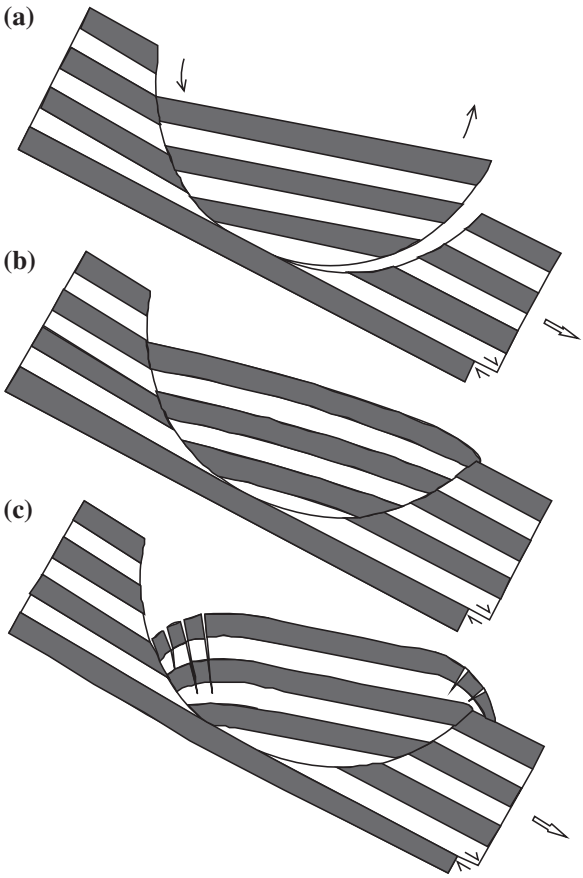

Fig. 5.13 Listric faults and adjustment of dilation spaces. Top surface of the lowermost bed represents a plane of decollement. **a.** The basic compatibility problem and formation of dilation space. *Two arrows* above the hanging wall show the sense of rotation of the hanging wall beds. **b** The dilation space is filled-up by curvature of the hanging wall beds. **c** Development of open fissures and curvature of hanging wall beds to fill-up the dilation space [From Ramsay and Huber (1987), © Elsevier. Published with permission of Elsevier.]

of listric faults. The domino-type or book-shelf gliding involves planar rotational faulting. The model requires a large number of nearly parallel planes with relatively easy slip, with or without a basal detachment surface. The dilation spaces formed during the rotation are filled-up by the basement material. Planar faults initiate at early stage of deformation and these faults do not involve rotation of hanging wall blocks or layers. Normal listric faults produced by extension were found to have similar geometry to those of compressional listric faults. Positive listric faults are common in nature but negative listric faults do exist. One of such models showing formation of negative listric fault is shown in Fig. 5.14. The first stage shows initiation of a positive listric fault (between blocks 'x' and 'y') and a planar fault (between blocks 'y' and 'z') during horizontal extension shown by the large arrow (Fig. 5.14a). Displacement along the listric fault leads to anticlockwise rotation of block 'y'. A dilation space is formed between blocks 'y' and 'z' with curvature (c) of the planar fault in the block 'y' (Fig. 5.14b). The anticlockwise rotation increases with increase in displacement along the listric fault and result in

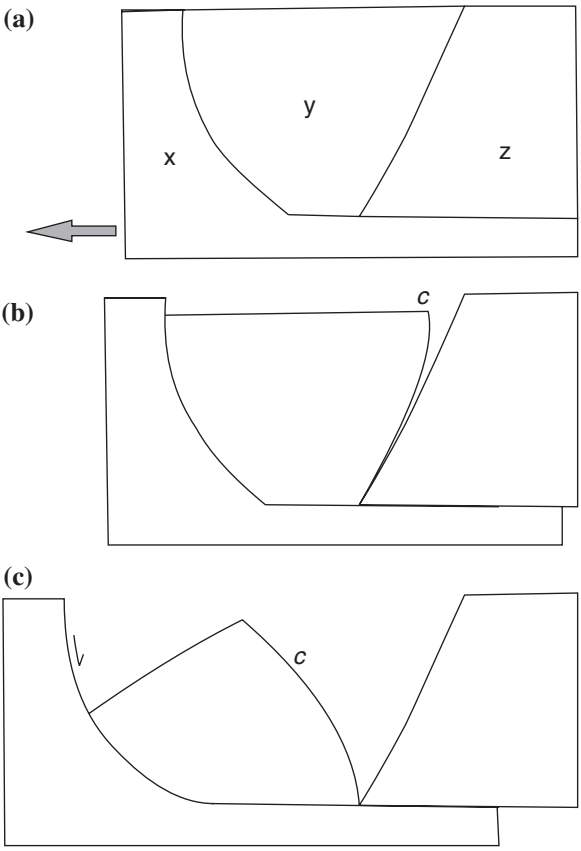

Fig. 5.14 Development of negative listric-fault geometry due to heterogeneous rotation within a rollover anticline. **a** Initial position at initiation of normal listric fault. The *arrow* denotes the direction of extension. **b** Block 'y' rotates anticlockwise along the listric fault of block 'x' with curvature (*c*) on the right side. **c** Increase in anticlockwise rotation of the fault and curvature in block *y* resulting in negative listric fault geometry [From McClay and Ellis (1987), © The Geological Society. Published with permission of the Geological Society of London.]

simultaneous increase in curvature of 'c' and formation of a negative listric fault (Fig. 5.14c).

Simultaneous development of planar and listric faults are shown in Fig. 5.15 (McClay and Ellis 1987). The diagram depicts a deformed sandbox model that underwent extension from one side. The sequence of initiation of faults (1, oldest to 6, youngest) indicates that steep extensional fault (1) with planar geometry initiated at an early stage. This was followed by footwall collapse on both sides (fault 2) and formation of a graben along listric faults. New faults with planar geometry initiated towards the centre of the graben in the hanging wall with the moving margin. The fault displacement gradually decreased towards the top indicating that the faults initiated at the base of the model. The diagram indicates that faults with smaller dimensions and displacement have a planar geometry and large faults with greater displacement have listric geometry.

A convincing mechanism for formation of listric faults was described by Vendeville and Cobbold (1988) (Fig. 5.16). Initiation of evenly spaced normal faults at an angle of ~60° to the horizontal bedding is shown in Fig. 5.16a. With

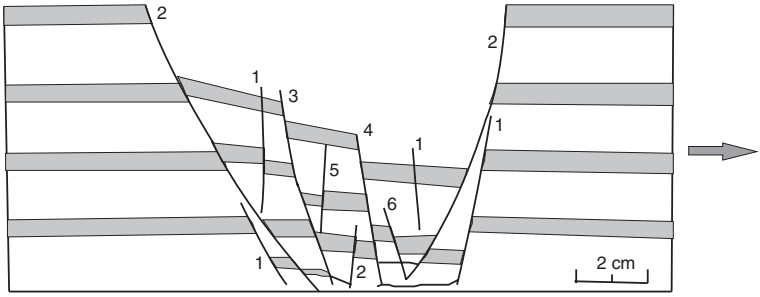

Fig. 5.15 Fault development after 25 % extension. The *arrow* denotes the direction of extension. Sequence of initiation of the faults is shown by *consecutive numbers*. The figure shows dominant nucleation of normal faults in the hanging wall of the graben [From McClay and Ellis (1987), © The Geological Society. Published with permission of the Geological Society of London.]

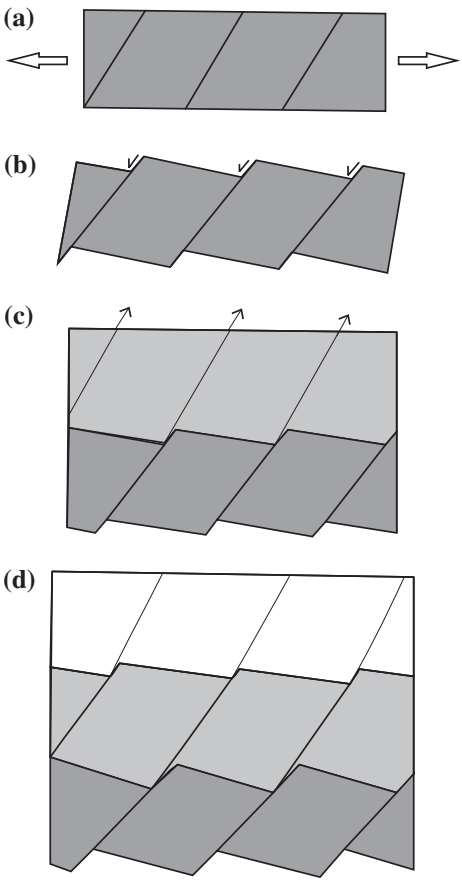

Fig. 5.16 A geometric model of stepwise sedimentation and formation of listric, normal faults. **a** Initiation of faults. The *large arrows* show extension direction. **b** Normal faulting and clockwise rotation of the blocks. **c** Upward propagation of the underlying faults (*arrows* shown by *broken lines*) with constant dips into younger sedimentary layers along with rotation of the fault blocks. **d** Listric geometry of the faults [From Vendeville and Cobbold (1988), © Elsevier. Published with permission of Elsevier.]

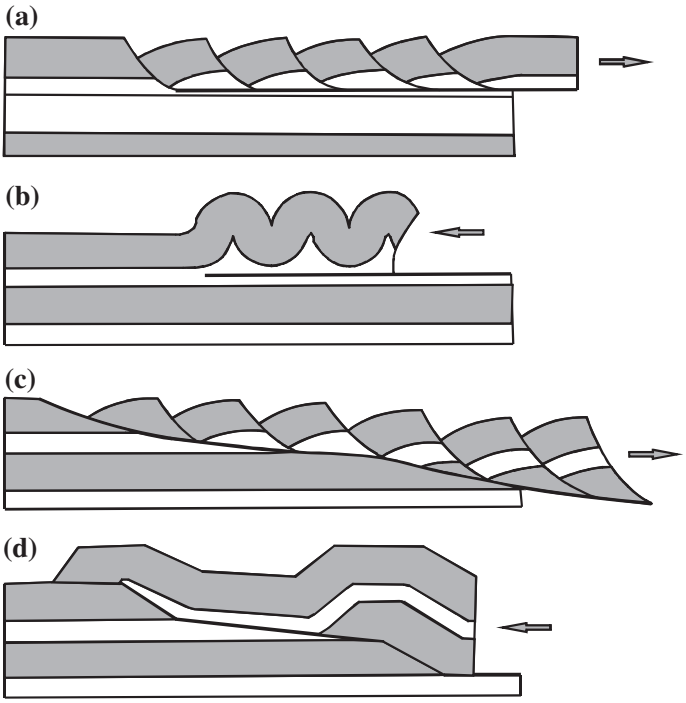

Fig. 5.17 Different geometries of normal and thrust faults. **a** Extensional decollement fault. **b** Compressional decollement fault. **c** Extensional detachment fault. **d** Compressional detachment fault [From Ramsay and Huber (1987), © Elsevier. Published with permission of Elsevier.]

increase in deformation, displacement along these faults lead to rotation and rigid tilting of domino type fault blocks (Fig. 5.16b). Deposition of younger sediments fills the surface depressions and creates a horizontal surface at the top (Fig. 5.16c). The faults propagate upwards with 60° dip to the bedding and a new cycle of displacements and sedimentation is followed. Gradual rotation of the lower faults leads to gentler dips and consequently faults with positive listric geometry are formed.

An important feature that supplements curvature of faults is variation of rheology with depth. In a brittle regime at shallow depths, the amount of rotation is less as compared to ductile regime at greater depths (Jackson and McKenzie 1983). The flattening of listric faults with depth is also attributed to a weak layer in the crust. Another significant point is that dip of the recent normal faults is often very steep at the surface because the top few tens of meters near the earth's surface fail in tension, not shear.

5.5 Decollement and Detachment Faults

Ramsay and Huber (1987) have classified the normal and thrust faults in two basic types, decollement and detachment faults. The term decollement is related to strata control of the sole fault in a particularly soft or incompetent rock. The term detachment is used when the fault is not parallel to any one horizon but cuts across the competent-incompetent geological horizons (Fig. 5.17).

5.6 Co-existence of Normal and Reverse Faults

Normal and reverse faults develop under different stress conditions but rotation of normal faults can resemble coexistence of normal and reverse faults as shown in Fig. 5.18. The natural example shows a monoclinal structure above a plane of decollement. The multilayer sequence is cut by three normal faults. Out of these, two faults represent the real displacement of normal faults whereas the third one shows the displacement pattern of a reverse fault. Evolution of the structure is shown in Fig. 5.18b, c, and d. Extension of the layer and initiation of a normal fault (A) is shown in Fig. 5.18b. With increase in deformation, the earlier fault rotates and a new fault (B) initiates in the layer (Fig. 5.18c). Both the faults rotate in a clockwise direction with formation of a new normal fault (C). A greater rotation of fault A creates an impression as if this is a reverse fault.

An alternate model for the formation of similar structure is presented in Fig. 5.19. The model incorporates formation of the monocline, which is a fold structure formed as a result of compression. The first stage (Fig. 5.19a) represents a series of normal faults (A, B, and C) formed during a tensional phase in the region. During a later compressional phase, the layer starts folding with formation of a monocline. Folding initiates from one end of the layer and fault A rotates in a clockwise direction (Fig. 5.19b). With increase in deformation, the folding gradually propagates along the layering with increase in rotation of Fault A and Fault B. If the deformation is arrested at this stage, coexistence of reverse and normal faults can be seen along the layering.

Another example of listric normal fault development resembling a thrust is shown in Fig. 5.20. Initial geometry of a listric fault and the axis of maximum extension are shown in Fig. 5.20a. The top layer is marked in gray to help in identifying the fault displacement pattern. The extension leads to creation of an open space providing condition for formation of an antithetic (dipping in opposite direction) normal fault (AF, Fig. 5.20b). The displacements continue along the synthetic and antithetic faults (Fig. 5.20c) along with initiation of a new normal fault. Greater displacement along the synthetic fault and consequent rotation of the hanging wall along the main listric fault result in resemblance of the antithetic fault (AF1) to a thrust. Open space is likely to be formed at the base of the hanging wall and another antithetic fault (AF2) initiates. Figure 5.20e represents collapse of the hanging wall and formation of listric fault “roll over” antiform. The

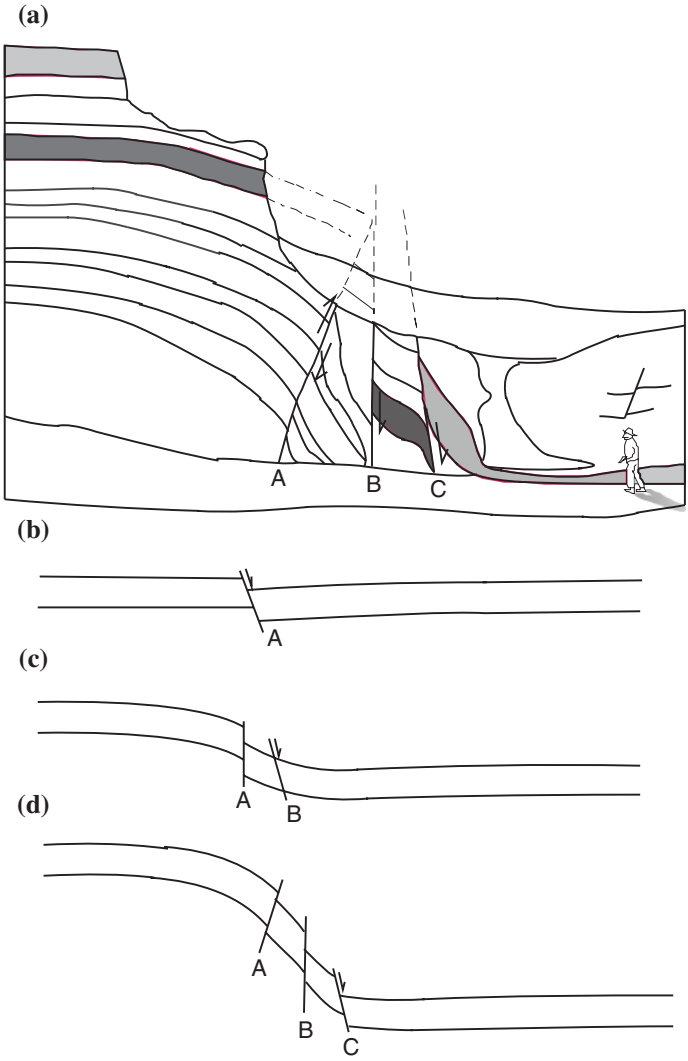

Fig. 5.18 Sequential initiation and gradual rotation of faults resulting in coexistence of normal and reverse faults. **a** Normal and reverse faults in a multilayer sequence (San Rafael Desert, Utah). **b** Initiation of a normal fault (*A*). **c** Clockwise rotation of Fault *A* to a sub-vertical position with increase in deformation and initiation of a new normal fault (*B*). **d** Further rotation of the earlier faults (*A* and *B*) and initiation of a new normal fault. A greater rotation of Fault *A* creates an impression of a reverse fault [From Fossen (2010), © Cambridge University Press. Published with permission of Cambridge University Press, Cambridge.]

two normal faults 'Th' and 'AF2' occur in a conjugate set but their opposite sense of relative movement can be used to identify the sequence of evolution.

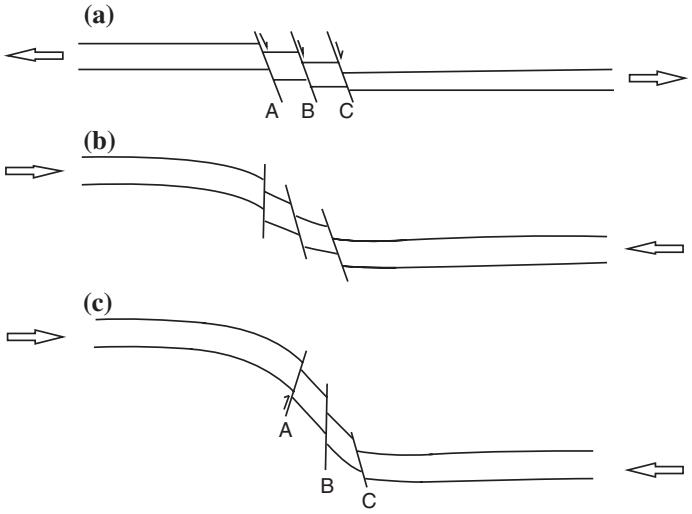

Fig. 5.19 Coexistence of normal and reverse faults in a developing monocline as a result of inversion tectonics. The stress orientations are shown by *arrows*

5.7 Evolutionary Stages of Normal Faults

Following the identification of listric normal faults in seismic reflection records of the Aegean region (McKenzie 1978), Rhine Graben (Murawski 1976), the Great Basin of the western USA (Wright 1976), and Canadian Rocky Mountains (Bally et al. 1966), McKenzie (1978) proposed a model for development of sedimentary basins. The model was based on stretching of continental lithosphere leading to thinning and passive upwelling of hot asthenosphere, normal listric faulting and subsidence. The model allows estimation of stretching from the slow subsidence, heat flow, and change in thickness of the continental crust caused by extension. It can explain epeirogenic subsidence but not uplift above sea level. The model was later applied to the formation of northern Bay of Biskay and Galicia continental margins in the northeast Atlantic.

Normal faults can develop in conjugate sets (i.e. fault dip in opposite directions; horst and graben structure), or in a single set. Displacement along the single set of listric faults leads to formation of half grabens in the down-thrown side (Fig. 5.21). These are of particular interest to geologists because of distinct deposition pattern, presence of angular unconformities, growth faults, and presence of hydrocarbons. A steady and slow displacement results in gradual variation of dip in penecontemporaneous sediments. The layers which were deposited at the onset of fault displacement lie at the greatest depth with the maximum dip amount whereas upper layers of the sequence show the minimum dip (Fig. 5.21a). The layer thicknesses also vary with distance from the fault and the maximum thickness occurs at the fault. However if the initial phase of displacement and

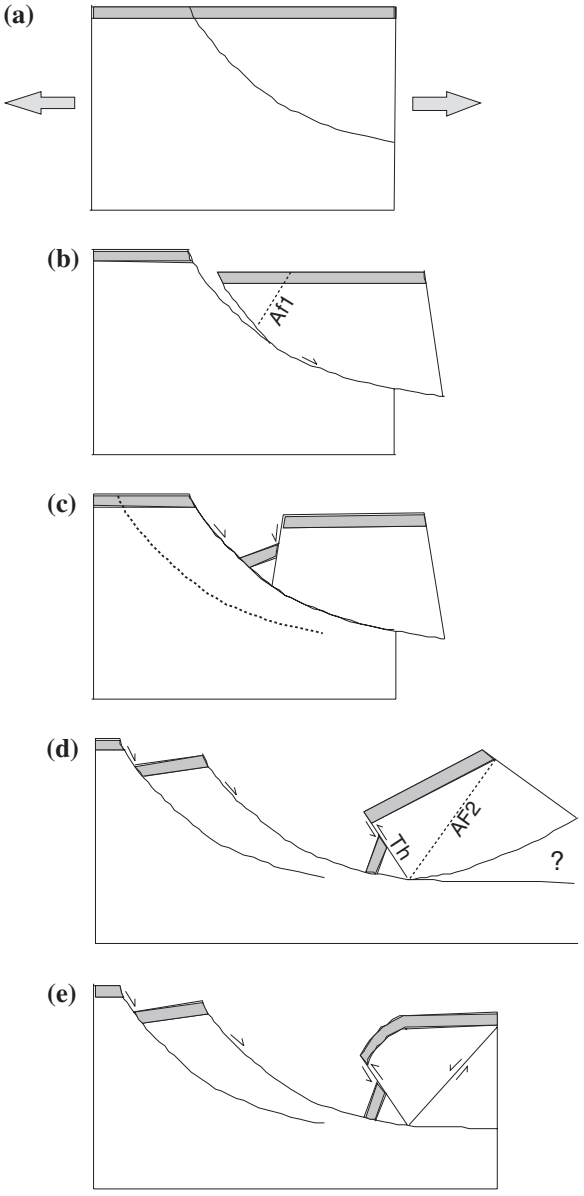

Fig. 5.20 Evolution of a normal fault system leading to pseudo thrust displacement and a roll-over antiform [From Profett (1977), © Geological Society of America. Published with permission of Geological Society of America.]

deposition is ceased for some time, the interval may be marked by an angular unconformity (Fig. 5.21b). Angular unconformities in the Himalaya have been described by Bhargava et al. (2011).

Angular unconformities play an important role in controlling the geometries of developing structures during a later compressional regime (Chap. 4). If a basin is formed on a scale of hundreds of km, it is called as rift basin, the rock in which pre-orogenic (prior to mountain building) listric faults are formed is called as

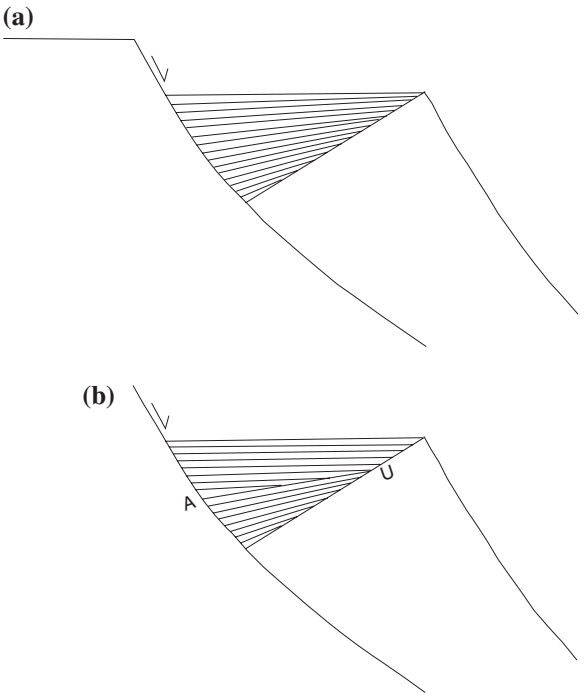

Fig. 5.21 Development of half grabens and their deposition pattern. **a** Continuous deposition of sedimentary layers during displacement along a listric fault. **b** Spasmodic fault reactivation and formation of an angular unconformity (*A–U*) in the sedimentary cover layers

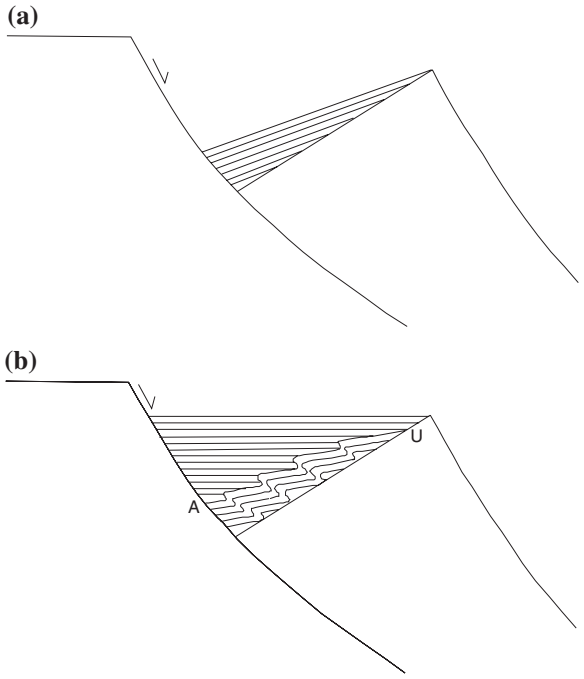

Fig. 5.22 Angular unconformity in a half graben. **a** Formation of a half graben and deposition of beds followed by displacement without deposition. **b** Formation of asymmetric folds in the older beds as a result of gravity gliding followed by an angular unconformity and later deposition of younger beds above the unconformity. The younger cover rock can be horizontal in case of fault locking

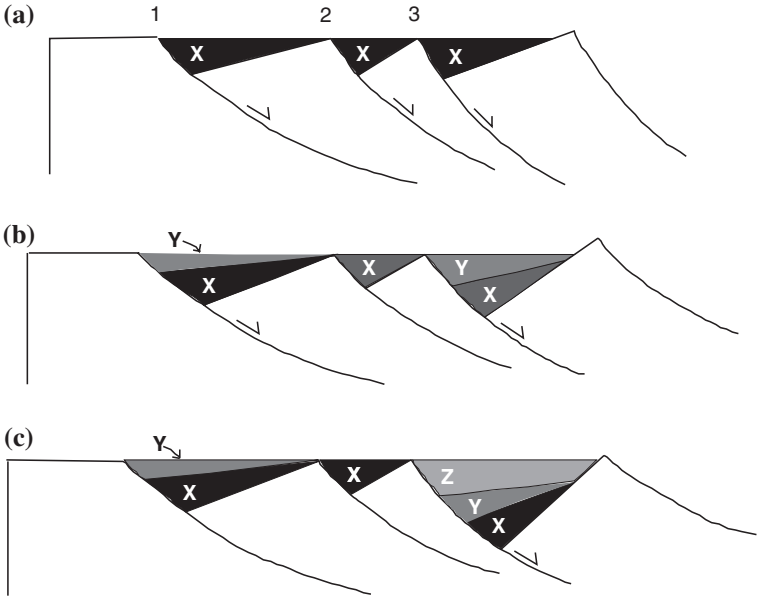

Fig. 5.23 A simplified diagram to illustrate deposition of different sediments in a series of half grabens. *1*, *2*, and *3* represents three listric faults. **a** Deposition of 'X' in all the three half grabens. **b** Displacements along Faults *1* and *3* with deposition of 'Y'. There is no displacement along Fault *2* hence no deposition. **c** Displacement only along Fault *3* and deposition of the youngest sediments 'Z'. Fault *2* shows the minimum and Fault *3* shows the maximum fault displacement

basement, and the overlying sedimentary layers deposited during or after the faulting are known as cover rocks.

Asymmetric folds are likely to develop in the older tilted sequence of rocks. Figure 5.22a shows formation of a half graben, and deposition of cover rocks. Continued displacement along the listric normal fault, accompanied by anticlockwise rotation of the hanging wall, can increase the slope for gliding of layers under the gravitational force resulting in development of asymmetric folds. These folds are called as growth folds. The process can be followed by deposition of younger beds (Fig. 5.22b) above an unconformity.

If the fault displacement is of a large magnitude, the folded layers may reach to a depth where they are metamorphosed under the prevalent P–T conditions. These folds may wrongly be identified as tectonic folds formed during an earlier orogeny (Tobisch 1984).

Deposition in a series of half grabens depends upon the number of listric basement faults and displacements along them (Fig. 5.23). Figure 5.23a shows simultaneous initiation of three listric faults (1, 2 and 3), formation of half grabens, and deposition of 'X' in all of them. After the deposition of 'X', displacement ceases at Fault 2 and the younger series 'Y' is deposited in the half grabens of Faults 1 and 3

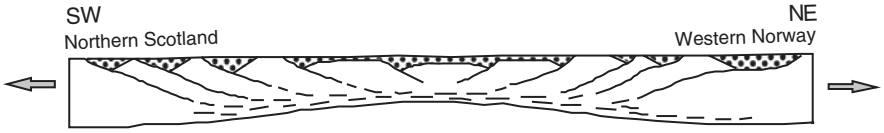

Fig. 5.24 A section of the North Sea during Middle Devonian times. The symmetrical low-angle shear zones bounding the basins at each margin merge in the lower crust within a zone of pervasive ductile flow (not to scale) [From Seranne and Seguret (1987), © The Geological Society. Published with permission of Geological Society of London.]

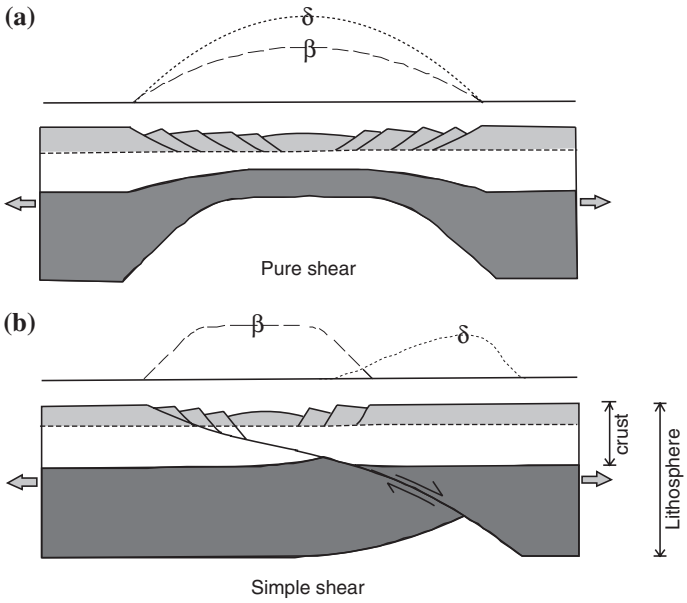

Fig. 5.25 Two models of lithospheric extension. **a** Pure-shear model. The lithosphere necks and thins below the developing sedimentary basin where a series of extensional listric faults have developed. **b** Simple shear model. The extension is accommodated along a low angle shear zone through the lithosphere. The distribution of β (extension of the crust) and δ (extension of the subcrustal lithosphere) are shown schematically [From Keen et al. (1987), © NRC Research Press, Published with permission of NRC Research Press.]

(Fig. 2.14b). This is followed by continued movement only along Fault 3 and deposition of 'Z'. Hence the complete sequence of rocks is available only at Fault 3.

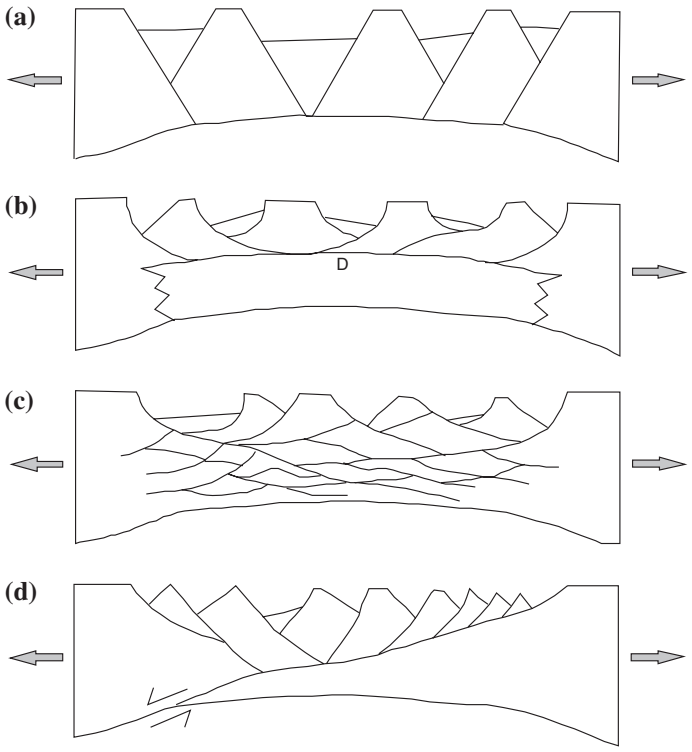

Fig. 5.26 Models of intracontinental extension. **a** Symmetrical rift grabens **b** Sub-horizontal, mid-crustal decoupling horizon (Eaton 1979; Miller et al. 1983; Smith and Bruhn 1984). **c** Lensoidal or anastomosing shear zones (Hamilton 1982; Kligfield et al. 1984). **d** Crustal penetrating shear zone (Wernicke 1981) [From Allmendinger et al. (1987), © The Geological Society. Published with permission of Geological Society of London.]

5.8 Models of Lithospheric Extension

Planar (or sigmoidal) normal faults occur on comparatively smaller scales and normal faults of continental scales are more commonly listric (e.g. Fig. 5.24). These extensional faults, arranged in a symmetric fashion across an axial zone and dipping in opposite directions on two sides of the zone, form during a large scale tensional (rift) phase. The faults are steep near the axial zone and gradually acquire gentle dips away from the zone. The crustal and subcrustal material may either extend by approximately the same amount (e.g. Nova Scotian Margin) or the mantle lithosphere may extend considerably more than the crust (e.g. Labrador) (Royden and Keen 1980).

Two models of lithospheric extension are shown in Fig. 5.25. The Pure shear model (Fig. 5.25a) involves ductile necking and thinning of the subcrustal lithosphere during a tensional phase. The pinching may be symmetrical and the basin develops immediately above the thinned crust and the subcrustal lithosphere. This is also

reflected by the distribution of β (extension of the crust) and δ (extension of the sub-crustal lithosphere). In contrast, the simple shear model is markedly asymmetrical. Position of the sedimentary basin is horizontally offset from the zones of thinning of the lower crust and lower lithosphere. This is indicated by the distribution of β and δ.

Other fault geometries, which form during an extensional phase are shown in Fig. 5.26. The horst and graben structures are illustrated in Fig. 5.26a. The Rhine graben in Germany and Leopargial horst in the Himachal Tethys Himalaya (Chap. 13) are well known examples. However on an intercontinental scale, the structure may not be very symmetrical as shown in the diagram and the fault surfaces may not be planar structures. Figure 5.26b displays a number of listric faults dipping in opposite directions and terminating into a mid-crustal decoupling horizon (D). When a conjugate set (opposite dipping) of listric shear zones form simultaneously, they divide the region into a large number of irregular lensoidal blocks by anastomosing shear zones and displace the individual blocks in a complicated manner (Fig. 5.26c) (Freund 1974; Ramsay and Huber 1987). These are somewhat deeper structures characteristic of ductile and brittle-ductile environment. The crustal penetrating shear zones appear to be the most common (Fig. 5.26d). The structure involves formation of a detachment fault and a conjugate set of listric faults in the hanging wall. The geometries of the extensional faults may vary but they have a common feature of formation in a conjugate set with a number of half graben structures. These half grabens are later filled-up by sedimentary infills. When the faults are deep enough, they act as conduits for upward movement of magma. The occurrence of these magmatic rocks along the faults is important because age of these rocks can help in deciphering the age of faulting.

5.9 Factors Responsible for Uplift in a Region

The early history of an orogenic belt is characterized by tensional regime in the region that lead to formation of rift basins along listric normal faults. Since this is related to either horizontal extension or vertical maximum compression, it is worthwhile to consider the factors that may cause uplift resulting in normal faults The tectonic development of young continental margins was attributed by Bott (1971) to progressive loss of gravitational energy and subsidence of the shelf as isostatic response to crustal thinning caused by hot creep of lower continental crustal material towards the sub-oceanic mantle. Normal faulting was particularly envisaged for the overlying brittle upper crust.

The various speculative models include accretion of low density material derived from the mantle to base of the crust (Fig. 5.27a) and subsequent rise into the high density material. The mechanism is comparable to an experiment in which low density oil is injected at the base of a beaker containing water. Centrifuge experiments of this kind in which an artificial gravitational force was created by rotation of the model container were performed by Ramberg (1967). Isochemical phase changes, hydration, or other metasomatic alterations leading to volume increase in the lower crust or upper mantle will also produce uplift of

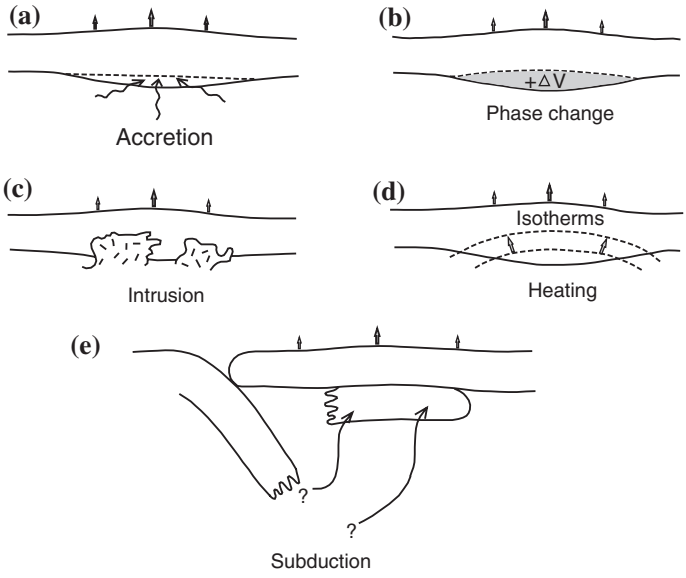

Fig. 5.27 Different mechanisms that may cause uplift in a region [From Hobbs et al. (1976), © B.E. Hobbs. Published with permission of B.E. Hobbs.]

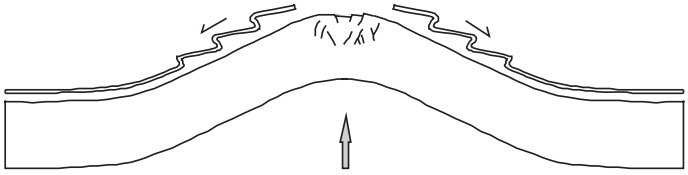

Fig. 5.28 Uplift of a region resulting in formation of normal faults at the crest and asymmetric folds on the limbs

the crust (Fig. 5.27b). Since the material of increased volume is not penetrating over a large part of the crust, the deformation pattern would be comparatively simpler. The reversal of these processes may result in subsidence. However whether it is uplift or subsidence, the result would be formation of normal faults because the axis of maximum compression acts in a vertical direction. Plutonic activity (Fig. 5.27c) and heating of the crust (including mantle plume) (Fig. 5.27d) will have similar effects. The resulting deformation structures will depend upon the size and density of the pluton and the force of intrusion. A mild force will result in antiformal structures whereas an intense force will result in a greater number of fractures. However in certain cases it may not be very clear whether the extension causes the upwelling or vice versa. The mechanism of subduction is not very well known but if the subducting plate breaks-up after reaching a certain depth and rise to occupy a position below the other colliding plate, the low density and high heat flow can also produce uplift (Fig. 5.27e).

Apart from formation of normal faults, uplift of a region can create slopes that will facilitate sliding of overlying layers under the influence of gravity (gravity collapse or gravity gliding) resulting in normal faults at the crest and asymmetric folds on the limbs (Fig. 5.28). The asymmetry of folds increases with steepness of the slope and amount of shear. The slope required for the gravitational collapse can also result from large scale folding, thrusting, igneous activity and natural slope at a basin margin.

5.10 Identification of a Rift Phase by Geochemical Method

Study of surface geology is a direct method of understanding the structural features. Subsurface structural interpretations can substantiate the interpretations. In addition to these, one of the indirect methods of obtaining information on tectonics is geochemical analysis of magmatic rocks that are now exposed on the surface in known tectonic environments. The inferences are then extrapolated to other similar areas. The chemical methods have been used on the ocean floor basalt (OFB) magma to estimate past spreading rates. It was found out by Bass (1971) that basalts from faster spreading ridges were low in Al and more silica saturated than basalts occurring at slow-spreading ridges. Anorthite content of plagioclase phenocrysts was found to be negatively correlated with spreading rate (Scheidegger 1973). An important correlation was established by Nisbet and Pearce (1973), and Pearce (1975) between mean TiO_2 concentrations and spreading rates in a rift zone. Many fine grained basic alkaline rocks associated with the rift systems contain ocelli (small spherical bodies of felsic material) which may have formed as immiscible droplets (Philpotts 1978).

Sun et al. (1979) have described two types of mid-ocean ridge basalts (MORB). The normal (N)-type MORB is characteristically depleted in highly incompatible elements (Cs, Rb, Ba, Th, U, NB, K, LREE, etc.) and isotopic evidence suggests that this is a long-term (>1b.y.) phenomenon. The Plume (P)-type or incompatible-element enriched basalts occur in several oceanic environments. However the long term history of islands located on a mid-ocean ridge (MOR) (e.g. Iceland) or volcanism in one mantle anchored spot (e.g. Hawaiian Islands) suggests that a continuous supply of P-type source has been sustained for a substantial period of time.

Rifts associated with a large crustal extension are characterized by tholeiitic rocks whereas alkaline rocks were formed on a limited scale where rifting has resulted mainly in down faulting. The extensional regime can also be identified by a dike swarm along fault zones. Since the dikes are intruding simultaneously with faulting, the dikes may be off-set by faults (e.g. northern side of the Ottawa graben). Instead of dikes, widely scattered stock-like bodies can also intrude in a rift system (e.g. St. Lawrence valley rift system) (Philpotts 1978). The vapour coexisting with rift valley magmas is deficient in water. It is strongly reducing with high concentrations of carbon and halogen gases with possibility of nitrogen. The vapour escapes from the deep mantle and passes through the lithosphere during its upward journey. The early

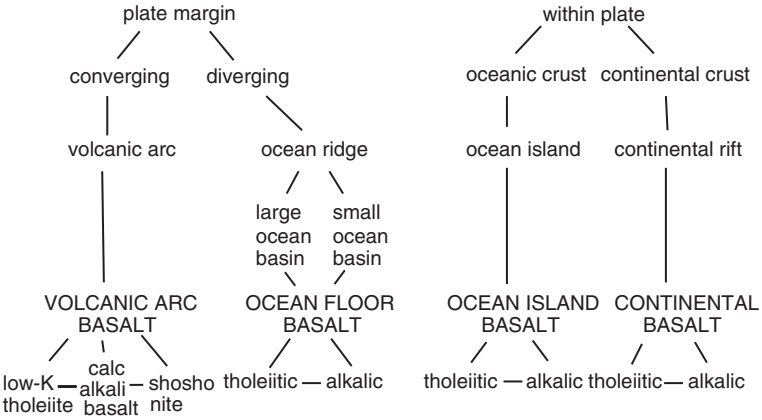

Fig. 5.29 Geological classification of volcanic rocks based on tectonic environment [From Pearce and Cann (1973), © Elsevier. Published with permission of Elsevier.]

stages are characterized by vapour producing metasomatic carbonates, and halogen bearing alkali silicates in the upper mantle and the lower crust. This is accompanied by continental uplift by thermal and metasomatic expansion of the lithosphere. As the flux cycle climbs through the lithosphere, the initial uplift is followed by devolatilization, melting, eruption and consequent subsidence (Bailey 1978).

It is to be noted that there are different geometrical and mechanical aspects of the oceanic and continental rifts (Bailey 1983). The continental rift is a split within one plate whereas the oceanic rift is a separation of two plates. In contrast to the oceanic rift, the continental rift is very slow, magmatism and high heat flux are sporadic, the magmatism is highly variable (typically gas and alkali rich), and the mantle sources are enriched in large ion lithophile elements (LILE).

Pearce and Cann (1973) have proposed a useful geological classification of volcanic rocks based on the tectonic environment associated with their eruption (Fig. 5.29). Four major groups that can be readily recognized and recent volcanic rocks were defined as follows.

5.10.1 Ocean Floor Basalts

Volcanic rocks from the ocean floor are extremely homogeneous. These are generally tholeiitic, but with transitional and alkalic varieties occurring in some areas. The rocks represent a single magma type of narrow compositional range and there is little chemical difference between the basalt from large ocean basins and small ocean basins.

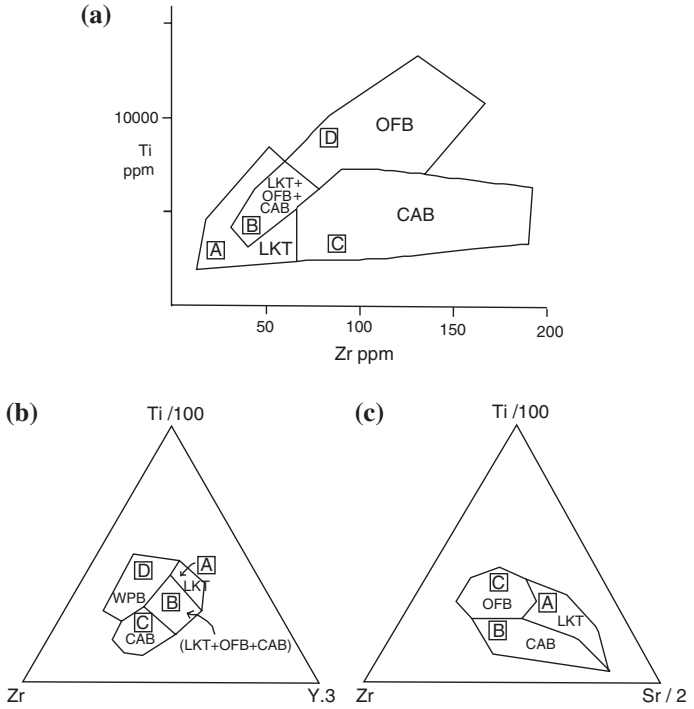

Fig. 5.30 Discrimination diagrams to understand the tectonic settings of basic volcanic rocks [From Pearce and Cann (1973), © Elsevier. Published with permission of Elsevier.]

5.10.2 Volcanic Arc Basalts

In volcanic arcs, the products of volcanicity vary both with stage of evolution of the arc and with the vertical distance of the eruption above the Benioff zone. Hence the rocks are divided into three rock series; (i) the low potassium tholeiitic series, (ii) the calc-alkali series, and (iii) the shoshonitic series. The series may be gradational from the low potassium tholeiites through calc-alkali rocks to shoshonites both in time (tholeiites typical of the earliest eruptions) and space (tholeiites occur closest to the trench).

5.10.3 Ocean Island Basalts

These basalts show a large chemical variation from the tholeiitic lavas through the more common intermediate alkali varieties to the ultra alkaline types. The products of fractionation are also common.

5.10.4 Continental Basalts

The ocean island and continental basalts cannot be distinguished on the basis of chemical compositions. Hence they are treated as one group in the 'within plate basalts'.

Pearce and Cann (1973) have used the trace element concentrations of over 200 basaltic rocks from known tectonic setting of the present day to determine the tectonic settings of older rocks. It was shown that the elements Ti, Zr, Y, Nb, and Sr can be applied to characterize basic volcanic rocks from different tectonic settings. The following three discrimination diagrams were proposed.

1. Ti–Zr diagram (Fig. 5.30a)
2. Ti ($\times 10^{-2}$)–Zr–Y ($\times 3$) diagram (Fig. 5.30b)
3. Ti ($\times 10^{-2}$)–Zr–Sr ($\times 0.5$) diagram (Fig. 5.30c)

Figure 5.30a is divided into four fields, A, B, C and D. Low potassium tholeiites plot within fields A and B, calc-alkali basalts within fields B and C, and ocean-floor basalts within fields B and D. The fields A, C and D are therefore distinctive but B is encroached by each group. Hence if the majority of analyses plot within field B, additional evidence is needed. The analyses should be first plotted on Fig. 5.30b because it has a distinctive field (D) for 'within plate' basalts (ocean island and continental basalts). The other magma types can be separated by using Fig. 5.30c. In order to reach a meaningful solution, it was suggested that a large sample set should be used because in many cases the rock series may be polygenetic, i.e. it may contain more than one magma type. This may occur when ocean floor and ocean island volcanic rocks have been emplaced together.

A similar approach has been used to subdivide the granites according to their intrusive settings into four main groups—ocean ridge granites (ORG), volcanic arc granites (VAG), within plate granites (WPG) and collision granites (COLG) (Pearce et al. 1984). These diagrams can be used to understand the tectonic environment during emplacement of the rocks.

References

Allmendinger RW, Hange TA, Hauser EC, Potter CJ, Oliver T (1987) Tectonic heredity and the layered lower crust in the Basin and Range Province, western United States. In: Coward MP, Dewey JF, Hancock PL (eds) Continental extensional tectonics, vol 28. Special Publication Geological Society of London, pp 223–246

Bailey DK (1978) Continental rifting and mantle degassing. In: Neumann ER, Ramberg IB (eds) Petrology and geochemistry of continental rifts. Reidel Publishing Company Dordrecht, Holland, pp 1–13

Bailey DK (1983) The chemical and thermal evolution of rifts. Tectonophysics 94:585–597

Bally AW, Gordy PL, Stewart GA (1966) Structure, seismic data and orogenic evolution of southern Canadian Rocky Mountains. Bull Can Pet Geol 14:337–381

Bass MN (1971) Variable abyssal basalt populations and their relation to sea-floor spreading rates. Earth Planet Sci Lett 11:18–22

Bhargava MN, Wolfgang F, Rufus B (2011) Late Cambrian deformation in the Lesser Himalaya. J Asian Earth Sci 40:201–212. doi:10.1016/j.jseaes.2010.07.015
Bott MHP (1971) Evolution of young continental margins and formation of shelf basins. Tectonophysics 11:319–327
Eaton GP (1979) Regional geophysics, Cenozoic tectonics, and geologic resources of the Basin and Range Province and adjoining regions. In: Newman GW, Goode HD (eds) Basin and Range symposium, Rocky Mountain Association of Geologists, pp 11–39
Fossen H (2010) Structural geology. Cambridge University Press, Cambridge, 463 p
Freund R (1974) Kinematics of transform and transcurrent faults. Tectonophysics 21:93–134
Hafner W (1951) Stress distribution and faulting. Bull Geol Soc Am 62:373–398
Hamilton W (1982) Structural evolution of the Big Maria Mountains, northeastern Riverside County, southeastern California. In: Frost EG, Martin DL (eds) Mesozoic-Cenozoic tectonic evolution of the Colorado River Region, California, Arizona, and Nevada. Cordilleran Publishers, San Diego, pp 1–28
Hobbs BE, Means WD, Williams PF (1976) An outline of structural geology. Wiley, New York, 571 p
Hubbert MK, Rubey WW (1959) Role of fluid pressure in mechanics of overthrust faulting: I. Mechanics of fluid filled porous solids and its application to overturned faulting. Bull Geol Soc Am 70:115–166
Jackson J, McKenzie D (1983) The geometrical evolution of normal fault systems. J Struct Geol 5:471–482
Keen CE, Stockmal GS, Welsink H, Quinlan G, Mudford B (1987) Deep crustal structure and evolution of the rifted margin northeast of Newfoundland: results from LITHOPROBE East. Can J Earth Sci 24:1537–1549
Kligfield R, Crespi J, Naruk S, Davis GH (1984) Displacement and strain patterns of extensional orogens. Tectonics 3:557–609
Larsen P-H (1988) Relay structures in a Lower Permian basement involved extension system, East Greenland. J Struct Geol 10:3–8
Maniatis G, Hampel A (2008) Along-strike variations of the slip direction on normal faults: insights from three-dimensional finite-element models. J Struct Geol 30:21–28. doi:10.1016/j.jsg.2007.10.002
McClay KR, Ellis PG (1987) Analogue models of extensional fault geometries. In: Coward MP, Dewey JF, Hancock PL (eds) Continental extensional tectonics, vol 28. Geological Society of London Special Publication, pp 109–125
McKenzie DP (1978) Some remarks on the development of sedimentary basins. Earth Planet Sci Lett 40:25–32
Miller EL, Gans PB, Garing J (1983) The Snake Rande decollement: an exhumed mid-Tertiary ductile-brittle transition. Tectonics 2:239–263
Murawski H (1976) Raum problem und Bewegungsablauf an listrischen Flachen, inbesondere bei Tifenstorungen. N Jahrb Geol Palaontol Monatsh 4:209
Nisbet E, Pearce JA (1973) TiO_2 as a possible guide to past oceanic spreading rates. Nature 246:468–470
Peacock DCP, Sanderson DJ (1995) Strike-slip relay ramps. J Struct Geol 17:1351–1360
Pearce JA (1975) Basalt geochemistry used to investigate past tectonic environments on Cyprus. Tectonophysics 25:41–67
Pearce JA, Cann JR (1973) Tectonic setting of basic volcanic rocks determined using trace element analyses. Earth Planet Sci Lett 19:290–300
Pearce JA, Harris NB, Tindle AG (1984) Trace element discrimination diagrams for the tectonic interpretation of granitic rocks. J Petrol 25:956–983
Philpotts AR (1978) Rift-associated igneous activity in eastern North America. In: Neumann ER, Ramberg IB (eds) Petrology and geochemistry of continental rifts. Reidel Publishing Co., Dordrecht, Holland, pp 133–154

Price NJ (1977) Aspects of gravity tectonics and the development of listric faults. J Geol Soc London 133:311–327
Proffett JM (1977) Cenozoic geology of the Yerington district, Nevada, and implications for the nature of Basin and Range faulting. Bull Geol Soc Am 88:247–266
Ramberg H (1967) Gravity, deformation and the earth's crust as studied by centrifuged models. Academic Press, New York, 241 p
Ramsay JG, Huber MI (1987) The techniques of modern structural geology, vol II. Folds and fractures. Academic Press, London, pp 309–700
Royden L, Keen CE (1980) Rifting process and thermal evolution of the continental margin of eastern Canada determined from subsidence curves. Earth Planet Sci Lett 51:343–361
Scheidegger KF (1973) Temperatures and compositions of magmas ascending along mid-ocean ridges. J Geophys Res 78:3340–3355
Seranne M, Seguret M (1987) The Devonian basins of western Norway: tectonics and kinematics of an extending crust. In: Coward MP, Dewey JF, Hancock PL (eds) Continental extensional tectonics, vol 28. Geological Society of London Special Publication, pp 537–548
Smith RB, Bruhn RL (1984) Intraplate extensional tectonics of the eastern Basin-Range: inferences on structural style from seismic reflection data, regional tectonics, and thermal mechanical models of brittle-ductile deformation. J Geophys Res 89:5733–5762
Sun S, Nesbitt RW, Sharaskin AY (1979) Geochemical characteristics of mid-ocean ridge basalts. Earth Planet Sci Lett 44:119–138
Tobisch OT (1984) Development of foliation and fold interference patterns produced by sedimentary processes. Geology 12:441–444
Vendeville B, Cobbold PR (1988) How normal faulting and sedimentation interact to produce listric fault profiles and stratigraphic wedges. J Struct Geol 10:649–659
Wernicke B (1981) Low-angle normal faults in the Basin and Range Province: Nappe tectonics in an expanding orogen. Nature 291:645–648
Wernicke B, Burchfiel BC (1982) Modes of extensional tectonics. J Struct Geol 4:105–115
Wright L (1976) Late Cenozoic fault patterns and stress fields in the Great Basin and westward displacement of the Sierra Nevada block. Geology 4:489–494

Chapter 6
Strike-Slip Fault

Abstract Stress orientation responsible for formation of strike slip fault is described along with rheological controls on development of the fault. Conjugate strike slip faults are discussed with special reference to necessity of rotation of faults with progressive deformation. Variation of displacement along the fault length and how this results in different types of fault terminations under different rheological conditions are discussed. Transpression and transtension zones occurring at curvature of strike slip faults are described. Positive and negative flower structures are illustrated. Relationship between folds and strike slip faults is discussed using natural example of the Jura mountains. Development of oblique fault ramps and significant criteria to distinguish between strike slip faults and oblique fault ramps are described.

All fractures can be broadly classified into faults and joints. A fault is marked by discontinuity of bed(s) and clear-cut displacement across the plane of fracture whereas joints do not show any visible displacement. A group of closely spaced parallel or sub-parallel faults constitute a fault zone. Displacement at depth under high temperature-pressure conditions, where the rock behaves as a ductile substance, results in shear zones. In a shear zone, beds on either side of the zone are displaced but they may not be discontinuous because of prevalent ductile condition. These are localized areas of concentration of high strains with sub-parallel walls.

6.1 Rheological Control on the Development of Faults

Based on the rheological condition of the deforming rock, the developing faults and shear zones can have different geometries as shown in Fig. 6.1. When a clear discontinuity exists across a fracture and the fracture walls are almost unstrained or brecciated, the structure is described as a brittle fault (Fig. 6.1a) (Ramsay

A. K. Dubey, *Understanding an Orogenic Belt*, Springer Geology,
DOI: 10.1007/978-3-319-05588-6_6,

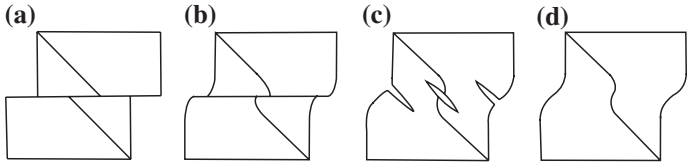

Fig. 6.1 Rheological control on development of faults and shear zones. **a** A clear-cut fault and displacement of bed under brittle condition. **b** A clear-cut fault and displacement of bed with ductile curvature in vicinity of the fault under predominant brittle and subdued ductile condition. **c** Continuous variation of deformation across a shear zone with development of extensional shear veins under predominant ductile and subdued brittle condition. **d** Continuous deformation across a shear zone resulting in ductile curvature of beds under predominant ductile condition. [From Ramsay (1980), © Elsevier. Published with permission of Elsevier]

1980). These are formed under essentially brittle condition when elastic limit of the rock is exceeded under orogenic stresses. When some ductile deformation is observed in the walls, the structure is termed as brittle-ductile fault (Fig. 6.1b). The walls may show permanent strain for a distance of up to 10 m on both sides of the fault surface. The structure is very similar to fault drag. It is possible that the brittle and ductile parts of the deformation have taken place at different times during the deformation history. The ductile-brittle shear zone may also lead to extensional openings, usually filled with fibrous crystalline material (Fig. 6.1c). The openings are generally formed at an angle of 30° to the shear zone but the angle increases with increase in deformation and the opening may also take a sigmoidal form (Ramsay and Huber 1983). In a ductile shear zone (Fig. 6.1d), deformation and differential displacement of the walls is accomplished entirely by ductile flow (i.e. no discontinuities are seen). Marker beds running across the shear zone may show change in their thickness in the zone but without any break.

6.2 Development of Strike-Slip Faults

All types of faults and shear zones can form under the above conditions including strike-slip faults. These faults differ from thrust and normal faults because the faults are vertical and displacement is predominantly horizontal, parallel to strike of the fault. The displacement is indicated by horizontal pattern of slicken lines or fibre growth on the fault surface, if not modified by a later deformation. The amount of displacement can vary from few mm to hundreds of km. Some of the large strike-slip faults are San Andreas Fault along the western coast of America; Great Glen Fault, Scotland; Anatolia Fault, Turkey; and Karakoram Fault in the Himalaya.

The essential condition for formation of these faults is orientation of maximum and minimum compression axes in horizontal direction and intermediate axis in vertical direction. The faults develop oblique to the axis of maximum and minimum

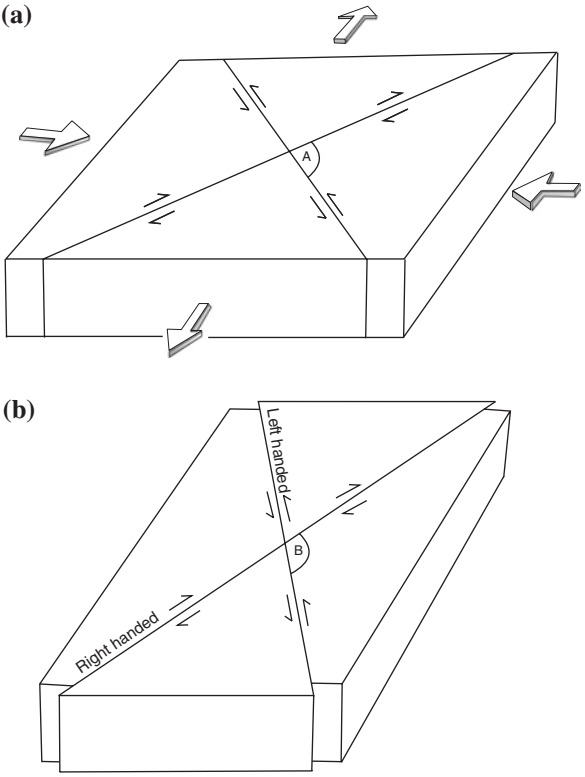

Fig. 6.2 Development of strike-slip faults. **a** A conjugate set of strike-slip faults. The *large arrows* denote the directions of compression and extension. The pattern of relative displacements (shown by *half arrows*) helps in determining the compression directions. **b** A later stage of fault development. The angle between the fault and the maximum compression direction gradually increases with progressive deformation

axes of compression (Fig. 6.2). Hence strike of the large-scale normal and thrust faults are generally parallel to orogenic belts but strike-slip faults are oblique to normal faults, thrusts and major fold structures comprising an orogenic belt. Because of this oblique nature, the strike-slip faults are also described as transcurrent faults. These faults are also described as transverse faults in the Himalaya.

The oblique orientation of the faults is explained in terms of their development along the direction of maximum shear planes (Ramsay and Huber 1983). Initial angle between the conjugate set of faults is about 60° (i.e. 30° to the axis of maximum compression). The fault planes rotate away from the axis of maximum compression with gradual increase in the angle (cf. angle A and B in Fig. 6.2). After acquiring a large angle, the faults are locked and a new set of faults develop. Hence strike-slip faults of one generation but with different orientations can occur in an area. Faults with larger angles with the axis of maximum compression are normally the early formed faults.

The strike-slip faults are basically of two types, right handed (dextral) and left handed (sinistral) (Fig. 6.2b). The terminology is based upon the relative displacement of the block opposite to an observer. When the opposite block moves towards right of the observer, the fault is right handed and if it moves towards left, the fault is left handed. Since the faults initiates in conjugate set, the sense of relative movements helps in identifying the orientation of the stress axes. When these faults form during early, and superposed deformations, the early and the later set of faults can be separated on the basis of typical relative movement patterns (Fig. 6.2).

6.3 Development of Two Sets of Faults Under Pure Shear

An alternate model (Anderson 1951) for the development of faults is based on non-rotational (pure shear) strain of a square area by two sets of faults (Fig. 6.3). However, Freund (1974) has pointed out the following difficulties with the model.

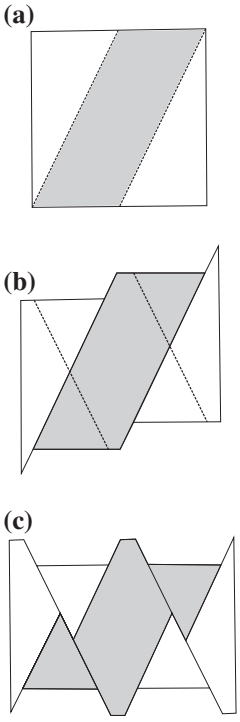

Fig. 6.3 Evolutionary stages of Anderson's (1951) geometric model of fault development by irrotational plane strain. The second set of faults at stage **b** has initiated after displacement along the first set of faults. Displacement along the second set of faults at stage **c** results in anticlockwise rotation of the upper and lower boundaries. [From Freund (1974), © Elsevier. Published with permission of Elsevier Scientific Publishing Company]

1. The faults maintain constant displacement along their lengths and as a result, the boundaries of the faulted area are disrupted. Hence there would be gaps or overlaps with the surroundings at the ends of the faults.
2. The two sets of simultaneously developing faults would interfere with one another and clear-cut displacements as shown at stage (Fig. 6.3c) are not possible.
3. The sinistral sense of fault movements would result in anticlockwise rotation of the faulted blocks whereas the dextral movement would result in clockwise rotation of the faulted blocks. This to and fro movement is difficult to sustain.

In view of the above, a more realistic model, based on differential displacement along a fault, is preferred as discussed below.

6.4 Differential Displacement Along Faults and Fault Terminations

All fractures initiate from a point and propagate by extending their lengths. Thus the maximum displacement takes place in central part of the fault and decreases gradually to zero at the terminations. The variation of displacement is accommodated at the fault tips where a number of structures can develop depending on the amount of displacement and sense of relative movements (Fig. 6.4). Transform faults are very large-scale structures that occur at plate boundaries. Termination of these faults is different from smaller strike-slip faults because the displacement does not vary along its length and the fault can terminate at ridges (ocean spreading centers) on either side (Fig. 6.4a). Hence the total displacement can be equal to the fault length. In strike-slip faults, one side of the fault termination undergoes compression whereas the other side undergoes extension. This can result in formation of smaller folds, thrusts or shear zones on one side. The other side may be characterized by formation of extensional structures like normal faults (Fig. 6.4c). On a micro-scale, stylolitic seams with solution activities can develop at the terminations (Fig. 6.4d). Fault development under predominant brittle condition leads to development of splay faults where the decrease in displacement is accommodated along a number of smaller faults (Fig. 6.4e). On the other hand if a fault develops under the brittle-ductile or ductile conditions, bending towards the receding side is formed at the terminations (Freund 1974). (Fig. 6.4f).

Extensional flow at the terminations under predominant ductile conditions can also give rise to second-order structures (Fig. 6.5) that are termed as extensional crenulation cleavage (Platt and Vissers 1980) or shear bands (White 1980). The extent of these bands reveals the extent of extensional flow in these zones.

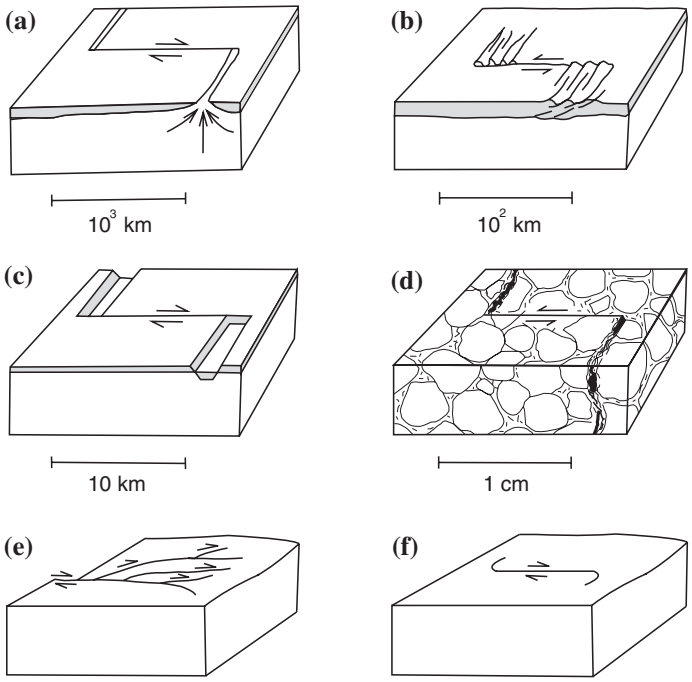

Fig. 6.4 Geological structures developed at fault terminations. **a** A large-scale transform fault (TF) terminating into ridge (R) structures. **b** Fault terminating into compressional structures. **c** Fault terminating in extensional structures. **d** Microfault terminating in stylolitic seams, from which coarse grains are removed in solution. **e** Fault termination by splay faulting. **f** Fault termination by bending towards the receding side (scale of e and f can vary from micro to map-scale). [From Hobbs et al. (1976), © B.E. Hobbs. Published with permission of B.E. Hobbs)

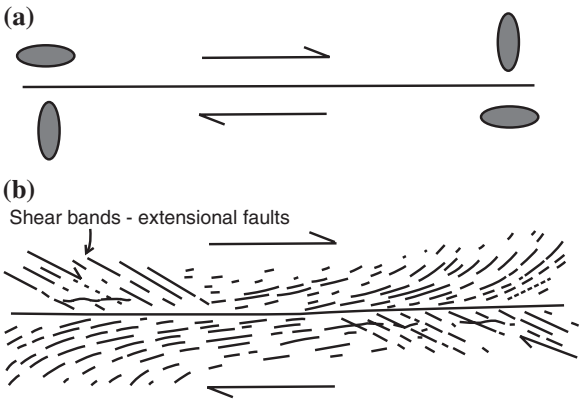

Fig. 6.5 **a** Strain patterns at fault terminations. **b** Second order shear zones or shear bands formed in zones of extensional strain at termination of ductile strike-slip shear zones. [From Coward and Potts (1983), © Elsevier. Published with permission of Elsevier]

6.5 Transpression and Transtension

Apart from curvature at the terminations, significant fault curvatures can result along their length during propagation. This can be a result of either prevalent heterogeneities or oblique linking of two simultaneously propagating faults. Depending on the nature of curvature and relative movements of the two faulted blocks, a transpression (restraining bend) or transtension (releasing bend) zone is created around the region of bending (Fig. 6.6). A transpression zone is characterized by additional compression in the zone resulting in compressional structures like folds and thrusts. In the transtension zone, the two faulted blocks move away from each other resulting in extensional structures like normal faults, veins, sag ponds, and pull-apart basins. The extension and formation of the pull-apart basin is a gradual process hence successively younger rocks (sediments) occur towards the central part of the basin.

The restraining and releasing bends can also result in formation of a flower structure (Fig. 6.7). The structure consists of a group of faults, inclined towards one another and finally terminating in a vertical fault at depth. Branching of the faults provide widening to the main strike-slip fault. The negative flower structure develops at a releasing bend which is a region of tensional stresses. A series of normal faults (mostly half graben type with listric geometry) are formed near the surface (Fig. 6.7a). The positive flower structure (Fig. 6.7b) is formed at a restraining bend under compressional stresses. A series of thrust faults are formed with listric geometry providing uplift of the near surface layers. The flower structures can be seen in seismic profiles of the Himalayan foreland foothill belt (Raiverman 2002).

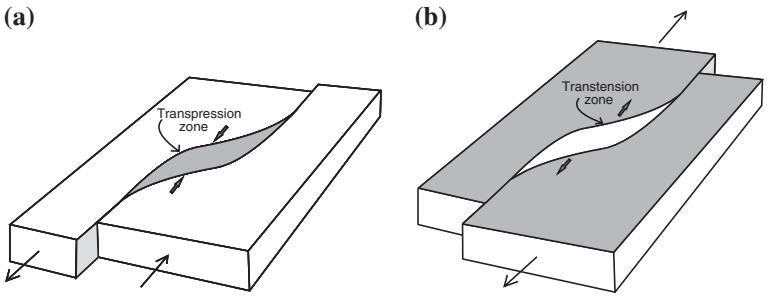

Fig. 6.6 Transpression and transtension zones at bends in strike-slip faults (after Ramsay and Huber 1987)

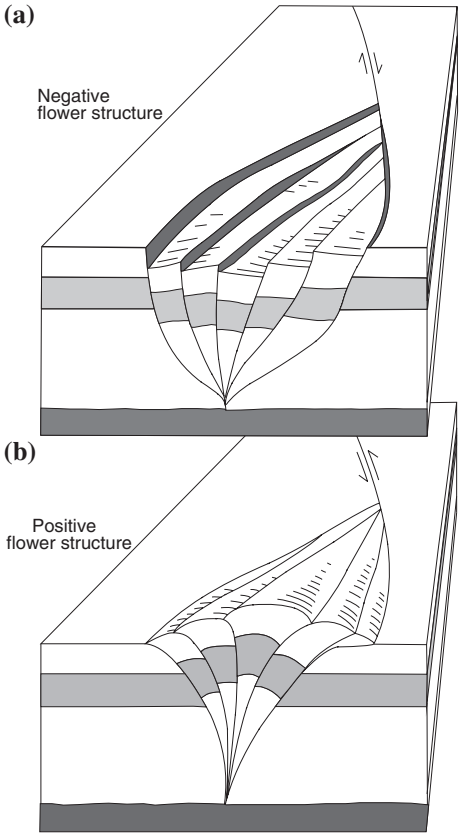

Fig. 6.7 Two kinds of flower structures associated with strike-slip faults. **a** Negative flower structure formed at releasing bend, and **b** Positive flower structure formed at restraining bend. [From H. Fossen (2010), © Cambridge University Press. Published with permission of Cambridge University Press, Cambridge.]

6.6 Relationships Between Folds and Strike-Slip Faults

One of the best associations between folds and strike-slip faults can be seen in the Jura Mountains (Fig. 6.8) (Heim 1919) between Switzerland and France. Here Mesozoic rocks have been folded and displaced by a large number of strike-slip faults. The faults are nearly vertical and many of them show horizontal slicken sides suggesting horizontal displacement. The faults have developed in a conjugate set, although one set (orientation ~N–S) is more prominent than the other (orientation ~WNW–ESE). Some of the faults are up to 48.27 km long and show a maximum displacement of ~9.65 km. The different fault displacements clearly reveal

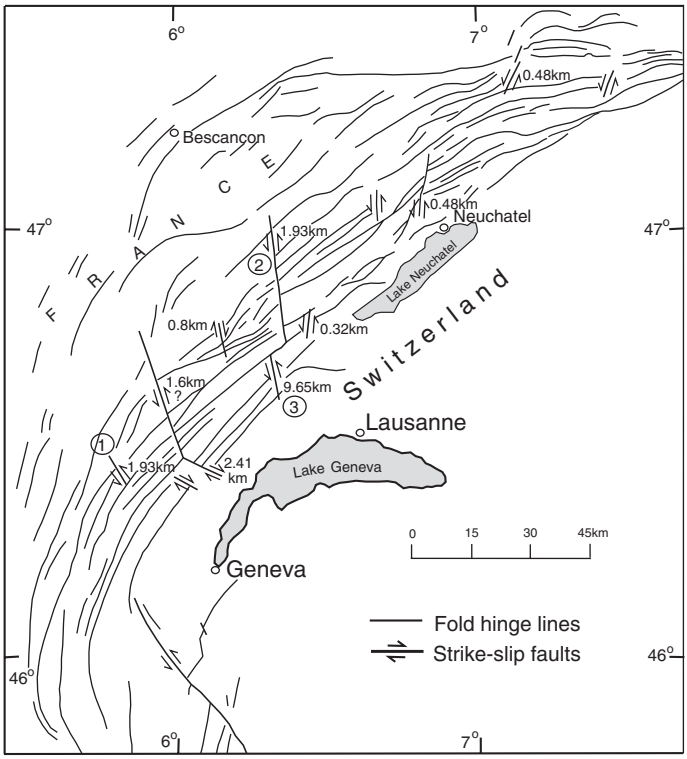

Fig. 6.8 A geological map of the Jura mountains showing arcuate fold pattern and transverse strike-slip faults. The predicted fault displacements are also marked on the map (after Heim 1919)

that there is no direct relationship between length of a fault and total displacement, e.g. Fault 1 and Fault 2 have different lengths but with the same amount of total fault displacement. On the contrary, Fault 3 is much smaller in length as compared to Fault 2 but reveals a much larger displacement. In central part of the region, strikes of the faults are oriented at an angle of ~30° to the axis of maximum compression (Fig. 6.9) but the angle increased on the two sides. The fold hinge lines are also orthogonal to the axis of maximum compression in the central part but deviates on either side of the mountain belt.

The variation in orientation of the faults and the fold hinge lines may be attributed to limited extent of the compressing piston (Fig. 6.9). The trends of fold hinge lines and faults have been used to obtain a generalized regional principal stress trajectory pattern. It is interesting to know that the picture is very close to the theoretical pattern of stress trajectories for uniform loading on surface of an elastic region (Fig. 6.10).

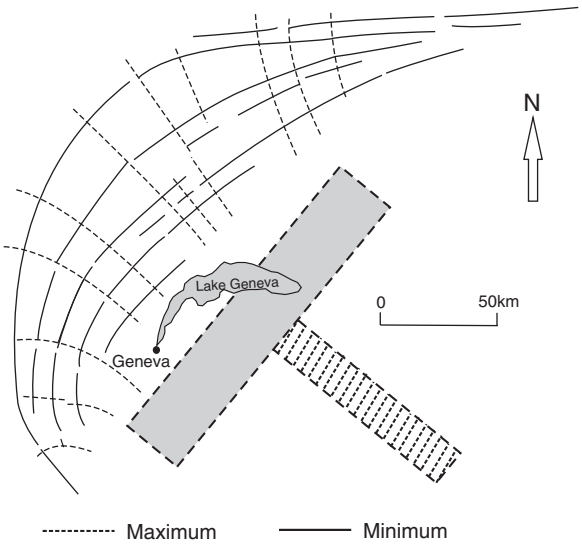

Fig. 6.9 Principal stress trajectories of the Jura system based on the trends of strike slip faults and fold hinge lines, and proposed mechanism for the formation of structural features by maximum compression from SE to NW (after Laubscher 1972)

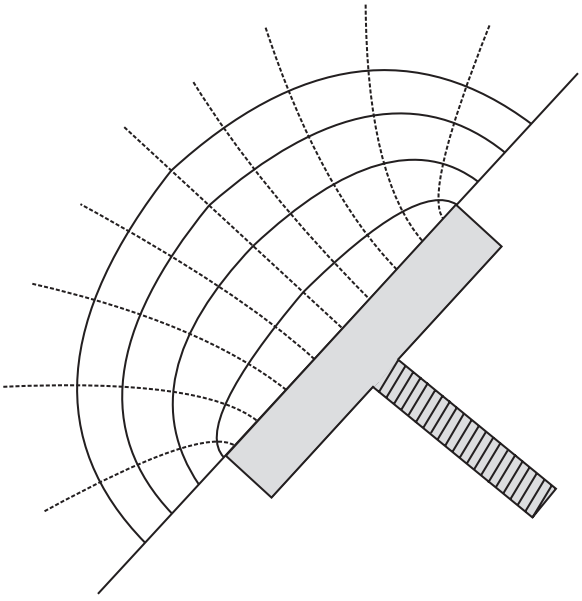

Fig. 6.10 Stress trajectories for uniform loading developed across a plane under compression (shown by *arrows*) (after Jaeger and Cook 1969)

Table 6.1 Significant criteria to distinguish between strike-slip faults and oblique fault ramps

Strike-slip fault	Oblique fault ramp
1. Faults are vertical	1. Transfer faults may be vertical but oblique ramps are inclined
2. Faults generally initiate in conjugate set	2. Conjugate set is not common. They are generally formed by linking of two faults
3. Displacement is horizontal	3. Displacement is oblique
4. The maximum displacement occurs in middle of the fault and the displacement gradually decreases towards the terminations where the displacement is nil	4. Isolated single faults follow this pattern but when they join two separate faults and transfer displacement from one to the other, the fault length and displacement appears to be the same on a geological map
5. Normally does not terminate in another type of fault	5. Normally these faults join two frontal ramps

6.7 Oblique Fault Ramp

It is sometimes difficult to differentiate between a strike-slip fault and an oblique fault ramp from a map pattern. However a careful field study can lead to their proper identification. The following criteria are of special significance (Table 6.1).

References

Anderson EM (1951) The dynamics of faulting. Oliver and Boyd, Edinburgh 206 pp
Coward MP, Potts GJ (1983) Complex strain patterns developed at the frontal and lateral tips to shear zones and thrust zones. J Struct Geol 5:383–399
Fossen H (2010) Structural geology. Cambridge University Press, Cambridge 463 pp
Freund R (1974) Kinematics of transform and transcurrent faults. Tectonophysics 21:93–134
Heim A (1919) Geologie der Schweiz. Bernhard Tauchnitz Verlag Gmbh, Stuttgart 1028 pp
Hobbs BE, Means WD, Williams PF (1976) An outline of structural geology. Wiley, New York 571 pp
Jaeger JC, Cook NGW (1969) Fundamentals of rock mechanics. Methuen & Co., London 513 pp
Laubscher HP (1972) Some overall aspects of Jura dynamics. Am J Sci 272:293–304
Platt JP, Vissers RLM (1980) Extensional structures in anisotropic rocks. J Struct Geol 2:397–410
Raiverman V (2002) Foreland sedimentation in himalayan tectonic regime: a relook at the orogenic process. Bishen Singh Mahendra Pal Singh, Dehra Dun 378 pp
Ramsay JG (1980) Shear zone geometry: a review. J Struct Geol 2:83–99. doi:10.1016/0191-8141(80)90038-3
Ramsay JG, Huber MI (1983) The techniques of modern structural geology, vol. 1: strain analysis. Academic Press, London 307 pp
Ramsay JG, Huber MI (1987) The techniques of modern structural geology, vol. II. Folds and fractures. Academic Press, London, pp 309–700
White S (1980) Large strain deformation: report on a tectonic studies group discussion meeting held at Imperial College, London. 14 November 1979. J Struct Geol 1:333–339

Chapter 7
Simultaneous Development of Folds and Faults

Abstract A large amount of information is now available on the development of folds and faults but these structures have been studied in isolation and their simultaneous development has not been studied in detail. The simultaneous development of folds and faults has been described under the following headings.

(i) Simultaneous development of folds and thrusts

- Formation of folds at an early stage of compressional phase
- Formation of folds at the null point
- Formation of folds after crossing the null point
- Thrust initiation later than folding
- Development of folds in vicinity of an arcuate thrust.

(ii) Simultaneous development of folds and strike-slip faults

- Simultaneous development of thrust and strike slip faults at different structural levels and superimposed folding as a result of boundary conditions.

(iii) Simultaneous development of folds and normal faults

- Syn-rift deformation
- Post-rift deformation.

(iv) Simultaneous development of folds and oblique fault ramps

- Interference patterns between simultaneously developing folds, frontal and oblique ramps
- Fault reactivation during superposed deformation.

Folds are formed under predominant ductile regime deep under the earth's surface. The folded rocks are gradually uplifted either by thrusting or by isostasy. During their upward migration, they shift their position from ductile to brittle–ductile regime where folds and faults can develop simultaneously. Ultimately they may be brought to the surface or closer to the surface in the predominant brittle regime where faulting is the predominant mechanism of deformation.

A. K. Dubey, *Understanding an Orogenic Belt*, Springer Geology,
DOI: 10.1007/978-3-319-05588-6_7,

The simultaneous development of folds and faults can be studied under the following headings.

(i) Simultaneous development of folds and thrusts
(ii) Simultaneous development of folds and strike-slip faults
(iii) Simultaneous development of folds and normal faults
(iv) Simultaneous development of folds and oblique fault ramps.

Out of the above four, simultaneous development of folds and thrusts is a common feature amongst many orogenic belts where deformation has taken place at comparatively upper levels of the earth's crust. At this level, it is easier for deforming layers to extend in vertical direction because of comparatively lighter load on the top thereby encouraging the formation of thrust faults.

7.1 Simultaneous Development of Folds and Thrusts

Depending on the sequence of formation of folds and thrusts, the discussion is subdivided into the following categories.

7.1.1 Fold Initiation with Reactivation of Early Normal Fault as Thrust

The mountain building activity is normally preceded by tensional phase in the region in which half grabens are formed by displacement along normal listric faults followed by deposition in the half grabens (Chap. 5). During later compressional phase of an orogeny (collision of two continental plates followed by subduction of one of the plates), these early normal faults may reactivate as thrust faults along with formation of new thrust faults. The reactivation can be studied under different categories depending on orientation of hanging wall layers prior to folding.

7.1.1.1 Formation of Folds at an Early Stage of Compressional Phase

The early normal faulting leads to tilting of the hanging wall layers towards the listric fault (i.e. layer dip opposite to dip of the fault; Fig. 7.1a) (Dubey and Bhakuni 1998). Thus orientation of layers at the onset of deformation is marked by horizontal layering in the footwall and tilted layers in the hanging wall. This leads to layer parallel compression in the footwall and layer oblique compression in the hanging wall (Fig. 7.1b). Asymmetric folds initiate in the hanging wall with axial surfaces dipping in dip direction of the thrust. The footwall folds initiate with box fold geometry. The main listric fault gradually rotates away from the axis of maximum compression (Dubey and Behzadi 1981; Kusznir et al. 1991; Coward 1996). The maximum rotation occurs in the middle part forming a sigmoidal geometry of the thrust (Fig. 7.1c). Part of the footwall layers, close to steep segment of the

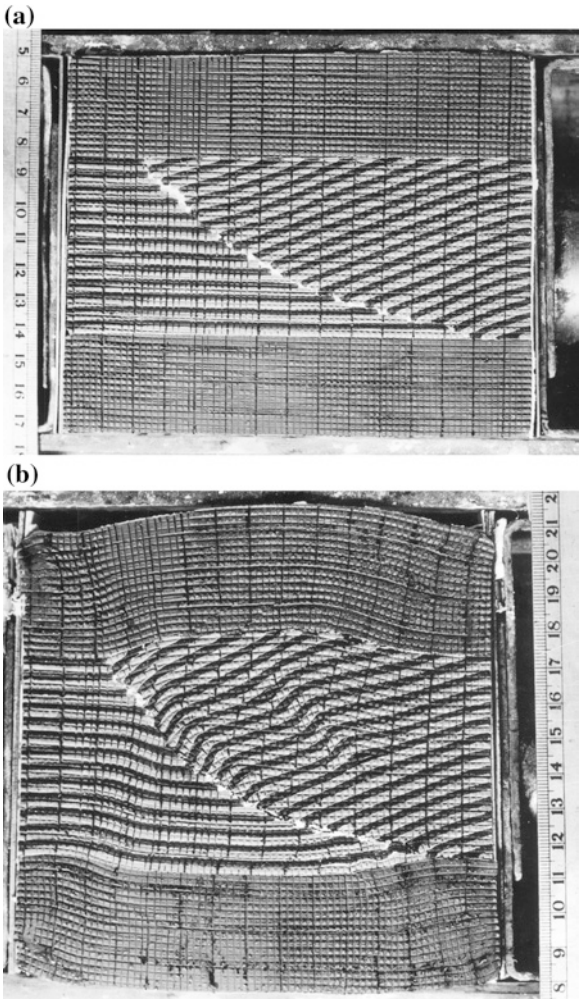

Fig. 7.1 Four stages in deformation of a multilayer model. The total model shortening is **a** 0 %, **b** 15 %, **c** 20 %, **d** 36 %. [From Dubey and Bhakuni (1998), © Elsevier. Published with permission of Elsevier]

thrust develops upright folds (Fig. 7.1d). It is to be noted that folds develop both in the hanging wall and the footwall (Ramsay 1992).

7.1.1.2 Formation of Folds at the Null Point

Null point is defined as the stage when hanging wall layers tilted during early normal faulting restores their initial disposition, in conformity with the footwall layers, during later thrusting (Fig. 7.2a). The important geometrical developments that took place during compression are as follows.

The displacement varies along the listric fault. The minimum displacement is observed in the top layer where the fault dip is steep and the maximum in lower part of the layer sequence where the dip is gentle.

Fig. 7.1 (continued)

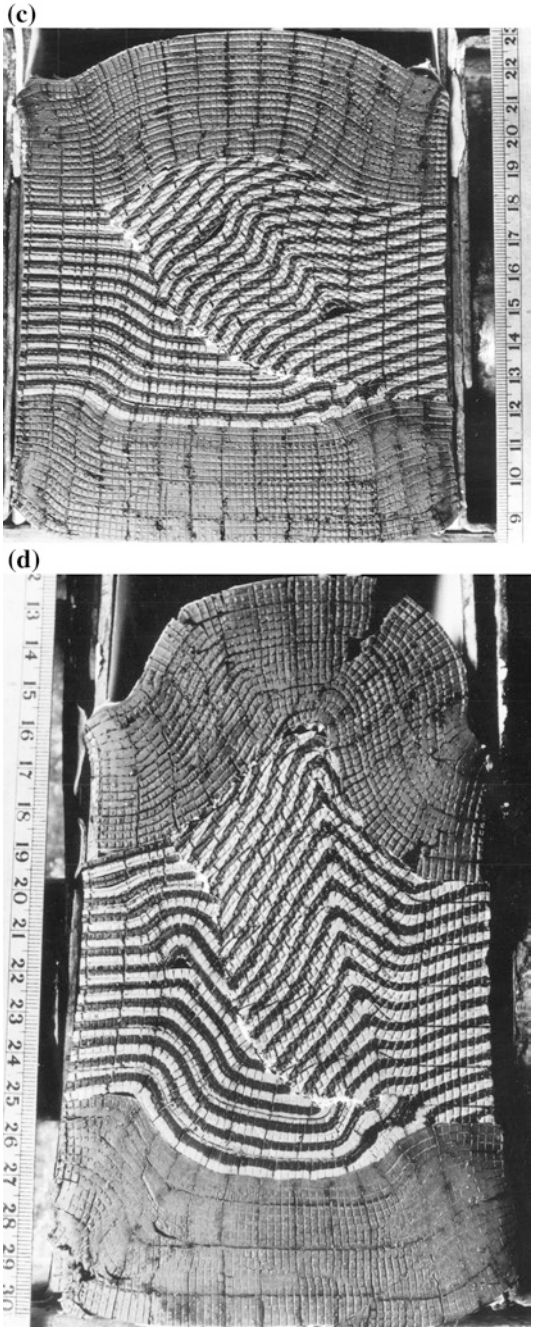

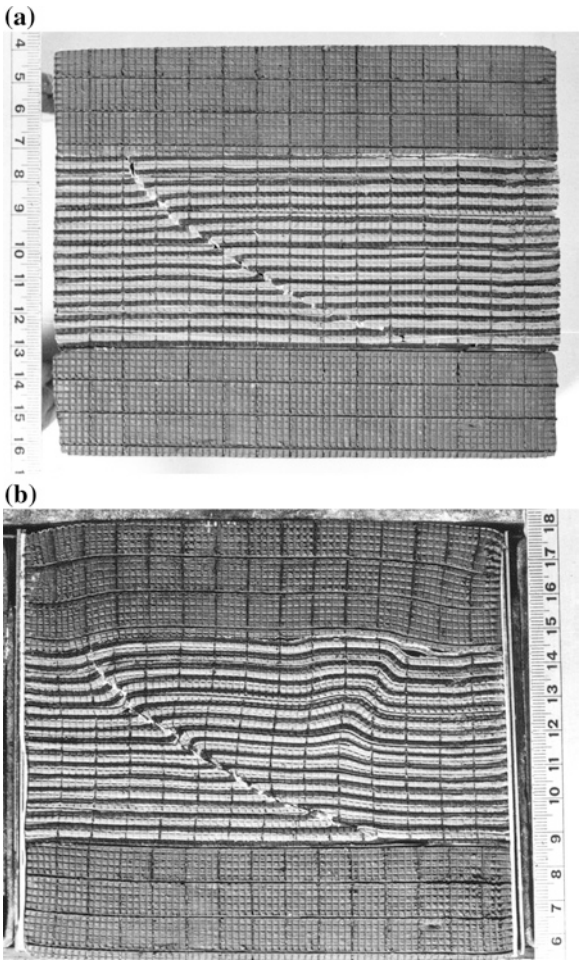

Fig. 7.2 Four stages in deformation of a multilayer model showing development of folds near a listric fault. The total model shortening is **a** 0 %, **b** 7 %, **c** 17 %, and **d** 24 %. [From Dubey and Bhakuni (1998), © Elsevier. Published with permission of Elsevier]

Asymmetric folds develop in vicinity of the thrust and symmetric folds at some horizontal distance from the thrust (Fig. 7.2b). Axial surfaces of the folds rotate with the hanging wall and after few stages of deformation, the asymmetric folds become upright and the initially upright symmetric folds modify to back folds or hanging wall vergent folds (Fig. 7.2c). Folds do not develop in lower layers of the hanging wall where the layers are characterized by reverse drag and extension along the layering (Fig. 7.2d). The features related to fold amplification, e.g. decrease in fold interlimb angles, limb thinning and hinge thickening, development of limb thrust, and fold locking at late stages of deformation are similar to multilayer folding described in Chap. 3.

The development of multilayer folds is followed by folding of the thick top and bottom slabs. Folding of the bottom slab corroborates that the thrust related deformation can be penetrative in the footwall as well.

Fig. 7.2 (continued)

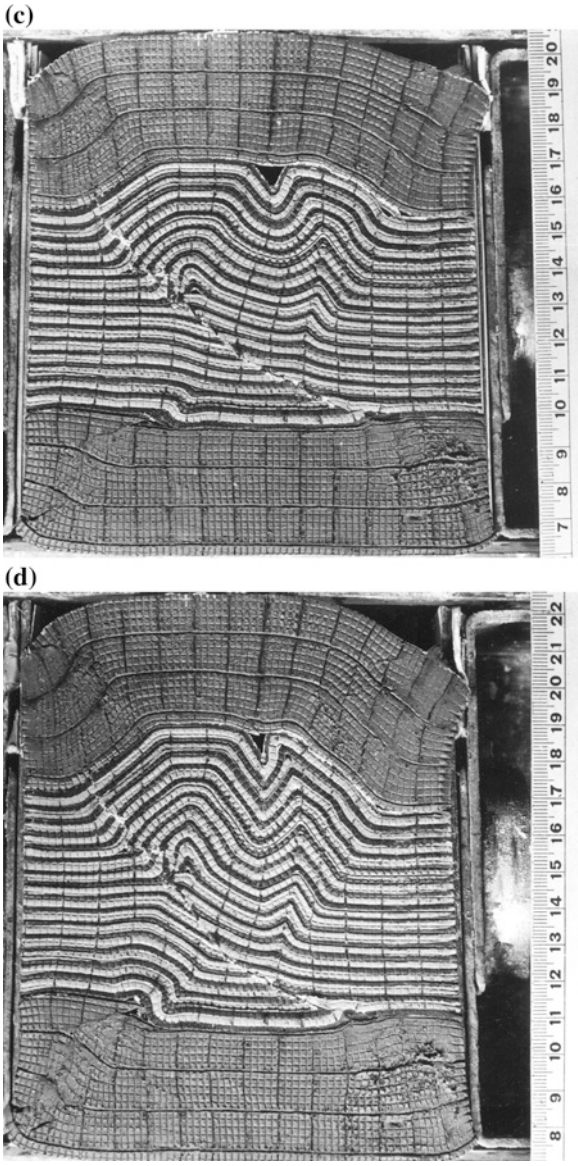

The thrust displacement varies and the minimum displacement occurs at fault termination at the upper slab. The ratio of buckle shortening to layer parallel strain also varied in the profile although all the layers were of the same competence.

The particle movement path field during progressive deformation helps in understanding the deformation pattern. The path field is determined by marking a grid pattern on the profile surface, prior to deformation. The intersection points

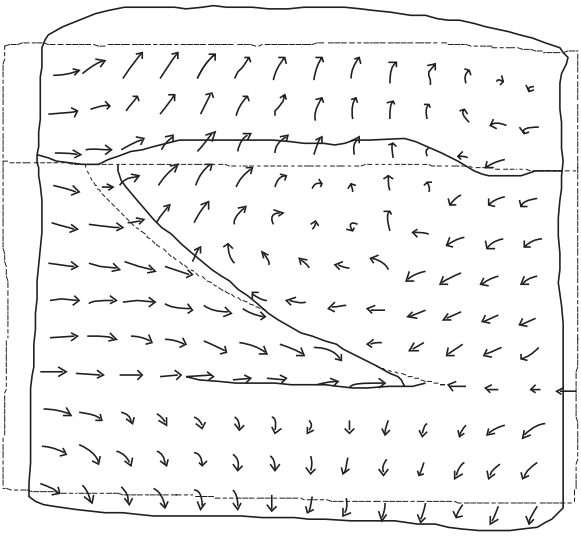

Fig. 7.3 Particle movement path field and rotation of the thrust in the experiment shown in Fig. 7.2. *Broken lines* represent initial outlines of the model and the listric fault; *continuous lines* represent configuration of the model and the thrust after 12 % shortening. [From Dubey and Bhakuni (1998), © Elsevier. Published with permission of Elsevier]

of the undeformed grid lines are marked on a tracing sheet. Later, the sheet is kept upon photographs of successive stages of deformation and new positions of the grid intersection points are marked (Cobbold 1975). The particle movement path field in the experiment (Fig. 7.2) shows a marked difference in the hanging wall and footwall deformation patterns (Fig. 7.3). In the footwall, the movement path pattern resembles to that of a pure-shear deformation (Ramsay and Huber 1983) except close to the thrust. In the hanging wall layers, the movement forms a nearly circular pattern. In the lower part, the directions are nearly parallel to the maximum compression direction whereas in the central part, close to the thrust, the directions are parallel to the thrust displacement. A sharp contrast can be observed in the upper part where prominent deflections are observed away from the thrust as a result of gradual increase in thrust dip with deformation (i.e. rotation of the thrust). A general practice is to show the relative movements across a fault by two half arrows parallel to the fault but it is evident from the diagram that the displacements are not always parallel to the fault because the relative movements are controlled by; (i) pure shear deformation, (ii) rotation of hanging wall along a listric fault, and (iii) folding of the multilayers (cf. Couples et al. 1994).

7.1.1.3 Formation of Folds After Crossing the Null Point During Thrusting

In this geometrical situation, the hanging wall layers rotate even after crossing the null point so that the layers dip in dip direction of the thrust (Fig. 7.4a). This orientation of the hanging wall layers results from good lubrication (presence of a lubricating horizon, e.g. graphite, gypsum, salt or suitable fluids) along the thrust surface and consequent easy slip.

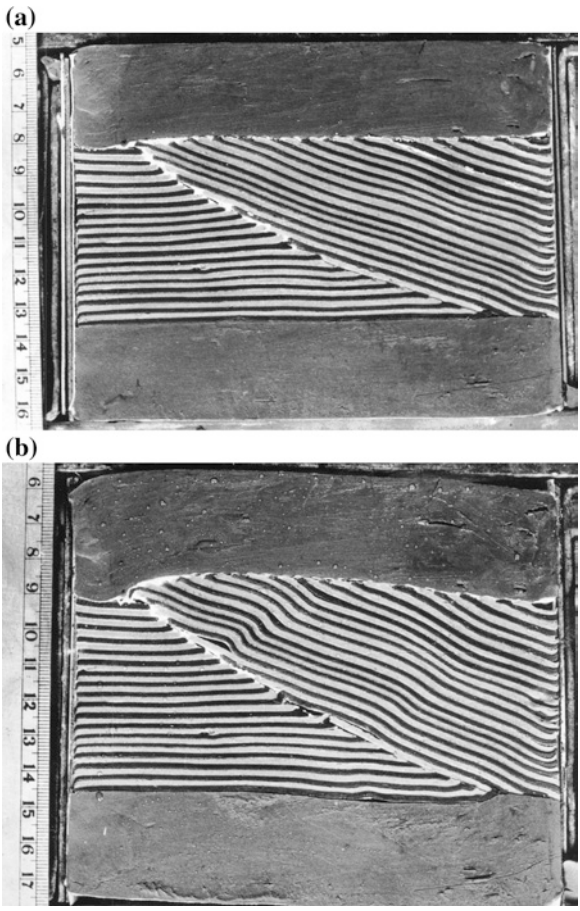

Fig. 7.4 Four stages in the deformation of a multilayer model. The total model shortening is **a** 0 %, **b** 10 %, **c** 29 %, and **d** 38 %. [From Dubey and Bhakuni (1998), © Elsevier. Published with permission of Elsevier]

Initiation of folds took place with formation of asymmetric folds in the hanging wall. Most of these are back folds (Fig. 7.4b) (cf. Cobbold et al. 1971; Mugnier et al. 1994). Hence the shear sense indicated by asymmetry of the folds is opposite to the thrust transport direction. Since the footwall layers are parallel to the axis of maximum compression, the footwall folds possess a symmetric geometry (Fig. 7.4c). At late stages of deformation, the hanging wall layers became nearly parallel to the thrust and developed extension faults (Fig. 7.4d).

The above experiments explicitly reveal that simultaneous thrusting and folding results in development of folds both in the hanging wall and the footwall although the fold initiation normally takes place early in the hanging wall where the fold magnitudes are also large. However it is to be noted that in an orogenic belt there are a series of thrust faults and footwall of one thrust is hanging wall of another thrust.

Fig. 7.4 (continued)

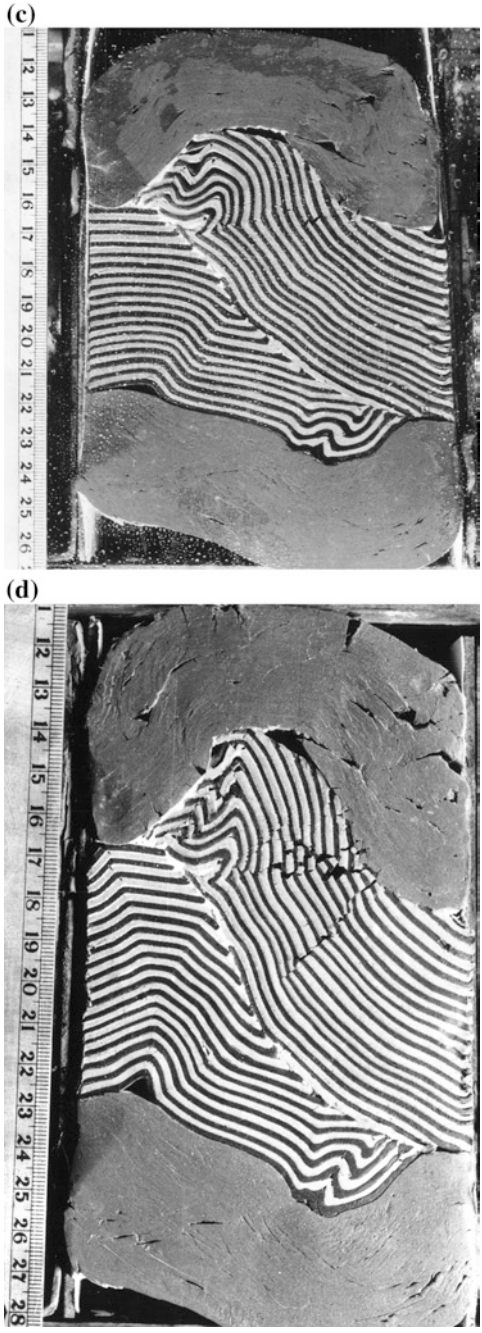

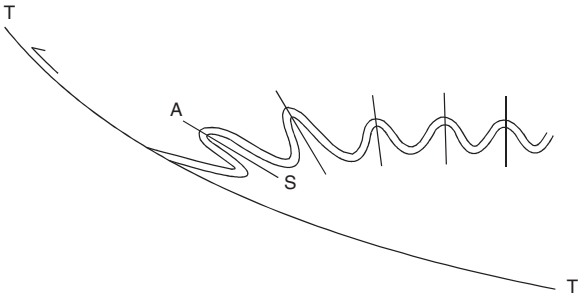

Fig. 7.5 Development of asymmetric folds in the hanging wall near the thrust and upright folds at a distance from the thrust. T–T, thrust; A–S, axial surface

The experiments also divulge that folds and thrusts develop simultaneously and they should be provided equal importance while studying the evolution of fold and thrust belts. The relative importance of the two may differ in different regions but none of these should be ignored during the analysis. It has been noticed that folding (especially small-scale folds) has been ignored by many while restoring deformed sections but this could lead to wrong interpretations. Allmendinger (1982) has also pointed out from microstructural data of the Idaho–Wyoming foreland thrust belt (USA) that most of the strain is directly related to folding and not to thrusting.

Progressive deformation results in decrease in fold interlimb angles and increase in fault dip. The rate of decrease of interlimb angle depends upon location of fold in a multilayer profile, sequence of fold initiation, distance from adjacent thrust, initial fold geometry, and amount of thrust displacement prior to initiation of folding. Rotation of fault depends upon the initial geometry of the fault. An initial gentle dip fault tends to rotate at a faster speed. With a large number of these variables, it is not possible to establish a systematic relationship between fault dip and fold interlimb angles (cf. Jamison 1987).

7.1.2 Variation of Fold Geometry with Increasing Distance from a Thrust

Figures 7.5 and 7.6 depict simultaneous development of thrust and folds. As a result of shearing along the thrust, developing folds in vicinity of the thrust are asymmetric. The asymmetry gradually decreases with increase in distance from the thrust and the folds acquire an upright geometry. Hence folds with different amounts of axial surface dip can develop during a single deformation.

The related variation in orientation of the strain ellipses is shown in Fig. 7.7. During the initial stages of deformation, the footwall strains have lower values but gradually the strain increases both in the hanging wall as well as footwall.

Fig. 7.6 An asymmetric fold at a thrust shear plane and an upright fold at some distance from the shear plane (Munsiari schist, Wangtu, Himachal Himalaya)

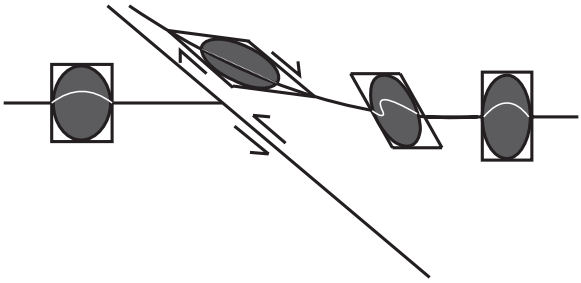

Fig. 7.7 Orientation of strain ellipses in vicinity of a thrust

7.2 Thrust Initiation Later than Folding

Compressive stress along multilayer sequence of competent and incompetent layers leads to formation of chevron folds. With variation in thickness of the layers, the thicker layers show a different rotation (i.e. rate of change of dip) as compared to the thinner layers and this results in formation of limb thrusts (thrusts across the fold limbs) or hinge collapse (bulbous hinge zone) or both (Ramsay 1974). In addition to this, late stages in development of folds are often marked by stretching of fold limbs thereby resulting in limb thinning and hinge thickening (Chap. 3). Weakening of the limbs may lead to initiation of conjugate thrusts across the fold limbs. The development of such fractures has been demonstrated by using a simple multilayer Plasticine model (Fig. 7.8).

The above experiment shows that an essential condition for formation of thrust faults is plane strain deformation with no extension parallel to fold hinge lines of the developing folds. In model experiments, where fold surfaces were allowed to extend parallel to the hinge, the resulting structures were second order folds (Chap. 3), and strike-slip faults. Extension of fold hinges can also be obstructed by presence of oblique fault ramps or transfer faults as shown in Fig. 7.9. A positive listric fault in the basement is shown in Fig. 7.9a. The fault is bounded by a

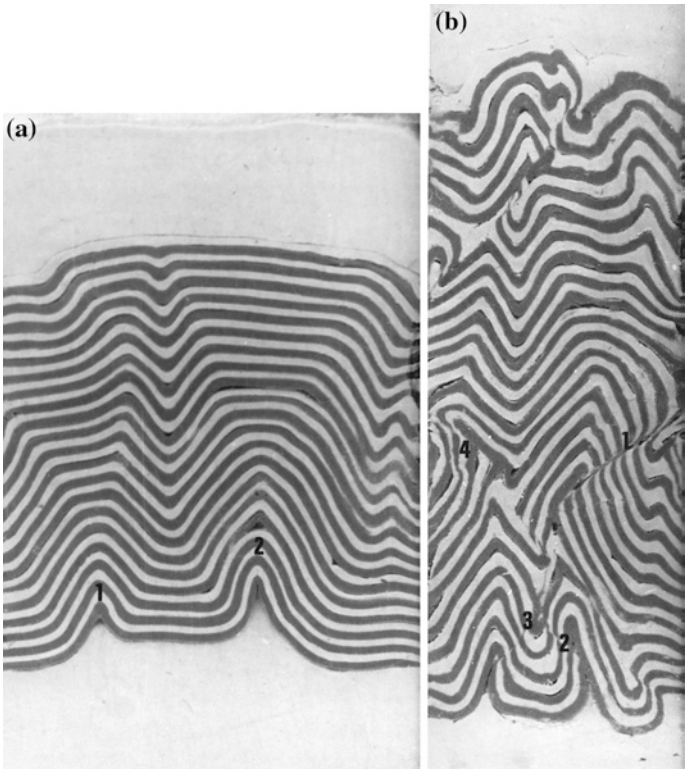

Fig. 7.8 Two stages in deformation of a multilayer Plasticine model. **a** Development of folds after 42 % shortening. Folds *1* and *2* have developed independently from separate irregularities. **b** Simultaneous development of folds and conjugate set of thrust faults (*1*, *2*, *3*, *4*) at 69 % shortening (after Dubey and Behzadi 1981)

transfer fault (TF) at the front face, and by an oblique ramp (OR) at the back face. An overlying undeformed layer is shown in gray. Thrusting along the listric fault results in development of an asymmetric fault propagation fold above the thrust and upright buckle folds at some distance from the thrust (Fig. 7.9b). The fold hinge lines are parallel to strike of the thrust. The progressive deformation results in rotation of the fault surface. The thrust locks at a steep dip and the folds also acquire rotation hardening at low interlimb angles (Fig. 7.9c). The locked fault tends to extend parallel to its strike. The fold surfaces also extend parallel to the hinge lines resulting in formation of a conjugate set of strike-slip faults. However the horizontal extension is restricted by the boundary condition imposed by the transfer fault and the oblique ramp. The restrain at the two ends results in curvature of the fold hinge lines and formation of folds whose hinge lines are parallel to the axis of maximum compression. These folds are likely to be described as superposed folds though they have formed because of the boundary conditions

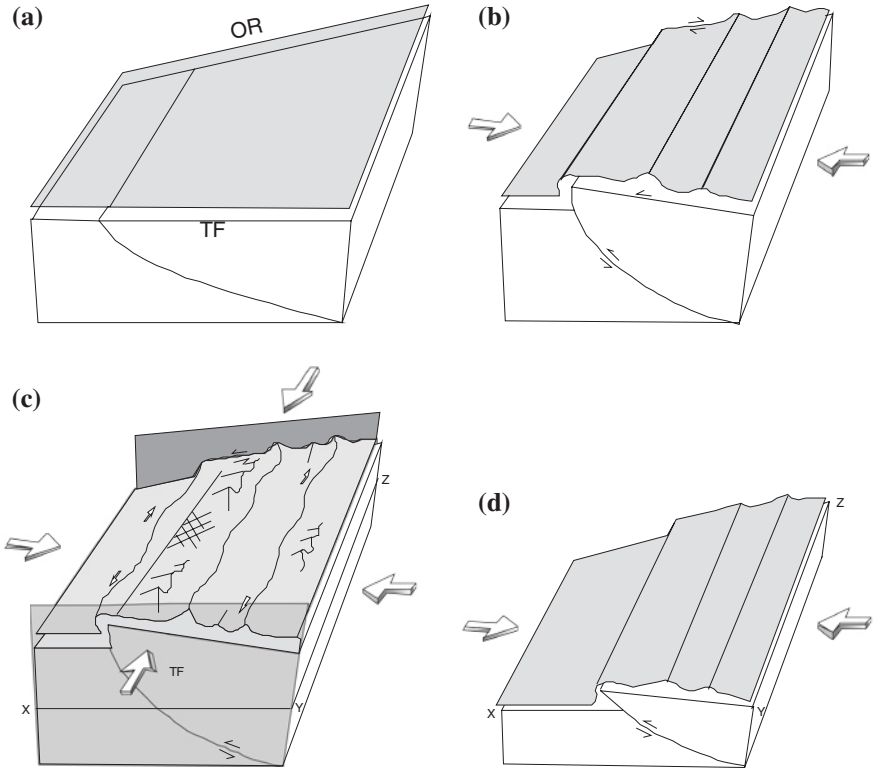

Fig. 7.9 Simultaneous development of cross folds, thrust and strike-slip faults at different structural levels. **a** A positive listric fault in the basement bounded by an oblique ramp (*OR*) and a transfer fault (*TF*) at the back and front faces, respectively. An overlying undeformed layer is shown in gray **b** Thrusting along the basement fault and folding of the cover layer. The oblique ramp and the transfer fault show a component of horizontal displacement as well. **c** Locking of the folds and thrust at late stages of deformation, extension of the fold surfaces parallel to hinge lines and extension of the hanging wall parallel to strike of the thrust leading to formation of a conjugate set of strike-slip faults. Obstruction in the extension as a result of barriers provided by the oblique ramp and the transfer fault thereby resulting in curvature of the fold hinge lines, and initiation of cross folds. The curvature of the fold hinge lines along with the cross folds give an impression as if the maximum compression direction is parallel to the early fold hinge lines. **d** Structures at depth along the x–y section shown in **c**. Because of gentler dip of the thrust, the strike-slip faults and cross folds have not developed at this depth

in the same phase of deformation. At the lower structural levels, the thrust with listric geometry does not lock because of gentle dips. Hence the later cross folds remain absent at the lower levels as shown in Fig. 7.9d. In the Himalaya, these cross folds trend N–S to NE–SW, i.e. nearly orthogonal to the early fold hinge lines and parallel to the axis of maximum compression imposed by movement of the Indian plate.

Fig. 7.10 A strike-slip fault marked by discontinuity of structures (Bude Bay, North Cornwall, England)

7.3 Simultaneous Development of Folds and Strike-Slip Faults

Simultaneous development of folds and strike-slip faults can be identified by different fold geometries or lack of complete correspondence in fold geometries on two sides of the fault. An excellent example of this kind is from the folded and faulted sedimentary strata at Bude, North Cornwall, England (Fig. 7.10). Structural map of the area shows that the fold sequence is cut by a prominent strike-slip fault. The fault shows a curvature in its trend (Fig. 7.11). Since the anticlinal fold hinge zones have been removed by erosion and the synclinal hinge zones are not exposed, it is not possible to observe the cross-sectional fold profile shapes. However, the two approximate cross-sections, prepared on each side of the fault, differ noticeably (Fig. 7.12). Some of the folds on one side of the fault appear to have counterparts on the other side and a few folds terminate at the fault. The lack of complete correspondence in fold geometry on either side of the fault suggests that folding and faulting were simultaneous.

Evolutionary stages in the development of such structures, using a deformed Plasticine model, are shown in Fig. 7.13. The initial multilayer consisted of ten layers of Standard Plasticine. The central layer was embossed by an orthogonal grid pattern for subsequent study of surface strains and for measuring displacements along possible faults. The model was enclosed in a matrix of Special Soft Plasticine. It was deformed under the plane strain boundary condition in which the maximum compression direction was parallel to the initial horizontal layering and the principal extension direction was also in this plane. However, the compression was applied from one side of the model and it resulted in some inhomogeneous deformation, which later became apparent from boundaries of the model and the deformed grid pattern.

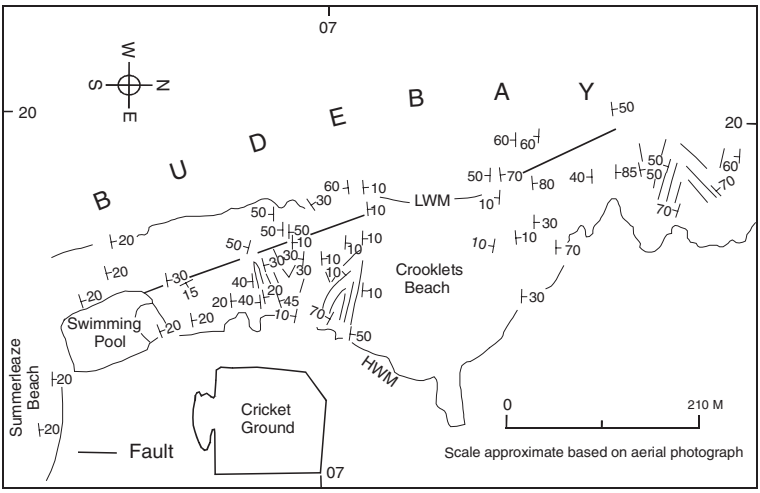

Fig. 7.11 A geological sketch map of the Bude Bay. [From Dubey (1980), © Elsevier. Published with permission of Elsevier]

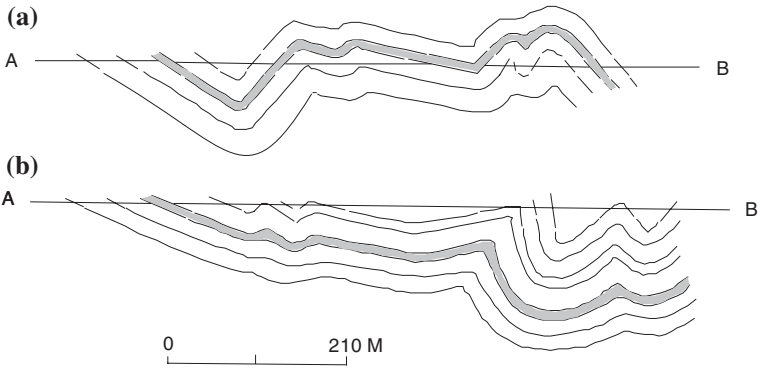

Fig. 7.12 Dissimilar cross-sections on two sides of the strike slip fault shown in Fig. 7.11. **a** Cross-section on west side of the fault. **b** Cross-section on east side of the fault. [From Dubey (1980), © Elsevier. Published with permission of Elsevier]

At the start of the deformation, noncylindrical folds initiated, amplified and interfered in the usual manner (Chap. 3) (Fig. 7.13a). After 20 % overall shortening, a number of strike-slip faults appeared on the layer surface. The faults initiated in conjugate set and the number increased with increase in shortening. Each fault propagated by increasing its length and displacement (Fig. 7.13b, c, d). The model was compressed up to 42 % shortening. The deformed layer surface revealed the following.

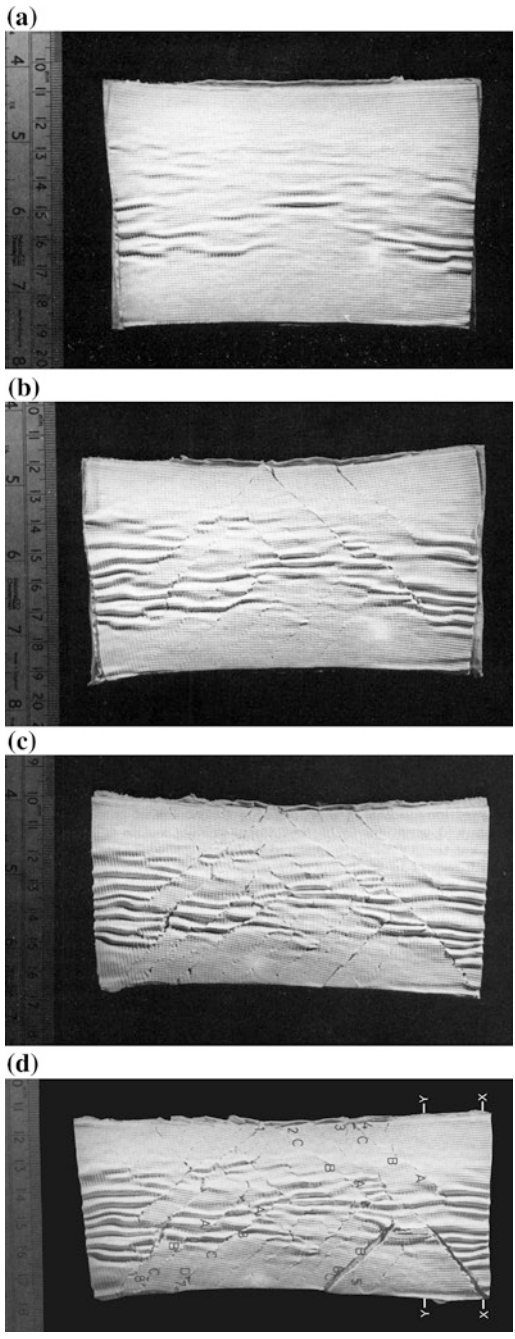

Fig. 7.13 Progressive deformation of a Plasticine model showing appearance of an internal layer surface. The one sided compression was applied from top side of the photographs. **a** 20 %, **b** 25 %, **c** 30 %, **d** 42 % overall shortening. [From Dubey (1980), © Elsevier. Published with permission of Elsevier]

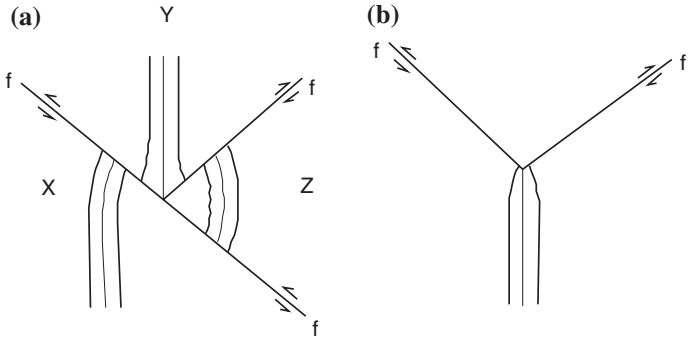

Fig. 7.14 Curvature of fold hinge lines in vicinity of strike-slip faults (*f*). The *continuous* and *broken lines* represent antiformal and synformal hinge lines. [From Dubey (1980), © Elsevier. Published with permission of Elsevier]

Initiation of the faults led to division of the layer surface into several independent segments in which the development of structures was different.

With the appearance of new faults and extension of early faults, additional fold curvatures were observed as a result of fold-fault interference as shown in Fig. 7.14. Folds in zone X (Fig. 7.14a) showed curved hinges near the fault due to shear whereas similar effects in zone Z produced arcuate folds. Zone Y is situated between a conjugate set of faults where in addition to fold hinge curvatures, the fold profile of the central syncline was modified by increase in interlimb angle. In another situation, noncylindrical folds terminated at the junction of two fault planes with decrease in fold interlimb angle at the termination (Fig. 7.14b).

Fold structures on either side of the faults were different (Fig. 7.15). Some of the folds, developed during early stages of deformation, can be traced on other side of the fault but the other folds have no direct counterpart across a fault plane. Fault displacement varied along the fault length. The maximum displacement was observed in central part of the faults with gradual decrease toward the terminations. The total fault displacement did not exceed 17 % of the fault length.

Initial angle between the conjugate fault sets was difficult to observe because fracturing could be seen only after completion of one stage of deformation when the model was taken out of the press and the internal deformed layer was exposed. The fractures were observed to be initiated at angles of 35°–45° to the principal compression direction. The angle increased with increase in shortening though the rate of increase was different for different faults (Fig. 7.16). The increase is in conformity with a theoretical model, obtained by deforming a homogeneous block under plane strain condition, with an initial fracture oriented at an angle of 30° to the maximum compression direction (Fig. 7.16). After 42 % overall shortening it was no longer possible to reassemble the multilayers and subject them to further deformation. Hence the later stages of fault rotation could not be observed.

The faults initiated sequentially with progressive deformation, some faults being younger than the others. The process was accompanied by rotation and

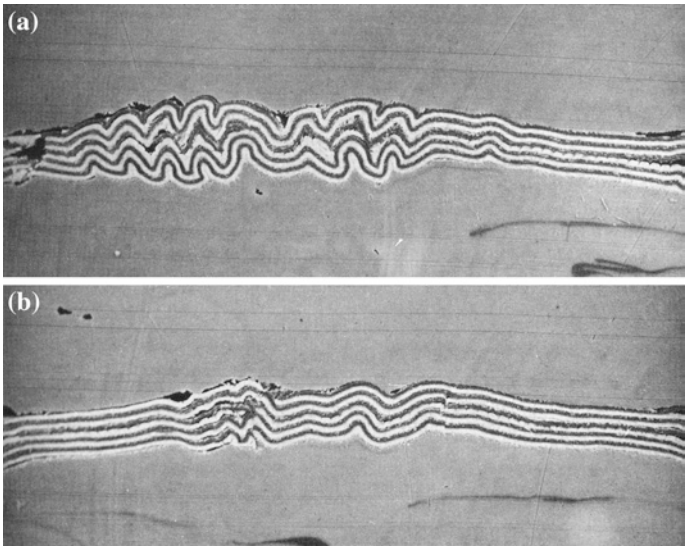

Fig. 7.15 Two cross-sections across the deformed model shown in Fig. 7.13. The different structures are the result of fold terminations at fault planes. **a** Cross-sectional fold profile along the section X–X. **b** Cross-sectional fold profile along the section Y–Y. [From Dubey (1980), © Elsevier. Published with permission of Elsevier]

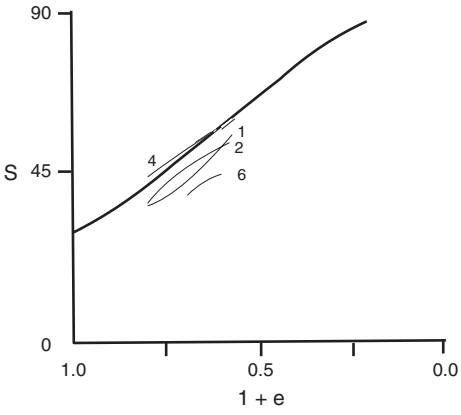

Fig. 7.16 Change in angle (*S*) between fault and principal compression direction with change in total model shortening (1 + e). The fault locations are shown on Fig. 7.13d. *The thick long line* illustrates the theoretical relationship (initial angle 30°) (after Dubey 1980)

linear propagation of the faults. Hence most of the larger length faults were older than the smaller length faults. This tempts to infer that the larger faults display a larger rotation. However the relationship between fault length and rotation (Fig. 7.17) shows that some faults did not follow this predicted behavior. It was observed that faults which did not cross-cut folds showed larger rotation than faults of nearly the same length but which cross cut folds. This suggests that fold formation makes rotation of faults less necessary for compatibility of displacement

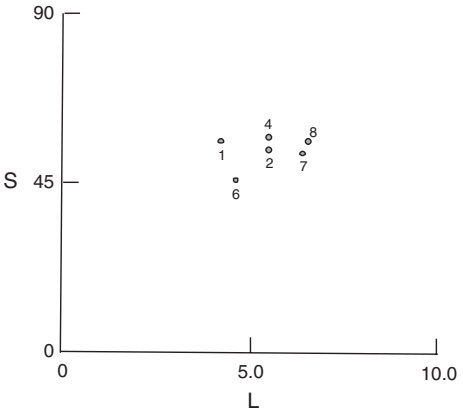

Fig. 7.17 Relationship between length of fault (*L*) and angle (*S*) between fault and principal compression direction. The locations of faults are shown on Fig. 7.13d. [From Dubey (1980), © Elsevier. Published with permission of Elsevier]

strain. This statement is supported by the fact that the fold hinge lines did not rotate with the same amount as the faults.

A general pattern of relationship between total model strain (1 + e) and displacement (D) is shown in Fig. 7.18. Increase in displacement with shortening along each fault was measured at different points marked as A, B, and C (also D at Fault 7) (Fig. 7.13d). The early stages of deformation are marked by development of folds. However when the fold amplification drops, the fault displacement becomes prominent. The fault locks after the total displacement reaches a value of ~17 % of the total fault length and then the displacement shifts to another fault or a new fracture forms. The general pattern remains similar though individual faults may occupy different places on the shortening—displacement graph. The faults terminated by bending towards the receding side.

7.4 Determination of Fault Displacement by Using a Fold Hinge Line

A method used to determine displacement along a fault is to identify a fold hinge line on either side of the fault (Hobbs et al. 1976, p. 307). The method can provide satisfactory results provided the fault has originated later than the fold. In geological situations where the two structures have developed concomitantly it could lead to incorrect estimation because the same fold hinge line may not exist on other side of the fault and the offset may be a result of oblique linking of folds. For example, Fig. 7.19a displays oblique linking of two fold complexes having the same wavelength. After initiation of faulting, they may be positioned so that true fault displacement cannot be measured by extending the general trend of the fold hinge lines. An observer might also deduce a wrong sense of movement along a fault if the region of oblique linking is wrongly attributed to fault drag. Another situation of oblique linking (left lateral or sinistral oblique linking) is shown in Fig. 7.19b where the estimated displacement will be more than the real value.

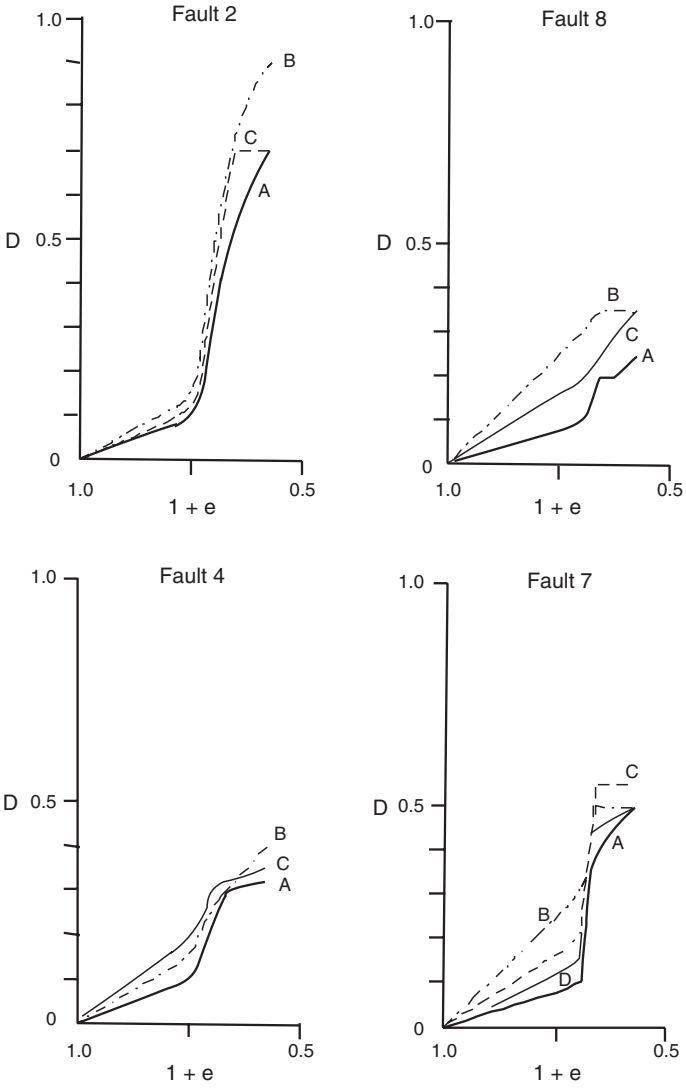

Fig. 7.18 Variation in fault displacement (D) with variation in total model shortening ($1 + e$). The locations of measurements are shown on Fig. 7.13d. [From Dubey (1980), © Elsevier. Published with permission of Elsevier]

When two fold complexes show fold bifurcation and steeply plunging termination, and the region of fold interference is cut by a fault then obviously the method cannot be used to deduce fault displacement.

Different fold structures on either side of a fault have also been reported from the Irish Variscan fold belt by Bamford and Ford (1990).

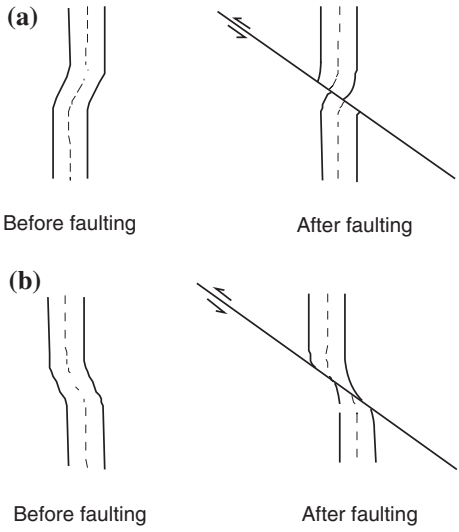

Fig. 7.19 Fault offsets of oblique linked folds where true displacement on faults cannot be determined by tracing the fold hinge lines. **a** Right lateral oblique linking. **b** Left-lateral oblique linking. [From Dubey (1980), © Elsevier. Published with permission of Elsevier]

7.5 Simultaneous Development of Folds and Normal Faults

Folds are contractional structures that develop in compressional regimes whereas normal faults develop in extensional regimes. Hence their simultaneous development appears to be contrary. However the simultaneous development of these structures takes place under certain special conditions as described below.

7.5.1 Normal Faults in Vicinity of a Thrust

Displacement along a thrust leads to curvature of hanging wall layers in its vicinity. Increase in the curvature may bring the layers to zone 3 of the strain ellipse (Ramsay 1967) thereby resulting in stretching of the layers and formation of normal faults. Normal faults can also develop in the overturned limb of a large fold nappe (Chap. 3).

7.5.2 Normal Faults During a Rift Phase

Tensional regime during a rift phase results in listric normal faulting and formation of half grabens, followed by deposition of sediments (Fig. 7.20a). Increase in rotation of the hanging wall block leads to tilting of the hanging wall layers and increase in layer dips. Gravity gliding ensues at steep layer dips resulting in formation of penecontemporaneous (primary) folds (Fig. 7.20b). These folds initiate as symmetric folds but modifies to asymmetric folds with increase in shear (cf. Fig. 5.22).

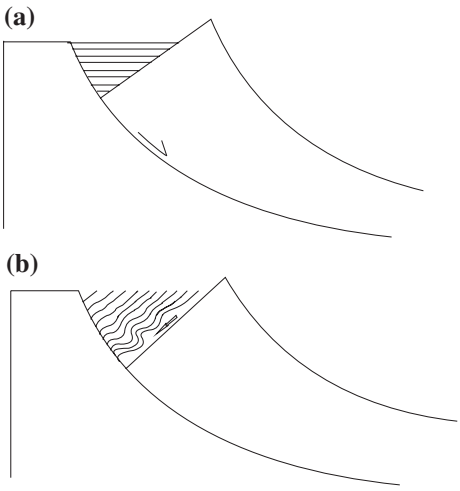

Fig. 7.20 Formation of penecontemporaneous folds during rifting. **a** Normal faulting in the basement, tilting of the hanging wall block and deposition of cover rocks in the half graben. **b** Gravity gliding along steeper slopes at the basement-cover interface and formation of folds

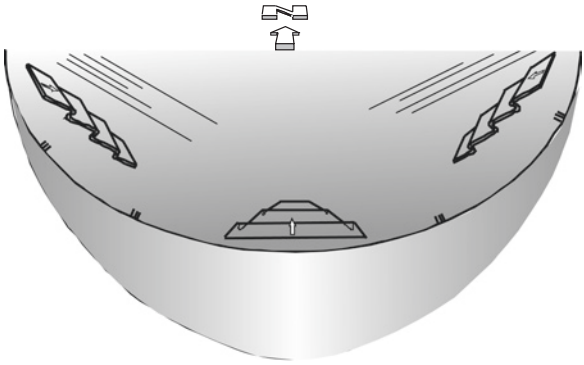

Fig. 7.21 An arcuate normal fault showing orientation of fold hinge lines at different locations. N, north direction

Orientation of the slope varies in an arcuate rift basin (e.g. the Himalaya) resulting in different orientations of primary folds along the basin. Such folds in the Himalaya are likely to be oriented in NW–SE to NE–SW directions from west to east, respectively (Fig. 7.21).

7.6 Simultaneous Development of Folds and Oblique Ramps

The above discussion was restricted to linear or arcuate strike of faults. However variations from this systematic geometry have also been observed. For example, Fig. 7.22a shows a thrust fault where orientation of the fault is normal to the axis, oblique to the axis, and parallel to the axis. The geometry of the fault is

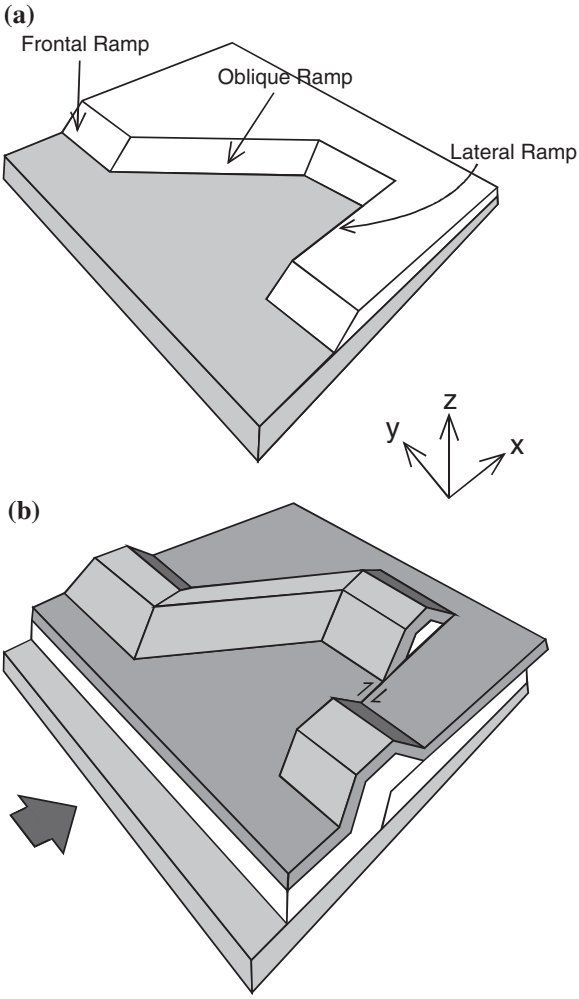

Fig. 7.22 Different types of fault ramp geometries. **a** Frontal, oblique, and lateral ramp geometries in the basement. **b** A simplified view of hanging wall folds in the cover rock assuming plane strain and a rigid footwall. x, axis of maximum shortening in horizontal direction; y, intermediate axis in horizontal direction; z, extension direction along the vertical axis. *Half arrows* indicate strike-slip displacement. The *black arrow* denotes the compression direction. [From Apotria (1995), © Elsevier. Published with permission of Elsevier Scientific Publishing Company]

also reflected in the geometry and orientations of folds developing in the cover rocks (Fig. 7.22b). When strike of a fault is normal to the axis of maximum compression, it is called as frontal ramp; when oblique to the axis with a gentle dip, oblique ramp; and when parallel to the axis, lateral ramp. The lateral ramp is characterized by a component of strike-slip displacement. When dip of an oblique ramp is near vertical, the fault is also called as transfer fault. The features are common in both thrust and normal faults. Fault curvatures are also observed in strike-slip faults but these curvatures result in transpressional and transtensional zones (Chap. 6). The oblique ramp shows oblique slip displacement. However it is to be noted that the frontal fault ramps can also show an oblique slip displacement along a frontal ramp as a result of fault propagation (Fig. 5.5a). At the centre

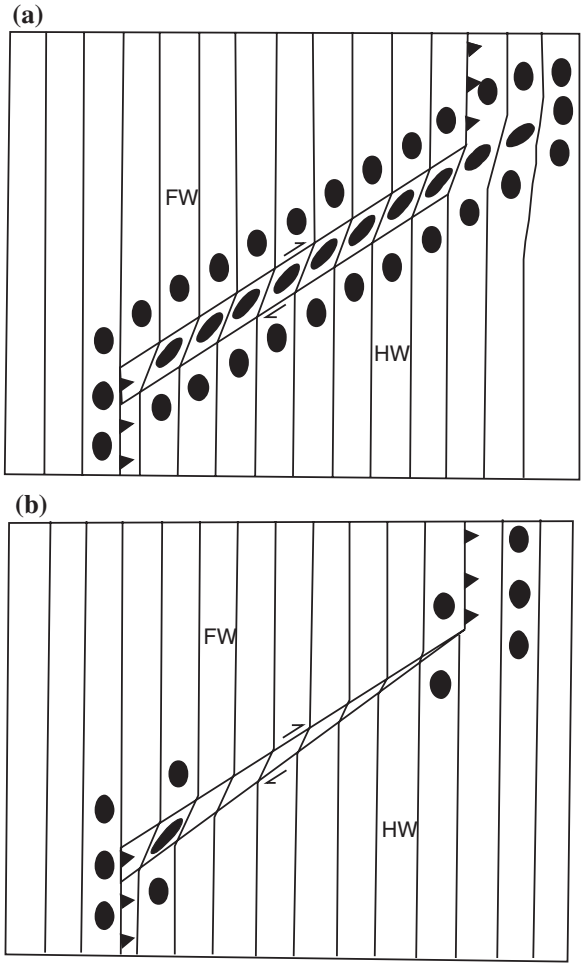

Fig. 7.23 Shear zones in vicinity of an oblique ramp and associated strains. **a** Shear zone with parallel walls. **b** Shear zone with walls tapering toward the trailing fault ramp. *HW* hanging wall, *FW* footwall. [From Dubey (1997), © American Geophysical Union. Published with permission of American Geophysical Union]

of the fault (location of fault initiation), the displacement is pure dip-slip but it becomes oblique towards the fault tip (fault termination). The oblique-slip gradually increases towards the termination (direction of fault propagation).

An oblique ramp can also act as a shear zone between two frontal fault ramps (cf. Ramsay and Allison 1979). The shear zone walls may be parallel (Fig. 7.23a) or taper towards one of the frontal ramps (Fig. 7.23b). Geometry of the shear zone controls orientation of developing fold hinge lines. When walls of a shear zone are parallel, noncylindrical folds demonstrate a uniform curvature opposite to the tectonic transport direction (normal drag but generally no fold counterpart on the other side of the fault) along the zone. With tapering shear zone walls, the fold curvature adjacent to the oblique ramp varies with maximum curvature near the junction of the transfer fault and the frontal ramp (Fig. 7.24) (or trailing ramp, if the width is maximum at the trailing ramp). The curvature is best seen in folds, which initiate near the boundary of the model and gradually propagate towards an active shear zone.

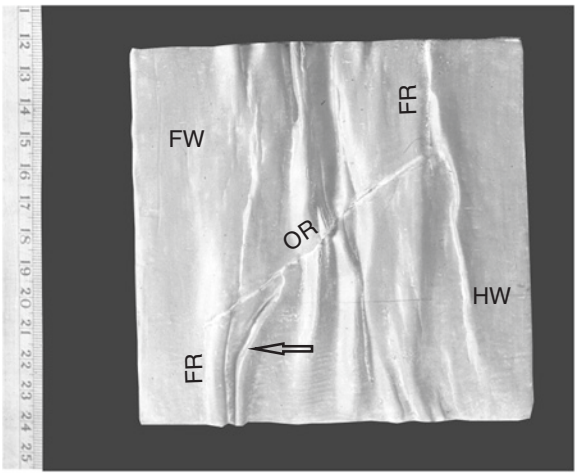

Fig. 7.24 Simultaneous development of thrusting and folding in a modeling clay multilayer model deformed under plane strain boundary condition (after 19 % shortening). *HW* hanging wall, *FW* footwall, *FR* frontal ramp, *OR* oblique ramp. The noncylindrical fold shown by an *arrow* displays a prominent curvature of hinge line as it approaches the oblique ramp. [From Dubey (1997), © American Geophysical Union. Published with permission of American Geophysical Union]

7.7 Interference Between Simultaneously Developing Folds, Frontal and Oblique Fault Ramps

A variety of fold hinge line curvatures can occur around an oblique ramp. Figure 7.25a, shows fold curvatures during an early deformation. The effect of oblique ramp is not visible away from the ramp and fold hinge lines are linear and parallel to the frontal ramp (Fig. 7.25a, fold a). A propagating noncylindrical fold shows a curvature towards the tectonic transport direction while approaching an oblique ramp (Fig. 7.25a, fold b). An opposite fold curvature will form at the junction of oblique and frontal ramps (Fig. 7.25a, fold d) as a result of shear strain inside the shear zone (cf. Figure 7.24). In the footwall region, fold curvatures towards the thrust transport direction form as a result of; (i) normal drag along an oblique ramp (fold e), and (ii) oblique ramp shear zone (fold f). Noncylindrical fold propagation towards an oblique ramp produces curvature opposite to the regional thrust transport direction (fold h). At late stages of deformation, a greater rotation of the ramp in the middle part forms a restraining bend resulting in extra curvature of the adjacent fold hinge lines both in the hanging wall and the footwall (Fig. 7.25a, folds c, and g). When an oblique ramp makes an angle of 70° or greater with the axis of maximum compression, fold hinge lines develop parallel to the trend of the oblique ramp but only in its vicinity (Fig. 7.26).

During early history of superposed deformation, the interference pattern is marked by orthogonal linking of the early and superposed folds (Chap. 3).

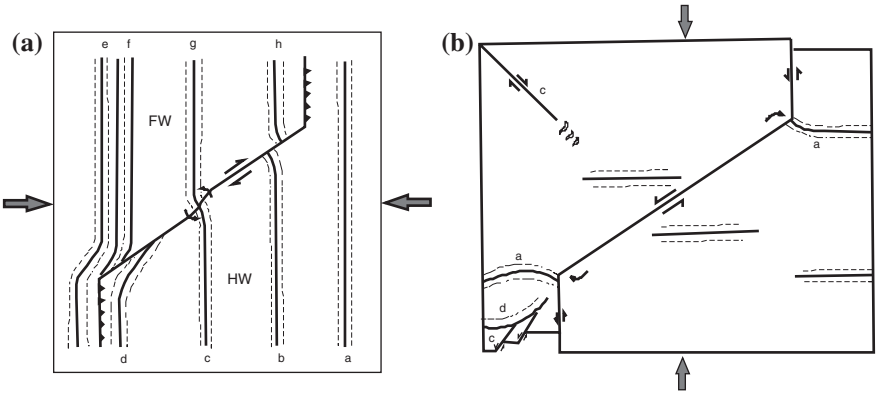

Fig. 7.25 Fold interference patterns produced by simultaneous development of noncylindrical folds, frontal and oblique fault ramps. *Thick arrows* represent the axis of maximum compression. The *continuous* and *broken lines* represent antiformal and synformal hinge lines, respectively. **a** Early deformation. **b** Superposed deformation. *HW* hanging wall, *FW* footwall. [From Dubey (1997), © American Geophysical Union. Published with permission of American Geophysical Union]

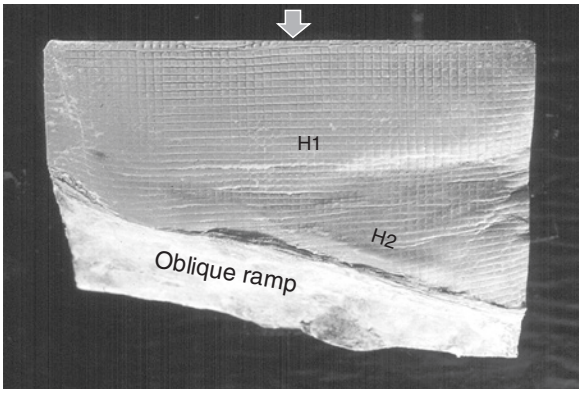

Fig. 7.26 A deformed modeling clay footwall layer (49 % shortening) showing two orientations of fold hinge lines. The *top arrow* denotes the axis of maximum compression. *H1* fold hinge normal to the compression direction, *H2* fold hinge oblique to the maximum compression direction, parallel to the trend of the oblique ramp (after Dubey 1999)

Additional fold curvatures result from interference between propagating noncylindrical folds and oblique ramp (Fig. 7.25b, fold a). A number of parallel strike-slip faults develop at late stages of superposed deformation (Fig. 7.25b, location c). Displacement along these faults can also result in curvature of adjacent noncylindrical folds (Fig. 7.25b, fold d). Folds 'd' and 'a' have opposite sense of curvature because of interference with different faults (cf. Fig. 7.27).

7.8 Fault Reactivation During Superposed Deformation

A change in direction of maximum compression (during superposed deformation) results in reversal of fault displacement along an oblique ramp and predominant strike-slip displacement along frontal ramps (Fig. 7.28). In sharp contrast to the

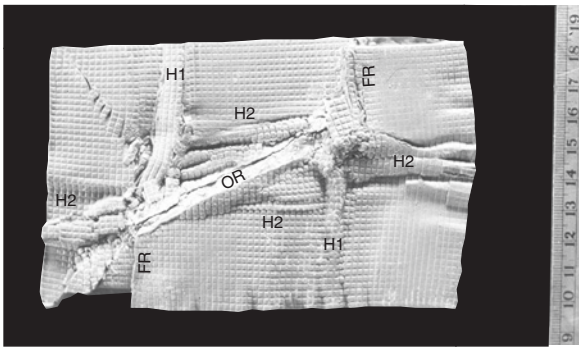

Fig. 7.27 A deformed modeling clay layer after 18 % shortening during the early deformation and 19 % during the superposed deformation (after Dubey 1999). *FR* frontal thrust ramp, *OR* oblique thrust ramp, *H1* Early fold hinge, *H2* Superposed fold hinge

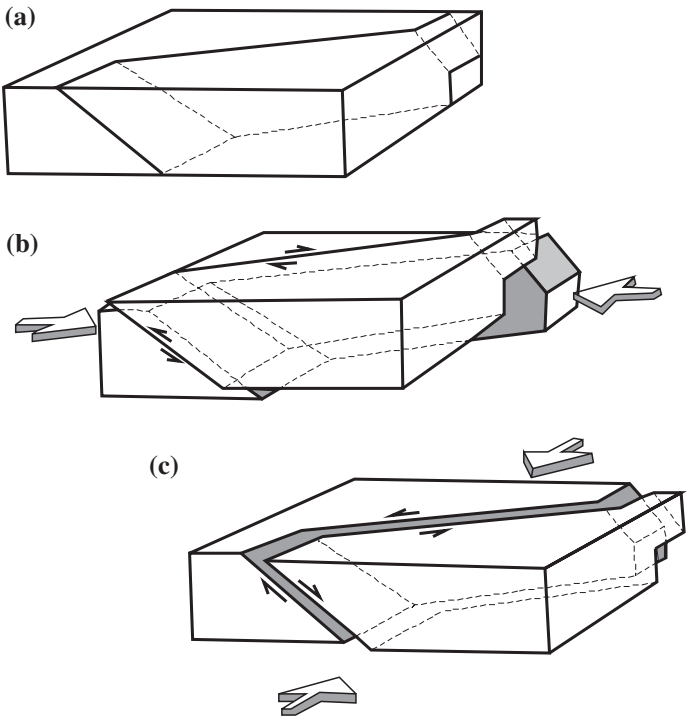

Fig. 7.28 Reversal of fault displacement and normal faulting during superposed deformation. **a** Initial configuration of a fault showing frontal ramp and oblique ramp geometries. **b** Thrusting along the fault during a compressional regime. The *thick arrows* represent the maximum compression direction. The oblique ramp has a horizontal and a vertical component of displacement. **c** A change in the direction of maximum compression during superposed deformation. Since the frontal ramps have a gentle dip, reversal of displacement along the oblique ramp results in normal fault displacement along the frontal ramps. [From Dubey (1997), © American Geophysical Union. Published with permission of American Geophysical Union]

geometry of strike-slip faults, the frontal ramp part of the fault has a gentle dip. The gentle dip results in normal faulting along the frontal ramp as a consequence of right lateral displacement along the oblique ramp. However this kind of normal faulting takes place only in vicinity of an oblique ramp. At some distance from an oblique ramp, the superposed deformation is likely to result in strike-slip displacement and folding of the frontal ramp.

References

Allmendinger RW (1982) Analysis of micro-structures in the Meade Plate of the Idaho-Wyoming foreland thrust belt, USA. Tectonophysics 85:221–251

Apotria TG (1995) Thrust sheet rotation and out-of-plane strain associated with oblique ramps: an example from the Wyoming salient, USA. J Struct Geol 17:647–662

Bamford MLF, Ford M (1990) Flexural shear in a periclinal fold from the Irish Variscides. J Struct Geol 12:59–67

Cobbold PR (1975) Fold propagation in single embedded layers. Tectonophysics 27:333–351

Cobbold PR, Cosgrove JW, Summers JM (1971) Development of internal structures in deformed anisotropic rocks. Tectonophysics 12:23–53

Couples GD, Stearns DW, Handin JW (1994) Kinematics of experimental forced folds and their relevance to cross-section balancing. Tectonophysics 233:113–123

Coward MP (1996) Balancing sections through inverted basins. In: Buchanan PG, Nieuwland DA (eds) Modern developments in structural interpretation, validation and modelling. Spec Publ Geol Soc London 99:51–77

Dubey AK (1980) Model experiments showing simultaneous development of folds and transcurrent faults. Tectonophysics 65:69–84

Dubey AK (1997) Simultaneous development of noncylindrical folds, frontal ramps and transfer faults in a compressional regime: experimental investigations of Himalayan examples. Tectonics 16:336–346

Dubey AK (1999) Oblique thrust ramps in the Himalaya: a study based on model experiments. Gondwana Research Group Memoir 6, Gondwana Research Group, Japan, pp 39–49

Dubey AK, Behzadi H (1981) Development of flexural slip folds, overlapping boudins and extension faults in multilayered materials: field evidence and experimental model. J Geol Soc India 22:274–284

Dubey AK, Bhakuni SS (1998) Hangingwall bed rotation and the development of contractional and extensional structures around a thrust fault: geometric and experimental models. J Struct Geol 20:517–527

Hobbs BE, Means WD, Williams PF (1976) An outline of structural geology. Wiley, New York, pp 571

Jamison WR (1987) Geometric analysis of fold development in overthrust terranes. J Struct Geol 9:207–219

Kusznir NJ, Marsden G, Egan SS (1991) A flexural-cantilever simple-shear pure-shear model of continental lithosphere extension: applications to the Jeanne d'Arc Basin, Grand Banks and Viking Graben, North Sea. In: Roberts AM, Yielding G, Freeman B (eds) The geometry of normal faults. Spec Publ Geol Soc London 56:41–60

Mugnier JL, Mascle G, Faucher T (1994) The structures of the frontal thrust belt of Himalaya (Siwaliks of western Nepal). Himalayan Geol 15:245–261

Ramsay JG (1967) Folding and fracturing of rocks. McGraw Hill, New York, pp 568

Ramsay JG (1974) Development of chevron folds. Bull Geol Soc Am 85:1741–1754

Ramsay JG (1992) Some geometric problems of ramp-flat thrust models. In: McClay KR (ed) Thrust tectonics. Chapman & Hall, London, pp 191–200

Ramsay JG, Allison I (1979) Structural analysis of shear zones in an Alpinised Hercynian granit, Maggia Lappen, Pennine Zone, Central Alps, Schweiz. Mineral Petrogr Mitt 59:251–279
Ramsay JG, Huber MI (1983) The Techniques of modern structural geology, vol 1, strain analysis. Academic Press, USA. pp 307

Chapter 8
Global Positioning System

Abstract Global positioning system is now generally used during field investigations for obtaining precise locations but more importantly it has been employed to determine the plate movements. The results are used for determining the strain build-up in an area and seismic predictions. However, the inferences are based upon surface observations whereas geological structures require study in three-dimensions. Velocity vectors are determined using a few fixed points. However, it is not possible to find fix points on the surface of the moving plates. Hence the velocity vectors can change their magnitude and direction with change in location of the fix points, leading to incorrect conclusions. Hence extra precautions are required when fix points are selected on moving surfaces. Some of these precautions are discussed in the light of an experiment where a physical model was deformed under controlled boundary conditions. Importance of location of GPS stations in an active orogenic belt, like the Himalaya, is emphasized where all the three types of faults (i.e. thrust, normal, strike slip) are developing simultaneously.

Global positioning system (GPS) is a useful device, which is commonly used to obtain precise location on land, at sea or in the air. This is comparatively a new technology as the first GPS satellite was launched in February 1978. This has an advantage over the land based navigation systems because the GPS signals are available to users 24 h a day in all weather conditions (unaffected by cloud or rain) and perhaps most importantly there are no user charges. This is resistant to jamming and is capable of providing simultaneous service to an unlimited number of users. It works on the latest atomic clock, which can deviate by only one second in 3 million years. The only essential condition is access to open air where it is possible to receive satellite signals. Hence it cannot be used inside buildings, under thick forests, or in tunnels. It is widely employed for general aviation, for navigation and for road vehicles to find out a short cut to destination. The obtained locations are precise with an accuracy of within a centimeter. Hence it is widely used by earth scientists to mark the locations where field data have been collected or a particular rock type or structure of geological importance is exposed.

A. K. Dubey, *Understanding an Orogenic Belt*, Springer Geology,
DOI: 10.1007/978-3-319-05588-6_8,

The GPS signals are sent by 24 satellites positioned 20,200 km above the earth in six different orbital paths. Each satellite is travelling in a 12 h circular orbit so that at least six are available nearly 100 % of time from any point on the earth. The signals are received by GPS receivers to detect, decode and process. With a minimum of three satellites, the receiver can determine a latitude–longitude position. However with the availability of four or more satellites it is possible to determine an approximate altitude as well.

8.1 Possible Sources of Error

Despite several advantages and applications of the GPS technique, care has to be taken for the following points, which may introduce error in the result.

1. The technique was originally designed and developed for military applications. In order to keep a safeguard against its reaching in wrong hands, some error, known as Selective Availability (SA), is deliberately introduced in the GPS position. Initially, the introduced error was of the order of 100 m.
2. For a better triangulation to obtain accuracy, it is essential that the receiver is placed so that the satellites are positioned in different directions (i.e. North, South, East and West of the receiver).
3. An ideal position for a receiver is a plane area, outside a vehicle, and away from tall buildings, Any obstruction to the GPS signal by buildings or by rock cliffs in mountainous and valley areas may introduce errors. However, a GPS receiver can indicate if the signal of a given satellite is being obstructed.
4. Another source of error is multipath, caused by reflection of the signal from an object (e.g. building or terrain) before reaching the GPS receiver. Since the signal has not taken a straight path, the additional time taken during the reflection can add to the error by an amount of ~5 m.
5. Radio signals travel at the speed of light in the outer space in a homogeneous medium. This homogeneity is disturbed by plasma, which are electrically charged particles distributed inhomogeneously in the ionosphere. If there are pockets (bubbles) of plasma particles in the ionosphere, they may affect the GPS signals because of local heterogeneity.

However, the good news is that with improving technology, the extent of these errors is gradually diminishing.

Despite the above limitations, GPS has provided useful data for interpreting plate movements and deformation at plate boundaries. Though the individual plates are regarded as rigid, all parts of the plates do not move with the same speed and in the same direction. Different GPS stations, located in different parts of a plate, provide velocity vectors at each site. These velocity vectors not only help in understanding the movement patterns at the plate boundaries but also inside the plate. The velocity vectors are similar to particle movement path field used in structural geology. The best method to obtain the particle movement path fields, is

experiments with physical models in laboratory. Hence a brief description of this method is given here for a better understanding of results normally obtained by the GPS technique.

8.2 Experiments with Physical Models

Physical models with known initial geometries can be deformed under controlled boundary conditions to understand the evolutionary processes of several geological structures. One of the useful parameters, which is obtained by the experiments, is deduction of particle movement path fields. These movement paths have led to understanding of a number of important geological processes, e.g. initiation, amplification and propagation of folds in a single layer, multilayers, and simultaneous development of folds and thrusts (Chaps. 3 and 7).

The paths are determined using a sequence of photographs of an experiment where an initial model surface (layer surface or cross-sectional multilayer profile) is embossed by a grid pattern to monitor the movements of the grid points (intersection points of the grid lines) with reference to a fixed point/points outside the deforming model. It has been observed in these experiments that displacement paths can take a circuitous route during progressive deformation. Hence a pattern obtained by using two widely spaced stages of deformation may lead to misleading information. The method is similar to obtaining the velocity fields using the GPS studies but it provides an advantage that the path fields are obtained for entire evolution of the observed structures. In contrast, conclusions are drawn in the GPS studies by keeping a fix point inside the body (e.g. Bangalore, Delhi, Dehradun for movement of the Indian plate) and the displacement paths are observed over an extremely short duration of time as compared to development of natural structures. Despite this limitation, results of the GPS studies have been employed for long term estimations of India-Asia convergence rate, crustal shortening rates in the Himalaya and in the Indian shield, splaying of the Himalayan mass through strike-slip faulting along the Karakoram Fault, prediction of seismic activity etc. (e.g. Bilham et al. 2001; Banerjee and Burgmann 2002). An experiment is described here to further elaborate on this point.

8.3 Experiment

An experiment was performed by deforming a modeling clay model. Initial dimensions of the model were 15 × 12 × 7 cm and a fault with frontal and oblique ramp geometries was induced in the model prior to its deformation (Fig. 8.1a). Dip of the frontal ramp was 30°. A 2 mm grid pattern was embossed on the top model surface and every fifth grid line was marked by black ink. The model was compressed normal to the model boundaries. Three fix points were

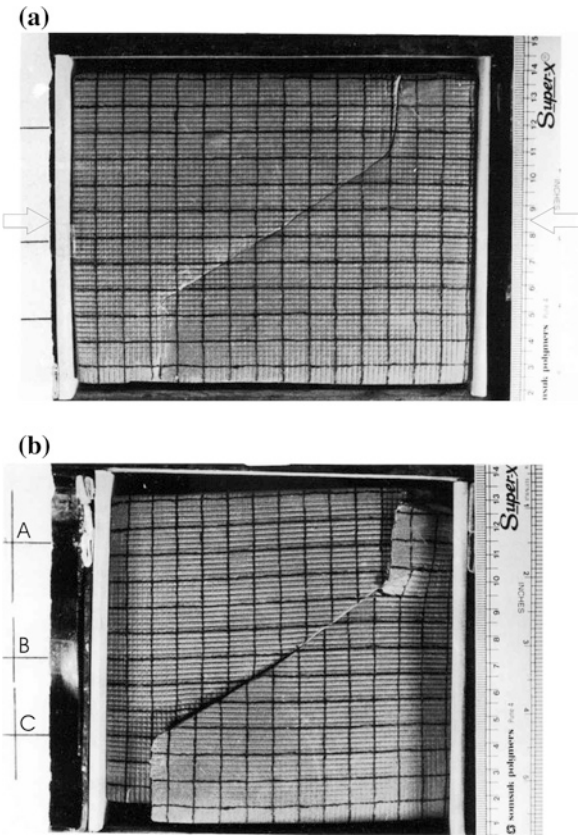

Fig. 8.1 Two stages in deformation of a modeling clay model. *Arrows* indicate the axis of maximum compression. The total model shortenings are 0 % (**a**), and 9 % (**b**). The displacement paths were determined using intersection points of the *black grid lines* with respect to three fix points (A, B, C) marked on the top Perspex plate. These points were outside the model and remained stationary throughout the deformation (Dubey 2005)

marked on top retaining Perspex plate. Since these points were outside the deforming model, they remained unaffected by the deformation process.

The outset of deformation led to displacement along the fault, observed by displacement of the grid lines. The deformed model, after 9 % shortening, is shown in Fig. 8.1b. Displacement of the grid points with reference to the three fix points (A, B, C) is shown in Fig. 8.2a. The footwall points are displaced parallel to the direction of maximum compression with nearly equal magnitudes. The direction of movement varies in vicinity of the trailing frontal ramp as a result of displacement out of the tectonic transport plane (Apotria et al. 1991; Dubey 1997), i.e. a component of strike-slip parallel to trend of the frontal ramp. This displacement was more pronounced in the hanging wall and it showed a gradual increase towards the leading frontal ramp. Rotation of the oblique ramp, along the vertical axis, away from the axis of maximum compression was also observed. Under the influence of displacement out of the tectonic transport plane and rotation of the oblique ramp, the movement paths were not parallel to strike of the oblique ramp. The pattern of deformation differed from the ideal pure-shear strain deformation (Ramsay and Huber 1983) because of presence of the oblique ramp.

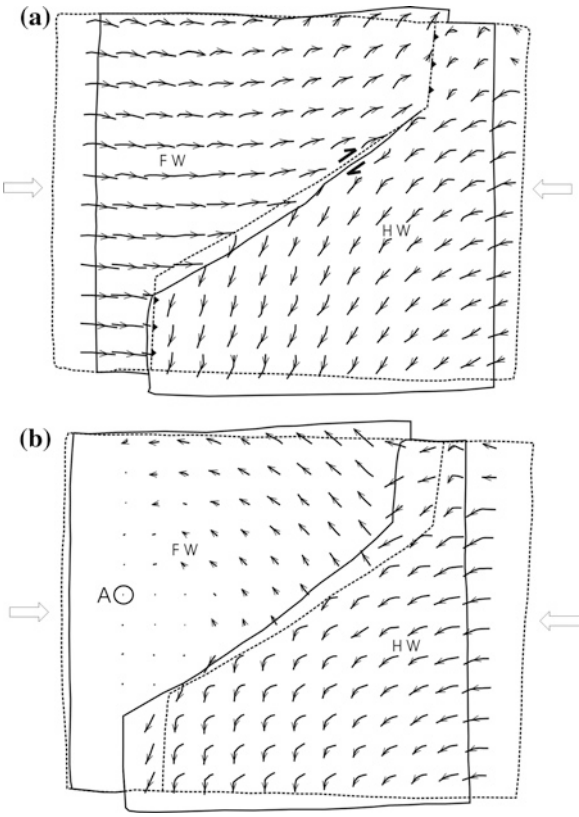

Fig. 8.2 The particle movement path fields obtained with reference to fix points outside the model (**a**), and with reference to a fix point 'A' inside the model, in footwall of the thrust (**b**). *Broken lines*, initial model; continuous line, deformed model after 9 % shortening. *FW* footwall, *HW* hanging wall (Dubey 2005)

The movement paths were significantly different when the fix point was placed in footwall of the deforming model (Fig. 8.2b). The direction of displacement in the footwall reversed and magnitude of displacement decreased from the trailing frontal ramp towards the fix point. The pattern of displacement also varied although the hanging wall points moved in one direction somewhat similar to Fig. 8.2a. Change in location of the fix point to the hanging wall (not illustrated) reflects a reversal of the footwall particle movements towards the hanging wall and a number of stationary points in the hanging wall. Since a change in location of fix points can alter the magnitude and direction of the movement paths, the fix points must be positioned outside the deforming body in order to obtain a true picture.

Similar variations in intensity and direction of velocity vectors in the Indo–Tibetan–Burmese region are shown in Fig. 8.3 (Holt et al. 2000; see also Zhang and Wang 2006). The model velocity field relative to Eurasia (Fig. 8.3a) clearly depicts the north-east movement of the Indian plate, and eastward extrusion of Tibet. However, a change in the reference point (i.e. relative to India) changes the whole scenario (Fig. 8.3b). The entire Indian plate remains stationary whereas the

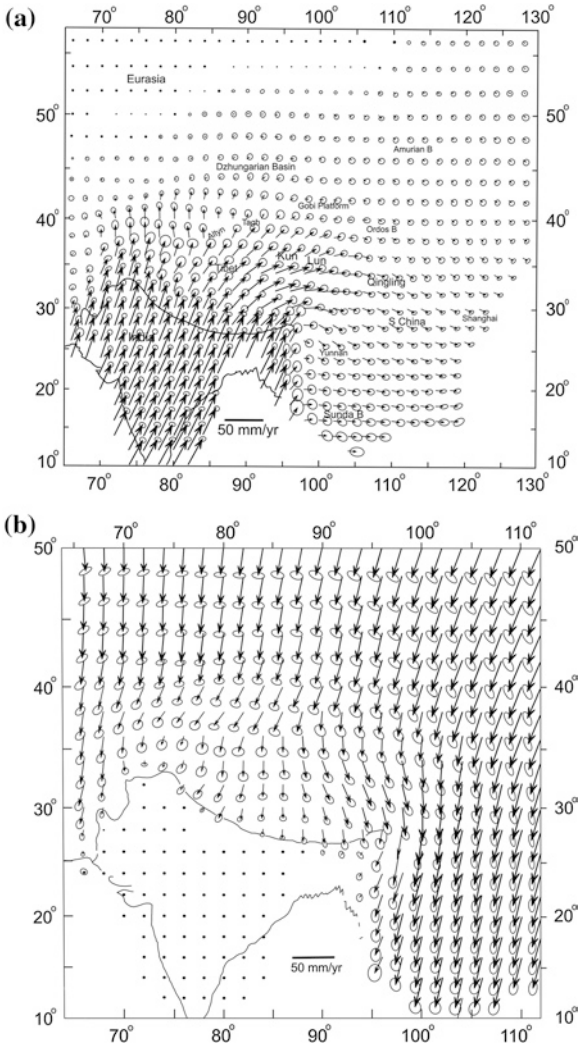

Fig. 8.3 Intensity and direction of velocity vectors showing movements in India and Eurasia with reference to different fix points. **a** Model velocity field relative to Eurasia showing northward movement of the Indian plate, eastward extrusion of Tibet and stationary Eurasian plate. **b** Velocity field solution defined relative to India shows a false picture of stationary Indian plate and southward movement of the Eurasian plate. [From Holt et al. (2000), © American Geophysical Union. Published with permission of American Geophysical Union]

Tibetan plate reveals a southward movement without eastward extrusion. Since it is known from other evidence (total plate reconstruction) that the Indian plate is moving towards north, the selection and interpretation of the diagrams are not difficult. However choice of a reference point can lead to significant errors while interpreting comparatively smaller structures like displacement along a fault or evolution of an active fold. The various discrepancies in the measurements were also pointed out by Holt et al. (2000). For example, the slip rate on the Karakoram Fault was assigned as 15 ± 12 mm as compared to the earlier estimate of 30 ± 10 mm (Avouac and Tapponier 1993). The results of Holt et al. (2000) appears to be more convincing because they have taken the Quaternary fault slip rates into account as well.

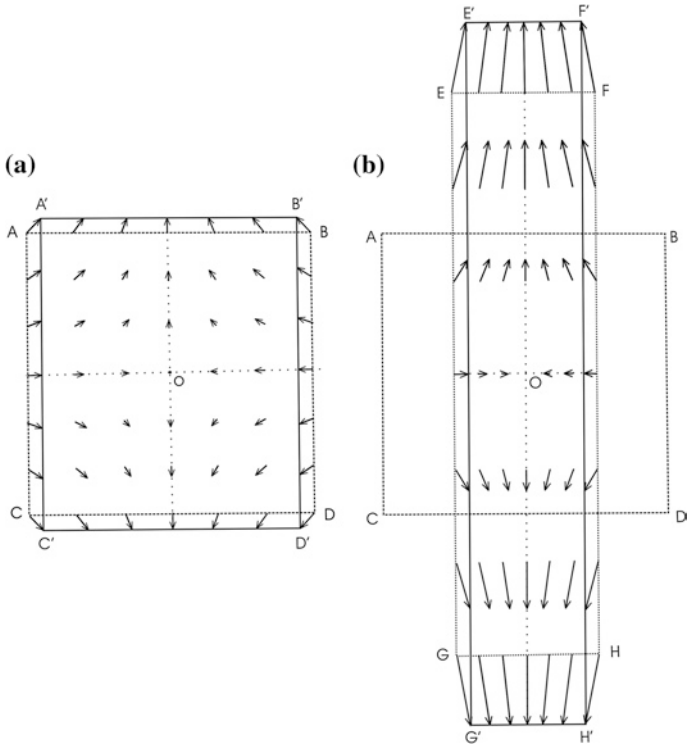

Fig. 8.4 Variation in magnitude and direction of movement paths between two stages of pure-shear deformation. **a** Movement paths between 0 and10 % shortening. **b** Movement paths between 50 and 60 % shortening. The *broken line* represents the initial shape of the body

8.4 Deformation of a Body Under Pure-Shear

Apart from location of the fix point, another important aspect is that the magnitude and direction of displacement paths vary at different stages of deformation between an equal amount of shortening. For example, Fig. 8.4a shows an undeformed body, ABCD, by broken lines. After 10 % shortening by pure-shear deformation, the body acquires a deformed shape, A′B′C′D′, shown by continuous lines (cf. Ramsay and Lisle 2002, p. 1031). The movement paths between the two stages of deformation are shown by arrows. The central point, O, remained fixed during the deformation. It is interesting to compare this with variation in magnitude and direction of movement paths of the same initial body between 50 % (broken line, EFGH) and 60 % shortening (continuous line, E′F′G′H′) (Fig. 8.4b). The shortening amount between Figs. 8.4a, b remains the same (i.e. 10 %) but the later stage of deformation reveals a greater displacement of points and their rotation towards the axis of maximum extension. Thus it is evident that the length and direction of movement paths vary during progressive deformation and any attempt

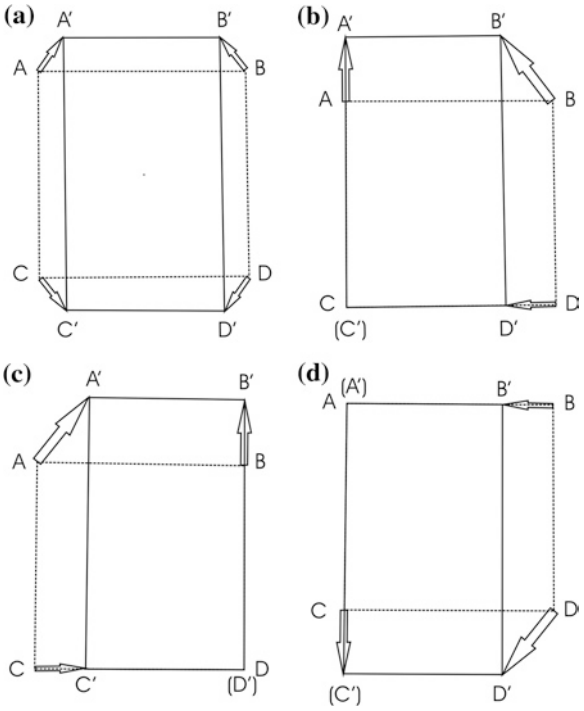

Fig. 8.5 Variation in magnitude and direction of movement paths with variation of the fix point

for determination of shortening amount between any two stages of deformation can be made only when initial shape of the body, shortening amount of the preceding stage, and mode of deformation are known.

In the above example, the reference point remained fixed at the central point (i.e. point O). However a change in position of the reference point can bring a significant change in magnitude and direction of displacement of the points. For example, Fig. 8.5a is similar to Fig. 8.4a where the reference point is the central point and point A moves to A′, B moves to B′, C moves to C′ and D moves to D′. The magnitude of displacement remains the same. In contrast to this, Fig. 8.5b shows a different situation where the fix point is selected at point C. With a change in position of the fix point, the magnitude and direction of displacement vectors change considerably although the shortening amount remains the same. The similar effect is shown in Figs. 8.5c, d where the fix points are selected as point D and point A respectively. The diagram illustrates it clearly that by a careful (cunning!) selection of the fix reference point, the magnitude and direction can be manipulated in a predetermined chosen direction.

The velocity fields are not absolute but always relative hence accuracy of the interpretation depends on proper selection of the reference point. Thus Bangalore or Delhi does not form good reference points to predict the movement of the Indian plate because these are situated on the moving plate itself. Places like Siberia that have not moved for millions of years could be better reference points. This is one of the reasons that the GPS velocity fields obtained by Avouac and

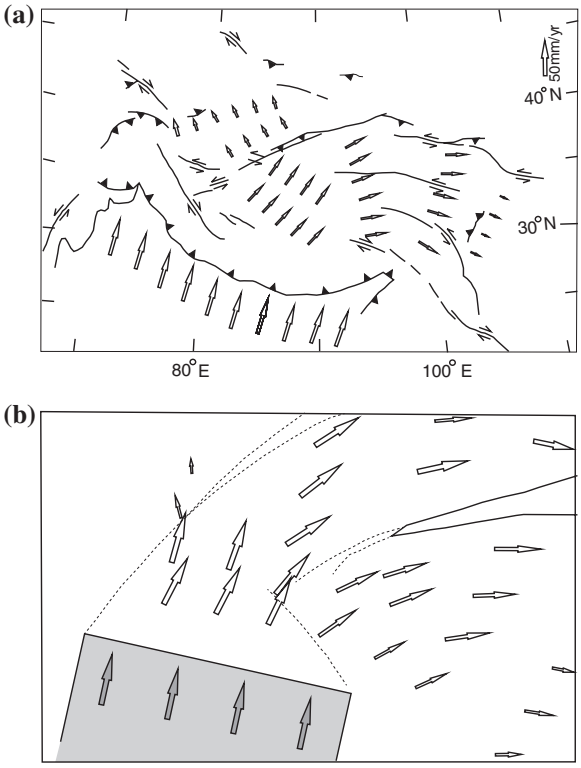

Fig. 8.6 A good correlation between GPS and experimental data obtained by deforming a Plasticine model. **a** GPS velocity vectors in the Indian and Tibetan regions (after Avouac and Tapponnier 1993). **b** Velocity field obtained by plane-strain indentation of a Plasticine block. [From Peltzer and Tapponnier (1988). © American Geophysical Union. Published with permission of American Geophysical Union]

Tapponnier (1993) can be compared very well with the velocity field of plane-strain indentation of a Plasticine block (Peltzer and Tapponnier 1988) (Fig. 8.6).

8.5 Development of Geological Structures During Internal Deformation and Translation

In an active orogenic belt, deformation is accomplished by a combination of internal strain and translation. It is also possible that more than one type of structure form simultaneously within the same deformation field. For example, folds can form simultaneously with thrust, normal, and strike-slip faults. One such example is shown in Fig. 8.7. Figure 8.7a displays an initial body ABCD, which has undergone translation without internal deformation to a new position A′B′C′D′. The body has moved with respect to the fix outer axis but not with respect to any point located inside the body. Figure 8.7b represents further translation of the body and development of a thrust, T–T′. The thrusting and associated bulk translation has modified the movement paths in two opposite directions along the y-axis. Displacements along the thrust have brought the points C′D′ to a new position EF.

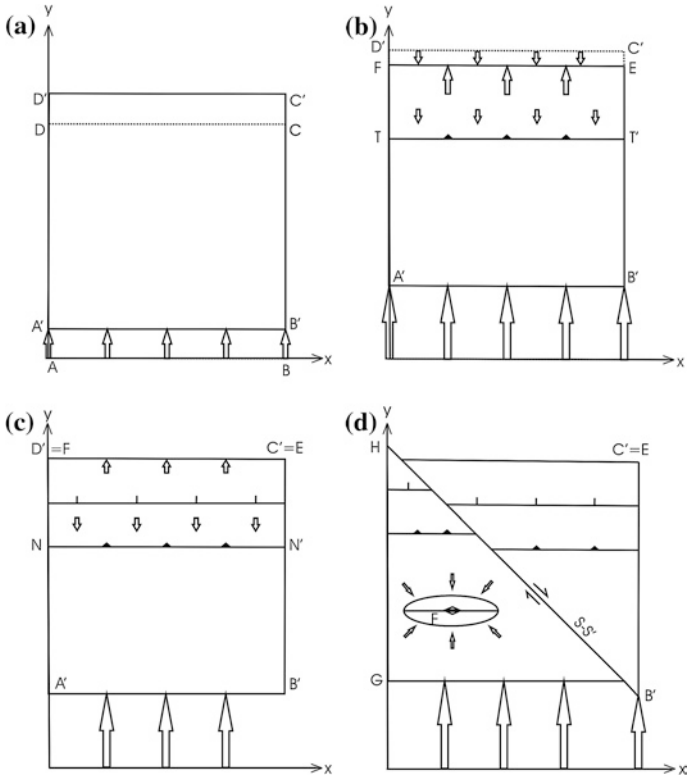

Fig. 8.7 Displacement paths (shown by *arrows*) during translation and internal deformation of a body with respect to an outer axis. **a** Translation of a body, ABCD, to a new position A′B′C′D′ without internal deformation. **b** Translation of the body, development of a thrust (T–T′) and modified displacement paths. The length of the body along the y-axis has decreased as a result of thrusting. **c** Movement paths as a result of thrust and normal faults. The normal faulting brings back the original length of the body along the y-axis. **d** Development of a strike-slip fault at a late stage of deformation. Part of the body has taken up a new position G–H (Dubey 2005)

During progressive deformation, these patterns are modified after development of a normal fault, N–N′, parallel to the thrust (Fig. 8.7c). As a result of normal fault displacement, the body acquires its initial length along the y-axis. Hence location of a fix point inside the body at this stage of deformation will not reveal any displacement. (It is to be noted that both extensional and thrust faults are active in the Quaternary Piedmont zone of the eastern Himalaya; Mullick et al. 2009).The sequence of structures is shown to be cut by a later strike-slip fault (S–S′) and formation of a noncylindrical fold (Fig. 8.7d) bringing about additional movement paths because amplification of the noncylindrical fold involves variation in movement directions around the fold culmination point. The direction is normal to the fold hinge line near the culmination and oblique to the hinge line away from the culmination (Price and Cosgrove 1990). Relative displacement along the strike-slip fault has resulted in part of the body taking up a new position GH.

In the above discussion, the following factors have been ignored.

1. Initial homogeneous shortening that may take place prior to formation of the structures.
2. Simultaneous development of folds and oblique thrust ramps, and displacement out of the transport plane, and
3. Inability of the GPS technique to accurately measure the vertical displacements.

In view of point 3, mentioned above, the GPS technique is better suited for strike-slip faults where displacements are predominantly horizontal.

The above discussion makes it abundantly clear that if the velocity vectors in GPS studies are obtained by location of a fix point inside the deforming body, the results are open to questions, especially in an active orogenic belt like the Himalaya. However the results have a greater credibility if the measurements are made with reference to a fix point outside of the body (e.g. a geostationary point above the surface of the earth).

The above discussion emphasizes that GPS data should be analyzed in light of the available geological information. A good combination of these two can provide useful results. Moreover, since the geological field data can be observed and rechecked, this should be regarded as of primary importance and most of the geophysical data, including GPS data, should be regarded as subsidiary. GPS data from an active orogenic belt is more effective when the stations are closely spaced and the data are presented with a good quality structural map showing the main structural features especially the active folds and type of faults with possible components of horizontal and vertical displacements.

8.6 Field Observations Versus GPS Data

The GPS has contributed to understanding of the present day plate movements but there are a number of contradictions between geological field observations and interpretations derived by GPS measurements. Some of these are listed below. These should be viewed in addition to the three factors mentioned above.

1. Geological data from the Himalaya and recent earthquakes in the region indicate thrust faulting in the Lower Himalaya (Uttarkashi, 20 October 1991, magnitude 6.5; Chamoli, 29 March 1999, magnitude 6.3), normal faulting in the Tethys Himalaya (Kinnaur, 19 January 1975, magnitude 6.8), and strike-slip faulting along the Karakoram Fault. The simultaneous development of these three types of faults in the region is not revealed by the available GPS data. This is mainly because of the fact that there are large distances between the GPS stations. Moreover, the GPS data deal with surface observations only and it is nothing to do with deformations taking place inside the earth.
2. The surface studies consisting of velocity fields and estimation of shortening amounts from the GPS data considers the bulk part of consumption of natural strain by faulting alone (e.g. 80 %, Peltzer and Saucier 1996). However structural

data reveal that the Simla Klippe shows displacement along a basal detachment thrust of the order of 40 km, and displacement along the Main Boundary Thrust is of the order of 33 km (Chap. 11). Displacements of these low magnitudes along the prominent thrusts cannot consume bulk of the shortening.

3. There is no consideration for reactivation of thrust faults as normal faults and initiation of new normal faults (e.g. the Tethys and Ladakh Himalaya; Herren 1987; Royden and Burchfiel 1987; Steck et al. 1993), and reversal of displacement along strike-slip faults during superposed folding (e.g. Yamuna Tear Fault in the Foreland Foothill Belt; Jayangondaperumal et al. 2010).
4. Surface expressions of geological structures in Tibet and higher reaches of the Himalaya may not be the real manifestation of crustal shortening. This is because of the fact that at higher elevations, where the rock has been brought up by early thrusting, effect of active horizontal compression is minimal (Dubey and Bhakuni 2004).

8.7 Indian Plate Movement and GPS Data

A variety of convergence rates between India and Tibet have been obtained by GPS studies, e.g. 58 ± 4 mm/year (Bilham et al. 1997), 50 mm (Larsen et al. 1999), 36 ± 3.5 mm/year (Holt et al. 2000), ≤20 mm (Paul et al. 2001), 15 ± 5 mm/year (Jouanne et al. 1999), and 12 mm/year (Seeber and Pecher 1998). Similarly, the extrusion rate of south China is estimated as 10 ± 5 mm/year (Peltzer and Saucier 1996), 9–11 mm/year (Holt et al. 2000), 6–11 mm/year (Wang et al. 2001).

The different rates show that the convergence is not uniform along the length of the Himalaya (~2,500 km). This is further exemplified by the following convergence rates from different parts of the Himalaya.

Ladakh Himalaya: 15 ± 2 mm year^{-1} (Banerjee and Burgmann 2002)

Sikkim Himalaya: 10–12 mm year^{-1} (Jade 2004)

Nepal Himalaya: 18 ± 2 mm year^{-1} (Bilham et al. 1997; Jouanne et al. 1999; Larson et al. 1999)

North Bengal Himalayan region: 11.1 ± 1.5 mm year^{-1} (Mullick et al. 2009)

Slip rates of India beneath southern Tibet are estimated to be 17 ± 1; 12.2 ± 0.4; 19 ± 1 mm/year on the western, central, and eastern segments respectively. The lower rate in the central Himalaya is significant. The variation in the slip rates has been attributed to geometries of the two most active rift systems, the Yedong–Gulu rift and Thakkola graben in southern Tibet and concentrated extension rates in the region (Chen et al. 2004). However it remains to be seen whether the Himalaya is controlling the structure of the Tibetan plateau or vice versa. One may also question whether the kinematics of collision is complicated or there is something basically wrong with the analysis of GPS data.

The different methods have also led to significant differences in estimation of shortening rates along the strike of the Himalaya. For example, the geological

estimate of convergence rate over the Holocene in central Nepal along the HFT is 21 ± 1.5 mm/year (Lave and Avouac 2000) whereas the GPS estimate is 20 ± 3 mm/year (Bilham et al. 1997). The two estimates are comparable but in the Indian part of the Himalaya, the convergence rate of Dehradun is 8.6–10 mm/year (Wesnousky et al. 1999; Kumar et al. 2006) whereas the GPS measurements reveal a convergence rate of 14 ± 1 mm/year (Banerjee and Burgmann 2002).

It is significant to note that even a difference of few mm/year becomes enormous when a time period of about 10,000 years is taken into account. Since these rates are used for predicting earthquakes in the region, their accuracy is of prime importance. Apart from the rates, the direction and amount of movement at different stations also display a wide variety depending on selection of the fix point (cf. Figs. 2b and 4a in Holt et al. 2000). Moreover all these data consider the two dimensional aspect only. The three dimensional kinematics involving deformation at depth and block rotations will add to the complexities (cf. Larson et al. 1999).

8.8 Importance of Location of GPS Stations in an Orogenic Belt

The problems highlighted above will increase manifolds if a large number of GPS stations are roving (e.g. Wang et al. 2001) because at one instant of time, the stations will be close to one set of geological structures and at another instant of time they will be close to another set of geological structures (Fig. 8.8). Roving stations are more appropriate away from an active orogenic belt where the number of geological structures and their varieties are limited.

Geophysical studies attribute high elevation of the Himalaya and Tibet to the collision between India and Tibet (e.g. Bilham et al. 1997) and while doing so an important geological fact is ignored that the elevation is, in fact, a result of folding and thrusting brought about by the collision. This is unfortunate that folding of the rocks has been completely ignored while estimation of crustal shortening. Holt et al. (2000) have accommodated 80 % of the India-Eurasia motion along narrow fault zones. This implies that the remaining 20 % is responsible for formation of billions and billions of folds (on different scales) spread over the length, breadth, and depth of the Himalaya. Data on recent fold amplification are not available from most parts of the Himalaya. However, Burg et al. (1997) have shown that the Eastern Namche-Barwa Syntaxis of the Himalaya is a fast growing, post collision antiform with considerable shortening component and the exhumation is caused by ~10 mm year^{-1} erosion coeval with the crustal scale folding. It was discussed in Chap. 4 that the method of restoration of cross-sections has several inherent problems and therefore the results are not reliable. Hence in view of these studies it becomes evidently clear that the crustal shortening estimates in the Himalaya are very approximate.

All the published GPS data, related to the Himalaya, showed northward displacement vectors (e.g. Banerjee and Burgmann 2002). However, a great

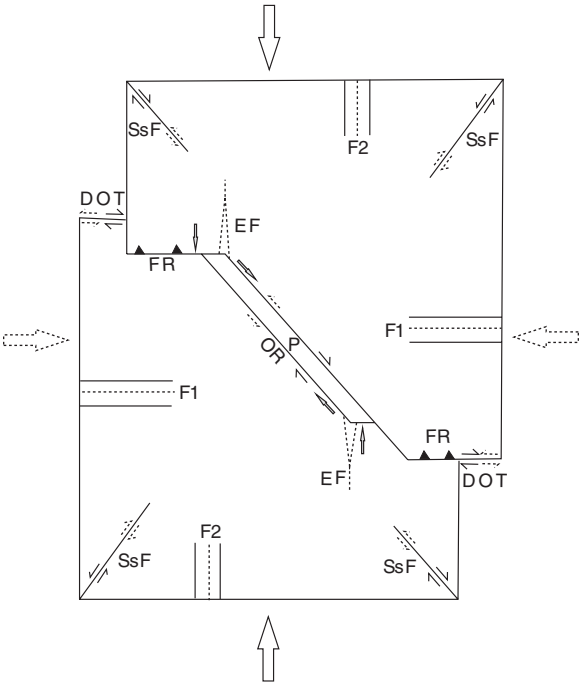

Fig. 8.8 Variety of structures, which can occur in close proximity in an orogenic belt (e.g. Foreland foothill belt and Lower Himalaya). *Arrows* with *continuous lines*, maximum compression direction during early deformation; *arrows* with *broken lines*, maximum compression direction during superposed deformation; *F1* early folds, *F2* superposed folds, *FR* frontal thrust ramp, *OR* oblique thrust ramp, *EF* extension fault, *P* pull-apart basin, *Ss F* Strike-slip fault (*half arrows with continuous lines* early strike-slip faults, *half arrows with broken lines* later strike-slip faults formed during the superposed deformation), *DOT* displacement out of the tectonic transport plane

earthquake occurred on 26 December 2004 along the Sumatra megathrust at the interface of the subsiding Indian plate with the overriding Andaman microplate. The earthquake rupture propagated to about 1,400 km in length. Analysis of coseismic GPS data from the surrounding regional permanent GPS stations revealed that the earthquake affected at least 4,000 km range area surrounding the source zone. The south Indian shield that was continuously moving towards north then shifted towards east by 10–16 mm. Consequently, the inter-station distance between Singapore and Bangalore decreased by ~30 mm (Banerjee 2005). Without questioning the authenticity of the data, it remains unanswered as to why no displacement of the south Indian shield was observed or reported prior to the Sumatra earthquake. Was it observed only after selection of new fix points! Moreover, if the velocity vectors can change their direction suddenly during an earthquake or immediately prior to an earthquake, the GPS data have very limited application for seismic predictions.

References

Apotria TG, Snedden WT, Spang JH, Wiltschko DV (1991) Kinematic models of deformation at an oblique ramp. In: McClay K (ed) Thrust tectonics. Chapman & Hall, New York, pp 141–154

Avouac JP, Tapponnier P (1993) Kinematic model of active deformation in Central Asia. Geophys Res Lett 20:895–898

Banerjee P (2005) Inter-seismic geodetic motion and far-field coseismic surface displacements caused by the 26 December 2004 Sumatra earthquake observed from GPS data. Curr Sci 88:1491–1496

Banerjee P, Burgmann R (2002) Convergence across the northwest Himalaya from GPS measurements. Geophys Res Lett 29:13. doi:10.1029/2002GL015184

Bilham R, Larson K, Freymueller J, Project Idylhim Members (1997) GPS measurements of present-day convergence across the Nepal Himalaya. Nature 386:61–64

Bilham R, Gaur VK, Molnar P (2001) Himalayan seismic hazard. Science 293:1442–1444

Burg J-P, Davy P, Nievergelt P, Oberli F, Seward D, Diao Z, Meier M (1997) Exhumation during crustal folding in the Namche-Barwa syntaxis. Terra Nova 9:53–56

Chen Q, Freymueller JT, Yang Z, Xu C, Jiang W, Wang Q, Liu J (2004) Spatially variable extension in southern Tibet based on GPS measurements. J Geophys Res 109:B09401. doi:10.1029/2002JB002350

Dubey AK (1997) Simultaneous development of noncylindrical folds, frontal ramps and transfer faults in a compressional regime: experimental investigations of Himalayan examples. Tectonics 16:336–346

Dubey AK (2005) Displacement paths around geological structures obtained from model deformation experiments: implications for GPS studies in the active Himalayan orogenic belt. Himalayan Geol 26:199–204

Dubey AK, Bhakuni SS (2004) Development of extension faults on the oblique thrust ramp hanging wall: example from the Tethys Himalaya. J Asian Earth Sci 23:427–434

Herren E (1987) Zanskar shear zone: northeast–southwest extension within the higher Himalaya (Ladakh, India). Geology 15:409–413

Holt WE, Chamot-Rooke N, Le Pichon X, Haines AJ, Shen-Tu B, Ren J (2000) Velocity field in Asia inferred from Quaternary fault slip rates and global positioning system observations. J Geophys Res 105:19185–19209

Jade S (2004) Estimates of plate velocity and crustal deformation in the Indian subcontinent using GPS geodesy. Curr Sci 86:1443–1448

Jayangondaperumal R, Dubey AK, Kumar BS, Wesnousky SK, Sangode SJ (2010) Magnetic fabrics indicating late Quaternary seismicity in the Himalayan foothills. Int J Earth Sci 99:S265–S278. doi:10.1007/s00531-009-0494-5

Jouanne F, Mugnier JL, Pandey MR, Gamond JF, Le Fort P, Serrurier L, Vigny C, Avouac JP (1999) Oblique convergence in the Himalaya of Western Nepal deduced from preliminary results of GPS measurements. Geophys Res Lett 26:1933–1936

Kumar S, Wesnousky SG, Rockwell TK, Briggs RW, Thakur VC, Jayangondaperumal R (2006) Paleoseismic evidence of great surface rupture earthquakes along the Indian Himalaya. J Geophys Res 111:B03304. doi:10.1029/2004JB003309

Larson KM, Burgmann R, Bilham R, Freymueller JT (1999) Kinematics of the India-Eurasia collision zone from GPS measurements. J Geophys Res 104:1077–1093

Lave J, Avouac JP (2000) Active folding of fluvial terraces across the Siwalik Hills, Himalaya of central Nepal. J Geophys Res 105:5735–5770

Mullick M, Riguzzi F, Mukhopadhyay D (2009) Estimates of motion and strain rates across active faults in the frontal part of eastern Himalaya in North Bengal from GPS measurements. Terra Nova 21:410–415. doi:10.1111/j.1365-3121.2009.00898.x

Paul J, Burgmann R, Gaur VK, Bilham R, Larson KM, Ananda MB, Jade S, Mukal M, Anupama TS, Satyal G, Kumar D (2001) The motion and active deformation of India. Geophys Res Lett 28:647–650

Peltzer G, Saucier F (1996) Present-day kinematics of Asia derived from geologic fault rates. J Geophys Res 101:27943–27956

Peltzer G, Tapponnier P (1988) Formation and evolution of strike-slip faults, rifts and basins during the India-Asia collision: an experimental approach. J Geophys Res 93(B12):15085–15117

Price NJ, Cosgrove JW (1990) Analysis of geological structures. Cambridge, 502 pp

Ramsay JG, Huber MI (1983) The techniques of modern structural geology, vol 1, strain analysis. Academic Press, USA 307 pp

Ramsay JG, Lisle RJ (2002) The techniques of modern structural geology, vol 3, applications of continuum mechanics in structural geology. Academic Press, USA, pp 701–1055

Royden LH, Burchfiel BC (1987) Thin-skinned N–S extension within the convergent Himalayan region: gravitational collapse of a Miocene topographic front. Spec Publ Geol Soc London 28:611–619

Seeber L, Pecher A (1998) Strain partitioning along the Himalayan arc and the Nanga Parbat antiform. Geology 26:791–794

Steck A, Spring L, Vinnay J-C, Masson H, Stutz E, Bucher H, Merchant R, Tiche J-C (1993) Geological transect across the Northwestern Himalaya in eastern Ladakh and Lahaul (A model for continental collision of India and Asia). Eclogae Geol Helv 86:219–263

Wang Q, Zhang P-Z, Freymueller JT, Bilham R, Larson KM, Lai X, You X, Niu Z, Wu J, Li Y, Liu J, Yang Z, Chen Q (2001) Present day crustal deformation in china constrained by global positioning system measurements. Science 294:574–577

Wesnousky SG, Kumar S, Mohindra R, Thakur VC (1999) Uplift and convergence along the Himalayan Frontal Thrust of India. Tectonics 18:967–976

Zhang X, Wang Y (2006) Seismic and GPS evidence for the kinematics and the state of stress of active structures in south and south-central Tibetan Plateau. J Asian Earth Sci 29:283–295. doi:10.1016/j.jseaes.2006.03.008

Part II
Evolution of the Himalaya

Chapter 9
The Himalaya

Abstract A brief introduction of the Himalaya is given. Evolution of the Himalaya began with break-up of the supercontinent Gondwanaland into Antarctica, Africa, Australia, and India around 140 Ma. The Indian plate moved towards north and the Indo-Eurasian collision took place somewhere between ~65 and ~43 Ma. The Himalaya started rising and led to monsoonal rains in the Indian region. Now the mountain has a vast reserve of fresh water in form of ice. It supports thick forests and is a source of many perennial rivers of north India. However, despite of several blessings, the active mountain has few inherent dangers as well, e.g. seismicity, landslides, floods, glacial lake outburst, etc. Hence the study of Himalaya is important not only from the scientific point of view but also from the societal point of view. Tectonic sub divisions of the Himalaya are illustrated.

The gigantic Himalaya is a part of the Alpine-Himalayan mountain chain. The mountain is about 240–320 km wide and 2,500 km long, bordered by the Indus River in the west and Brahmputra in the east. The youngest mountain with the highest peak (Everest, 8,850 m) is an arcuate fold belt convex towards south. In order to fully understand the evolution of the Himalaya, one must begin with pre-Himalayan events that led the foundation.

Break-up of the supercontinent Gondwanaland into Antarctica, Africa, Australia and India took place around 140 Ma and journey of the Indian plate began in the northern direction. While considering the collision between the Indian and the Tibetan (Eurasian) plates, relative motion of each has to be taken into account. The largest Eurasian plate is regarded as the slowest moving continental block. As described by Ali and Aitchison (2004), very few palaeomagnetic data are available for the Eurasian plate for the last 100 Ma. The problem is aggravated by the fact that all the poles are from Lower Plaeogene rocks (~11 Ma) within a limited geographical area of the plate (NW Britain and the Faeroe islands). Beloussov (1968) has also presented data in support of the fact that some regions (e.g. Moscow basin) have been over the same part of the mantle for hundreds of millions of years. Notwithstanding the dilemma of the European plate movement, the timing of collision between the

A. K. Dubey, *Understanding an Orogenic Belt*, Springer Geology,
DOI: 10.1007/978-3-319-05588-6_9,

Indian and Tibetan plates can be obtained from the geological evidence mainly; (1) end of marine sedimentation and beginning of continental molasse sedimentation in the Indus Suture Zone (ISZ), (2) end of Andean type calc-alkaline magmatism along the Trans-Himalayan (Ladakh–Kohistan–Gangdese) batholith, and (3) initiation of thrusting in the Himalaya (Searle et al. 1988). The age for the onset of Indo-Asian collision is not well constrained and the different estimates range from ~65 to ~43 Ma (Yin 2006) though the results of the collision became apparent around the Eocene-Oligocene boundary (~34 Ma).

The Himalaya is a great gift by the Mother Nature to the people of the Indian sub-continent. The monsoonal rains are possible only because of great heights of the mountain, many of the large perennial rivers of north India (e.g. Jhelum, Satluj, Ganga, Yamuna, Tista, and their tributaries) initiate from the mountain, it supports thick forests, and Siberian cold winds from the north are blocked to make the life cozy for the habitats. It is now called as the third pole because of vast reserves of fresh water in form of glacier ice. Having a vast treasure of natural gifts, the mountain also has an inherent danger of seismic risk. Apart from a very large number of minor earthquakes, the region has experienced some great and high intensity earthquakes as well. Hence study of the Himalaya is extremely important not only from scientific but also from societal point of view. On one hand, the study helps in exploitation of minerals and rocks of economic importance, construction of roads, bridges, tunnels etc. and on the other hand it is crucial for understanding the kinematics of seismic events.

Geological studies of the Himalaya are now more than one hundred and fifty years old. The study was initiated by a civil engineer Sir Proby Thomas Cautley while digging the 560 km long Ganga canal between Hardwar and Kanpur. The work began in 1843 in the foothills of the Garhwal–Kumaun Himalaya and the Indo-Gangetic alluvial plain. A large number of mammalian fossils were obtained from the region (Siwalik Group of rocks) indicating that the area was once a swampland. The fossil collection was extremely useful for later generation of palaeontologists, who established the age of different stratigraphic horizons. Another important aspect that led to the progress of geological studies was prevalent seismicity in the region. A catalogue of Indian earthquakes was first prepared by Oldham (1883). This was followed by a detailed report by Middlemiss (1910) on the great earthquake (4 April 1905; Mw = 7.0 magnitude on the Richter scale) of the Kangra region (Himachal Himalaya) and minor quakes near Dehra Dun (Garhwal Himalaya). Later, the western Himalaya was studied by Wadia (1931) and the concept of Western Himalayan Syntaxis was formulated.

Thrusts and folds are the most prominent structures of the Himalaya. The prominent thrusts extend throughout its length. Folds with different dimensions, orientations and geometry have developed throughout the region. It was established in the earlier studies that asymmetric folds occur near the thrusts and upright folds at a distance from the thrusts (Fig. 9.1).

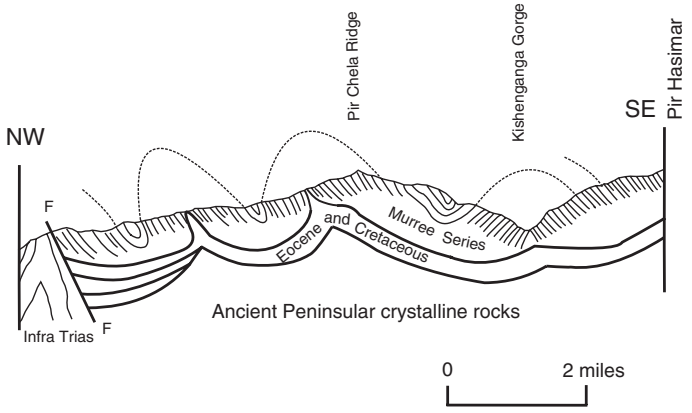

Fig. 9.1 A geological cross-section across a part of the western Syntaxial bend showing asymmetric folds near thrust and upright folds away from the thrust. Also note that both hanging wall and footwall are affected by thrust related shear strain and the Archaean basement is also folded with the upper rock sequence. (After Wadia 1931) (2 miles = 3.218 km)

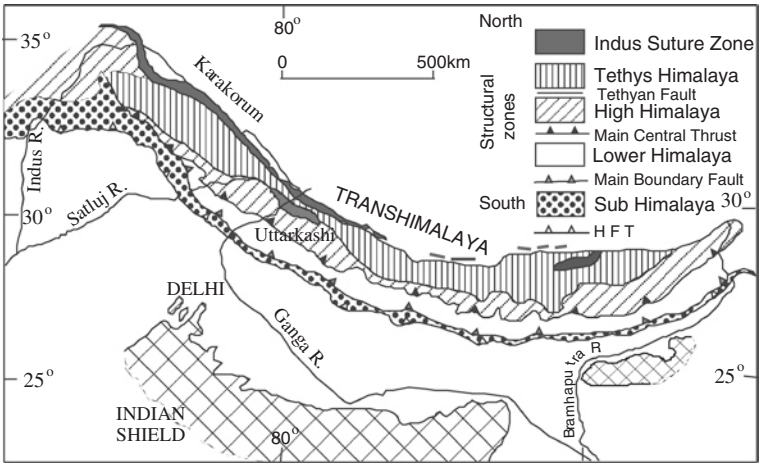

Fig. 9.2 Tectonic subdivisions of the Himalaya. (After Gansser 1964)

9.1 Tectonic Subdivisions of the Himalaya

The Himalaya can be divided in the following six main tectonic subdivisions from south to north (Fig. 9.2) (Gansser 1964). The division is based on major rock types and prominent structural features. Each subdivision is separated by a prominent fault.

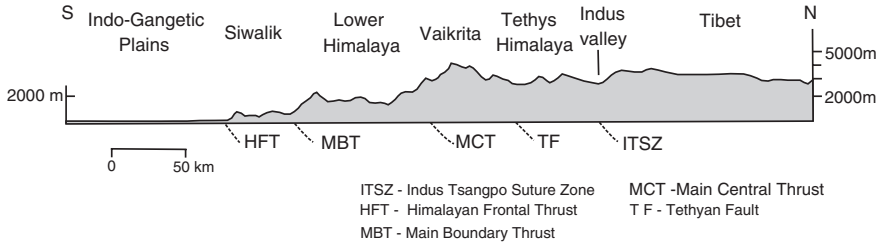

Fig. 9.3 A topographic profile across the Garhwal–Kumaun Himalaya [From Valdiya (1998), Geodynamic Himalaya. Universities Press, Hyderabad. Published with permission of K.S. Valdiya]

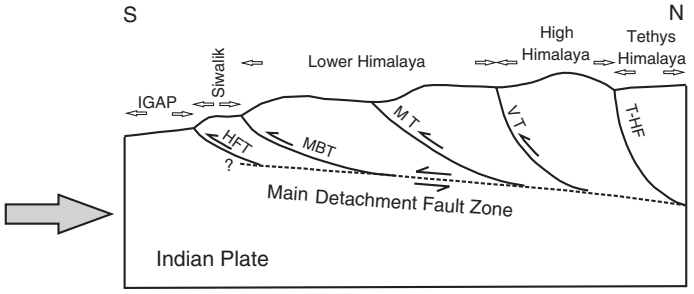

Fig. 9.4 A simplified S–N section across the Himalaya showing prominent Himalayan thrusts and distribution of important rock units (*IGAP* Indo-Gangetic Alluvial Plain; *HFT* Himalayan Frontal Thrust; *Siwalik* Foreland Foothill Belt; *MBT* Main Boundary Thrust; Lower Himalaya, sedimentary and metasedimentary rocks; *MT* Munsiari Thrust, (MCT I); *VT* Vaikrita Thrust (MCT II); *High Himalaya* medium to high grade rocks of the Vaikrita Group; *T-HF* Trans-Himadri Fault (= South Tibetan Detachment (STD)) Fault; *Tethys Himalaya* metasedimentary, and sedimentary rocks of the Tethyan sequence

1. Foreland Basin or Foothill Belt or Sub-Himalaya
2. Lower Himalaya or Lesser Himalaya
3. High Himalaya or Central Himalaya
4. Tethys Himalaya
5. Indus Suture Zone
6. Trans Himalaya or Tibetan Himalaya

All the subdivisions are characterized by similar structural features, lithological settings and evolutionary history. A topographic profile across the Garhwal–Kumaun Himalaya is shown in Fig. 9.3 and a simplified N–S geological cross-section across the Himalaya is shown in Fig. 9.4.

Description of each subdivision is given in the subsequent chapters.

References

Ali JR, Aitchison JC (2004). Problem of positioning Paleogene Eurasia: a review; efforts to resolve the issue; implications for the India-Asia collision. In: Clift PD et al. (ed), Continent-Ocean interactions within the East Asia Marginal Seas. Geophysical Monograph Series, American Geophysical Union, Wasington, DC., 149, 23–35

Beloussov VV (1968) An open letter to J. Tuzo Wilson. Geotimes 13:17–19

Gansser A (1964) Geology of the Himalaya. Interscience, New York, p 289

Middlemiss CS (1910) The Kangra earthquake of 4th April 1905. Memoir Geological Survey of India 37, 409 pp (Reprinted 1981)

Oldham T (1883) A catalogue of Indian earthquakes. Mem Geol Surv India 19:163–215

Searle MP, Cooper DWJ, Rex AJ (1988) Collision tectonics of the Ladakh-Zanskar Himalaya. Philos Trans Roy Soc London Ser A 326:117–150

Valdiya KS (1998) Geodynamic Himalaya. Universities Press, Hyderabad, p 178

Wadia DN (1931) The syntaxis of northwest Himalaya: its rocks, tectonics and orogeny. Rec Geol Surv India 65:189–220

Yin A (2006) Cenozoic tectonic evolution of the Himalayan orogen as constrained by along-strike variation of structural geometry, exhumation history and foreland sedimentation. Earth Sci Rev 76:1–131. doi:10.1016/j.earscirev.2005.05.004

Chapter 10
The Foreland Basin

Abstract The foreland basin is the southernmost part of the Himalaya. It is separated from the Indo-Gangetic Alluvial Plain by the Himalayan Frontal Thrust (HFT). The HFT is an active thrust evidenced by scarps, uplifts, folding of Late Quaternary and Holocene deposits, and paleo-seismic studies. Available data on slip rates suggest a general increase from North-west to Central (Nepal) Himalaya. Thrusting in the region has resulted in fault propagation folds. The basin has formed during uplift of the Himalaya and is characterized by sedimentary succession of rocks. Stratigraphic sequence and sedimentological characters are described along with a brief remark on paleoclimate. Two generations of strike slip faults formed during the early and superposed deformations are present. A pull-apart basin is described from the Kangra region. Normal faults are the youngest structures. Results of cross-section balancing and various problems related to the balancing are discussed in the light of development of foreland basins, along with possible solutions.

The Indo-Gangetic Alluvial Plain (IGAP), spread over north India along the Ganga and Yamuna rivers, is not a litho-tectonic subdivision of the Himalaya but this is an integral physiographic part because the Ganga and Yamuna rivers and their tributaries originating from the Himalaya deposit their sediments in this region. The Foreland Basin lies north of the IGAP.

The Alluvial Plain is separated from the Basin by the Himalayan Frontal Thrust (HFT, also called as Main Frontal Thrust, MFT). The thrust continues as a fault zone along the Himalayan foothills, although the contact is not exposed everywhere (Karunakaran and Ranga Rao 1979; Raiverman 2002). The HFT delineates northern limit of the exposed Indian plate. It is an active Himalayan thrust as it displaces the Tertiary and Quaternary sediments of the hanging wall Siwalik Group over the IGAP. The active deformation is also evident by scarps, uplift, and folding of Late Quaternary and Holocene deposits (Nakata 1989). Thrusting along the HFT is estimated to have absorbed 21 $\pm$ 1.5 mm/year of N–S shortening during the Holocene period (Lave and Avouac 2000).

A. K. Dubey, *Understanding an Orogenic Belt*, Springer Geology,
DOI: 10.1007/978-3-319-05588-6_10,

Table 10.1 Lithologies and depositional environments of the late cretaceous and early tertiary Himalayan foreland basin sediments (after Najman et al. 1993)

Formation	Age	Lithologies	Facies interpretation
Kasauli	Early Middle Miocene	Gray sandstones, siltstones and mudstones. Much woody material	Humid climate, braided fluvial regime
Dagshai	Late Eocene–Late Oligocene	Red sandstones, siltstones, mudstones and caliche	Semi-arid climate, meandering fluvial and floodplain regime
Subathu	Palaeocene–Middle Eocene	Limestones, shale and green mudstones	Shallow marine environment
Singtali	Late Cretaceous–Palaeocene	Limestones	Shallow marine environment

10.1 Stratigraphic Succession

Rock sequence of the Foreland basin lies over Tal Formation, which is a Lower Himalayan sequence of Cambrian age. After deposition of Tal, there was a great hiatus and the next succession of Singtali Formation deposited from the Late Cretaceous to Palaeocene (Table 10.1). The Singtali Formation mainly consists of limestone with ill preserved fragments of shells. The fossils are not identifiable hence the age is not certain and could range from 75 to 65 Ma. The Singtali deposition is attributed to flexure in the propagating Indian craton. Rock sequence of the region represents synorogenic sedimentation but under various depositional environments from shallow marine to transitional to fluvial. A useful review of sedimentary history of the region, provided by Kumar et al. (2011), is the main source of the following description.

Singtali Formation is overlain by Subathu Formation consisting of limestones, shales, and green mudstones. The rocks are rich in fossils indicating a shallow marine environment. Presence of large foraminifers revealed the Late Thanetian to Middle Lutetian age (48.6–40.4 Ma). Subsurface data of the Oil and Natural Gas Corporation (ONGC), India in SW part of the Himachal Himalaya does not show the Subathu Formation up to a depth of 6,000 m. Hence there appears to have been greater subsidence in this part as a result of flexural bending of the lithospheric plate, and greater thrust displacement in the eastern part where these rocks are exposed.

A major disconformity was suggested by Najman (2007) between the marine facies (Subathu Formation) and the overlying alluvial facies (Dagshai Formation) at <31 Ma. However based on sedimentologic observations, Kumar et al. (2011) have inferred an erosional discontinuity at the Subathu–Dagshai contact with a much smaller magnitude at <12 Ma (Kumar et al. 2011). The presence of fresh water deposits suggests that the Subathu Formation was deposited during suturing of India with Eurasia. After the suturing, regression of the sea ensued as a result of rise of the Himalaya and fresh water condition initiated with onset of monsoon. The rise of the Himalaya was facilitated by crustal shortening and displacement along a series of thrusts.

The Dagshai Formation consists of sandstones, siltstones, and mudstones. Petrographic and geochemical evidence indicate that Subathu Formation has received its detritus from the proto-Himalayan suture belt whereas metamorphic rocks of the High Himalaya were the main source for the Dagshai Formation. The overlying Kasauli Formation consists of fresh water deposits consisting of sandstones, siltstones and mudstones. The Dagshai and Kasauli formations constitute the Dharamsala Group that represents the oldest exposed continental foredeep sediments.

The Siwalik Group is a continental deposit that overlies the Dagshai, Kasauli and Murree formations throughout the NW Himalaya (Table 10.2). The Group is also called as 'molasse', which is a Swiss term applied to detritus derived from uplifting ranges and deposited in gradually subsiding foredeep at the foot of the rising mountain. The Siwalik ranges are up to 280 m high and are well known for their abundant vertebrate fossil assemblages. The base is dated at ~13 Ma in the Indian part (Meigs et al. 1995). The Group is divided into three fold classification based on coarsening upward succession from mudstone–sandstone (Lower Siwalik), to sandstone dominated (Middle Siwalik), to conglomerate, sandstone and mudstone (Upper Siwalik) facies.

The Lower Siwalik (~13–10 Ma) consists of dark gray, medium- to fine-grained sandstone interbedded with purple mudstone. More than 50 % mudstone was derived from a northerly source over a long period of low sediment accumulation in an extensive region. The total thickness of the succession is ~1.4 km. Intensification of the Indian monsoon took place after 10 Ma when a suitable elevation was achieved during the Lower Siwalik period.

A detailed sedimentological analysis of the Middle Siwalik subgroup (between 9 and 5.23 Ma) of Dehradun area was described by Kumar (1993), Kumar and Ghosh (1994) and Kumar et al. (2003). The Middle Siwalik succession of the area represents a multistorey sandstone complex, with facies variation from sandstone–mudstone (300–450 m thick) to sandstone (900–1,200 m thick) and finally to sandstone–mudstone–conglomerate (100–250 m thick). The medium- to fine-grained gray sandstones occur as multistorey units with sheet geometry. The individual storeys (thickness from 0.5 m to >3 m) can be recognized by presence of intra- and extraformational clasts along the base, and differences in paleocurrent azimuths (in order of +90°). Each storey is underlain by a major erosional surface, which extends laterally for hundreds of meters. The erosional surfaces are generally planar but a relief of the order of 1 m is also visible at some places. The proportion of sandstones (channel deposit) is >50 % throughout the Middle Siwalik succession. These sandstones are lithic arenite derived from a source comprising sedimentary, low to medium grade metamorphic, and igneous rocks in different proportions. There is a significant increase in metamorphic component around 7.50 Ma suggesting wide spread erosion of the High Himalayan Crystalline gneisses due to displacement along the Main Central Thrust.

Conglomerate facies is also observed in the Middle Siwalik succession between ~8.7 and 7 Ma. These conglomerates are well stratified, imbricated and fining upward beds of 1–2 m thick, comprising of rounded to well-rounded

Table 10.2 Neogene and Quaternary formations of the Himalayan foothills (after Valdiya 1998)

Epoch	Sindh	Potwar-Jammu		Himachal-Kumaun	Nepal	Arunachal Pradesh	Assam	Myanmar plains
Early Pleistocene	Upper Mancher	Upper Siwalik Boulder Conglomerate		Upper Siwalik Boulder Conglomerate	Devrali Boulder Beds	Kimin	Dihing	Irrawady group
Pliocene		Upper Siwalik	Pinjor Tatrot	Upper Siwalik	Chitwan			
Late Miocene		Middle Siwalik	Dhokpathan Nagri	Middle Siwalik	Binaikhola	Subansiri	Namsang Dupitila	
Middle Miocene	Lower Mancher	Lower Siwalik	Chinji Kamlial	Lower Siwalik	Arungkhola	Dafla	Girujan Tipam	Upper Pegu group
Early Miocene	Gaj	Murree		Kasauli	Dumri	–	Surma	

clasts of quartzite, basic rock, granite/gneiss, and sandstone. The rock shows coarsening up succession up to ~7.2 Ma followed by fining upward. A thick accumulation of conglomerate facies (10 and 7.2 Ma), deposited as alluvial fan, is exposed at extreme NE part of the basin (Kumar et al. 2011).

The Middle Siwalik deposits have been attributed to a southeasterly flowing large braided stream, parallel to the axis of the basin. The thickly bedded (>40 m) stack of gray sandstone beds was formed by repeated and rapid migration of the channel network over an alluvial plain. This sandstone contains minor intervening overbank (flood plain) mudstones that display trough cross-stratification. The flood plain to channel deposit thickness ratio is generally <0.2 but locally as high as 1. The intervening massive mudstones are brown to gray with presence of calcrete nodules. Immature paleosols and reworking of soils and sediments by animals or plants (bioturbation features) are commonly observed in the mudstone. At outcrop level, the data sets show clustering around the mean paleoflow direction. However, temporally and spatially there is high variability of the order of +90°. The sedimentary succession of Dehradun region (9–5.23 Ma) was deposited by sheet floods in a braided channel environment in the form of a southward prograding sandy alluvial fan. The Middle Siwalik succession gradually terminates in the northwest direction (Kumar 1993).

The Middle Siwalik succession is overlain by the Upper Siwalik with a transitional contact (Kumar and Ghosh 1994; Kumar et al. 2003). At the boundary of Middle and Upper Siwalik between ~5.5 and 5 Ma, the thick gray multistoried sandstone bodies are replaced by both minor sheet and ribbon shape bodies with increase in proportion of overbank mudstone. The lower part of the Upper Siwalik succession around Dehradun is represented by conglomerate, sandstone and mudstone facies. These facies form 3 to 25 m thick upward fining cycles with erosional bases. The conglomerate facies gradually increases upward in the section by laterally and vertically amalgamated sheets of gravel beds. The rock dominantly consists of clasts of quartzite (70–85 %), both from the Inner and Outer Lower Himalaya, with minor argillite (5–10 %; including slate and phyllite), limestone (5–20 %), granitoid gneiss (1–3 %), and mafic volcanic rocks (<1 %). The paleoflow data, obtained mainly from clast imbrications, suggest a southwestward drainage pattern. These were deposited by gravelly braided rivers in medial to distal alluvial fan settings. The paleoflow data and upward-coarsening trend of facies in the Upper Siwalik succession suggest progradation of conglomerate towards southwest. The clast composition data indicate that the Lower and part of the High Himalayan region acted as source area for these sediments (Kumar and Ghosh 1994). Thus, the depositional setting of sedimentary succession of Dehradun region is marked by two overlapping sandy (Middle Siwalik) and gravelly (Upper Siwalik) alluvial fans. The deposition initiated at ~1.77 Ma and has a time transgressive lower contact ranging from 1.77 to 1.1 Ma. The time transgressive boundary of the Boulder Conglomerate Formation indicates that the central part of the basin represents an inter-fan area in which alternations of sandstone–mudstone were deposited on alluvial slopes and coalesced with side fans after ~1.1 Ma. These fans are restricted along the basin margin and show rapid lateral variation in clast size from

proximal to distal fans. The facies architecture of these fans indicates syntectonic origin in a rapidly subsiding basin (Kumar et al. 1999).

The Upper Siwalik succession represents three formations, i.e. Tatrot, Pinjor and Boulder Conglomerate (Table 10.2). The Tatrot Formation (~5–2.58 Ma) was deposited by anastomosing streams and its thickness decreases in the northwest direction. The Formation includes three types of sandstone bodies; (1) major gray sheet bodies, (2) minor gray sheet bodies, and (3) gray and buff ribbon bodies. The buff ribbon sandstone bodies appeared at ~4.8 Ma with gradual increase in frequency and size upward in the section. These bodies are associated with higher proportion of overbank deposits (overbank to channel deposit ratio >5). In the early sequence, gray and buff sandstones interfinger, but buff sandstones became dominant after 1.77 Ma. The gray sandstone is lithic arenite whereas buff sandstone is sublithic arenite to lithic arenite. In both the sandstones, rock fragments vary from 0 to 49 %. Conglomerate beds increase in abundance after 2.6 Ma. Mudstones are plentiful, and the overbank/channel deposit ratio exceeds 5 near the Tatrot–Pinjor contact at around 2.58 Ma. In the Pinjor Formation, minor gray sheet sandstone is common and occurs in association with pre-Tertiary clast bearing conglomerates. The frequency and thickness of buff sandstone, which is multistoried at places, increase upwards. The conglomerates are stratified, imbricated, and are composed of subangular to subrounded clasts of quartzite with minor limestone, phyllite, slate, chert, granitoid, and basic igneous rocks. The clast size generally ranges from 10 to 15 cm with the largest clasts ~20 cm. The paleoflow directions of buff and gray sandstones are almost perpendicular to each other showing SE and SW trends, respectively. These sediments were deposited by gravelly main stream with broad floodplain at the mountain foot. Extensive soil formation of the mudstone facies and lateral variability of its maturation indicate that vertical accretion took place on a broad floodplain under subaerial condition. This period records interfingering of gravelly braided transverse main stream and piedmont stream(s) (Kumar et al. 2011).

The contact between the Pinjor and the Boulder Conglomerate formations is marked by a change in the conglomerate clast composition from the Lower Himalaya derived quartzite to sub-Himalaya derived (Tertiary) sandstone. Basal part of the Boulder Conglomerate Formation consists of stratified and imbricated conglomerates (1–6 m thick) composed of subrounded to subangular clasts embedded in buff sandy muddy matrix. These are interbedded with buff sandstones and abundant mudstones with overbank to channel deposit ratio >5. Size of the conglomerate bodies, clast size (up to 50 cm) and angularity increase in the upward direction. The predominance of Tertiary clast bearing conglomerate suggests that the southwesterly flowing main stream gradually migrated in response to progradation of piedmont alluvial fan. Massive, poorly sorted, disorganized, sandy and muddy, matrix supported conglomerates were formed by rapid sedimentation in form of cohesive debris flow in proximal part of the alluvial fan. Kumar et al. (2011) have assigned the initiation of the Boulder Conglomerate Formation at ~1.77 Ma with a time transgressive lower contact ranging from 1.77 to 1.1 Ma. The alluvial fan sedimentation was initiated at ~1.77 Ma in the southeastern and northwestern part.

Based on the magnetic studies, Ranga Rao et al. (1988) have estimated the rate of sedimentation as 45–71 cm/1,000 year for the Siwalik Group in the western Himalaya in Gilbert and Gauss times, and 21–37 cm/1,000 year in the Mohand Rao section, south of Dehradun during the Matuyama magnetic reversal of the earth. Later, Ranga Rao (1993) observed a decrease in sedimentation in the northern part and accelerated rates in the southern part during Matuyama as a result of migration of depocentre. Sangode et al. (1999) have estimated an average rate of sedimentation as 38 cm/1,000 year for the Middle Siwalik succession.

The Upper Siwalik succession (~2,000 m thick) initiated at ~3 Ma in which 1–2 m thick conglomeratic beds were deposited (Quade et al. 1995; Sanyal et al. 2005). The conglomerates are poorly to moderately sorted, with subrounded to rounded clasts, crudely stratified with transverse imbrication clast fabric. The clasts (10–25 cm, rarely up to 30 cm) are matrix supported but framework supported pebble, cobble, boulder conglomerates are also present. Conglomerate facies, in upper part of the succession, is clast supported (rarely matrix-supported), subrounded to rounded pebble to boulder size conglomerates with sandy to granular matrix (devoid of clayey matrix). The clast size ranges from 25 to 40 cm, rarely reaching to a maximum of 50 cm. The conglomerates are massive with poorly developed imbrication, crude upward fining and irregular lower bounding surfaces. These conglomerates include—crystalline white quartzite (40–60 %) and pink quartzite (10–15 %), limestone (15–20 %), granite/gneiss (5–10 %), Tertiary sandstone (14–18 %), basic volcanic (1–4 %) and others (4–10 %). The composition indicates complex provenance from hanging walls of the MBT and Chail Thrust. Some clasts (up to 18 %) have been cannibalized from foreland basin sediments (Subathu–Dharamsala formations). The Upper Siwalik Conglomerate shows southwesterly paleoflow with trends towards south and west in form of radial pattern that suggests sheet flood dominated proximal to distal alluvial fan setting with decrease in clast size and simultaneous increase in sandstone percentage (Kumar et al. 2011). The succession varies laterally across the foreland basin exhibiting an increase in conglomerate percentage towards the MBT. The Lower Siwalik and older strata are well indurated, whereas the Middle and Upper Siwalik strata are mostly friable except at few places where it is cemented by calcium.

Besides predominant tectonic control on the basin fill, climate has also influenced the overall distribution of grain size and rate of sediment supply. Presence of purple and brown paleosols with calcareous nodules suggests humid warm climate during the Middle Siwalik time in the Kangra region, partially in Dehradun region, and during the Upper Siwalik time in the Subathu region. Fluvial architecture around 10 and 5 Ma suggests increased precipitation and consequent increase in river size and discharge.

The Siwalik Group is overlain by Quaternary conglomerates in broad synclines, e.g. the Dehradun syncline.

The stromatolite bearing Lower Himalayan Bilaspur Limestone is exposed south of the MBT (Thakur and Rawat 1992). Presence of the basement rock in the basin suggests reactivation of a basement fault. The fault cuts through the Siwalik rocks indicating that the reactivation is younger than the rocks.

In Nepal, Jurassic and Cretaceous rocks are exposed north of the MBT, a feature not seen in the western Himalaya. One of the explanations for this observation could be that normal faulting during the rift phase had a less displacement in the western Himalaya and larger magnitude of displacement in the central part of the Himalaya. Because of the greater displacement, the region was not positive even up to the Cretaceous time allowing deposition of the rocks.

10.2 Structural Features

The pre-tertiary sequence consists of sedimentary and low grade metasedimentary rocks (mainly quartzite, limestone, shale, slate, with some phyllite) whereas the overlying cover rocks are sedimentary. There is a large variation in thickness of individual formations and the rocks have undergone superimposed folding (Raiverman et al. 1990). The early folds are characterized by fault propagation folds near thrusts and large wavelength buckle folds away from the thrusts where thrust-related shear strains are not significant. Hence the anticlines show asymmetric fold geometry (wavelength small, amplitude large; steep southern limb and a gentle northern limb) with a pinched appearance (Gansser 1964) whereas the synclines show broad open fold geometry (wavelength large, amplitude small). The superposed folds are represented by weakly developed dome and basin pattern. In vicinity of oblique ramps, the fold hinge lines are markedly curved. Some of the faults occur along the anticlinal fold hinge lines (Raiverman 2002). Back thrusts have developed at a later stage of development of foreland propagating listric thrusts. Presence of these faults, development of syntectonic veins and flexural-slip mechanism of folding suggest that the deformation has taken place at comparatively upper levels of the earth's crust in a predominant brittle regime. The subsurface structures (Raiverman et al. 1995) reveal that the plane of decollement at the pre-Tertiary–Tertiary boundary is not prominent as the contact is involved in thrusting and also marked by decollement upwarps (Chap. 4).

The Mio-Pliocene unroofing history of the Himalayan thrust belt in western Nepal reveals that the High Himalayan metamorphic rocks, K-feldspar and metasedimentary fragments have contributed to the Middle Siwalik deposition (~11–5.5 Ma), in response to displacement along the Main Central Thrust and the Ramgarh Thrust (≈Chail Thrust; De Celles et al. 1998). One of the activation phases of the Chail Thrust has been identified around 10 Ma in the Kangra region (Himachal foothill belt) and this has also contributed to the deposition (Sangode and Kumar 2003; Kumar et al. 2004).

In central part of the Kangra recess (oblique fault ramp), there is a prominent rhomboid shaped pull-apart basin containing Tertiary and subsidiary Siwalik rocks. Presence of these rocks suggests that the pull-apart basin has formed simultaneously with thrusting at the frontal ramps. The basin shape lies between basin nucleation and lazy-z-shape (Mann et al. 1983). The characteristic age relationship of successively younger rocks towards the middle of the basin (Crowell 1974)

cannot be established because of lack of systematic geochronological data for the rocks. Quaternary sediments suggest that deposition and basin development continued into the Pleistocene (Srivastava and Sah 1993). At some distance from the pull-apart basin, outcrops of the Siwalik rocks gradually straightens out and follows a NW-SE trend near the Himalayan Frontal Thrust (HFT). At the southern end of the Kangra recess (termination of the oblique thrust ramp), the foothill belt is marked by a number of imbricate thrust faults along which rocks of the Subathu Formation and the Dharamsala Group have come in contact with the Siwalik Group.

Since the southern boundary of the Siwalik rocks is marked by a thrust (HFT), the southern face is steep as compared to the northern gentle slope where a large number of synclinal structures have developed along the strike of the thrust. These synclinal valleys are called as duns (e.g. Dehra Dun, Pinjaur Dun, Solan Dun etc.). Dehra Dun (or Dehradun) area is also characterized by a small recess structure (Fig. 10.1). The lithostratigraphy exhibits coarsening upward succession and comprises of the Middle Siwalik (sandstone-dominated) and Upper Siwalik (conglomerate-dominated) formations.

A large number of conjugate strike-slip faults, oblique to the fold hinge lines, have divided the foreland into a number of blocks. The relative displacement along these faults suggests that some of these faults have formed during the early deformation (Tapponnier and Molnar 1976) whereas the others have formed during the superposed deformation (Jayangondaperumal et al. 2010). The later strike-slip faults were regarded as the youngest structures (Nakata 1989) but now normal faults have been identified as the youngest structure (Srivastava and John 1999; Kandpal et al. 2006). Efforts have been made to estimate the relative tectonic rotations amongst these faulted blocks (Sangode et al. 1999) using the mean of palaeomagnetic directions (direction-space approach) from the magneto-stratigraphically constrained sections but more data are needed to obtain a regional picture of the rotational pattern.

The Ganga and Yamuna Tear faults lie to the east and west of Dehradun region, respectively (Fig. 10.1). Extension of the Dehradun oblique ramp (OR) can be seen in the Doon valley, NE of Nagsidh Hill. A sub-parallel oblique slip right lateral fault (E2) is exposed SE of the Hill. The western side of the MBT (trailing frontal ramp) is characterized by three subsidiary thrusts, i.e. Santurgarh Thrust (ST), Majhaun back Thrust (MT), and Bhauwala Thrust (BT). The Santurgarh Thrust was initiated post 500 Ka and the Bhauwala Thrust between 29 and 20 Ka (Thakur and Pande 2004).

The most prominent early fold in the Siwalik foothill belt is Mohand asymmetric anticline which initiated as a fault propagation fold along the HFT (Raiverman et al. 1983). Displacement along the Santurgarh Thrust resulted in Santurgarh anticline. A few noncylindrical folds developed in eastern part of the area (i.e. Raiwala anticline, R, and subsidiary synclines) plunge towards the Ganga Tear (Raiverman 2002).

A series of right lateral oblique-slip normal faults trending NE–SW (e.g. Ganga Tear, S1, S2, S3; Fig. 10.1) (footwall on the eastern side) and complimentary left lateral oblique-slip faults trending NW–SE (e.g. Yamuna Tear) are exposed in the area

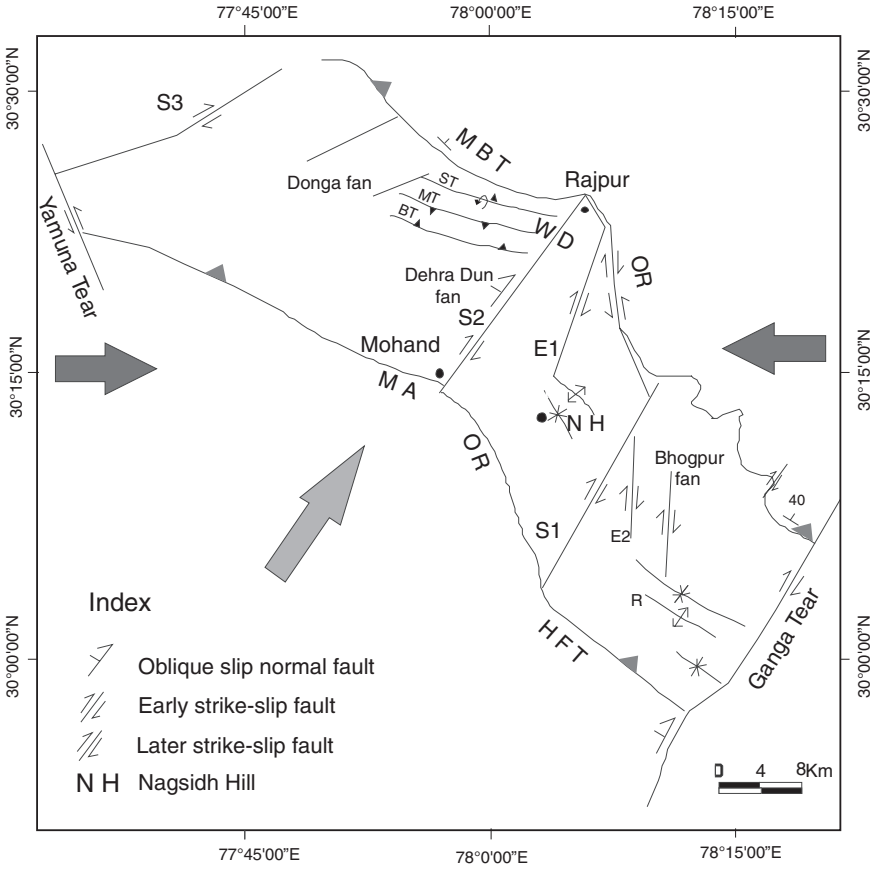

Fig. 10.1 Structural lineaments of Dehradun valley (Garhwal Himalaya) between the rivers Yamuna and Ganga drawn from IRS-1D PAN imagery (resolution 5.6 m). The *gray* and *black arrows* represent the axis of maximum compression during the early and superposed deformations, respectively. *ST* Santurgarh Thrust; *MT* Majhaun Thrust; *BT* Bhauwala Thrust; *OR* oblique ramp; *MA* Mohand anticline; *R* Raiwala anticline; *WD*, water divide; *E*1 *E*2, early structures; *S*1, *S*2, *S*3 superposed structures. The Saharanpur bench mark is located ~50 km *SW* of Dehradun (after Jayangondaperumal et al. 2010)

(Arur and Hasija 1986). The difference in vertical relief across the faults is clearly visible in field, PAN imagery, and topographic map (Raiverman 2002) as older Siwalik rock on the western side and younger alluvium on the eastern side. One of these faults (S2), between Rajpur and Mohand, acts as water divide in the area.

The HFT is responsible for upliftment of the Tertiary and Siwalik Group of rocks. Recent geomorphological and paleoseismic studies reveal that the long term slip-rate along the HFT is 20 ± 3 mm/year in central Nepal (Lave and Avouac 2000; Mugnier et al. 2004), 13.8 ± 3.16 mm/year near Mohand, south of Dehradun (Wesnousky et al. 1999), 14 ± 2 mm/year in Kangra

reentrant, 11 ± 5 mm/year across the Dehradun reentrant (Powers et al. 1998), 9.62 + 7.0/−3.5 along southern Himachal foothills (the Black mango tear fault; Kumar et al. 2001), and 6.3 ± 2 mm/year near Chandigarh (Malik and Nakata 2003). The data suggest a general increase from NW to the Central (Nepal) Himalaya.

The HFT folds and displaces the late Holocene sediments at several places in the western Himalaya. Paleoseismic studies at some of these sites (Kumar et al. 2006) using freshly dug trenches estimated a vertical uplift rate of ~4–6 mm/year as a result of slip on an underlying thrust dipping at ~20°–45°. This is equivalent to fault slip rates of ~6–18 mm/year or shortening rates of ~4–16 mm/year. Radiocarbon ages of samples taken from the displaced Holocene sediments suggest surface ruptures at the studied sites after ~A.D. 1,200 and prior to ~A.D. 1,700. Similar uplift rates, measured by abandoned terraces of the Markanda River (Himachal Pradesh), were estimated to be 4.8 ± 0.9 mm per year or more since the mid-Holocene (Kumar et al. 2001). In the Siwalik Hills of central Nepal, uplift of up to 1.5 cm/year was estimated from river incision (Lave and Avouac 2000). In the Punjab Himalaya, topography of the Chandigarh anticlinal ridge was generated as a result of coseismic deformation produced by cumulative slip of repeated earthquakes recurring at every 1,000 years interval between 0.1 and 0.5 Ma.

Increase in thickness of the Siwalik sediments in the central Himalaya has been correlated with acceleration of surface erosion in the hinterland part. The erosion and basin deposition have increased since the Late Miocene (Wang et al. 2010).

10.3 Results of Cross-Section Balancing

A geological map of the area, along with location of different transects is shown in Fig. 10.2. The cross-sections were restored by the line length balancing technique (Ramsay and Huber 1987). Transects 1 and 4 were restored by Powers et al. (1998) and the rest by Dubey et al. (2001). A short description of the sections is provided here.

10.3.1 Transect One

Transect one extends from Hoshiarpur (Punjab) to Palampur (Himachal Pradesh) (Fig. 6 in Powers et al. 1998). The Lower Himalayan sequence of rocks pinches in the northern part of the transect and is exposed only for a short distance of 2–3 km. The sequence is followed by Tethyan rocks across the Panjal Thrust. The transect is at a distance of ~55 km from the Central Crystalline rocks in N–S direction. A shortening of 22 % or 23.4 km was envisaged along the transect.

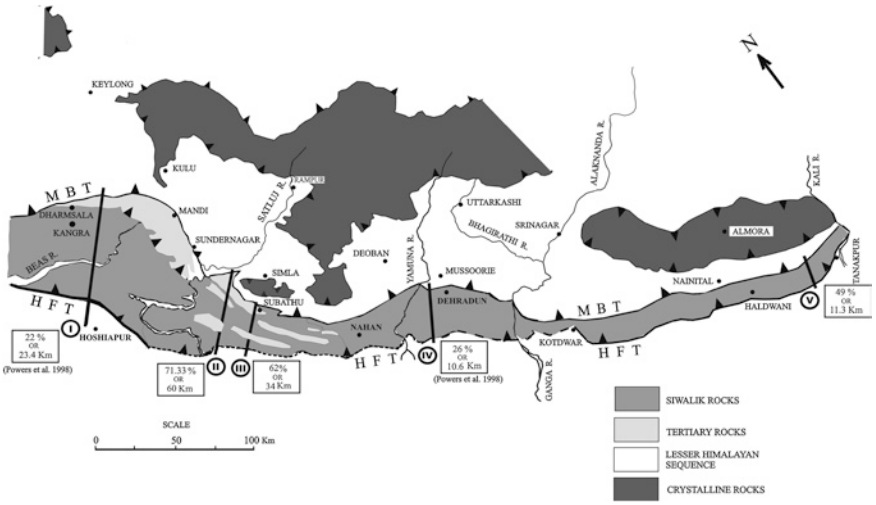

Fig. 10.2 A geological map of the Western Himalaya showing locations of different cross-sections (*encircled numbers*) and estimated shortenings along them. [From Dubey et al. (2001), © Elsevier. Published with permission of Elsevier]

10.3.2 Transect Two

The section falls in Himachal Pradesh, south of the Satluj (also Sutlej) River. Deformed and restored cross-sections along the transect are shown in Fig. 10.3. The Cheri asymmetric anticline is an initial fault propagation fold in which the thrust has later propagated through the fold hinge. The Mundkhar syncline occurs as a pop-up structure between the foreland propagating Nalagarh Thrust and the Barsar back thrust. Northeast of Cheri anticline, the beds show a consistent dip towards NE. Exposure of the pre-Tertiary and Subathu formations, NE of the Bilaspur Thrust, suggests a larger displacement along the thrust. In view of repetition of Subathu rocks and their parallelism with the adjacent thrust, the section could not be balanced after the Surajpur Thrust. Other problems in restoration of the section were thickness variation of the beds across the Cheri anticline and other thrusts, and involvement of pre-Tertiary rocks in the thrusting. The Subathu rocks appear to continue beneath the MBT.

A shortening of 71.3 % or 60 km was estimated from the balanced section (Fig. 10.3). The estimated shortening amount is intriguing, because cleavage is not developed in the rocks, no consideration is made for initial layer parallel shortening, volume reduction, displacement out of the tectonic transport direction, inversion tectonics, etc.

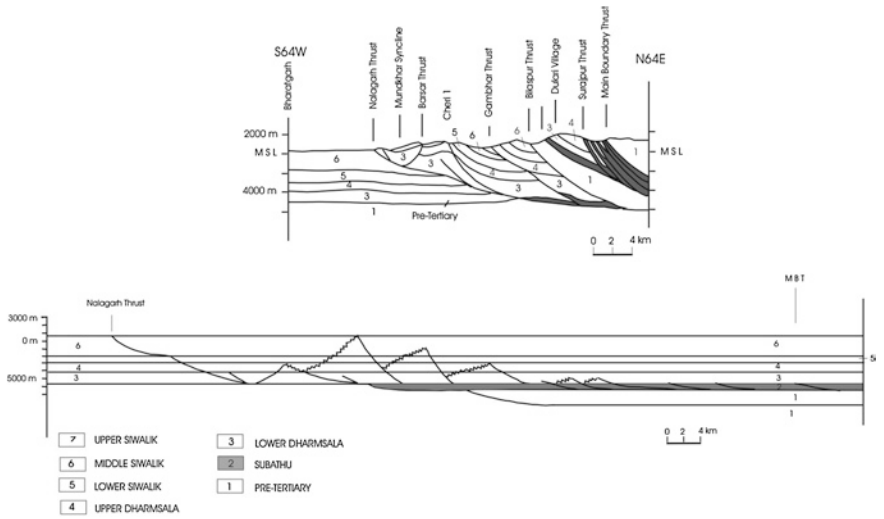

Fig. 10.3 Deformed (Task Force, Oil and Natural Gas Corporation 1998) and restored cross-sections of transect two. [From Dubey et al. (2001), © Elsevier. Published with permission of Elsevier]

10.3.3 Transect Three

The transect incorporates a geological cross-section of the Subathu depression, Himachal Pradesh. The deformed section (Fig. 10.4) represents an energy sequence or time stratigraphic units. The concept of energy sequence was introduced in the Himalaya by Raiverman et al. (1983) for rock units deposited at a specific time in the foothill belt.

The contact between the pre-Tertiary and E1 sequence (equivalent to the Subathu rocks) is marked by an unconformity. The decollement plane lies inside the pre-Tertiary rocks, that are involved in imbricate thrusting. The maximum displacement occurs along the Bilaspur Thrust where the pre-Tertiary rocks are in contact with E5 sequence. The other displacements are of the order of several meters to few kilometers. Thickness of E1 sequence increases in northeasterly direction and the rocks continue beneath the MBT. The estimated shortening amount between Paonta thrust and the Krol thrust (MBT) is 62 % or 34 km. However the following points should be noted.

1. The depicted lengths of the thrust faults have to be manipulated considerably in order to balance the section. Hence the shortening amount is not precise.
2. In contrast to the previous sections, the basal decollement is within the pre-Tertiary (PT) rocks.
3. The rocks are different on either side of the Bilaspur thrust hence the fault displacement shown is approximate.

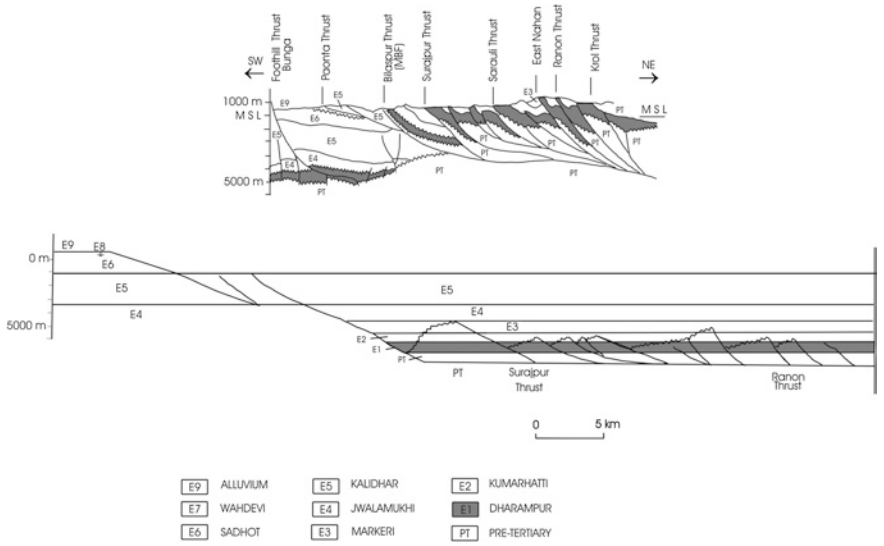

Fig. 10.4 Deformed (Raiverman et al. 1995) and restored cross-sections of transect three. [From Dubey et al. (2001), © Elsevier. Published with permission of Elsevier]

10.3.4 Transect Four

Transect four (Powers et al. 1998) incorporates the Dehradun valley in the Garhwal Himalaya. The anticlines are sharp having a pinched appearance (e.g. Mohand Anticline and Santurgarh Anticline) divided by a broad synclinal structure (i.e. Doon Syncline) suggesting that these folds were formed as fault propagation folds. A shortening of 26 % or 10.6 km was estimated along the restored section.

10.3.5 Transect Five

The transect incorporates the Tanakpur area, Kumaun Himalaya (Fig. 10.5). Energy sequences are shown in the deformed section where the oldest Tertiary sequence (No. 1) is equivalent to the Subathu Formation. The pre-Tertiary–Tertiary boundary is marked by an unconformity and the pre-Tertiary rocks are also involved in imbricate thrusting. The section displays variable thickness of the pre-Tertiary rocks above the decollement indicating that the decollement is not a planar surface. The southerly dipping beds suggest the possibility of a growth fold. The maximum displacement of 5.25 km occurs along the MFT whereas displacements of 1.65 and 0.26 km occur near the MBT. The other fault

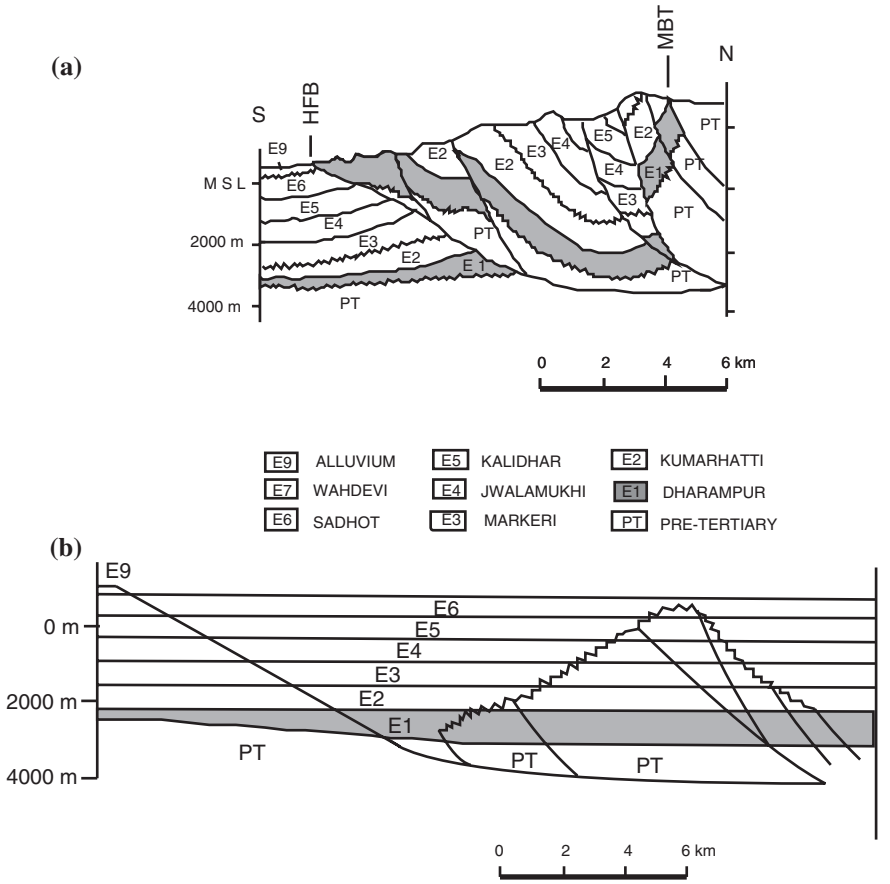

Fig. 10.5 Deformed (Raiverman et al. 1995) and restored cross-sections along transect five. [From Dubey et al. (2001), © Elsevier. Published with permission of Elsevier]

displacements are <1 km. The cumulative fault displacement is 8.09 km for a cross-section length of 5.25 km. A shortening of 49 % or 11.3 km was estimated from the restored section.

The various crustal shortening estimates from the western Himalaya are shown in Fig. 10.2. The variation in shortening amounts from 22 to 71.3 % (or 10.6–60 km) over a lateral distance of ~85 km is intriguing as none of the tectonic models can explain such a large variation over a short distance. A large number of plates moving with different rates and separated by strike-slip faults (transform faults!) can possibly suggest a solution but in the Himalayan belt, the entire compression is attributed to a single plate (the northward moving Indian plate). Even a conceptual model involving rotation of the plate cannot account for the enormous variation in shortening over a small distance.

10.4 Possible Sources of Error

Some of the possible reasons that can account for the shortening variations are summarized as follows.

1. The sections are not parallel to the tectonic transport direction.
2. Some of the sections are situated in vicinity of oblique fault ramps. For example, transects 1, 2 and 3 are close to the Kangra recess and transect 4 is across the Mohand and Dehradun recesses. However no consideration is made for oblique-slip displacement along the thrusts.
3. Palaeomagnetic data are not available for determination of rotation of thrust sheets about the vertical axis (cf. McCaig and McClelland 1992).
4. Some of the seismic lines are disconnected and the sections are completed by extrapolating the surface geological information.
5. Initial compaction and layer parallel shortening at the outset of deformation are not taken into account (Ramsay 1997). Since there is no lubricating horizon for easier slip along the Sub Himalayan thrust surfaces, the layer parallel shortening is likely to be of significant amount. Further, no consideration is made for variation of ratio of buckle shortening to layer parallel strain across the multilayer profile (cf. Dubey and Bhakuni 1998).
6. Presence of superposed folds and strike-slip faults is ignored. These structures suggest shortening or extension normal to the plane of cross-section thereby resulting in deviation from the plane strain deformation.
7. Initial extension during normal faulting of the rift phase has not been taken into account. It is to be noted that the Tertiary compressional phase of the Himalayan orogeny led to reactivation of the early normal faults as thrusts and brought the fault blocks closer to the null point (i.e. the point of change from net extension to net contraction; Williams et al. 1989). Since the method of restoration considers the beds as initially horizontal, a large amount of initial shortening prior to their restoration at the null point has not been taken into account.

In order to further understand the estimated large variations over short distances, one has to look deeper into the process of development of a foreland basin.

10.5 Development of a Foreland Basin

A classical model for evolution of foreland basin was proposed by Beaumont (1981). The model envisages development of a thrust fault during collision of two continents. The hanging wall of the thrust acts as advancing orogenic load and forms a depression (down warping) in the footwall as foreland basin. During development of the thrust, eroded material is deposited in the foreland basin. If the erosion and deposition are rapid in a gradually subsiding basin, the result is a shallow deposition sequence even in a deep basin. The foreland basin and the peripheral forebulge (a domal structure) advance and gradually migrate

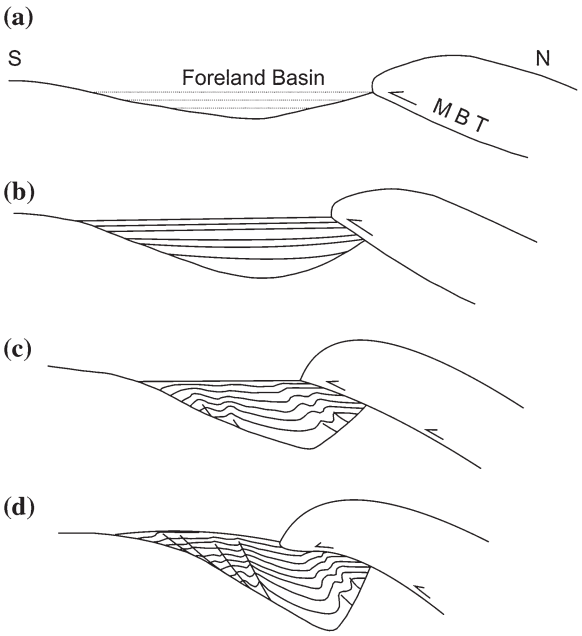

Fig. 10.6 Stages in development of the Himalayan foreland basin. **a** Displacement along the basin boundary thrust (*MBT*) and initiation of foreland basin. *N* north; *S* south. **b** Advancement of orogenic load and deepening of the basin causing synclinal structure with a greater thickness of the beds above the depocentre. **c** Increase in displacement along the boundary thrust, initiation of thrusts from the basement-cover interface, and initiation of fault propagation folds. **d** Further deepening of the basin with advancing orogenic load and amplification of the fault propagation folds. It is to be noted that straightening of the older beds during restoration will unravel a higher shortening as compared to the younger beds. [From Dubey et al. (2001), © Elsevier. Published with permission of Elsevier]

cratonwards, with the depocentre of the basin remaining close to the advancing thrust stack. The model forms a basis for proposing a model for evolution of the Siwalik foreland basin.

The Himalayan foreland basin has evolved by a combination of flexural bending of the Indian plate margin and thrust faulting (Lyon-Caen and Molnar 1983; Najman et al. 1993; Burbank et al. 1994; Singh 1999; Beaumont 1981; Meigs 1997; Storti et al. 1997). Stages in evolution of the basin are shown in Fig. 10.6. Initiation of the basin started in the Eocene times with displacement along the MBT (the basin margin thrust) and development of a flexure in front of the rising mountain (Fig. 10.6a). Increase in displacement along the basin margin thrust leads to gradual subsidence of the basin, synformal curvature of the older beds and deposition of younger beds (Fig. 10.6b). With progressive deformation, thrust faults initiate inside the basin (Fig. 10.6c). Upward propagation and displacement along these thrusts produce fault propagation folds (Fig. 10.6d) with south vergence. Some of the thrusts in the northern flank of the basin may be overlapped by

the advancing orogenic load along the basin margin thrust. Since older beds show a greater synformal curvature, unfolding of these beds during restoration would reveal a greater shortening as compared to the younger beds.

The thrust displacements and basin subsidence act simultaneously and control transgression and regression in the basin, depending on locations of the depocentre and active thrust(s). This may also result in thickness variation across the thrusts. The southward displacement along the MBT is likely to result in a southern shift of the depocentre and gradual reactivation of thrusts towards south. Detachment or listric faults can emanate from the basement-cover interface at late stages of the evolution.

The width and depth of the foreland basin depend upon thickness and rheological properties of the foreland lithosphere, size and weight of the hanging wall load, nature of the sedimentary fill, rate of convergence, and slip rate along the boundary thrust (Burbank et al. 1994).

10.6 Corrections to be Applied

The relationships between depth of a basin and possible error in restoration can be established using simple trigonometry, as follows.

10.6.1 Case 1

Figure 10.7 shows an inclined layer AB dipping at an angle θ. The layer inclination is a result of subsidence during basin evolution. Considering that there is no change in its length during the subsequent compressional phase, the layer will be rotated to a position AC (AB = AC) during restoration. The result will be a greater shortening

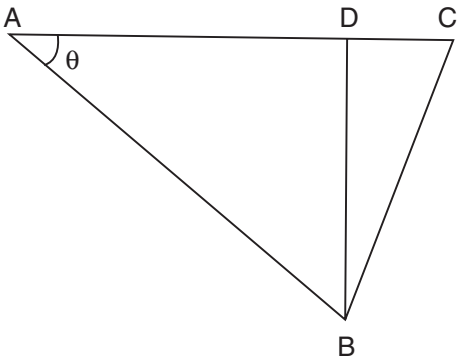

Fig. 10.7 A geometric representation of an inclined layer (*AB*) rotated to a horizontal position (*AC*) during restoration (after Dubey et al. 2001)

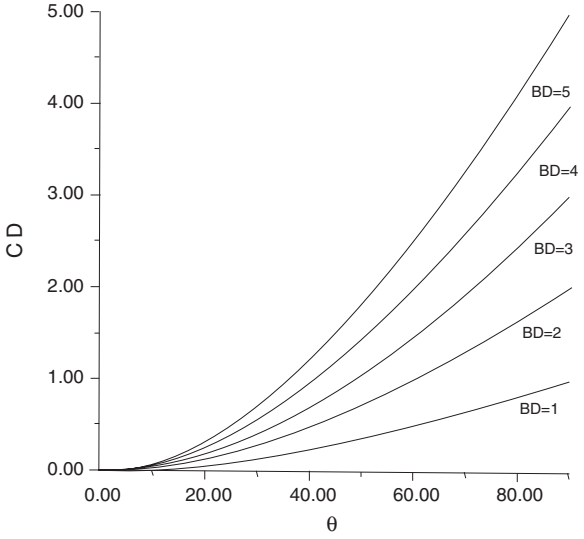

Fig. 10.8 Relationships of estimated excess shortening (*CD*) with different amounts of layer dip (θ) and maximum depth of the layer (*BD*). [From Dubey et al. (2001), © Elsevier. Published with permission of Elsevier]

estimate and the distance CD will provide the amount of error. The trigonometric relationship reveals that

$$CD = AB\,(1 - \cos\,\theta)$$

Hence the error CD depends upon length of the layer AB and its dip amount. These two factors also control the maximum depth of the section (or depth of the depocentre). The relationship is shown graphically in Fig. 10.8. It is apparent from the diagram that the estimated error (CD) is minimum up to 10° layer dip and increases rapidly with increase in dip. The error shows an explosive increase at greater depths and higher dips. The relationship can be used when a part of the basin is covered by the advancing basin boundary thrust and the initial disposition of the layer is known.

10.6.2 Case 2

The method can be applied when subsidence of a basin results in symmetric fold geometry and the fold interlimb angle is known.

Figure 10.9 demonstrate an initial symmetric fold ABC with an interlimb angle 2θ, formed during the basin subsidence. Unfolding of the fold will reveal a greater shortening amount because the real shortening should be measured with reference to AC, as follows:

$$AC = (AB + BC)\,\sin\,\theta$$

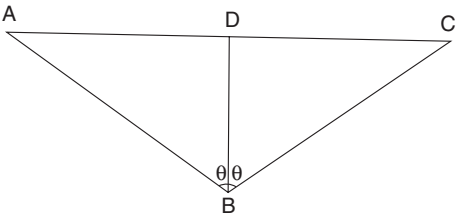

Fig. 10.9 A geometric representation of layer *ABC* folded symmetrically during subsidence of a basin, maximum depth of the layer (*BD*), and distance *AC*, which should be considered as initial length of the layer for estimation of shortening (after Dubey et al. 2001)

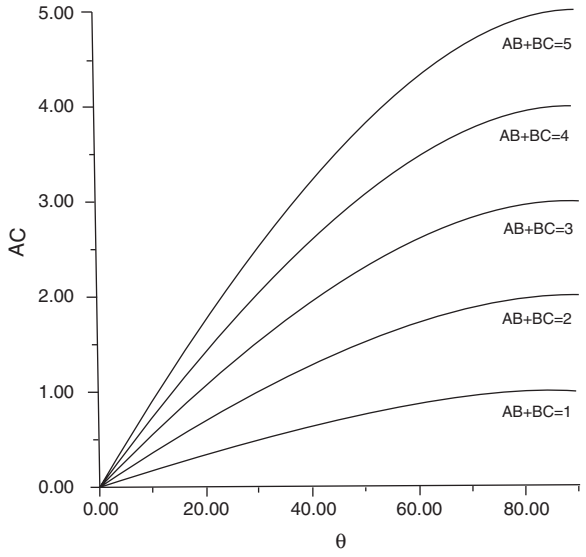

Fig. 10.10 Variation of initial reference length (*AC*) with different fold limb lengths and angles between fold limb and axial plane. [From Dubey et al. (2001), © Elsevier. Published with permission of Elsevier]

The above relationship, shown graphically in Fig. 10.10, demonstrates that the rate of increase in AC is higher for large limb lengths and low interlimb angles. Hence a greater subsidence (i.e. small interlimb angle) in a large basin (i.e. large fold limbs) is likely to provide a greater error in the shortening estimate.

Similar relationships for an asymmetric fold are shown in Fig. 10.11. The real shortening can be calculated from the following relationship and its graphical representation (Fig. 10.12) provided the angles θ_1, θ_2, and depth of the basin (BD) are known.

$$\mathrm{AC} = \mathrm{BD}\ (\tan\theta_1 + \tan\theta_2)$$

Present knowledge of the Himalayan foreland basin is still in its infancy and data are not available on depth of the basin, three dimensional basin geometry,

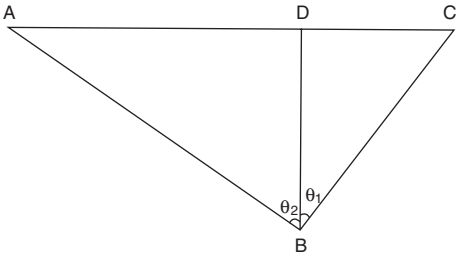

Fig. 10.11 A geometric representation of layer *ABC* folded asymmetrically during subsidence of a basin, maximum depth of the layer (*BD*), and distance *AC*, which should be considered as initial length of the layer for estimation of shortening (after Dubey et al. 2001)

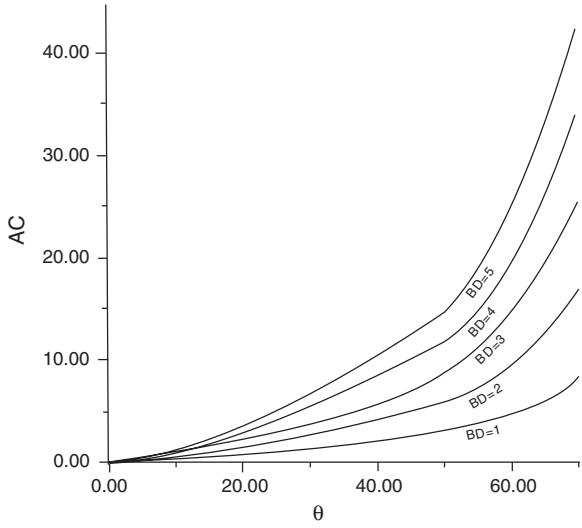

Fig. 10.12 Relationships of initial reference length (*AC*) with maximum depth of the layer (*BD*) and angle θ (θ_1 or θ_2). [From Dubey et al. (2001), © Elsevier. Published with permission of Elsevier]

extension of the basin beneath the Lower Himalaya, total displacement and displacement rates along the MBT, and load of the Lower Himalayan hanging wall rocks at the basin margin. Hence the suggested corrections cannot be applied to the estimated shortenings.

10.7 The Estimated Crustal Shortening with Reference to Distance from the Central Crystalline Thrust

A better understanding of the shortening estimates emerges when a High Himalayan crystalline thrust is taken into consideration. The estimated shortenings are plotted against the minimum distance between the MBT and the

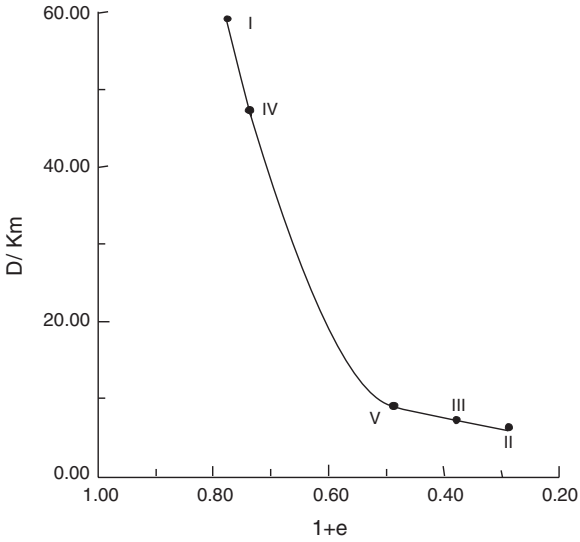

Fig. 10.13 Relationships between shortening $(1 + e)$ and distance (D) between the *MBT* and a central crystalline thrust. The transect numbers are shown on the diagram. [From Dubey et al. (2001), © Elsevier. Published with permission of Elsevier]

MCT (/Chail Thrust/Jutogh Thrust/South Almora Thrust/Central Crystalline rocks of the High Himalaya) along linear continuity of the transect line (Fig. 10.13). The relationship shows that the estimated shortening amounts appear to depend upon the distance (D) between the foreland basin and the Central Crystalline rocks. A smaller distance (i.e. large displacement) results in greater shortening and vice versa. The observation leads to the following inferences.

1. The basin geometry is controlled not only by the basin boundary (margin) thrust (i.e. MBT) but also by a major thrust in the hinterland (i.e. MCT),
2. A large displacement in the hinterland thrust results in a deeper foreland basin and a deeper basin leads to a larger error by providing higher shortening estimates.
3. Results obtained from balancing a few isolated sections in a large region can be misleading because of three-dimensional variation in the basin geometry.
4. The present shortening estimates are deceptive and provide an unsound basis for strain rates and earthquake prediction.

10.8 Smooth Trajectory Thrust Versus Flat and Ramp Structure

In addition to the above, the technique of restoration unfolds and balances a section by bringing in the flat and ramp geometry of the thrust even though the initial thrust may be a smooth trajectory thrust as shown below.

Sequential restoration of a deformed layer is shown by a simple model in Fig. 10.14 (Cooper et al. 1989). Figure 10.14a shows a folded layer with a thrust

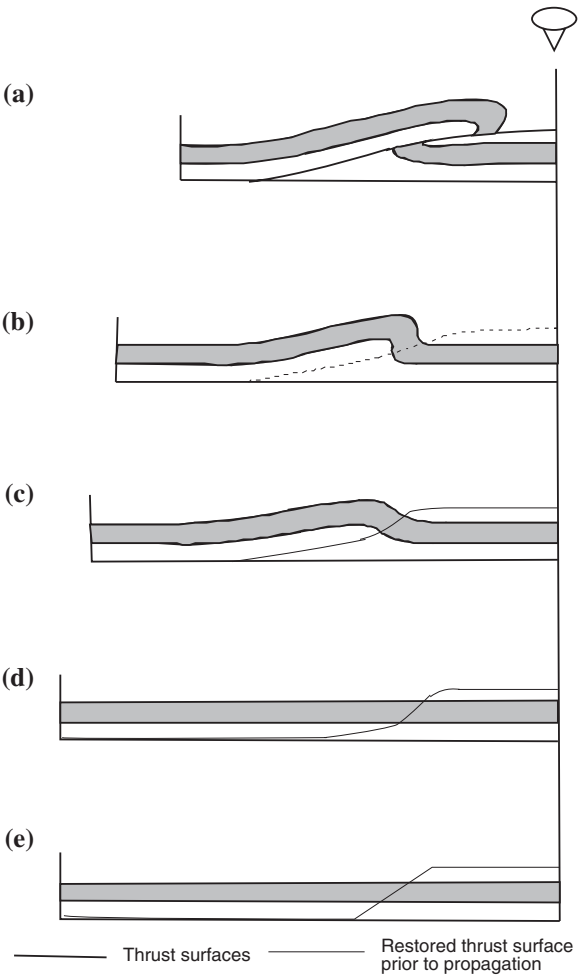

Fig. 10.14 Sequential restoration of a simple fold and thrust structure assuming a basal decollement. **a** The deformed state. **b** No thrust displacement, i.e. prior to propagation of the thrust from the decollement. **c** Fold initiation prior to thrusting. **d** Restoration of the thrust trace onto the stratigraphic template. **e** Restoration of the section based on thin-skinned tectonics. [From Cooper and Trayner (1986), © Elsevier. Published with permission of Elsevier]

fault. Figure 10.14b displays a stage of restoration when the layer is brought to a position prior to thrust displacement. The layer is then gradually unfolded (Fig. 10.14c) and brought to a position of an accurate restoration of the thrust trace onto the stratigraphic template (Fig. 10.14d). The ideal restoration of the thrust trace as per the thin-skinned tectonics model is shown in Fig. 10.14e where the initial smooth trajectory thrust assumes a flat and ramp geometry. It is clear from the illustration that restoration of deformed sections from fold-and-thrust belts results in staircase trajectory onto the stratigraphic template though the initial thrust may deviate significantly from the flat and ramp geometry. It is also to be noticed that all the sections in the Himalaya do not have a plane of basal decollement.

In view of the above, one can conclude that the technique of restoration of deformed cross-sections is useful but the results are based on over-simplification.

They cannot accommodate such real phenomena as erosion, syn-orogenic sedimentation, compaction, pressure solution, veining, halotectonics (salt tectonics), igneous intrusions, non-isochoric strain (where volume is not preserved), strike-slip faulting, and structural inversion.

The problems associated with restoration of deformed sections were already known to the Himalayan workers but the warning note was largely ignored. Searle (1986) had pointed out that the amount of inference (fiddling) that has to be made while restoring a section is unacceptably great. This comment was made with reference to the Ladakh and Zanskar regions but it is equally applicable to other parts of the Himalaya. Coward (1996) has also acknowledged that the earlier calculations for shortening across the frontal Himalaya (e.g. Coward and Butler 1985) considered only one component, the thin-skinned shortening due to plate collision, and hence the results are probably incorrect.

10.9 Future Directions of Research

In view of the above discussion, future directions of research should be focused on the following points (Kumar et al. 2011).

1. Importance of the Chail Thrust in evolution of the Foreland is also evident from the sedimentological studies of Ghosh et al. (2009). The sedimentary succession in the Kangra region consists of dark gray sandstone interbedded with purple mudstone in the lower part, overlain by salt-and-pepper grey sandstone, and variegated mudstone capped by thickly bedded conglomerate with minor amounts of coarse grained sandstone and mudstone. The sedimentologic parameters show change in palaeochannel pattern from meandering to braided streams at 10 Ma and inception of alluvial fan settings at around 5.5 Ma. A remarkable variation in detrital modes was also noticed between 10 and 9.0 Ma. The depocenter received high amount of Lower- and Sub-Himalayan footwall sedimentary and metasedimentary fragments prior to 10 Ma. After 10 Ma, the detritus from the metamorphic rocks of the Chail hanging wall became more abundant. The study inferred that the variations in the drainage pattern, sedimentation accumulation rate and detrital modes noticed in the 11–5.5 Ma part of HFB-fill of the Kangra sub-basin were collectively related to activity along the Chail Thrust at around 10 Ma and not to the MBT as proposed by Meigs et al. (1995).
2. Subsurface data are needed to establish the 3-D geometry of the Basin.
3. Investigations on exhumation history, using detrital mineral modes, are essential for understanding the late evolutionary aspects.
4. Detailed work on paleosols with reliable isotopic attempts is required for long term reconstructions on paleoclimate variability.
5. A high resolution stratigraphy of the conglomerate succession is needed for lateral correlations and deducing the accurate rates of gravel progradation and to trace the extra-dynamic climatic/tectonic events.

6. Integration of existing data and generation of new data are required for estimation of modern geomorphic parameters such as stream power.
7. Chronologically constrained regional data are required to establish a relationship between the foreland sedimentation of the Ganga basin and the Bay of Bengal.

The northern boundary of the Foreland Basin is marked by the Main Boundary Thrust (MBT).

References

Arur MG, Hasija NL (1986) Crustal movement studies across Ganga tear fault (in Siwalik) at Haridwar in Uttar Pradesh, India. In: Proceedings of international symposium on neotectonics in South Asia. Survey of India, Dehradun, pp 18–21

Beaumont C (1981) Foreland basins. Geophys J Roy Astron Soc 65:291–329

Burbank DW, Beck R, Mulder T (1994) The Himalayan foreland basin. In: Yin A, Harrison TM (eds) Tectonic evolution of Asia. Cambridge University Press, Cambridge, pp 149–188

Cooper MA, Trayner PM (1986) Thrust surface geometry: implications for thrust belt evolution and section balancing techniques. J Struct Geol 8:305–312

Cooper MA, Williams GD, de Graciansky PC, Murphy RW, Needham T, de Paor D, Stoneley R, Todd SP, Turner JP, Ziegler PA (1989) Inversion tectonics—a discussion, vol 44. In: Cooper MA, Williams GD (eds) Inversion tectonics. Special Publication Geological Society of London, London, pp 335–347

Coward MP (1996) Balancing sections through inverted basins. In: Buchanan PG, Nieuwland DA (eds) Modern developments in structural interpretation, validation and modelling, vol 99. Special Publication Geological Society of London, London, pp 51–77

Coward MP, Butler RWH (1985) Thrust tectonics and the deep structure of Pakistan Himalaya. Geology 13:417–420

Crowell JC (1974) Origin of the late Cenozoic basin in Southern California. In: Dickinson WR (ed) Tectonics and sedimentation, vol 22. Special Publication of Society of Economic Geologists, Paleontologists and Mineralogists, Tulsa, pp 190–204

DeCelles PG, Gehrels GE, Quade J, Ojha TP, Kapp PA, Upreti BN (1998) Neogene foreland basin deposits, erosional unroofing, and the kinematic history of the Himalayan fold thrust belt, western Nepal. Bulle Geol Soc Am 110:2–21

Dubey AK, Bhakuni SS (1998) Hangingwall bed rotation and the development of contractional and extensional structures around a thrust fault: geometric and experimental models. J Struct Geol 20:517–527

Dubey AK, Misra R, Bhakuni SS (2001) Erratic shortening from balanced cross-sections of the western Himalayan foreland basin: causes and implications for basin evolution. J Asian Earth Sci 19:765–775

Gansser A (1964) Geology of the Himalaya. Interscience, New York, 289 p

Ghosh SK, Sinha S, Kumar R (2009) Response of 10 Ma thrusting event in the Himalayan foreland sediments, Kangra sub-basin, Himachal Pradesh, India. Himalayan Geol 30:1–15

Jayangondaperumal R, Dubey AK, Sen K (2010) Structural and magnetic fabric studies of recess structures in the western Himalaya: Implications for 1905 Kangra earthquake. J Geol Soc India 75:225–238

Kandpal GC, Joshi KC, Joshi DD, Singh BK, Singh J (2006) Signature of Quaternary tectonics in a part of Dehra Dun valley, Uttaranchal. J Geol Soc India 67:147–150

Karunakaran C, Ranga Rao A (1979) Status of exploration for hydrocarbon in the Himalayan region—contributions to stratigraphy and structure. Himalayan Geology Seminar, New Delhi, 1976, section III, vol 41. Geological Survey of India Miscellaneous Publications, pp 1–66

Kumar R (1993) Coalescence megafan: multistorey sandstone complex of the late-orogenic (Mio-Pliocene) sub-Himalayan belt, Dehra Dun, India. Sed Geol 85:327–337
Kumar R, Ghosh SK (1994) Evolution of the Mio-Pleistocene alluvial fan system in the Siwalik foreland basin, Dehra Dun, India. In: Kumar R, Ghosh SK, Phadtare NR (eds) Siwalik foreland basin of Himalaya, vol 15. Himalayan Geology, pp 143–159
Kumar R, Ghosh SK, Sangode SJ (1999) Role of thrusting in the evolution of fluvial system, Himalayan foreland basin, India. In: Macfarlane A, Sorkhabi RB, Quade J (eds) Himalaya and Tibet: mountain roots to mountain tops, vol 328. Geological Society of America Special Publication, pp 239–256
Kumar R, Ghosh SK, Mazari RK, Sangode SJ (2003) Tectonic impact on fluvial deposits of Plio–Pleistocene Himalayan foreland basin, India. Sed Geol 158:209–234
Kumar R, Ghosh SK, Sangode SJ (2004) Depositional environment of Mio—Pleistocene coarse clastic facies in the Himalayan foreland basin, India. Himalayan Geol 25:101–120
Kumar R, Ghosh SK, Sangode SJ (2011) Sedimentary architecture of late Cenozoic Himalayan foreland basin fill: an overview, vol 78. In: Bhargava ON (ed) Facets of phanerozoic. Memoir of the Geological Society of India, pp 245–280
Kumar S, Wesnousky SG, Rockwell TK, Ragona D, Thakur VC, Seitz GG (2001) Earthquake recurrence and rupture dynamics of Himalayan Frontal Thrust, India. Science 294:2328–2331
Kumar S, Wesnousky SG, Rockwell TK, Briggs RW, Thakur VC, Jayangondaperumal R (2006) Paleoseismic evidence of great surface rupture earthquakes along the Indian Himalaya. J Geophys Res 111:B03304. doi:10.1029/2004JB003309
Lave J, Avouac JP (2000) Active folding of fluvial terraces across the Siwalik Hills, Himalaya of central Nepal. J Geophys Res 105:5735–5770
Lyon-Caen H, Molnar P (1983) Constraints on the structure of the Himalaya from an analysis of gravity anomalies and a flexural model of the lithosphere. J Geophys Res 88:8171–8191
Malik JN, Nakata T (2003) Active faults and related late Quaternary deformation along the northwestern Himalayan frontal zone India. Ann Geophys 46:917–936
Mann P, Hampton MR, Bradley DC, Burke K (1983) Development of pull-apart basins. J Geol 91:529–554
McCaig AM, McClelland E (1992) Palaeomagnetic techniques applied to thrust belts. In: McClay KR (ed) Thrust tectonics. Chapman & Hall, London, pp 209–216
Meigs AW (1997) Sequential development of selected pyrenean thrust faults. J Struct Geol 19:481–502
Meigs AJ, Burbank DW, Beck RA (1995) Middle-late miocene (>10 Ma) formation of the Main Boundary Thrust in the western Himalaya. Geology 23:423–426
Mugnier J-L, Huyghe P, Leturmy P, Jouanne F (2004) Episodicity and rates of thrust-sheet motion in the Himalaya (Western Nepal). In: McClay KR (ed) Thrust tectonics and hydrocarbon systems, vol 82. Memoir American Association of Petroleum Geologists, pp 91–114
Najman Y (2007) Comment on biochronological continuity of the paleogene sediments of the Himalayan foreland basin: paleontological and other evidences—Bhatia SB, Bhargava ON (2006) JAES 26:477–487. J Asian Earth Sci 30:417–421. doi:10.1016/j.jseaes.2006.12.001
Najman Y, Clift P, Johnson MRW, Robertson AHF (1993) Early stages of foreland basin evolution in the Lesser Himalaya, N. India, Himalayan tectonics. In: Treloar PJ, Searle MP (eds) Himalayan tectonics, vol 74. Special Publication Geological Society of London, London, pp 541–558
Nakata T (1989) Active faults of the Himalaya of India and Nepal. Geol Soc Am Spec Pap 232:243–264
Powers PM, Lillie RJ, Yeats RS (1998) Structure and shortening of the Kangra and Dehra Dun re-entrants sub-Himalaya India. Geol Soc Am Bull 110:1010–1027
Quade J, Cater JML, Ojha TP, Adam J, Harrison TM (1995) Late Miocene environmental change in Nepal and the northern Indian subcontinent: stable isotope evidence from Paleosols. Bull Geol Soc Am 107:1381–1397
Raiverman V (2002) Foreland sedimentation in Himalayan tectonic regime: a relook at the orogenic process. Bishen Singh Mahendra Pal Singh, Dehra Dun, 378 p

Raiverman V, Kunte SV, Mukherjea A (1983) Basin geometry, Cenozoic sedimentation and hydrocarbon prospects in northwestern Himalaya and Indo-Gangetic plains. Petrol Asia J 6:67–92
Raiverman V, Ganju JL, Ram J, Mishra VN (1990) Geological map of Himalayan Foothills between Ravi and Yamuna rivers. Scale 1:250,000. Oil and Natural Gas Corporation, Dehra Dun
Raiverman V, Srivastava AK, Prasad DN (1995) On the foothill thrust of northwestern Himalaya. Himalayan Geol 16:237–256
Ramsay JG (1997) The geometry of a deformed unconformity in the Caledonides of NW Scotland. In: Sengupts S (ed) Evolution of geological structures in micro to macro-scales. Chapman & Hall, London, pp 445–472
Ramsay JG, Huber MI (1987) The techniques of modern structural geology, vol II. Folds and fractures. Academic Press, Waltham, pp 309–700
Ranga Rao A (1993) Magnetic-polarity stratigraphy of Upper Siwalik of north-western Himalayan foothills. Curr Sci 64:863–873
Ranga Rao A, Agarwal RP, Sharma VN, Bhalla MS, Nanda AC (1988) Magnetic polarity stratigraphy and vertebrate palaeontology of the Upper Siwalik Subgroup of Jammu hills. J Geol Soc India 31:361–365
Sangode SJ, Kumar R (2003) Magnetostratigraphic correlation of the late Cenozoic fluvial sequences from NW Himalayans India. Curr Sci 84(8):1014–1024
Sangode SJ, Kumar R, Ghosh SK (1999) Palaeomagnetic and rock magnetic perspectives on the post-collisional continental sediments of the Himalaya, India. In: Radhakrishna T, Piper JDA (eds) The Indian subcontinent and Gondwana: a palaeomagnetic and rock magnetic perspective, vol 44. Memoir Geological Society of India, pp 221–248
Sanyal P, Bhattacharya SK, Prasad M (2005) Chemical digenesis of Siwalik sandstone: isotopic and mineralogical proxies from Surai Khola section. Nepal Sediment Geol 180:57–74
Searle MP (1986) Structural evolution and sequence of thrusting in the High Himalayan, Tibetan-Tethys and Indus Suture Zones of Zanskar and Ladakh, western Himalaya. J Struct Geol 8:923–936
Singh IB (1999) Tectonic control on sedimentation in Ganga Plain Foreland Basin: constraints on Siwalik sedimentation models. In: Jain AK, Manickvasagam RM (eds) Geodynamics of the NW Himalaya, vol 6. Gondwana Research Memoir, pp 247–262
Srivastava DC, John G (1999) Deformation in the Himalayan frontal fault zone: evidence from small-scale structures in Mohand-Khara area, NW Himalaya. Gondwana Res Group Mem Osaka J 6:273–284
Srivastava RAK, Sah MP (1993) The Sundernagar basin of Himachal Himalaya: its pull-apart nature and palaeoclimatology. (Abstract), Seminar on Himalayan Geology and Geophysics. Wadia Institute of Himalayan Geology, Dehra Dun, pp 72–73
Storti F, Salvini F, McClay K (1997) Fault-related folding in sandbox analogue models of thrust wedges. J Struct Geol 19:583–602
Tapponnier P, Molnar P (1976) Slip-line field theory and large-scale continental tectonics. Nature 264:319–324
Thakur VC, Rawat BS (1992) Geological map of the western Himalaya. Scale 1:1,111,111. Wadia Institute of Himalayan Geology, Dehradun
Thakur VC, Pande AK (2004) Late Quaternary tectonic evolution of Dun in fault bend propagated fold system, Garhwal Sub-Himalaya. Curr Sci 87:1567–1576
Valdiya KS (1998) Geodynamic Himalaya. Universities Press, Hyderabad, 178 p
Wang A, Garver JI, Wang G, Smith JA, Zhang K (2010) Episodic exhumation of the Greater Himalayan Sequence since the Miocene constrained by fission track thermochronology in Nyalam, central Himalaya. Tectonophysics 495:315–323. doi:10.1016/j.tecto.2010.09.037
Wesnousky SG, Kumar S, Mohindra R, Thakur VC (1999) Uplift and convergence along the Himalayan frontal thrust of India. Tectonics 18:967–976
Williams GD, Powell CM, Cooper MA (1989) Geometry and kinematics of inversion tectonics. In: Cooper MA, Williams GD (eds) Inversion tectonics, vol 44. Geological Society London Special Publication, London, pp 3–15

Chapter 11
The Lower (Lesser) Himalaya

Abstract Litho-tectonic set-up and inverted metamorphism are described. A large number of curvatures in the trend of the Main Boundary Thrust are attributed to oblique fault ramps formed during the pre-Himalayan tensional regime. The pre-Himalayan origin of the curvatures differentiates it from arcuate structures observed in other fold and thrust belts of the world. A model is proposed for arcuate geometry of the Mandi-Karsog Pluton. The Kangra recess is the longest oblique ramp of the Himalaya. The structural evolution is proposed using a three-dimensional model. A comparison is made between petrofabric and magnetic strains measured in the region. Reasons for low magnitudes of magnetic strain are mentioned. Geometrical relationships are established between displacement along oblique fault ramps and displacement out of the tectonic transport plane. Models are proposed for allochthonous (Simla) and pop-up klippen (Satengal, Banali, and Garhwal) models along with field examples. The new evidence suggests that the actual thrust displacement is much less than the previously conceived large amounts. Using the structural data from the Uttarkashi area (Garhwal Himalaya) a model is proposed for simultaneous development of thrust and normal faults at different structural levels.

In the early literature (e.g. Auden 1937) the area was referred to as the Lower Himalaya but following Gansser (1964), the tectonic sub-division is also called as the Lesser Himalaya. It extends from the Main Boundary Thrust (MBT) in the south to the Main Central Thrust (MCT) in the north and consists of sedimentary and metasedimentary rocks ranging in age from Precambrian to Eocene but mostly older rocks. No tectonic window with outcropping Siwalik rocks is noticed indicating that the MBT is a steep thrust, horizontal component of displacement along the MBT is of a lower order of magnitude, and the foreland basin does not extend much beneath the MBT. The dip of the MBT in the Himachal Himalaya varies from 44° to 60°.

A. K. Dubey, *Understanding an Orogenic Belt*, Springer Geology,
DOI: 10.1007/978-3-319-05588-6_11,

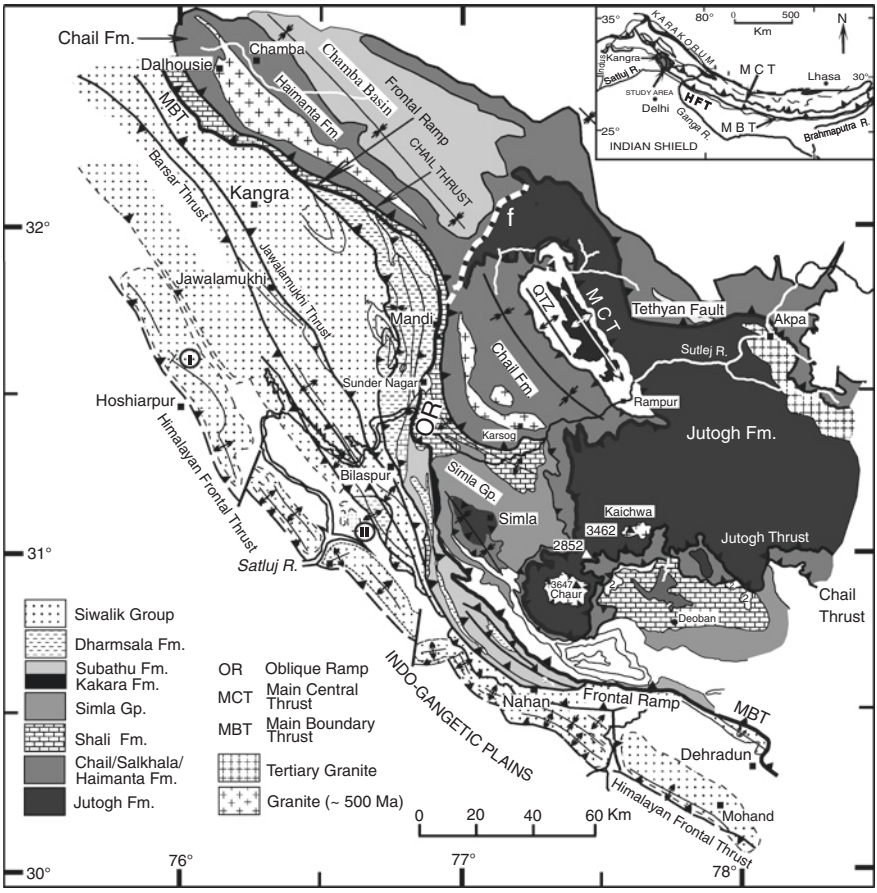

Fig. 11.1 A geological map of a part of the Himachal Himalaya [from Dubey (2009), © Geological Society of America. Published with permission of Geological Society of America]

11.1 Pre-Himalayan Curvature of the MBT

An early geological investigation in the Himachal Lower Himalaya was made by Pilgrim and West (1928) for construction of a railway track from Kalka to Simla (=Shimla) town. This was followed by Srikantia and Sharma (1976), Chatterji and Swaminath (1977), and Srikantia and Bhargava (1998). The area is geologically very significant because the MBT shows a prominent curvature described as the Kangra reentrant (recess) (Fig. 11.1). The trend of the MBT in the north and south is NW–SE whereas in the central part, the trend is ~N16E–S16W. However it is to be noticed that the younger thrusts of the Foreland basin, i.e. the Himalayan Frontal Thrust (HFT), the Jwalamukhi, and the Barsar thrusts have a linear NW–SE trend, not affected by the curvature of the MBT, suggesting that the

Table 11.1 Litho-tectonic succession in the Lower Himalaya

Subathu Group	(Green nummulitic shale and limestone)	Paleocene to Eocene
Kakara series	(Green, gray and purple shale with siltstone intercalations, lenticular bands of limestone)	Paleocene
Unconformity/Krol Thrust/Main Boundary Thrust		
Tal Formation	Orthoquartzite and calc-arenite with pebbly quartzite;shale; black phosphoritic and cherty layers	Early Cambrian
Krol Formation	Dolomitic limestone and shale alteration	
Blaini Formation	Slate and muddy quartzite, conglomerate, greywacke, and limestone	
Nagthat Formation	Orthoquartzite (locally pebbliferous) and subordinate shale	
Chandpur Formation	Olive green and gray phyllite with subordinate slate	
Mandhali Formation	Arenaceous limestone, gritty and slaty quartzite; Phyllite.	
Giri Thrust		Precambrian
Simla Group	Slate, sandstone, and quartzite	
Shali Thrust		
Shali Formation	Cherty limestone and stromatolitic limestone	
Chail Thrust		
Chail Formation (=Haimanta)	Low to medium grade metamorphic rocks, metasedimentary rocks	
Jutogh Thrust		
Jutogh Formation	Medium to high grade metamorphic rocks	

curvature is a pre-Himalayan feature. The pre-Himalayan origin of the curvature differentiates it from arcuate structures observed in other fold and thrust belts, e.g. Espinhaco thrust belt in Minas Gerais, Brazil (Marshak and Wilkerson 1992), northern sub-Alpine chain, France (Ferril and Groshong 1993), Tennessee salient, eastern United States (Macedo and Marshak 1999).

11.2 Lithotectonic Set-Up

A large number of thrusts are exposed in the area and the most characteristic feature is occurrence of klippen structures. The Chaur region, SE of the Simla klippe, has a special significance because the Jutogh and Chail formations show large horizontal translation but are still attached to their crystalline root in the High Himalaya (Fig. 11.1).

A lithotectonic set-up of the region is displayed in Table 11.1.

The highest grade of metamorphism is observed in the Jutogh Formation, which is characterized by muscovite-biotite-garnet-staurolite mineral assemblage

(Ray and Naha 1971). The presence of staurolite distinguishes the rock from the overlying Chail Formation. The Jutogh and Chail formations are regarded as parts of the High Himalayan crystallines. In view of small variations in the lithology and metamorphic grade, the two formations can be put together as undifferentiated crystallines. North of the Simla klippe, mylonitic gneiss (~1,800 Ma) is developed along the Chail thrust. The Chail metamorphic rocks show a decrease in the grade of metamorphism in a northwesterly direction, and the rocks around Chamba are described as the Haimanta/Salkhala Formation (low grade metasedimentary rocks). The variation could be a result of one of the following features.

1. The Kangra oblique fault ramp extends further in the north direction dividing the crystalline and metasedimentary rocks (white broken line, Fig. 11.1), or
2. There is a greater magnitude of displacement along the frontal part of the oblique ramp resulting in exposure of the higher grade rocks from depth.

The Chail rocks in the Simla syncline are surrounded by Simla slates, sandstones and quartzites. North of the Simla syncline, the Shali Formation is exposed as hanging wall rock along the Shali thrust. The strike is curved and follows the trend of the Kangra recess and Mandi-Karsog granite (~500 Ma). Further in the NE direction, metabasalts are associated with clastic metasediments in the basal sedimentary succession (Rampur Formation). Zircons from the metabasalts, dated by single grain evaporation technique, yielded an age of 1,800 ± 13 Ma (1σ) (Miller et al. 2000).

Southeast of the Kangra recess, the Lower Himalayan sequence is very well exposed in and around the Mussoorie Syncline (Fig. 11.2) (Auden 1937; Jayangondaperumal and Dubey 2001). This is a noncylindrical fold extending in NW–SE direction and occurs as a hanging wall structure of the MBT. The lowermost Mandhali Formation is best exposed around western termination of the syncline and in the synclinal core forming the Satengal klippe. The formation essentially consists of blue, grayish fawn arenaceous limestone, yellowish to white gritty and slaty quartzite with phyllite. The rock is weakly deformed but slate and phyllite in the Satengal klippe show good development of foliation and boudins of the interbedded competent rocks. Jain (1972) has classified the klippen rocks into three distinct members. The lowermost unit is boulder beds of the Mandhali Formation and comprises grayish green, laminated to non-laminated slate and pebbly slate. The pebbles (0.5–3 cm) are mostly of slate, phyllite and quartzite. The unit is overlain by grayish buff, coarse, massive quartzite and purple gray slate. The uppermost member consists of limestone characterized by grayish fawn, thinly bedded, recrystallized arenaceous limestone weathering to granular surface as a result of protruding sand grains. Gray slate intercalations are common.

The overlying Chandpur Formation consists of olive green, gray phyllite and subordinate slate interbedded and finely interbanded with quartzites, metasiltstone, and finely grained wackes. In the southern part of the syncline, the Chandpur Formation consists of banded green slate, phyllite, and ash beds whereas in the northern part, the slate gradually changes to chlorite-sericite phyllite and shows well developed foliation. In the southern part, the Mandhali and Chandpur formations are in contact with the MBT. In the core of the Mussoorie Syncline, the Chandpur Formation

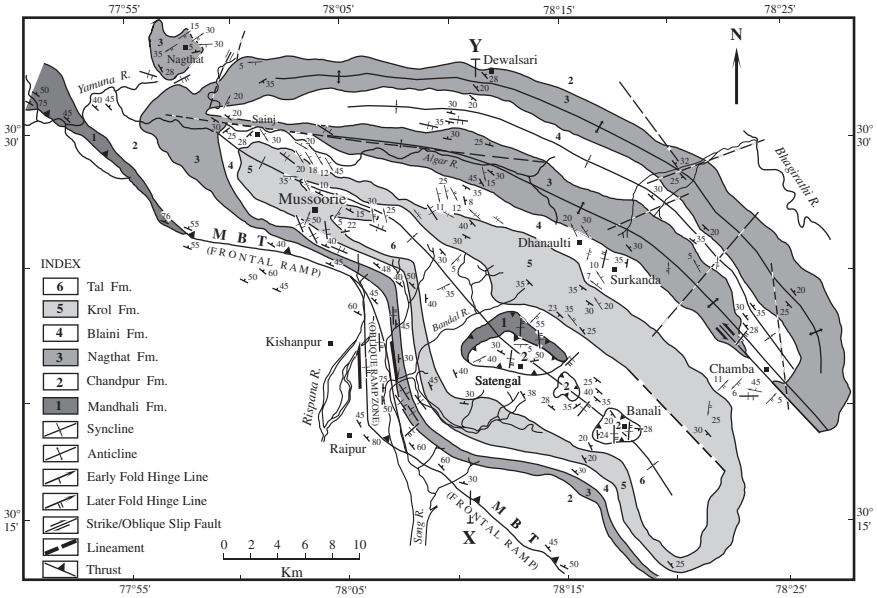

Fig. 11.2 Structural map of the Mussoorie Syncline, Garhwal Lower Himalaya [from Jayangondaperumal and Dubey (2001), © Elsevier. Published with permission of Elsevier]

occurs in three small detached klippen; the Satengal, Darak, and Banali klippen. Phyllites of the klippen units are gray and grayish green. Thin-sections reveal alignment of quartz, mica, chlorite, and opaque minerals forming cleavage. The southern contact of the Satengal klippe between the Chandpur and Tal formations is marked by Kathu-ki-chail thrust. The northern contact of the klippe is marked by two back thrusts, bringing the Mandhali Formation in contact with the Tal Formation.

In northern part of the Mussoorie Syncline, Nagthat quartzite is represented by multistoried purple green, fawn, gray, cherry red, and white, fine to coarse grained, locally pebbliferous sandstone with lenses of siltstone/shale. In southern part of the syncline, the quartzite is massive and made up of sandstone and quartz with secondary silica cement. Under a microscope, it shows anchimetamorphic characters, with recrystallized matrix. Margins of the quartz grains are preserved with corroded boundaries. Deformed quartzite shows stretched quartz grains surrounded by mantles of fine recrystallized grains as cleavage wrapping. In the northern part of the area, the rock is chlorite-sericite-quartzite, whereas distinct facies changes along the strike from sandstone to siltstone and shale were observed NW of Mussoorie.

The Subathu Formation occurs as a thin patch around the Satengal Klippe. The rock lies unconformably over the Precambrian–Cambrian Lower Himalayan sequence. It consists of ferruginous shale with lateritic/limonitic nodules, greenish gray, purple and dark gray shales. A thin patch of bluish gray arenaceous

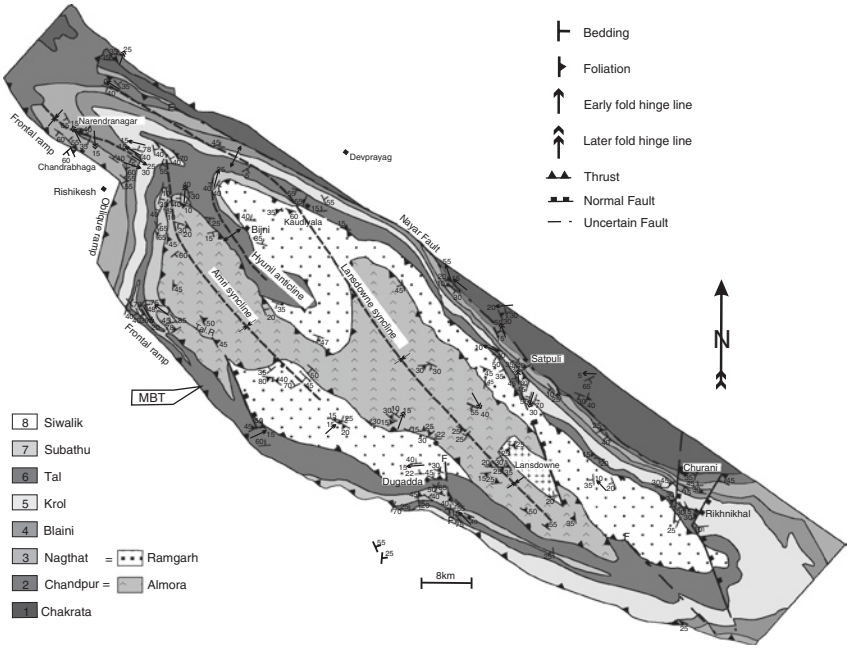

Fig. 11.3 A geological map of the Garhwal Synform [from Devrani and Dubey (2008), © Blackwell Publishing Asia Pty Ltd.. Published with permission of Blackwell Publishing Asia Pty Ltd.]

limestone occurs at the northern contact of the Satengal klippe. The limestone is a result of later marine transgression but the age cannot be ascertained because of lack of identifiable fossils. It extends roughly E–W with low to moderate dips and is crushed and brecciated during thrusting.

The adjacent Garhwal Syncline is also characterized by presence of klippen structures in the core (Fig. 11.3). The Garhwal Syncline slightly differs from the Mussoorie Syncline because, (1) the klippen are of larger size, (2) in addition to major thrusts, numerous small-scale normal and strike-slip faults are also present, and (3) some of the stratigraphic formations exposed in the northern limb are absent in the southern limb as a result of truncation by the MBT. The klippen rocks are described as Almora and Ramgarh groups of the Precambrian age. The highest grade of metamorphism is shown by the Almora Group, which is metamorphosed up to the garnet grade whereas the Ramgarh Group is metamorphosed up to the chlorite grade. The phyllite, exposed in the klippen, consists of quartz, plagioclase, K-feldspar, chlorite, biotite and muscovite with accessory minerals including tourmaline, hematite, magnetite, and pyrite. The quartz grains vary in size from fine to coarse and show undulose extinction. Biotite and plagioclase are sometimes altered to chlorite and sericite, respectively as a result of retrograde metamorphism. Alignment of chlorite and mica has resulted in weak foliation. However in the klippen phyllite, well developed

foliation is formed by preferred orientation of chlorite, biotite, and muscovite. Quartz, feldspar, and chlorite are concentrated in lenticular domains. Secondary quartz locally occupies the foliation and fractures. Plagioclase is locally altered to sericite-rich matrix. The rock has suffered lower greenschist facies metamorphism. The mineral assemblages are; (1) chlorite-quartz-plagioclase-sericite, (2) muscovite-biotite-chlorite-sericite-quartz-plagioclase, and (3) chlorite-biotite-garnet-quartz-plagioclase-K-feldspar. Hence the klippen phyllite differ from the surrounding phyllite in better development of foliation and occasional presence of garnet (near a granite intrusion at Lansdowne) (Devrani and Dubey 2008). These phyllites are absent in the High Himalaya, where the rocks are metamorphosed up to the sillimanite grade.

The Nagthat quartzite consists of medium to coarse, subangular to rounded, well sutured grains of quartz with subsidiary K-feldspar, plagioclase, and chlorite. Recrystallization of quartz is rare and plagioclase is locally altered to sericite. A few thin-sections show fine grained chloritic and micaceous matrix. Magnetite, hematite, and pyrite are present as accessory minerals. The klippen quartzite is composed of quartz with subordinate plagioclase and K-feldspar. Mica, chlorite, tourmaline, magnetite, and hematite occur as accessory minerals. The quartz grains are fine to coarse with well sutured grain boundaries and mostly recrystallized grains, especially near the Lansdowne granite. Garnet is absent. Conjugate set of fractures are common and weak foliation can be seen at few localities. The Nagthat quartzite differs from the High Himalayan quartzite, which is coarse, recrystallized, garnetiferous with subsidiary feldspar and small prisms of muscovite and biotite as accessory minerals. Triple junction and subgrain structures are present. The High Himalayan crystalline rock exhibits ribbon texture, deformed lamellae, undulose extinction and well developed foliation. In addition to these petrographic observations, basic rocks, Ca-rich metasediments, and migmatite gneisses are characteristic of the High Himalayan succession.

The Nagthat Formation has a conformable contact with the overlying Blaini Formation consisting of conglomerate, siltstone, graywacke, slates and limestone. The argillaceous, arenaceous, and calcareous sediments are slightly metamorphosed. The slates are purple, olive green and gray while the limestone is purple and gray. A lensoidal boulder bed often occurs at the base, consisting of quartzitic and calcareous pebbles (1–50 cm) in random orientation.

The Krol Formation consists mainly of bluish gray crystalline dolomitic limestone, green shaly limestone with chert and bluish gray shale. At some places, pinch and swell structure can be observed in the more competent limestone beds. Joints are widely spaced and often filled with quartz and calcite. Thin bedded sandy limestone, associated with chert layers, occurs at the top.

The Tal Formation lies over the Krol Formation. The Lower Tal consists of gritty quartzite, black chert, carbonaceous shale and dark greywacke. The Upper Tal mainly consists of massive arkosic sandstone, quartzitic pebble (up to 5 cm) beds, shale, dark limestone, calcareous sandstone and quartzite. The quartzite is pure white to brownish yellow and has undergone intense crushing along the

thrusts. After the Cambrian there was no deposition till Paleocene when the Kakara and Subathu rocks were deposited as a result of marine transgression.

Illite crystallinity data from the Lower Himalaya of Garhwal reveal that regional metamorphism in the Upper Precambrian–Lower Palaeozoic sequence occurred prior to the Cenozoic, i.e. it was pre-collisional (Oliver et al. 1995). K–Ar ages confirm that the Lower Himalayan rocks occurring below the MCT zone, obtained their peak metamorphism before the Cenozoic Himalayan orogeny (Johnson and Oliver 1990). Abundance of hornfels recorded from the Arunachal Lower Himalaya provides additional information on the pre-Himalayan contact metamorphism and suggests that the Lower Himalayan Granitoids were intruded as granite into the Lower Himalayan rocks during the Palaeoproterozoic and later deformed into gneisses during the Himalayan orogeny (Bikramaditya Singh 2012).

11.3 Inverted Metamorphism

At lower topographic levels, the rocks are sedimentary or metasedimentary with slate and phyllite grades. The grade of metamorphism increases with increase in topographic level (reverse or inverted metamorphism). For example, the peak metamorphic P–T conditions in the Lower Himalaya of central Nepal reveal ~550 °C and 8 kbar. These increase suddenly at higher elevations to ~725 °C and 10–12 kbar in vicinity of the Munsiari and Main Central thrusts (Kohn 2008). This pattern of metamorphic variation can be observed throughout the Lower Himalaya.

The upward increase in metamorphic grade from chlorite, to biotite, garnet, kyanite and sillimanite grade rocks was noticed in the eighteenth century by early geologists like Medlicott (1864) and Mallet (1874). The earliest interpretation proposed for the inverted metamorphism was a large scale recumbent folding (Pilgrim and West 1928; Gansser 1964) but no evidence of overturning (e.g. primary structure, cleavage-bedding relationship etc.) was cited as evidence. Further, no large-scale recumbent folding has been observed elsewhere in the Lower Himalaya. The recumbent and overturned folds are exposed only on minor and outcrop scales. In absence of large-scale recumbent folding, alternate mechanisms were proposed where inversion of the rock sequence is not involved. The feature was interpreted either as evidence for a thermal structure with recumbent isotherms (e.g. Le Fort 1975) or as a result of post-metamorphic shearing of isograds (e.g. Brunel et al. 1979). Frictional heat along the MCT was also attributed for the inversion of isograds. Caddick et al. (2007) have reported a peak temperature of 600–640 °C and a burial depth of ~25 km for a part of the Lower Himalaya. Based on the PTt history, the inverted metamorphic sequence was described as a result of footwall heating due to rapid overthrusting of hot High Himalayan rocks. The continued thrusting exhumed the rock sequence rapidly enough to preserve an inverted metamorphic gradient. However, there is still very little knowledge about precise age and total displacement along the MCT. The strain rates are also

very approximate. Hence it is not certain whether the slip rates along the MCT can generate the required friction for the inversion.

Inverted metamorphism in the central Himalaya (Nepal) was studied by Raman spectroscopy of carbonaceous material (Bollinger et al. 2004). It shows a temperature of <330 °C in the lower part increasing gradually upward towards the MCT to 520–550 °C. The temperatures describe structurally a 20–50 °C inverted apparent gradient. The inverse thermal gradient was interpreted as a result of combination of underplating and post metamorphic shearing of the underplated units. The Ar muscovite ages suggested that the Lower Himalaya has exhumed jointly with the overlying thrust sheets by about 5 mm/year. If the convergence rate is taken to be about 20 mm/year, the underthrusting of the Indian basement below the Himalaya comes out to be about 15 mm/year.

In the NE Himalaya, development of inverted thermal profile in the Bomdila Gneiss (~400 °C at the lower zone increasing at the upper levels, i.e. towards the MCT to 500–600 °C) is attributed to imbrications and post-metamorphic shearing within the Lower Himalayan crystalline rocks (Bikramiditya Singh and Gururajan 2011).

11.4 Structure

A combination of frontal and oblique ramp structures form recess (or re-entrant; part of an orogenic belt in which geological structures like faults and folds are concave towards the foreland) and salient (part of an orogenic belt in which geological structures like faults and folds are convex towards the foreland) along the MBT. Formation of these recesses was earlier attributed to basement ridges in the Indian Craton. For example, the Dehradun recess (NE of Dehradun) was attributed to the Delhi—Aravalli Ridge, which is a basement structure of the Penisular shield. However a large number of recess and salient structures occur along the MBT (Fig. 11.4), even where there is no basement ridge. Hence their formation is attributed to linking of frontal and oblique fault ramps. These structures are not imitated along the HFT confirming that they are pre-Himalayan structures (cf. Marshak 1988). The study of these oblique fault ramps is important because some of these ramps are associated with recent earthquakes in the Himalaya. For example, the Uttarkashi earthquake (20 October, 1991; M 7.0) (Gupta and Gupta 1995), and Chamoli earthquake (29 March 1999; M 6.6) (Mandal et al. 2002) have their epicenters in vicinity of oblique ramps. One of the important earthquakes of the century, the Kangra earthquake (4 April, 1905; M 7.0) (Middlemiss 1910; Molnar 1987) also occurred along the Kangra oblique ramp.

An oblique ramp can be identified as follows.

1. It is confined to offset thrust segments, i.e. the fault displacement appears to be equal to length of the fault. This is in sharp contrast to strike-slip faults where the maximum displacement takes place in the central part, and total displacement cannot be equal to the fault length.

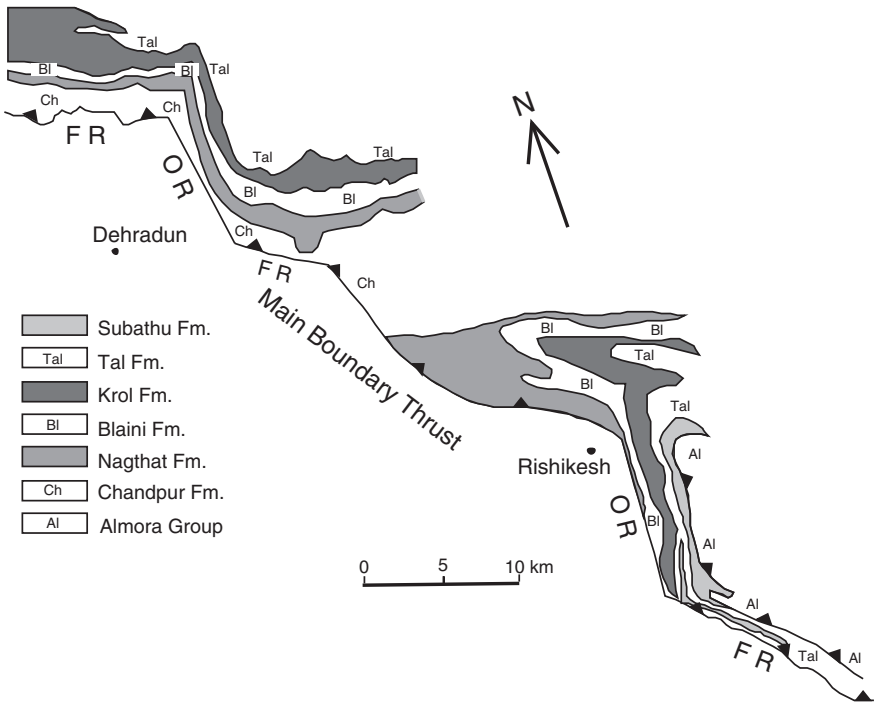

Fig. 11.4 A series of recess and salient structures along the MBT in the Garhwal Himalaya. The Precambrian and Cambrian rock formations follow the trend of the frontal and oblique ramps indicating that the fault is pre-Himalayan

2. When the fault is prior to deposition (e.g. rift basin) it does not displace stratigraphic horizons but the stratigraphic horizons follow the trend of the fault.
3. A single fold hinge line is not traceable across the fault, and
4. The sense of fold hinge line curvature in vicinity of the fault is opposite to the tectonic transport direction, and the amount of curvature varies in different folds, implying that the folds have not been displaced by the same amount and in proportion to the depicted fault displacement (Fig. 11.5).

These frontal and oblique ramps are older normal faults reactivated later as thrusts along with simultaneous development of noncylindrical folds.

Thrust faults are the dominant structure but normal and strike-slip faults also occur in the region. Normal faults of the following four generations are clearly distinguishable. Out of these, the first one is pre-orogenic whereas the other three were formed during successive stages of the Himalayan orogeny.

1. Rift faults and associated minor normal faults formed during the rift phase.
2. Orogenic normal faults attributed to large shear strain along thrusts (Sect. 11.8).
3. Normal faults associated with reactivation of oblique thrust ramps during superposed deformation (Fig. 7.28).

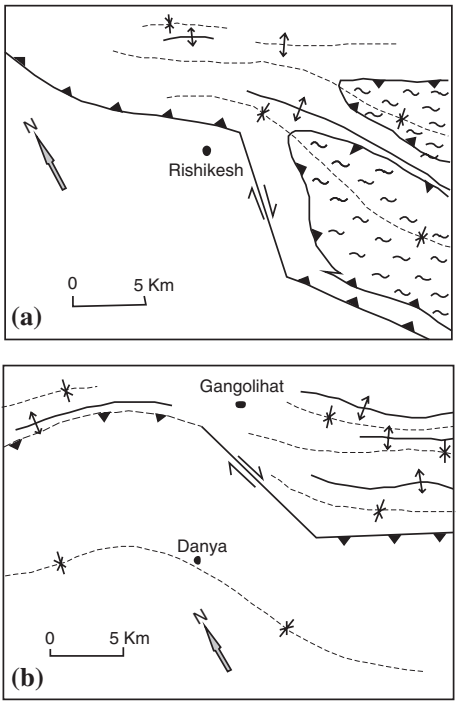

Fig. 11.5 Curvature of fold hinge lines adjacent to an oblique fault ramp. **a** A part of the Garhwal Lower Himalaya around Rishikesh. **b** A part of the Kumaun Lower Himalaya around Gangolihat [from Valdiya (1980), © K.S. Valdiya. Published with permission of K.S. Valdiya]

4. Youngest normal faults formed as a result of gravity gliding and lateral spreading (Herren 1987; Royden and Burchfiel 1987; Dubey and Bhakuni 2008). These can be identified by the fact that they displace all the foliations and are unaffected by superposed folding.

Structural studies in the region indicate two prominent phases of folding, i.e. early and superposed. A series of fold structures, trending NW–SE to E–W, along the Main Boundary Thrust, are early folds. These were formed simultaneously with displacement along the thrusts. The superposed folds, whose hinge lines trend NE–SW to N–S, were formed at a later stage after locking of the prominent thrusts and early folds. The superposed folds occur on all scales and are exposed throughout the Himalaya. The general orientation of folds may vary locally depending upon the interference between simultaneously developing folds, and faults and folds. The early folds are absent in close vicinity of the thrusts but the superposed folds are distributed throughout the region. Formation of superposed folds in fold and thrust belts has been explained earlier (Coward and Potts 1983) as a result of simultaneous development and interference of two thrust sheets. The structure has a characteristic geometry where the superposed folds are concentrated in the region of fold interference (Fig. 11.6). The uniform distribution of superposed folds in the Himalaya provides evidence that they have formed as buckle folds due to compression rather than as a result of interference between two propagating thrust sheets.

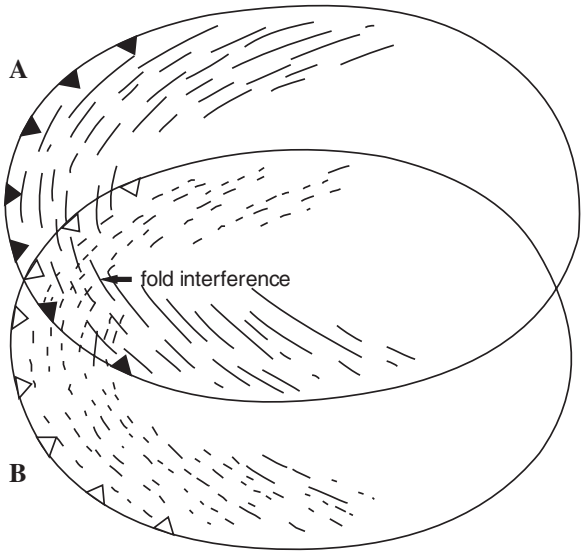

Fig. 11.6 Interference between two simultaneously developing thrust sheets (*A* and *B*) resulting in fold interference and formation of superposed folds in the region of interference [from Coward and Potts (1983), © Elsevier. Published with permission of Elsevier]

In the Lower Himalayan region, emplacement of numerous granitic bodies, between 450 and 600 Ma, involved both explosive volcanism and syntectonic intrusion (Valdiya 1993, 1995). The Mandi-Karsog pluton is one of these bodies, lying within the Chail Formation, and covering an area of ~30 km^2 (Fig. 11.7). The regional trend of the pluton is parallel to curvature of the adjacent Chail Thrust (Fig. 11.1), i.e. N–S in the northern part and E–W in the southern part. Age of the pluton is constrained by Rb–Sr dating to around 507 ± 100 Ma (Jager et al. 1971). Miller et al. (2001) have carried out geochemistry and geochronology of the Kaplas pluton (north of the Mandi-Karsog pluton) and tholeiitic mafic rocks in the Mandi-Karsog area. The study provides evidence of magma mingling and close association of granitic and mafic magma in the Mandi-Karsog area. It was also revealed that the mafic magma, crystallized at 496 ± 14 Ma, has a mantle source whereas the granitic part was derived from a crustal source and crystallized at 553 ± 2 Ma. Based on these data, an asthenospheric upwelling and passive crustal extension model was preferred for generation of the pluton. These studies suggest that fissures generated during the rifting assisted the ascent and emplacement of the granitic magma.

The pluton intrudes quartzites, schists and calc-silicate rocks of the Proterozoic Chail Formation. The host rock exhibits a foliation parallel to the pluton margin with low to moderate dip towards east or NE (Jayangondaperumal et al. 2010) except in areas of superimposed folding. The stretching mineral lineation shows a moderate plunge towards NE (Steck 2003; Dubey et al. 2004). Variation in the direction of plunge can be observed as a result of noncylindrical folding. The host rock shows evidence of brittle deformation at a late stage. The pluton is coarse and porphyritic granite essentially made up of quartz, feldspar, muscovite and biotite. This has later been intruded by injections of aplitic veins. The veins have a dominant NW–SE trend implying that the granitic body has undergone stretching in a

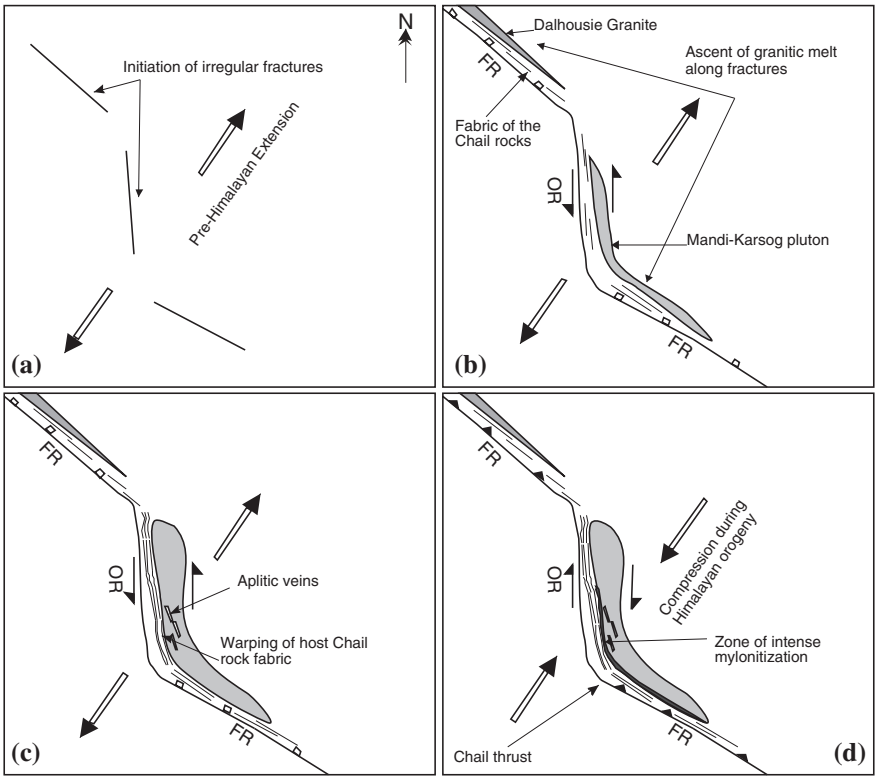

Fig. 11.7 A simplified diagram showing structural evolution of the Mandi-Karsog pluton (not to scale). **a** Initiation of irregular fractures in heterogeneous Chail Formation during the pre-Himalayan tensional regime. The predominant stretching direction was NE-SW. **b** Propagation and linking of fractures as frontal (*FR*) and oblique (*OR*) normal fault ramps. The oblique ramp shows a component of sinistral strike-slip displacement. Ascent and emplacement of granitic melt along the fault. **c** Emplacement of the pluton results in deflection of the host rock fabric that acquires parallelism with the intrusion. Minor extensional fractures were filled-up by the aplitic melt. **d** Reactivation of the early normal fault as thrust during the Tertiary compressional phase. Note the reversal of slip-sense along the oblique ramp (*OR*) fault. Mylonitization took place along the western margin of the pluton, close to the Chail Thrust [from Jayangondaperumal et al. (2010), © Cambridge University Press. Published with permission of Cambridge University Press, Cambridge]

NE–SW direction, which coincides with the pre-Himalayan extension direction (Bhat 1987). In the core of the pluton, feldspar laths show random orientation whereas in the marginal parts they define a well developed margin parallel foliation. The western margin of the pluton is characterized by exposures of mylonite in its central and southern parts. The mylonite shows stretching lineation with dominant northeasterly moderate plunge. Microstructures in the mylonite indicate 'top to the SW' shearing related to the regional thrusting. The western margin is also intruded by tourmaline granite striking N–S. The tourmaline crystals show

mostly NW–SE to N–S trends. The field relationship suggests that the aplitic veins and the tourmaline bearing granites are younger than the coarse-grained and porphyritic varieties of the two-mica granite. The mesoscopic features show primary magmatic fabric defined by preferred orientation of euhedral to subhedral feldspar laths in northern part of the pluton and a tectonic fabric defined by deformed granitic gneiss with feldspar porphyroclasts in the southern part. Contact between the granite and the Chail rock is parallel to foliation of the host rock. At some places, the granite shows interfingering with quartzite and schist of the Chail Formation.

The Mandi-Karsog pluton shows an almost concordant relationship between the field and magnetic fabrics (Jayangondaperumal et al. 2010). In the northern sector it is expected, since this has not suffered much post-crystallization deformation during the Tertiary orogeny. Despite intense mylonitization, the central and southern sectors show almost similar strike in their field and magnetic fabrics. This may be a result of extension (pre-Himalayan) and compression (Himalayan orogeny) in the same direction (i.e. NE–SW).

11.5 Structural Evolution of the Mandi-Karsog Pluton

Structural evolution of the pluton has been explained in the following stages (Fig. 11.7). The pre-Himalayan tensional regime led to initiation of fractures in the region. The heterogeneous nature of the crust was responsible for formation of irregular geometry and orientation of the fractures (Fig. 11.7a). These fractures propagated by extending their lengths and linked to form frontal and oblique fault ramps (Fig. 11.7b). The oblique fault ramp shows vertical and sinistral horizontal components of displacements. Ascent and emplacement of granitic melt took place along this fracture and forced its way into the country rock by lateral extension. The arcuate geometry of the fault led to arcuate pattern of the granitic body. During expansion of the pluton, the initial host rock fabric deflected and warped around the pluton (Fig. 11.7c). Folding in the host rock suggests that the expansion was accompanied by ductile shortening of the host rock. Minor extensional fractures that are syn- to post-emplacement were filled up by late injections of aplitic veins. Finally, during the Tertiary compressional phase, reactivation of the early normal fault took place as thrust. The initial sinistral displacement was also reactivated as right lateral displacement (Fig. 11.7d). Development of the mylonites can be attributed to displacement along the Chail Thrust. These evolutionary stages suggest that the arcuation of the pluton was pre-Himalayan.

11.6 Structural Evolution of the Kangra Region

Structural evolution of the Kangra region has a special significance because of presence of the largest Himalayan recess structure. The strain studies show mild deformation in the region. Two dimensional magnetic susceptibility ellipses along

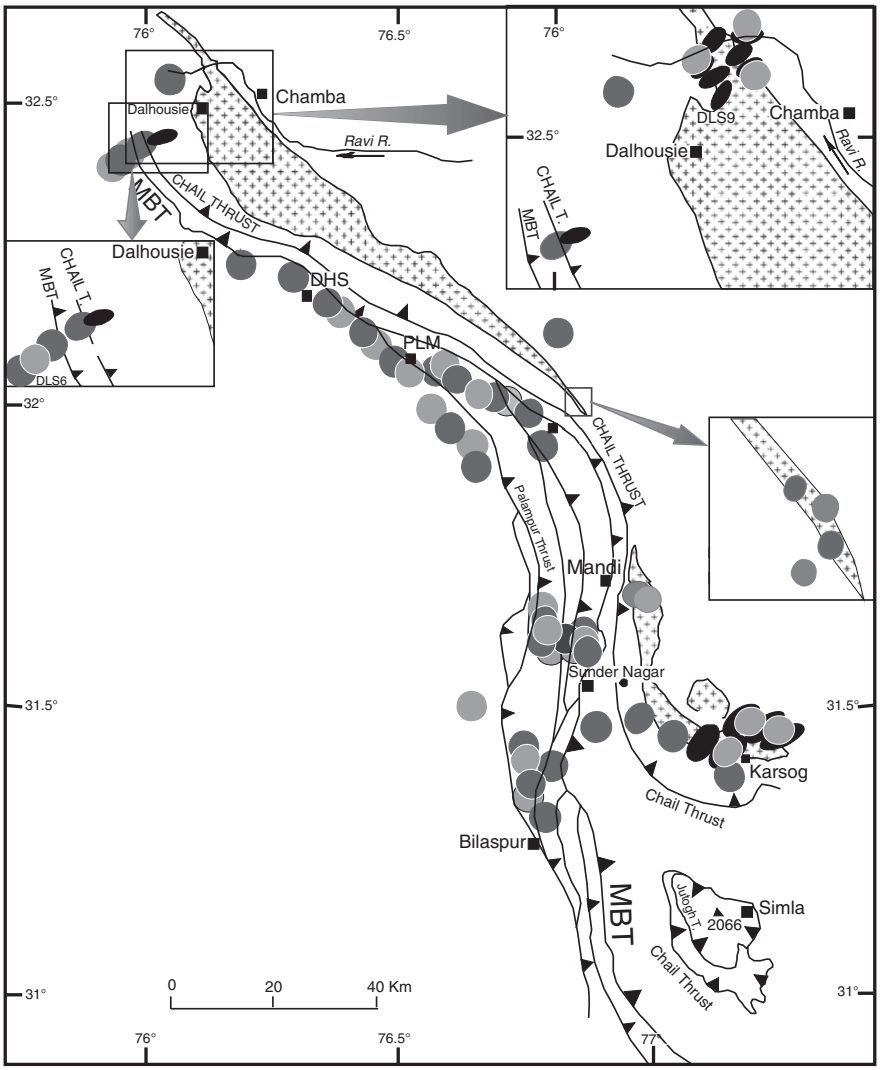

Fig. 11.8 Distribution of magnetic susceptibility ellipses (containing the maximum and minimum axes in various *shades of gray*) and petrofabric strain ellipses (XZ plane, *black*) [from Dubey et al. (2004), © Elsevier. Published with permission of Elsevier]

with their orientations are shown in Fig. 11.8. The hanging wall strain ellipses show slightly higher axial ratios and a greater variation in their orientation. Strain ellipses obtained by the R_f/φ method, from the MBT hanging wall samples, are also shown in Fig. 11.8. The weakly deformed sedimentary rocks of the footwall are not suitable for determining strain from this method. Strain ratios ($X \geq Y \geq Z$) in the Dalhousie area vary from 1.71:1.22:1 to 2.36:1.62:1. In the Karsog area, rock samples from vicinity of the oblique ramp shows higher strain values from 1.87:1.26:1 to 2.7: 1.5:1.

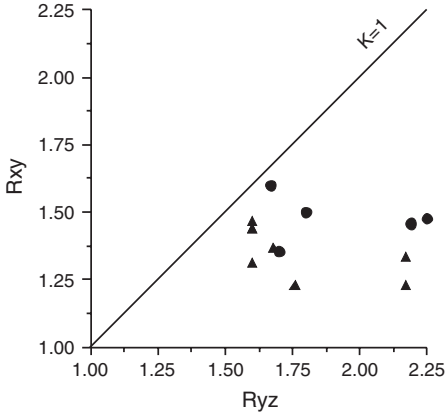

Fig. 11.9 Flinn diagram depicting shapes of petrofabric strain from the hanging wall region. The *circles* and *triangles* represent samples from oblique ramp and frontal ramp, respectively [from Dubey et al. (2004), © Elsevier. Published with permission of Elsevier]

The higher values of petrofabric strain as compared to magnetic strain can be attributed to the following (cf. Borradaile 1988).

1. Petrofabric strain represents the shape anisotropy whereas magnetic strain is a combined result of grain shape, grain distribution, and crystallographic orientation (Kelso and Tikoff 2001).
2. Granite represents a multiphase system where different minerals may have different orientations of magnetic ellipsoids (Kelso and Tikoff 2001).
3. Since the superposed maximum compression is orthogonal to the early maximum compression, a part of the early strain may have been obliterated by the later deformation.

Flinn diagram of strain data from the MBT hanging wall samples, obtained by the R_f/φ method, is shown in Fig. 11.9. Since ellipsoids from the frontal and oblique ramps occupy the oblate field, no obvious distinction can be made between the deformation patterns of the two areas.

Hrouda double plot from the footwall and hanging wall data is shown in Fig. 11.10a, b respectively. The pattern is independent of distance from the thrust and location with respect to frontal and oblique ramps. The footwall region is characterized by small values of degree of magnetic anisotropy (Pj) and large variation in the angle between magnetic foliation and bedding (f). The hanging wall region shows high values of Pj and large variation in the angle f. The pattern is characteristic of a combination of lateral shortening and simple shear (Chap. 2).

11.6.1 The Model

Based on the knowledge of geometry of the MBT (Dubey and Misra 1999, Balancing of cross-sections across the Lesser Himalaya. Report of joint collaboration between Wadia Institute of Himalayan Geology and Oil and natural Gas

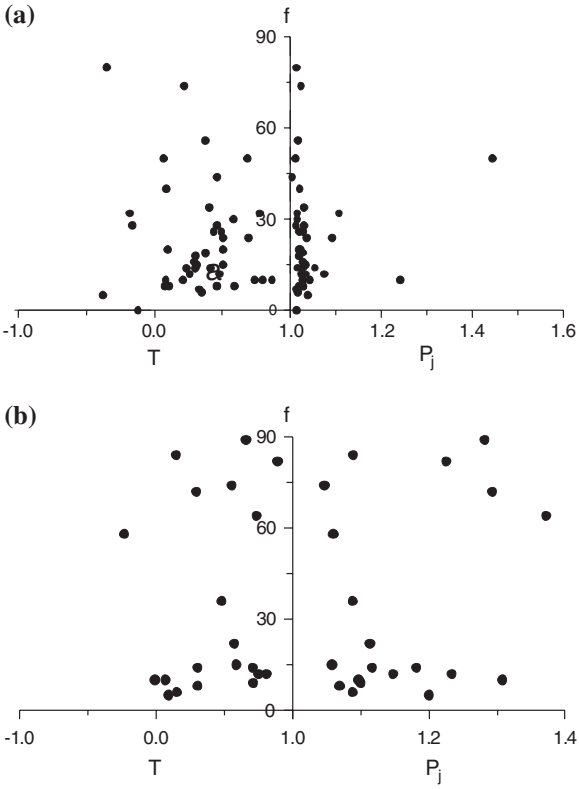

Fig. 11.10 Angle between the magnetic foliation and bedding (f) plotted against the shape (T) and degree of anisotropy (Pj). **a** Footwall region, **b** hanging wall region [from Dubey et al. (2004), © Elsevier. Published with permission of Elsevier]

corporation, p 45, unpublished) and development of frontal and oblique fault ramps, structural evolution of the area has been proposed in the following stages (Fig. 11.11) (Dubey et al. 2004).

Stage 1: *Initiation of fractures during the extensional phase*

During the earlier tensional phase in the region, a number of fractures initiated depending on available planes of weakness. The fractures propagated by extending their lengths and some of the fractures linked-up to form frontal and oblique ramp structures. One such fault is shown in Fig. 11.11a. FR1 is a frontal fault ramp dipping at an angle of 20° and FR2 is a frontal fault ramp dipping at an angle of 35°. The oblique ramp (OR) makes an angle of 30° and FR2 makes an angle of 70° to the axis of maximum compression.

Stage 2: *Development of extensional faults*

Figure 11.11b shows normal faulting and sinistral strike slip displacement during the rift phase. The steeper dip at the leading frontal ramp resulted in a larger fault displacement as compared to the trailing frontal ramp. The larger displacement and recess structure resulted in formation of a new extensional fault 'f_1', which is a continuation of the frontal ramp. The new fault gradually propagated by extending its length.

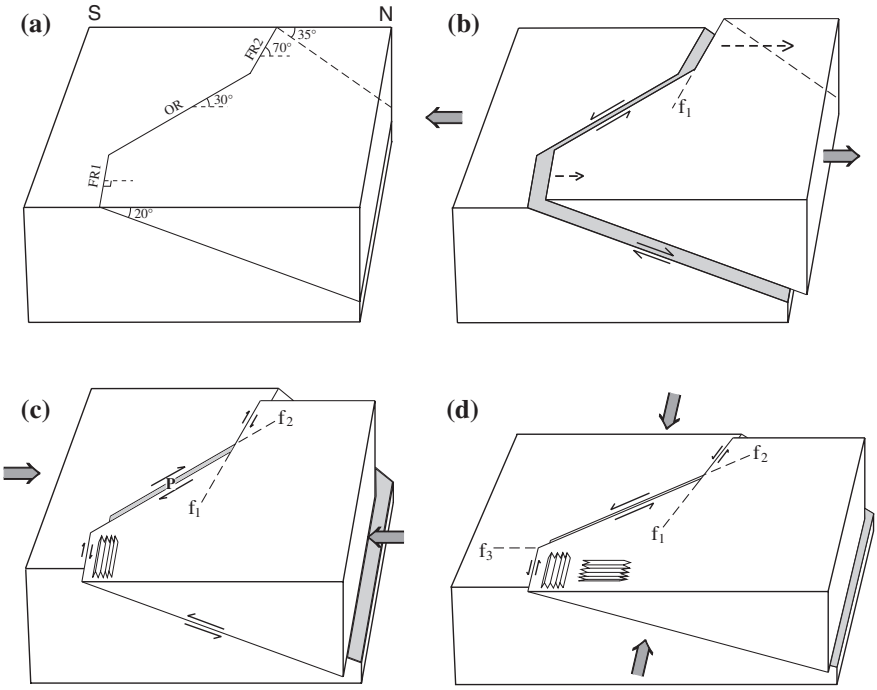

Fig. 11.11 A schematic model showing stages in structural evolution of the Kangra region. **a** Initiation of fractures during tensional phase in the region. *FR* Frontal fault ramp; *OR* oblique fault ramp; *N* north; *S* south. **b** Normal faulting and formation of extensional fault f1 as a result of variation of displacement along the leading and trailing frontal normal ramps. **c** Reactivation and reversal of the early normal fault as thrust during the compressional phase, formation of early folds and pull-apart basin (P) at the central part of the oblique ramp, and extension of the oblique ramp as f2. **d** Superposed deformation during the Himalayan orogeny, formation of superposed folds and f3 fault [from Dubey et al. (2004), © Elsevier. Published with permission of Elsevier]

Normal faulting in the Kangra region is supported by the following geological findings (Srikantia and Bhargava 1979; Virdi 1994).

(1) The various litho-units show an eastward increase in thickness indicating that the basin has deepened towards the east.
(2) The area west of the oblique ramp remained exposed from the Late Proterozoic to Jurassic, and
(3) Palaeocurrents indicate an eastward palaeoslope (Gaetani et al. 1990).

Stage 3: *Compressional Phase*

The compressional phase resulted in reversal of fault displacement as thrust (Fig. 11.11c). The central oblique ramp showed dextral oblique slip displacement and displacement out of the tectonic transport plane, resulting in formation of a pull-apart basin (P) where Tertiary rocks were deposited. Presence of the

Kakara Series (Srikantia and Sharma 1970) (Table 11.1) suggests that the basin was initiated in the Paleocene, simultaneously with thrusting along the MBT and flexural bending of the Indian plate margin (Chap. 10). The Lower Tertiary and the Upper Tertiary Siwalik rocks were deposited in the foreland basin. Increase in compression at a later stage led to thrusting in the pull-apart basin. The early folds were formed at this stage of deformation. The central oblique ramp propagated by extending its length (i.e. f_2). The strike-slip component of fault displacement varies along the oblique ramp. The maximum displacement occurs in central part of the oblique ramp with gradual decrease towards the frontal ramps. The decrease in displacement was accompanied by increase in fold intensity near the frontal ramps. The folds were developed by a combination of normal stress and shearing along the oblique ramp. Hence the developing minor folds reveal a wide variation in their orientation.

The initial gentle dip of the leading frontal thrust ramp (earlier trailing normal fault frontal ramp) resulted in larger thrust displacement so that rocks from a deeper level (i.e. low to medium grade Chail Formation) cropped-out on the surface. The steeper dip of the trailing frontal ramp led to smaller thrust displacement hence rocks from a higher stratigraphic level (i.e. metasedimentary rocks, Haimanta Formation) outcrop on the surface (Fig. 11.1).

Stage 4: *Superposed deformation*

The axis of maximum compression changed to an orthogonal horizontal direction thereby resulting in reversal of fault displacement at the oblique ramp and formation of superposed folds (Fig. 11.11d). The hinge lines of these later folds have an orthogonal relationship with the early folds. Reversal of displacement on the oblique ramp resulted in normal fault displacement (Fig. 7.28). Sinistral strike slip displacement may be attributed to the formation of f_3 fault in the footwall at the junction of the frontal and oblique ramps (i.e. Rupar lineament; Virdi 1979).

11.7 Geometrical Relationships Between Shortening, Displacement Along Thrust and Displacement Out of Tectonic Transport Plane

Consider a simple two-dimensional case where layering is horizontal and the axis of maximum compression also acts in a horizontal direction. Figure 11.12 denotes a line AB, which is parallel to the axis of maximum compression. The oblique ramp (BC) is oriented at an angle α to the axis of maximum compression. Displacement along the oblique ramp results in displacement out of the tectonic transport plane. When the shortening is equal to AB, the displacement along the oblique ramp is BC and the displacement out of the tectonic transport plane is equal to AC, which can be calculated by the following geometrical relationships.

$$\mathrm{AC} = \mathrm{AB}\ \tan\alpha = \mathrm{BC}\sin\alpha$$

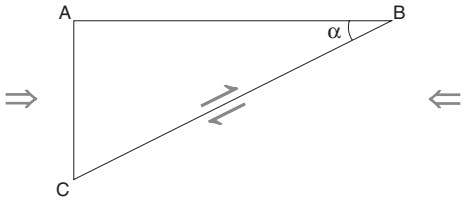

Fig. 11.12 A geometric representation of orientation of axis of maximum compression (*AB*) and an oblique ramp (*BC*) at an angle α with *AB* on a horizontal plane. *AC* represents displacement out of the tectonic transport plane

The relationship demonstrates that displacement out of the tectonic transport plane is directly proportional to shortening, displacement along the oblique ramp and the angle between the oblique ramp and the axis of maximum compression.

Problem 1

The relationships discussed above can help in determination of displacement out of the tectonic transport plane (i.e. AC) as follows.

In the Kangra recess, the shortening along the Hoshiarpur–Dharamsala section has been estimated as 23.4 km by Powers et al. (1998). The general strike of the rock formations and the regional fold hinge lines (away from the oblique ramp) are NW–SE, hence the axis of maximum compression may be taken as NE–SW. The angle α between the axis of maximum compression and the oblique ramp is 45°, hence

$$\mathrm{AC} = 23.4 \times \tan 45^\circ = 23.4 \text{ km}$$

In the Cheri section, the estimated shortening is 60 km (Dubey et al. 2001), hence

$$\mathrm{AC} = 60 \times \tan 45^\circ = 60 \text{ km}$$

The two values of 23.4 and 60 show a large difference because the estimated shortening amounts are different over a very small area (Chap. 10).

Another attempt to determine the amount of shortening can be made with the available geological data as follows.

Problem 2

Considering the pull-apart basin at the footwall of the MBT to have formed during the Tertiary as a result of displacement along the MBT, displacement out of the tectonic transport plane can be measured on the geological map. The frontal ramps on either side of the oblique ramp are not parallel hence the strike-slip displacement is likely to be greater at the trailing frontal ramp, which is oriented at an acute angle to the predicted axis of maximum compression. However the maximum width of the basin, parallel to strike of the frontal ramp, (23.68 km), provides the maximum displacement. This distance is taken into consideration for estimation of the maximum horizontal displacement along the oblique ramp during the Tertiary as follows.

$$\begin{aligned} \mathrm{AC} &= \mathrm{BC} \sin \alpha \\ 23.68 &= \mathrm{BC} \sin 45 \\ \mathrm{BC} &= 33.48 \text{ km} \end{aligned}$$

In the absence of a marker horizon, it is difficult to determine the component of strike-slip displacement along the oblique ramp. However, considering the hanging wall granite as an initial continuous body and excluding the possible ductile extension, the horizontal displacement comes out to be ~33 km (Virdi 1979).

The above displacement estimate can be used to find out the amount of shortening in the region as follows.

$$\begin{aligned} \mathrm{AB} &= \mathrm{BC}\cos\alpha \\ &= 33.48 \times \cos 45 = 23.67 \text{ km} \end{aligned}$$

The shortening estimate of 23.67 km during Tertiary time agrees very well with the estimate of Powers et al. (1998) made for the trailing ramp. In the central part of the oblique ramp, the estimated shortening is 60 km (Fig. 10.2) but it is difficult to further substantiate the result, since displacement in the central part of the ramp is not known. The experimental results suggest a greater displacement in central part of an oblique ramp (Dubey 1997) and this can provide a higher shortening amount. In order to obtain the maximum amount of shortening, the maximum displacement along an oblique ramp should be taken into account.

The above discussion leads to the following inferences.

1. The Kangra recess is a combination of frontal and oblique ramp structures.
2. The stratigraphic and structural evidence suggest that the Main Boundary Thrust was formed as a normal fault during pre-Himalayan extensional phase in the region. The fault later reactivated as thrust during the Tertiary Himalayan orogeny.
3. Formation of a pull-apart basin at the oblique ramp is attributed to large strike slip displacement along the trailing frontal ramp because of its orientation at an acute angle to the axis of maximum compression.
4. Geometry of the Tertiary pull-apart basin suggests a horizontal translation of ~33 km along the MBT oblique ramp.
5. The anisotropy of magnetic susceptibility data reveal that the deformation is by a combination of pure and simple shear. A larger part of the shear strain is supposed to be confined to a narrow zone characterized by the presence of salt (thickness >236 m; Srikantia and Sharma 1976).
6. Orthogonal relationship of the leading frontal ramp with the axis of maximum compression resulted in formation of a large number of folds in the hanging wall (e.g. Rampur window, Simla klippe etc.).
7. The Fugtal–Manali–Rupar Megalineament is an extension of the MBT oblique ramp. The northern part of the lineament occurring in the hanging wall appears to be older than the southern part in the foothill belt.
8. The study of magnetic strain is ideal for areas that have undergone a weak deformation whereas the study of petrofabric strain is more suited to areas of strong deformation. These techniques are complimentary to each other in areas of repeated deformations because the collective data can unravel the early (petrofabric strain) and superposed (magnetic strain) deformations.

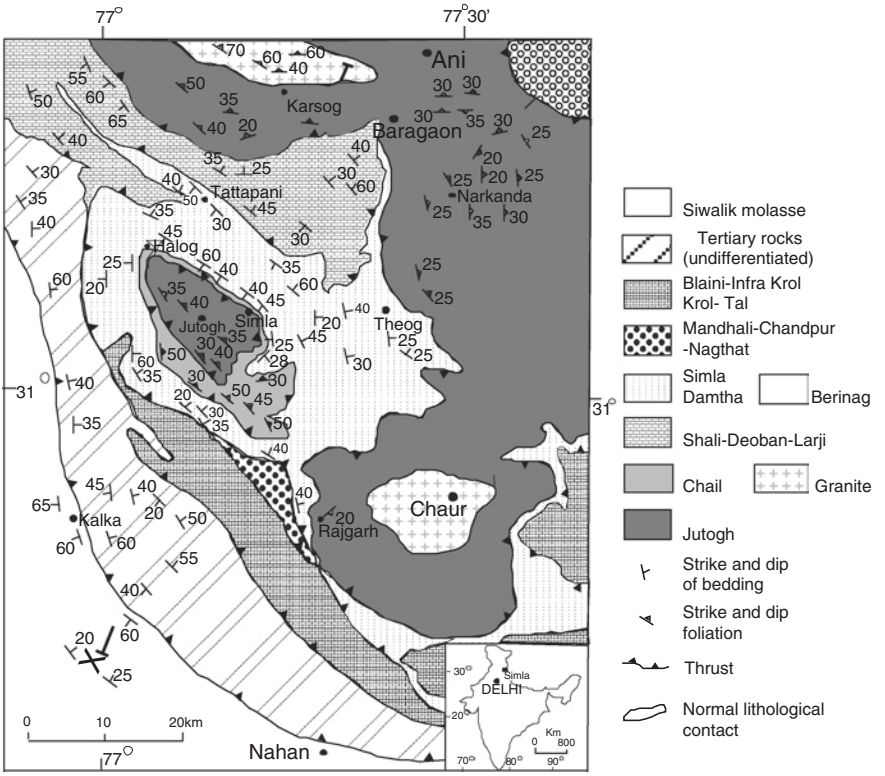

Fig. 11.13 A geological map of the Simla klippe and surrounding region, Himachal Himalaya [from Dubey and Bhat (1991), © Elsevier. Published with permission of Elsevier]

11.8 Structural Evolution of the Simla Klippe

The Simla klippe, a major syncline, is composed of Jutogh and Chail formations surrounded by the younger Simla Group of metasedimentary rocks (Fig. 11.13). The concepts of root-zone, klippe and window were introduced in the Himalaya after study of this area (Pilgrim and West 1928; West 1939).

The first formed (early) folds are mostly tight or isoclinal, upright, recumbent or reclined. The trend of the gently plunging fold hinge lines varies from NW–SE to E–W. Some of these folds have been refolded coaxially (type 3 interference pattern) in open to tight, upright, overturned, and recumbent styles. The later (superposed) folds are characterized by upright and asymmetric chevron folds, conjugate folds and kink bands. The hinge lines trend from NE–SW to N–S (i.e. nearly perpendicular to the early folds) with gentle plunge in both directions. The two generations of folds are associated with axial plane foliations. The allochthonous Jutogh and Chail formations, and the autochthonous Simla Group have the similar fold

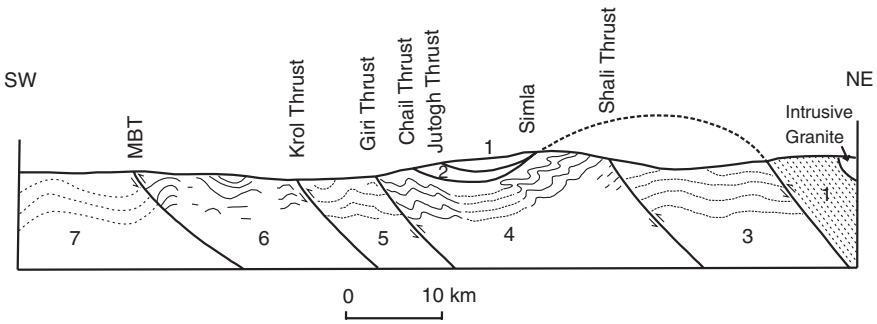

Fig. 11.14 A geological cross-section of the Simla Himachal Himalaya along the line X–Y in Fig. 11.13. *MBT* Main Boundary Thrust [from Dubey and Bhat (1991), © Elsevier. Published with permission of Elsevier]

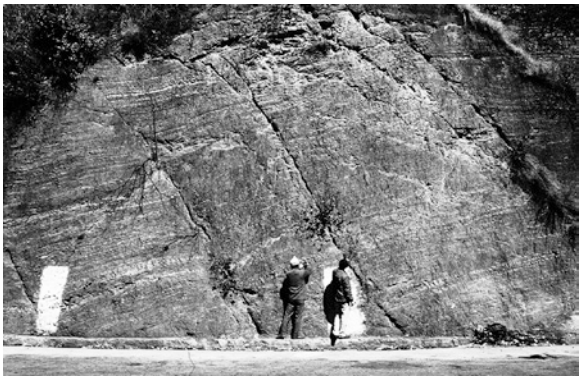

Fig. 11.15 Normal faults in the Simla Group of rocks near the Giri Thrust at Kandaghat

geometries (Dubey and Bhat 1991) indicating that there is no earlier deformation of the klippe rocks in the root-zone.

A cross-section of the area is shown in Fig. 11.14. The Chail and Jutogh thrusts are distinctly spaced in SW part of the klippe but they nearly merge in NE thereby reducing the thickness of the Chail Formation to a few meters. Hence the two thrusts are termination splays of a single master thrust. The maximum horizontal translation along the klippe detachment thrust, determined by the "klippe to fenster method" is ~40 km. The large displacement was possible because of presence of a lubricant graphitic schist band at the thrust surface.

The characteristic features of the Simla Group are as follows.

1. Occurrence of normal faults in the hanging wall in vicinity of the Giri Thrust (Fig. 11.15).
2. Upright folds at some distance from the Giri Thrust (Fig. 11.16), and
3. Asymmetric folds at the northern contact with the klippe (Fig. 11.17).

Fig. 11.16 An upright early fold, ~1 km from the Giri Thrust (north of Kandaghat)

Fig. 11.17 An overturned fold in the Simla Group of rocks, ~8 km south of the Shali Thrust (north of Simla town)

The section cannot be balanced for the following reasons.

1. There is no marker bed across the thrusts.
2. Minor strike-slip faults (post thrusting) are present in the Krol-Tal sequence around Solan. These faults indicate extension normal to the plane of the cross-section hence assumption of plane strain deformation is not valid for the region.
3. Depth of basal decollement and dip of the sole thrust are not known. Hence no estimates can be made for the original area or length of the section restored.

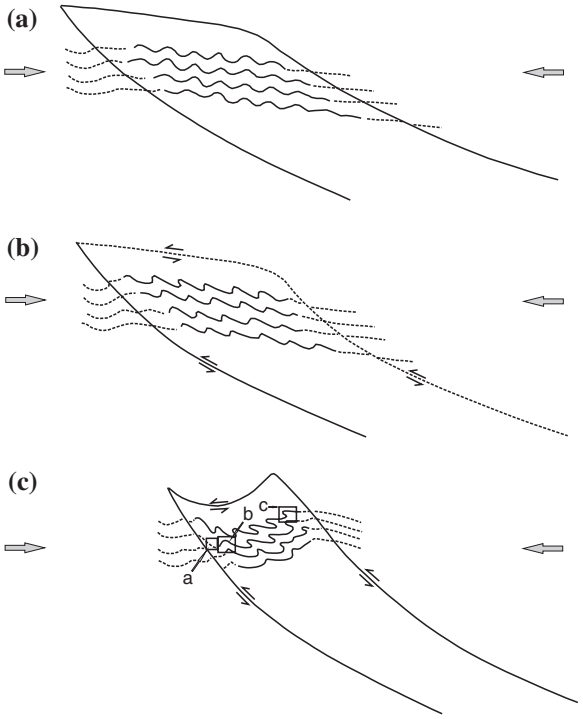

Fig. 11.18 A simplified model for structural evolution of the Simla area. **a** Simultaneous development of upright folds and thrusts. The *arrows* indicate the axis of maximum compression. **b** Modification of the upright fold geometry to asymmetric and overturned forms as a result of increase in displacement along the sub-horizontal Chail-Jutogh thrust. **c** Formation of second order folds, increase in dip of the thrusts, and folding of the sub-horizontal part of the thrust resulting in thrust locking. The structural features developing at locations a, b, and c are shown in Figs. 11.15, 11.16 and 11.17, respectively [from Dubey and Bhat (1991), © Elsevier. Published with permission of Elsevier]

A model for structural evolution of the area is shown in Fig. 11.18. The model considers simultaneous development of folding and thrusting. Since the faults had listric geometry, the hanging wall beds were tilted in dip direction of the thrusts. Oblique orientation of the beds with reference to the thrusts conforms to zone 1 of the strain ellipse developed by progressive simple shear (Fig. 7.7). The shear strain in vicinity of the thrust resulted in extension of the layering and formation of normal faults near the thrust (Fig. 11.18a). At some distance from the thrust, layer parallel shortening was prominent resulting in formation of upright folds. Progressive increase in shear strain, associated with the roof thrust, modified the upright fold geometry to asymmetric and overturned fold patterns (Fig. 11.18b). The modification was accompanied by a decrease in fold interlimb angles leading to rotation hardening of the folds. Finally, the sequence was folded into second order folds (Fig. 11.18c) along with folding of the roof thrust. The folded sequence was not favourable for further translation hence this resulted in thrust locking. In view of the locking, the minimum displacement of 40 km appears to be very

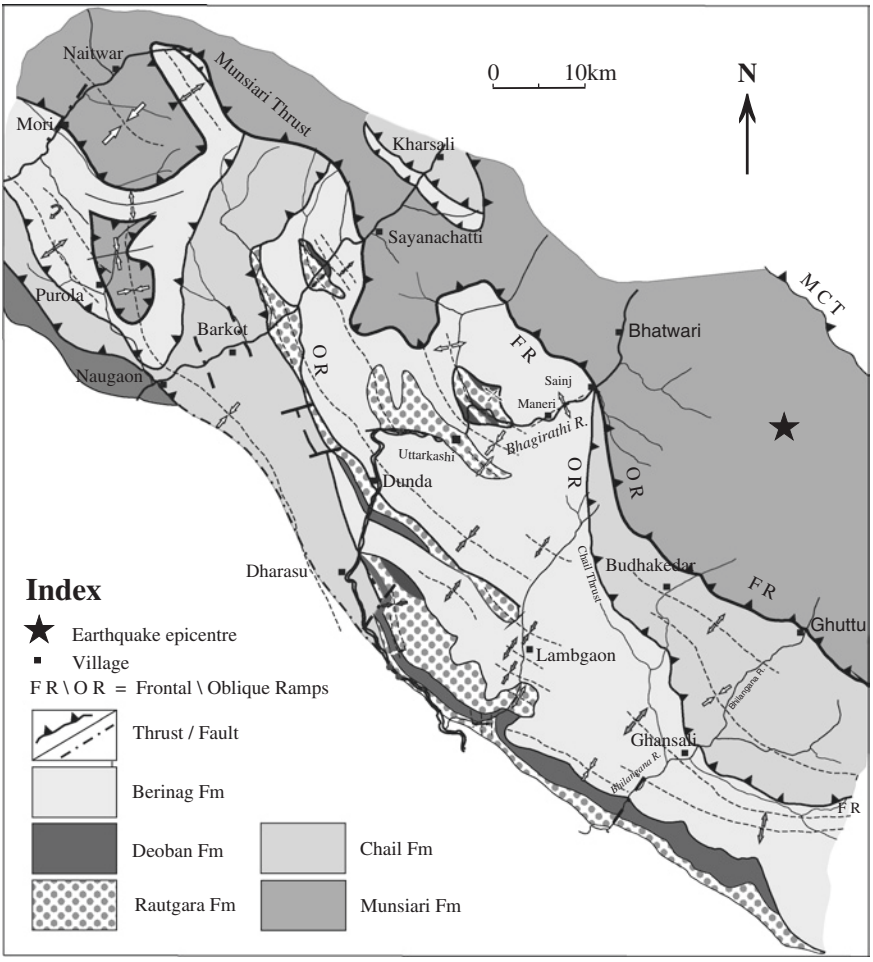

Fig. 11.19 Geological map of a part of the Inner Lower Himalaya (Garhwal) around Uttarkashi (after Dubey and Bhakuni 2008)

close to the maximum possible displacement along the thrust. Another implication of thrust locking is that the superposed folds, which formed after the locking show a uniform occurrence throughout the area, irrespective of their distance from the thrusts.

11.9 Structural Evolution of the Uttarkashi Area

The Uttarkashi area is situated SE of Simla syncline. A geological map of the area is shown in Fig. 11.19 and the lithotectonic set-up in Table 11.2. Two prominent thrusts (Munsiari and Chail) are exposed in the area along with some minor thrusts. Total displacement along the thrusts cannot be determined because of different rock types on the two sides. The early folds are oriented around NW–SE axis whereas

Table 11.2 Tectonostratigraphy of the Inner Lower Himalaya (Garhwal) around Uttarkashi (after Dubey and Bhakuni 2008)

Formation	Gross lithology
Munsiari Formation	Variety of schists, micaceous quartzites, and gneisses of the lower amphibolite facies
	Munsiari Thrust
Chail Formation	Quartz-porphyry and porphyritic granite suite in a succession of phyllites, quartzwackes and metasiltstones
	Chail Thrust
Berinag Formation	Coarse grained to pebbly sericitic quartz arenite with basalt and tuffites.
Deoban Formation	Cherty dolomite and dolomitic limestone with intercalations of blue limestone and gray slate
Rautgara Formation	Intercalations of slate and sub-graywacke with extensive basic sills, dykes and lava flows
	North Almora Thrust

the superposed folds show variable trends from N–S to NE–SW. Curvature of fold hinge lines in vicinity of oblique ramps suggests that the early folds and thrusts have developed simultaneously. A prominent lineation, formed as a result of flexural-slip during the early folding and thrusting, trends in NE–SW direction. Folding of the thrusts during the superposed deformation can be seen in NW part of the area.

The magnetic strains are of low values as most of the axial ratios are ~1:0.9 (Fig. 11.20). No systematic relationship can be established between the axial ratios and distance of the sample from a thrust. Petrofabric strain, determined from seven samples using the R_f/φ technique, was slightly higher than the magnetic strain as the axial ratios range from 1.18:1 to 1.67:1. There is no systematic relationship between distance from a thrust and the magnitude of strain. Hence the strain pattern was not controlled by thrusting alone and folding has also played a significant role. The low strain patterns are suggestive of the following.

1. Displacements along the thrusts are of low order of magnitude.
2. The folds were formed by flexural-slip mechanism where the internal layer strain is minimum except at the hinge zone. Presence of slicken sides on bedding surfaces and geometry of dilational veins on the limbs and hinge zones support the flexural-slip mechanism.
3. The thrusting was confined to a narrow zone but in absence of a lubricating horizon, which can act as a plane of decollement, the possibility appears to be remote.

11.9.1 The Model

Earlier studies in the area (Dubey and Bhakuni 2008) have brought out the following significant features.

1. Neotectonic stress pattern in most of the area is favourable for formation of normal faults. The only exception is southern part of the area at the North Almora Thrust where the pattern is representative of thrust faulting, indicating that the thrust is still not locked.

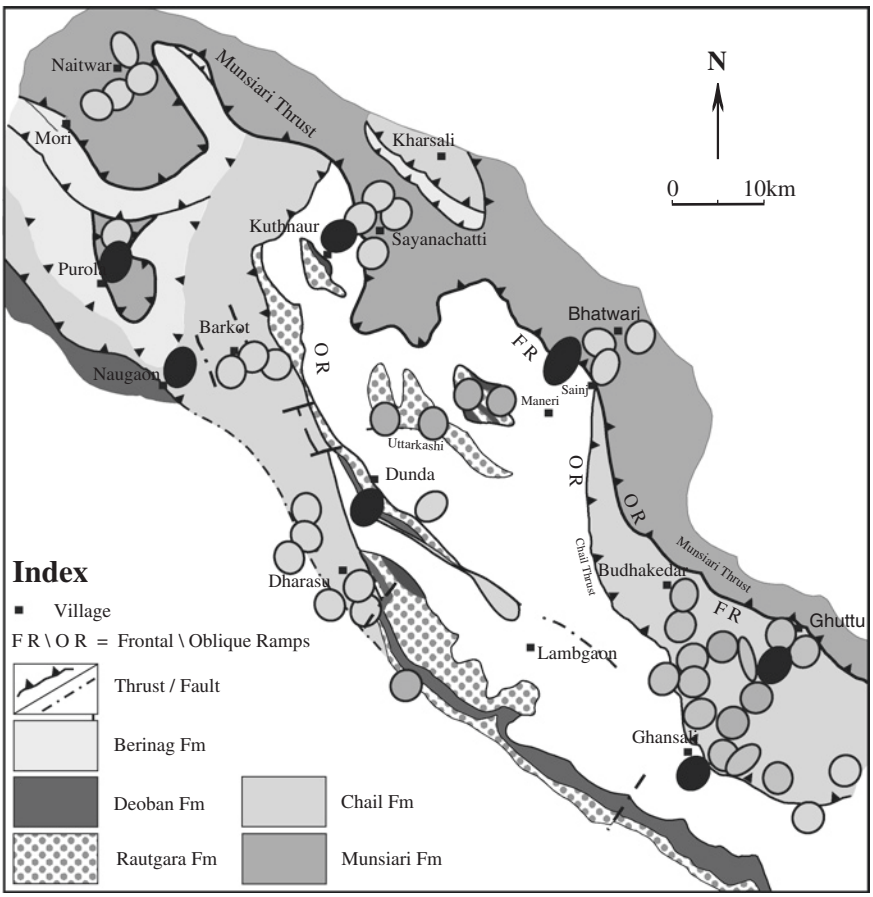

Fig. 11.20 The distribution of magnetic susceptibility ellipses (*gray*) (containing the maximum and minimum axes), and petrofabric ellipses (*black*, X–Z plane). The small axial ratios suggest flexural-slip mechanism of folding (after Dubey and Bhakuni 2008)

2. Hanging wall of the Munsiari Thrust is characterized by stress conditions favourable for normal faulting with some oblique slip component. This suggests locking of Munsiari thrust.
3. The Uttarkashi antiformal fold in central part of the area was formed as a fault propagation fold due to displacement along a blind thrust (Thakur and Kumar 1995).

A schematic model for evolution of structures in the area is shown in Fig. 11.21. The first stage of deformation (Fig. 11.21a) shows displacement along a gently dipping thrust fault with maximum extension in the vertical direction during compressive strain. With increase in deformation, the fault surface rotates in a clockwise direction thereby resulting in increase in thrust dip (Fig. 11.21b). The model extends in the

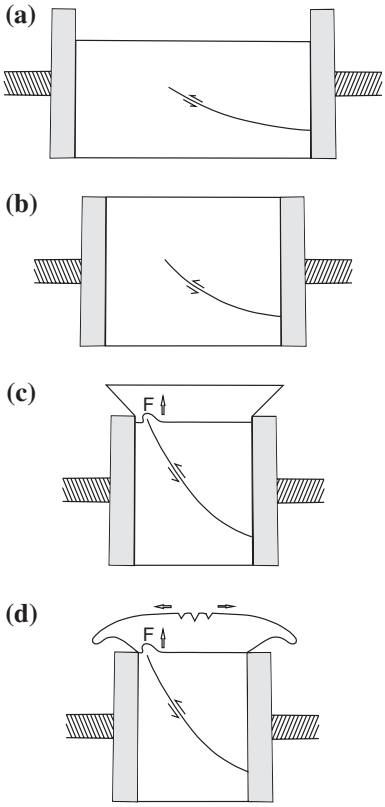

Fig. 11.21 Schematic diagrams showing development of compressional strains at depth and extensional strains at upper levels resulting in different types of faults. **a** Compression of a geological body, extension in the vertical direction and initiation of a gently dipping listric thrust fault. **b** Rotation of the thrust in a clockwise direction resulting in increase in dip. The upper part of the body reaches to the height of the pistons. **c** Overflow of the upper part of the body. The thrust at the lower level can form a fault propagation fold within the compressional regime. **d** Collapse of the upper part as a result of gravity with formation of extensional faults. The new location of the fault propagation fold is in the extensional regime hence the fold amplification is dropped (after Dubey and Bhakuni 2008)

vertical direction and reaches up to the height of the pistons. Increase in displacement along the fault led to initiation of a fault propagation fold (F, Fig. 11.21c). The degree of asymmetry of the fold depends upon the dip of the thrust. A gentle dip results in a greater asymmetry. The upward extension of the model, after surpassing the height of the pistons, leads to overflow of the upper part in horizontal directions. The overflow results in extensional regime at higher levels creating conditions suitable for formation of normal faults. The described mechanism may be responsible for development of recent shallow normal faults in several parts of the Himalaya where similar deformation condition exists (e.g. Kandpal et al. 2006; Rautela and Sati 1996; Valdiya et al. 1984; Srivastava and John 1999).

The model explains the absence of young thrusts at the surface. The active blind thrust cannot propagate in an upward direction because of prevalence of extensional strains near the surface. Thus the proposed model brings a tiding for the regional habitats. The contrasting stress condition at the upper level can reduce or confine the displacement along an active thrust fault thereby lowering the intensity of a possible earthquake. The model is suggested for the Uttarkashi area but the inference can be extended to other parts of the Himalaya as well. For example, the following four major earthquakes have occurred in the Himalayan belt.

1. Shillong earthquake (12 June 1897, M 8.1)
2. Kangra earthquake (4 April 1905, M 7.8)
3. Bihar–Nepal earthquake (15 January 1934, M 8.1)
4. Assam earthquake (15 August 1950, M 8.6)

However none of these events has produced coseismic surface ruptures (Yeats and Thakur 1998). The above model can explain the termination of thrust faults beneath the surface because of prevalence of extensional strains at the surface.

The described variation of the stress state with depth is significant for understanding of seismicity in the Himalayan region. The inference has implication for GPS studies as well where all the data are collected from surface displacements alone.

11.10 Structural Evolution of the Mussoorie Syncline

The Garhwal Lower Himalaya should be regarded as the most crucial region for study of thrust tectonics because the maximum displacement along a Himalayan thrust (~80 km) was proposed in this region. The contradictory view of pop-up klippen with a limited displacement was also introduced in this region. Since crustal shortening and earthquake predictions are based on displacement along thrusts, it is always better to work on alternate or multiple choices of evolutionary models. With development of new techniques, evidence can be obtained in favour of one of these models. This is more so important because the knowledge of earthquake prediction is still in its infancy.

A large number of klippen are exposed in the Garhwal–Kumaun (now Uttarakhand) region. The klippen detachment thrust was assumed to have root-zone in the High Himalaya (Gansser 1964). However, some of these klippen were re-examined in view of emerging knowledge on thrust tectonics, and the earlier model was either modified or an alternate model was proposed (Dubey and Paul 1993; Srivastava and Mitra 1994; Jayangondaperumal and Dubey 2001; Devrani and Dubey 2008).

The Mussoorie noncylindrical syncline lies south of the Uttarkashi area. It extends in NW–SE direction and occurs as a hanging wall structure above the MBT (Fig. 11.2). The Satengal, Banali, and Darak klippen occur in the synclinal core.

Middlemiss (1887) suggested an autochthonous model for structural evolution of the area based on field observations and petrological similarities of the klippen

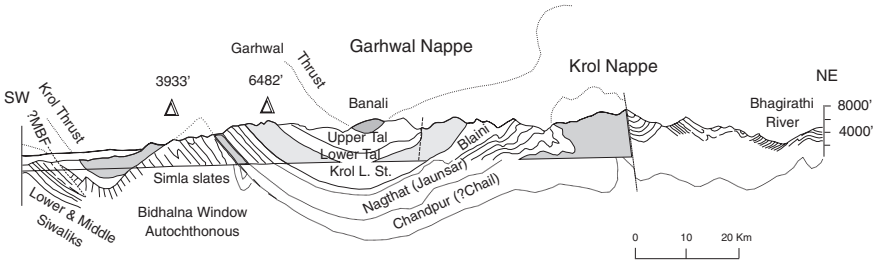

Fig. 11.22 An earlier geological cross-section across the Mussoorie Syncline showing an allochthonous klippe (after Auden 1937)

and the adjacent rocks (Chandpur Formation). This was the time when the concept of large-scale translation along thrust sheets was introduced in the Scottish highlands (Peach and Horne 1884; Peach et al. 1907) and was followed later in the Alps (Heim 1919). Influenced by this, Pilgrim and West (1928) proposed a large-scale thrust displacement model in the Simla Lower Himalaya. The area of Garhwal Lower Himalaya was assigned by the Geological Survey of India to J.B. Auden, who proposed a geological cross-section of the area (Fig. 11.22; Auden 1937). The Garhwal Lower Himalaya was classified in two dominant structural units, namely, Krol Nappe and Garhwal Nappe. The Garhwal Nappe was depicted as occurring in form of a detached klippe over the Krol Nappe with displacement of nearly 80 km southward from its root in the Central Crystallines of the High Himalaya. Most of the later workers (e.g. Gansser 1964; Valdiya 1980) have followed the Auden's work despite that there is a marked contradiction in his stratigraphic observation and structural interpretation. The stratigraphic table (Auden 1937) describes the uppermost horizon of the Garhwal Nappe as metamorphosed Chandpur Formation (a lower Himalayan Formation) whereas the cross-section brings the klippe rocks from the High Himalaya where the Chandpur Formation does not exist. Later, Jain (1972) confirmed that the klippe rocks resemble the older Lesser Himalayan formations and inferred that the tectonic units of Garhwal Thrust are of local origin, developed somewhere near the base of the Krol Thrust Sheet in the north. Hence he found it difficult to visualize their large-scale displacement from the base of the Central Himalaya and to connect the Garhwal thrust with the Main Central Thrust. Saklani (1993) also mapped the klippen rocks as Chandpur phyllite.

It is evident from the above discussion that the earlier workers have clearly identified the klippen rocks as the Lower Himalayan formations but the regional structure was explained in terms of large-scale displacement along a thrust from an assumed root zone in the High Himalaya. In the backdrop of these information, the area was remapped by Jayangodaperumal (1998) on 1:50,000 scale. Additional information on lineaments and lithological boundaries were obtained from the computer compatible tape of IRS LISS II/A2 (Fig. 11.2).

The rocks were subjected to two phases of folding. The first phase was initiated simultaneously with development of the thrusts. These early folds show a wide

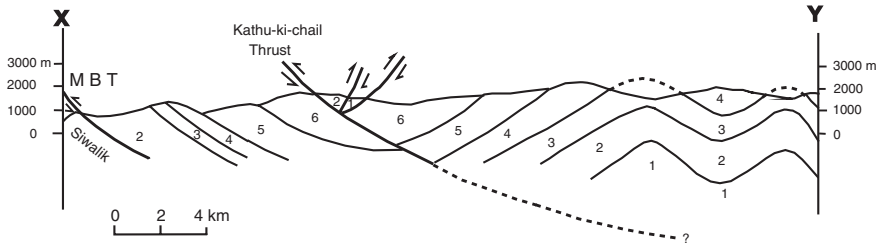

Fig. 11.23 A revised geological cross-section of the Mussoorie Syncline (along *X–Y line* marked on Fig. 11.2) showing development of a klippe in the core. Legend same as Fig. 11.2 [from Jayangondaperumal and Dubey (2001), © Elsevier. Published with permission of Elsevier.]

variation in geometry from open to isoclinal and occasionally recumbent. The fold hinge lines vary in trend from NW–SE to E–W directions and asymmetry of the folds indicate a sense of shear from top to the SW. Superposed folds developed after locking of the thrusts. Minor superposed folds are mostly upright to asymmetric kinks and chevrons, and vary in trend from NE–SW to N–S. The klippen rocks are characterized by fold interference patterns and two sets of prominent foliations, which are axial planar to the early and superposed folds. Considering the klippen rocks as Lower Himalayan formations, a revised cross-section was presented by Jayangondperumal and Dubey (2001) (Fig. 11.23). The section shows a prominent listric thrust (Kathu-ki-chail) and two back thrusts that are exposed east of Anand Chowk (near Satengal). The Satengal klippe consists of the older Mandhali and Chandpur formations overlying the younger Tal Formation.

As a result of fold interference between the early and superposed folds, dips of the klippen rocks are not always centripetal. The inward dips were observed in the surrounding rocks outside the klippen. The superposed synformal hinge lines separate the Satengal, Darak (Ringalgarh) and Banali klippen (Fig. 11.2).

The rocks have undergone a weak deformation resulting in either absence or poor development of linear and planar structures. The weak deformation is further confirmed by Flinn plots of magnetic susceptibility ellipsoids (Fig. 11.24). The plot represents variation in ellipsoid shapes from prolate to plane strain to oblate shapes, without any systematic variation across the area.

The two dimensional data of magnetic strain (Fig. 11.25) reveal small axial ratios and random orientations of the Kmax axes. The strain pattern is oblique to the thrusts and seems to be unaffected by the trailing frontal ramp, oblique ramp or the klippen detachment thrust.

Similar observations were made in orientation pattern of the petrofabric ellipses obtained by the Centre to centre (Fry 1979) and Surfor wheel (Panozzo 1987) methods (Fig. 11.26). Samples for the petrographic studies were collected from quartzites of Chandpur, Nagthat and Tal formations. The longer axes of the strain ellipses (Kmax) are parallel to the early or superposed axial plane foliations. In the NW (around Nagthat village), the ellipses are arranged in diverse orientations because of prominence of superposed folds and their interference patterns. In the

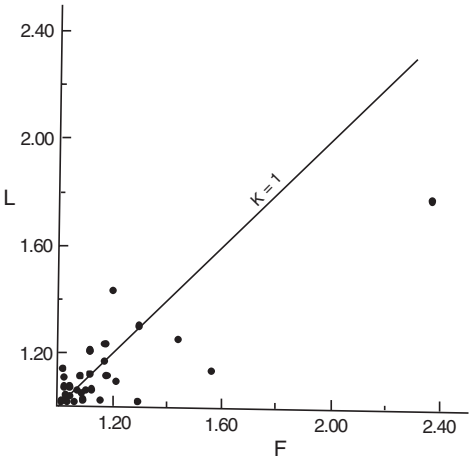

Fig. 11.24 Flinn diagram depicting shapes of AMS ellipsoids. The *vertical* axis is magnetic lineation (L = Kmax/Kint and the *horizontal* axis is magnetic foliation (F = Kint/Kmin) [from Jayangondaperumal and Dubey (2001), © Elsevier. Published with permission of Elsevier]

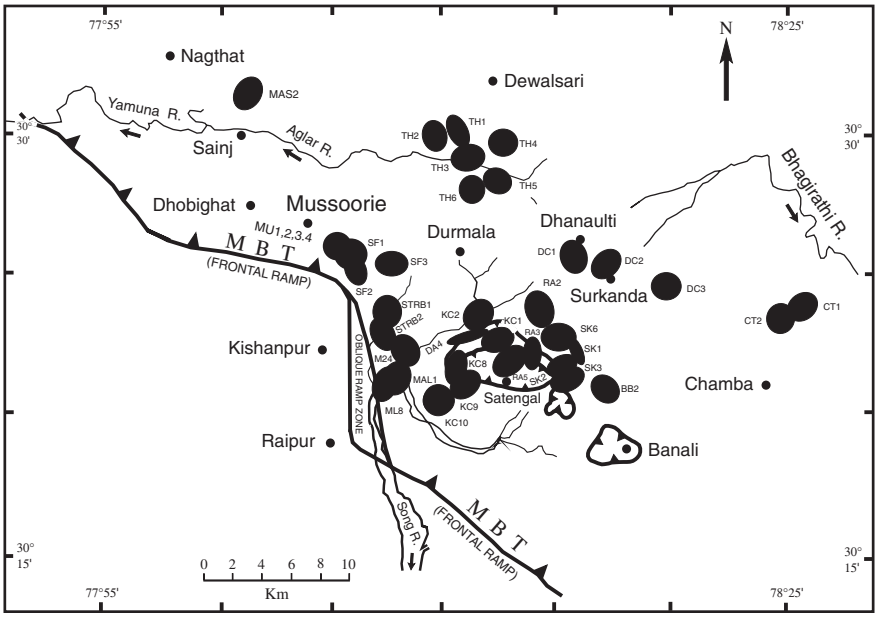

Fig. 11.25 Distribution of magnetic susceptibility ellipses (containing the maximum and minimum axes) in and around the Mussoorie Synclinal region [from Jayangondaperumal and Dubey (2001), © Elsevier. Published with permission of Elsevier]

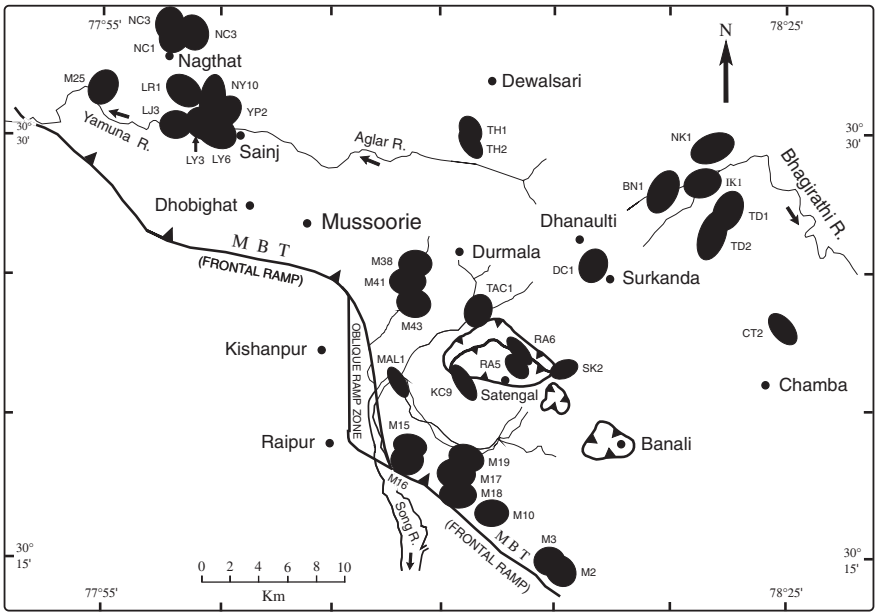

Fig. 11.26 Distribution of petrofabric strain ellipses (*XZ plane*) in and around the Mussoorie Syncline [from Jayangondaperumal and Dubey (2001), © Elsevier. Published with permission of Elsevier]

NE, the ellipses follow the trend of superposed fold hinge lines. In the central part of the map (east of the oblique ramp), the axial trace of the Mussoorie Syncline shows a prominent curvature (Fig. 11.2) as a result of interference between the simultaneously developing folds, frontal and oblique fault ramps. Following the trend of the syncline, the ellipses are also arranged oblique to the oblique ramp and parallel to trace of the axial surface. Along the leading frontal ramp of the MBT, the axial ratios are low and the longer axes are parallel to strike of the formations rather than the trend of the thrust. This indicates that displacement along the MBT is of a low order of magnitude and the strains are related to development of the Mussoorie Syncline (i.e. early folding).

A simplified orientation pattern of strain ellipses during early and superposed deformations is illustrated in Fig. 11.27. During the early deformation, the Kmax showed E–W orientation (considering the vertical edge of the diagram pointing towards north), normal to the axis of maximum compression. The oblique ramp shear zone with right lateral displacement resulted in NW–SE trend of the longer axes. During the superposed deformation (Fig. 11.27b), change in the direction of maximum compression led to reactivation with left lateral displacement along the oblique ramp shear zone resulting in rotation of the Kmax in the zone. The precise orientation depended upon the amount of simple shear along the zone. Away from the oblique ramp, the Kmax showed N–S orientation, normal to the axis of maximum compression during the superposed deformation. Additional orientations resulted because of different rotations of the earlier ellipses.

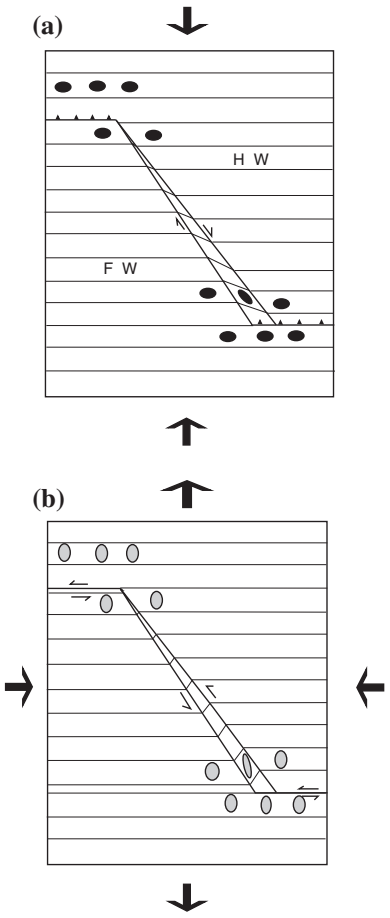

Fig. 11.27 The orientations of strain ellipses during early (**a**) and superposed deformations (**b**) around frontal ramps and oblique ramp shear zone. *HW* hanging wall; *FW* footwall. Note reversal of displacements along the initial frontal thrust ramps and oblique ramp during the superposed deformation [from Jayangondaperumal and Dubey (2001), © Elsevier. Published with permission of Elsevier]

The Hrouda double plot (Fig. 11.28) shows a low degree of anisotropy and a large variation in the angle between magnetic foliation and bedding. All the samples show a similar pattern irrespective of their distance from the thrusts suggesting a combination of lateral shortening and simple shear.

11.10.1 The Model

A two dimensional evolutionary model is shown in Fig. 11.29. The different layers designated as A to F roughly correspond to thicknesses of the Lower Himalayan formations. 'A' represents Mandhali, 'B' represents the next younger formation, Chandpur, 'C' Nagthat, 'D' Blaini, 'E' Krol, and 'F' Tal Formation. An initial listric fault (Fig. 11.29a) was formed during tensional regime in the region. Normal faulting took place along the fault (Fig. 11.29b) accompanied by

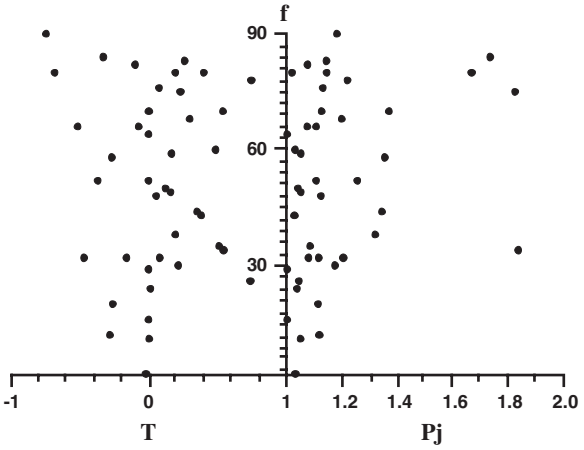

Fig. 11.28 Angle between magnetic foliation and bedding (f) plotted against shape (T) and degree of anisotropy (Pj) [from Jayangondaperumal and Dubey (2001), © Elsevier. Published with permission of Elsevier]

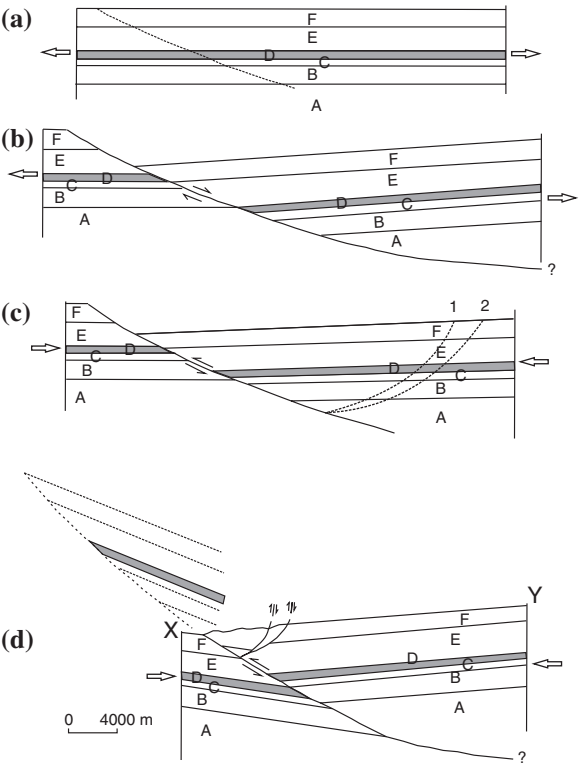

Fig. 11.29 Schematic diagram showing sequential development of klippen in the core of the Mussoorie Syncline. **a** Initiation of a fracture during tensional regime in the region. **b** Normal fault displacement along the fault. **c** During the later compressional regime, initiation of a conjugate set of fracture in the hanging wall. **d** Large displacement along the main thrust and minor displacements along the back thrusts leading to the development of pop-up klippen. *X*–*Y* represents the present erosion level (scale approximate) [from Jayangondaperumal and Dubey (2001), © Elsevier. Published with permission of Elsevier]

anticlockwise rotation of the hanging wall block and tilting of the beds opposite to the fault dip. The Tertiary compressional phase resulted in reactivation of the normal fault as thrust and clockwise rotation of the hanging wall beds. This was

followed by initiation of a conjugate set of faults (back thrusts; marked 1 and 2 in Fig. 11.29c) to fill-up the space generated by displacement of the main listric fault (Kathu-ki-chail thrust). The main thrust brought the lower formations (Mandhali and Chandpur) to higher topographic levels. A larger displacement along back thrust 2, as compared to back thrust 1, brought up the Mandhali Formation at the uppermost horizon and in thrust contact with the Chandpur Formation. Thus, a combination of displacements along the main thrust and back thrusts resulted in formation of the klippe. Subsequent regional shortening led to an open synformal structure in the region. The cross-sectional geometry suggests that relative displacement can be of a higher order of magnitude along a steep thrust but in geological situations a higher dip results in increased friction hence early locking. It is also to be noted that a larger displacement along the main thrust could have brought the rocks from a deeper level. Thus, presence of rocks in klippen depends upon the extent, geometry, and total displacement along the main thrust. In the Satengal klippe, it is not possible to estimate the maximum translation along the thrust, because of absence of data on the attitude of the main thrust. However, geometrical considerations suggest that the translation should be considerably less than 80 km proposed earlier.

A pictorial evolution of the area in three-dimensions is illustrated in Fig. 11.30. Frontal and oblique fault ramp geometries of the basement are shown in Fig. 11.30a. The oblique, leading and trailing frontal ramps are marked as 'OR', 'L', and 'T', respectively. Deposition of the cover rocks took place on the faulted basement. At the onset of the compressional phase, the trailing frontal ramp propagated by extending its length and a rejoining back thrust 'BT' initiated in the basement (Fig. 11.30b). Fault propagation folds formed in the cover rocks at the propagating thrust tips. The rejoining back thrust formed a pop-up structure and an arcuate noncylindrical fold. The number of folds increased with increase in shortening (Fig. 11.30c). During the subsequent superposed deformation, the maximum compression axis changed its orientation and became parallel to strike of the frontal ramps (Fig. 11.30d). A number of superposed folds initiated and interfered with the early folds. The dome and basin pattern was prominent because of orthogonal relationship between the early and the superposed fold hinge lines. One such pattern is shown above the back thrust. Subsequent erosion of the folds led to exposure of older rocks surrounded by younger rocks (Fig. 11.30e) thereby resulting in the formation of klippen. Superimposed folding of the trailing frontal ramp has provided limited exposure of the thrust around the domes and it remained as a blind thrust along the remaining part of the strike. Figure 11.30e is labeled for comparison with the geological map ((Fig. 11.2). Point 'J' represents the junction between the leading frontal ramp of the MBT and the oblique ramp, NE of Raipur, 'OR' represents the oblique ramp along the Song River, 'T' represents the trailing frontal ramp NE of Kishanpur, 'BT' represents exposed part of the blind thrust (Kathu-ki-chail thrust), 'S' and 'B' are present outcrops of the Satengal and Banali klippen.

The proposed 3-D evolution of the region was partially simulated by performing an experiment using modeling clay model (Dubey and Jayangondaperumal

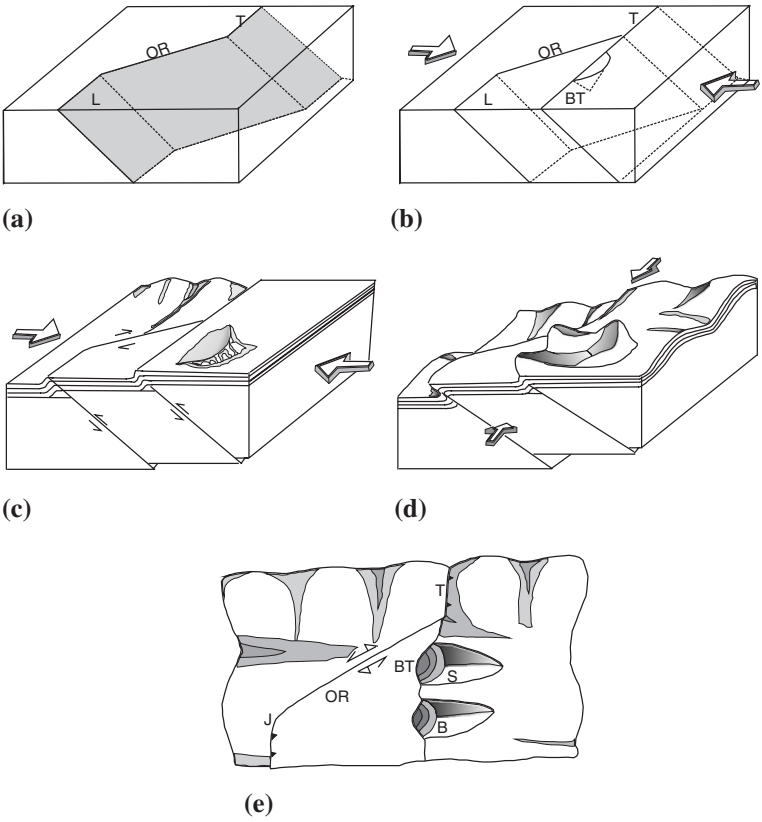

Fig. 11.30 A schematic diagram showing sequential development of Satengal and Banali klippen. **a** Geometry of an initial basement fault at the onset of compressional phase. *T* trailing frontal ramp; *L* Leading frontal ramp; *OR* oblique ramp. **b** Extension of the trailing frontal ramp along the strike followed by formation of a back thrust. Large arrows indicate the maximum compression direction. **c** Thrusting and development of fault propagation folds above the frontal ramps during early deformation. Extension of the trailing ramp remains a blind thrust. **d** Change in the compression direction resulting in superposed deformation and interference between early and superposed folds. Prominent folds occur above the pop-up structure. **e** Erosion of hanging wall with exposure of older rocks surrounded by younger rocks. [From Jayangondaperumal and Dubey (2001), © Elsevier. Published with permission of Elsevier.]

2005) (Fig. 11.31). The external dimensions of the model were 15 × 11 × 7 cm. Five layers of modeling clay, each approximately 1 mm thick, formed the multilayer packet that was sandwiched between two thick slabs of modeling clay. The models were cut to predetermined geometries for simulation of thrust faults that were initiated as normal faults. In the basement, the trailing frontal ramp extended to the other end of the model and the leading frontal ramp terminated in the oblique ramp that acted as a connecting splay with the trailing frontal ramp (Fig. 11.31a). The multilayers were cut for two parallel frontal ramps joined by an

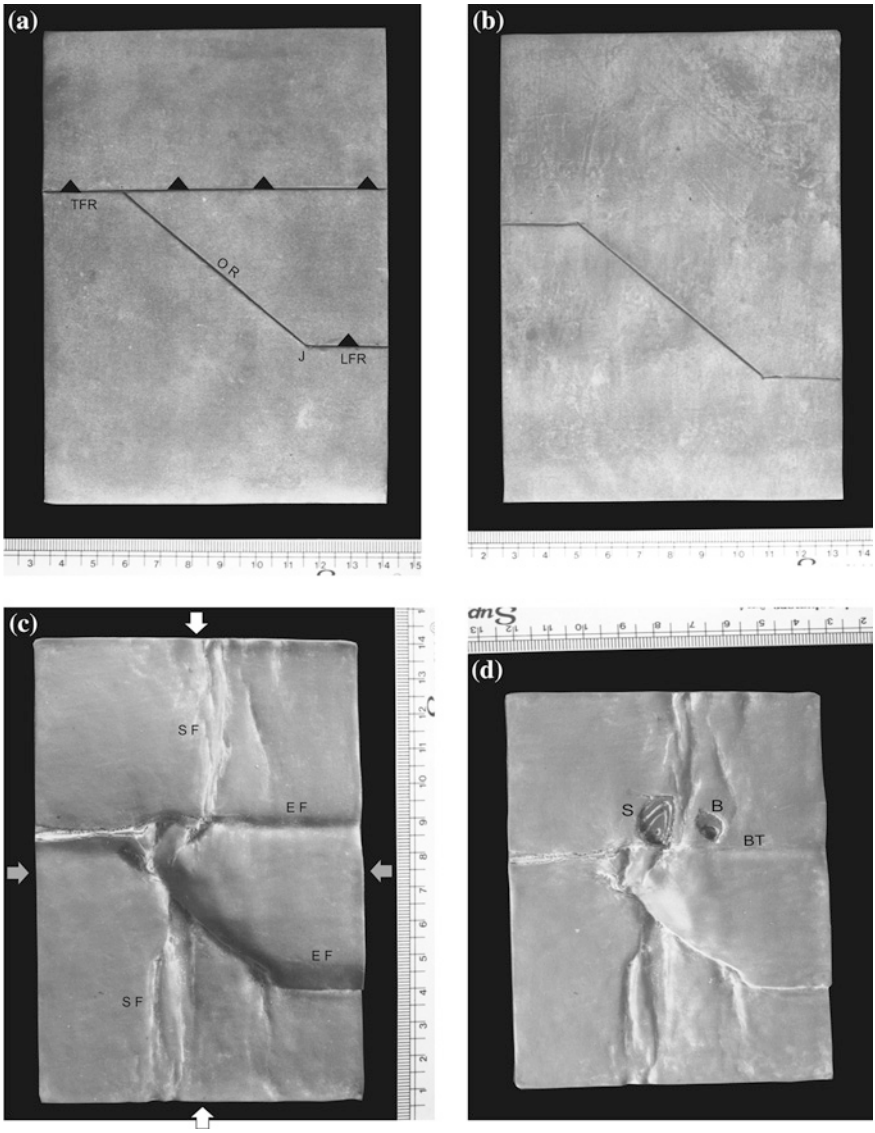

Fig. 11.31 **a** Frontal and oblique ramp geometries of the initial basement faults in a homogeneous block of modeling clay. *TFR* trailing frontal ramp; *LFR* leading frontal ramp; *OR* oblique ramp; *J* junction of frontal and oblique ramps. **b** Frontal and oblique fault ramp geometries in a cover layer consisting of modeling clay. **c** Development of early folds (*EF*) and superposed folds (*SF*) on a deformed layer surface. White arrows, early compression direction; gray arrows, superposed compression direction. **d** A horizontal slice was cut and removed from the layer surface at stage 'c' to expose lower layers of the sequence along the blind thrust (*BT*) of the trailing frontal ramp. *S* Satengal klippe; *B* Banali klippe (after Dubey and Jayangondaperumal 2005)

oblique ramp (Fig. 11.31b). Hence the fault geometries were slightly different in the basement and in the multilayers. Initial angle between the basement oblique ramp and the axis of maximum compression was 50° and initial dip of the fault was 30°. The model was deformed under the general strain boundary condition, i.e. the model was allowed to extend along the horizontal as well as vertical axes of the press when the axis of maximum compression acted along the layering in a horizontal direction.

Formation of cylindrical fault propagation folds was observed in the multilayers during early stages of deformation. The blind frontal thrust ramp of the basement was also reflected in the development of cover folds. The model was shortened up to 12 % overall shortening during the first phase of deformation and then it was compressed in horizontal direction normal to the earlier compression direction under the general strain boundary conditions. After 17 % shortening during the superposed deformation, superposed folds became prominent on the layer surfaces (Fig. 11.31c). In contrast to the early folds, these folds were mostly buckle folds that initiated both, on the hanging wall and footwall unaffected by the thrust. At this stage, a horizontal slice was cut from the deformed hanging wall layers to expose the internal structures above the blind thrust (Fig. 11.31d). Noncylindrical geometry of the antiformal superposed folds revealed close outcrop patterns resembling klippen structure (minus the development of back thrusts).

Apart from the prominent Himalayan thrusts, large strike-slip and minor normal faults are also exposed in the area. The strike-slip faults have formed after locking of the thrusts and indicate a change in orientation of the minimum stress axis from vertical to horizontal. The strike-slip faults are exposed at lower horizons and the klippen rocks exposed at higher elevations are not affected by these faults. In northern part of the area, a major E–W trending strike-slip fault is exposed along the Aglar River. The fault plane is characterized by abrupt termination of Nagthat Formation against the Blaini Formation. The fault is exposed south of Dewalsari (Magra–Dewalsari section) as well.

11.11 Structural Evolution of the Garhwal Syncline

The Garhwal Syncline is a regional noncylindrical fold trending in NW–SE direction. The polyharmonic Synform incorporates a number of synclines and anticlines (e.g. Lansdowne Syncline, Hyunil Anticline, Amri Syncline) (Fig. 11.3). Part of the Lansdowne synclinal core is occupied by intrusive granite.

The southern synclinal boundary is marked by the MBT. The general trend of the thrust is WNW–ESE forming a frontal ramp structure. However at the western termination of the fold, the trend changes to nearly N–S forming an oblique fault ramp. The northern boundary of the Synform is marked by Nayar thrust, where the Chakrata Formation of the Inner Lower Himalaya is exposed on the hanging wall. Recent studies suggest that the thrust has a component of strike-slip displacement (Devrani and Dubey 2008). Fold hinge line orientation and bedding-cleavage

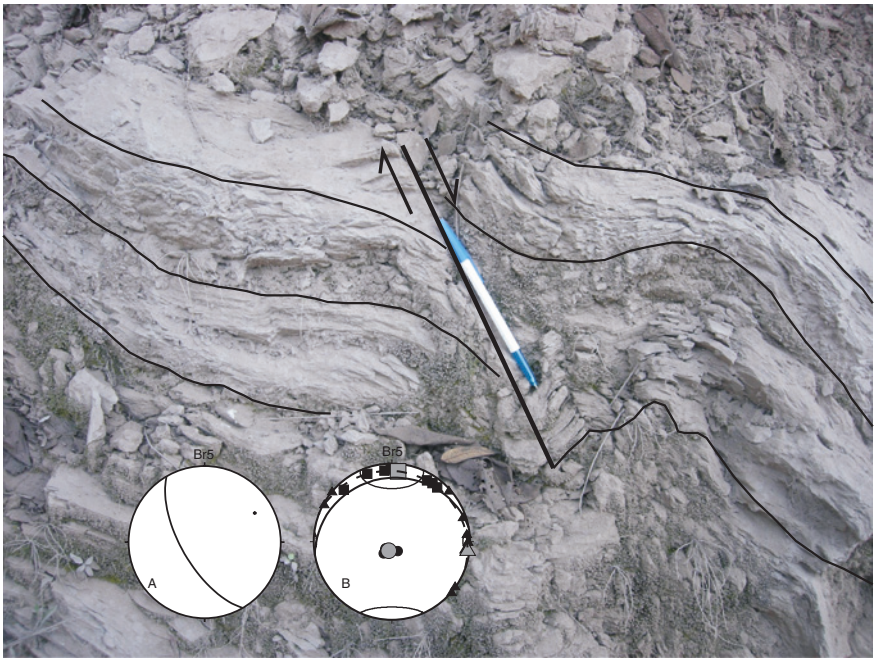

Fig. 11.32 A young normal fault showing curvature of bedding foliation at the fault surface (Krol Formation, NE of Rishkesh). Inset A shows orientation of the fault in the lower hemisphere stereographic plot. Inset B shows orientation of magnetic susceptibility axes near the fault in the lower hemisphere stereographic plot [from Devrani and Dubey (2008), © Blackwell Publishing Asia Pty Ltd. Published with permission of Blackwell Publishing Asia Pty Ltd.]

relationship indicate presence of two phases of folding episodes. Development of early folds with NW–SE to E–W fold hinge line orientations was coeval with the regional thrusts. Superposed NE–SW to N–S oriented fold hinge lines suggest maximum compression in NW–SE to E–W directions. These folds are generally small-scale chevron folds associated with upright to asymmetric kink bands that formed after locking of the thrusts. Several normal faults, which formed at different times, are exposed throughout the region. Some of the minor normal faults observed in the Blaini and Tal formations have thicker beds in the footwall and they do not displace the earlier axial plane cleavage indicating their formation as growth faults during the pre-Himalayan times. The youngest normal faults (Fig. 11.32) displace the foliations, which were formed during the early and superposed foldings. The minimum magnetic susceptibility axes at these locations are oriented in a vertical direction confirming that the principal magnetic susceptibility axes can be used to infer the neotectonic stress pattern (Chap. 2).

Petrofabric strain was determined by the Fry method using samples from the Nagthat, Tal, and klippen quartzites (Fig. 11.33a). In the western part of the area, the strain ellipses are arranged in diverse orientations with the longest axis oriented in

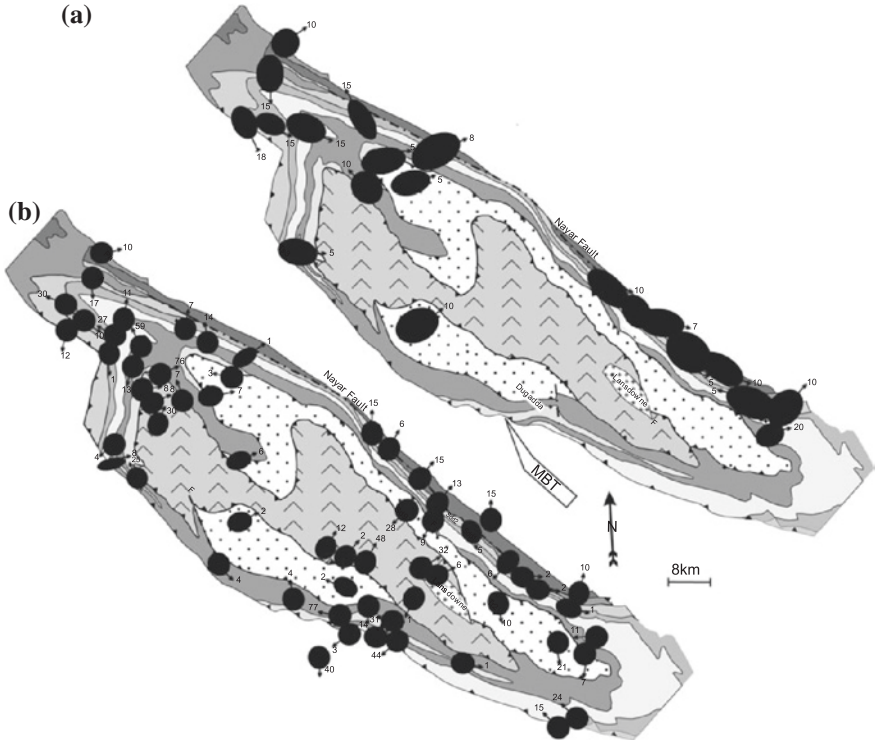

Fig. 11.33 Distribution, orientation and geometry of strain ellipses in the Garhwal Syncline. **a** Petrofabric strain ellipses. **b** Magnetic strain ellipses [from Devrani and Dubey (2008), © Blackwell Publishing Asia Pty Ltd. Published with permission of Blackwell Publishing Asia Pty Ltd.]

NW–SE direction parallel to the early fold trends and the MBT, or NE–SW to N–S directions parallel to the superposed fold hinge lines. In the eastern part of the area, the longest axes are oriented nearly E–W following the trend of the thrust, which separates the Chakrata and Chandpur formations. The ellipticity is low and varies between 1.18 and 2.17 along the strike direction and between 1.06 and 2.09 in the dip direction suggesting weak deformation in the area. The quartzites of the Nagthat Formation and the outer klippen show the highest strain ratios varying between 1:1.16 and 1:2.09. The magnetic susceptibility ellipses, reveal smaller axial ratios varying from 1:1.01 to 1:1.71 (Fig. 11.33b). The smaller strain values can be attributed to the fact that the AMS mainly reflects the later deformation.

The Hrouda double plot reveals a low degree of anisotropy (<2), and a large variation in the angle (0°–90°) between magnetic foliation and bedding (Fig. 11.34). This suggests that a combination of lateral shortening and simple shear was responsible for deformation in the area. The inference is also supported by absence of a prominent lubricating horizon, which can facilitate a large translation under simple shear. Similar patterns were obtained from the Kangra, and

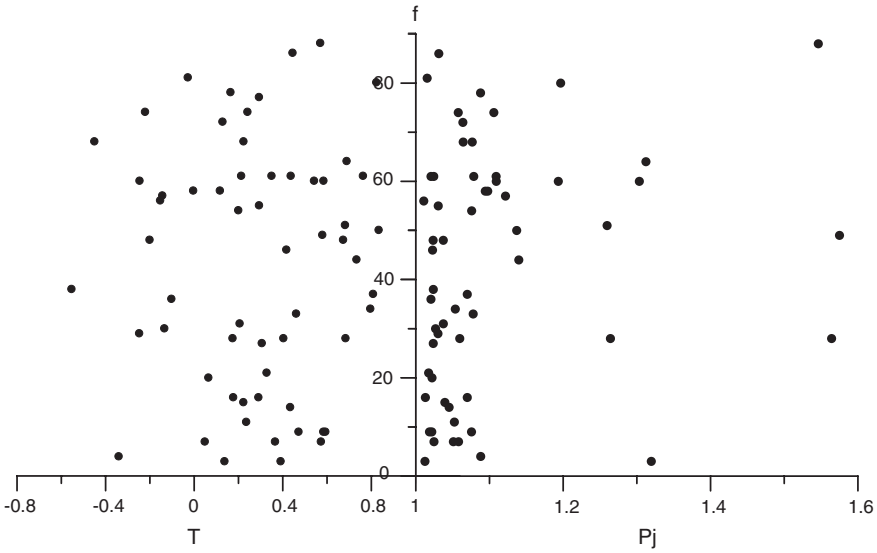

Fig. 11.34 Hrouda double plot depicting relationships between degree of anisotropy (Pj), shape parameter (T), and angle between magnetic foliation and bedding (f) [from Devrani and Dubey (2008), © Blackwell Publishing Asia Pty Ltd. Published with permission of Blackwell Publishing Asia Pty Ltd.]

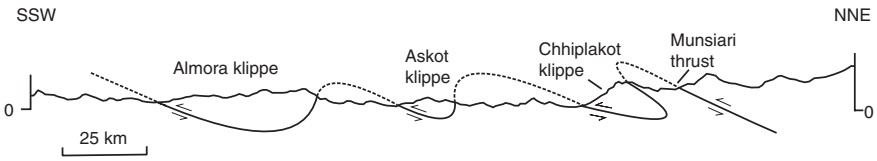

Fig. 11.35 Allochthonous model of thrust tectonics. Large scale displacement along a single thrust is interpreted to have resulted in a number of klippen in the Garhwal-Kumaun Lower Himalaya [from Valdiya (1980), © K.S. Valdiya. Published with permission of K.S. Valdiya.]

Mussoorie areas. Hence it can be inferred that the hanging wall rocks along the MBT in the western Himalaya have undergone a similar deformation pattern.

11.11.1 The Model

Evolution of the Garhwal klippe (Almora klippe) was earlier described as a result of large-scale displacement along a klippen detachment thrust (Fig. 11.35; Valdiya 1980) whose root-zone lies in the High Himalaya and the displacement initiated from the Munsiari Thrust.

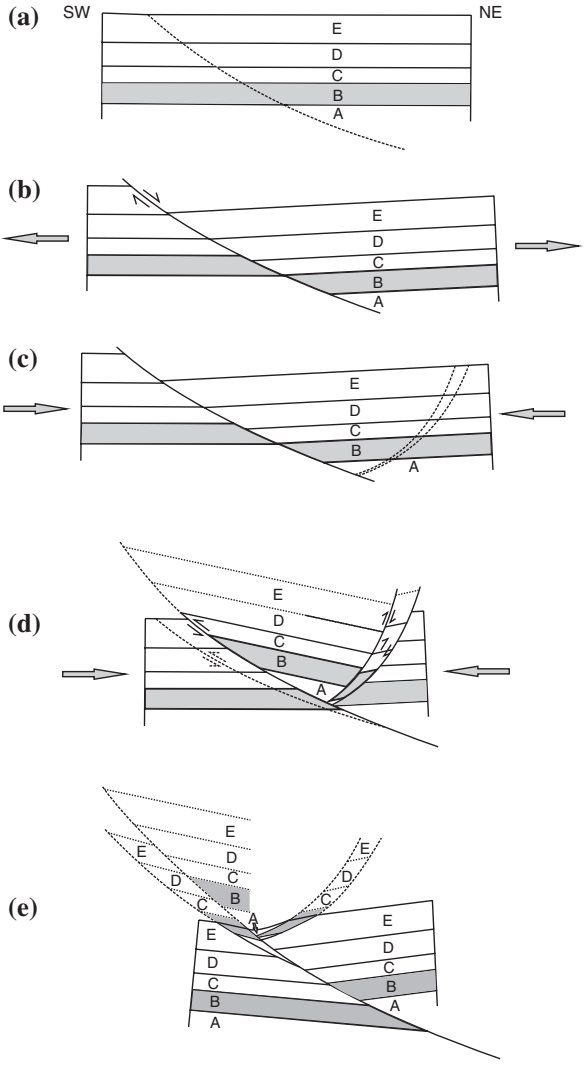

Fig. 11.36 Schematic diagram showing development of pop-up klippen in the Garhwal synform. **a** Initiation of a fracture during tensional regime. *A* Chandpur; *B* Nagthat; *C* Blaini; *D* Krol; *E* Tal. **b** Normal fault displacement along the listric fault. **c** Reactivation of the normal fault as thrust during the Tertiary compressional regime and initiation of a conjugate set of fractures. **d** Initiation of a new thrust in the footwall of the main thrust. **e** Progressive displacement along the main and back thrusts. Erosion of the upper layers to the present surface level reveals exposure of older rocks surrounded by younger rocks with thrust contacts (pop-up klippen) [from Devrani and Dubey (2008), © Blackwell Publishing Asia Pty Ltd. Published with permission of Blackwell Publishing Asia Pty Ltd.]

Later, an alternate model was proposed considering a limited thrust displacement (Fig. 11.36). The Outer Lower Himalaya consists of five main formations as shown by different layers in Fig. 11.36a. Initiation of a listric fault took place

during the tensional regime in the region. Displacement along the normal fault led to anticlockwise rotation of the hanging wall rocks along a subhorizontal axis (Fig. 11.36b). During the Tertiary compressional regime, a conjugate set of faults initiated in the hanging wall (Fig. 11.36c) to compensate the space formed as a result of displacement along the main listric fault. The normal faults reactivated as thrust faults with clockwise rotation of the hanging wall rocks (Fig. 11.36d). The conjugate set of faults became active as back thrusts. The progressive compression led to development of a new thrust in the footwall. Displacement along the main listric fault (Garhwal Thrust) and the subsidiary faults brought the lower formations (Chandpur and Nagthat) at upper levels as pop-up structure (Fig. 11.36e). Subsequent erosion of the upper layers to the present surface level reveals exposure of older rocks surrounded by younger rocks with thrust contacts. Subsequent deformation led to formation of a number of synclines and anticlines (not shown in the diagram) resulting in an open polyharmonic Garhwal Synform.

The structural evolution of Simla, Satengal, and Garhwal klippen reveals two types of klippe structure. The first one is allochthonous klippe, which shows a larger component of horizontal translation from a root zone along a basal detachment thrust (e.g. Simla klippe). The second type is known as parautochthonous klippe (e.g. Satengal, Banali and Garhwal klippen), which lies above its root and forms as pop-up structure. Their characteristic feature is a combination of simple shear and lateral shortening.

The pop-up klippe possibly exist in Nepal as well because Upreti and Le Fort (1999) have observed that rocks in the Lower Himalayan crystalline nappes of Nepal have not come from the High Himalayan Crystallines or the Main Central thrust zone. These rocks represent a separate unit characterized by their own stratigraphy, lithology and metamorphism.

The fault slip rates are based on duration of thrusting and total displacement along the thrust. Since these two estimates in the Himalaya are very approximate, the estimated slip rates can be far from the real. Hence the available slip rates cannot be used for prediction of seismicity in the region.

The northern boundary of the Lower Himalaya is marked by the Main Central Thrust (Munsiari Thrust).

References

Auden JB (1937) The structure of the Himalaya in Garhwal. Records Geol Surv India 71:407–433

Bhat MI (1987) Spasmodic rift reactivation and its role in the pre-orogenic evolution of the Himalaya. Tectonophysics 134:103–127

Bikramaditya Singh RK (2012) Discovery of hornfels from the Arunachal Lesser Himalaya: evidence for the pre-Himalayan contact metamorphism in the Himalaya. Curr Sci 103:405–413

Bikramaditya Singh RK, Gururajan NS (2011) Microstructures in quartz and feldspars of the Bomdila Gneiss from western Arunachal Himalaya, Northeast India: Implications for the geotectonic evolution of the Bomdila mylonitic zone. J Asian Earth Sci 42:1163–1178. doi:10.1016/j.jseaes.2011.06.014

Bollinger L, Avouac JP, Beyssac O, Catlos EJ, Harrison TM, Grove M, Goffe B, Sapkota S (2004) Thermal structure and exhumation history of the Lesser Himalaya in central Nepal. Tectonics 23:TC5015. doi:10.1029/2003TC001564

Borradaile GJ (1988) Magnetic susceptibility, petrofabrics and strain. Tectonophysics 156:1–20

Brunel M, Colchen M, Le Fort P, Mascle G, Pecher A (1979) Structural analysis and tectonic evolution of the central Himalaya of Nepal. In: Saklani PS (ed) Structural evolution of the Himalaya, vol 2. Today and Tomorrow's Printers and Publishers, New Delhi, pp 247–264

Caddick MJ, Bickle MJ, Harris NBW, Holland TJB, Horstwood MSA, Parrish RR, Ahmad T (2007) Burial and exhumation history of a Lesser Himalayan schist: recording the formation of an inverted metamorphic sequence in NW India. Earth Planet Sci Lett 264:375–390. doi:10.1016/j.epsl.2007.09.011

Chatterji GC, Swaminath J (1977) The stratigraphy and structure of parts of the Simla Himalaya—a synthesis. Mem Geol Surv India 106:408–488

Coward MP, Potts GJ (1983) Complex strain patterns developed at the frontal and lateral tips to shear zones and thrust zones. J Struct Geol 5:383–399

Devrani U, Dubey AK (2008) Anisotropy of magnetic susceptibility and petrofabric studies in the Garhwal synform, Outer Lesser Himalaya: evidence of pop-up klippen. Island Arc 18:428–443. doi:10.1111/j.1440-1738.2008.00628.x

Dubey AK (1997) Simultaneous development of noncylindrical folds, frontal ramps and transfer faults in a compressional regime: experimental investigations of Himalayan examples. Tectonics 16:336–346

Dubey AK (2009) The leading edge of the Greater Himalayan Crystalline complex revealed in the NW Indian Himalaya: Implications for the evolution of the Himalayan region: comment. Geology 37:e189–e190. doi:10.1130/G24745C.1

Dubey AK, Bhakuni SS (2008) Neotectonic stresses and active tectonics in the Garhwal Inner Lesser Himalaya: anisotropy of magnetic susceptibility studies. Himalayan Geol 29:35–47

Dubey AK, Bhat MI (1991) Structural evolution of the Simla area, NW Himalaya: implications for crustal thickening. J SE Asian Earth Sci 6:41–53

Dubey AK, Paul SK (1993) Map patterns produced by thrusting and superposed folding: model experiments and example from the NE Kumaun Himalaya. Eclogae Geol Helv 86:839–852

Dubey AK, Bhakuni SS, Selokar AD (2004) Structural evolution of the Kangra recess, Himachal Himalaya: a model based on magnetic and petrofabric strains. J Asian Earth Sci 24:245–258

Dubey AK, Jayangondaperumal R (2005) Pop-up klippen in the Mussoorie syncline Lesser Himalaya: evidence from field and model deformation studies. In: Saklani PS (ed) Himalaya (geological aspects), vol 3. Satish Serial Publishing House, Delhi, pp 203–222

Dubey AK, Misra R, Bhakuni SS (2001) Erratic shortening from balanced cross-sections of the western Himalayan foreland basin: causes and implications for basin evolution. J Asian Earth Sci 19:765–775

Ferrill DA, Groshong RH Jr (1993) Kinematic model for the curvature of the northern Subalpine Chain, France. J Struct Geol 15:523–541

Fry N (1979) Random point distributions and strain measurement in rocks. Tectonophysics 60:89–105

Gaetani M, Garzanti E, Tintori A (1990) Permo-Carboniferous stratigraphy in SE Zanskar and NW Lahaul (NW Himalaya, India). Eclogae Geol Helv 83:143–161

Gansser A (1964) Geology of the Himalaya. Interscience, New York, 289 pp

Gupta HK, Gupta GD (eds) (1995) Uttarkashi earthquake (20 Oct 1991). Memoir Geological Society of India 30, Bangalore, 233 pp

Heim A (1919) Geologie der Schweiz. Bernhard Tauchnitz Verlag Gmbh, Stuttgart, 1028 pp

Herren E (1987) Zanskar shear zone: Northeast- southwest extension within the Higher Himalaya (Ladakh, India). Geology 15:409–413

Jager E, Bhandari AK, Bhanot VB (1971) Rb-Sr age determination of biotites and whole rock samples from the Mandi-Karsog and Chor granite (H.P.), India. Eclogae Geologicae Helvetiae 64:523–527

Jain AK (1972) Structure of Bidhalna-Pharat windows and Garhwal Thrust Unit, Garhwal, U.P. Himalayan Geol 2:188–205
Jayangondaperumal R (1998) Structural evolution of Mussoorie syncline, Lesser Himalaya, U.P. Ph. D. Thesis (unpublished), HNB Garhwal University, Srinagar, (Garhwal)
Jayangondaperumal R, Dubey AK (2001) Superposed folding of blind thrust and formation of klippen: results of anisotropic magnetic susceptibility studies from the Lesser Himalaya. J Asian Earth Sci 19:713–725
Jayangondaperumal R, Dubey AK, Sen K (2010) Mesoscopic and magnetic fabrics in arcuate igneous bodies: an example from the Mandi-Karsog pluton, Himachal Lesser Himalaya. Geol Mag 147:652–664. doi:10.1017/S0016756810000105
Johnson MRW, Oliver GJH (1990) Precollision and postcollision thermal events in the Himalaya. Geology 18:753–756
Kandpal GC, Joshi KC, Joshi DD, Singh BK, Singh J (2006) Signature of Quaternary tectonics in a part of Dehra Dun valley, Uttaranchal. J Geol Soc India 67:147–150
Kelso P, Tikoff B (2001) Separation of paramagnetic and ferromagnetic susceptibility anisotropy using high field and low field methods: or adventures at 1 am with a VSM. The Institute of Rock Magnetism Quarterly, Minnesota, Minneapolis 11, p 2
Kohn MJ (2008) P-T-t data from Central Nepal support critical taper and repudiate large-scale channel flow of the Greater Himalayan sequence. Bull Geol Soc Am 120:259–273. doi:10.1130/B26252.1
Le Fort P (1975) Himalaya: the collided range. Present knowledge of the continental arc. Am J Sci 275:1–44
Macedo J, Marshak S (1999) Controls on the geometry of fold-thrust belt salients. Bull Geol Soc Am 111:1808–1822
Mallet FR (1874) On the geology, etc., of the Darjiling district and the Western Duars. Mem Geol Surv India 11
Mandal P, Rastogi BK, Kousalya M (2002) A fault model for the Chamoli earthquake from after shock studies. Himalayan Geol 23:25–38
Marshak S (1988) Kinematics of orocline and arc formation in thin-skinned orogens. Tectonics 7:73–86
Marshak S, Wilkerson MS (1992) Effect of overburden thickness on thrust belt geometry and development. Tectonics 11:560–566
Medlicott HB (1864) On the geological structure and relations of the southern portion of the Himalayan range between rivers Ganges and Ravee. Mem Geol Surv India 3:1–206
Middlemiss CS (1887) Crystalline and metamorphic rocks of the Lower Himalaya, Garhwal and Kumaun. Mem Geol Surv India 20:134–143
Middlemiss CS (1910) The Kangra earthquake of 4th April 1905. Mem Geol Surv India 37:409 (Reprinted 1981)
Miller C, Klotzli U, Frank W, Thoni M, Grasemann B (2000) Proterozoic crustal evolution in the NW Himalaya (India) as recorded by circa 1.80 Ga mafic and 1.84 Ga granitic magmatism. Precambr Res 103:191–206
Miller C, Thoni M, Frank W, Graseman B, Klotzli V, Guntli P, Draganits E (2001) The early Palaeozoic magmatic event in the northwest Himalaya, India: source, tectonic setting and age of emplacement. Geol Mag 138(3):237–251
Molnar P (1987) The distribution and intensity associated with the 1905 Kangra earthquake and bounds on the extent of the rupture zone. J Geol Soc India 29:221–229
Oliver GJH, Johnson MRW, Fallick AE (1995) Age of metamorphism in the Lesser Himalaya and the main central thrust zone, Garhwal India: results of illite crystallinity, 40Ar–39Ar fusion and K-Ar studies. Geol Mag 132:139–149
Panozzo R (1987) Two dimensional strain determination by the inverse SURFOR wheel. J Struct Geol 1:115–119
Peach BN, Horne J (1884) Report on the geology of north-western Sutherland. Nature 31:31
Peach BN, Horne J, Gunn W, Clough MA, Hingxman LW (1907) The geological structure for the northwest Highlands of Scotland. Mem Geol Surv Great Britain 1:668

Powers PM, Lillie RJ, Yeats RS (1998) Structure and shortening of the Kangra and Dehra Dun re-entrants sub-Himalaya, India. Geol Soc Am Bull 110:1010–1027
Pilgrim GE, West WD (1928) The structure and correlation of the Simla rocks. Mem Geol Surv India 53:1–140
Rautela P, Sati D (1996) Recent crustal adjustments in Dehra Dun valley, western Uttar Pradesh, India. Curr Sci 71:776–780
Ray SK, Naha K (1971) Structural and metamorphic history of the "Simla klippe": a summary. Himalayan Geol 1:1–24
Royden LH, Burchfiel BC (1987) Thin-skinned N-S extension within the convergent Himalayan region: Gravitational collapse of a Miocene topographic front. Geol Soc London 28:611–619 (Special Publication)
Saklani PS (1993) Geology of the Lower Himalaya. IBS, Delhi
Srikantia SV, Sharma RP (1970) The occurrence of rocks of Kakara (Paleocene) affinity in the Bakhalag-Bughar Belt, Himachal Pradesh. J Geol Soc India 11:185–188
Srikantia SV, Sharma RP (1976) Geology of Shali Belt and the adjoining areas. Mem Geol Surv India 106:31–166
Srikantia SV, Bhargava ON (1979) The Tandi Group of Lahaul—its geology and relationship with the Central Himalayan Gneiss. J Geol Soc India 29:531–539
Srikantia SV, Bhargava ON (1998) Geology of Himachal Pradesh. Geological Survey of India, Bangalore, 406 pp
Srivastava DC, John G (1999) Deformation in the Himalayan frontal fault zone: evidence from small-scale structures in Mohand-Khara area, NW Himalaya. Gondwana Res Group Mem Osaka, Japan 6:273–284
Srivastava P, Mitra G (1994) Thrust geometries and deep structure of the outer and Lesser Himalaya, Kumaon and Garhwal (India): implications for evolution of the Himalayan fold-and-thrust belt. Tectonics 13:89–109
Steck A (2003) Geology of the NW Indian Himalaya. Eclogae Geol Helv 96:147–196. doi:10.1007/s00015-003-1091-4
Thakur VC, Kumar S (1995) Seismotectonics of the 20 October 1991 Uttarkashi earthquake in Garhwal Himalaya, north India. Mem Geol Soc India 30:101–108
Upreti BN, Le Fort P (1999) Lesser Himalayan crystalline nappes of Nepal: Problems of their origin. Geol Soc Am 328:225–238 (Special Paper)
Valdiya KS (1980) Geology of Kumaun Lesser Himalaya, Wadia Institute of Himalayan Geology, Dehra Dun, 291 pp
Valdiya KS (1993) Evidence for Pan-African—cadomian tectonic upheavals in Himalaya. J Palaeontol Soc India 38:51–62
Valdiya KS (1995) Proterozoic sedimentation and Pan-African geodynamic development in the Himalaya. Precambr Res 74:35–55
Valdiya KS, Joshi DD, Sanwal R, Tandon SK (1984) Geomorphic development across the active Main Boundary Thrust: an example from the Nainital Hills in Kumaun Himalaya. J Geol Soc India 25:761–774
Virdi NS (1979) On the geodynamic significance of magalineaments in the outer and Lesser regions of western Himalaya. Himalayan Geol 9:79–99
Virdi NS (1994) Basement structures and their possible relation to sedimentation and tectonics in the Tethyan basin of western Himalaya. J Himalayan Geol 5:11–19
West WD (1939) Structure of the Shali Window near Simla. Rec Geol Surv India 74:133–163
Yeats RS, Thakur VC (1998) Reassessment of earthquake hazard based on a fault-bend fold model of the Himalayan plate-boundary fault. Curr Sci 74:230–233

Chapter 12
The High Himalaya

Abstract Age of the Main Central Thrust, at different places, obtained by different methods is described. Litho-tectonic subdivisions are mentioned along with magmatic events. Both Vaikrita and Munsiari rocks represent two distinct rock assemblages and both have undergone pre-Himalayan metamorphism. A model is proposed to explain the occurrence of younger Vaikrita rocks on the thrust hanging wall and older Munsiari rocks in footwall of the Vaikrita thrust. The model is based on reactivation of early rift related normal fault as thrust fault. Details of structural features along the Satluj valley are described primarily to explain the interference between Karcham oblique fault ramp and two generations of folds. Change in orientation of early and superposed folds in vicinity of Vaikrita thrust is illustrated. Field evidence suggests that after locking of the Vaikrita thrust, the maximum extension has taken place along the strike of the thrust. Different models proposed for structural evolution of the High Himalaya are reviewed.

The High Himalaya constitutes the core of the Himalaya and is separated by the Lower Himalaya by the Main Central Thrust (MCT). The thrusting has brought the deeper level rocks to the surface. It is to be noted that undeformed basement rocks are nowhere exposed in the Himalaya as all the available rock sequences are deformed and represent the supracrustal rocks.

The MCT was defined by Heim and Gansser (1939) as the thrust, which separates the gneisses, migmatites and schists of the Central Crystalline rocks (High Himalayan Crystallines, HHC) from the lower grade metasediments and sediments of the Lower Himalaya. The MCT has also been described as Vaikrita, Munsiari, and Chail thrusts in the Himachal Himalaya, and Almora thrust in the Garhwal-Kumaun Himalaya. The thrust is characterized by a broad ductile shear zone but base of the thrust is marked by brittle faults in some areas. The thrust may be marked either at the top or at the basal surface of the shear zone (Arita 1983).

A. K. Dubey, *Understanding an Orogenic Belt*, Springer Geology,
DOI: 10.1007/978-3-319-05588-6_12,

12.1 Age of the MCT

Efforts have been made to determine the age of the MCT using various methods. The $^{40}Ar/^{39}Ar$ hornblende ages indicate that amphibolite grade metamorphism associated with displacement along the MCT occurred at 23–20 Ma (Hodges et al. 1992; Hubbard and Harrison 1989; Parrish and Hodges 1996). The age of the High Himalayan crystallines in Garhwal region is constrained to be 22–14 Ma by K–Ar cooling ages of muscovite (Metcalfe 1993). Below the Vaikrita thrust, Th–Pb ion-microprobe dating of monazites reveals that the thrusting was active between 6 and 2 Ma (Catlos et al. 2002a) confirming the youngest K–Ar muscovite cooling ages (5.7–5.9 Ma) from the same locality (Metcalfe 1993). Muscovite dates from the hanging wall and footwall from the Kathmandu Nappe indicate that the MCT shear zone was cooled below 350 °C between 21 and 14 Ma. The southernmost part of the MCT ceased movement since 14 Ma (Arita et al. 1997). In the Sikkim Himalaya, Sm–Nd growth ages of garnet cores and rims indicate pre-decompression garnet growth at 23 ± 3 Ma and near-peak temperatures at 16 ± 2 Ma (Harris et al. 2004). These ages are indicative of MCT activeness at ~23 Ma during the prograde metamorphism.

The MCT, south of the Mount Everest, corresponds to a 3–5 km thick mylonite zone developed at temperatures between 500 and 730 °C (Hodges et al. 1992). Hornblende from amphibolites of the lower MCT zone yielded a $^{40}Ar/^{39}Ar$ isochron age of 20.9 ± 0.4 Ma. This date was suggested to be an approximate age of displacement along the MCT in this region (Hubbard and Harrison 1989). U–Pb dating of monazite and xenotime suggests that the MCT in Bhutan Himalaya was active at 22 Ma and continued its displacement during and after ~14 Ma (Daniel et al. 2003). Catlos et al. (2002b) have obtained similar Th–Pb monazite ages between 22 and 14 Ma for the MCT zone in Sikkim. An active age of ~10 Ma, based on ion-microprobe dating of monazite inclusions in garnet from the MCT zone, has come from the Arunachal Himalaya (Yin 2006). A subsequent study by $^{40}Ar/^{39}Ar$ thermochronometry of the MCT in the eastern Himalaya indicated initiation at ca. 13–10 Ma (Yin et al. 2010). Structural and geochronological studies in Nepal have revealed at least three distinct phases of displacement along the MCT; between 25 and 15 Ma, between 9 and 7 Ma, and at ~2.3 Ma (Hodges et al. 1988a; Macfarlane 1993). Crustal shortening in the Himalaya is a continuous process but spasmodic displacements suggest lack of good lubrication along the fault and displacement after a considerable strain build-up in the region. Now the MCT is an inactive thrust as it does not cut Quaternary deposits anywhere along its length (Nakata 1989). Earthquake of moderate magnitudes are concentrated beneath the MCT at depths of about 10–20 km where the dip is gentle.

Small-scale folds and their interference patterns are well preserved in schistose rocks. These folds, in association with micro-structures, help in determination of sense of shear, which reveals a general top-to-south sense of displacement along the thrust.

12.2 The Central Crystalline Rocks

The Central Crystalline rocks represent the main metamorphic belt and root-zone of a few allochthonous klippen of the Lower Himalaya. The sequence is up to 40 km thick and is divided into two units, Munsiari Formation and Vaikrita Group separated by the Vaikrita thrust (Valdiya 1998) (Table 12.1). The Munsiari Formation consists of two different lithological components; an older undifferentiated basement complex composed of a magmatic suite (1,800–2,600 Ma granite gneisses and associated amphibolites) and a younger metasedimentary suite. These two suites of rocks now occur as imbricate slices, especially within the imbricate faults (schuppen zone) of the Munsiari thrust. The constituent minerals of the Munsiari rocks are fine to medium grade (size <1 mm). Mylonitization is a common feature throughout the sequence and kyanite is present only rarely in small pockets.

The Vaikrita Group comprises the metamorphic equivalents of sedimentary rocks and impure limestone with subordinate disseminated volcanic rock. The constituent minerals are coarse grained (size 1–2 mm), kyanite is uniformly distributed, and mylonitization occurs only at the base. The basal part of the Pindari Formation, which forms the upper limit in the Group, is intruded by ~500 Ma old porphyritic biotite granite, whereas the upper part is injected by ~20 Ma tourmaline-bearing leucogranite with associated pegmatitic and aplitic veins and subordinate unfoliated porphyritic granite.

Based mainly on the higher grade of metamorphism in the Vaikrita Group of rocks, Valdiya (1973, 1980) suggested that the Vaikrita thrust should be regarded as the real MCT. Subsequently, supporting evidence in favour of Valdiya's interpretation has come from the isotopic study of Ahmad et al. (2000), suggesting that though the rocks of the Munsiari Formation are older than the Vaikrita Group of rocks they have closer geochemical affinities with the Lower Himalayan formations. The criterion suits well for the western Himalaya and appears to be well defined but it may be difficult to identify the MCT because the geochemical affinity cannot be observed in field. Moreover, the occurrence of Munsiari (Chail) rocks as klippen in the Lower Himalaya advocate for Munsiari thrust to be regarded as the MCT. Hence it is suggested that in order to avoid any confusion, the two thrusts may be described as Munsiari (or MCT I) and Vaikrita (or MCT II) thrusts.

In absence of marker horizons, displacements along the Munsiari and Vaikrita thrusts are a matter of speculation. However the Munsiari rocks occur as klippen in the Lower Himalaya, and the klippe-to-fenster method of determining fault displacement showed that the maximum displacement along the klippen thrust in the Simla klippe is ~40 km (Chap. 11). A number of bows formed by Munsiari thrust can be observed on a geological map (Fig. 12.1) whereas trace of the Vaikrita thrust is nearly linear with occasional curves at oblique thrust ramps (e.g. Karcham oblique ramp). Moreover, the Vaikrita thrust has a weak geomorphic expression, which does not allow mapping by remote sensing.

Table 12.1 Litho-tectonic subdivisions of the Central crystalline rocks in the Garhwal Himalaya (after Ahmad et al. 2000; Miller et al. 2000; Myrow et al. 2003; Parrish and Hodges 1996; Valdiya et al. 1999)

Tethyan facies	Martoli Formation	Graywacke—slate alternations	Precambrian (Ma)
Trans Himadri/Malari fault			
	Pindari Formation	The Upper part, Budhi Schist, consists of biotite porphyroblastic calc-schist, interbedded with micaceous schist and phyllite, locally carbonaceous, pyritic or staurolite—bearing phyllite. Banded calc-silicate gneisses and calc-schists interbedded with subordinate psammitic gneisses and schists characterized by presence of sillimanite and/or kyanite. Extensively penetrated by tourmaline—bearing leucogranite, and a network of dykes and veins of aplite, pegmatite and adamellite near top; Cambro-Ordovician biotite granite in the lower part	No precise age data
Pindari thrust			
Vaikrita Group	Pandukeshwar Formation	Biotite and/or muscovite rich quartzite intercalated with garnet-kyanite- bearing mica schists and subordinate psammatic gneiss. Locally lenses and layers of calc-silicate gneisses and garnet bearing amphibolite	No precise age data
	Joshimath Formation	Streaky and banded psammitic gneisses and schists including migmatitic gneisses. Biotite-garnet-kyanite rich schists, calc-silicate gneisses with amphibolite and phyllonites at base	800–1,000
Vaikrita thrust (*MCT II*)			
Lower Himalaya	Munsiari Formation	Mylonitized body of granodioritic, granitic, and aplitic composition grading locally into augen mylonite or porphyry schist. Interbedded with chlorite—sericite schist, graphitic schist, and crystalline bluish gray limestone	2,600–1,800
Munsiari thrust (*MCT I*)			
	Berinag/Deoban Formation	Quartz arenite with penecontemporaneous basic volcanic rocks	1,800

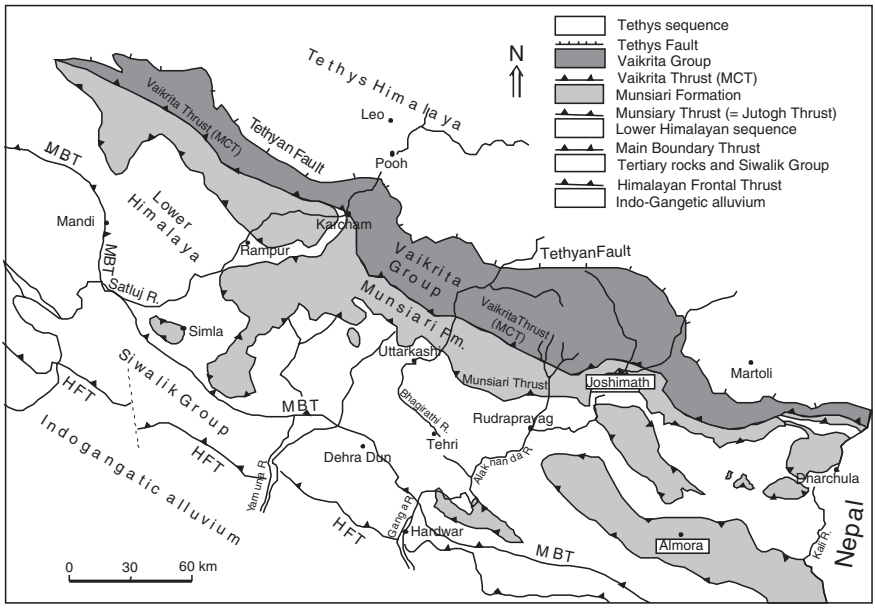

Fig. 12.1 A geological map of a part of the western Himalaya highlighting the distribution of Vaikrita and Munsiari rocks. [From Paul and Roy (1991), © S.K. Paul. Published with permission of S.K. Paul]

12.3 Metamorphism

Metamorphism in the region took place mainly in two episodes: (i) pre-Himalayan metamorphism, and (ii) Tertiary Himalayan metamorphism. Stratigraphic and palaeontological evidence from the Hazara-Swat belt were provided by Baig et al. (1988) for at least one metamorphic episode of late Precambrian to Earliest Cambrian age. Subsequently, a metamorphic event, prior to emplacement of early Palaeozoic granitoids, was recognised in the SE Zanskar (NW Himalaya) by Pognante and Lombardo (1989) and Pognante et al. (1990). The early metamorphic event is characterized by mineral assemblages indicating high T and P conditions of crystallization ($T = 750 \pm 50$ °C; $P = 12.0 \pm 0.5$ kbar), whereas the second (Himalayan) metamorphism occurred at a similar or lower T and at a lower P. The results of these studies were further confirmed by Walker et al. (1999), who found evidence of monazite growth during pre-Himalayan (ca. 500 Ma—Early palaeozoic) metamorphism from the U–Pb analysis of monazite. The pre-Himalayan episode of metamorphism, with occurrence of sillimanite and pyrope-rich cores of garnet crystals in the Vaikrita rocks, was also observed by Arita (1983).

In the eastern Bhutan Himalaya, geothermometry and mineral assemblages display an increase in temperature structurally upwards across the MCT. The peak metamorphic pressure remains similar across the boundary and correspond

to depths of 35–45 km. Garnet bearing samples from the uppermost Lower Himalayan sequence yield metamorphic conditions of 650–675 °C and 9–13 kbar. Kyanite bearing migmatites from the High Himalayan sequence yield pressures of 10–14 kbar at 750–800 °C. The southward thrusting is synchronous to postdate the peak metamorphic mineral growth (Daniel et al. 2003).

The different phases of the later Himalayan metamorphism are now well established (Hodges 2000; Hubbard 1989). In their interpretation of thermal evolution of the Garhwal High Himalaya, Hodges et al. (1988b) have established that during the initial collision between India and Tibet, the Vaikrita rocks were buried and metamorphosed at depths of up to 36 km. Hence the Vaikrita rocks underwent a higher grade of metamorphism (lower granulite facies) than the Munsiari rocks and show a normal metamorphic gradient, decreasing upwards in grade towards the overlying Tethyan sediments (Arita 1983). Subsequent metamorphism was related to thrusting along the MCT. The studies of Harrison et al. (1996) and Hodges et al. (1996) suggest that the high-grade metamorphism and anatexis in the High Himalayan rocks began in the earliest Miocene and continued till at least Late-Middle Miocene (ca. 12 Ma; Edwards and Harrison 1997). The metamorphic event may have extended up to even Pleistocene (Hodges 2000). The temperature increased to ~825 °C whereas the pressure decreased to 8 kbar (Kohn 2008).

In view of the above data, it is evident that: (i) the Vaikrita and Munsiari represent two distinct rock assemblages and both have undergone a pre-Himalayan metamorphism (ii) The Vaikrita rocks are younger than the Munsiari rocks, but the former were affected by a higher grade of metamorphism and deformed in a more ductile regime, and (iii) The Munsiari thrust has a greater displacement than the Vaikrita thrust. These characteristics fit in the following model of structural evolution.

12.4 A Model to Explain the Younger Vaikrita Rocks on the Thrust Hanging Wall

A model to explain the occurrence of younger high grade metamorphic rocks on hanging wall of the Vaikrita thrust is presented in Fig. 12.2. The first stage (Fig. 12.2a) represents the initial disposition of rocks and initiation of normal listric faults during a pre-Himalayan tensional regime. The top gray bed is a reference horizon to understand the subsequent displacement patterns along the thrusts. Faults 1 and 2 represent the present day Vaikrita and Munsiari thrusts, respectively. The normal faulting led to anticlockwise rotation of the hanging wall rocks along the horizontal axis and tilting of the rocks towards the foreland (Fig. 12.2b). The dip of the fault is likely to be steeper towards the Indus Suture, which forms the main axial zone of the tensional stress. Consequently, the northern fault represents a steeper dip and a larger displacement. The hanging wall rocks have gone down to a deeper crustal level and therefore suffered a higher grade of metamorphism. Deposition of fresh sediments in the rift basin and subsequent metamorphism took place during the rift related subsidence.

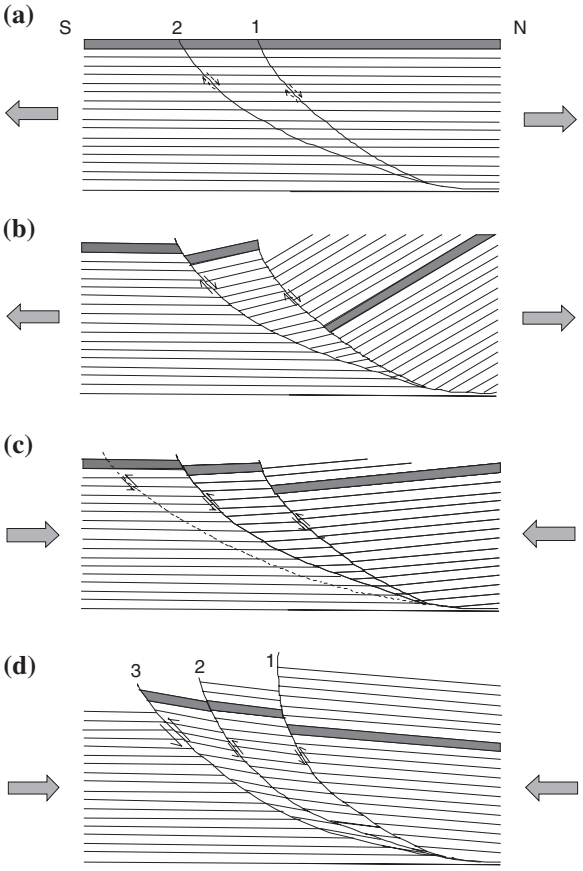

Fig. 12.2 A simplified model for structural evolution of a part of the High Himalaya illustrating occurrence of younger rocks on the thrust hanging wall and older rocks in the footwall. **a** Initial disposition of strata and initiation of listric faults during the tensional regime. The *gray bed* represents a marker stratigraphic horizon for reference. *N* and *S* represent the north and south directions, respectively. **b** Normal faulting and *anticlockwise rotation* of the hanging wall rocks along the *horizontal axis*. **c** Reversal of fault displacement during inversion tectonics and initiation of a thrust in the footwall sequence. **d** Thrusting along the listric faults and rotation of the hanging wall blocks in a *clockwise direction* along *horizontal axes*. A limited thrust displacement along Fault 1 (i.e. thrust locking prior to crossing the null point) has resulted in the occurrence of younger hanging wall rocks along Thrust 1 (1, Vaikrita Thrust; 2, Munsiari Thrust; 3, Ramgarh Thrust). [From Dubey and Bhakuni (2007), © Elsevier. Published with permission of Elsevier]

At the onset of Tertiary compressional phase, the early normal faults reactivated as thrust faults (Fig. 12.2c). The steeper dip of Fault 1 led to an early thrust locking, prior to reaching the null point so that younger but higher grade rocks (i.e. Vaikrita) lies on the hanging wall of the thrust. The structure indicates that the normal fault displacement along the Vaikrita thrust was of greater magnitude than the subsequent thrust displacement. However the amount of displacement during the

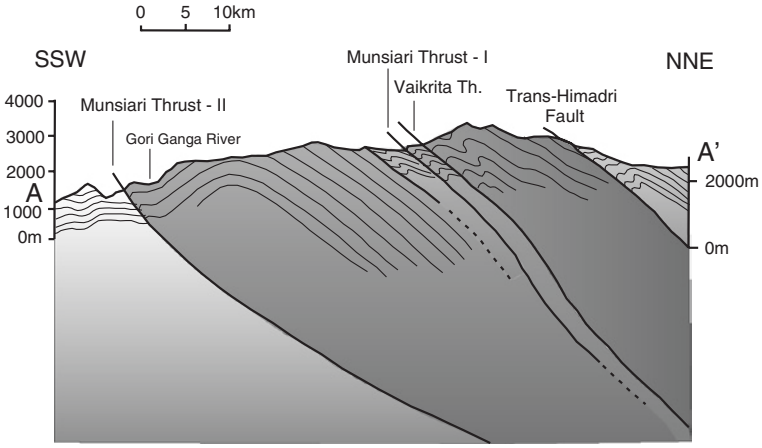

Fig. 12.3 A SSW-NNE geological cross-section of a part of the NE Kumaun Himalaya showing structures from the Lower Himalaya to the Tethys Himalaya (after Dubey and Paul 1993). The vertical scale is true for the surface profile and approximate for the vertical section at depth

inversion may vary along the strike of Fault 1, so that it is possible that younger hanging wall rocks do not occur everywhere along the strike of the Vaikrita thrust. A larger thrust displacement is envisaged to have occurred along the Munsiari thrust (Fault 2). This is also envisaged by the fact that along the Munsiari thrust, the Munsiari rocks are also in contact with the Berinag Formation (Valdiya 1980), which is considered to be of the same age (1,800 $\pm$ 13 Ma, $^{207}Pb/^{208}Pb$, single zircon ages for Rampur metabasaltic rocks; Miller et al. 2000). Initiation of a new thrust further south (Fault 3, Ramgarh thrust, Fig. 12.2c) and subsequent displacements led to clockwise rotation (Fig. 12.2d) and tilting of the hanging wall rocks so that they dip in the same direction as the thrusts.

The layer orientations as shown in Fig. 12.2d are unlikely to be preserved after the Tertiary deformation. Since folding occurred together with the Himalayan metamorphism, the resulting fold styles do not conform to the expected fold patterns characteristic of this particular orientation. The final geometry will also be modified by development of later thrusts, back thrusts, pop-up structures and fold patterns.

A geological cross-section from the Kumaun Himalaya is shown in Fig. 12.3 (Dubey and Paul 1993). The section incorporates rocks from the Lower, High, and Tethys Himalaya. The increasing metamorphism is shown in increasing shades of gray. Early folds in the area have developed simultaneously with the thrusts. The Munsiari thrust II brought the hanging wall Munsiari rocks over the Inner Lower Himalayan metasediments. A large shear strain along the Munsiari thrust is indicated by presence of sheath folds close to the thrust surface. The anticlinal structure shown by the Munsiari Formation is a dome formed as a result of interference between the early and superposed folds. Tilting of the hanging wall layers along a listric fault (e.g. Fig. 12.2d) leads to gradual younging of rocks with increasing distance in dip direction of the thrust. Further north, these rocks are cut by

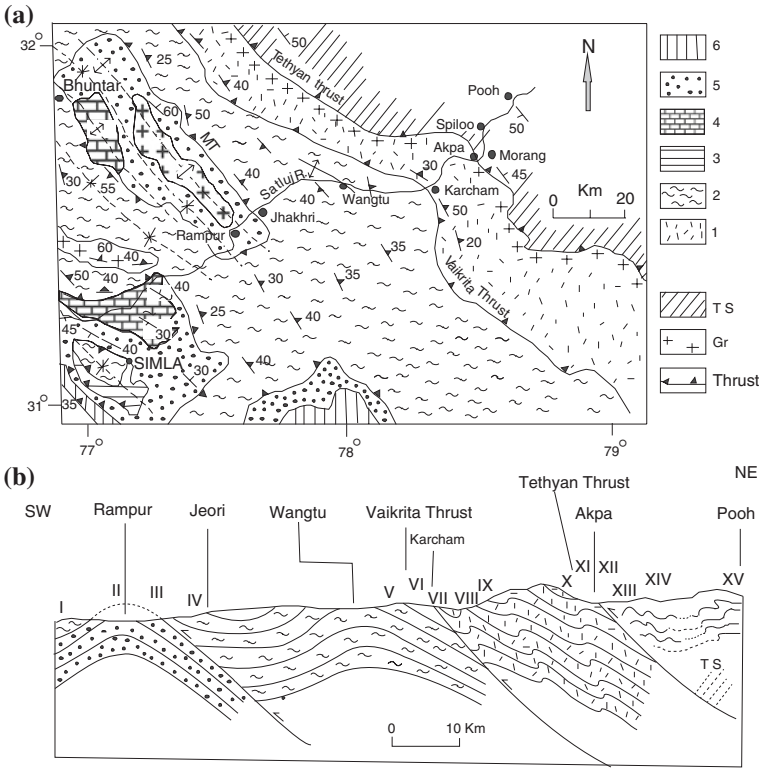

Fig. 12.4 **a** A geological map of a part of the Himachal Himalaya along the Satluj valley. *1* High grade metamorphic rocks of the Vaikrita Group. *2* Medium to high grade rocks of the Munsiari Formation. *3* Low grade metamorphic rocks (mainly quartzite and phyllite) of the Chail Formation. *4* Shali Limestone. *5* Simla slate and quartzite. *6* Sedimentary rocks of the Krol Group. *G* granite. *TS* metasedimentary rocks of the Tethyan sequence. Note the curvature of the thrusts at Karcham and Akpa due to oblique fault ramps. **b** A geological cross-section along the Satluj valley showing locations of domains *I* to *XV* (Fig. 12.5) (after Dubey 1999)

Munsiari thrust I. A narrow slice of the Munsiari rocks is followed by the Vaikrita thrust, which brought younger but higher grade Vaikrita Group rocks above the Munsiari Formation. Absence of sheath folds in the hanging wall of the Vaikrita thrust suggests a low magnitude of shear strain as compared to the Munsiari thrust.

12.5 Structural Features Along the Satluj Valley

The High Himalaya of the Himachal region has been studied in great details. Regional geological studies have been described by Le Fort (1975), Srikantia and Sharma (1976), and Srikantia and Bhargava (1998). A geological map of a part of the Himachal Himalaya is shown in Fig. 12.4a along with a simple cross-section

along the Satluj valley (Fig. 12.4b). General trend of the rock units is parallel to the prominent thrusts and early fold hinge lines. Medium to high grade mica schist and quartzite of the Munsiari Formation (including the Palaeo-proterozoic Wangtu Gneissic Complex, WGC) thrust south-westward over the Lower Himalayan metasedimentary sequence along the Munsiari thrust. Towards the north-eastern direction, high grade metamorphic rocks of the Vaikrita Group thrust over the Munsiari Formation along the Vaikrita thrust. Further in the NE direction, the Vaikrita rocks are over ridden by metasedimentary rocks of the Tethyan sequence along the South Tibetan Detachment (STD).

The rock sequences present a variety of fold structures with differing geometries and orientations. The orientations of minor early and superposed folds and dip of axial surfaces are shown in Fig. 12.5.

The Rampur tectonic window (Fig. 12.4a) consists of a thick quartzite sequence, metamorphosed to the lower greenschist facies. The rock surrounded by the Munsiari thrust (MT) is folded into an open upright antiformal fold trending NW–SE. The Munsiari thrust at the NE boundary of the window occurs near Jakhri. The Munsiari rocks on the SW limb are mostly characterized by asymmetric, overturned or reclined early folds scattered around the E–W axis with northerly dip of the axial surfaces (Fig. 12.5; Sub-area I). The superposed fold hinge lines are oriented N–S to NE–SW with varying directions of the axial surface dip. The orientation is in conformity with the general pattern of the western Himalayan folds. Within the Rampur window, bedding foliation in the weakly metamorphosed (lower green schist facies) thick quartzite sequence is poorly developed hence the number of minor folds is small. Available data from the anticlinal fold hinge zone reveal a wide variation in trends of the early and superposed minor folds (Fig. 12.5; Sub-area II). The folds are mostly upright with open or gentle interlimb angles. The prominent lineation is defined by intersection of early and superposed axial plane foliations and plunges NE. The fold geometry and the lineation do not show a change in vicinity of the northerly dipping Munsiari thrust, thereby suggesting a low magnitude of footwall strain. Poor rock exposure prohibits collection of data on minor folds near the thrust contact.

The northerly dipping MT is associated with a large number of thrust shear planes which are responsible for development of asymmetric folds. The density of these shear planes gradually decreases with increase in distance from the thrust. Hence asymmetric folds occur in vicinity of the thrust (Fig. 12.6a) and upright folds at some distance (Fig. 12.6b) as a result of pure-shear buckling. Quartz boudins formed during the early folding are refolded during the superposed deformation (Fig. 12.6c).

North-east of the Rampur window, the Munsiari thrust is overlain by medium to high grade metamorphic rocks of the Munsiari Formation and the Wangtu Gneissic Complex (WGC). The zircon U–Pb age of crystallization of the WGC is 1,840 ± 16 Ma (Miller et al. 2000). The WGC is transformed into granitic gneiss during the Cenozoic Himalayan orogeny and was exhumed in the Pliocene-Pleistocene time along the Vaikrita thrust (Jain et al. 2000; Vannay et al. 2004). The thrust is folded into a broad syncline paired with an anticline to the north

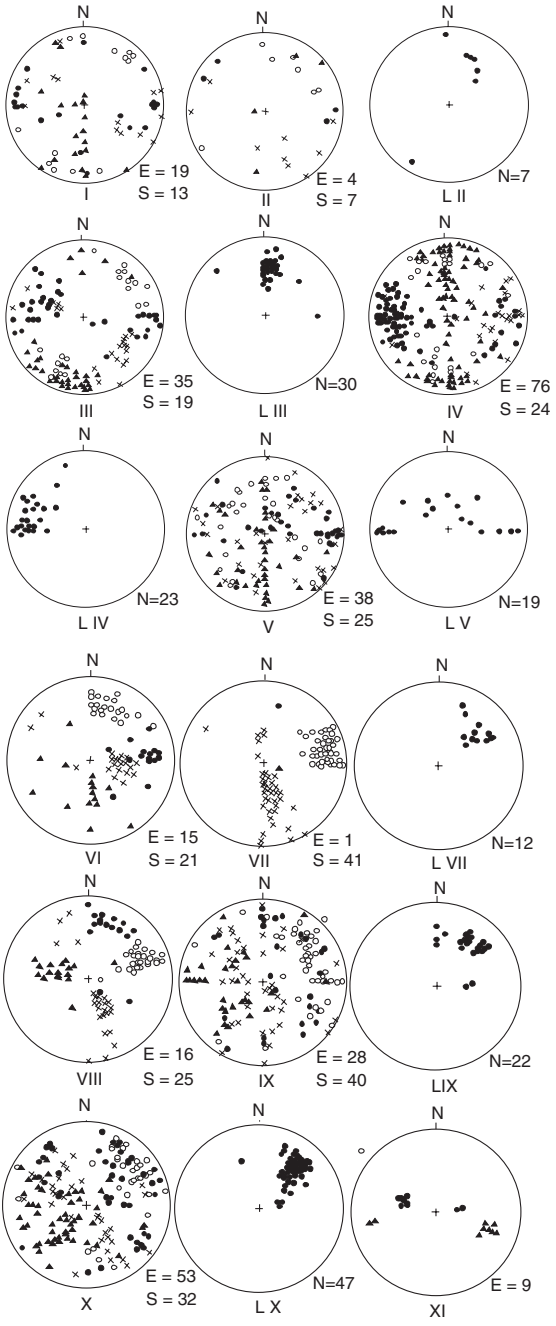

Fig. 12.5 Orientations of minor folds along the Satluj valley. The sub-areas are shown in Fig. 12.4b. *Dot*, plunge of early fold *hinge line*; *open circle*, plunge of superposed fold *hinge line*; *triangle*, pole to the early axial surface; cross, pole to the superposed axial surface; *L* plunge of lineation. Note a marked variation in the orientation of folds across the Vaikrita thrust at Karcham. All equal area lower hemisphere plots (after Dubey 1999)

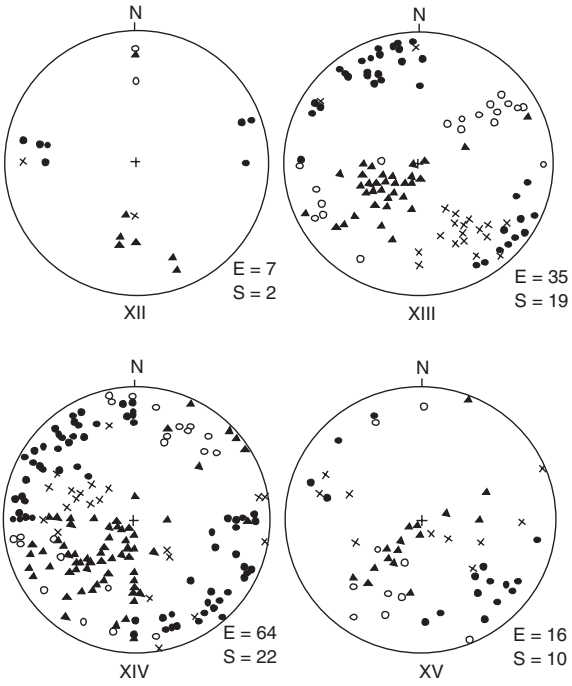

Fig. 12.5 (continued)

direction. Further NE of the thrust, the early fold hinge lines are oriented around the E–W axis and plunge in both directions (Fig. 12.5; Sub-area IV, V). Dip of the axial surfaces and asymmetry of the folds indicate a flexural-slip model for the large-scale fold. The superposed folds show a large variation in their trend because of interference and their development on initially undulatory surfaces. Majority of the superposed axial surfaces dip towards north and asymmetry of the folds denotes a sense of shear from top to the SE i.e. parallel to the trend of the Munsiari thrust. The mineral lineation, defined by stretched feldspar and mica, is parallel to the early fold hinge lines suggesting an extension in this direction. The lineation was later folded by superposed folds.

The orientation of folds gradually acquires a more uniform pattern in the footwall of the Vaikrita thrust at Karcham (Fig. 12.5; Sub-area VI). The early folds have an E–W trend with plunge towards east and most of the axial surfaces dip towards north, except reclined folds which plunge towards east. The early fold geometry indicates a sense of shear from top to the south i.e. oblique to general trend of the Vaikrita thrust. The superposed folds are oriented N–S to NE–SW with majority of the axial surfaces dip towards NW. The sense of shear as revealed by asymmetry of the superposed folds is sinistral (i.e. top to NW), parallel to general trend of the Vaikrita thrust.

In NE part of the gneissic body, biotite rich mylonitic gneiss is present in vicinity of the Vaikrita thrust. Migmatisation is also evident from leucocratic melts segregated

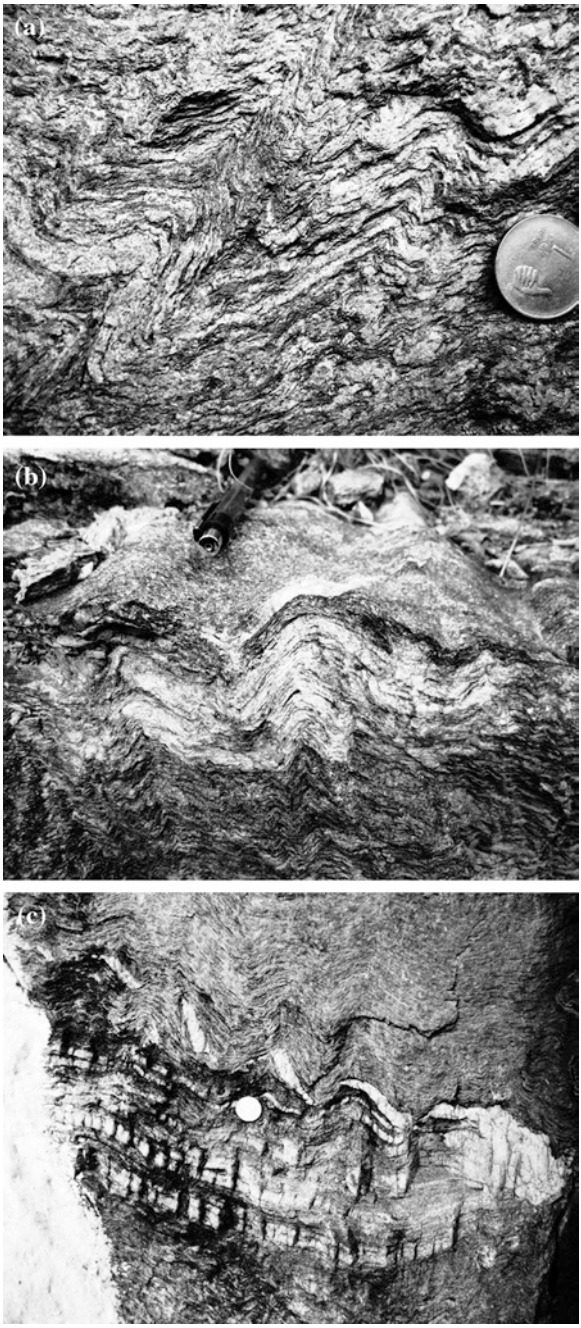

Fig. 12.6 Mesoscopic structures at the Rampur–Karcham section along the Satluj valley in the Himachal High Himalaya. **a** *Asymmetric folds* in mica schist in vicinity of the Munsiari Thrust. **b** *Upright folds* in the Munsiari Formation, at some distance from the Munsiari Thrust. **c** An early recumbent and later upright *superposed folds*. Quartz boudins formed along an early fold limb have been folded during the superposed deformation. [From Sen et al. (2012), © Elsevier. Published with permission of Elsevier]

along the foliation. The Vaikrita thrust is marked by different rock formations on either side of the thrust and presence of fault breccia. Asymmetric geometry of early folds shows top to the SW sense of shear along the thrust. The geological map shows a marked curvature in trend of the thrust at Karcham indicating an oblique fault ramp structure (Fig. 12.4a). On the hanging wall, close to the thrust, the early minor folds are absent (Fig. 12.5b; Sub-area VII). The exposed superposed folds have a moderate to gentle plunge towards east or NE with variable axial surface dips mostly towards north or NW. Absence of early folds at the hanging wall close to the thrust is a known phenomenon (Raj 1983; Dubey and Bhat 1991), but the different orientation of the superposed folds is a remarkable feature. Secondary silica veins cut the fold surfaces normal to the fold hinge line and the vein fibres indicate extension parallel to the hinge line in a sub-horizontal direction. The sense of shear indicated by the asymmetric superposed folds is sinistral and parallel to the Vaikrita thrust. The mineral lineation shows a variable plunge around NE and appears to be related to thrusting. The early folds gradually appear at a distance (~50 m) from the thrust with a marked variation from their general trend (Fig. 12.5; Sub-area VIII). These folds plunge towards north to N40E with moderate dips of the axial surface toward east. The superposed folds plunge towards N50E to N80E with majority of axial surfaces dipping towards NW. These folds are mostly asymmetric kink and chevron.

At some distance from the Vaikrita thrust (Fig. 12.5b; Sub-area IX), the early fold geometry is dominated by asymmetric, overturned and recumbent folds. The superposed folds are characterized by both harmonic and disharmonic types. The asymmetric fold geometry suggests a sense of sinistral shear parallel to the trend of the thrust. Despite a large shear strain in the sub-area, indicated by presence of sheath folds, orientation of the folds show a variable trend. The stretching mineral lineation plunges towards north to NE and is related to the thrusting. A reversal in the sense of shear from thrust to normal fault was observed in the sub-area (cf. Royden and Burchfiel 1987; Coward et al. 1987).

The southern contact of granite at Akpa is marked by interfingering of granite with the country rock thereby indicating an intrusive contact. Only a few minor folds are exposed. The early folds are reclined plunging towards east or west.

The Tethyan fault represents a prominent zone of reversal of displacement. It was not possible to record minor folds adjacent to the fault due to lack of rock exposures but at some distance from the contact, minor asymmetric folds are present. The bedding-cleavage relationship is prominent and helps in locating overturned limbs. There is a large variation in orientation of folds but majority of axial surfaces dip towards NE. Sheath folds and reclined folds are absent in the Tethyan rocks in the sub-areas (Fig. 12.5; Sub-area XIII to XV). The early folds show a sense of shear from NE to SW, whereas the superposed folds show a sense of shear from SE to NW (i.e. parallel to the thrust trace). Late Miocene (syn- to late emplacement of the leucogranitic plutons) dextral shearing has also been observed by Pecher (1991) in Nepal.

The last stage of tectono-metamorphic evolution from Pliocene to late Pleistocene was associated with rapid exhumation and cooling of the rocks (Vannay et al. 2004). This stage was associated with brittle extensional structures

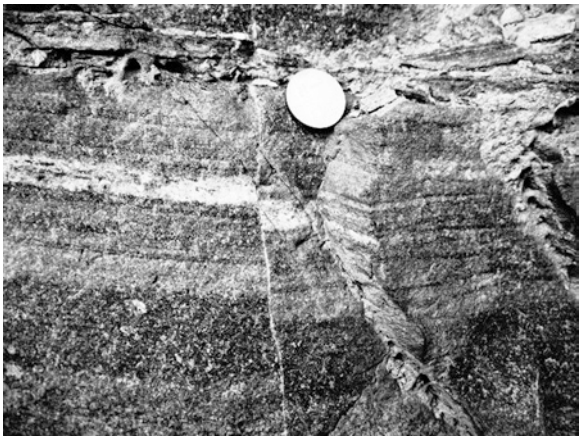

Fig. 12.7 A late stage brittle normal fault in the Vaikrita gneiss, Sangla valley, Himachal High Himalaya

(Fig. 12.7). Since these structures cannot form along with the ductile compressional structures, this stage should be post superposed deformation.

12.6 Tectonic Evolution of the WGC

Modification in the curvatures of the hanging wall folds is explained with the help of a simple diagram. Figure 12.8a displays map pattern of a thrust, which is characterized by frontal and oblique fault ramp geometries. Simultaneous development of noncylindrical folds and oblique thrust ramp results in curvature of hanging wall fold hinge lines in vicinity of the thrust (cf. Fig. 11.5). During the superposed deformation, with a change in the direction of maximum shortening, the early thrust fault reactivate as strike-slip fault with a prominent restraining bend at the oblique fault ramp (Fig. 12.8b). An increase in curvature of the early folds takes place in vicinity of the restraining bend and the fold hinge line orientation varies from NE–SW to N–S. The noncylindrical superposed folds during their longitudinal propagation display a curvature at the restraining bend, and the fold hinge lines rotate towards the E–W direction. Thus the early and superposed folds demonstrate different orientations from their regional trend, across the oblique ramp.

Figure 12.9 is a simplified diagram showing evolution of different structures in the area. The initial frontal and oblique fault ramp geometries are shown in Fig. 12.9a. At the onset of the Himalayan orogeny the fault acted as a thrust fault. The frontal ramp showed dip-slip displacement whereas the oblique ramp showed oblique-slip displacement with dextral sense of movement. Simple shear along the oblique ramp led to formation of a shear zone with the longer axes of the ellipses at an acute angle to the axis of maximum compression. Early fold hinge lines developed orthogonal to the compression direction. Folds, which initiated at the hanging wall close to the frontal ramp, propagated by longitudinal fold propagation towards the oblique ramp. After entering the oblique ramp shear zone, the

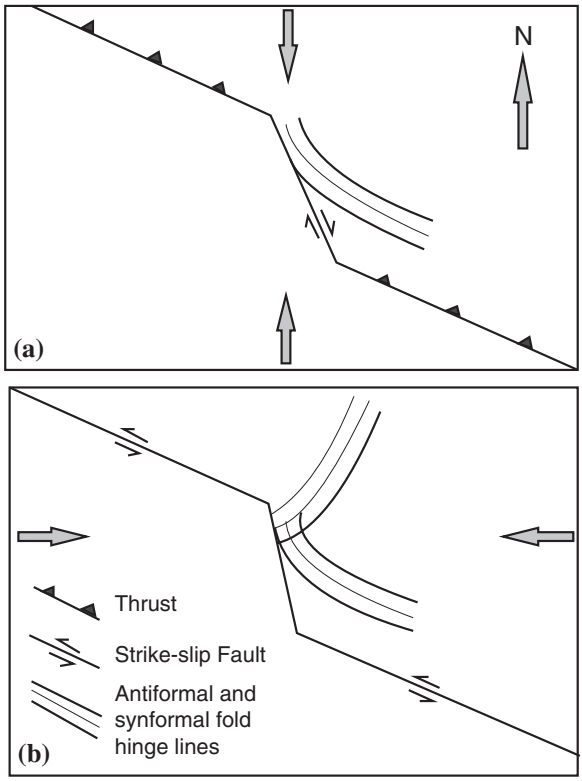

Fig. 12.8 Effect of fault geometry and displacement on curvature of developing *fold hinge lines*. *Arrows* indicate the axis of maximum compression. **a** Curvature of propagating noncylindrical early fold hinge lines at the oblique thrust ramp. **b** Change in the type of fault from thrust to strike-slip during superposed deformation, modification in the early fold orientation, and curvature of propagating superposed fold hinge lines at the restraining bend. North is marked on the diagram to compare these folds with the described natural folds at Karcham (after Dubey 1999)

hinge line showed a curvature (C1) towards the longer axis of the strain ellipse and became nearly parallel to the trend of the oblique ramp (Fig. 12.9b). Two new fold complexes (F) initiated at a distance from the oblique ramp. During the superposed deformation, the axis of maximum compression changed its orientation and became orthogonal to the early direction. With the change in orientation of the compression direction, the early dextral displacement along the oblique ramp reactivated as sinistral (Fig. 12.9c) that led to normal fault displacement in vicinity of the oblique ramp (cf. Fig. 7.28). Superposed folds developed with orientation of fold hinge lines orthogonal to the early folds. Interference took place between the early and superposed folds, and the superposed folds and oblique ramp. The interference between folds resulted in orthogonal linking of the fold hinge lines (C2, Fig. 12.9c) whereas interference between the propagating superposed folds and sinistral oblique ramp resulted in curvature of the fold hinge lines due to drag along the oblique ramp (C3, Fig. 12.9c). Hence the following two patterns emerged.

1. The initial thrust fault reactivated as normal fault, and
2. A large variation in orientation of the fold hinge lines.

Caddick et al. (2007) have carried out pseudo-section analysis and in situ monazite dating of the Lower Himalayan metasediments and inferred a peak temperature

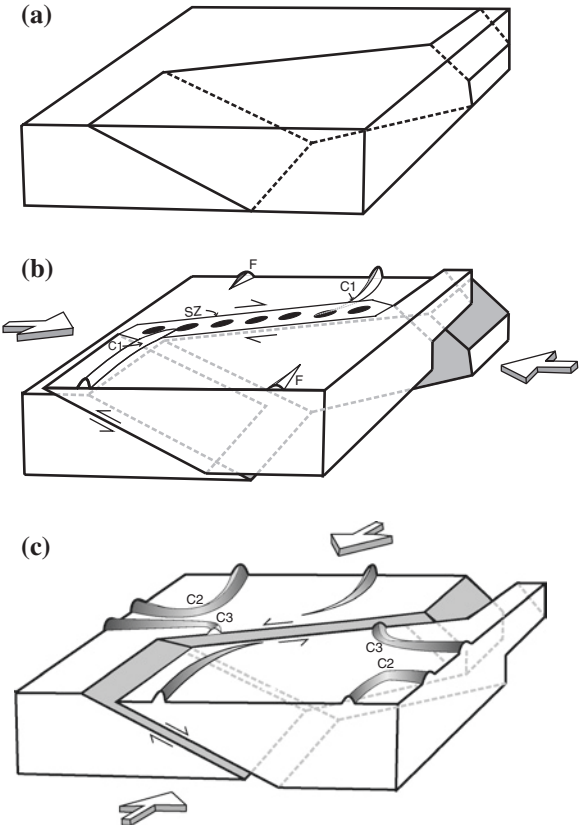

Fig. 12.9 A schematic model to explain the structural evolution of the area around Karcham, Himachal High Himalaya. [From Sen et al. (2012), © Elsevier. Published with permission of Elsevier Scientific Publishing Company]

of 600–640 °C at ~25 km depth at around 10 Ma. The study also interpreted that the relatively hotter HHC rapidly rode over the Lower Himalayan metasediments along the MCT instead of deep underthrusting along the MCT zone (Vannay et al. 2004). The field and AMS studies (Tripathi et al. 2011) vindicates the inference of Caddick et al. (2007) that deep underthrusting along the MCT did not take place after locking of the thrust and superposed folding was the only manifestation of deformation at later stages.

12.7 Reverse (Inverse) Metamorphism

The reverse metamorphism has been observed for nearly 1,700 km along the length of the belt. Both the High Himalayan and Lower Himalayan sequences display inverted metamorphic gradients but the two are not of the same age (Hodges 2000) because the metamorphic event in the High Himalaya extended up to early Miocene or even Pleistocene. The inverted metamorphic zonation is characterized

by a gradual superposition of garnet, staurolite, kyanite, sillimanite + muscovite and sillimanite + K-feldspar isograds from base to top of the unit (Vannay and Grasemann 2001). The P–T conditions associated with this inverted metamorphism suggest peak conditions characterized by temperature (T) increase from 570 to 750 °C at a constant pressure (P) around 8 kbar from the base to top of the sequence.

In the Zanskar region, temperature and pressure increase dramatically upward in the section across the MCT zone from biotite through garnet, staurolite and kyanite grades to sillimanite + muscovite, and then decrease towards the top beneath the Zanskar Shear zone (Searle et al. 1999). In Zanskar, peak P–T conditions of the M1 kyanite-grade rocks are 550–680 °C and 9.5–10.5 kbar, and M2 sillimanite grade gneisses were formed at 650–770 °C and 4.5–7 kbar. The core of the High Himalayan zone was described as 30 km wide zone of sillimanite + K-feldspar-grade gneisses, migmatites and anatectic leucogranites with a right way-up isograd sequence above and an inverted sequence below.

Inverted metamorphism along the Main Central Thrust zone is one of the unresolved problems of the Himalaya. Various models have been proposed to explain the feature, e.g. (i) shear heating along the thrust (Le Fort 1975), (ii) recumbent folding of earlier formed metamorphic isograds along the hanging wall of the later thrust (Searle et al. 1988, 1992), (iii) downward transfer of heat from Miocene High Himalayan leucogranites and thermal buffering (Hodges et al. 1988a), (iv) ductile shear displacements along ubiquitous, closely spaced S–C shear planes across a broad shear zone within the basal part of the MCT (Thoni 1977; Jain and Manickavasagam 1993), and by tectonic imbrications along thrusts (Treloar et al. 1989). Vannay and Grasemann (2001) have presented a useful synthesis and review of the inverted metamorphism in the Himalaya.

In the Nepal Himalaya, metamorphic grade in the Crystallines increases upward in its lower part and then decreases from the middle to the upper part towards the South Tibetan Detachment (STD) (Hubbard 1989) whereas in the Himachal Himalaya, the inverted metamorphism span the whole Crystallines from MCT zone to the STD (Vanay and Grasemann 1998).

Initial attempts to explain the inverted isotherms involve thermal or hot iron models. Le Fort (1975) proposed that displacement along the MCT led to inverted metamorphism of the Lower Himalayan footwall. It incorporated displacement of the hot Crystalline rocks over the cool footwall rocks and downward conduction of heat (Frank et al. 1973). The model involves continuous increase of temperature across the thrust zone, to reach a maximum at some structural level within the hanging wall rocks and then decrease upwards but such feature has not been observed everywhere in the Crystalline rocks. Hence the hot iron model can explain the pro-grade inverted isotherms and isograds in footwall of the MCT but is not consistent with preservation of metamorphic peak assemblages in the hanging wall. Moreover conduction of heat to the footwall cannot extend to several kilometres of depth. Lyon-Caen and Molnar (1983) have suggested that the occurrence of high-grade metamorphic rocks over the Main Central Thrust is a result of transport of lower crustal material to the surface and not to heating during the orogenesis. The structural and thermobarometric data provided by Searle et al. (1999)

also did not support the thermal models of thrusting a hot slab over a cold slab, and frictional heating along the MCT. Mechanical models of post-metamorphic folding and thrusting of a pre-existing, right way-up metamorphic sequence was found to be compatible with the structural and P–T data. It was suggested that ductile shearing along the MCT zone has structurally condensed the isograds.

Later work by Jaupart and Provost (1985) suggested that high temperatures near the top of the High Himalayan sequence are related to focussing of the heat near the contact because of a difference in thermal conductivity of High Himalayan and Tibetan units. The inverted metamorphism was also explained by shear heating as a result of large displacement along the MCT (e.g. Bird et al. 1975) but the model fails to explain the occurrence of highest temperature hanging wall assemblages at high structural levels above the MCT. Moreover, the shear heating can result in inverted geotherm in the footwall but not in the hanging wall (England and Molnar 1993; Harrison et al. 1998). Such a process predicts maximum temperature near the MCT but temperature field gradient measures for the Satluj valley and other Himalayan sections are not in support of the assumption (Vannay and Grasemann 2001). Another thermal model that involves a combination of accretion of crustal material enriched in radioactive heat producing elements and erosion controlled heat advection (Royden 1993) is also not convincing because the process is slow. The radiogenic heat production and erosion can enhance the geothermal gradient in the thickened crust but the slow time dependent processes alone cannot induce inverted isotherms in the entire crystalline sequence during the c. 30 m.y. time interval between the onset of collision and activation of the MCT (Vannay and Grasemann 2001).

Since large-scale recumbent fold do not occur in the High Himalaya, folding of metamorphic isograds were postulated by Searle et al. (1992) but as pointed out by Hodges (2000), closures of postulated folds in isograd patterns have not been established so far. Moreover, most isograds in the High Himalayan sequence do not correspond to mapped structural discontinuities as expected if discrete thrust imbrication of pre-existing isograds was responsible for inverted metamorphism. Evidence against overturning of isograds by isoclinal folding have also come from the petrologic analysis of Daniel et al. (2003). The study suggests that the peak pressure remains constant across the MCT zone at about 11–13 kbar while the peak temperature decreases across the shear zone from ~660 °C at the base to 780 °C at the top of the shear zone. If the pressure profile is not inverted then the isograds cannot be overturned by isoclinal folds.

12.8 Structural Evolution of the High Himalaya

Some of the models depicting evolution of the High Himalaya are shown in Fig. 12.10. The orogenic wedge model (Burchfiel et al. 1992) (Fig. 12.10a) is based on High Himalayan Crystalline (HHC) wedge sandwiched between the MCT (below) and the South Tibetan Detachment (STD) (above). The STD is a

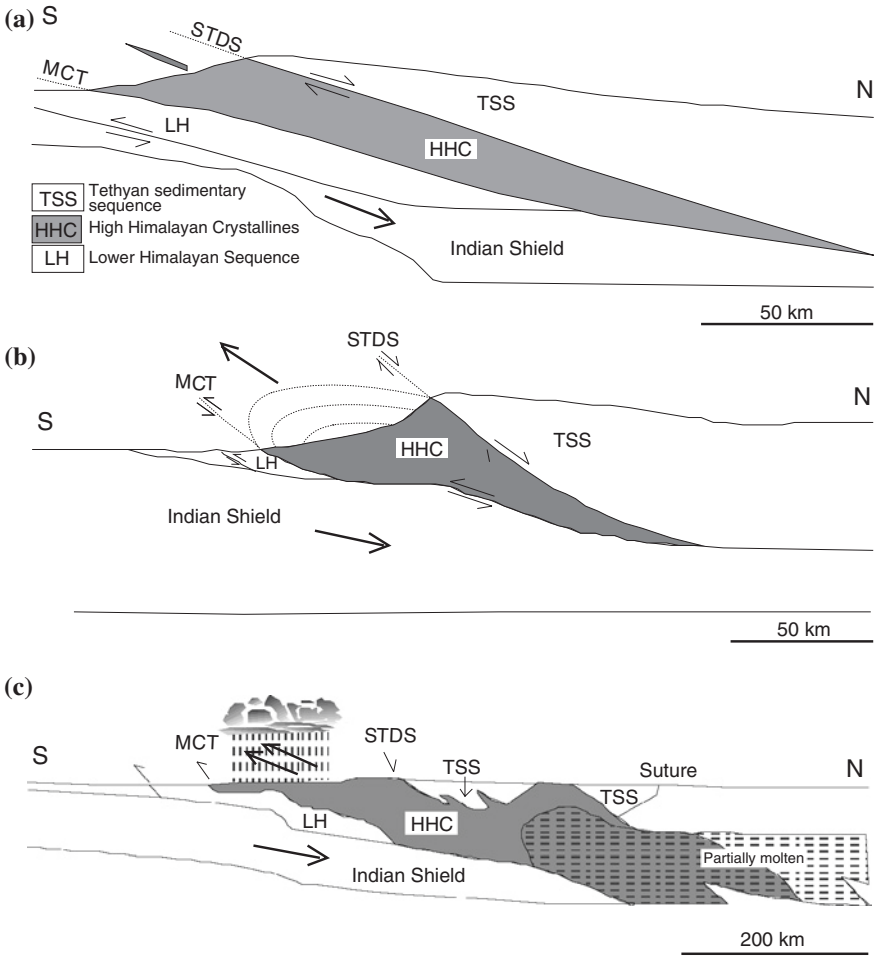

Fig. 12.10 Three schematic sections depicting evolution of mechanical and thermo-mechanical models of the extrusion of the High Himalaya Crystallines. **a** Orogenic wedge model (after Burchfiel et al. 1992). **b** Pervasive ductile flow indicated by folded isograds in High Himalayan Crystalline wedge (after Grujic et al. 1996). **c** Section based on INDEPTH profile (after Nelson et al. 1996) modified to accommodate the essential elements of mid-crustal channel flow predicted by Beaumont et al. (2004). [From Harris (2007), © The Geological Society. Published with permission of Geological Society of London]

normal fault whereas the MCT is a thrust fault. This opposite sense of movement at the same time (Early Miocene?) has facilitated the extrusion of the HHC. Melting in the middle crust at depths of 25–30 km was attributed to be responsible for lowering the shear stress along the base of the wedge.

Based mainly on top-to-the-south shearing, coaxial thinning across the High Himalaya and concomitant north–south stretching parallel to the thrusting direction, Grujic et al. (1996) have proposed a tectonic model to explain the

ductile southward extrusion of the High Himalayan crystalline rocks of Bhutan. The inverted metamorphic sequence was explained as a result of deformation of the metamorphic isograds into a crustal-scale antiform by ductile shearing (Fig. 12.10b). Locally, the peak metamorphic isograds were inverted during deformation due to heat advection from a large leucogranite intrusion leading to the inversion of isotherms. In this model, rapid exhumation is a prerequisite necessity for preserving the deformed isograds.

The model is described as a qualitative channel flow model. It considers the High Himalayan Crystalline sequence as a wedge of hot metamorphic rocks, ductily deformed between colder and more rigid rocks of the MCT footwall and the Tethyan sequence. The flow is characterized by highest velocity at the centre of the channel and opposite relative movements in the upper and lower parts of the unit. The flow was attributed to an orogen perpendicular pressure gradient c. 1–2 kbar/km, induced by a topographic gradient of 4–6 km over a horizontal distance of about 100 km. However as pointed out by Vannay and Grasemann (2001), such a strong topographic gradient, similar to the present one, did not exist before exhumation of the High Himalayan Crystallines during the Miocene times. The elevation of Tibet at that time was likely to be about 2 km. Moreover, exhumation of the crystalline rocks which occur in the core of the High Himalaya is more likely the cause rather than the consequence of the present day topographic gradient across the Himalaya.

Two essential components of the model are; shear at the boundaries, and induced pressure gradients, which generate highest velocities in the centre of the channel and opposite vorticity at the top and bottom of the channel. However, in contradiction to the highest flow in the centre, field observations suggest greater asymmetry of the folds near the faults (Fig. 12.11) and gradual upright fold geometry with increasing distance from the faults (Fig. 12.12).

A modified model is based on movement of a low-viscosity crustal layer in response to topographic loading and provides an explanation for eastward flow of the Asian lower crust resulting in peripheral growth of the Tibetan plateau, and southward flow and extrusion of the Indian middle crust along the MCT (Fig. 12.10c). The thermo-mechanical models for such extrusion attribute the phenomenon to focussed orographic precipitation and erosion at the surface causing isostatic inequilibrium. Isotopic constraints on the timing of the extrusion indicate the flow during the Early to Mid-Miocene. The viscosity reduction required for the channel flow was a result of melt weakening along the upper surface (STD) and strain softening along the base (MCT). The brittle Quaternary faults, south of the MCT were correlated with spatial distribution of precipitation across a north–south transect, suggesting climate-tectonic linkage over a million year time-scale.

The changing lithological viscosities are the crucial aspect of the channel flow model. The evidence for this was cited from the INDEPTH seismic survey of southern Tibet that showed a zone of bright reflection spots, low seismic velocities and low resistivities at depths of about 15–20 km. Nelson et al. (1996) interpreted this finding as evidence for a zone of partial melting in the crust and suggested the HHC as an extrusion of the fluid middle crust. The extrusion may have facilitated by isostatic imbalance created by large precipitation and erosion of the surface

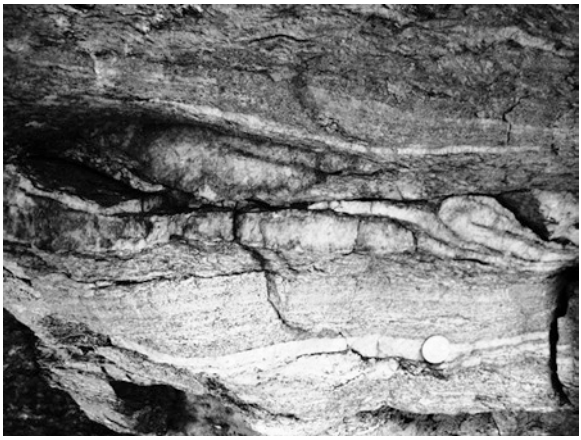

Fig. 12.11 Isolated fold hinges and transposed foliation in the hanging wall Vaikrita gneisses at the Vaikrita Thrust, Karcham, Himachal High Himalaya

Fig. 12.12 Initiation and development of folds by internal buckling in the Vaikrita gneiss, at a distance from the Vaikrita Thrust (Sangla valley, Himachal High Himalaya)

material. The significance of focussed orographic precipitation was applied to extrusion of the high-grade rocks by Wu et al. (1998). Since there is no focussed orographic precipitation in Tibet, the weak crustal layer does not reach the surface and extrusion of the eastern Tibet has been described as "channel tunnelling" (Beaumont et al. 2001). However, Makovsky et al. (1996) contradicted the presence of a widespread melt fraction and argued that the low seismic velocities may represent a zone of saline aqueous fluid percolation. Hence melting of the crust throughout the length of the Himalaya to promote channel flow is open to questions.

Another modified model involves radioactive self heating and rheological weakening of the orogenic crust that led to the formation of a hot, low-viscosity mid-crustal channel and a broad plateau (Fig. 12.13) (Jamieson et al. 2004). The channel material (High Himalayan sequence) flows outward from beneath the plateau in response to topographically induced differential pressure. The material was exhumed at the plateau flank and juxtaposed with cooler, newly accreted material corresponding to the Lower Himalayan sequence. The channel is supposed to

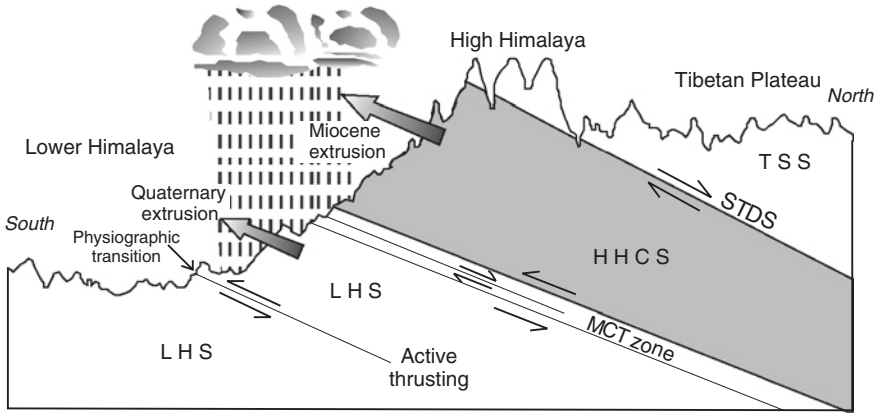

Fig. 12.13 A schematic N–S geological section through the central Himalaya showing Miocene extrusion bounded by Main Central Thrust zone and South Tibetan Detachment. The Quaternary extrusion is bounded by brittle reactivation of the Main Central Thrust and thrusting along the physiographic transition. [From Harris (2007), © The Geological Society. Published with permission of Geological Society of London]

be bounded by the Main Central Thrust zone in the south and the South Tibetan Detachment in the north. The inverted metamorphism associated with the MCT was interpreted as combined effects of distributed ductile shear within the MCT zone and extrusion of the hot channel above the Lower Himalaya.

According to the channel flow model, if the Miocene channel was bounded below by the MCT, then the locus of extrusion had migrated southward by the Late Pliocene to expel the top lithologies of the Lower Himalaya (Fig. 12.13).

In the channel flow model, movement of a low-viscosity crustal layer in response to topographic loading was attributed to (i) eastward flow of the Asian lower crust causing the peripheral growth of the Tibetan plateau, and (ii) southward flow of the Indian middle crust (Harris 2007). Thermomechanical models for channel flow linked this extrusion to focussed orographic precipitation at the surface. Isotropic constraints on the timing of fault movement, anatexis and thermobarometric evolution of the exhumed garnet- to sillimanite-grade metasedimentary rocks were provided as support for mid-crustal channel flow during the Early to Mid-Miocene. Study of exhumed metamorphic assemblages was used to suggest that the dominant mechanism of the viscosity reduction (an essential requirement for channel flow) was melt weakening along the upper surface (STD) and strain softening along the base (MCT) (Harris 2007). The eastward extrusion of Tibet was explained by eastward flow of the lower crust. However, Oreshin et al. (2008) could not find any evidence for a low-velocity layer at mid-crustal depths, making the crustal channel flow unlikely. The study was based on integrated analysis of teleseismic body wave recordings from the linear array of 16 portable broadband seismographs along the western Himalaya-Karakoram section.

Evidence against the channel flow model has also been cited by Sachan et al. (2010) using the age of Malari leucogranite from the Garhwal Himalaya. The

leucogranite lies between the High Himalaya Crystallines and the Tethys Martoli Formation. The leucogranite cuts through the STD and ductile normal-sense shear fabrics, and has experienced relatively little subsolidus brittle deformation or alteration. Hence the leucogranite is younger than the STD and the related shear fabric. Emplacement age of the granite is estimated as 19.0 ± 0.5 Ma suggesting that the normal-shear on the STD must have ceased by 19 Ma. Since initiation of the STD is estimated at between 24–22 Ma, the short duration of extension (≤5 and likely ~3 m.y.) contradicts the basic assumption of the channel flow model. The model predicts long duration of ductile normal shear and large fault displacements after ca. 20 Ma.

Another evidence against the channel flow model was described by Copley et al. (2011). The channel flow model is primarily based on the assumption of poor coupling between the upper crust of the Tibetan plateau and the underthrusting Indian crust because of an intervening low viscosity channel. However, the contrast in tectonic regime between primarily strike-slip faulting in northern Tibet and dominantly normal faulting in southern Tibet requires mechanical coupling between the upper and the lower crusts. Such coupling is not consistent with the presence of active 'channel flow' beneath southern Tibet. Hence the Indian crust retains its strength as it underthrusts the plateau.

Geochronological data suggest that the north Indian region has experienced four magmatic events at 1,760–1,745, 878–825, 520–480, and 28–20 Ma. The first three events also occurred in the north-eastern Indian craton, whereas the last (youngest) one is unique to the Himalaya. The correlation of magmatic events suggests that the Himalayan units were derived from the Indian craton and the formation of the eastern Himalaya was accomplished by vertical stacking of basement involved thrust sheets of the Indian cratonal rocks. The correlation rules out the possibility of derivation of the High grade Himalayan rocks from Tibetan middle crust by channel flow (Yin et al. 2010).

Robinson et al. (2006) have also observed that the channel flow model that require ductile extrusion of the High Himalayan rocks from beneath the Tibetan plateau in a channel, cannot explain the regional-scale structural features of western Nepal. These structures were explained by the orogenic wedge models for thrust belts with inclusion of ductile deformation.

In view of the above, the most convincing hypotheses seem to be those that involve distributed shearing of a pre-existing, right way-up metamorphic sequence in the High Himalaya (Frank et al. 1973; Jain and Manickvasagam 1993; Searle and Rex 1989).

12.9 Tectonic Exhumation of the High Himalaya

Thermal modelling and ZFT and AFT dating across the High Himalayan root-zone in the central Himalaya (Nepal) suggest that the thermochronological structure of the region is a combined result of two distinct cooling episodes. The first tectonic exhumation, took place in the middle Miocene (16–12 Ma). The exhumation was

facilitated by gravity driven slip on the STD and it caused systematic cooling at different structural positions in the High Himalayan crystallines. The second climate driven erosional exhumation took place in the late Miocene–Pliocene (Wang et al. 2010). However, the concept of climate controlled exhumation may not be applicable everywhere. For example, Patel and Carter (2009) have presented the cooling and exhumation history of two structurally identical sections of the HHC exposed along the Dhauliganga and Goriganga river valleys in the Garhwal-Kumaun Himalaya. The two river sections are separated by only 60 km and share the same climate but they have experienced very different exhumation histories. The difference was attributed to variation of recent slip on the Vaikrita thrust (slip rate ~2–3 mm a^{-1}) in the region. The low-temperature chronological studies across the Himalaya in western Nepal and NW India further suggest that the High Himalayan crystallines have experienced faster exhumation than the adjacent Lower and Tethys Himalaya.

Najman et al. (2009) have interpreted that exhumation rate of the High Himalaya decreased markedly just before 16 Ma. The High Himalaya continued to exhume the deeper metamorphic rocks but at much slower rates and the thrusting transferred southward towards the footwall of the MCT. The sedimentary succession of the Lower Himalaya was exhumed to the surface by 9 Ma. Major exhumation of the Lower Himalaya, including the Lower Himalayan klippen rocks occurred at 6 Ma.

The northern boundary of the High Himalaya is marked by the Tethyan fault. The fault was initially a thrust fault, which later reactivated as a normal fault. Gravity gliding could be responsible for the reactivation. A conformable boundary between the Tethyan metasedimentary rocks and the underlying Central Crystalline rocks has also been reported by Gansser (1964), and Pecher (1991). Evidence in support of the conformable contact were provided by apparent structural and metamorphic continuity from the gneisses to the sedimentary series of the Tethyan rocks and no hiatus in the metamorphic isograd succession. The axial plane slaty cleavage of the isoclinal folds observed in the Tethyan rocks could also be traced in the metamorphic cleavage of the gneisses.

References

Ahmad T, Harris N, Bickle M, Chapman H, Bunbury J, Prince C (2000) Isotopic constraints on the structural relationships between the Lesser Himalayan Series and the High Himalayan Crystalline series, Garhwal Himalaya. Geol Soc Am Bull 112:467–477

Arita K (1983) Origin of the inverted metamorphism of the Lower Himalaya, Central Nepal. Tectonophysics 95:43–60

Arita K, Dallmeyer RD, Takasu A (1997) Tectonothermal evolution of the Lesser Himalaya, Nepal: constraints from Ar/Ar ages from the Kathmandu Nappe. The Island Arc 6:372–385

Baig MS, Lawrence RD, Snee LW (1988) Evidence for late Precambrian to Early Cambrian orogeny in north-west Himalaya, Pakistan. Geol Mag 125:83–86

Beaumont C, Jamieson RA, Nguyen MH, Lee B (2001) Himalayan tectonics explained by extrusion of a low-viscosity crustal channel coupled to focused surface denudation. Nature 414:738–742

Beaumont C, Jamieson RA, Nguyen MH, Medvedev S (2004) Crustal channel flows: 1. Numerical models with applications to the tectonics of the Himalayan-Tibetan orogen. J Geophys Res 109, B06406. doi:10.1029/2003JB002809

Bird P, Toksoz MN, Sleep NH (1975) Thermal and mechanical models of continent-continent collision zone. J Geophys Res 80:4405–4416

Burchfiel BC, Chen Z, Hodges KV, Liu Y, Royden LH, Deng C, Xu J (1992) The South Tibetan Detachment System, Himalayan orogen: extension contemporaneous with and parallel to shortening in a collisional mountain belt. Geol Soc Am, Special Paper 269:1–41

Caddick MJ, Bickle MJ, Harris NBW, Holland TJB, Horstwood MSA, Parrish RR, Ahmad T (2007) Burial and exhumation history of a Lesser Himalayan schist: recording the formation of an inverted metamorphic sequence in NW India. Earth Planet Sci Lett 264:375–390. doi:10.1016/j.epsl.2007.09.011

Catlos EJ, Harrison TM, Manning CE, Grove M, Rai SM, Hubbard MS, Upreti BN (2002a) Records of the evolution of the Himalayan orogen from in situ Th–Pb ion microprobe dating of monazite: Eastern Nepal and western Garhwal. J Asian Earth Sci 20:459–479

Catlos JE, Harrison TM, Dubey CS, Edwards MA (2002b) P-T-t constraints on the evolution of the Sikkim Himalaya (Abstract). In: 17th Himalaya-Karakoram-Tibet Workshop, Gangtok, Sikkim, India, pp 6–7

Copley A, Avouac JP, Wernicke BP (2011) Evidence for mechanical coupling and strong lower crust beneath southern Tibet. Nature 472:79–81. doi:10.1038/nature09926

Coward MP, Butler RWH, Khan AM, Knipe RJ (1987) The tectonic history of Kohistan and its implications for Himalayan structure. J Geol Soc London 144:377–391

Daniel CG, Hollister LS, Parrish RR, Grujic D (2003) Exhumation of the Main Central Thrust from lower crustal depths, Eastern Bhutan Himalaya. J Metamorph Geol 21:317–334

Dubey AK (1999) Oblique thrust ramps in the Himalaya: a study based on model experiments. Gondwana Research Group Memoir 6, Gondwana Research Group, Japan, pp 39–49

Dubey AK, Bhakuni SS (2007) Younger hanging wall rocks along the Vaikrita Thrust of the High Himalaya: a model based on inversion tectonics. J Asian Earth Sci 29:424–429

Dubey AK, Bhat MI (1991) Structural evolution of the Simla area, NW Himalaya: implications for crustal thickening. J SE Asian Earth Sci 6:41–53

Dubey AK, Paul SK (1993) Map patterns produced by thrusting and superposed folding: model experiments and example from the NE Kumaun Himalaya. Eclogae Geol Helv 86:839–852

Edwards MA, Harrison TM (1997) When did the roof collapse? Late Miocene north-south extension in the High Himalaya revealed by Th–Pb monazite dating of the Khula Kangri granite. Geology 25:543–546

England P, Molnar P (1993) The interpretation of inverted metamorphic isograds using simple physical calculations. Tectonics 12:145–157

Frank W, Hoinkes G, Miller C, Purtscheller F, Richter W, Thoni M (1973) Relations between metamorphism and orogeny in a typical section of the Indian Himalaya, NW Himalaya, S-Lahaul, Kulu, Himachal Pradesh: first comprehensive report. Tschermaks Mineralogische Petrographische Mitteilungen 20:303–332

Gansser A (1964) Geology of the Himalaya. Interscience, New York 289 pp

Grujic D, Casey M, Davidson C, Hollister LS, Kundig R, Pavlis T, Schmid S (1996) Ductile extrusion of the Higher Himalayan Crystalline in Bhutan: evidence from quartz microfabrics. Tectonophysics 260:21–43

Harris N (2007) Channel flow and the Himalayan-Tibet orogen: a critical review. J Geol Soc London 164:511–523

Harris NBW, Caddick M, Kosler J, Goswami S, Vance D, Tindie AG (2004) The pressure-temperature-time path of migmatites from the Sikkim Himalaya. J Metamorph Geol 22:249–264

Harrison TM, Ryerson FJ, McKeegan KD, Le Fort P, Yin A (1996) Th–Pb monazite ages of Himalayan metamorphic and leucogranitic rocks: Constraints on the timing of inverted metamorphism and slip on the MCT and STD. In: Macfarlane AM, Sorkhabi RB, Quade J (eds) 11th Himalaya-Karakoram-Tibet Workshop Abstracts: Flagstaff, Northern Arizona University, pp 58–59

Harrison TM, Grove M, Lovera M, Catlos EJ (1998) A model for the origin of Himalayan anatexis and inverted metamorphism. J Geophys Res 103:27017–27032

Heim A, Gansser A (1939) Central Himalaya: geological observation of the Swiss expedition in 1936. Mémoires de la Société Helv'tique des Sciences Naturelles 73:1–245

Hodges KV (2000) Tectonics of the Himalaya and southern Tibet from two perspectives. Geol Soc Am Bull 112:324–350

Hodges KV, LeFort P, Pecher A (1988a) Possible thermal buffering by crustal anatexis in collisional orogens: Thermobarometric evidence from the Nepalese Himalaya. Geology 16:707–710

Hodges KV, Hubbard MS, Silverberg DS (1988b) Metamorphic constraints on the thermal evolution of the central Himalayan Orogen. Roy Soc London Philosophical Trans 326:257–280

Hodges KV, Parrish RR, Housh TB, Lux DR, Burchfiel BC, Royden LH, Chen Z (1992) Simultaneous Miocene extension and shortening in the Himalayan orogeny. Science 258:1466–1470

Hodges KV, Parrish RR, Searle MP (1996) Tectonic evolution of the central Annapurna Range, Nepalese Himalaya. Tectonics 15:1264–1291

Hubbard MS (1989) Thermobarometric constraints on the thermal history of the Main Central thrust zone and Tibetan slab, eastern Himalaya. J Metamorph Geol 7:19–30

Hubbard MS, Harrison TM (1989) $^{40}Ar/^{39}Ar$ age constraints on deformation and metamorphism in the Main Central Thrust zone and Tibetan Slab, eastern Nepal Himalaya. Tectonics 8:865–880

Jain AK, Manickavasagam RM (1993) Inverted metamorphism in the intracontinental ductile shear zone during Himalayan collision tectonics. Geology 21:407–410

Jain AK, Kumar D, Singh S, Kumar A, Lal N (2000) Timing, quantification and tectonic modelling of Pliocene–Quaternary movements in the NW Himalaya: evidence from fission track dating. Earth Planet Sci Lett 179:437–451. doi:10.1016/S0012-821X(00)00133-3

Jamieson R, Beaumont C, Medvedev S, Nguyen MH (2004) Crustal channel flows: 2. Numerical models with implications for metamorphism in the Himalayan-Tibetan orogen. J Geophys Res 109:B06407. doi:10.1029/2003JB002811

Jaupart C, Provost A (1985) Heat focusing, granite genesis and inverted metamorphic gradients in continental collision zones. Earth Planet Sci Lett 73:385–397. doi:10.1016/0012-821X(85)90086-X

Kohn MJ (2008) P-T-t data from Central Nepal support critical taper and repudiate large-scale channel flow of the Greater Himalayan sequence. Bull Geol Soc Am 120:259–273. doi:10.1130/B26252.1

Le Fort P (1975) Himalaya: the collided range. Present knowledge of the continental arc. Am J Sci 275:1–44

Lyon-Caen H, Molnar P (1983) Constraints on the structure of the Himalaya from an analysis of gravity anomalies and a flexural model of the lithosphere. J Geophys Res 88:8171–8191

Macfarlane (1993) Chronology of tectonic events in the crystalline core of the Himalaya, Langtang National Park, central Nepal. Tectonics 12:1004–1025

Makovsky Y, Klemperer SL, Ratschbacher L, Brown L, Li M, Zhao W, Meng F (1996) INDEPTH wide-angle reflection observation of P-wave to s-wave conversions from crustal bright spots in Tibet. Science 274:1690–1691

Metcalfe RP (1993) Pressure, temperature and time constraints on metamorphism across the Main Central Thrust zone and High Himalayan slab in the Garhwal Himalaya. In: Treloar PJ, Searle MP (eds) Himalayan Tectonics. Geol Soc London, Special Publication 74:485–509

Miller C, Klotzli U, Frank W, Thoni M, Grasemann B (2000) Proterozoic crustal evolution in the NW Himalaya (India) as recorded by circa 1.80 Ga mafic and 1.84 Ga granitic magmatism. Precambr Res 103:191–206

Myrow PM, Hughes NC, Paulsen TS, Williams IS, Parcha SK, Thompson KR, Bowring SA, Peng S-C, Ahluwalia AD (2003) Integrated tectonostratigraphic analysis of the Himalaya and implications for its tectonic reconstruction. Earth Planet Sci Lett 212:433–441

Najman Y, Bickle M, Garzanti E, Pringle M, Barfod D, Brozovic N, Burbank D, Ando S (2009) Reconstructing the exhumation history of the Lesser Himalaya, NW India, from a multi-technique provenance study of the foreland basin Siwalik Group. Tectonics 28, TC5018. doi:10.1029/2009TC002506

Nakata T (1989) Active faults of the Himalaya of India and Nepal. Geol Soc Am Special Paper 232:243–264

Nelson KD and Project INDEPTH Team (1996) Partially molten middle crust beneath Southern Tibet: synthesis of project INDEPTH results. Science 274:1684–1696

Oreshin S, Kiselev S, Vinnik L, Prakasam KS, Rai SS, Makeyeva L, Savvin Y (2008) Crust and mantle beneath western Himalaya, Ladakh and western Tibet from integrated seismic data. Earth Planet Sci Lett 271:75–87

Parrish RR, Hodges KV (1996) Isotopic constraints on the age and provenance of the Lesser and Greater Himalayan sequences, Nepalese Himalaya. Geol Soc Am Bull 108:904–911

Patel RC, Carter A (2009) Exhumation history of the Higher Himalayan Crystalline along Dhauliganga-Goriganga river valleys, NW India: new constraints from fission track analysis. Tectonics 28, TC3004. doi:10.1029/2008TC002373

Paul SK, Roy AK (1991) Significance of satellite imagery in the elucidation of tectonic set-up of Himachal and UP Himalaya. In: Gupta PN, Roy AK (eds) Mountain resource and management and remote sensing. Surya Publication, Dehradun, pp 27–37

Pecher A (1991) The contact between the Higher Himalaya crystallines and the Tibetan sedimentary series: Miocene large-scale dextral shearing. Tectonics 10:587–598

Pognante U, Lombardo B (1989) Metamorphic evolution of the High Himalayan Crystallines SE Zanskar, India. J Metamorph Geol 7:9–17

Pognante U, Castelli D, Benna P, Genivese G, Oberli F, Meier M, Tonarini S (1990) The crystalline units of the High Himalaya in the Lahul-Zanskar region (north-west India): metamorphic–tectonic history and geochronology of the collided and imbricated Indian plate. Geol Mag 127:101–116

Raj S (1983) Variation of structural elements across the Jutogh thrust and its implications: a study based on field evidence and model experiments. Geosci J 4:157–168

Robinson D, DeCelles PG, Copeland P (2006) Tectonic evolution of the Himalayan thrust belt in western Nepal: implications for channel flow models. Geol Soc Am Bull 118:865–885. doi:10.1130/B25911.1

Royden LH (1993) The steady state thermal structure of eroding orogenic belts and accretionary prisms. J Geophys Res 98:4487–4507

Royden LH, Burchfiel BC (1987) Thin-skinned N-S extension within the convergent Himalayan region: Gravitational collapse of a Miocene topographic front. Geol Soc London, Special Publication 28:611–619

Sachan HK, Kohn MJ, Saxena A, Corrie SL (2010) The Malari leucogranite, Garhwal Himalaya, northern India: chemistry, age, and tectonic implications. Bull Geol Soc Am 122:1865–1876. doi:10.1130/B30153.1

Searle MP, Rex AJ (1989) Thermal model for the Zanskar Himalaya. J Metamorph Geol 7:127–134

Searle MP, Cooper DWJ, Rex AJ (1988) Collision tectonics of the Ladakh-Zanskar Himalaya. Philosophical Trans Roy Soc London Series A 326:117–150

Searle MP, Waters DJ, Rex DC, Wilson RN (1992) Pressure, temperature and time constraints on Himalayan metamorphism from eastern Kashmir and western Zanskar. J Geol Soc London 149:753–773

Searle MP, Waters DJ, Dranfield MW, Stephenson BJ, Walker CB, Walker JD, Rex DC (1999) Thermal and mechanical models for the structural and metamorphic evolution of the Zanskar High Himalaya. In: Mac Niocaill C, Ryan PD (eds) Continental tectonics. Geol Soc London, Special Publication 164:139–156

Sen K, Dubey AK, Tripathi K, Pfänder JA (2012) Composite mesoscopic and magnetic fabrics of the Paleo-Proterozoic Wangtu Gneissic Complex, Himachal Himalaya, India: implications for ductile deformation and superposed folding of the Himalayan basement rocks. J Geodyn 61:81–93

Srikantia SV, Sharma RP (1976) Geology of Shali Belt and the adjoining areas. Memoir Geological Survey of India 106:31–166

Srikantia SV, Bhargava ON (1998) Geology of Himachal Pradesh. Geological Survey of India, Bangalore 406 pp

Thoni M (1977) Geology, structural evolution and metamorphic zoning in the Kulu valley (Himachal Himalaya, India) with special reference to the reverse metamorphism. Mitt Gesch Bergbaustud Ostern 24:125–187

Treloar PJ, Rex DC, Guise PG, Coward MP, Searle MP, Windley BF, Petterson MG, Jan MQ, Luff IW (1989) K–Ar and Ar–Ar geochronology of the Himalayan collision in NW Pakistan: constraints on the timing of suturing, deformation, metamorphism and uplift. Tectonics 8:881–909. doi:10.1029/TC008i004p00881

Tripathi K, Sen K, Dubey AK (2011) Modification of fabric in pre-Himalayan granitic rocks by post-emplacement ductile deformation: insights from microstructures, AMS and U–Pb geochronology of the Paleozoic Kinnaur Kailash Granite and associated Cenozoic leucogranites of the South Tibetan Detachment zone, Himachal High Himalaya. Int J Earth Sci. doi 10.1007/s00531-011-0657-z

Valdiya KS (1973) Lithological subdivision and tectonics of the Central Crystalline zone of Kumaun Himalaya. In: Seminar proceedings of geodynamics Himalayan region. National Geophysical Research Institute, Hyderabad, pp 304–305

Valdiya KS (1980) Geology of Kumaun Lesser Himalaya. Wadia Institute of Himalayan Geology, Dehra Dun 291 pp

Valdiya KS (1998) Geodynamic Himalaya. Universities Press, Hyderabad 178 pp

Valdiya KS, Paul SK, Chandra T, Bhakuni SS, Upadhyay RC (1999) Tectonic and lithological characterization of Himadri (Great Himalaya) between Kali and Yamuna rivers, central Himalaya. Himalayan Geol 20:1–17

Vannay JC, Grasemann B (1998) Inverted metamorphism in the High Himalaya of Himachal Pradesh (NW India): phase equilibria versus thermobarometry. Schweizerische Mineralogie ssche und Petrographische Mittecilungen 78:107–132

Vannay J-C, Grasemann B (2001) Himalayan inverted metamorphism and syn-convergence extension as a consequence of a general shear extrusion. Geol Mag 138:253–276

Vannay J-C, Grasemann B, Rahn M, Frank W, Carter A, Baudraz V, Cosca M (2004) Miocene to Holocene exhumation of metamorphic crustal wedges in the NW Himalaya: evidence for tectonic extrusion coupled to fluvial erosion. Tectonics 23(1):1–24, TC 1014. doi:10.1029/2002TC001429,2004

Walker JD, Martin MW, Bowring SA, Searle MP, Waters DJ, Hodges KV (1999) Metamorphism, melting, and extension: age constraints from the High Himalayan slab of southeast Zanskar and northwest Lahaul. J Geol 107:473–495

Wang A, Garver JI, Wang G, Smith JA, Zhang K (2010) Episodic exhumation of the Greater Himalayan Sequence since the Miocene constrained by fission track thermochronology in Nyalam, central Himalaya. Tectonophysics 495:315–323. doi:10.1016/j.tecto.2010.09.037

Wu C, Nelson KD, Wortman G (1998) Yadong cross structure and South Tibetan Detachment in the east central Himalaya (89°–90°E). Tectonics 17:28–45. doi:10.1029/97TC03386

Yin A (2006) Cenozoic tectonic evolution of the Himalayan orogen as constrained by along-strike variation of structural geometry, exhumation history and foreland sedimentation. Earth Sci Rev 76:1–131. doi:10.1016/j.earscirev.2005.05.004

Yin A, Dubey CS, Kelty TK, Webb AAG, Harrison TM, Chou CY, Celerier J (2010) Geologic correlation of the Himalayan orogen and Indian craton: Part 2. Structural geology, geochronology, and tectonic evolution of the Eastern Himalaya. Geol Soc Am Bull 122:360–395. doi:10.1130/B26461.1

Chapter 13
The Tethys Himalaya

Abstract Lithostratigraphy (including leucogranites) is described along with structural features. The nature and age of the intrusive granite are discussed. The South Tibetan Detachment System (STDS) has a complicated history of fault reactivations. It initiated as a normal fault during pre-Himalayan rifting and reactivated as thrust during early phase of Himalayan orogeny. Sheath folds in the hanging wall have formed during thrusting. During the late stages of deformation, it showed normal faulting. Two trends of normal faults, parallel and transverse to the Himalayan trend, and their origin are discussed. Some of the normal faults are a result of gravity gliding. Formation of transverse extensional faults (e.g. Leopargial Horst) in a predominant compressional regime is explained. The latest displacement along the STDS is that of right lateral slip. Evidence for the reactivations are discussed.

The high grade metamorphic core of the Himalaya is separated from the weakly metamorphosed supra-structure by the Tethyan fault or the South Tibetan Detachment System (STDS) (Burg et al. 1984; Burchfiel et al. 1992). The STDS has acted as a thrust at the onset of the compressional phase and later reactivated as a normal fault. The inference is supported by the following observations.

1. Presence of sheath folds at the hanging wall (Lahaul-Spiti region, Himachal Himalaya) followed by normal faulting demonstrated by a number of later secondary veins.
2. Asymmetric folds showing early sense of shear from top to south followed by reversal in the sense of shear from top to north.
3. Locally preserved (e.g. Annapurna of Nepal) higher grade over lower grade relationship (Yin 2006).
4. Exposure of older rocks over younger rocks (e.g. Zanskar of NW Himalaya).

The later northward sense of shear has been attributed to gravitational collapse of the Tethyan sequence after acquiring higher topographic elevation by thrusting. There is only one prominent mineral stretching lineation plunging gently at N15°

A. K. Dubey, *Understanding an Orogenic Belt*, Springer Geology,
DOI: 10.1007/978-3-319-05588-6_13,

to 35°E suggesting that the displacement was in the NE–SW direction throughout its history, i.e. during the early thrusting and later normal faulting.

13.1 The South Tibetan Detachment System

The STDS extends along the entire length of the Himalaya. Thrusting along the STDS initiated prior to 22 Ma (Early Miocene) (Hodges et al. 1996) but later displacements younger than 12.5 Ma have also been recorded (Hodges 2000; Hodges et al. 1992, 1998). Searle et al. (1999) have obtained $^{40}Ar/^{39}Ar$ and K–Ar cooling ages and age of a cross-cutting leucogranite from the Garhwal Himalaya. The ages suggest that the STDS was active between 23 and 21 Ma. Thermochronological data from the Nepal Himalaya suggest that the displacement prevailed till 15–13 Ma (Godin et al. 2001). If the MCT has initiated as thrust at c. 22 Ma, then the STDS and the MCT were active simultaneously (or spasmodic) for a considerable amount of time (Hodges et al. 1995).

Burchfiel and Royden (1985) have estimated the displacement along the STDS to be of the order of 15–18 km whereas a minimum displacement of 35 km has been predicted along the Qomolangma Detachment between 22 and 16 Ma (Burchfiel et al. 1992; Hodges et al. 1992, 1998).

In Satluj and Baspa river valleys of the Himachal Himalaya, the STDS is characterized by presence of Paleozoic (~475 Ma) granite called as Kinnaur Kailash Granite (KKG) (Marquer et al. 2000). The granite was later intruded by Cenozoic leucogranites (~18 Ma). Magnetic fabric in interior parts of the KKG is the original emplacement related fabric. U–Pb geochronology of zircons from two samples of the KKG yielded crystallization age of 477.6 ± 3.4 and 472 ± 4 Ma. The leucogranite gives a crystallization age of 18.5 ± 0.6 Ma. Zircons from the KKG also reveal signatures of a deformation event (20.6 ± 2.3 Ma) at its rim. Deformation of the external rim of the KKG and crystallization of the leucogranites are synchronous and triggered by ductile deformation associated with the STDS (Tripathi et al. 2011). The Garhwal Himalaya provides a similar lithological setting where the Gangotri leucogranite intrudes the Paleozoic, S-type Bhaironghati Granite.

The latest displacement along the STDS indicates a right-lateral slip (Pecher et al. 1991; Dubey 1999). Fabrics of both the KKG and the leucogranite are related to displacement along the STDS and later modification by the Cenozoic right-lateral slip. The mylonites of the KKG shows evidence of shearing related to eastward extension along the STDS (Vannay et al. 2004). Petrological and geochemical signatures of the KKG indicate emplacement in an extensional setting. Islam et al. (1999) have carried out a detailed geochemical study of some of the Himalayan granites and inferred them to be peraluminous S-type granites derived from a crustal source related to rift magmatism. The Mandi-Karsog pluton (Himachal Lower Himalaya), which is contemporaneous with the KKG, also shows evidence of emplacement in an extensional oblique-slip

environment (Jayangondperumal et al. 2010). Hence the region of the Himachal Himalaya has suffered extensional tectonics in both Paleozoic and Cenozoic times.

13.2 Leucogranites

The presence of leucogranites along the STDS can be observed throughout the Himalaya at top of the High Himalayan Crystallines. This magmatism is one of the youngest magmatic activities and it continued from 23 to 12 Ma. In the Zanskar shear zone, leucogranite magmatism has been dated to be around 22.2 ± 0.2 Ma (Dezes et al. 1999). Th–Pb monazite date from the Annapurna-Manaslu region of the Nepal central Himalaya yielded two pulses of magmatism at 22.9 ± 0.6 Ma and at 19.3 ± 0.3 Ma (Harrison et al. 1999). In the Khula-Kangri region of Bhutan High Himalaya the age of leucocratic magmatism obtained by Th–Pb dating of monazite is as young as 12.5 ± 0.4 Ma (Edwards and Harrison 1997). In the Garhwal Himalaya, U–Pb geochronology of zircon revealed 23 Ma age of crystallization for the Shivling leucogranite (Hodges et al. 1996), and 19.0 ± 0.5 Ma for the Malari leucogranite (Sachan et al. 2010). The leucogranite occurring with the KKG differs in occurrence with other leucogranites as it occurs in hanging wall of the STDS and instead of cross-cutting the High Himalayan Crystallines in footwall of the STD, it intrudes the KKG.

Vannay et al. (2004) have carried out $^{40}Ar/^{39}Ar$ thermochronology in mylonites of the Sangla detachment and obtained ages of 19.2–17.2 Ma for deformation in the hanging wall. Zircon fission track (16.3–13.6 Ma) and apatite fission track (4.9–2.6 Ma) ages indicated that deformation in the STDS (Satluj valley) continued till ~2.5 Ma with decreasing temperature.

Rb–Sr dating of a mylonitic orthogneiss unit (Baragaon gneiss in the Kulu-Larji-Rampur window) revealed an age of ~1,840 Ma for basement of the Tethys sequence. The rocks have a thickness of more than 8 km and consist of metamorphic, metasedimentary, and sedimentary rocks (Thakur 1992; Srikantia and Bhargava 1998). The rock sequence is continuous from Precambrian to Eocene. The sedimentary rocks are predominantly fossiliferous and range in age from Late Precambrian to Cretaceous and at places up to Eocene.

13.3 Lithostratigraphy

The lithostratigraphy of the Tethys region (Table 13.1) varies along and across the Tethyan fault. Brookfield (1993) has pointed out that sedimentation of the Tethyan sequence is markedly different in east and west of the Nanga Parbat syntaxis prior to onset of the Indo-Asia collision. The difference was attributed to two rifting events; one in the Permian along the northern margin of India and two in the Jurassic along the western margin of India.

Table 13.1 Palaeozoic sedimentary formations in the Tethys domain of the Himalaya (after Valdiya 1998)

Age								
Period		Time Range (my ago)	Kashmir	Himachal		Kumaun	Nepal	Sikkim	Bhutan
Permian	L	-250 –	Zewan Fm.	Kuling Shale		Kuling Shale	Thinichu Fm.	Lachi Fm.	Shodung
	M	-260-	Panjal volcanics	Panjal volcanics					
		-270-	Agglomeratic Slate	Ganmachidam Congl.					
	E	-290-							Wachila
Carboniferous	L	-310-	Fenestella Shale	Po Shale					
	M	-325							
	E	-355-	Syringothyris Ls.	Lipak Ls.					Tongchu
Devonian			Muth Quartzite	Muth Quartzite		Muth Quartzite	Tilicho Lake Fm.		
Silurian		-426-	Marhaum/ Margam Fm..	Takche / Pin		Variegated Silurian	Dark Band Fm.		Nakechu
		-438-		Thango/ Thaple		Shiala Fm.	North Face Qz.		
Ordovician	L	-446-				Garbyang Fm.	Nilgiri Ls.		
	M	-455-						Everest Ls.	Maneting
	E	-510-						Everest Pelites	
Cambrian	L	-523-	Tragaham Fm.	Parahio/ Kurgiakh	Haimanta	Ralam Congl.			
	M	-525-	Karikul/ Nutunus	Karsha Ls.		Martoli			
	E	-570-	Lolab/ Khaiyar Fm.	Kunzamla					

-------,unconformity; Fm., formation; Ls., limestone; Qz., quartzite; Congl., conglomerate.

13.4 Structural Features

Reclined and recumbent folds are characteristic structures of the subdivision. The reclined folds have formed as a result of superposed folding of the early recumbent folds.

Two trends of recent normal faults have been observed in the Himachal Tethys Himalaya. The first trend is parallel to the general trend of the Tethyan fault (i.e. NW–SE). These faults can be explained either by gravity gliding (Burg et al. 1984; Herren 1987; Royden and Burchfiel 1987) or by pull-apart structure (Ni and Barazangi 1985; Mazari and Bagati 1991). The brittle normal faults, developed in response to differences in gravitational potential energy is marked by a 3–10 m wide zone of fault breccias at some places and dips between 5° to 15° towards the northeast (Hodges et al. 1992). The second trend is nearly orthogonal to the general trend of the Tethyan fault. These N–S trending normal faults have a wide occurrence and are described from the central Himalaya and also from the Tibetan Himalaya. The faults initiated around 4 Ma in the Lower Himalaya and between 14 and 16 Ma in the High and Tethys Himalaya (Hintersberger et al. 2010). On a larger scale these faults are responsible for the formation of the Leo Pargial Horst (Fig. 13.1) and are characterized by shallow crustal seismicity (Ni and Barazangi 1985).

The fault plane solution of the Kinnaur earthquake (19 January 1975; depth of focus, 37 km; magnitude, Ms, 6.8) indicated a nearly vertical axis of maximum compressive strain, which was regarded as contradictory to the plate tectonics model, where the axis is regarded as oriented in NE–SW horizontal direction

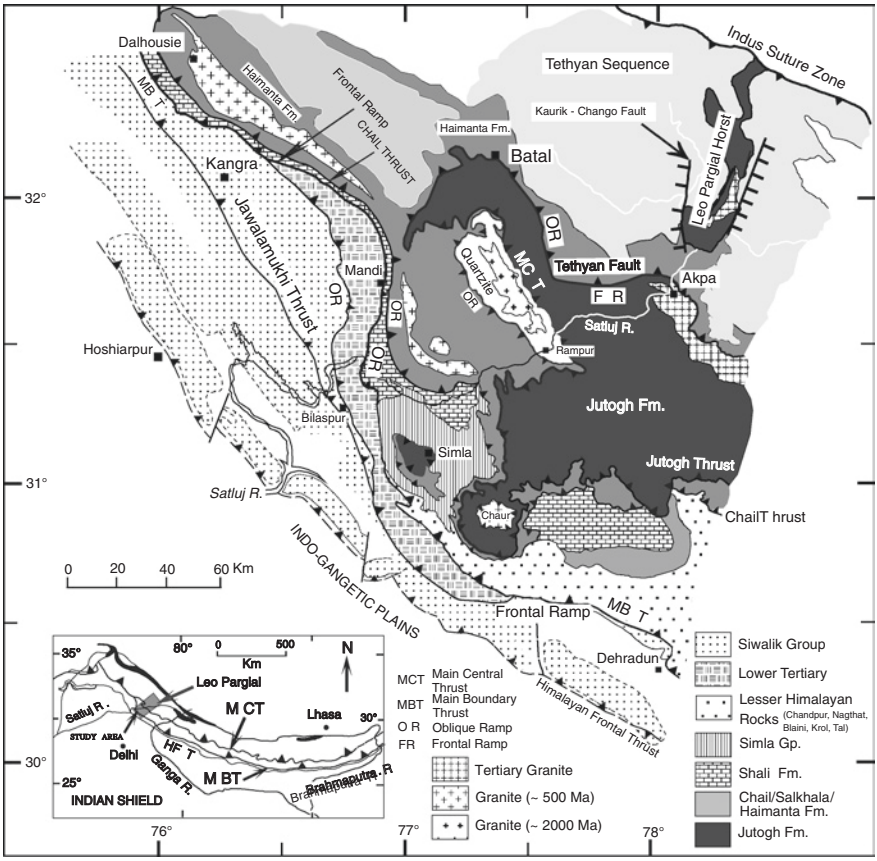

Fig. 13.1 Geological map of a part of the western Himalaya including the Leo Pargial Horst (after Ni and Barazangi 1985; Thakur and Rawat 1992; Dubey and Bhakuni 2004)

(Khattri et al. 1978). In order to explain these faults, Chandra (1978) postulated an extension of the Aravalli Ridge for a distance of ~235 km across the Himalaya into the Leo Pargial region and underthrusting of the Ridge causing local uplift and consequent normal faulting. However the basement ridge is not prominent even below the HFT in the Himalayan Foothill Belt (Raiverman et al. 1995). Based on model deformation studies, Dubey and Bhakuni (2004) have explained these faults in terms of extension in vertical direction by predominant pure-shear followed by horizontal extension (Fig. 11.21). These deformation conditions prevail at higher topographic elevations (e.g. height of the Leo Pargial Horst is ~7,100 m) when effect of the horizontal compression is minimal (see also Hintersberger et al. 2010). Some of the normal and strike-slip faults have formed simultaneously at different structural levels; normal faults at higher elevations and strike-slip faults at lower elevations.

Two schematic models for initiation of extensional faults in the hinterland were proposed by Coward et al. (1987). Figure 13.2a shows subduction of the Indian plate beneath Tibet and increase in thickness of the crust below Tibet. This was

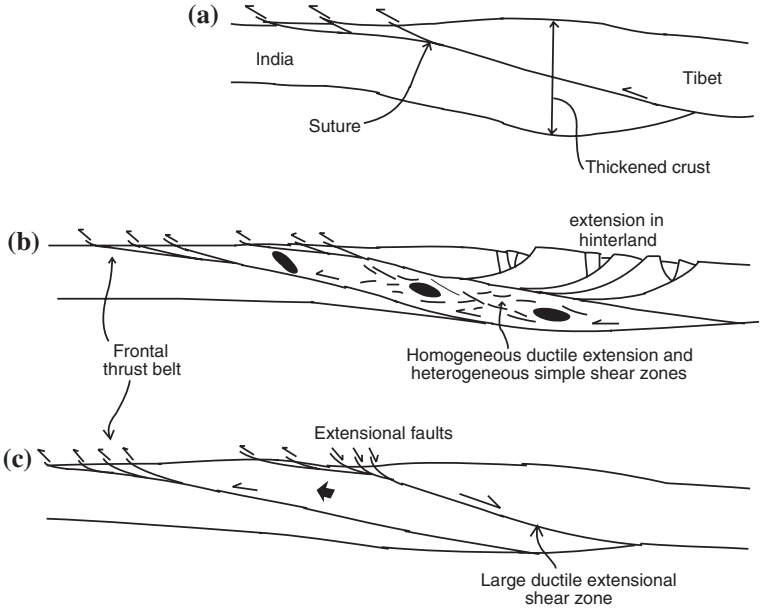

Fig. 13.2 Models for initial thrusting, thickening of the crust and later extensional faults. **a** Subduction of the Indian plate beneath Tibet and thickening of the crust. **b** Spreading of the weak lower crust and formation of brittle extensional faults in the *upper part* of the thrust sheets. **c** Extrusion of the *weak lower* thrust beneath hinterland dipping extensional fault systems [From Coward et al. (1987) © The Geological Society. Published with permission of Geological Society of London]

followed by ductile extension of the weak lower crust and formation of heterogeneous simple shear zones. The extension in the lower crust led to development of brittle listric, extensional faults in the upper crust of the hinterland (Fig. 13.2b). These faults have not been observed in the Tethys or Tibetan Himalaya as the exposed faults are dipping towards north (hinterland). An alternate explanation was development of large ductile extensional shear zone in the lower crust thereby resulting in extensional faults at upper levels of the upper crust (Fig. 13.2c).

The northern boundary of the Tethys Himalaya is marked by the Indus Tsangpo Suture Zone (ITSZ) which is the zone of collision between the Indian and Tibetan plates. The ITSZ is followed by the Trans Himalaya or Karakoram Mountains.

References

Brookfield ME (1993) The Himalayan passive margin from Precambrian to Cretaceous. Sed Geol 84:1–35

Burchfiel BC, Royden LH (1985) N-S extension within the convergent Himalayan region. Geology 13:679–682

Burchfiel BC, Chen Z, Hodges KV, Liu Y, Royden LH, Deng C, Xu J (1992) The South Tibetan Detachment System, Himalayan orogen: extension contemporaneous with and parallel to shortening in a collisional mountain belt. Spec Pap Geol Soc Am 269:1–41

Burg JP, Brunel M, Gapais D, Chen GM, Liu GH (1984) Deformation of leucogranites of the crystalline Main Central Sheet in southern Tibet (China). J Struct Geol 6:535–542
Chandra U (1978) Seismicity, earthquake mechanisms and tectonics along the Himalayan mountain range and vicinity. Phys Earth Planet Inter 16:109–131
Coward MP, Butler RWH, Khan AM, Knipe RJ (1987) The tectonic history of Kohistan and its implications for Himalayan structure. J Geol Soc London 144:377–391
Dezes PJ, Vannay JC, Steck A, Bussy F, Cosca M (1999) Synorogenic extension: quantitative constraints on the age and displacement of the Zanskar shear zone (northwest Himalaya). Bull Geol Soc Am 111:364–374
Dubey AK (1999) Oblique thrust ramps in the Himalaya: a study based on model experiments. Gondwana Research Group Memoir 6, Gondwana Research Group, Japan, pp 39–49
Dubey AK, Bhakuni SS (2004) Development of extension faults on the oblique thrust ramp hanging wall: example from the Tethys Himalaya. J Asian Earth Sci 23:427–434
Edwards MA, Harrison TM (1997) When did the roof collapse? Late Miocene north-south extension in the High Himalaya revealed by Th-Pb monazite dating of the Khula Kangri granite. Geology 25:543–546
Godin L, Parrish RR, Brown RL, Hodges KV (2001) Crustal thickening leading to exhumation of the Himalayan metamorphic core of central Nepal: insight from U–Pb geochronology and Ar-40/Ar-39 thermochronology. Tectonics 20:729–747
Harrison TM, Grove M, Lovera OM, Catlos EJ, D'Andrea J (1999) The origin of Himalayan anatexis and inverted metamorphism: models and constraints. J Asian Earth Sci 17:755–772
Herren E (1987) Zanskar shear zone: Northeast-southwest extension within the Higher Himalaya (Ladakh, India). Geology 15:409–413
Hintersberger E, Thiede RC, Strecker MR, Hacker BR (2010) East-west extension in the NW Indian Himalaya. Geol Soc Am Bull 122:1499–1515. doi:10.1130/B26589.1
Hodges KV (2000) Tectonics of the Himalaya and southern Tibet from two perspectives. Geol Soc Am Bull 112:324–350
Hodges KV, Parrish RR, Housh TB, Lux DR, Burchfiel BC, Royden LH, Chen Z (1992) Simultaneous Miocene extension and shortening in the Himalayan orogeny. Science 258:1466–1470
Hodges KV, Parrish RR, Searle MP (1995) Structural evolution of the Annapurna Sanctuary region, central Nepal. In: Spencer DA, Burg J-P, Spencer-Cervato C (eds) 10th Himalaya-Karakoram-Tibet workshop, Ascona. Mitt Geol Inst Eidg Tech Hochsch Univ Zurich 298:89–90
Hodges KV, Parrish RR, Searle MP (1996) Tectonic evolution of the central Annapurna Range, Nepalese Himalaya. Tectonics 15:1264–1291
Hodges KV, Bowring S, Davidek K, Hawkins D, Krol M (1998) Evidence for rapid displacement on Himalayan normal faults and the importance of tectonic denudation in the evolution of mountain ranges. Geology 26:483–486
Islam R, Upadhyay R, Ahmad T, Thakur VC, Sinha AK (1999) Pan-African magmatism and sedimentation in the NW Himalaya. Gondwana Res 2:263–270
Jayangondaperumal R, Dubey AK, Sen K (2010) Mesoscopic and magnetic fabrics in arcuate igneous bodies: an example from the Mandi-Karsog pluton, Himachal Lesser Himalaya. Geol Mag 147:652–664. doi:10.1017/S0016756810000105
Khattri KN, Rai K, Jain AK, Sinvhal H, Gaur VK, Mithal RS (1978) The Kinnaur earthquake, Himachal Pradesh, India of 19 January 1975. Tectonophysics 49:1–21
Marquer D, Chawla HS, Challandes N (2000) Pre-Alpine high-grade metamorphism in High Himalaya crystalline sequences: evidence from Lower Paleozoic Kinnaur Kailash Granite and surrounding rocks in the Satluj valley (Himachal Pradesh, India). Eclogae Geol Helv 93:207–220
Mazari RK, Bagati TN (1991) Post-collision graben development in the Spiti Valley, Himachal Pradesh. J Himalayan Geol 2:111–117
Ni J, Barazangi M (1985) Active tectonics of the western Tethyan Himalaya above the underthrusting Indian plate: the upper Sutlej river basin as a pull-apart structure. Tectonophysics 112:277–295

Pecher A (1991) The contact between the Higher Himalaya crystallines and the Tibetan sedimentary series: Miocene large-scale dextral shearing. Tectonics 10:587–598

Raiverman V, Srivastava AK, Prasad DN (1995) On the foothill thrust of northwestern Himalaya. Himalayan Geol 16:237–256

Royden LH, Burchfiel BC (1987) Thin-skinned N-S extension within the convergent Himalayan region: gravitational collapse of a Miocene topographic front. Spec Pub Geol Soc London 28:611–619

Sachan HK, Kohn MJ, Saxena A, Corrie SL (2010) The Malari leucogranite, Garhwal Himalaya, northern India: chemistry, age, and tectonic implications. Bull Geol Soc Am 122:1865–1876. doi:10.1130/B30153.1

Searle MP, Noble SR, Hurford AJ, Rex DC (1999) Age of crustal melting, emplacement and exhumation history of the Shivling leucogranite, Garhwal Himalaya. Geol Mag 136:513–525

Srikantia SV, Bhargava ON (1998) Geology of Himachal Pradesh. Geol Surv India, Bangalore, 406 pp

Thakur VC (1992) Geology of Western Himalaya. Pergamon, 363 pp

Thakur VC, Rawat BS (1992) Geological map of the western Himalaya. Scale 1:1,111,111. Wadia Institute of Himalayan Geology, Dehra Dun

Tripathi K, Sen K, Dubey AK (2011) Modification of fabric in pre-Himalayan granitic rocks by post-emplacement ductile deformation: insights from microstructures, AMS and U-Pb geochronology of the Paleozoic Kinnaur Kailash Granite and associated Cenozoic leucogranites of the South Tibetan Detachment zone, Himachal High Himalaya. Int. J. Earth Sci. doi: 10.1007/s00531-011-0657-z

Valdiya KS (1998) Geodynamic Himalaya. Universities Press, Hyderabad, 178 pp

Vannay J-C, Grasemann B, Rahn M, Frank W, Carter A, Baudraz V, Cosca M (2004) Miocene to Holocene exhumation of metamorphic crustal wedges in the NW Himalaya: evidence for tectonic extrusion coupled to fluvial erosion. Tectonics 23, TC 1014:1–24. doi:10.1029/2002TC001429,2004

Yin A (2006) Cenozoic tectonic evolution of the Himalayan orogen as constrained by along-strike variation of structural geometry, exhumation history and foreland sedimentation. Earth Sci Rev 76:1–131. doi:10.1016/j.earscirev.2005.05.004

Chapter 14
The Ladakh Himalaya

Abstract The timing of collision between the Indian and Tibetan plates along with significant evidence is described. The tectono-stratigraphy of the region is described under four major zones, Zanskar, Indus-Suture, Shyok Suture, and Karakoram. The plate tectonics model of subduction of the Indian plate beneath the Tibetan plate is illustrated. Tectonics of the dextral-slip Karakoram strike-slip fault is discussed with special reference to age, temperature of formation, and displacement. Deformation features characteristic of a transpressional zone are described from Tangtse area. Sequential formation of asymmetric folds, minor thrust faults, and subsequent extension resulting in irregular orientations of aplite veins is illustrated. Zanskar shear zone and simultaneous development of normal and strike-slip faults in the Tibetan region are described. The model proposed for simultaneous development of different types of faults in the Himalaya appears to be applicable to the Tibetan region.

The Tethys Himalaya is followed by the Indus Tsangpo Suture Zone (ITSZ) where the collision had taken place between the Indian and Tibetan plates (Fig. 14.1). There is a gradual decrease in metamorphism from the High Himalaya to the Ladakh Himalaya. The High Himalayan crystalline rocks show the upper amphibolites grade whereas in the ITSZ the rocks are characterized by low grade anchimetamorphism. The collision zone is marked by complicated structures of the ophiolite sequence (Molnar and Tapponnier 1975). The zone extends through the length of the Himalaya for a distance of about 2,500 km. The suture and the adjacent tectonic zones, marked by a large number of thrusts, are well exposed in the Ladakh region. The timing of collision between the Indian and Tibetan plates was estimated as ca. 50–40 Ma by Searle et al. (1987). Closing of the Tethys was shown by (i) change from marine (flysch-like) to continental (molasse-like) sedimentation in the ITSZ (ii) end of Gangdese I-type granitoid injection (iii) Eocene S-type anatectic granites and migmatites in the Lhasa block, and (iv) initiation of compressional tectonics (south facing asymmetric folds, and south-directed thrusts). The deformation then gradually shifted towards south across the Tethys Himalaya to the High Himalaya.

A. K. Dubey, *Understanding an Orogenic Belt*, Springer Geology,
DOI: 10.1007/978-3-319-05588-6_14,

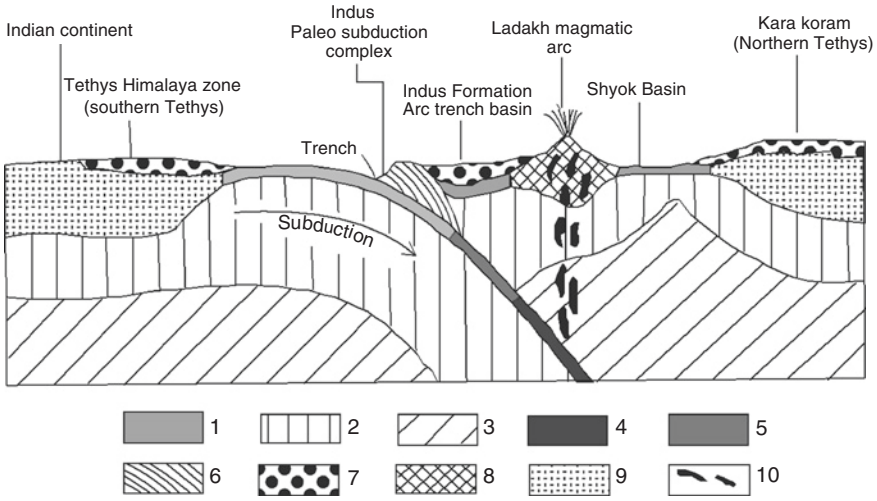

Fig. 14.1 A schematic cross-section across the ITSZ in Ladakh region during the late Cretaceous—early Tertiary times. *1* Basaltic oceanic crust; *2* Bottom of the lithosphere; *3* Asthenosphere; *4* Eclogite layer; *5* Transitional zone of eclogite to basalt; *6* Deformed crust; *7* Marine sediments; *8* Crust of the arc; *9* Continental crust; *10* Magma [From Thakur (1983), © V.C. Thakur. Published with permission of V.C. Thakur]

A second suture called as Shyok suture lies further north of the Indus suture. The two suture zones are divided by Ladakh Batholith. A characteristic feature of the region is double crustal thickness below the Tibetan plateau. The feature is attributed to subduction of the Indian plate below the Tibetan block. The geology and tectonics of the region have been described by Sharma and Kumar (1978), Srikantia et al. (1978), Srikantia and Razdan (1980), Thakur (1981), Thakur and Sharma (1983), Thakur and Misra (1984), and Upadhyay (2002).

14.1 Tectonostratigraphy

The tectono-stratigraphic framework of the region is followed after Thakur (1981) (Table 14.1). The area, from south to north is divided into four major zones; (i) Zanskar (ii) Indus suture (iii) Shyok suture, and (iv) Karakoram. A geological map of the region is shown in Fig. 14.2 and the cross-sections are shown in Fig. 14.3. A brief description of the different zones is as follows.

14.1.1 Zanskar Zone

The zone consists of three major stratigraphic units, i.e. Zanskar Crystalline Complex, Zanskar Supergroup, and Tso Morari Crystalline Complex. The area

Table 14.1 Tectonostratigraphy of the Ladakh Himalaya (after Thakur 1981)

Tectonic zone	Stratigraphic unit	Age
Karakoram zone	Karakoram Group	Permian to Cretaceous
	Intrusive junction	
	Karakoram plutonic complex	Eocene-Miocene
	Intrusive junction	
Shyok Suture zone	Pangong Group	Precambrian to lower palaeozoic ?
	Thrust	
	Gondwana Group	Upper jurassic
	Thrust	
	Shyok Group	Cretaceous-Eocene with permian blocks
	Shyok thrust	
	Khardung Formation	Cretaceous
	Intrusive junction	
	Ladakh plutonic complex	Eocene-Miocene
	Transgressive boundary	
Indus Tsangpo Suture Zone	Kargil Formation	Neogene
	Thrust	
	Indus Formation	Cretaceous-Eocene
	Thrust	
	Nidar complex	Cretaceous
	Thrust	
	Shergol mélange	Cretaceous
	Thrust	
	Dras Formation	Cretaceous
	Thrust	
	Lamayuru division	Triassic, Jurassic ?
	Zanskar thrust	
Zanskar zone	Tso Morari Crystalline complex	Middle–upper Palaeozoic
	Thrust	
	Zanskar Supergroup	Upper Proterozoic–Cretaceous-Eocene
	Zanskar crystalline complex	Precambrian

is deformed into large-scale noncylindrical folds of early generation. The Zanskar Crystalline Complex and the Tso Morari Crystalline Complex occur in antiformal cores whereas the Zanskar Supergroup is exposed in the intervening synformal core.

14.1.1.1 Zanskar Crystalline Complex

This is the oldest sequence (1830 my by Rb-Sr whole-rock) forming basement for the Upper Proterozoic to Cretaceous-Eocene Zanskar Supergroup. The complex consists of metasedimenary, gneisses and migmatite rocks metamorphosed from greenschist to granulite facies, along with deformed granites (500–600 my; Bhanot et al.

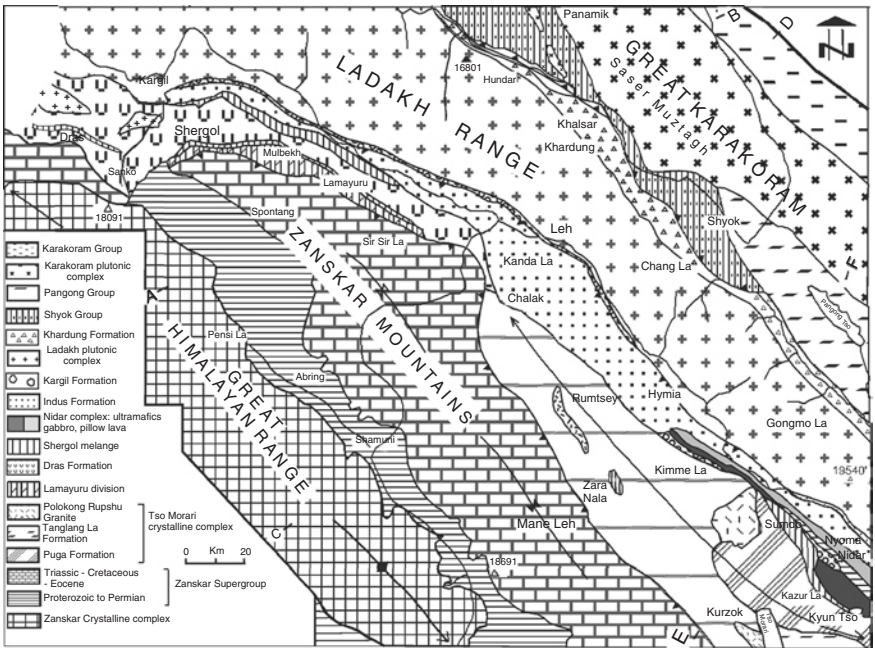

Fig. 14.2 A geological map of the Ladakh region [From Thakur (1981), © Royal Society of Edinburgh. Published with permission of Royal Society of Edinburgh]

1976; Mehta 1977). On the basis of lithological similarities, the complex is correlated with Central Crystalline rocks of the western Himalaya, south of the Tethyan zone.

14.1.1.2 Zanskar Supergroup

The Supergroup consists of fossiliferous sequence (~9,000 m thick) of Upper Proterozoic and Palaeozoic argillites along with Permian volcanic rocks and carbonates of Mesozoic to Eocene age. The sequence is correlated with the Tethys sediments of the Spiti valley and Kashmir basin. The palaeo-current analysis of the Spiti and Zanskar regions support a common provenance in the southern direction (Thakur 1981).

14.1.1.3 Spongtang Klippe

The Spongtang klippe in Zanskar area is composed of ultramafic and gabbroic rocks and dikes overlying a tectonic melange, embodying volcanic rocks, limestone and chert. The Spongtang ophiolite has been dated by hornblende at 130–140 Ma (Reuber et al. 1990).

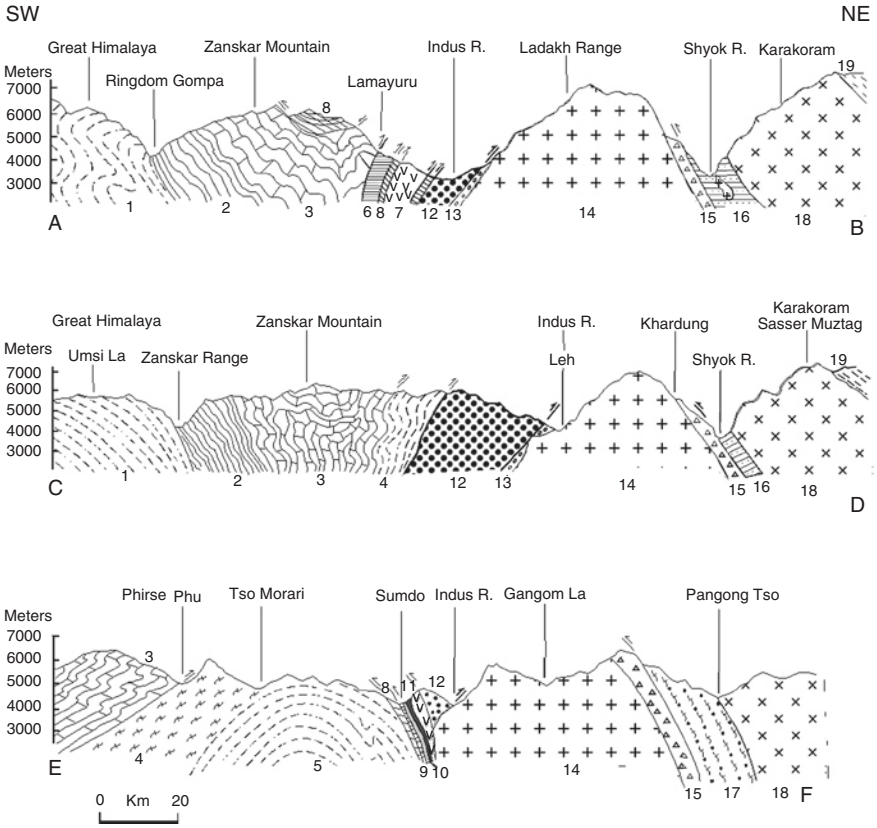

Fig. 14.3 Geological cross sections of the Ladakh region. Locations of the sections are shown in Fig. 14.2 [From Thakur (1981), © Royal Society of Edinburgh. Published with permission of Royal Society of Edinburgh]

14.1.2 Tso Morari Crystalline Complex

The Tso-Morari Crystalline complex occurs as a dome between the Indus Tsangpo Suture Zone to the north and Zanskar sedimentary unit (low-grade metasedimentary rocks) to the south. Rocks in the core are metamorphosed up to sillimanite grade gradually decreasing to chlorite grade towards the outer arc.

The complex is further divided into two groups. The lower Puga Group consists of gneisses with amphibolite bands and lenses whereas the upper Tanglang La Group is made up of phyllite, schist, marble and amphibolites. The Polokong and Rupshu granites intrude into the two groups. Based on the age (presence of Lower Permian conodonts), lithostratigraphy, structural setting, and magmatic history it has been suggested that the complex is different from the Central Crystalline rocks. Moreover, the presence of coesite inclusions in eclogites, in the fold core, suggests

ultra-high pressure metamorphism (28 kbars at 700–800°C, a depth of >120 km) event in the ITSZ (Mukherjee and Sachan 2001, 2009). Unaltered nature of the rock suggests a very rapid exhumation to the surface although the rapid exhumation remains an unsolved puzzle. The finding also suggests that the Indian plate in the Ladakh Himalaya subducted at a steeper angle as compared to the western Himalaya of Pakistan.

14.1.3 Indus Tsangpo Suture Zone

The ITSZ is separated from the Zanskar Supergroup by a prominent Zanskar thrust to the south and Shyok thrust to the north. The zone is represented by obducted material of the oceanic crust together with deep marine Triassic to Eocene sediments. Hence the complex includes turbidites, ophiolitic melanges with seamounts and calc-alkaline volcanic rocks.

The rocks of the zone have been subdivided into a number of lithostratigraphic units as described below. The older units are separated by thrusts (Table 14.1).

14.1.3.1 Lamayuru Division

The Lamayuru division or complex comprises of fossiliferous shales, siltstones and graded sandstones that preserve sedimentary structures. These rocks were deposited on the leading passive edge of the Indian subcontinent (Upadhyay 2002). The sequence varies in thickness from 1,000 to 1,500 m. Large blocks and lenticular bodies of limestone (up to a few kilometers by hundreds of meters) occur as exotic blocks in the rocks. Shelf, fore-reef and basin margin (slope) olistoliths (exotic blocks of limestone) of Permian-Jurassic age are tectonically juxtaposed within the complex.

14.1.3.2 Dras Formation

The formation consists of volcanic rocks (mainly andesite and basalt) and associated sedimentary rocks. Pillow lava, rhyolite, agglomerate and volcanoclastic products occur along with radiolarian chert and jasper. The sedimentary rocks consist of shales and sandstones with occurrence of chert, jasper and limestone, which has yielded fossils of the Upper Cretaceous age. The volcanic rocks have petrochemical characters of island—arc environment (Gergan 1978).

14.1.3.3 Shergol Melange

The melange occurs as narrow belts, two in western Ladakh and one in eastern Ladakh. The belts consist of serpentinite, peridotite and dunite with jasperoid

shales, cherts, pillow lavas and basic rocks. Mica schist occurs as blocks with lenses of oliostromal limestone. The assemblage is described as ophiolitic melange. Virdi et al. (1977) have reported blueschist facies metamorphism suggesting high-pressure metamorphism related to subduction of the Indian plate. Klippen of the melange occur at Spongtang, Zaranala, and Kurzok overlying the rocks of the Zanskar Supergroup and the Tso Morari Crystalline Complex.

14.1.3.4 Nidar Complex

This is a part of the ophiolite sequence consisting of three main units, viz. ultramafic rocks (pyroxinite with peridotite and dunite), gabbros (intrusive within the ultramafic rocks) and pillow lavas (basic to intermediate volcanic assemblage with pillow structure with interbedded layers of lava, chert, jasper, grit, and sandstone), occurring in eastern Ladakh. The Nidar complex occurs as hanging wall rocks over the Shergol melange along a steep thrust, which may be a surface manifestation of a listric thrust.

14.1.3.5 Indus Formation

The Indus Formation has a steep thrusted contact with the other older formations. The 4,000–5,000 m thick sequence consists of conglomerate, sandstone, siltstone and shale. Dolerite sills, ~1 m thick and bands of limestone up to 30 m thick occur in Upshi-Rumtsey section. Pebbles present in the conglomerate consist of volcanic rocks (basalt, andesite, rhyolite), vein quartz, carbonates, sandstone, shale, granite, and gneiss. Turbidites of the Indus Formation were interpreted as fore-arc sediments. The northern boundary of the formation is transgressive on the Ladakh batholith. Elsewhere it has a thrusted contact on both sides.

14.1.3.6 Kargil Formation

The formation consists of clastic sediments (~1,000 m thick), mainly conglomerate and sandstone with occasional shale bands, rests directly and transgressively over the Ladakh Plutonic Complex. Pebbles in the conglomerate consist of granite, vein quartz, radiolarites, carbonates, volcanic rocks and gneiss. These pebbles are somewhat similar to the Indus Formation. Fresh water molluscs and plant remains indicate Upper Oligocene to Lower Pliocene age.

14.1.4 Ladakh Plutonic Complex

The Ladakh batholith forms the southern margin of the Tibetan plate. This is a NW-SE trending batholithic body striking parallel to the Indus Suture Zone. It essentially consists of intrusions of tonalite, granodiorite and granite with

muscovite, muscovite-biotite, and hornblende bearing types. The rock contains bodies of an igneous mafic complex consisting of gabbro, gabbro-norite, gabbroic anorthosite to diorite. Petrochemical studies suggest calc-alkaline affinities of the plutonic suite with multiphase intrusive history. Crosscutting relationships with the surrounding rocks indicate post-Cretaceous, pre-Miocene age of the emplacement. The K/Ar, Rb-Sr and other radiometric age data suggest that the batholith has evolved through multiple phases of magmatic activity. U-Pb ages of 101 ± 2 Ma and 60.8 ± 4 Ma were obtained from a granodiorite and diorite respectively (Sharma 1990). At Chumathang (NE Ladakh), U-Pb ID-TIMS zircon age from the subduction related hornblende bearing granodiorite reveals 57.7 ± 0.2 Ma. In view of the youngest marine sedimentary rocks in the suture zone (Nummulitic Limestone; 50.5 Ma), Early Eocene was proposed as the time for collision of the two continents (St-onge et al. 2010). The age is further supported by the fact that Ar–Ar analysis of the batholith indicates that these rocks have not experienced temperatures above 150°C since 36 Ma (Weinberg and Searle 1998).

14.1.4.1 Khardung Formation

The Khardung Formation comprises predominantly of rhyolite, trachyte, karatophyre, dacite, andesite, tuff and agglomerate with subsidiary basalt. Interbedded chert, limestone and shale occur in upper part of the formation. The limestone and shale have yielded *Orbitolina parma* indicating Early–Middle Cretaceous age.

14.1.5 Shyok Suture Zone

The Shyok Suture Zone lies north of the Indus Suture Zone and is older than the Indus Suture as it was closed between 100–75 Ma ago. This is an oceanic suture or relict of a back-arc basin. The sedimentary, volcanic and plutonic rocks of the Shyok Suture Zone are intensely deformed and occur as tectonic slices between the Ladakh and Karakoram batholiths.

14.1.5.1 Gondwana Group

The Group is named because plant fossils of Jurassic age with Gondwana affinities have been reported from the horizon. The sequence consists of orthoquartzite, calcareous sandstone, breccia and carbonaceous shale.

14.1.5.2 Shyok Group

The Group overlies the Khardung Formation along the Shyok thrust. The lower sequence consists of chlorite, schist, quartzite, limestone, basalt, and andesite

intruded by diorite and hornblendite. The upper sequence comprises of platy limestone, amphibolites, mica schist, serpentinite lenses, sandstone, shale, conglomerate, pyroxenite, peridotite, gabbro, basalt and andesite. All the units occur as tectonic melange. Limestone in both the units has yielded crinoids ossicles and fusilinids of Permian age. The lithological units of the Shyok Group occur as thrust slices and tectonic lenses forming a tectonic melange with the ophiolite components.

14.1.5.3 Pangong Group

The Group varies in thickness from 2 to 10 m and lies between the Karakoram Plutonic complex in the north and the Shyok Group and Khardung Formation in the south. Rocks of the Group have suffered low to medium grade dynamothermal metamorphism. The low grade rocks consists of calcareous phyllite, mica schist, foliated metavolcanic rocks and chlorite schist with bands of limestone and quartzite. The medium grade rocks consist of garnet, kyanite and hornblende bearing schists, biotite gneiss, calc-silicate rocks, marbles and migmatites with aplite and pegmatite veins.

It is evident from the above description that the ITSZ and the Shyok suture have significantly different tectonostratigraphy. The ITSZ represents the rock assemblages that are typical of a subduction zone whereas the Shyok suture represents a back-arc basin.

14.1.6 Karakoram Zone

The Karakoram zone lies above the Pangong Group with an intrusive contact. Two units have been recognized in this zone.

14.1.6.1 Karakoram Plutonic Complex

The Karakoram plutonic complex or Karakoram batholith lies immediately north of the Shyok Ophiolitic Melange in the Nubra-Shyok valleys. At several places, the boundary is marked by a NW-SE trending strike-slip fault zone called as Karakoram fault. The complex consists of biotite, muscovite-biotite, and hornblende bearing granites enclosing large xenoliths of metasedimentary and mafic rocks. Aplitic veins, pegmatite dikes, fine-grained quartzo-feldspathic veins and dikes of intermediate composition are common. The geochemical data indicate that the Karakoram batholith contains both volcanic-arc granites and syn-collision granites. The collision between the Kohistan-Ladakh arc and the Karakoram block took place at 83 ± 9 Ma (Upadhyay 2002). Near Pangong Tso (Tangtse), the batholith is composed of older granodiorite-tonalite phases (120–85 Ma) (Weinberg and Searle 1998). The leucogranite has similar modal and chemical composition to the Baltoro granite (Pakistan) and crystallized at 17 Ma (U-Pb zircon age; Searle et al. 1998).

In vicinity of the suture zone, the granites are gneissic. This has an intrusive contact with the underlying and the overlying sequences. The plutonic activity occurred in two main phases. The first one was initiated at the start of the orogenic phase (Late Cretaceous—Eocene) and the second one took place during the Neogene times (Desio 1979).

The Karakoram and Ladakh plutonic complexes are petrographically similar. The intervening Shyok suture zone pinches out and the two complexes join to form one (outside the region shown in Fig. 14.2).

14.1.6.2 Karakoram Group

Rocks of the Group range in age from the Early Permian to Early Cretaceous. The Permian sequence consists of limestone, shale and sandstone. These are conformably overlain by the Triassic sequence consisting of thinly bedded cherty limestone, dolomitic limestone and dolomite with interstratified shale and conglomerate. The Jurassic rocks consist of shale, marly limestone and shallow water deposits. The lower Cretaceous rocks consist of limestone and shale.

14.2 Tectonics of the Region

The concept of two sutures in the region has come from the early works of Stocklin (1977), and Sengor et al. (1980) who observed Neo-Tethys and Palaeo-Tethys sutures in Turkey, Iran, Afghanistan, and central Asia. Later Thakur (1981) proposed a model for tectonic evolution of the Ladakh-Karakoram region. The model envisages that the Karakoram block was a part of India (Gondwanaland) till Permian and later it was separated by a rift. The resulted opening led to formation of the Neo-Tethys during the Triassic time. The fragmentation of the continental crust was followed by generation of oceanic crust in Jurassic-Cretaceous times. Onset of the Himalayan orogeny during the late Cretaceous led to closing of the Neo-Tethys and subduction of the Oceanic Indian plate beneath the Tibet-Karakoram block. The ophiolite melange, dismembered ophiolites and the trench sediments represent the subduction complex. Melting of the subducted oceanic crust resulted in generation of the Ladakh-Gandise magmatic belt. Between the evolving magmatic arc to the north and subduction complex to the south, a basin was formed in the arc-trench gap region. The Indus Formation of Ladakh and the Xigase Formation of southern Tibet were deposited in this gap (Thakur 1983). Collision of the Indian continent with the Ladakh-Gandise magmatic arc occurred in Middle Eocene. The molasse sedimentary rocks and Kargil Formation of Ladakh were deposited in Miocene-Pliocene times after convergence of the Indian continental crust with the Karakoram-Tibet block and closure of the Shyok basin.

In contrast to the Indian part of the Himalaya, the ITSZ in the Pakistan Himalaya was initiated as a thrust fault, which reactivated as a normal fault. The thrusting is related to collision between the Kohistan Complex and passive margin of the Indian

plate (beginning at c. 55 Ma) and the later reactivation is attributed to backsliding of the Kohistan arc. The earliest backsliding initiated at 47 Ma. A second phase of normal faulting started at c. 5 Ma (early Pliocene times) when the syntaxes were formed. The normal faulting is still active in parts of the region (Zeilinger et al. 2007).

14.3 Karakoram Fault

This is an active fault, which strikes NW-SE and is traceable from the Shyok suture to the Pamir in the NW direction for a distance of ~800 km. Alignment of 70 km long Siachen glacier and the Nubra-Shyok valley is controlled by the Karakoram fault. The Karakoram fault exhibits a dextral strike-slip displacement and is responsible for east-west extension of southern Tibet and westward motion of the northwest Himalaya towards Nanga Parbat (Banerjee and Burgmann 2002). A detailed mapping of the fault has revealed both transtensional and transpressional segments along the fault (Searle et al. 1998) with a large number of splays. Apparent offset of the Indus River for a distance of ~120 km suggests a dextral motion at a long-term rate of $\geq 8.5 \pm 1.5$ mm yr^{-1} (Valli et al. 2007). Study of minerals has recorded a deformation temperatures at 600–400°C. The $^{40}Ar/^{39}Ar$ ages reveal the oldest age of initiation of the fault as 21.2 ± 1.0 Ma and the U-Th/Pb ages constrain the onset of deformation at ≥25–22 Ma. Biotite from the Karakoram fault zone provides an age of 12 Ma suggesting initiation of the fault at this time (Wang et al. 2009). Thermochronological results show slow cooling for the period ~21–14 Ma, followed by rapid cooling between ~14 and 4 Ma (Valli et al. 2007). In another study, based on relationship between magmatism and strike-slip faulting, Phillips and Searle (2007) have shown that the magmatism (~15 Ma leucogranites, U-Pb age) preceded shearing because the rocks are crosscut by central segment of the fault. The offset does not exceed 150 km. In view of these data, a long-term slip-rate for the Karakoram fault was suggested as 3–10 mm/yr. It was also suggested that the Karakoram fault has not played a dominant role in accommodating the lateral extrusion of Tibet because the lateral extrusion model is based on lithospheric-scale faults and the Karakoram fault is only crustal in scale. However, various aspects regarding the age, total displacement, slip rate etc. are still controversial (review in McCarthy and Weinberg 2010). The total displacement on the fault has been variously estimated from 40 to ~300 km. The central part of the Karakorum fault shows displacement of ~120 km (Searle 1996; Searle et al. 1998) whereas the southern end of the fault reveals displacement of ~65 km (Murphy et al. 2000, 2002). Hence the displacement is maximum in the central part gradually decreasing towards the termination. The age of initiation is assigned from 34 Ma to 13.9 ± 0.1 Ma.

The Karakoram fault is very well exposed along the Tangtse gorge (Fig. 14.4). Slickenside is well developed and the horizontal slicken lines confirm strike-slip displacement along the fault (Fig. 14.5). In contrast to other parts of the batholith (Fig. 14.6), the granite is deformed in vicinity of the fault. Very well developed mylonite is exposed trending N45W and dipping 80° towards southeast (Fig. 14.7).

Fig. 14.4 The Karakoram fault along the road (Tangtse, Ladakh)

Fig. 14.5 *Horizontal* quartz fibers on the Karakoram fault surface (Tangtse, Ladakh)

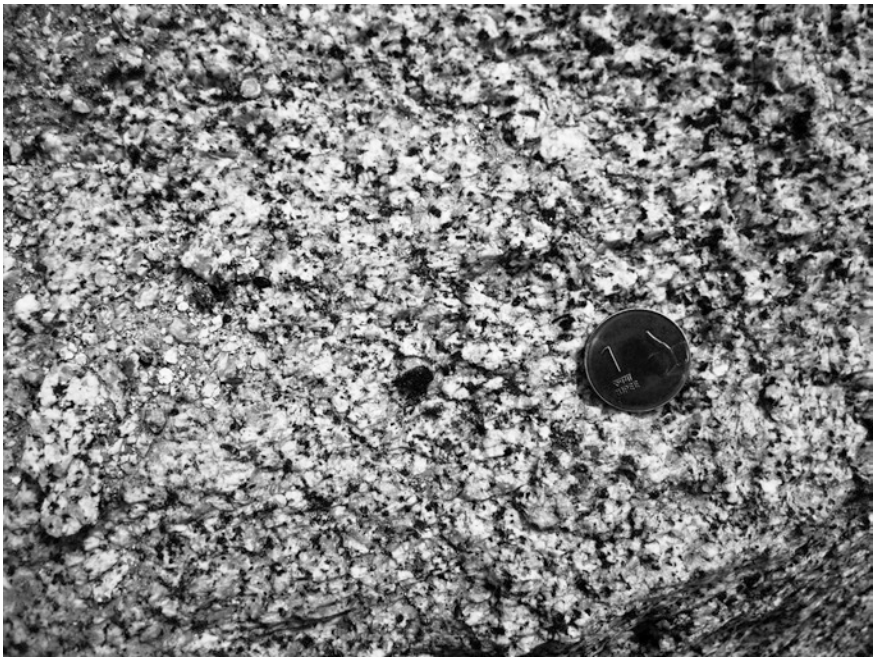

Fig. 14.6 Undeformed granite at some distance from the fault

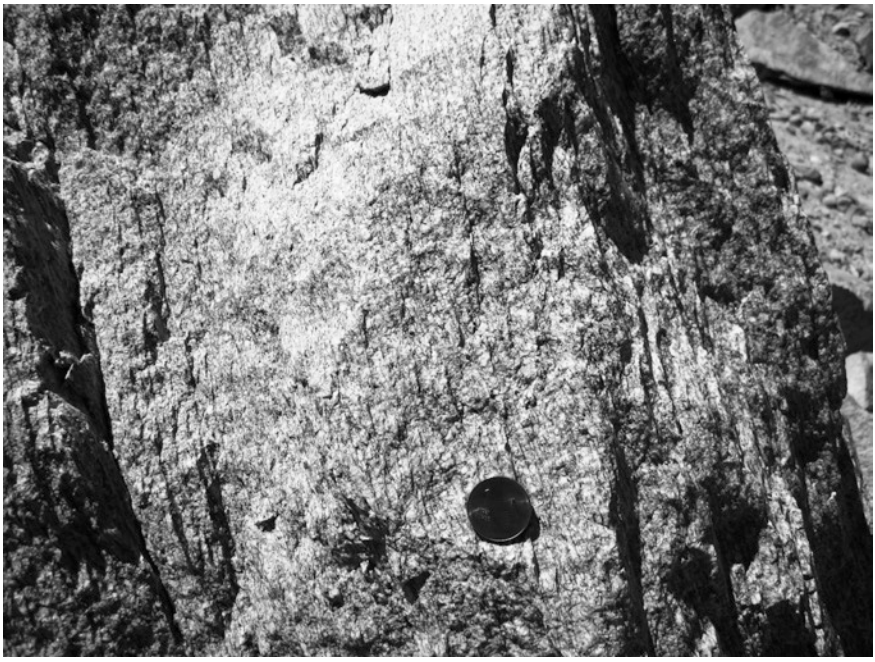

Fig. 14.7 Mylonite along the Karakoram fault (near Tangtse, Ladakh)

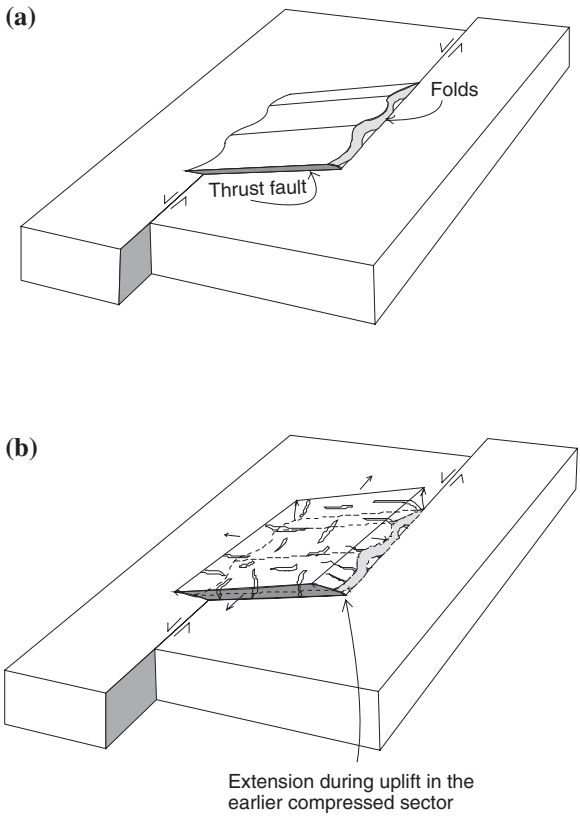

Fig. 14.8 **a** Uplift region developed in a *left-hand* shear, *right-hand* en-echelon or transpression zone [From Ramsay and Huber (1987), © Elsevier. Published with permission of Elsevier] **b** Formation of extensional veins as a result of extension during uplift in the earlier compressed sector of the transpression zone

The area between Tangtse and Vimgul lies in the Pangong Transpressional Zone (Searle and Phillips 2007) of the Karakoram fault and presents a characteristic deformation feature that can be observed in a transpressional zone. The zone is characterized by compressional strain (Fig. 14.8a), which has resulted in formation of asymmetric folds and minor thrust faults. Progressive deformation resulted in extension of the initially compressed rocks during subsequent uplift in the transpressional zone (Fig. 14.8b).

The dilational phase was simultaneous with intrusion of irregular leucocratic granitic dykes. The dykes trend in different directions and can be seen cutting the fold axial surfaces (Fig. 14.9). Some of these dykes are vertical whereas the others are inclined and horizontal. The age of these dykes is ascribed as circa 18 Ma (Ahmad et al. 2008). The dilational feature also led to formation of normal faults and book-shelf gliding (Fig. 5.8). Additional evidence for dilation can be seen in the development of extensional orthogonal joints in the host rock (Fig. 14.10).

Fig. 14.9 Irregular orientation of aplite veins inside the Karakoram fault developed as a result of extension during uplift in the earlier compressed sector of a transpressional zone (Tangtse, Ladakh)

Fig. 14.10 Extensional orthogonal joints in granite (Ladakh batholith) developed as a result of extension during uplift (on way to Pangong Tso from Tangtse, Ladakh)

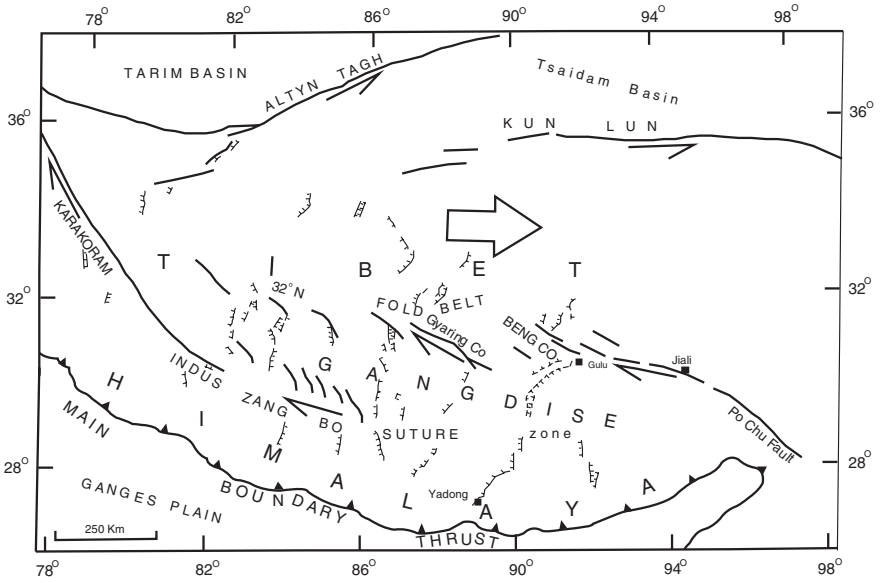

Fig. 14.11 Larger strike-slip faults (*thick lines*) and comparatively smaller normal faults (*thin lines* with hatures) in the Tibetan Himalaya. The two types of faults are developing simultaneously. Normal faults are *shallower* structures whereas the strike-slip faults are *deeper* structures. *Right-lateral* strike-slip faults suggest eastward extrusion of Tibet [From Tapponnier et al. (1986), © The Geological Society. Published with permission of Geological Society of London]

14.4 Zanskar Shear Zone

Another important structural feature in the region is the Zanskar shear zone in the Zanskar area. The shear zone is 2.25–6.75 km wide and extends for at least 80 km in NW-SE direction. A minimum ductile slip of 35 km was estimated during 22–19 Ma (Herren 1987; Dezes et al. 1999). In contrast to the regional structures, this is an extensional structure in which the extension is parallel to the main compression direction in the Himalaya. The minimum horizontal extension is ~16 km and the vertical displacement is of the order of 19 km. The shear zone separates the Late Precambrian—Early Cambrian sedimentary sequence (Phe Formation) from the underlying Zanskar crystalline unit. The shear zone displaces the older granitic rocks, various metasedimentary rocks, and leucogranites of Miocene age indicating its formation after the Miocene. The metamorphism also suggests its movement at a late stage under the greenschist or lower metamorphic condition. The late stage displacement along the Zanskar shear zone post-dated leucogranite crystallization (21.5–19.5 Ma; U-Pb monazite ages) and emplacement in the footwall (Searle et al. 1999). Apatite fission track ages obtained from footwall of the Zanskar shear zone indicate ceased movement by 11–9 Ma (Kumar et al. 1995).

14.5 Simultaneous Development of Normal and Strike-Slip Faults

Further north in Tibet, the region is marked by simultaneous development of normal faults and eastward extrusion along strike-slip faults. The normal faults are smaller in their dimensions as compared to the strike-slip faults (Fig. 14.11) (Tapponnier et al. 1986).

The right-lateral strike-slip faults are attributed to have formed as a result of northward migration and indentation of the rigid Indian plate into Tibet (Tapponnier et al. 1982, 1986). These faults occur as far north as Kunlun mountains and are essentially responsible for eastward extrusion of Tibet. However, the normal faults are more prevalent in southern Tibet. These normal faults trend nearly N–S and also show extension in E–W direction perpendicular to strike of the faults. Some of these faults are hundreds of km long, about 200 km apart and the vertical offsets on major normal faults are 2–4 km. Some of these normal faults form rift valleys with a width of 10–20 km. All of these normal faults reveal shallow depth of earthquake epicentres. The strike-slip faults have initiated with the outset of the collision and have continued throughout the Tertiary period. However, the normal faults have initiated about 14–8 my ago in southern Tibet, and about 13.5–4 my in central Tibet (Blisniuk et al. 2001). Since the normal faults occur at higher elevations they are attributed to have formed as a result of variation in gravitational potential energy of the lithosphere.

References

Ahmad T, White L, Forster M, Ireland TR, Lister G (2008) New SHRIMP ages for Ladakh and Karakoram batholiths—inherited zircons indicate involvement of older crust (abstract). Himalayan J Sci 5:19

Banerjee P, Burgmann R (2002) Convergence across the northwest Himalaya from GPS measurements. Geophys Res Lett 29:13. doi:10.1029/2002GL015184

Bhanot VB, Singh VP, Kansal AK, Thakur VV (1976) Early Proterozoic Rb-Sr whole-rock age for Central Crystalline Gneiss of Higher Himalaya. J Geol Soc India 18:90–91

Blisniuk PM, Hacker BR, Glodny J, Ratschbacher L, Bi S, Wu Z, McWilliams MO, Calvert A (2001) Normal faulting in central Tibet since at least 13.5 my ago. Nature 412:628–632

Desio A (1979) Geological evolution of Karakoram. In: Farah A, de Jong KA (eds) Geodynamics of Pakistan. Geological Survey of Pakistan, Quetta, pp 11–124

Dezes PJ, Vannay JC, Steck A, Bussy F, Cosca M (1999) Synorogenic extension: quantitative constraints on the age and displacement of the Zanskar shear zone (north–west Himalaya). Bull Geol Soc Am 111:364–374

Gergan JT (1978) Stratigraphy and tectonic studies on the Indus suture belt between Dras and Kargil. Ph. D. thesis (unpublished), Jammu University

Herren E (1987) Zanskar shear zone: northeast–southwest extension within the Higher Himalaya (Ladakh, India). Geology 15:409–413

Kumar A, Lal N, Jain AK, Sorkhabi RB (1995) Late Cenozoic-Quaternary thermo-tectonic history of Higher Himalayan Crystalline (HHC in Kishtwar-Padar-Zanskar region, NW Himalaya: evidence from fission ages. J Geol Soc India 45:375–391

McCarthy MR, Weinberg RF (2010) Structural complexity resulting from pervasive ductile deformation in the Karakoram Shear Zone, Ladakh, NW India. Tectonics 29, TC3004. doi:10.1029/2008TC002354

Mehta PK (1977) Geochronology of the Kulu-Manali belt: its implications for the Himalayan tectonogenesis. Geol Rundsch 6:156–188

Molnar P, Tapponnier P (1975) Cenozoic tectonics of Asia: effects of a continental collision. Science 189:419–426

Mukherjee BK, Sachan HK (2001) Discovery of coesite from Indian Himalaya: a record of ultra-high pressure metamorphism in Indian continental crust. Curr Sci 81:1358–1361

Mukherjee BK, Sachan HK (2009) Fluids in the coesite-bearing rocks of the Tso Morari Complex, NW Himalaya: evidence for entrapment during peak metamorphism and subsequent uplift. Geol Mag 146:876–889. doi:10.1017/S0016756809990069

Murphy MA, Yin A, Kapp P, Harrison TM, Lin D, Jinghui G (2000) Southward propagation of the Karakorum fault system, southwest Tibet: timing and magnitude of slip. Geology 28:451–454

Murphy MA, Yin A, Kapp P (2002) Structural evolution of the Gurla Mandhata detachment system, southwest Tibet: implications for the eastward extent of the Karakorum fault system. Bull Geol Soc Am 114:428–447

Phillips RJ, Searle MP (2007) Macrostructural and microstructural architecture of the Karakoram fault: relationship between magmatism and strike-slip faulting. Tectonics 26, TC 3017. doi:10.1029/2006TC001946

Ramsay JG, Huber MI (1987) The techniques of modern structural geology, vol 2. Folds and fractures. Academic Press, London, pp 309–700

Reuber I, Montigny R, Thuizat R, Heitz A (1990) K/Ar ages of ophiolites and arc volcanic of the Indus Suture Zone (Ladakh): comparison with other Himalaya-Karakorun data. J Himalayan Geol 1:115–125

Searle MP (1996) Geological evidence against large-scale pre-Holocene offsets along the Karakorum fault: implications for the limited extrusion of the Tibetan Plateau. Tectonics 15:171–186

Searle MP, Windley BF, Coward MP, Cooper DJW, Rex AJ, Rex D, Tingdong L, Xuchang X, Jan MQ, Thakur VC, Kumar S (1987) The closing of Tethys and the tectonics of the Himalaya. Bull Geol Soc Am 98:678–701

Searle MP, Waters DJ, Dranfield MW, Stephenson BJ, Walker CB, Walker JD, Rex DC (1999). Thermal and mechanical models for the structural and metamorphic evolution of the Zanskar High Himalaya. In: Mac Niocaill C, Ryan PD (eds) Continental tectonics. Special Publication Geological Society of London 164, pp 139–156

Searle MP, Phillips RJ (2007) Relationships between right-lateral shear along the Karakoram fault and metamorphism, magmatism, exhumation and uplift: evidence from the K2–Gasherbrum–Pangong ranges, north Pakistan and Ladakh. J Geol Soc London 164:439–450

Searle MP, Weinberg RF, Dunlap WJ (1998) Transpressional tectonics along the Karakorum fault zone, northern Ladakh: constraints on Tibetan extrusion. In: Holdsworth RE, Strachan RA, Dewey JF (eds) Continental transpressional and transtensional tectonics. Special Publication Geological Society of London 135, pp 307–326

Sengor AMC, Vilmaz Y, Kati I (1980) Ramanent of a pre-late Jurassic ocean in northern Turkey: fragments of Permian-Traissic Palaeotethys? Bull Geol Soc Am 191:599–609

Sharma KK (1990) Petrology, geochemistry and geochronology of the Ladakh batholiths and its role in the evolution of Ladakh magmatic arc. In: Sharma KK (ed), Geology and geodynamic evolution of the Himalayan collision zone. Physics and Chemistry of the Earth 17, pp 173–194

Sharma KK, Kumar S (1978) Contributions to the geology of Ladakh. Himalayan Geol 8:252–287

Srikantia SV, Ganesan TM, Rao PM, Sinha PK, Tirkey B (1978) Geology of Zanskar area, Ladakh Himalaya. Himalayan Geol 8:1009–1033

Srikantia SV, Razdan ML (1980) Geology of part of central Ladakh Himalaya with particular reference to Indus tectonic zone. J Geol Soc India 21:523–545

Stocklin J (1977) Structural correlation of the Alpine ranges between Iran and central Asia. Mem Ser Soc Geol Fr 8:33–353

St-Onge MR, Rayner N, Searle MP (2010) Zircon age determinations for the Ladakh batholith at Chumathang (Northwest India): implications for the age of the India–Asia collision in the Ladakh Himalaya. Tectonophysics 495:171–183

Tapponnier P, Peltzer G, Le Dain AY, Armijo R, Cobbold P (1982) Propagating extrusion tectonics in Asia: new insights from simple experiments with Plasticine. Geology 10:611–616

Tapponnier P, Peltzer G, Armijo R (1986) On the mechanics of the collision between India and Asia. In: Coward MP, Ries AC (eds) Collision tectonics. Special Publication Geological Society of London 19, pp 115–157

Thakur VC (1981) Regional framework and geodynamic evolution of the Indus-Tsangpo suture zone in the Ladakh Himalaya. Trans R Soc Edinb: Earth Sci 72:89–97

Thakur VC (1983) Palaeotectonic evolution of Indus-Tsangpo suture zone in Ladakh and southern Tibet. In: Thakur VC, Sharma KK (eds) Geology of Indus Suture zone of Ladakh. Wadia Institute of Himalayan Geology, Dehradun, pp 195–204

Thakur VC, Sharma KK (1983) Geology of Indus Suture Zone of Ladakh. Wadia Institute of Himalayan Geology, Dehradun, p 204

Thakur VC, Misra DK (1984) Tectonic framework of Indus and Shyok suture zones in eastern Ladakh, Northwest Himalaya. Tectonophysics 101:207–220

Upadhyay R (2002) Stratigraphy and tectonics of Ladakh, eastern Karakoram, western Tibet and western Kunlun. J Geol Soc India 59:447–467

Valli F, Arnaud N, Leloup H, Sobel ER, Maheo G, Lacassin R, Guillot S, Li H, Tapponnier P, Xu Z (2007) Twenty million years of continuous deformation along the Karakorum fault, western Tibet: a thermochronological analysis. Tectonics 26, TC4004. doi:10.1029/2005TC001913

Virdi NS, Thakur VC, Kumar S (1977) Blue schist facies metamorphism from the Indian suture zone of Ladakh and its significance. Himalayan Geol 7:479–482

Wang S, Fang X, Lai Q, Zheng D, Wang Y (2009) New radiometric dating constrains the time for initiation of the Karakorum fault zone (KFZ), SW Tibet. Tectonophysics 475:503–513. doi:10.1016/j.tecto.2009.06.016

Weinberg RF, Searle MP (1998) The Pangong injection complex, Indian Karakoram: a case of pervasive granite flow through hot viscous crust. J Geol Soc London 155:883–891

Zeilinger G, Seward D, Burg J-P (2007) Exhumation across the Indus Suture Zone: a record of back sliding of the hanging wall. Terra Nova 19:425–437. doi:10.1111/j.1365-3121.2007.00767.x

Chapter 15
The Model

Abstract Geochronological data from some of the important tectonic events of the Himalaya are summarized. A brief introduction of pre-Himalayan structures, including the basic rocks and four phases of acid magmatism, is given along with distribution of volcanic rocks in the Himalaya. Distribution of significant structural features, which form the basis for the proposed model are described. These include evidence of seismicity below the plane of basal detachment, inconsistency between surface and subsurface fold geometries, arcuate shape of the Himalaya as a primary structure, locking of the prominent Himalayan thrusts followed by formation of strike-slip faults, occurrence of younger rocks on the thrust hanging wall, and formation of superposed folds, which indicate maximum compression in E–W direction. The model is based on inversion tectonics and explains many of the previously unexplained features. Finally, the recent concept of tectonics versus climate is briefly discussed. It is concluded that the Himalayan structures are a result of gigantic tectonic forces that drive the plates and make the Indian plate to subduct beneath the Tibetan plate.

Geochronological data from the Himalaya are still limited and approximate but the available ages bring out the following picture.

Pre-Himalayan magmatic events during rift tectonics: Proterozoic to Upper Cretaceous.
Initial junction: ~55–57 Ma (Acton 1999; Klootwijk et al. 1992; Molnar and Tapponier 1975; Patriat and Achache 1984; Searle et al. 1987).
Cessation of marine sedimentation in the Tethys Himalaya: ~52 Ma (Rowley 1996).
Beginning of molasse sedimentation along the Tibetan part of the suture zone: Eocene (~55–34 Ma).
Initiation of deposition of the correlative Indus molasse along the Indus Suture: Eocene (~55–34 Ma) (Searle et al. 1987).

A. K. Dubey, *Understanding an Orogenic Belt*, Springer Geology,
DOI: 10.1007/978-3-319-05588-6_15,

Youngest calc-alkaline magmatism: ~40 Ma (Coulon et al. 1986; Debon et al. 1986).
Age of the MCT (reactivation age?): 25 Ma (Hodges et al. 1988; Macfarlane 1993).
Age of the MBT (reactivation age?): 11–10 Ma (Meigs et al. 1995).
Clear-cut evidence of the collision (≤35 Ma) (Aitchison et al. 2007).

In order to have a model for structural evolution of the Himalaya, the pre-Himalayan tectonics is of prime importance. Hence a short description of the tectonic activity, which took place in the region prior to onset of the compressional phase, is made here.

15.1 Pre-Himalayan Rift Tectonics

It is now known that formation of rift valleys and sedimentary basins involves rifting of lithosphere by a series of normal listric faults (e.g. Bott 1971; Lowell and Genik 1972; McKenzie 1978; Royden and Keen 1980). These faults are later reactivated as thrust faults at the initiation of compressional phase and mountain building starts after most of these early fault displacements reach to the null-point. All the normal faults, present in the region, may not reactivate as thrusts. Some of them can show partial reactivation and new thrusts also develop during an orogenic phase. Identification of the early rifting events is mainly done on the basis of geophysical, geochemical and large scale structural studies but minor structures can also indicate reactivation of early normal faults. Geophysical methods rely on prediction of subsurface structures where "fossilized" early normal faults are identified in the basement. However, geophysical surveys have not been carried out in most of the Himalayan region because the techniques are expensive and the region is not potentially viable for economic mineral deposits. The only exception is the foothill belt where few geophysical surveys and drillings have been done for finding out the possibility of natural oil and gas.

The geochemical evidence consists of studying detailed geochemistry of rocks from different tectonic environments of the present time, identifying the crucial parameters and applying the inferences to ancient rocks of unknown tectonic environments. Systematic and extensive geochemical investigations leading to a better understanding of the pre-collision history of the Himalayan region have been carried out by Bhat and his coworkers (Bhat 1982, 1984, 1987, 2001; Bhat et al. 1981, 1998; Bhat and Zainuddin 1982).

Reactivation of normal faults as thrusts during a later compressional regime is a common feature of several orogenies. Some of the restored sections also reveal the presence of early normal faults. One such example is shown in Fig. 15.1. The restored section clearly reveals that the Chelungpu–Sani thrust is a reactivated normal fault. The section has a similarity with the restored sections of the Himalayan Foreland Foothill belt in the fact that both the cover and part of the basement were involved in the later shortening.

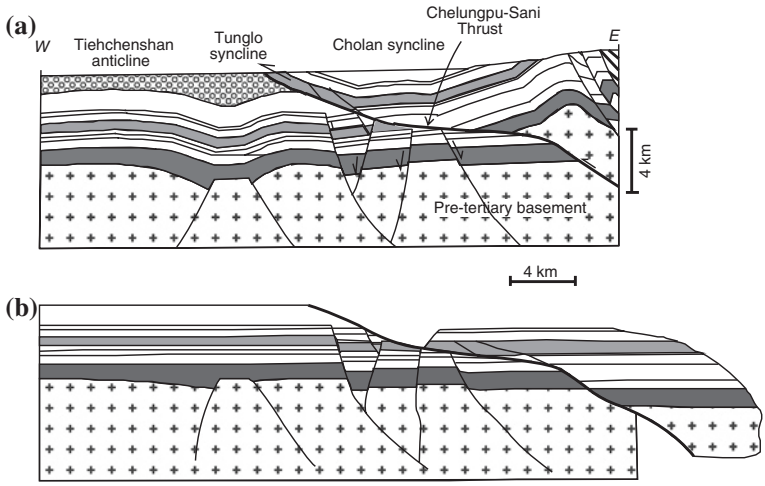

Fig. 15.1 Normal faults in a balanced section. **a** A deformed geological section across the Sani thrust in the Miaoli area, NW Taiwan. **b** Restored section showing earlier normal faults involving the basement [From Lacombe et al. (2003), © American Geophysical Union, Published with permission of American Geophysical Union]

15.2 Distribution of Basic Lava

The pre-collision history of the Himalayan region can best be studied by geochemistry of basic volcanic rocks, exposed in isolated patches, along the prominent Himalayan thrusts. These rocks unravel the mechanism and timing of the continental break-up during formation of the Tethys Ocean. Following the evolution of the plate tectonic concept and emerging data on spreading centers of the earth, it was envisaged that the Tethys Ocean was opened-up by rifting of the continental crust (Kamen-Kaye 1972; Burrette 1972). The concept was later applied in the Himalaya to suggest that the basic volcanic rocks in the Himalaya were erupted from the Tethyan spreading centers. Figure 15.2 shows locations of the major mafic–ultramafic and granitic-gneiss bodies in different regions of the Himalaya from the Late Precambrian to Cretaceous times (pre-collision magmatism) (Bhat 1987). In addition to these, there are numerous dikes, sills, small metadolerite and orthoamphibolite bodies in Central Crystallines of the High Himalaya and metasedimentary rocks of the Lower Himalaya. These rocks are regarded as Precambrian although age demarcation and succession of the rocks is not possible because of scanty fossils and lack of enough radiometric age data. However based on field relationships, the Sundernagar Formation of the Lower Himalaya is considered to be the oldest sedimentary rock (Srikantia 1977). Hence the metabasic volcanic flows associated with the formation may be regarded as the oldest magmatic phase. The second phase is represented by the Rampur, Srinagar–Rudraprayag (Garhwal Himalaya), and the Bhowali–Bhimtal (Kumaun Himalaya) volcanic rocks. Both these phases belong to the Middle and Late Proterozoic.

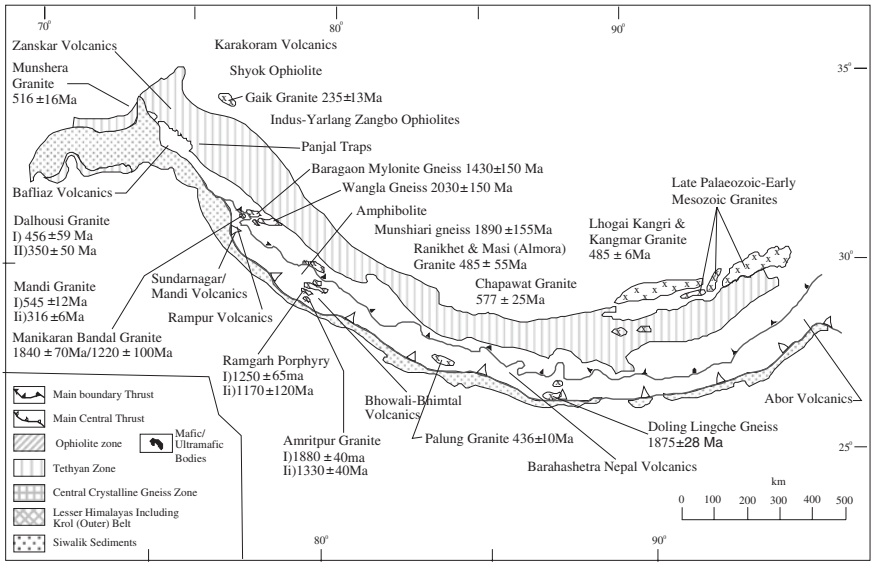

Fig. 15.2 Distribution of volcanic rocks in the Himalaya [From Bhat (1987), © Elsevier. Published with permission of Elsevier]

These are succeeded by the Bafliaz volcanic rocks (Kashmir Himalaya) of Ordovician age (Shah et al. 1978).

The Late Palaeozoic–Early Mesozoic volcanism (LP–EM) was on a large scale and wide spread from west to east. This includes Phe-Zanskar-Ralakung, and Panjal Traps, volcanic rocks associated with Lamayuru Formation (Jammu and Kashmir region), small potassium-rich volcanic breccia of west-central Nepal, volcanic rocks of Sikkim, and Abor volcanics of Arunachal Pradesh. The youngest phase is represented by mafic and ultramafic Cretaceous ophiolites of the Indus-Suture Zone. The different magmatic phases are characterized by some important systematic changes. The Proterozoic and Early Paleozoic magmatism was confined to northwest and west-central parts of the Himalaya. The LP–EM phase covers nearly the entire length of the Himalaya with intermittent breaks, and the last Cretaceous phase is exposed almost from the western to the eastern end of the region along the Indus Tsangpo Suture Zone (ITSZ). Apart from this longitudinal variation, a change can also be observed from south to north. The early magmatic phases are mostly confined to the Lower Himalayan region whereas the LP–EM phase is exposed in the Inner Lower Himalaya and the Tethyan zone. The Cretaceous phase is exposed exclusively to north of the Tethys Himalaya along the Indus-Suture Zone. The systematic variation suggests a gradual shift of the magmatic activity from the outer region to the suture zone (i.e. from south to north). The other important feature of the magmatic activity is that the earliest (Proterozoic) phases occur as relatively thin flows intercalated with sedimentary beds, the LP–EM phase is dominated by thick successive flows with minor

intercalations of sedimentary beds towards the waning phase of the eruption, and the Cretaceous phase is devoid of any intercalations. Hence volume of the volcanism shows a progressive increase from the oldest to the youngest phase. All these observations led Bhat (1987) to conclude that the initial diffused activity gradually became concentrated and intensified in inner parts of the Himalaya. The localization of the activity was interpreted in terms of stress regime changing from an initial diffused pattern to later concentration along a narrow belt. The faults are steep near the axial zone (ITSZ) and gradually acquire gentle dips away from the zone. The basaltic rocks occur in large isolated patches parallel to the trend of the Himalaya and this suggests that the tensional regime in this belt was oriented ~N–S throughout the tensional history of the region. The stress regime and the accompanying magmatism resulted in lithospheric uplift, stretching and development of anastomosing normal faults.

15.3 Acid Magmatism

Apart from the basic magmatic activities, four distinct phases of acid magmatism have been recognized in the Himalayan region (Thakur 1983). The first three phases, dated 2,000–1,800 Ma, 1,400–1,200 Ma, and ~500 Ma are quite voluminous and spatially wide spread in contrast to the fourth phase of Permian–Triassic age. Initially, there was a misconception that the earlier granitic magmatism was associated with pre-Himalayan orogenies namely, the Hercynian, Caledonian, and Pan-African. Angular unconformities were cited as evidence for the orogeny. However, the idea was later shelved because of the following reasons (Bhat 1987).

1. Angular unconformities are common in regions of normal listric faulting (Chap. 5).
2. The rift zones are associated with high volatile flux coming from deeper parts of the mantle thereby carrying the subsurface heat with them. The phenomenon results in; (i) increase in temperature of the region causing buoyancy in the lithospheric rocks with consequent epeirogenic uplift and erosion, producing unconformity and peripheral transgression, and (ii) predominantly CO_2 rich volatile flux, high temperature gradient and reduced lithospheric pressure facilitating sub crustal partial melting (Mason and Heaslip 1980; Bickle et al. 1985) even at relatively lower temperature, producing acidic magma intrusions and extrusions. Hence the generation of granitic magma is not the sole prerogative of compressional tectonics (i.e. orogeny).
3. There is no structural evidence for the presence of pre-Himalayan orogenies. The so called pre-Himalayan folds may be a result of gravitational tectonics (Fig. 5.22). Carey (1976) has explained these folds by syntepheral tectonics where the deformation is produced due to gliding of sediments from the continental shelf and slope regions. If these folds are subjected to metamorphism (Tobisch 1984) their identification as gravity folds would be difficult.

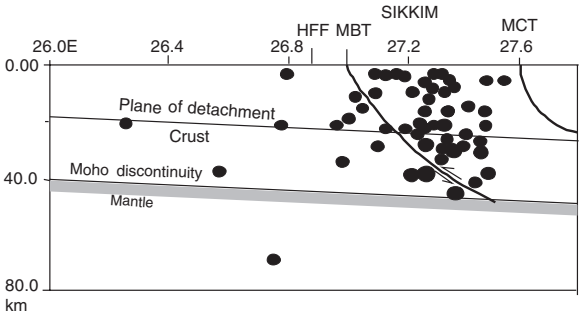

Fig. 15.3 Subsurface cross-section across the Sikkim Himalaya showing seismic activities below the plane of detachment (decollement) [From De and Kayal (2003), © Seismological Society of America. Published with permission of Seismological Society of America]

4. If the Tertiary Himalayan orogeny can generate superposed deformation with distinct geometry and orientations of the superimposed folds, associated foliations and lineations, why there is only very limited and sparsely reported pre-Himalayan deformation trend?

15.4 Significant Structural Features of the Himalaya

Inversion tectonics is common to many orogenic belts along with some of the structural features, e.g. arcuation in their trend, tectonic subdivisions from foreland foothill belt to inner core consisting of high grade metamorphic rocks, pre- and syn-orogenic metamorphism, fold- and thrust belts, early and superposed deformation, reactivation of faults, etc. However there are certain features, which are characteristic of an orogenic belt and these features help in formulating a model for its structural evolution. Some of the characteristic, enigmatic, and often misinterpreted features of the Himalaya are as follows.

Some of the Geological cross-sections of the Himalayan Foothill belt demonstrate folding and thrusting of the 'plane of decollement' (contact between pre-Tertiary and Tertiary rocks) along with the cover rocks. Upwarp structures (subthrust anticlines) are also present at the contact of thrust ramps with the basal décollement. Deformation of footwall rocks, very close to the thrusts is a rule rather than an exception. Moreover, many of the available seismic sections reveal a large number of activities below the projected plane of décollement (e.g. De and Kayal 2003; Sheehan et al. 2008; Nabelek et al. 2009; Caldwell et al. 2013) (Fig. 15.3). Hence the deformation is not confined to the cover rocks and the basement is still undergoing deformation as revealed by seismic activities. In view of this, the ideal thin-skinned model of thrust tectonics cannot be applied to the Himalaya.

It is interesting to note here that the earlier Deep Seismic Section (DSS) across the Himalaya revealed a number of vertical faults without any plane of basal décollement

(Kaila et al. 1978). However, acceptance of the thin-skinned tectonic model in some of the orogenic belts was followed by emergence of another seismic profile, which displays a prominent plane of basal decollement and various thrusts emanating from the plane (Allegré et al. 1984).

There appears to be some inconsistency between surface and subsurface fold geometries. The exposed large-scale fold structures are polyharmonic and show a rounded profile (e.g. Dubey and Bhat 1991; Thakur 1992; Devrani and Dubey 2008) except in areas of fault propagation folds (e.g. Mohand anticline: Raiverman 2002) but the subsurface folds are shown with typical kink band geometry without any second order folds (e.g. Powers et al. 1998). This has been done so that the cross-sections can be easily used for palinspastic reconstructions. Rheological properties of rocks that control the geometry of evolving folds, can change with increase in depth but an abrupt variation of fold geometries across the ground surface is difficult to justify.

The Himalayan fold belt presents an arcuate geometrical shape with the convex side facing towards south. Sufficient strain data are not available from different parts of the Himalayan arc but it is known that there is a general uniformity of structural pattern throughout the region reflecting a uniform pattern of distribution of strain. The observation can be viewed in the light of pattern of strain ellipses in different types of primary and secondary arcs (Fig. 15.4; Ries and Shackleton 1976). The points to be noted are;

1. the maximum forward motion is not from the centre of the arc (cf. Fig. 15.4a),
2. sinistral and dextral shear zones at the flanks are absent and the central part is also deformed in harmony with the rest of the area (cf. Fig. 14.5b), and
3. the outer arc is characterized by thrust faults and the inner arc by normal and strike-slip faults. Hence the tangential longitudinal fold model is not applicable to the Himalaya (cf. Fig. 15.4c).

Hence the primary arc model (Fig. 15.4d) appears to be the most appropriate.

Development of fold hinge lines in a primary arc pattern is shown in Figs. 15.5 and 15.6. Figure 15.5 shows initial stage of a model in which the basement block of modeling clay was cut by three faults with arcuate strikes. The top modeling clay block was homogeneous without any fault. A multilayer packet was sandwiched between the basement and the top blocks. The maximum compression was along the layering and the maximum extension was normal to the layering so that the basement faults can act as thrusts. The arcuate strike of the basement was reflected in geometry of the developing folds, which developed with arcuate hinge lines (Fig. 15.6). In case of secondary arcuation, the outer arc shows extensional structures whereas the inner arc shows compressional structures (Fig. 3.70).

A significant structural feature of the Himalaya is locking of the prominent thrusts at steep dip angles during late stages of deformation accompanied by change in the maximum extension direction from vertical to horizontal. This led to initiation of strike-slip faults cross-cutting the thrusts (Fig. 15.7) (Khattri and Tyagi 1983; Mattauer 1986). This also has significant implication for restoration of deformed sections because the extension direction became normal to the plane of the cross-section.

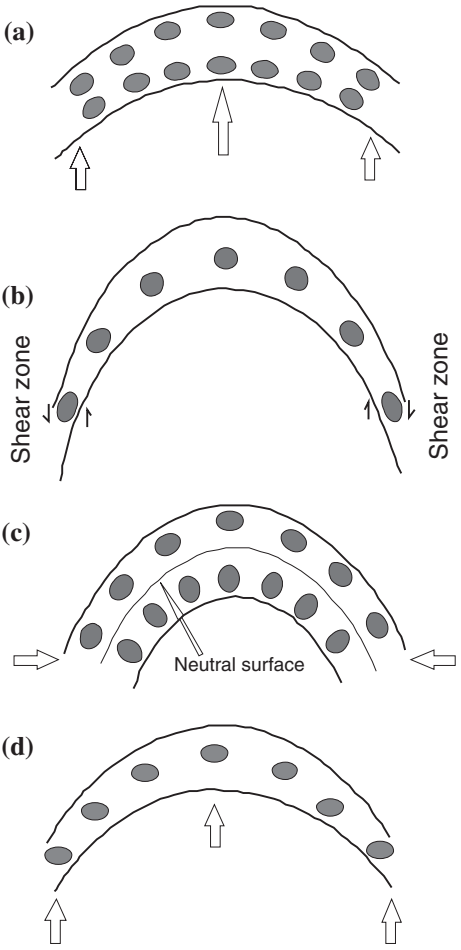

Fig. 15.4 Pattern of strain ellipses in different types of arcs. (**a**, **b**, **c**) secondary arcs, (**d**) Primary arc. **a** Maximum forward motion in centre of the arc. **b** Dextral and sinistral shear zones on flanks of the arc. **c** Flanks moving towards one another. **d** Uniform compression and strain patterns [From Ries and Shackleton (1976), © Royal Society of London. Published with permission of Royal Society of London]

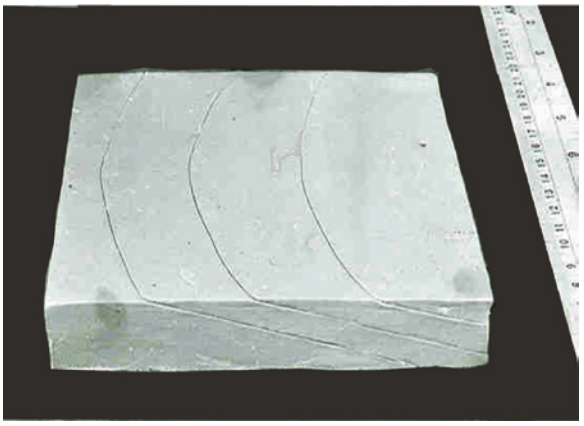

Fig. 15.5 Initial arcuate strikes of basement faults in a modeling clay model (after Dubey and Bhat 1986)

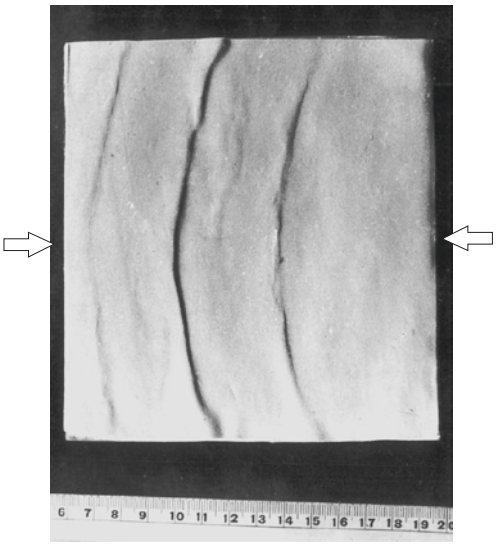

Fig. 15.6 Development of arcuate folds in a layer lying over the arcuate basement faults (7 % overall shortening). The *arrows* show the axis of maximum shortening (after Dubey and Bhat 1986)

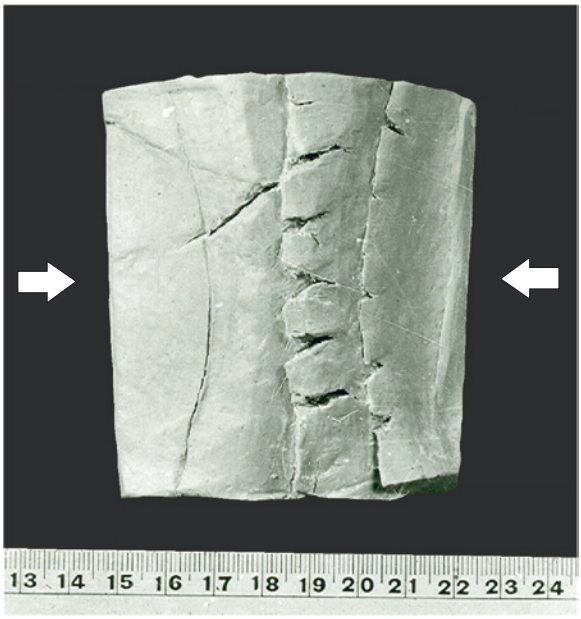

Fig. 15.7 Internal appearance of top of the basement after removing the multilayer sequence. Strike of the locked basement thrusts and later conjugate set of strike-slip faults are visible (after 47 % overall shortening). The *white arrows* show the axis of maximum shortening (after Dubey and Bhat 1986)

The Himalayan thrusts are characterized by listric geometry. After acquiring steep dips, they are locked near the surface but thrusting continues at greater depths where the dips are gentle. Normal faults also develop by gravity gliding and horizontal spreading. Hence all the three types of faults are active simultaneously in the region.

The occurrence of younger rocks at the hanging wall and older rocks at the footwall of the Vaikrita Thrust has been reported. The only available model to explain this feature is based on inversion tectonics.

15.5 A Model for Structural Evolution of the Himalaya

In view of the above facts, a model was proposed for structural evolution of the Himalaya (Fig. 15.8). The model is based on reactivation of pre-Himalayan normal listric faults as thrusts during the Tertiary compressional phase of the Himalayan orogeny (Dubey and Bhat 1986).

The first stage (Fig. 15.8a) depicts initiation of normal listric faults during the pre-Himalayan rift phase. Because of heterogeneous nature, the lithosphere yields in a number of irregular and anastomosing patterns of fractures including oblique ramps (not shown in the diagram). Increase in the tensional stresses led to increase in fault displacement, which was accompanied by tilting of the hanging wall blocks toward the fault surface, i.e. toward south (Fig. 15.8b). The tilt amount depended on the fault dip and displacement along the fault. The northernmost hanging wall block reached the deepest level as a result of cumulative displacements along the faults and consequently underwent relatively higher temperature–pressure gradients. After reaching a deeper level, the faults have acted as conduits for upward movement of magma. This can explain the occurrence of metabasic rocks along the MBT, MCT, and ITSZ.

The initial geometry of the basement faults was slightly arcuate because of presence of a large number of recess structures in the western Himalaya (Figs. 11.1 and 11.4). The arcuate geometry was later enhanced, by shear effects along the Ninetyeast Ridge and by fractures emanating from the Owen Fracture, Murray Ridge Zone. Hence the arcuation was prior to the Himalayan orogeny (Fig. 15.8c). At the outset of the Tertiary compressional phase, the normal faults reactivated as thrust faults. The initial response of the reactivation was to acquire the stage of null-point (Fig. 15.8d). However, it is to be noted that the null point cannot be reached simultaneously by all the faults because of variation in fault displacements along the faults. The fault displacement also varies along the strike of a single fault and the null-point cannot be reached all along the fault at one instant of deformation. Some of the faults (or fault segments) may not reach the null point because of early locking.

It is also evident from the diagram (Fig. 15.8d) that considerable amount of shortening has taken place prior to reaching the null point. This shortening cannot be taken into account while restoring a deformed cross-section as the method considers initial disposition of layers as horizontal. This shortcoming of the method adds to the facts that there is no consideration for possible viscosity contrast between different layers of the succession, initial layer parallel (homogeneous) shortening, amount of displacement along basin margin fault (MCT and MBT in the Himalaya), departure from plane-strain deformation as a result of displacement out of the tectonic transport plane, etc.

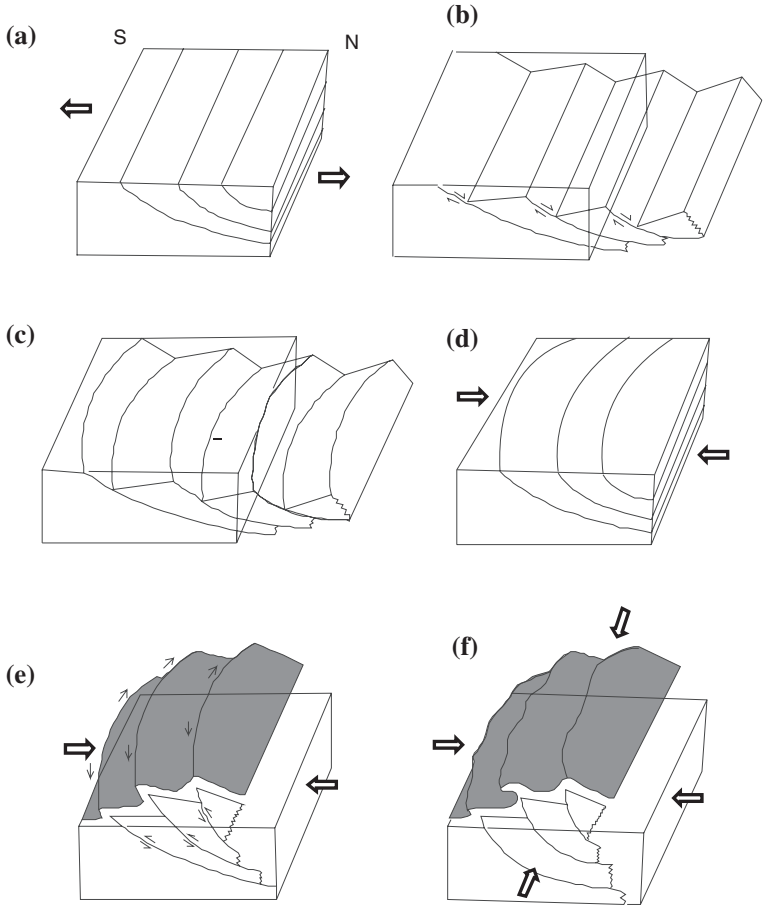

Fig. 15.8 A simplified model illustrating stages in structural evolution of theHimalaya by reactivation of listric faults. N and S represents north and southdirections, respectively. **a** Initiation of normal listric faults during the tensionalphase **b** Displacement along the faults **c** Arcuation in the trend of the faults **d** Initiation of compressional phase, reactivation of early normal faults as thrusts andstage of null points **e** Displacement along thrusts and formation of early folds in thecover rocks **f** Locking of the thrusts at steep dips and formation of superimposedfolds (details in text) (after Dubey and Bhat 1986)

Folding of the cover rocks was simultaneous with thrusting (Fig. 15.8e). Fault propagation folds initiated above the thrusts and buckle folds at some distance from the thrusts. The developing fold hinge lines followed the trend of underneath/adjacent thrust except in areas where oblique ramps were present and/or fold interference took place. Displacement along the arcuate basement faults led to arcuation of the cover folds. Thus the arcuate fold belt is a primary structure. The lower thrust sheets have carried the upper thrust sheets during thrusting and hanging wall tips, which were initially at lower altitudes during the normal faulting now occur at higher elevations. Hence, the highest region represents the highest metamorphic grade. The thrusting has also tilted

the hangingwall blocks toward the north thereby arranging the successively younger rocks with gradual decrease in metamorphism with increasing distance from the thrust (Metcalfe 1993). The syn-Himalayan metamorphism, which is controlled by mainly folding and thrusting, is a later phenomenon that could vary with the intensity of deformation. The overprinting of this Tertiary metamorphism over the pre-Himalayan metamorphism needs to be studied in detail.

At late stages of fold formation, the folds acquired rotation hardening at low interlimb angles and further decrease in interlimb angles was not possible. Initially, the developing folds showed maximum extension parallel to the axial surface and normal to hinge line but after the rotation hardening, the maximum extension direction changed its orientation and became parallel to the fold hinge lines (Chap. 3) (Fig. 15.8f). The fold amplification was concomitant with rotation of the faults. At steep dips the thrusts were also locked and the maximum extension took place parallel to its strike resulting in formation of strike-slip faults oblique to the early folds and thrusts. Restriction in the E–W extension because of boundary conditions imposed by transverse strike-slip and oblique faults resulted in formation of superposed folds and associated structures. Intensity of the superposed deformation may vary with position of local boundary faults. The early and superposed folds have developed during a single compressional regime hence the different geometries should not be attributed to different phases of deformation. There is only one phase of deformation that has resulted in different folding episodes.

Since the superposed folds are formed at a late stage after locking of the thrusts, their intensity and development are not controlled by thrusting and they are distributed throughout the region. The precise timing of their formation is not known and it is possible that thrusting along low dip faults and formation of early folds in one area was simultaneous with formation of superposed folds in an adjacent region characterized by steep (locked) thrusts. Similar variations may have taken place at depth because of listric fault geometry. At lower levels the fault dips are gentle or moderate hence the faults are likely to act as thrust. However because of steep dips near the surface, the thrust faults lock and strike-slip faults develop in a conjugate set oblique to the trend of the thrusts and early folds. At the same stage of deformation, normal faults may develop at higher elevations because of gravity gliding. Hence different phases of folding or different types of faults do not represent different phases of deformation.

The model can also explain the occurrence of allochthonous klippe and pop-up klippe in the Lower Himalaya. A gentle thrust dip and a lubricating horizon along the thrust surface (e.g. graphite schist along the klippe detachment thrust in the Simla klippe) promotes a large displacement thereby resulting in formation of an allochthonous klippe whereas displacement along a listric fault followed by initiation of back thrust(s) results in formation of a pop-up klippe. Listric geometry, poor lubrication along fault surface and deformation at comparatively upper levels of the earth's crust favour the development of pop-up klippe.

The listric faults in the model do not merge in a basal decollement because seismic activity has been observed beneath the predicted basal decollement and the subsurface sections of the Foothill belt reveal folding and thrusting of the decollement along with the cover rocks. For development of the Himalayan structures, horizontal compression in nearly N–S direction is needed and this can be attributed to northward movement of

the Indian plate. Locking of the thrusts and folds indicate that the "young mountain" has started showing signs of ageing. The deformation is now concentrated in the formation of superposed structures including the transverse deformation zones. Hence, initiation of more thrusts in the southern direction is not envisaged.

The Himalaya presents a good example of how the oceanic structures are continuing into the continental part. The eastern part is characterized by extension of the Ninetyeast Ridge and associated faults whereas the western part is characterized by fractures emanating from the Owen Fracture. The Indian plate is moving towards north between these two prominent faults producing a maximum compression direction in nearly N–S direction and strike-slip displacements on the two sides where the structures are more complex.

15.6 Tectonics and Climate

Recently, there has been a greater emphasis on understanding the relationship between tectonics and climate. The two are described as intimately associated and can influence each other. Beaumont et al. (1992) have suggested that when erosional forces removes mass from an active orogenic belt, gravitational stabilization is reduced and strain rates increase in such regions. The increased strain along with isostatic adjustment induces enhanced uplift which is a result of the erosion. The process supplements the tectonic strain in exhumation of rock from deep within an orogen. For example, uplift of the Himalaya in the Cenozoic times brought down the temperature of the rising mountain and the process led to onset of the Monsoon. Precipitation in the region led to enhanced erosion and increase in the uplift rate with deposition of sediments at the base of the mountain front. A greater accumulation of the sediments was followed by isostatic readjustments with uplift of the mountain and the cycle continues. Evidence for this hypothesis has come from the young mineral cooling ages obtained by apatite fission track (Thiede et al. 2004). The authors have suggested that the denudational loss of material is balanced by tectonic uplift and thus the surface processes control the internal deformation along the southern Himalayan Front. In a subsequent complimentary publication, Thiede et al. (2005) have suggested that the tectonic processes have played a dominant role until the middle Miocene but since the Pliocene erosion may have been the most important factor.

Molnar and England (1990) have evaluated the phenomenon of late Cenozoic uplift in the mountain ranges and came to a conclusion that the different criteria (e.g. geomorphology, sedimentation, palaoebotany), which are followed to infer recent uplift can be deceptive. Many of the reports of surface uplift in mountain ranges are based on wrongly considering the exhumation of rocks or uplift of rocks for surface uplift. A large-scale correlation between elevation and climate change requires uplift of the earth's surface relative to sea level, which is the change in mean elevation. This cannot be measured directly and must be inferred indirectly. The uplift of rocks relative to the local earth surface, measured by using geochronology and petrological

geobarometers and geothermometers is "exhumation". This is equal to the thickness of rock removed from the earth's surface. The uplift of rocks relative to sea level is the sum of the uplift of the earth's surface and exhumation.

In the Himalaya, recent uplift is based not on measures of uplift of the earth's surface but on estimate either of uplift of rocks or of exhumation. Molnar and England (1990) have also suggested that some of the phenomena used as indicators of uplift may have caused by climate change. For example, a change towards a cooler and stormier climate could be responsible for the geomorphological evidence ('youthful landscapes') but it may be wrongly used to infer recent uplift. Similarly, increased denudation and exhumation can lead to an increase in the rate of coarse terrigenous sedimentation, a phenomenon also attributed to uplift. Based on these they have suggested that global cooling during the late Cenozoic era has contributed to the change in mountain flora from warmth loving species to those characteristic of cooler environments. Hence it was agreed that the Himalaya and Tibet rose in Cenozoic time but the palaeoclimatic inferences of an accelerating rise throughout Cenozoic time are likely to be exaggerated, if not simply false. It leads us to conclude that changes in mean elevation, climate change, tectonic uplift, and phenomena commonly used to infer uplift are intimately related to one another. The resultant uplift is a sum of tectonic and climate factors. Their individual components may differ from region to region but it is certain that in the Himalaya, the tectonic factor is the dominant cause.

Another interesting concept was put forward by Simpson (2004) that river erosion can unload the crust and the process causes enhanced local deformation in vicinity of the rivers provided the river incision occurs simultaneously with deformation of the crust in response to regional compression. A mathematical model was cited as an example, where a river cuts through the axial culmination of a noncylindrical fold. However the following points are to be noted in this context.

1. Noncylindrical folds do not normally initiate on the surface. Even if a fold is developing at the surface, the prevalent brittle conditions are likely to produce a hinge fault.
2. The model does not hold good where the fold is developing as a fault propagation fold.
3. The intensity of the subsurface processes (e.g. magnitude of forces associated with plate motion) are nowhere comparable to the forces that may result from river erosion (England and Molnar 1990).

The knowledge regarding importance of precipitation and erosion in tectonic evolution of an active orogen is essentially based on assumption that abrupt spatial gradient in erosion can cause high strain rates. These models invoke a "stream power rule" considering increased discharge or steeper channel slopes as cause for higher erosion rates (Burbank et al. 2003). The hypothesis was tested in the Nepal Himalaya on the basis of meteorology, apatite fission-track dating, topographic analysis, equilibrium-line altitude, and stream power. The results indicated that a north dipping crustal-scale thrust ramp structure beneath the High Himalaya is responsible for the observed uplift (i.e. upward particle velocities with respect to geoid). The

study also suggested that uniform erosion is maintained across the High Himalaya but does not provide answer as to why hill slopes steepen or absence of uniform erosion elsewhere though the precipitation remains nearly the same.

A good comparison between tectonics versus climate related exhumation was provided by Patel and Carter (2009). The study document the cooling and exhumation history of two structurally identical sections of Kumaun High Himalaya in Dhauliganga and Goriganga river valleys. The two sections are separated by only 60 km and share the same climate. Despite this they have experienced different exhumation histories. Fission track (FT) data from the Dhauliganga section show systematic changes in age while passing from south (Munsiari thrust) to north (Vaikrita thrust). The individual apatite FT ages range from 0.9 ± 0.3 to 3.6 ± 0.5 Ma, $r^2 = 0.82$. The zircon FT ages ranging from 2.3 ± 0.3 to 5.0 ± 0.4 Ma, $r^2 = 0.98$ record faster exhumation but not differential slip across the zone extending between the two thrusts. On the contrary, FT results from the Goriganga valley show a stepwise change in ages across the Vaikrita thrust. Footwall samples yielded a weighted mean apatite age of 1.6 ± 0.1 Ma as against 0.7 ± 0.04 Ma in the hanging wall. A constant zircon fission track age of 1.8 ± 0.4 Ma across the hanging wall and footwall shows the 0.9 Ma difference in apatite ages as a consequence of movement along the Vaikrita thrust that initiates after ~1.8 Ma (slip rates ~ 2-3 mm a^{-1}). Hence there is a clear tectonic signal in the Goriganga valley.

The Himalayan exhumation has reached three peaks. The first one occurred at a rate of ~40 mm/yr during 55–45 Ma in the western Himalaya. The second one occurred during 12–8 Ma at a rate of 6–7 mm/yr in northern Himalayan gneiss domes and the third one at a rate of 3–5 mm/yr since 7 Ma in Nepal above the reactivated MCT zone (Yin 2006). Between these most active events, much of the Himalayan orogen has experienced slow exhumation and erosion, with rates between 0.1 and 1.0 mm/yr. The eastern Himalaya has experienced a greater exhumation as compared to the western Himalaya and it has also acquired a greater elevation as compared to the western Himalaya. The high exhumation rate regions are associated with prominent Himalayan structures suggesting that the mode of deformation rather than climate conditions has played a decisive role in localizing high rates of exhumation in the Himalaya (Yin 2006).

Finally, the climatic factors may be more active in the stable plate regions but in collision zones, gigantic tectonic forces that drive the plates to thousands of kilometers are much more effective.

References

Acton GD (1999) Apparent polar wander of India since the Cretaceous with implications for regional tectonics and true polar wander. In: T. Radhakrishna et al. (ed) The Indian Subcontinent and Gondwana: A Palaeomagnetic and rock magnetic perspective, vol 44. Memoir Geological Society of India, pp 129–175

Aitchison JC, Ali JC, Davis AM (2007) When and where did India and Asia collide? J Geophys Res 112(B05423):1–19

Allegre CJ, 34 Authors (1984) Structure and evolution of the Himalaya–Tibet orogenic belt. Nature 307:17–22

Beaumont C, Fullsack P, Hamilton J (1992) Erosional control of active compressional orogens. In: McClay KR (ed) Thrust tectonics. Chapman & Hall, London, pp 1–18

Bhat MI (1982) Thermal and tectonic evolution of the Kashmir basin vis-à-vis petroleum prospects. Tectonophysics 88:117–132

Bhat MI (1984) Abor volcanics: further evidence for the birth of the Tethys Ocean in the Himalayan segment. J Geol Soc Lond 141:763–775. doi:10.1144/gsjgs.141.4.0763

Bhat MI (1987) Spasmodic rift reactivation and its role in the pre-orogenic evolution of the Himalaya. Tectonophysics 134:103–127

Bhat MI (2001) Untenability of the neo-Tethys: Okeanos was not a polygamist. Himalayan Geol 22:5–15

Bhat MI, Zainuddin SM, Rais A (1981) Panjal trap chemistry and the birth of Tethys. Geol Mag 118:365–375

Bhat MI, Zainuddin SM (1982) Strontium depleted nature of the Panjal Traps in relation to lithospheric rift tectonics. Indian J Earth Sci 9:18–28

Bhat MI, Claesson S, Dubey AK, Pandey K (1998) Sm–Nd age of the Garhwal–Bhowali volcanics, western Himalaya: vestiges of the Late Archaean Rampur flood basalt province of the northern Indian Craton. Precambr Res 87:217–231

Bickle MJ, Wickham SM, Taylor HP Jr (1985) Strontium and oxygen isotope evidence for crustal melting and mantle input during the Hercynian metamorphism in the Pyrenees. Terra Cognita 5:118

Bott MHP (1971) Evolution of young continental margins and formation of shelf basins. Tectonophysics 11:319–327

Burbank DW, Blythe AE, Putkonen J, Pratt-Sltaula B, Gabet E, Oskin M, Barros A, Ojha TP (2003) Decoupling of erosion and precipitation in the Himalaya. Nature 426:652–655. doi:10.1038/nature02187

Burrette CF (1972) Plate tectonics and the Hercynian orogeny. Nature 239:155–157

Caldwell WB, Klemperer SL, Lawrence JF, Rai SS, Ashish (2013) Characterizing the main Himalayan Thrust in the Garhwal Himalaya, India with receiver function CCP stacking. Earth Planet Sci Lett 367:15–27. http://dx.doi.org/10.1016/j.epsl.2013.02.009

Carey SW (1976) Expanding Earth. Elsevier, New York 488 pp

Coulon C, Maluski H, Bollinger C, Wang S (1986) Mesozoic and Cenozoic volcanic rocks from central and southern Tibet: 39 Ar–40Ar dating, petrological characteristics and geodynamic significance. Earth Planet Sci Lett 79:281–302

De R, Kayal JR (2003) Seismotectonic model of the Sikkim Himalaya: constraint from microearthquake surveys. Bull Seismol Soc Am 93:1395–1400

Debon F, Le Fort P, Sheppard SMF, Sonnet J (1986) The four plutonic belts of the Transhimalaya-Himalaya: a chemical, mineralogical, isotopic, and chronological synthesis along a Tibet-Nepal section. J Petrol 27:219–250

Devrani U, Dubey AK (2008) Anisotropy of magnetic susceptibility and petrofabric studies in the Garhwal synform, Outer Lesser Himalaya: evidence of pop-up klippen. Island Arc 18:428–443. doi:10.1111/j.1440-1738.2008.00628.x

Dubey AK, Bhat MI (1986) The role of reactivation of pre-rift basement listric faults in the structural evolution of the Himalaya: an experimental study. Himalayan Thrusts and Associated Rocks. Curr Trends Geol 9:265–290

Dubey AK, Bhat MI (1991) Structural evolution of the Simla area, NW Himalaya: implications for crustal thickening. J SE Asian Earth Sci 6:41–53

England P, Molnar P (1990) Surface uplift, uplift of rocks, and exhumation of rocks. Geology 18:1173–1177. doi:10.1130/0091-7613

Hodges KV, LeFort P, Pecher A (1988) Possible thermal buffering by crustal anatexis in collisional orogens: thermobarometric evidence from the Nepalese Himalaya. Geology 16:707–710

Kaila KL, Krishna VG, Roy Chowdhury K, Narain H (1978) Structure of the Kashmir-Himalaya from deep seismic soundings. J Geol Soc India 19:1–20
Kamen-Kaye M (1972) Permian Tethys and Indian Ocean. Bull Am Assoc Petroleum Geol 56(107):1984–1999
Khattri KN, Tyagi AK (1983) The transverse tectonic features in the Himalaya. Tectonophysics 96:19–29
Klootwijk CT, Gee JS, Peirce JW, Smith JM, McFadden PL (1992) An early India-Asia contact; paleomagnetic constraints from ninetyeast Ridge, ODP Leg 121; with supplementary Data 92-15. Geology 20:395–398
Lacombe O, Mouther F, Angelier J (2003) Frontal ramp curvature and oblique ramp development at an obliquely colloided irregular margin: geometry and kinematics of the NW Taiwan fold-thrust belt. Tectonics 22(3):9-1, 9-16
Lowell JD, Genik GJ (1972) Sea-floor spreading and structural evolution of southern Red Sea. Bull AAPG 56:247–259
Macfarlane (1993) Chronology of tectonic events in the crystalline core of the Himalaya, Langtang National Park, central Nepal. Tectonics 12:1004–1025
Mason DR, Heaslip JE (1980) Tectonic setting and origin of intrusive rocks and related porphyry copper deposits in the Western Highland of Papa New Guinea. Tectonophysics 63:125–138
Mattauer M (1986) Intracontinental subduction, crust-mantle decollement and crustal-stacking wedge in the Himalaya and other collision belts. In: Coward MP, Ries AC (eds) Collision tectonics, vol 19. Special Publication Geological Society of London, pp 37–50
McKenzie DP (1978) Some remarks on the development of sedimentary basins. Earth Planet Sci Lett 40:25–32
Meigs AJ, Burbank DW, Beck RA (1995) Middle-late Miocene (>10 Ma) formation of the Main Boundary Thrust in the western Himalaya. Geology 23:423–426
Metcalfe RP (1993) Pressure, temperature and time constraints on metamorphism across the Main Central Thrust zone and High Himalayan slab in the Garhwal Himalaya. In: Treloar PJ, Searle MP (eds) Himalayan tectonics, vol 74. Special Publication Geological Society of London, pp 485–509
Molnar P, England P (1990) Late Cenozoic uplift of mountain ranges and global climate change: chicken or egg? Nature 346:29–34
Molnar P, Tapponnier P (1975) Cenozoic tectonics of Asia: effects of a continental collision. Science 189:419–426
Nabelek J, Hetenyi G, Vergne J, Sapkota S, Kafle B, Jiang M, Su H, Chen J, Huang B, the Hi-CLIMB Team (2009) Underplating in the Himalaya-Tibet collision zone revealed by the Hi-CLIMB experiment. Science 325:1371–1374
Patel RC, Carter A (2009) Exhumation history of the Higher Himalayan Crystalline along Dhauliganga-Goriganga river valleys, NW India: new constraints from fission track analysis. Tectonics 28:TC3004. doi:10.1029/2008TC002373
Patriat P, Achache J (1984) India–Eurasia collision chronology has implications for crustal shortening and driving mechanism of plates. Nature 311:615–621
Powers PM, Lillie RJ, Yeats RS (1998) Structure and shortening of the Kangra and Dehra Dun re-entrants sub-Himalaya, India. Geol Soc Am Bull 110:1010–1027
Raiverman V (2002) Foreland sedimentation in Himalayan tectonic regime: a relook at the orogenic process. Bishen Singh Mahendra Pal Singh, Dehra Dun 378 pp
Ries AC, Shackleton RM (1976) Patterns of strain variation in arcuate fold belts. Philos Trans R Soc Lond A283:281–288
Rowley DB (1996) Age of initiation of collision between India and Asia: a review of stratigraphic data. Earth Planet Sci Lett 145:1–13
Royden L, Keen CE (1980) Rifting process and thermal evolution of the continental margin of eastern Canada determined from subsidence curves. Earth Planet Sci Lett 51:343–361
Searle MP, Windley BF, Coward MP, Cooper DJW, Rex AJ, Rex D, Tingdong L, Xuchang X, Jan MQ, Thakur VC, Kumar S (1987) The closing of Tethys and the tectonics of the Himalaya. Bull Geol Soc Am 98:678–701

Shah SK, Sharma TR, Gupta KR (1978) Trilobite trace fossils from the Bafliaz Formation, western Pir Panjal and their significance. J Geol Soc India 19:273–276

Sheehan AF, de la Torre T, Monsalve G, Schulte-Pelkum V, Bilham R, Blume F, Bendrick R, Wu F, Pandey MR, Sapkota S, Rajaure S (2008) Earthquakes and crustal structure of the Himalaya from the Himalayan Nepal Tibet seismic experiment (HIMNT). J Nepal Geol Soc 38:1–8

Simpson G (2004) Role of river incision in enhancing deformation. Geology 32:341–344

Srikantia SV (1977) The Sundernagar Group: its geology, correlation and significance as stratigraphically the deepest sediment in the Peninsular or Lesser Himalaya. J Geol Soc India 18:7–22

Thakur VC (1983) Palaeotectonic evolution of Indus-Tsangpo suture zone in Ladakh and southern Tibet. In: Thakur VC, Sharma KK (eds) Geology of Indus suture zone of Ladakh. Wadia Institute of Himalayan Geology, Dehradun, pp 195–204

Thakur VC (1992) Geology of Western Himalaya. Pergamon, 363 pp

Thiede RC, Bookhagen B, Arrowsmith JR, Sobel ER, Strecker MR (2004) Climatic control on rapid exhumation along the southern Himalayan Front. Earth Planet Sci Lett 222:791–806. doi:10.1016/j.epsl.2004.03.015

Thiede RC, Arrowsmith JR, Bookhagen B, McWilliams MO, Sobel ER, Strecker MR (2005) From tectonically to erosionally controlled development of the Himalayan orogen. Geology 33:689–692. doi:10.1130/G21483.1

Tobisch OT (1984) Development of foliation and fold interference patterns produced by sedimentary processes. Geology 441–444

Yin A (2006) Cenozoic tectonic evolution of the Himalayan orogen as constrained by along-strike variation of structural geometry, exhumation history and foreland sedimentation. Earth Sci Rev 76:1–131. doi:10.1016/j.earscirev.2005.05.004

Errata to: Understanding an Orogenic Belt

Ashok Kumar Dubey

Errata to:
A. K. Dubey, *Understanding an Orogenic Belt*, Springer Geology, DOI 10.1007/978-3-319-05588-6

1. In Chap. 5, on page 143: The word "Abstract" is missing. The blank line between Abstract and beginning of chapter text is missing. The first 4 lines of the chapter text are missing and need to be inserted as below:

   In brittle or brittle-ductile regimes, when maximum compression acts in vertical direction and minimum compression in a horizontal direction, normal faults are formed. Initially, these are steeply inclined faults in which hanging wall moves down relative to footwall (Fig. 5.1). Strike of the fault remains parallel to intermediate axis of compression (i.e. normal to the cross-section shown in Fig. 5.1).

2. In Chap. 5, on page 162, the citation of Fig. 2.14b has been changed to Fig. 5.23b.
3. In Chap. 6, on page 183, the third line of the text must read: "The above criteria …" instead of "The following criteria …".

The online version of the original book can be found under DOI 10.1007/978-3-319-05588-6

A. K. Dubey (✉)
Wadia Institute of Himalaya
Dehradun
India
email: akdubey123@gmail.com

DOI: 10.1007/978-3-319-05588-6_16,

Index

A. K. Dubey, *Understanding an Orogenic Belt*, Springer Geology,
DOI: 10.1007/978-3-319-05588-6, © Springer International Publishing Switzerland 2014